PONTIFICA UNIVERSIDAD CATÓLICA DEL PERÚ

ESCUELA DE POSGRADO

STRATEGIC MINERALS EXPLORATION IN THE CENTRAL ANDES:
SUSTAINABLE SOURCES OF RAW MATERIALS FOR GREEN TECHNOLOGIES

EXPLORACIÓN DE MINERALES ESTRATÉGICOS EN LOS ANDES CENTRALES:
ABASTECIMIENTO DE MATERIAS PRIMAS PARA LA PRODUCCIÓN DE TECNOLOGÍAS VERDES

Tesis para obtener el grado de Doctor en Ingeniería

Autor:
Diego Benites Negrón

Asesor:
Lisard Torró I Abat

Miembros del Jurado:

Blanca Silvia Rosas Lizárraga – Pontificia Universidad Católica del Perú
Lisard Torró i Abat – Pontificia Universidad Católica del Perú
Joaquín Antonio Proenza Fernández – Universidad de Barcelona
Lluís Fontboté – Universidad de Ginebra
José María González-Jiménez – Universidad de Granada

Noviembre, 2021 - Lima, Perú

AGRADECIMIENTOS

Al mirar en retrospectiva mientras escribo estas líneas, me doy cuenta de que el camino recorrido ha sido largo y a veces duro. Sin embargo, son muchas las personas que me han acompañado en este trayecto, brindándome su apoyo tanto académico y profesional como personal. Es así, que me gustaría dejar constancia de mi agradecimiento a todas aquellas personas e instituciones que, de distintas formas, han contribuido en el desarrollo de este trabajo.

Quisiera, en primer lugar, agradecer a la Pontificia Universidad Católica del Perú por la oportunidad de realizar esta tesis de Doctorado en Ingeniería y por otorgarme la beca Huiracocha. Asimismo, agradezco al CONCYTEC-FONDECYT-Banco Mundial 107-2018-FONDECYT-BM-IADT-AV, coordinado a través de PROCIENCIA, por haber financiado económicamente el proyecto de investigación conducente a mi tesis doctoral.

A la Sección Ingeniería de Minas por ofrecerme el ambiente adecuado y por haber puesto a disposición los recursos necesarios para desarrollar mi doctorado. Agradezco, asimismo, a las empresas Panamerican Silver Corp., Tinka Resources Ltd., Minera Colquisiri, Perliya-CORMIDOM, SIMSA-Unidad Minera San Vicente, y Minera Nexa Resources, por el apoyo logístico y de campo, y por haberme proporcionado las muestras para el desarrollo de la tesis. A Marc Polliand por brindarme, de manera desinteresada, las muestras de su tesis doctoral en la Universidad de Ginebra.

Deseo expresar mi profundo agradecimiento al doctor Lisard Torró, mi asesor y director de esta tesis doctoral, por haberme introducido en el mundo de la investigación y de los yacimientos, por sus conocimientos compartidos, por confiar en mis capacidades y por haberme animado a ir siempre un poco más adelante. Gracias por su paciencia e invaluable ayuda.

Es importante para mí agradecer de manera muy especial al Dr. Lluís Fontboté, profesor de la Universidad de Ginebra, por sus valiosos aportes y recomendaciones durante la elaboración de los artículos que forman parte de esta tesis doctoral.

A la especialidad de Ingeniería Geológica y a todas las personas que forman parte de ella, en especial a la doctora Silvia Rosas, Directora de la Carrera, por sus consejos e interés en mi trabajo; a los profesores Jorge Sáez y Jean Vallance, por su gran ayuda en las interpretaciones petrográficas y por su amable disposición a colaborar en todo momento. Asimismo, quiero agradecer a Xavier Llovet de la Universidad de Barcelona en el proceso de adquisición de datos por microsonda electrónica (EPMA), y a Peter Tollan de la ETHZ por la adquisición de datos por ablación láser (LA-ICP-MS). Un especial agradecimiento a Andrea, Brayam, Johan, Johann, Pablo y Patrick por tantas horas de apoyo durante estos tres años

Al laboratorio de Caracterización mineralógica BIZALAB.SAC, por haberme formado en el campo de la microscopía de minerales desde mi inicio profesional. Quiero agradecer especialmente a la CEO Erika Gabriel por el apoyo incondicional para el uso de las instalaciones cuando lo he requerido.

También quiero agradecer a todos los co-autores por las revisiones de los textos elaborados: Jean Vallance, Silvia Rosas, Oscar Laurent, Pablo Valverde, Kalin Kouzmanov, Cyril Chelle-Michou, Brayam Ortiz, Joaquín Proenza, Patrick Quispe, María Francisca Uzieda, Christopher Holm-Denoma, Laura Pianowski, Antoni Camprubí, Andrea Millán, Álvaro Fernández-Baca, Luis Giraldo y Lluís Fontboté. Un agradecimiento especial a todos los revisores de los artículos publicados: Richard Sillitoe, Andreas Dietrich, Graham Carman, Bernd Lehmann, Fredrik Sahlström, Max Frenzel y Franco Pirajno por sus comentarios constructivos.

Es imposible olvidarme del apoyo recibido por parte de mis queridos y entrañables amigos Rubén, Natalia, Víctor, Sandra, Carlos, Janeth y Alejandro, por animarme a realizar este doctorado, por sus palabras de aliento, por recordarme que avanzaba sobre la senda correcta y por disipar mis dudas.

Finalmente, quiero dar las gracias a las personas que constituyen el pilar fundamental de mi vida: mi familia. A mi madre Rosana, a mi hermano David y a mis muy queridos tíos, Gabriela, Jenny y Óscar, y a mi sobrina Abigail; por estar siempre ahí para apoyarme en todo lo que hago y por haberme ofrecido siempre la posibilidad de elegir. Sin su sacrifico y esfuerzo nunca hubiera podido llegar hasta aquí.

ABSTRACT

Securing a sustainable supply of critical raw materials such as In, Ge, and Ga has become a global concern in recent years. These elements are essential for the manufacture of modern digital and green technologies. The central-Andean metallogenetic belts in Peru bear potential for strategic metal/metalloid resources in some of the great variety of magmatic-hydrothermal and other hydrothermal mineral deposits they host. This doctoral thesis aims to provide a detailed survey on the ore mineralogy and mineral geochemistry at different metalliferous districts in the Central Andes of Peru, including constraints on the temporal and spatial distributions of trace elements with particular focus on In, Ge, and Ga. This contribution also expects a better understanding regarding the geochemical behavior of In, Ge, and Ga during magmatic-hydrothermal and other hydrothermal processes, as well as the metallogenetic preference of each of these elements, contributing to the development of exploration guidelines.

In general, the highest In, Ge, and Ga contents are found in sphalerite. Amongst analyzed samples, sphalerite is particularly rich in In in low-sulfidation assemblages in Cordilleran mineralization (up to 1.7 wt.% in Ayawilca); however, in the Morococha district, the highest In values are found in sphalerite from high-sulfidation assemblages (up to 1456 ppm), followed by sphalerite from low-sulfidation assemblages (up to 459 ppm in the Manto Italia body), whereas in intermediate-sulfidation assemblages its content is highly variable. The highest Ga contents are recorded in sphalerite from epithermal veins overprinting the Toromocho porphyry (up to 1739 ppm). Sphalerite from MVT deposits is remarkably Ge-rich, with values up to 1861 ppm in the San Vicente deposit. Chalcopyrite (up to 1185 ppm In in the Ayawilca deposit) and stannite (up to 1908 ppm in the Ayawilca deposit) can also host significant In contents. Tetrahedrite-tennantite samples from intermediate-sulfidation assemblages in the Morococha district occasionally host significant Ge contents (up to 266 ppm); however, values are in general low. In analyzed galena In, Ge, and Ga contents are mostly at the sub-ppm level. In sphalerite, In, Ge, and Ga are incorporated into the crystal lattice via coupled substitutions. Substitution schemes for the incorporation of In, Ge, and Ga in the other analyzed ore minerals remain unclear.

Some spatial and temporal trends in In, Ge, and Ga contents, mostly in sphalerite, have been observed. In intermediate-sulfidation assemblages from the Morococha district, sphalerite shows continuous In and Cu depletion from proximal-to-porphyry Cu metalliferous zone to distal-to-porphyry Ag-Pb metalliferous zone, and within single sampled orebodies, sphalerite records In depletion and Ge enrichment from early to late generations. These observations have led to the conclusion that in porphyry-related polymetallic mineralization, the distribution of In in sphalerite is controlled by i) sourcing of In via metal-rich magmatic-hydrothermal fluids; ii) a relatively high availability of Cu in the mineral system; iii) a relatively high temperature of the mineralizing fluid (> 250ºC) or low pH favoring the stability Cl complexes, and iv) availability of Cl to form In (and Cu) chloride complexes. Chalcopyrite from intermediate-sulfidation assemblages in the Morococha district shows a trend toward Se and Hg depletion and Sn and Ag enrichment from proximal to distal orebodies. As for VMS deposits, in the Sofía-D zone-refined massive sulfide body in the María Teresa deposit, there is a progressive enrichment in In, Cu, Mn, and Se and a depletion in Ge in sphalerite towards the chalcopyrite-rich basal domain. Finally, in the San Vicente and Shallipayco MVT deposits, Ge-richest sphalerite, which shows bright orange and yellow colors, crystalized relatively late in the respective paragenetic sequences.

RESUMEN

Asegurar un suministro sostenible de materias primas críticas como el indio, el germanio y el galio se ha convertido en un interés global en los últimos años. Estos elementos son esenciales para la fabricación de tecnologías digitales modernas y limpias. Los cinturones metalogenéticos del área centro-Andina del Perú tienen un gran potencial para albergar importantes recursos de metales/metaloides estratégicos debido a la gran variedad de depósitos magmático-hidrotermales y otros depósitos hidrotermales que alojan. Esta tesis doctoral tiene por finalidad proporcionar un estudio detallado sobre la mineralogía y la geoquímica mineral de menas en diferentes distritos metalíferos en los Andes Centrales del Perú, incluyendo la definición de la distribución temporal y espacial de elementos traza con un enfoque particular en In, Ge y Ga. El presente aporte también espera una mejor comprensión respecto al comportamiento geoquímico del In, Ge y Ga durante los procesos magmático-hidrotermales y otros procesos hidrotermales, así como la preferencia metalogenética de cada uno de estos elementos, permitiendo el desarrollo de posibles guías de exploración.

En general, los contenidos más altos de In, Ge y Ga se encuentran en la esfalerita. De las muestras analizadas, la esfalerita es particularmente rica en In en ensambles de baja sulfuración en mineralización Cordillerana (hasta 1,7% wt.% en Ayawilca). Sin embargo, en el distrito de Morococha, los valores más altos de In se encuentran en la esfalerita de ensambles de alta sulfuración (hasta 1456 ppm), seguida de la esfalerita de ensambles de baja sulfuración (hasta 459 ppm en el cuerpo de Manto Italia), mientras que en ensambles de sulfuración intermedia su contenido es muy variable. Los mayores contenidos de Ga se registran en esfalerita de vetas epitermales que sobreimprimen el pórfido de Toromocho (hasta 1739 ppm). La esfalerita de depósitos MVT es notablemente rica en Ge, con valores de hasta 1861 ppm en el depósito San Vicente y de hasta 1119 ppm en el depósito Shallipayco. La calcopirita (hasta 1185 ppm de In en el depósito de Ayawilca) y la estannita (hasta 1908 ppm en el depósito de Ayawilca) también pueden albergar contenidos importantes de In. La tetraedrita y tennantita provenientes de ensambles de sulfuración intermedia en el distrito de Morococha alberga ocasionalmente contenidos significativos de Ge (hasta 266 ppm); sin embargo, los valores son en general bajos. En la galena analizada, los contenidos de In, Ge y Ga son principalmente a nivel de sub-ppm. En la esfalerita, el In, Ge y Ga se incorporan a la red cristalina mediante sustituciones acoplada. Los esquemas de sustitución para la incorporación de In, Ge y Ga en los otros minerales analizados siguen sin poder ser definidos de forma clara.

Se han observado algunas tendencias espaciales y temporales en los contenidos de In, Ge y Ga, principalmente en esfalerita. En ensambles de sulfuración intermedia del distrito de Morococha, la esfalerita muestra un empobrecimiento continuo en In y Cu desde la zona metalífera de Cu, proximal al pórfido, hasta la zona metalífera de Ag-Pb, distal al pórfido. Dentro de algunos cuerpos minerales en particular, la esfalerita también registra un empobrecimiento en In y Cu y enriquecimiento en Ge desde generaciones tempranas a tardías. Estas observaciones han permitido concluir que en mineralizaciones polimetálicas en sistemas de pórfido Cu(-Mo), la distribución de In en la esfalerita está controlada por i) el suministro de In a través de fluidos magmático-hidrotermales ricos en metales; ii) una disponibilidad relativamente alta de Cu en el sistema mineral; iii) una temperatura relativamente alta del fluido mineralizante (> 250ºC) o pH bajo favoreciendo la estabilidad de los complejos de Cl, y iv) disponibilidad de Cl para formar complejos clorurados de In y Cu. La calcopirita de ensambles de sulfuración intermedia en el distrito de Morococha muestra un empobrecimiento de Se y Hg y un enriquecimiento de Sn y Ag desde cuerpos minerales proximales a distales en relación al pórfido. En cuanto a los depósitos VMS, en el cuerpo de sulfuro masivo en la zona-refinada de Sofía-D del depósito María Teresa, se produce un enriquecimiento progresivo en In, Cu, Mn, Se y un empobrecimiento en Ge en la esfalerita hacia el dominio basal, rico en calcopirita. Finalmente, en los depósitos MVT de San Vicente y Shallipayco, la esfalerita más rica en Ge, que se caracteriza por colores de cristal naranja y amarillo, cristalizó relativamente tarde en las respectivas secuencias paragenéticas.

TABLE OF CONTENTS

OVERVIEW OF THE THESIS

The thesis is organized in five parts or chapters. Part I is an introduction on critical raw materials and Parts II, III, IV y V provide detailed study cases for selected ore deposits in Peru and are presented as journal articles

Part I (**"Introduction to critical raw materials"**)
This part provides information on how the term "critical raw materials" is approached in different countries, regions and international organizations and the importance of these materials in the production of modern digital and green technologies. Likewise, geochemical, mineralogical, and use information is given for the metals/metalloids indium, germanium, and gallium, central study elements in this thesis. Finally, some data on mining production in Peru and its impact on its economy are provided.

Part II ("Geology, mineralogy, and cassiterite geochronology of the Ayawilca Zn-Pb-Ag-In-Sn-Cu deposit, Pasco, Peru")
This part corresponds to the first scientific article on the geology and mineralogy of the Ayawilca deposit, in Central Peru, that is one of the largest undeveloped base-metal and indium resource in the Andes. Cassiterite U-Pb dating was performed, allowing to place the deposit in the Oligocene-Miocene polymetallic belt in central and northern Peru. The exhaustive petrographic study points to strong similarities with the Cerro de Pasco Cordilleran polymetallic deposit. The occurrence of a tin economic mineralization at Ayawilca, ~ 1,000 km to the north of the northern end of the Central Andean tin belt is discussed from a metallogenetic point of view. Minor and trace elements contents in sphalerite, chalcopyrite, galena, tetrahedrite-tennantite, and cassiterite, their contextualization along the produced paragenetic sequences, and substitution mechanisms with particular interest in In, Ge, and Ga are provided.

Part III (" Distribution of indium, germanium, gallium and other minor and trace elements in polymetallic ores from a porphyry system: The Morococha district, Peru")
This part presents detailed petrographic information from different styles of polymetallic mineralization in the Morococha mining district, including skarn and skarn-free (Cordilleran) low-, intermediate-, and high-sulfidation assemblages. Minor and trace element contents are analyzed in sphalerite, chalcopyrite, galena, and tetrahedrite-tennantite from orebodies and veins distributed at different distances from causative porphyritic intrusives, mainly along metalliferous zones belonging to the "Morococha district-scale polymetallic event" (Catchpole et al. 2015) around the giant Toromocho porphyry Cu-Mo stock. Furthermore, substitution mechanisms with emphasis on In, Ge, and Ga in the sphalerite structure are proposed. The geothermometer of Frenzel et al. (2016), which uses trace element contents in sphalerite, was applied to compare crystallization temperatures with available microthermometry data in the district. Finally, principal component analysis diagrams were

carried out to evaluate/overview minor and trace element distributions in analyzed ore minerals throughout the polymetallic mineralization. Main parameters controlling the distribution of In in sphalerite from porphyry Cu(-Mo)-related polymetallic mineralization are suggested.

Part IV ("Trace element geochemistry of sphalerite and chalcopyrite in arc-hosted VMS deposits")

This part provides detailed information on trace element contents in sphalerite and chalcopyrite from the four arc-hosted Cretaceous VMS deposits Maria Teresa, Perubar, and Palma in Peru, and Cerro de Maimón in the Dominican Republic. New data are compared with previous studies on trace element contents in sphalerite and chalcopyrite from other VMS and active seafloor massive sulfides (SMS) worldwide to assess distinctive geochemical signatures in massive sulfide mineralizations formed in this particular tectonic environment. Substitution mechanisms with emphasis on the incorporation of In and Ga into the sphalerite crystal lattice are presented. In addition, detailed petrography and ore mineral geochemistry on a zone-refined massive sulfide body has allowed to describe trace element distribution trends in sphalerite and chalcopyrite that may help determine the polarity of massive sulfide bodies in strongly tectonized VMS districts.

Part V ("Trace element composition of sphalerite from the San Vicente and Shalipayco Mississippi Valley-Type deposits, Peru")

This part provides textural and compositional information on minor and trace elements, with particular emphasis on Ge, in sphalerite from the San Vicente and Shalipayco MVT deposits in Peru. Trace element contents are correlated with different sphalerite types, with contrasting crystal colors, deposited at different stages along the respective mineralization sequences. Substitution mechanisms for the incorporation of Ge into the sphalerite structure are suggested. Finally, it is intended to establish a possible correlation between trace element contents and crystal colors that may serve as a guide to target Ge-rich sphalerite in MVT deposits.

OBJECTIVES

Main objective:

To determine the mineralogy, contents, and parameters that control the local and regional concentration of the critical elements In, Ge, and Ga in ore assemblages from different mineralization styles in the Central Andes of Peru.

Specific objectives:

To representatively sample different types of mineralization at the deposit and mining district scales in order to correlate trace element contents with particular mineralization styles along different metalliferous zones.

To contextualize the contents of In, Ge, and Ga in detailed paragenetic sequences produced for each deposit in order to understand the preferential distribution of these elements during the mineralization lifespan.
To assess the mechanisms that rule the incorporation of In, Ge, and Ga in ore minerals.

To determine favorable physicochemical conditions enhancing transportation and deposition of In, Ge, and Ga during magmatic-hydrothermal and hydrothermal mineralization.

To contextualize potential In, Ge, and Ga enrichment along the metallogenetic evolution of the Andean polymetallic belts in Peru.

SUMMARY OF THE OVERALL RESULTS

The main results derived from the study of polymetallic ore from the porphyry Cu-Mo system in the Morococha district include:

1. Amongst analyzed ore minerals, sphalerite displays the highest In and Ga contents, particularly in high-sulfidation epithermal veins overprinting the Toromocho porphyry (interquartile range [IQR] = 1291 – 726 ppm, up to 1456 ppm In; IQR = 1269 – 706 ppm, up to 1739 ppm Ga). Germanium contents in sphalerite are systematically low (IQR = 0.89 – 0.18 ppm) with significant values only in late, Fe-poor colloform sphalerite from an intermediate sulfidation assemblage in the Ivette Manto orebody (IQR = 129 – 74 ppm). Sphalerite is volumetrically the most abundant mineral component in polymetallic ore at Morococha and therefore represents the main host for In and Ga. Chalcopyrite also displays relatively high In and Ga contents, mainly in intermediate-sulfidation assemblages at the Morro Solar vein (IQR = 941 – 891 ppm, up to 1070 ppm In; IQR = 295 – 160 ppm, up to 630 ppm Ga). Germanium contents in chalcopyrite are generally low (< 20 ppm). In coeval generations of sphalerite and chalcopyrite, the average In content is at least two times higher in the former than in latter. Tetrahedrite-tennantite only displays significant In contents in the Morro Solar vein (IQR = 257-239 ppm, up to 266 ppm) whereas Ge and Ga contents are systematically low (< 10 ppm). Contents of In, Ge, and Ga in galena are also systematically low (< 5 ppm).

2. The highest In contents in sphalerite are found in Stage C (following the nomenclature defined by Rottier et al., 2016, 2018 and Fontboté, 2020), high-sulfidation epithermal veins overprinting causative Toromocho porphyry stock followed by Stage A, low-sulfidation assemblages in the Porvenir (IQR = 209 – 171 , up to 217 ppm) and Manto Italia (IQR = 323 – 39, up to 459 ppm) orebodies. In Stage C intermediate-sulfidation assemblages, In values decrease from porphyry-proximal Cu and Cu-Zn zones (e.g., Morro Solar vein: IQR = 471 – 8, up to 1804 ppm) to porphyry-distal Ag-Pb zone (e.g., Rosita/Rubí: IQR = 1.5 – 0.032 ppm, up to 25 ppm). Within individual orebodies and veins, sphalerite

in Stage C intermediate-sulfidation assemblages record a depletion in In and an enrichment in Ge from early to late generations.

3. Indium was incorporated into the sphalerite crystal lattice mostly through a $In^{3+} + Cu^{1+} \leftrightarrow 2Zn^{2+}$ coupled substitution. However, more complex coupled substitutions involving other elements probably operated for sphalerite from some particular mineral assemblages (e.g., $Cu^{1+} + Ga^{3+} \leftrightarrow 2Zn^{2+}$; $(Sn, Ge)^{4+} + (Ga, In)^{3+} + (Cu, Ag)^{+} \leftrightarrow 4Zn^{2+}$). Mechanisms of substitution for chalcopyrite, galena, and tennantite involving In, Ge, and Ge are not fully constrained.

4. The GGIMFis geothermometer (Frenzel et al. 2016), which uses Ga, Ge, In, Mn, and Fe contents in sphalerite, yields temperatures between 400 ◦C to below 100 ◦C which are broadly comparable to the microthermometric data of fluid inclusions available for different mineralization stages and zones at Morococha. The highest crystallization temperatures are registered in skarn-hosted polymetallic mineralization including both Stage A (e.g., Porvenir: 407 ± 8 ◦C, 2-sigma error ◦C) and Stage C (e.g., Lower Ombla: 358 ± 26 ◦C) sphalerite grains. Instead, Stage C sphalerite from high-sulfidation assemblages in veins overprinting the Toromocho porphyry yields a much lower crystallization temperature (157 ± 33 ◦C). Stage C sphalerite grains from intermediate sulfidation assemblages yield crystallization temperatures in the range between 323 ± 39◦ and 81 ± 26 ◦C. As expected, crystallization temperatures drop from Stage A to Stage C mineral assemblages, from proximal- to distal-to-porphyry locations, and from early to late sphalerite generations within a single mineralization stage.

The main results derived from the study of the Ayawilca Zn-Pb-Ag-In-Sn-Cu deposit in Pasco include:

1. Mineral assemblages define three stages of evolution: stage A (low sulfidation), stage B (intermediate sulfidation), and stage C (intermediate sulfidation), similar to other Cordilleran-type deposits. In “mantos”, Stage A is predated by relicts of a magnesian retrograde skarn mainly composed of Mg-siderite + talc + magnetite, as well as by cassiterite; these “pre-A stage” assemblages are restricted to the deepest mantos. Stage A is the economically and volumetrically most important and comprises arsenopyrite, pyrrhotite, chalcopyrite, Fe-rich sphalerite (two generations), stannite, and herzenbergite [SnS]. Stage A mineralization is overprinted by coarse pyrite ± marcasite (Stage B). Stage C comprises Fe-moderate to Fe-poor sphalerite, chalcopyrite, galena, Cu-Ag sulfosalts, kaolinite, dickite, and carbonates (siderite and undetermined Mn-Fe carbonates). Stage C overprinted the assemblages of stages A and B. Veins in NE Ayawilca display similar mineralogy and micro-textural relationships as in stages A and B in mantos. In contrast, veins in NW Ayawilca are mainly composed of Fe-moderate and Fe-poor sphalerite, galena, Ag-Cu sulfosalts (pyrargyrite and stephanite), and pyrite.

2. In mantos, high In contents were found in Stage A Fe-rich sphalerite (IQR = 986 – 16 ppm, up to 1.7 wt.%), particularly in second-generation sphalerite (IQR = 1299 – 227 ppm), and in stannite (IQR = 1168 – 869ppm, up to 1908 ppm) and chalcopyrite (IQR = 1078 – 900 ppm, up to 1185 ppm). In veins, In contents in sphalerite are much higher in the NE (IQR = 2676-993 ppm, up to 2702 ppm) than in the NW (IQR = 1.0 – 0.0036 ppm, up to 2.3 ppm) zones. Germanium and Ga contents in sphalerite from both mantos and veins are of some tens of ppm.

3. Indium is incorporated within the sphalerite structure via $Cu^{+} + In^{3+} \leftrightarrow 2Zn^{2+}$ and $(Sn, Ge)^{4+} + (Ga, In)^{3+} + (Cu + Ag)^{+} \leftrightarrow 4Zn^{2+}$ coupled substitutions. Indium incorporation mechanisms for chalcopyrite and stannite remain unclear.

4. U-Pb isotopic analyses of cassiterite yield dates of ca. 23.1-22.7 Ma contextualizing the Ayawilca deposit in the Miocene polymetallic belt of central Peru.

The main results from the study of arc-hosted VMS deposits (Palma, Perubar, and María Teresa in Peru and Cerro de Maimón in the Dominican Republic) include:

1. Sphalerite from the studied VMS deposits hosts Fe, Mn, Cd, Hg, Ag, Sb, Se, In, Ge, and Ga in solid solution. Other elements such as Sn, Tl, Bi, and Pb in sphalerite may be related to mineral microinclusions as suggested by occasional ragged ablation spectra. In chalcopyrite from Maria Teresa and Cerro de Maimón deposits, trace elements as solid solution include Zn, Ag, Sn, Cd, Se, In, Ga, and Ge while Au, Tl, Sb, Pb, and Bi probably occur as mineral microinclusions. In general, In, Ge, and Ga contents are low in analyzed ore minerals. Indium (IQR = 42–1.6 ppm, up to 415 ppm) and Ga (IQR = 31–5.9 ppm, up to 96 ppm) contents are higher in sphalerite, whereas Ge is higher in chalcopyrite (IQR= 5.9–0.70 ppm, up to 80 ppm). Sphalerite from arc-hosted VMS and SMS deposits yields distinctively high Cd, Hg, and to a lesser extent, Sb and Tl contents, relative to sphalerite from VMS and SMS located in back-arc basins or mid-ocean ridges.

2. Binary correlation plots for trace element contents in sphalerite suggest $Cu^{+} + In^{3+} \leftrightarrow 2Zn^{2+}$ and $Cu^{+} + Ga^{3+} \leftrightarrow 2Zn^{2+}$ coupled substitutions as the main mechanisms for the incorporation of In and Ga to the crystal lattice. More complex substitution mecanisms involving other monovalent (Cu^{+}, Ag^{+}), divalent ($Ge^{2+?}$), trivalent (In^{3+}, Ga^{3+}, $[Sn^{3+?}]$), and quadrivalent ($Ge^{4+,}$ Sn^{4+}) cations are also plausible for some of the analyzed sphalerite grains. In chalcopyrite, positive correlations between Zn, Cd, In, Ge, and Ga points to varied coupled substitution mechanisms of Fe (+2 and +4) and Cu (+1 and +3).

3. The ore mineralogy and sphalerite and chalcopyrite geochemistry were studied in detail for the zone-refined Sofía-D massive sulfide body in the María Teresa deposit. The ore assemblage includes sphalerite, chalcopyrite, tetrahedrite-group minerals, and galena,

and lesser proportions of pyrite, pyrrhotite, and barite. The mineralization has undergone contact metamorphism and foam textures are ubiquitous. Metal zoning at the sulfide body scale includes a lower part with dominant pyrite sheathed upwards by a Cu zone rich in chalcopyrite grading to sphalerite ± fahlore ± galena ± chalcopyrite (Zn zone) and galena + sphalerite ± fahlore ± barite (Pb – Zn – Ag zone). Bottom to top, sphalerite records a progressive depletion in In, Cu, Mn, and Se, and enrichment in Ge. As for chalcopyrite, Se content tends to decrease from bottom to shallower levels.

The main results derived from the study of the San Vicente and Shalipayco MVT deposits include:

1. A detailed petrographic study has disclosed different types of sphalerite discriminated according to their color (including the color of internal reflections under the petrographic microscope) and textural relationships. In San Vicente, up to 7 types of sphalerite grouped into two steps of mineralization were recognized. Sphalerite of the first mineralization step, which volumetrically represents the main ore at San Vicente, yields Fe contents mostly > 1 wt.% and includes, in chronologic order of deposition, black, reddish-brown, yellowish-brown, and yellow sphalerite types. The second mineralization step is volumetrically more restricted and contains Fe-poorer (<100 ppm) sphalerite which shows colors ranging from orange to yellow and to white/colorless along the paragenetic sequence. In Shalipayco, up to 5 types of sphalerite were identified, all attributed to a single ore-forming episode including, in order of deposition, black, reddish-brown, yellowish-brown, yellow, and white/colorless sphalerite types.

2. LA-ICP-MS analyses reveal that Ge is the main critical element hosted in sphalerite from the San Vicente (IQR = 118-44 ppm) and Shalipayco (IQR = 425-101 ppm) deposits. In San Vicente, the highest Ge values are found in orange sphalerite belonging to the second mineralization step (IQR = 1207-375 ppm, up to 1861 ppm), while in Shalipayco, yellow sphalerite yielded the highest Ge contents (IQR = 375-267 ppm, up to 1119 ppm). Therefore, in both deposits, Ge-richest sphalerite crystallized relatively late in the respective paragenetic sequences.

3. According to binary elemental correlation plots, Ge was incorporated to the sphalerite crystal lattice via $Ge^{4+} + 2Ag^{+} \leftrightarrow 3Zn^{2+}$, $Ge^{4+} + 2Cu^{+} \leftrightarrow 3Zn^{2+}$, $Ge^{4+} + 2(Cu + Ag + Tl)^{+} \leftrightarrow 3Zn^{2+}$, and $Cu^{+} + (Ga, In)^{3+} + Sn^{4+} \leftrightarrow 4Zn^{2+}$coupled substitutions. Germanium molar contents show no correlation with those of Ga and In thus suggesting independent substitution mechanisms relative to the latter elements.

SUMMARY OF THE OVERALL CONCLUSIONS

1. Indium, germanium, and gallium are critical elements because of their economic and strategic importance for the manufacture of modern digital and green technologies framing our development and evolution as a society. These elements do not form own mineral deposits but are recovered as by-products. Their chalcophile geochemical affinity favor their concentration in sulfide minerals.

2. Systematic petrographic study and trace element analysis have been conducted in ore minerals (sphalerite, chalcopyrite, stannite, galena, tetrahedrite-tennantite) from different polymetallic deposits of the Central Andes in Peru. Studied mineralization styles include i) skarn-hosted and skarn-free (Cordilleran) polymetallic deposits associated with porphyry Cu systems in the world-class Morococha district and the recently discovered Ayawilca deposit, ii) VMS mineralization in the María Teresa, Palma, and Perubar deposits, and iii) MVT mineralization in the San Vicente and Shalipayco deposits.

3. Of the analyzed minerals, sphalerite yields the highest contents in In (up to 1.7 wt.%), Ge (up to 1861 ppm), and Ga (up to 2137 ppm) followed by stannite (up to 1908 ppm In) and chalcopyrite (up to 1185 ppm In; up to 630 ppm Ga). Tetrahedrite and tennantite occasionally yield significant Ge values (up to 266 ppm). In galena, In, Ge, and Ga contents are low, mostly at the sub-ppm level.

4. Sphalerite is particularly rich in In in low-sulfidation assemblages in Cordilleran mineralization (up to 1.7 wt.% in Ayawilca). Nevertheless, the highest In values in the Morococha district are found in sphalerite from high-sulfidation assemblages (up to 1456 ppm), followed by sphalerite from low-sulfidation assemblages (up to 459 ppm in the Manto Italia body). Instead, highly variable In contents are found in sphalerite from intermediate-sulfidation assemblages at Morococha. The highest Ga contents are registered in sphalerite from epithermal veins overprinting the Toromocho porphyry (up to 1739 ppm). The highest Ge contents are recorded in sphalerite from the San Vicente (up to 1861 ppm) and Shallipayco (up to 1119 ppm) MVT deposits.

5. The incorporation of In, Ge, and Ga to the sphalerite crystal lattice was in the form of coupled substitutions involving monovalent (Cu^{+}, Ag^{+}), divalent ($Ge^{2+?}$), trivalent (In^{3+}, Ga^{3+}, [$Sn^{3+?}$]), and quadrivalent (Ge^{4+}, Sn^{4+}) cations. Table 1 summarizes the coupled substitutions that have been deduced for sphalerite in this thesis. The substitution mechanisms driving to the incorporation of In, Ge, and Ga into the crystal lattice of chalcopyrite, galena, stannite, and tetrahedrite-tennantite remain unclear.

Table 1. Substitution mechanisms reported from different mineralization styles studied in this thesis.

Substitution mechanism	Type of deposit
$In^{3+} + Cu^{+} \leftrightarrow 2Zn^{2+}$	Cordilleran and skarn-hosted (Morococha and Ayawilca) VMS (María Teresa)
$Ga^{3+} + Cu^{+} \leftrightarrow 2Zn^{2+}$	Cordilleran (Morococha) VMS (María Teresa, Perubar, and Cerro de Maimón)
$(Ge,Sn)^{4+} + (In,Ga)^{3+} + (Cu,Ag)^{+} \leftrightarrow 4Zn^{2+}$	Cordilleran and skarn-hosted (Morococha and Ayawilca) VMS (María Teresa, Perubar, and Cerro de Maimón)
$Ge^{4+} + 2Cu^{+} \leftrightarrow 3Zn^{2+}$	MVT (San Vicente)
$Ge^{4+} + 2(Cu, Ag, Tl)^{+} \leftrightarrow 3Zn^{2+}$	MVT (San Vicente and Shalipayco)
$Sn^{4+} + (Ga, In)^{3+} + Cu^{+} \leftrightarrow 4Zn^{2+}$	MVT (San Vicente)
$Ge^{4+} + 2Ag^{+} \leftrightarrow 3Zn^{2+}$	MVT (San Vicente and Shalipayco)

6. Coupling of trace element content determinations with detailed petrography has allowed unveil some trace-element distribution patterns involving the high-tech metals In, Ge, and Ga along paragenetic sequences (i.e., stages of mineralization – temporal distribution) and across deposits/districts (i.e., spatial distribution).

   <u>Spatial distribution patterns include:</u>

   a) In the Morococha district, sphalerite from intermediate-sulfidation assemblages shows continuous In and Cu depletion from proximal-to-porphyry Cu metalliferous zone to distal-to-porphyry Ag-Pb metalliferous zone. Within single sampled orebodies, sphalerite records In depletion and Ge enrichment from early to late generations. Likewise, from proximal to distal locations relative to the causative magmatic-hydrothermal center, chalcopyrite displays a depletion in Se and Hg and an enrichment in Sn and Ag, and galena records a depletion in In.

   b) In the Sofía-D zone-refined massive sulfide body in the María Teresa deposit, there is a progressive enrichment in In, Cu, Mn, Se and a depletion in Ge in sphalerite towards the chalcopyrite-rich basal domain. As for chalcopyrite, Se content decreases steadily from bottom to shallower levels.

   <u>Temporal distribution patterns include:</u>

   a) In Stage C intermediate-sulfidation assemblages at Morococha, In-richest sphalerite (up to 4608 ppm) crystallized during the base-metal substage with early sphalerite generations enriched in In relative to late generations regardless of their location in the district. From early to late sphalerite generations within the mineralization Stage C intermediate-sulfidation assemblages at the Ivette manto, the abrupt In depletion coincides with a drastic increase of Ge (up to 215 ppm in third-generation sphalerite).

Gallium only shows limited depletion from early to late sphalerite in Stage C assemblages.

b) In Ayawilca, the highest In contents in sphalerite are hosted in low sulfidation (stage A) assemblages, particularly in second-generation sphalerite (up to 1.7 wt.%), whereas stage C sphalerite is In-poor.

c) In the San Vicente and Shallipayco MVT deposits, Ge-richest sphalerite, which shows bright orange and yellow colors, crystalized relatively late in the respective paragenetic sequences.

7. Copper is involved in almost all substitution schemes for the incorporation of In and Ga into the sphalerite crystal lattice, and hence its availability in minerals systems defines the spatial and temporal distribution of these elements. Therefore, a high availability of Cu in metal-rich magmatic-hydrothermal fluids may enhance In enrichment in sphalerite. In the particular case of magmatic-hydrothermal deposits, the distribution of In in sphalerite is controlled by i) sourcing of In via metal-rich magmatic-hydrothermal fluids; ii) a relatively high availability of Cu in the mineral system; iii) a relatively high temperature of the mineralizing fluid (> 250ºC) or low pH favoring the stability Cl complexes, and iv) availability of Cl to form In (and Cu) chloride complexes.

8. Further similar studies on other Peruvian mineral deposits need to be carried out to complete the database on critical element contents in the central Andes and elsewhere.

References

Catchpole H, Kouzmanov K, Putlitz B, Seo J, Fontboté L (2015) Zoned base metal mineralization in a porphyry system: origin and evolution of mineralizing fluids in the Morococha District, Peru. Econ Geol 110:39–71

Fontboté L (2020) Systematic trends in the evolution of porphyry-related Zn-Pb-(Ag) deposits. Swiss Geoscience Meeting. 18th, Zurich, Switzerland, 2020. Extended Abstracts

Frenzel M, Hirsch T, Gutzmer J (2016) Gallium, germanium, indium, and other trace and minor elements in sphalerite as a function of deposit type – a meta-analysis. Ore Geol Rev 76:52–78

Rottier B, Kouzmanov K, Wälle M, Bendezú R, Fontboté L (2016) Sulfide replacement processes revealed by textural and LA-ICP-MS trace element analyses: example from the early mineralization stages at Cerro de Pasco, Peru. Econ Geol 111:1347–1367

Rottier B, Kouzmanov K, Casanova V, Wälle M, Fontboté L (2018) Cyclic dilution of magmatic metal-rich hypersaline fluids by magmatic low-salinity fluid: a major process generating the giant epithermal polymetallic deposit of Cerro de Pasco, Peru. Econ Geol 113:825–856

CHAPTER I: INTRODUCTION

CHAPTER 1: INTRODUCTION ON CRITICAL RAW MATERIALS (CRM)

a. Critical raw materials (CRM): definitions and applications

i. Definitions

Since the term "criticality" was first used in 1939 by the US government to ensure independent access to raw materials considered essential in military technology production, its definition has broadened and currently embraces a much complex and heterogeneous context (US Public Laws 1939; Achzet and Helbig 2013; Humphries 2013). In the last decade, industrial demand has increased on supply for the manufacture of digital and clean (*"green"*) technologies (Skirrow et al. 2013; Kesler and Simon 2015). Supply adjustment for those materials deemed as "critical" by certain economies has generated concern in most consumer countries (Barteková and Kemp 2016). The attribution of "criticality" comes, in general, from the same conceptual idea: supply disruption risk of raw materials that are fundamental for economy (Buijs and Sievers 2011; Erdmann and Graedel 2011; Sykes et al. 2016; Zepf 2020; Andersson 2020). However, given the contrasting objectives, criteria or indicators used for the "criticality" assessment vary from one country to another and may change over the years, preventing a standardized methodology for a single definition (Kristof and Hennicke 2010; Achzet 2012; Lloyd et al. 2012; Hayes and McCullough 2018; Zhou et al. 2021). In this sense, the following shows how major economies approach, according to their reality, the concept of "critical raw materials".

United States

In 1974, the US government issued a memorandum listing imported products considered essential to its economy (The White House 1974). This would be the first record (both in the United States and worldwide) in which "critical materials" are closely addressed (Jin et al. 2016). A couple of years later, the Government Printing Office (GPO), in charge of producing various security documents, defined critical (and strategic) materials as "those that would be needed to supply the US military, industrial, and civilian needs during a national emergency, and are not found or produced in the United States in sufficient quantities to cover such needs" (GPO 1979).

After almost three decades, the term "critical material" was officially discussed by the US National Research Council (NRC) based on the importance in use and availability. It was defined as a "raw material that meets only one essential function for which there are few or no substitutes and in turn, with a high

probability of supply restriction, which leads to higher prices for such material" (NRC 2008). The definition above would later become the basis for future assessment as those carried out by the European Commission (Jin et al. 2016).

From that moment on, due to the rapid development and increasing global demand for new technologies, certain raw materials rapidly gained importance (e.g., rare earth elements, REE; Balaram 2019). Consequently, the US National Academy of Science (NAS) established that "all minerals can be or become critical depending on their importance and availability" (NAS 2008). Along the same lines, other US organizations have also provided their definition for critical materials. A similar but more concise meaning of criticality was given by the US Department of Energy (DOE) as a "measure that combines both importance for clean energy economy, and supply risk" (Bauer et al. 2010). The American Physical Society, a member of the Material Research Society (APS-MRS), argues that “if a new technology that uses a rare element was sufficiently implemented to make a significant contribution to our energy needs, quantities of this element could be necessary to the point of exceeding current production. We will refer to such an element as (potentially) critical energy element (ECE)” (Jaffe et al. 2011; Jin et al. 2016).

According to the NRC (2008), criticality condition changes over time as new technologies are developed, based mainly on the following indicators: i) increasing demand and low production (leading to higher prices), ii) the difficulty of increasing production from small markets, iii) country and company raw materials concentration, iv) dependence on by-products (which main products determined their availability), and v) low recycling rates (from old scrap).

In the United States, the organization in charge of periodically publish the catalog of critical minerals, which currently includes a total of 35, is the US Department of Interior (DOI) (Fortier et al. 2018). Within the critical minerals list, the US National Science and Technology Council (NSTC) includes “strategic minerals” as a subcategory to those crucial for national security. However, it remains to be determined which critical minerals should be considered “strategic” (Nassar et al. 2016).

European Community

The European Commission lists as critical those raw materials of importance for the development of key technologies and strategic sectors for the European Union, but with a high supply restriction or high environmental risk, causing a

direct impact on the economy and regional stability (European Commission 2020). Thus, the term "critical" for the European Commission does not stem from the scarcity of the resource but from the impediment to access the product which makes its sustainable use impossible over time (Graedel et al. 2014; Zepf 2020). Since they comprise mainly metals, they are usually called, as in the United States, "critical metals", but they are also called "strategic metals", "E-Tech elements", or "technological metals" without a particular distinction (Zhou et al. 2021).

According to the European Commission (2020), the indicators or parameters that tend to increase the supply risk shortages and supply vulnerability are: i) the geopolitical and social stability of the producing countries (known as country risk), ii) the high production concentrations established in certain countries (mainly China), iii) low recycling rates, and iv) deficit or higher cost of substitutes for new technologies. Other authors such as Ferro and Bonollo (2019) include as indicators the risk of the level of abundance (in the earth's crust) and the environmental country risk (restriction of supply by producing countries due to environmental protection measures). Additionally, supply risk may increase because imported metals are processed and refined in a reduced number of countries (European Commission 2020).

The promotion of recycling is one of the main objectives of the European Commission to increase resource efficiency, avoid a possible supply shortage, and reduce environmental impacts. Although more sophisticated and improved technologies allow the recycling of critical metals, the low concentrations and the presence of other materials in the waste are challenging facts (Buchert et al. 2009). This situation becomes more complicated considering that, to date, critical metal applications are relatively new, limiting a considerable accumulation of material for recycling.

In order to improve access to essential raw materials, the European Raw Materials Initiative (EU RMI) produced in 2011 the first “critical raw materials” catalog for the European economy, where 14 of 41 non-energy materials were included. Since then, the number has steadily increased due to periodic reviews and updates based on the market and political priorities (European Commission 2020). Hence, by 2014 and 2017, this number increased from 20 to 26 critical materials (European Commission 2020). The latest evaluation conducted in 2020 includes 30 critical raw materials out of 83 candidates.

China

In China, "strategic mineral" is the official term given by various governmental agencies, so the use of "critical mineral" and "critical raw material" has been only restricted to academic discussions (Andersson 2020). The first registers of strategic mineral in Chinese communications are between 1980 and 2000; however, they commonly lack theoretical basis and are rather oriented to criticize the United States and the Soviet Union strategies for controlling resources considered “strategic" (Zhang 1980; Hu 1982).

It is not until the early 2000s that "strategic mineral" is not only defined but widely cited from three Chinese-language publications (Andersson 2020). Chen Yuchuan, former director of the Chinese Geological Survey, defined strategic minerals as those "essential for the country's economy, social development, and national defense that cannot be guaranteed domestically, and that can influence the international market" (Chen 2002). A similar definition was given by Qi (2002), who added that strategic minerals are "those that must be imported in wartime and when domestic supply is lacking or abundant (the latter means, minerals that China has in abundance, and can use its dominant position in global supply)." Finally, Zhang (2002) established that strategic minerals are "essential for national security where domestic supply cannot meet the demand”, and “when the foreign supply situation is unreliable, there may be an urgent supply shortage".

A few years later, Chen and Wang (2007) established two criteria to define a mineral as "strategic": i) minerals that China relies heavily on imports due to lack of resources or production, having a direct impact on its economy, security and national defense and ii) minerals that China possesses in abundance, being able to control the global market. At present, the meaning for strategic minerals has followed the same line, as minerals destined to safeguard the economy, defense, and the development of Chinese strategic industries (Andersson 2020).

The assessments to attribute the strategic nature of minerals in China are ruled in addition to industrial demand, by a series of complex political perceptions and regulations (Andersson 2020), based on a series of parameters, the most important being i) importance for development/economic security, ii) importance for national defense, iii) supply risk, and iv) substitutability (Andersson 2020).

Based on these criteria, "strategic minerals" were divided into the following subcategories, which coincide with the ones that appear in the National Mineral Resources Plan of China:

-*Basic minerals or basic pillars*: these are minerals or raw materials that China needs in large quantities, such as iron, copper, oil, and gas (Peng 2017).

-*Emerging strategic minerals* (SEI minerals): these are minerals or raw materials considered essential to guarantee development in China's emerging industries (Zhang et al. 2013). This list includes, for example, lithium, tungsten, REE, molybdenum, tin, among others (CGS 2016; Hebei Provincial Department of Land and Resources 2017). They are often comparable to "critical mineral" (US) and "critical raw materials"(CE) (Hu 2016; Wang 2019).

-*Advantageous and protected minerals*: minerals that China has in abundance and can gain a competitive advantage compared to other countries to control or influence global markets (Chen and Wang 2007; Wang 2009). Currently, this subcategory has no mineral examples. However, during 2008-2015, REE were included along with tin, antimony, graphite, among others (Bu et al. 2009; Ye and Zhao 2014). On the other hand, protected minerals are considered irreplaceable for defense and the Chinese economy (Yuan 2010).

In order to "coordinate the development of the exploration, use, and protection of mineral resources", the Ministry of Lands and Resources (today the Ministry of Natural Resources) drafted the National Mineral Resources Plan (NPMR), which included the first official catalog of "China's strategic minerals" (Sina 2016). This list has been further refined in 2018 and currently includes China's list of critical metals (Zhai et al. 2019; Zhou et al. 2021).

***

As stated in the World Trade Organization (WTO), the most visible example in recent years of the aforementioned criticality of raw materials is the case of REE, mainly used in permanent magnets for electric motors and electricity generators (European Commission 2020). The United States, Japan, and the European Community consider this mineral group as critical/strategic since their industries depend to a great extent on their importation for the production of a wide variety of high-tech products (Kiggins and David 2015; Schmid 2019; Calvo et al. 2019; Andersson 2020). This criticality assessment, on the other hand, will not be the same for China. Although its production share has fallen slightly as new rare earth mines have come into operation outside China (Castilloux 2016),

it still concentrates 85% of world supply, dominating and widely regulating the world market without representing a supply risk in the short or medium-term (Wang 2009; Mancheri 2015; Andersson 2020). However, China classifies them as strategic because they are essential raw materials for developing its emerging strategic industries (SEI minerals), thus contributing to an increasingly technological, wealthy, and integral Chinese society (Zhang et al. 2013).

Table 2 shows a compilation of raw materials classified as critical or strategic by various countries since 1996.

Table 2. Raw materials classified as "critical" or "strategic" by various countries. US Department of Energy (Bauer et al. 2010); US Department of Defense (DOD 2013); US Department of Interior (Fortier et al. 2018); United Kingdom Government (UK House of Commons 2011); Russian Federation government (from Chakhmouradian et al. 2015); Geoscience Australia (Skirrow et al. 2013); European Commission (European Commission 2020), Ministry of Natural Resources of China (Zhou et al. 2021). Modified from McFall (2016).

Organization – Year	Elements defined as critical	Category
US Department of Energy – 2010	Dy, Eu, Nd, Tb, Y, Ce, **In**, La, Te, Li	Critical material
US Department of Defense – 2013	Sn, Sb, Al_2O_3, SIC, Y, W, Ta, Bi, **Ge**, Mn, Dy, fluorite, Be, Er, Cr, **Ga**, Tb, Tm, Sc	Strategic commodities
US Department of Interior – 2018	Bauxite, Sb, As, barite, Be, Bi, Cs, Cr, Co, fluorite, Ga, Ge, graphite, Hf, He, In, Li, Mg, Mn, Nb, PGMs, potash, REE, Re, Rb, Sc, Sr, Ta, Te, Sn, Ti, W, U, V, Zr	Critical minerals
United Kingdom government – 2011	Sb, Be, Cr, Co, **Ga**, **Ge**, Au, Hf, **In**, Li, Mg, Ni, Nb, EGP, REE, Ta, Ti, W, V	Strategically important metals
Russian Federation government – 1996	U, Mn, Cr, Ti, Al_2O_3, Cu, Ni, Pb, Mo, W, Sn, Zr, Ta, Nb, Co, Sc, Be, Sb, Li, **Ge**, Re, REE, Au, Ag, PGE, diamonds, quartz	Strategic resources
Geoscience Australia – 2013	REE, Ga, **In**, W, PGE, Co, Nb, Mg, Mo, Sb, Li, V, Ni, Ta, Te, Cr, Mn	Critical elements
European Commission – 2020	Barite, Be, Bi, borate, Co, coal, fluorite, **Ga**, **Ge**, REE, **In**, Mg, graphite, Nb, PGE, phosphorite, rubber, Sc, Si, Ta, W, V, bauxite, Li, Ti, Sr	Critical raw materials
Ministry of Natural Resources of China – 2019	Li, Be, Rb, Cs, Nb, Ta, Zr, Hf, W, La, Ce, Pr, Nd, Sm, Eu, Gd, Tb, Dy, Ho, Er, Tm, Yb, Lu, Sc, Y, **Ga**, **Ge**, Se, Cd, PGMs, **In**, Te, Re, Tl, Cr, Co	Strategic minerals

ii. Importance of CRM for technological progress and clean technologies

Critical raw materials are part of our daily life and are essential for our evolution as a society. In recent years, its worldwide demand has exponentially grown due to numerous factors, including population growth, a vertiginous technological innovation, increasing industrialization, decarbonization of transport systems, and sustained economic growth in emerging countries (Skirrow et al. 2013; Kesler and Simon 2015; European Commission 2020).

Critical raw materials are used in key sectors: environmental technologies, health, national defense, consumer electronics, plastic and textile industries, chemical applications, pharmaceutical and animal feed industries, steel, automotive, aviation, and space exploration. Hence, they are linked to practically all industries and, in many cases, as irreplaceable supplies (e.g., European Commission 2020, Ferro and Bonollo 2019).

An example of massive new needs on critical elements is electrical storage batteries, which have led to an increase in the consumption of metals such as aluminum, cobalt, iron, lead, lithium, manganese, and nickel (European Commission 2020). Another case is in solar panels made up by silicon, germanium, indium, gallium, tellurium and cadmium (Grandell et al. 2016). Likewise, certain magnets contain high amounts of REE. Electric vehicles comprise small amounts of palladium, gold, germanium, indium, gallium, and silver. Hence, ensuring critical raw materials for the present and in the future is crucial for an environmentally sustainable and competitive society (Hagelüken 2012).

iii. Chalcophile high-tech metals and metalloids: the In-Ge-Ga triad

1. Indium

Indium (In) is a soft, malleable, silvery-white metal with an atomic number 49 and crustal abundance of ~0.05 ppm (Taylor and McLennan 1995; Alfantazi and Moskalyk 2003). It most often occurs in a +3-oxidation state, with chemical properties similar to Sn, Ga, and Tl (Schroll 1999). Indium is mainly considered a chalcophile element, arranged in covalent tetrahedral coordination in sulfide compounds (Schwarz-Schampera and Herzing 2014). Hydrothermal solutions mainly transport In under chloride complexes at average temperatures of 350ºC (Seward et al. 2000; Shimizu and Morishita. 2012). However, it can also be transported as hydroxide, sulfide, phosphate, carbonate, and arsenate complexes (Schroll 1999) and vapor in higher temperature systems (i.e., fumaroles; Chaplygin et al. 2007). Currently, only a few and rare minerals (12)

are known for hosting In as a structural component (Schwarz-Schampera 2014). The most abundant mineral containing essential In is roquesite (tetragonal; [$CuInS_2$]), the indium analogue of chalcopyrite (Picot and Pierrot 1963). The scarcity of In minerals normally prevents them from being economically extracted (Cook et al. 2009, 2011a). Indium tends to concentrate in the crystal structure of certain sulfides and oxides substituting elements of similar atomic radius (Schwarz-Schampera 2014), being sphalerite the main In-hosting mineral (Ishihara and Endo 2007; Andersen et al. 2009; Cook et al. 2011a; Shimizu and Morishita 2012; Lokanc et al. 2015; Márquez-Zavalía 2020). Although indium in sphalerite does not usually exceed 1 wt.% (Alfantazi and Moskalyk 2003), higher values have been reported in Sn-Zn polymetallic deposits (e.g., up to 18 wt.%, Murakami and Ishihara 2013), skarn deposits (e.g., up to 20 wt.%; Bauer et al. 2019a) and VMS deposits (e.g., up to 2.13 wt.%, Carvalho et al. 2018). Significant In contents can be hosted in chalcopyrite from skarn (e.g., up to 0.25 wt.%, Bauer et al. 2019a) and VMS deposits (e.g., up to 0.10 wt.%; Carvalho et al. 2018), and in stannite from VMS (e.g., up to 1.47 wt.%, Carvalho et al. 2018) and Sn-Zn polymetallic deposits (e.g., up to 2.64 wt.%, Torró et al. 2019a).

Indium has multiple applications in forefront technologies. It is currently considered essential for the consumer electronics and renewable energy industries (Werner et al. 2015, 2017). One of the main uses is in the form of indium tin oxide - ITO (In_2O_3 + SnO_2). This alloy behaves as a conductor when deposited as a thin film on a screen's surface, transforming electrical data into an optical form (Shanks et al. 2017). ITO is used in practically all flat screen and touch screen equipment including computers, optical, and electronic products (Tolcin 2017). Indium is also employed in alloys and welds, reducing the propagation of cracks and fatigue temperatures, and as semiconductor in LED (Indium Gallium Nitride - InGaN) and laser diodes (Indium phosphide - InP). It is also used in photovoltaic panels and batteries (Schwarz-Schampera and Herzing 2002; Alfantazi and Moskalyk 2003).

Although In consumption has increased thanks to the high demand for digital technological equipment (Frenzel et al. 2017), prices had been declining previous to 2021. Between 2014-2018, the scandal over collecting illegal funds by the failed Fanya Metal Exchange (FME) caused a sustained decrease, from 700 to 200 USD/kg (Anderson 2018). In 2018, even though there was a slight recovery, prices by 2020 reached 150 USD/kg, its lowest level to date (European Commission 2020). In 2021, In has reached a price of 447 USD/kg (https://www.kitco.com/strategic-metals/). In the future (2030 to 2050), an increase in the demand for indium is expected, especially for solar photovoltaics, electric vehicles, and nuclear technology manufacture (Watari et al. 2020).

2. Germanium

Germanium (Ge) is a hard, brittle silver-gray metalloid with an atomic number of 32 and a crustal abundance of 1.5 ppm (Wedepohl 1995). It has chemical properties similar to Sn and Si (González et al. 2018) and occurs in 4+ and 2+ oxidation states. Nevertheless, the former is considered more characteristic and stable. Due to its complex fractionation behavior, it usually occurs in different environments (Frenzel et al. 2014). It is considered a siderophile element in the presence of metallic iron (Wai et al. 1968), lithophile in the absence of Fe (and of certain sulfides) replacing Si^{4+} (Hörmann 1963), chalcophile in hydrothermal processes (Bernestein 1985), and organophilic, related to surface processes such as the first stages of coal formation (Yudovich and Ketris 2003). Germanium forms different complexes in aqueous solution and low temperatures, including fluoride, hydroxide, phosphate, and sulfate. It also forms germanic acid (H_4GeO_4) at hydrothermal temperatures of 300ºC (Wood and Samson 2006). Due to its high reactivity, Ge does not appear in its native state and, like In, it rarely forms its own minerals (27 mineral species documented), mainly as Ag-Cu sulfides (i.e., germanite ($[Cu_{13}Fe_2Ge_2S_{16}]$; Bernstein 1985). Instead, it mainly occurs as solid solution in sphalerite, with average contents between the tens to hundreds of ppm and, therefore, recovered as a byproduct (Ye et al. 2011; Frenzel et al. 2014). Germanium does not form specific mineral deposits (Shanks et al. 2017). It is exploited from Zn-rich deposits, mainly in MVT (Leach et al. 2010; Paradis 2015; Mondillo et al. 2018a, b) and sedimentary exhalative massive sulfide (SEDEX) deposits (Emsbo et al. 2016). It can also be hosted in VMS, carbonate replacement (CRD), polymetallic vein, porphyry Cu-Mo-Au, sedimentary-hosted massive sulphide (SHMS), and coal and lignite deposits (Höll et al. 2007).
Germanium can also be concentrated in supergene environments by weathering of Ge-rich sphalerite leading to the formation of secondary minerals such as hemimorphite and goethite as described at the MVT Crystal deposit (Mondillo et al. 2018b). Exceptional Ge contents in primary and secondary minerals (between 500 and 5000 ppm) were reported at the Tsumeb carbonate hosted-breccia pipe Cu-Pb-Zn-Ag deposit in Namibia, including enargite ($[Cu_3AsS_4]$, anglesite ($[PbSO_4]$, duftite ($[PbCu(AsO_4)(OH)]$, olivenite ($[Cu_2(AsO_4)(OH)]$, and bayldonite ($[(Cu,Pb)_2(AsO_4)(OH)]$ (Frondel and Ito 1957).

Due to its unique properties, Ge is transcendental in multifarious commercial, industrial, and military applications (Shanks et al. 2017). It is mainly commercialized as crude germanium oxide (GeO_2), which is in turn used to produce processed materials such as germanium tetrachloride (GeCl4), refined germanium oxide, and metallic germanium, each one with specific applications (Melcher and Buchholz 2014; European Commission 2020). Germanium

tetrachloride is used in the manufacture of fiber optic cables (Guberman 2015). Processed germanium oxide is employed in optical lenses and as polymerization catalysts to make plastic bottles (PET) (Thiele 2001). Metallic germanium is used as a semiconductor in electronic devices and infrared optics (lenses and windows for IR radiation). Other uses include solar cells in satellites, night vision devices, and solar energy panels (Bleiwas 2010).

Reliable information regarding Ge prices is obscure (Moskalyk 2004). After the 2008 crisis, prices considerably recovered due to the closure of three germanium dioxide plants, increased tariffs, and market restrictions by China, the world's leading producer of Ge. By 2015, an increase in Ge recycling rates coupled with the collapse of Fanya Metal Exchange (FME) drove prices down. Since then, the market value of germanium has evolved mainly between 1300 and 2000 USD/kg (Tolcin 2021). Its price in 2021 has reached 2120 USD/kg (https://www.kitco.com/strategic-metals/).

3. Gallium

Gallium (Ga) is a soft, silvery-white metal with an atomic number 31 and crustal abundance of 15-19 ppm (Foley and Jaskula 2013; Gray et al. 2005; Rudnick and Gao 2014). This lithophile/chalcophile element shares many chemical properties with Al, including 3+ oxidation state, similar ionic radius, tetrahedral or octahedral coordination, and amphoterism (Foley et al. 2017). Due to its similar ionic radio with Fe^{3+} and Zn^{2+} (Shannon 1976) Ga can also be present in Fe-Zn oxides and sulfides such as magnetite, franklinite, and sphalerite. In aqueous solution, gallium forms complexes mainly as fluoride, phosphate, sulfate, and hydroxide, the latter ($Ga(OH)^{4-}$), considered dominant in supergene environments (Wood and Samson 2006). Gallium does not occur in its elemental form, and only a few compounds (4 mineral species documented) are known for hosting significant amounts of this element (i.e., gallite [$CuGaS_2$]). However, none of them are economically attractive for extraction (Gray et al. 2005). Instead, Ga mainly occurs as solid solution in bauxite, an Al-rich rock and currently the primary Ga source (10-160 ppm average; Mordberg et al. 2001) recovered as byproduct (Butcher and Brown 2014). According to Deschamps et al. (2002), bauxite is formed from Al-rich rock-forming minerals (i.e., feldspars or nepheline), which in turn can host significant Ga contents. Both Al and Ga are released during weathering processes under tropical conditions and concentrate due to their limited mobility (Dittrich et al. 2011). Other Al-rich compounds that can host significant contents of Ga include minerals from the alunite supergroup, mainly in Jarosite [$KFe_3(SO_4)_2(OH)_6$], up to 3120 ppm; Dutrizac et al. 1986) and alunite ([$KAl_3(SO_4)_2(OH)_6$], up to 339 ppm; Sahlström et al. 2017). Exceptionally

high Ga contents have been reported in the oxidized zones of the Tsumeb deposit hosted in supergene gallobeudantite [$PbGa_3(AsO_4)(SO_4)(OH)_6$] (Jambor et al. 1996) and galloplumbogummite [$Pb(Ga,Al)_3(PO_4)_2(OH)_6$] (Mills et al. 2009; Schlüter et al. 2014). Sphalerite is the only sulfide described to contain significant amounts of Ga, representing <1% of the supply (Schroll 1999). Gallium contents in sphalerite usually increase as deposition temperature decreases (Cook et al. 2009; Frenzel et al. 2016a, 2016b), occasionally ranging between 100-1000 ppm (Gray et al. 2005).

Gallium is an excellent heat and electricity conductor and is essentially used in the development of compound semiconductor materials in the form of gallium arsenide (GaAs) and gallium nitride (GaN) (Huy and Liedtke 2016). They are mainly employed to manufacture optoelectronic devices (directly converting electricity into laser light) and integrated circuits (Foley et al. 2017). They are also used in thin-film photovoltaic production with CIGS technology (Copper, Indium, Gallium, Selenium/Sulfur) and military technology (i.e., satellites, radars, night vision equipment). Other applications include gallium nitrate ($Ga(NO_3)_3$), used in the pharmaceutical industry for cancer treatment. Likewise, in Nd (NdFeB) magnets, Ga is usually added to improve magnetism and corrosion resistance (European Commission 2020).

Since Ga is not traded on any metal exchange, prices tend to be negotiated bilaterally, taking as reference past deals between private parties (Rongguo et al. 2016). In general, prices have been relatively stable since the 1980s ranging between 400 and 600 USD/kg (https://www.kitco.com/strategic-metals/). However, in 2007, the sudden increase in demand for technological devices and energy resources brought a metal shortage and a considerable rise in prices close to 750 $/kg (Rongguo et al. 2016) with peaks of nearly 940 USD/kg in 2011. From then on, oversupply from China, considered the world's leading producer of Ga, caused a drop in prices, with a rebound in early 2021, year in which its price reached 534 USD/kg. Demand for Ga is expected to increase in the coming years as the need for increasingly smaller and integrated devices continues (Monnet and Abderrahim 2018).

b. Critical elements in sulfides and sulfosalts: beyond base and precious metals

i.Sphalerite

Sphalerite [ZnS] is the major zinc ore mineral and the sulfide with one of the largest critical metals/metalloids endowment in its composition, including In, Ge, and Ga. High concentrations of these elements have been reported in sphalerite from deposits belonging to a diverse range of mineralization styles (Schwarz-

Schampera and Herzing 2002; Cook et al. 2009; Frenzel et al. 2016a). The highest average In contents have been reported in sphalerite from VMS and SEDEX deposits including the Neves Corvo VMS deposit in Portugal (e.g., up to 2.13 wt.%; Carvalho et al. 2018), the Murchison greenstone belt VMS deposits in South Africa (up to 690 ppm; Schwarz-Schampera et al., 2010), the Laochang VMS deposit in South China (up to 566 ppm; Ye et al. 2011), and the Dabaoshan SEDEX deposit in China (e.g., up to 415 ppm; Ye et al. 2011). Exceptionally high In values in sphalerite were reported in tin polymetallic base metal deposits. These included the Toyoha deposit in Japan (e.g., up to 8.86 wt.%; Ohta 1989) and the Huari-Huari (e.g., up to 3.5 wt.% In; Torró et al. 2019a) and Ánimas-Chocaya-Siete Suyos (up to 10 wt.% In; Torró et al. 2019b) deposits in Bolivia. Sphalerite can also host significant Ge contents, particularly in MVT deposits. For example, sphalerite from the Tres Marías MVT deposit in Chihuahua, Mexico yield up to 3200 ppm Ge (Saini-Eidukat et al. 2009). High Ge contents in sphalerite are also found in the Tennessee MVT district, USA (e.g., up to 800 ppm; Bonnet et al. 2016), the Zn-Cristal deposit in Bongará, Peru (e.g., up to 336 ppm; Mondillo et al. 2018b), the Fankou deposit in China (e.g., up to 110 ppm; Song and Tan 1996). As for SEDEX deposits, sphalerite from the Red Dog deposit in Alaska has up to 426 ppm Ge (Kelley et al. 2004). Relative significant Ga contents in sphalerite are mainly found in low temperature carbonate-hosted replacement deposits (Cook et al. 2009). Gallium contents in the range of hundreds to thousands of ppm have been reported in sphalerite from a number of Namibian Pb-Zn deposits (up to 3120 ppm; Melcher et al. 2006). Indium, Ge and, Ga are incorporated into the sphalerite crystal lattice through a number of substitution mechanisms. A compilation of the proposed substitution mechanisms involving these three elements is provided in Table 3. Noteworthy, it is common that some minor and trace elements that are reported to occur within the sphalerite crystal lattice may actually occur as submicron to nano mineral inclusions. Although LA-ICP-MS profiles can give us some light regarding the presence of sub-micron-scale mineral inclusions, high-resolution imaging by using Transmission Electron Microscopy (TEM) techniques provides information for determining micro to nano-scale textural, compositional heterogeneity, and crystal structure modification. Since TEM analyses have not been performed in this thesis, we will not elaborate on this question and refer the reader to recent publications on the topic such as Ciobanu et al. (2011), Cook et al. (2015), and Xu et al. (2021) for background reading.

Table 3. Main substitution mechanisms involving In, Ge and Ga in sphalerite that have been proposed in previous works.

Element	Main Substitution mechanisms
In	**$Cu^{+} + In^{3+} \leftrightarrow 2Zn^{2+}$** (Burke and Kieft 1980; Johan 1988; Ohta 1989; Pattrick and Dorling 1991; Pattrick et al. 1993, 1998; Schwarz-Schampera and Herzig 2002; Benzaazoua et al. 2003; Schorr and Wagner 2005; Cook et al. 2009, 2011a, 2011b, 2012; Ye et al. 2011; Shimizu and Morishita 2012; Lindeberg 2013; Murakami and Ishihara 2013; Lockington et al. 2014; Belissont et al. 2016; Bauer et al. 2019a, 2019b; Torró et al. 2019a, 2019b, Wilson 2019; Xu et al. 2020, 2021) **$Ag^{+} + In^{3+} \leftrightarrow 2Zn^{2+}$** (Johan 1988; Pattrick et al. 1998; Shimizu and Morishita 2012; Murakami and Ishihara 2013; Kołodziejczyk et al. 2016; Wilson 2019, Xu et al. 2020) **$In^{3+} + Sn^{3+} + \square \leftrightarrow 3Zn^{2+}$** (Belissont et al. 2014; Wei et al. 2018; Yuan et al. 2018) **$In^{3+} + (Cu,Ag)^{+} + Sn^{2+} \leftrightarrow 3Zn^{2+}$** (Johan 1988; Belissont et al. 2014; Wei et al. 2018; Yuan et al. 2018) **$Cu^{+} + In^{3+} + Fe^{2+} \leftrightarrow 3Zn^{2+}$** (Johan 1988; Moura et al. 2007) **$Sn^{4+} + 2In^{3+} + 2\square \leftrightarrow 5Zn^{2+}$** (Li et al. 2020) **$Ag^{+} + Sn^{2+} + In^{3+} \leftrightarrow 3Zn^{2+}$** (Xu et al. 2020) **$In^{3+} + Sn^{4+} + (Cu,Ag)^{+} + \square \leftrightarrow 4Zn^{2+}$** (Belissont et al. 2014; Wei et al. 2018; Yuan et al. 2018)
Ge	**$2Fe^{2+} + Ge^{4+} + \square \leftrightarrow 4Zn^{2+}$** (Bernstein 1985; Cook et al. 2009; Yuan et al. 2018) **$2Ag^{+} + Ge^{4+} \leftrightarrow 3Zn^{2+}$** (Belissont et al. 2014; Yuan et al. 2018) **$2Cu^{+} + Ge^{4+} \leftrightarrow 3Zn^{2+}$** (Bernstein 1985; Belissont et al. 2016; Bonnet et al. 2016; Yuan et al. 2018; Wei et al. 2019; Cave et al. 2020) **$Ge^{4+} + \square \leftrightarrow 2Zn^{2+}$** (Bernstein 1985; Belissont et al. 2016; Sahlström et al. 2017) **$Ge^{4+} + \square \leftrightarrow 2Zn^{2+}$** (Cook et al. 2015; Belissont et al. 2016; Bonnet et al. 2016) **$4(Cu^{+} + Sb^{3+}) + (Ge^{4+} + 2Ag^{+}) + 2\square \leftrightarrow 13Zn^{2+}$** (Li et al. 2020)
Ga	**$Cu^{+} + Ga^{3+} \leftrightarrow 2Zn^{2+}$** (Johan 1988; Cook et al. 2009; Murakami and Ishihara 2013; Bonnet et al. 2016; Wei et al. 2018; Wilson 2019) **$Ag^{+} + Ga^{3+} \leftrightarrow 2Zn^{2+}$** (Johan 1988; Cook et al. 2009; Wei et al. 2018) **$2Ga^{3+} + \square \leftrightarrow 3Zn^{2+}$** (Bonnet et al. 2016)
In, Ge, Ga	**$(Cu,Ag)^{+} + (In,Ga)^{3+} + (Ge,Sn)^{4+} \leftrightarrow 4Zn^{2+}$** (Johan 1988; Cook et al. 2009; Rottier et al. 2018; Bauer et al. 2019b) **$(Cu,Ag,Tl)^{+} + (In,Ga,Sb)^{3+} + (Ge,Sn)^{4+} \leftrightarrow 4Zn^{2+}$** (Cave et al. 2020) **$(Cu,Ag)^{+} + (In,Ga)^{3+} \leftrightarrow 2Zn^{2+}$** (Sahlström et al. 2017)

ii. Chalcopyrite

Chalcopyrite [$CuFeS_2$] is the primary copper ore and, like sphalerite, can host a wide variety of trace elements (e.g., Co, Se, and Ag), becoming in cases economically profitable (George et al. 2018). Information regarding critical metals/metalloids in chalcopyrite is relatively scarce in comparison with

sphalerite. Indium is one of the most widely reported potential by-product in chalcopyrite (Wittmann 1974). Significant In contents were registered in chalcopyrite from skarn deposits in South-East England (e.g., up to 2214 ppm; Andersen et al. 2016) and from the Kidd Creek VMS deposit in Canada (e.g., up to 1119 ppm; Cabri et al. 1985). Likewise, Carvalho et al. (2018) recorded 660 ppm In average content in chalcopyrite from Neves Corvo VMS deposit. In contrast, significant Ga contents are rare, and Ge values are systematically of few ppm. According to George et al. (2016), Ga and In are preferentially hosted in chalcopyrite structure during recrystallization in high metamorphic grades (for example, in the amphibolite facies). However, significant amounts of trace elements in chalcopyrite can only occur in the absence of other base metals (e.g., sphalerite or galena) or when formed at high temperatures. On the other hand, Bauer et al. (2019a) argue that a pre-enrichment of In in chalcopyrite (average 0.15 wt.%, standard deviation of 0.08 wt.%; Hämmerlein skarn deposit, Erzgebirge, Germany) allows the subsequent enrichment in sphalerite (at borders or along microfractures) by diffusion. In general, the incorporation of trace elements into the chalcopyrite structure is not fully constrained yet. The fact that there is no agreement in the valence states of Cu and Fe requires caution in establishing substitution mechanisms. However, incorporation of trace elements is presumed to take place in the form of various coupled substitutions, including monovalent, divalent, trivalent (e.g., In and Ga), and tetravalent (e.g., Ge) ions (Belissont et al. 2019; Reich et al. 2020).

iii. Galena

Galena [PbS] is the main ore lead and an important silver ore mineral. Most of the publications related to the evaluation and incorporation mechanisms of elements in the galena structure have focused on those that tend to be concentrated in relatively large quantities (i.e., Ag, Sb, and Bi). For example, the mechanism for Ag enrichment in galena is via $Ag^{1+}+(Sb,Bi)^{3+} \leftrightarrow 2Pb^{2+}$ coupled substitutions (Van Hook 1960; Foord et al. 1988; Lueth et al. 2000; Chutas et al. 2008; Renock and Becker 2011; Wei et al. 2021). The studies of minor and trace elements carried out by George et al. (2015) allow improving the understanding of the incorporation of the mentioned elements and others not so well known to be present in galena. For example, ICP-MS analyses revealed lead sulfide could host traces of $Tl^{(1+)}$ and $Cu(^{1+})$, invoking a $(Ag,Cu,Tl)^{1+}+(Bi, Sb)^{3+} \leftrightarrow 2Pb^{2+}$ coupled substitution (George et al. 2015). Nevertheless, caution is needed since Ag, and the other elements may be present in galena as nanoparticles that are not detectable in time-resolved laser ablation spectra (e.g., Pb-Bi-Sb sulfosalts), requiring the use of TEM techniques (Ciobanu et al. 2011). Regarding critical

metals/metalloids, In, Ge, and Ga contents can become detectable by ICP-MS, but they are usually low and therefore, not economically significant.

iv. Stannite

Stannite [Cu_2FeSnS_4] is the most common tin sulfide mineral. It mainly occurs in magmatic-hydrothermal systems, usually intergrown with sphalerite and chalcopyrite (Kołodziejczyk et al. 2016; Shimizu and Shikazono 1985; Watanabe et al. 1994). Among critical metals/metalloids that can be hosted in stannite, In is reported in higher proportions related to Ge and Ga due to the similarity of In-S and Sn-S bond lengths, allowing higher temperature solid solutions of this element in its structure (Schroll 1999). Sphalerite and stannite usually display an oscillatory zonation, which has been attributed to an isothermal oscillatory crystallization due to possible fluctuations in fluid temperatures (Oen et al. 1980). The incorporation of indium in stannite can be contextualized in a sphalerite–stannite–roquesite pseudoternary system with a limited solid solution between the three endmembers (Oen et al. 1980).

Exceptionally high In contents were registered in stannite from the Toyoha Pb-Zn-Ag-In vein deposit (e.g., up to 9.85 wt.%; Ohta 1989) and in the Nghe An Sn sulfide vein deposits in Vietnam (e.g., up to 6 wt.%; Pavlova et al. 2015). Torró et al. (2019b) reported In values up to 4.11 wt.% in stannite from the Ánimas Volcanic Dome-Hosted Polymetallic deposit in Bolivia. Torró et al. (2019a) found contents up to 2.64 wt.% In in stannite from the Huari-Huari xenothermal vein deposit also in Bolivia. Significant In values were registered in Neves Corvo VMS deposit (e.g., up to 1.47 wt.%; Carvalho et al. 2018). Gallium and Ge contents, in contrast, are commonly present at much lower contents and often, below its lower limit of detection. Indium incorporation mechanisms into the stannite structure are, in general, poorly constrained. Torró et al. (2019a) suggest a $In^{3+} \leftrightarrow (Cu^{+} + 1/2Sn^{4+})$ coupled substitution with the release of Fe^{2+} to the system.

v. Tetrahedrite-tennantite series

"Tetrahedrite group" minerals are the most common sulfosalts present in many hydrothermal sulfide deposits (Moëlo et al., 2008). This group is formally divided into five series regarding its constituents, including tetrahedrite, tennantite, freibergite, hakite, and giraudite series (Biagioni et al. 2020). The tetrahedrite-tennantite series [$Cu_{12}(Sb,As)_4S_{13}$], traditionally known as "fahlore", is the most widespread in the tetrahedrite group. Both minerals form a complete solid solution with a high capacity to contain major, minor, or trace elements not included in the theoretical formula (Makovicky and Karup-Møller 1994).

Studies on to minor and trace element contents in tetrahedrite-tennantite are scarce, with limited information regarding critical metals/metalloids. Significant In contents were reported in tennantite (e.g., up to 2.7 wt.%; Gaspar 2002) and tetrahedrite (e.g., up to 0.2 wt.%; Gaspar 2002, up to 178 ppm; Serranti et al. 2002, and up to 400 ppm; Pinto et al. 2014) from the Neves-Corvo VMS deposit. Likewise, notable Ge values were detected in tennantite from the Tsumeb deposit (e.g., up to 0.14 wt.%; Kriesel 1924; up to 0.5 wt.%.; Frondel and Ito 1957, and up to 700 ppm; Lombaard et al. 1986). However, the replacement of germanite [$Cu_{13}Fe_2Ge_2S_{16}$] by tetrahedrite-tennantite in Tsumeb would suggest the possibility that impurities (nano- or micro-inclusions) of the first occur in the analyzed tennantite grains (Klünder et al. 2003). Important Ge contents were also reported in tennantite from the Lisheen Irish-type carbonate-hosted Zn–Pb deposit in Ireland (e.g., up to 1000 ppm; Wilkinson et al. 2005). However, the contents of the three elements in fahlore are normally very low, often below their detection limits and hence, the abovementioned examples can be considered exceptional.

c. Mining industry in Peru: some data and a realization that little is still known about critical metals in Peruvian deposits

The mining industry is considered one of the most important economic activities in Peru. It is the main source of foreign exchange income, contributing 10% of GDP and 60% of tax collection (SNMPE 2020). In addition, it represents about 55% of the country's total exports. As a mining country, Peru is one of the most attractive destinations worldwide due to its privileged mineralogical variety and its reserves. Currently, Peru occupies the first positions not only in the Latin American context but also worldwide regarding raw materials production, mainly metallic (USGS 2021). Table 4 shows a summary table.

In Peru, most mining companies that exploit deposits with reported or potential economically significant contents of critical metals/metalloids (including those studied in this thesis) do not take into account these potential by-products to enhance ore value. This omission may be harmful both for the potential economic benefit these companies can obtain as the derived benefit for the country. Furthermore, the lack of mineralogical knowledge of the carrier phases of these elements and their distribution may hinder an efficient mineralurgical and metallurgical extraction.

Table 4. Peru's position in the world ranking of mining production (From USGS 2021)

Product	L. America	World
Gold	**1**	8
Copper	2	2
Silver	2	2
Zinc	**1**	3
Lead	**1**	4
Tin	**1**	4
Molybdenum	2	4
Cadmium	2	9
Phosphate rock	2	10
Diatomite	**1**	5
Indium	**1**	7
Andalusite (and related. minerals)	**1**	4
Selenium	**1**	10

Few studies regarding the evaluation of trace element contents (particularly In, Ge, and Ga) in Peruvian deposits have been carried out. The first work, pioneer, focused on identifying critical metal/metalloid contents in mineral deposits from Peru was carried out by Soler (1987). The study was based on whole-rock geochemistry of 1500 polymetallic concentrates and composite samples from 89 polymetallic deposits in the Central Andes. The elements analyzed by the author include Cd, In, Ge, Ga, Ag, Bi, Se, Hg, and Sn. The elements preferentially concentrated in Zn concentrates (i.e., sphalerite-rich) were Cd, In, Ge, and Ga. Soler (1987) divided the deposits into two large groups: a first group with low Cd and high In (In / Cd > 0.10) and a second group with medium to high Cd and low In (In/Cd <0.05). In low-temperature MVT type deposits hosted in the Pucará Group, Soler (1987) reported low In and high Ge values in Zn concentrates (e.g., up to 130 ppm Ge in Shalipayco). In contrast, in Cordilleran-type deposits the author reports low Ge and high In contents (e.g., Carahuacra, up to 290 In). However, the above is not an absolute rule since some meso- to epithermal deposits presented significant Ge contents. For example, the Sayapullo deposit (Hualgayoc area) yielded the highest Cd (5840 ppm), In (240 ppm), Ge (310 ppm), and Ga (855 ppm) values in the polymetallic province of the Central Andes in Peru. Thus, it can be deduced that, in general, deposits with high In content and high In/Cd ratios can also present high contents of Ga. For this reason, Soler (1987) concluded that the abundance of In, Ge, and Ga is not only controlled by the crystallization temperature but also by other factors such as the typology of the ore deposit, the age and nature of the host rocks, and the geographical position of the deposits. Noteworthy, the study performed by Soler (1987) was carried out in few samples per deposit and lacked systematic petrography of the studied samples. Consequently, few conclusions can be drawn on the relative distribution of In, Ge, and Ga throughout the mineralized

districts (i.e., spatial control) and the evolution of their concentration over time throughout the life of the mineralizing system (i.e., temporary control).

In recent years, the evaluation of trace elements in Peruvian deposits has been developed using the LA-ICP-MS technique on single ore minerals. Indium, Ge, and Ga evaluation in minerals of Peruvian ore deposits were carried out by Rottier et al. (2016, 2018) from the giant Cerro de Pasco Cordilleran deposit. Rottier et al. (2018) estimated significant contents of In (165 - 17 ppm; up to 1449 ppm), Ga (58–1.7 ppm, up to 423 ppm), and Ge (4.3–3.5 ppm, up to 71 ppm) in sphalerite. Likewise, Mondillo et al. (2018b) analyzed sphalerite samples from the Cristal MVT project (Bongará province) with significant Ge contents (up to 231-31 ppm; up to 386 ppm).

References

Achzet B (2012) Empirische analyse von preis-und verfügbarkeitsbeeinflussenden indikatoren unter Berücksichtigung der Kritikalität von Rohstoffen. Hamburg, disserta Verlag

Achzet B, Helbig C (2013) How to evaluate raw material supply risks—an overview. Resour Policy 38:435–47

Alfantazi AM, Moskalyk RR (2003) Processing of indium: a review. Miner Eng 16:687–694

Andersen JCØ, Dendle JE, Stickland RJ (2009) Indium in main stage polymetallic mineralisation in West Cornwall. Appl Earth Sci 118: 24–25

Andersen JC, Stickland RJ, Rollinson GK, Shail RK (2016) Indium mineralisation in SW England: host parageneses and mineralogical relations. Ore Rev 78:213–238

Anderson CS (2018) Indium. U.S. Geological Survey, Mineral Commodity Summaries 2018. Washington DC, United States

Andersson P (2020) Chinese assessments of “critical” and “strategic” raw materials: concepts, categories, policies, and implications. Extr Ind Soc 7:127–137

Biagioni C, George LL, Cook NJ, Makovicky E, Moëlo Y, Pasero M, Sejkora J, Stanley CJ, Welch MD, Bosi F (2020) The tetrahedrite group: nomenclature and classification. Am Mineral 105:109–122

Balaram V (2019) Rare earth elements: a review of applications, occurrence, exploration, analysis, recycling, and environmental impact. Geosci Front 10:1285–1303

Bauer D, Diamond D, Li J, Sandalow D, Telleen P, Wanneret B (2010) Critical materials strategy, US Department of Energy, 171 p

Bauer ME, Seifert T, Burisch M, Krause J, Richter N, Gutzmer J (2019a) Indium-bearing sulfides from the Hämmerlein skarn deposit, Erzgebirge, Germany: evidence for late-stage diffusion of indium into sphalerite. Miner Deposita 54:175–192

Bauer ME, Burisch M, Ostendorf J, Krause J, Frenzel M, Seifert T, Gutzmer J (2019b) Trace element geochemistry of sphalerite in contrasting hydrothermal fluid systems of the Freiberg district, Germany: insights from LA-ICP-MS analysis, near-infrared light microthermometry of sphalerite-hosted fluid inclusions, and sulfur isotope geochemistry. Miner Deposita 54:237–262

Barteková E, Kemp R (2016) National strategies for securing a stable supply of rare earths in different world regions. Resour Policy 49:153–164

Belissont R, Boiron MC, Luais B, Cathelineau M (2014) LA-ICP-MS analyses of minor and trace elements and bulk Ge isotopes in zoned Ge-rich sphalerites from the Noailhac - Saint-Salvy deposit (France): insights into incorporation mechanisms and ore deposition processes. Geochim Cosmochim Ac 126:518–540

Belissont R, Muñoz M, Boiron MC, Luais B, Mathon O (2016) Distribution and oxidation state of Ge, Cu and Fe in sphalerite by µ-XRF and K-edge µ-XANES: insights into Ge incorporation, partitioning and isotopic fractionation. Geochim Cosmochim Ac 177:298–314

Belissont R, Munoz M, Boiron M, Luais B, Mathon O (2019) Germanium crystal chemistry in Cu bearing sulfides from micro-XRF mapping and micro-XANES spectrometry. Minerals 9:227–238

Benzaazoua M, Marion P, Pinto A, Migeon H, Wagner FE (2003) Tin and indium mineralogy within selected samples from the Neves Corvo ore deposit (Portugal): a multidisciplinary study. Miner Eng 16:1291–1302

Bernstein LR (1985) Germanium geochemistry and mineralogy. Geochim Cosmochim Ac 49:2409–2422

Bleiwas D (2010) Byproduct mineral commodities used for the production of photovoltaic cells. U.S. Geological Survey Circular 1365, pp 1-8

Bonnet J, Mosser-Ruck R, Caumon MC, Rouer O, Andre-Mayer AS, Cauzid J, Peiffert C (2016) Trace element distribution (Cu, Ga, Ge, Cd, and Fe) in sphalerite from the Tennessee

MVT deposits, USA, by combined EMPA, LA-ICP-MS, Raman spectroscopy, and crystallography. Can Mineral 54:1261–1284

Bu X, Meng G, Zhao Y, Shang Y, Zhang C (2009) Analysis and suggestions concerning China's advantageous strategic mineral resources. J Ind Technol Econ 5:27–30

Buchert M, Schüler D, Bleher D (2009) Critical metals for future sustainable technologies and their recycling potential. United Nations Environment Programme, 112 p

Buijs B, Sievers H (2011) Critical thinking about critical minerals: assessing risks related to resource security. Clingendael International Energy Programme, Hannover, Germany, 19 p

Butcher T, Brown T (2014) Gallium. In: Gunn G (ed) Critical Metals Handbook, Chicester, UK, pp 150- 176

Burke EAJ, Kieft C (1980) Roquesite and Cu–In-bearing sphalerite from Långban, Bergslagen, Sweden. Can. Mineral 18:361–363

Cabri LJ, Campbell JL, Gilles Laflamme JH, Leigh RG, Maxwell JA, Scott JD (1985) Proton-microprobe analysis of trace elements in sulfides from some massive-sulfide deposits. Can Mineral 23:133–148

Cacho A, Melgarejo JC, Camprubí A, Torró L, Castillo-Oliver M, Torres B, Artiaga D, Tauler E, Martínez A, Campeny M, Alfonso P, Arce-Burgoa OR (2019) Mineralogy and distribution of critical elements in the Sn-W-Pb-Ag-Zn Huanuni Deposit, Bolivia. Minerals 9:753–779

Calvo G, Valero A, Valero A (2019) How can strategic metals drive the economy? Tungsten and tin production in Spain during periods of war. Extr Ind Soc 6:8–14

Carvalho JRS, Relvas JMRS, Pinto AMM, Frenzel M, Krause J, Gutzmer J, Reis T (2018) Indium and selenium distribution in the Neves-Corvo deposit, Iberian Pyrite Belt, Portugal. Mineral Mag 82:S5–S41

Castilloux R (2016) Rare earth elements: market issues and outlook. Adamas intellingece Report, USA, 10 p

Cave B, Lilly R, Hong W (2020) The effect of co-cristallising sulphides and precipitation mechanisms on sphalerite geochemistry: a case study from the Hilton Zn-Pb (Ag) deposit, Australia. Minerals 10:797–820

CGS (2016) Serving National Energy and Mineral Resources Security. Achievements of China Geological Survey, Beijing: Dizhi Chubanshe 2016

Chakhmouradian AR, Smith MP, Kynicky J (2015) From “strategic” tungsten to “green” neodymium: a century of critical metals at a glance. Ore Geol Rev 64:455– 458

Chaplygin IV, Mozgova NN, Mokhov AV, Koporulina EV, Bernhardt HJ, Bryzgalov IA (2007) Minerals of the system ZnS-CdS from fumaroles of the Kudriavy volcano, Iturup Island, Kuriles, Russia. Can Mineral 45:709–722

Chen Y (2002) Establishing a reserve system of strategic mineral resources in China. Land Resour 1:20–21

Chen Q, Wang G (2007) Definition of China’s non-energy strategic minerals and evaluation of their importance. Resour Econ 1:18–21

Chutas NI, Kress VC, Ghiorso MS, Sack RO (2008) A solution model for high-temperature PbS-$AgSbS_2$-$AgBiS_2$ galena. Am Mineral 93:1630–1640

Ciobanu CL, Cook NJ, Utsunomiya S, Pring A, Green L (2011) Focussed ion beam-transmission electron microscopy applications in ore mineralogy: bridging micro- and nanoscale observations. Ore Geol Rev 42:6–31

Cook NJ, Ciobanu CL, Pring A, Skinner W, Shimizu M, Danyushevsky L, Saini-Eidukat B, Melcher F (2009) Trace and minor elements in sphalerite: a LA-ICP-MS study. Geochim Cosmochim Ac 73:4761–4791

Cook NJ, Ciobanu CL, Williams T (2011a) The mineralogy and mineral chemistry of indium in sulphide deposits and implications for mineral processing. Hydrometallurgy 108:226–228

Cook NJ, Sundblad K, Valkama M, Nygård R, Ciobanu CL, Danyushevsky L (2011b) Indium mineralisation in A-type granites in southeastern Finland: insights into mineralogy and partitioning between coexisting minerals. Chem Geol 284:62–73

Cook NJ, Ciobanu CL, Brugger J, Etschmann B, Howard DL, de Jonge MD, Ryan C, Paterson D (2012) Determination of the oxidation state of Cu in substituted Cu-In-Fe-bearing sphalerite via µXANES spectroscopy. Am Mineral 97:476–479

Cook NJ, Etschmann B, Ciobanu CL, Geraki K, Howard DL, Williams T, Rae N, Pring A, Chen G, Johannessen B, Brugger J (2015) Distribution and substitution mechanism of Ge in a Ge-(Fe)-bearing sphalerite. Minerals 5:117–132

Department of Defense (2013) Strategic and critical materials report on stockpile requirements. Office of the Under Secretary of Defense for Acquisition, Technology and Logistics, 189 p

Deschamps Y, Bailly L, Bouchot V, Gentilhomme P, Hocquard C, Lerouge C, Milesi JP, Nicol N, Ollivier P, Pelon R, Save M, Thomassin JF (2002) Métaux rares à forte demande industrielle. Tantale, germanium, indium et gallium. Etat de l'art en économie, traitement des minerais, gîtologie, 284 p

Dittrich T, Seifert T, Gutzmer J (2011) Gallium, can future demand be met by geological and technological availability? Department of Mineralogy, Technische Universität Bergakademie Freiberg, Germany, 3 p

Dutrizac JE, Jambor JL, Chen TT (1986) Host minerals for the gallium-germanium ores of the Apex Mine, Utah. Econ Geol 81: 946–950

Erdmann L, Graedel TE (2011) Criticality of non-fuel minerals: a review of major approaches and analyses. Environ Sci Technol 45:7620–7630

European Commission (2020) Study on the EU's list of Critical Raw Materials. European Commission, Brussels, Belgium, 158 p

Ferro P, Bonollo F (2019) Materials selection in a critical raw materials perspective. Mater Des 177:107848

Foley N, Jaskula B (2013) Gallium—a smart metal. U.S. Geological Survey Fact Sheet 2013–3006, 2 p

Foley N, Jaskula B, Kimball B, Schulte F (2017) Gallium. In: Critical Mineral Resources of the United States, Economic and Environmental Geology and Prospects for Future Supply, U.S. Geological Survey, Virginia, pp 1–26

Foord EE, Shawe DR, Conklin NM (1988) Coexisting galena, PbS and sulfosalts: evidence for multiple episodes of mineralization in the Round Mountain and Manhattan Gold districts, Nevada. Can Mineral 26:355–376

Fortier SM, Nassar NT, Lederer GW, Brainard J, Gambogi J, McCullough EA (2018) Draft critical mineral list—summary of methodology and background information—U.S. Geological Survey technical input document in response to Secretarial Order No. 3359: U.S. Geological Survey Open-File Report 2018–1021, 15 p

Frenzel M, Ketris MP, Gutzmer J (2014) On the geological availability of germanium. Miner Deposita 49:471–486

Frenzel M, Hirsch T, Gutzmer J (2016a) Gallium, germanium, indium, and other trace and minor elements in sphalerite as a function of deposit type – a meta-analysis. Ore Geol Rev 76:52–78

Frenzel M, Ketris MP, Seifert T, Gutzmer J (2016b) On the current and future availability of gallium. Resour Policy 47:38–50

Frenzel M, Mikolajczak C, Reuter MA, Gutzmer J (2017) Quantifying the relative availability of high-tech by-product metals – the cases of gallium, germanium and indium. Res Policy 52:327–335

Frondel C, Ito J (1957) Geochemistry of germanium in the oxidized zone of the Tsumeb mine, South-West Africa. Am Mineral 42:743–753

Gaspar OC (2002) Mineralogy and sulfide mineral chemistry of the Neves Corvo ores, Portugal: insight into their genesis. Can Mineral 40:611–636

George L, Cook NJ, Cristiana C, Wade BP (2015) Trace and minor elements in galena: a reconnaissance LA-ICP-MS study. Am Mineral 100:548–569

George LL, Cook NJ, Ciobanu CL (2016) Partitioning of trace elements in co-crystallized sphalerite–galena–chalcopyrite hydrothermal ores. Ore Geol Rev 77:97–116

George LL, Cook NJ, Crowe BB, Ciobanu CL (2018) Trace elements in hydrothermal chalcopyrite. Mineral Mag 82:59–88

González A, Córdoba P, Moreno N (2018) Germanium: current and novel recovery processes. In: Lee S (ed) Advanced Material and Device Applications with Germanium, InterchOpen, London, UK, pp 9–29

Government Printing Office (1979) Strategic and critical materials stockpilling Act. 96th Congress

Graedel TE, Gunn G, Tercero Espinoza L (2014) Metal resources, use and criticality. In: Gunn G (ed) Critical Metals Handbook, Chicester, UK, pp 1–19

Gray F, Kramer DA, Bliss JD (2005) Gallium and gallium compounds. In: Kirk-Othmer R (ed) Kirk-Othmer Encyclopedia of Chemical Technology, New York, USA, pp 337–364

Grandell L, Lehtilä A, Kivinen M, Koljonen T, Kihlman S, Lauri LS (2016) Role of critical metals in the future markets of clean energy technologies. Renew Energy 95:53–62

Guberman DE (2015) Germanium. U.S. Geological Survey, Mineral Commodity Summaries 2015. Washington DC

Hagelüken C (2012) Recycling the platinum group metals: a European perspective. Platin Met Rev 56:29–35

Hayes SM, McCullough EA (2018) Critical minerals: a review of elemental trends in comprehensive criticality studies. Resour Policy 59:192–199

Hebei Provincial Department of Land and Resources (2017) Classification of Strategic Emerging Minerals

Höll R, Kling M, Schroll E (2007) Metallogenesis of germanium—a review. Ore Geol Rev 30:145–180

Hörmann PK (1963) Zur Geochemie des Germaniums. Geochim Cosmochim Ac 8:861–876

Hu P (1982) The battle for the world's strategic mineral resources. Geol Prospect 6:68–70

Humphries M (2013) Rare earth elements: the global supply chain. Congressional Research Service Report, pp 1–27

Huy D, Liedtke M (2016) Supply and demand of lithium and gallium: Hannover, Germany, Bundesanstalt für Geowissenschaften und Rohstoffe, 50 p

Ishihara S, Endo Y (2007) Indium and other trace elements in volcanogenic massive sulphide ores from the Kuroko, Besshi and other types in Japan. Bulletin of the Geological Survey of Japan, 58:7–22

Jaffe R, Price J, Ceder G, Eggert R, Graedel T, Gschneider K, Hitzman M, Houle F, Hurd A, Kelley R, King A, Milliron D, Skinner B, Slakey F (2011) Energy critical elements:

securing materials for emerging technologies. A report by APS panel on public affairs and the Material Research Society, 29 p

Jambor JL, Owens DR, Grice JD, Feinglos MN (1996) Gallobeudantite, $PbGa_3[(AsO_4),(SO_4)]_2(OH)_6$, a new mineral species from Tsumeb, Namibia, and associated new gallium analogues of the alunite-jarosite family. Can Mineral 34:1305–1315

Jin Y, Kim J, Guillaume B (2016) Review of critical material studies. Resour Conserv Recycl 113:77–87

Johan Z (1988) Indium and germanium in the structure of sphalerite: an example of coupled substitution with copper. Mineral Petrol 39:211–229

Kelley KD, Leach DL, Johnson CA, Clark JL, Fayek M, Slack JF, Anderson VM, Ayuso RA, Ridley WI (2004) Textural, compositional, and sulfur isotope variations of sulfide minerals in the Red Dog Zn-Pb-Ag deposits, Brooks Range, Alaska: Implications for Ore formation. Econ Geol 99:1509–1532

Kesler SE, Simon AC (2015) Mineral resources, economics and the environment. Cambridge University Press, 434 p

Kiggins RD (2015) The political economy of rare earth elements: rising powers and technological change, first ed. Palgrave Macmillan, Basingstoke, UK, 242p

Kitco (2021) Strategic Metals. https://www.kitco.com/strategic-metals/ (Accessed October 27, 2021)

Kołodziejczyk J, Pršek J, Voudouris P, Melfos V, Asllani B (2016) Sn-bearing minerals and associated sphalerite from lead-zinc deposits, Kosovo: an electron microprobe and LA-ICP-MS study. Minerals 6:42–58

Kriesel FW (1924) Über die analyse des neuen germanium-gallium-minerals “Germanit”. Chem Zeit 48:961–972

Kristof K, Hennicke P (2010) Material efficiency and resource conservation (MaRess) project. Wuppertal Institute for Climate, Environment and Energy

Klünder Hansen M, Makovicky E, Karup-Møller S (2003) Exploratory studies on substitutions in tetrahedrite-tennantite solid solution. Part IV. Substitution of germanium and tin. N Jb Miner Abh 179:43–71

Leach DL, Taylor RD, Fey DL, Diehl SF, Saltus RW (2010) A deposit model for Mississippi Valley-type lead-zinc ores, chap A. In: mineral deposit models for resource assessment, U.S Geological Survey Scientific Investigations Report 2010–5070–A, 52 p

Li Z, Ye L, Hu Y, Wei C, Huang Z, Yang Y, Danyushevsky L (2020) Trace elements in sulfides from the Maozu Pb-Zn deposit, Yunnan Province, China: implications for trace-element incorporation mechanisms and ore genesis. Am Mineral 105:1734–1751

Lindeberg T (2013) Indium analysis and small-scale distribution in sulphides from the Lindbom prospect, Långban area, western Bergslagen Ore Province. Uppsala universitet, Självständigt arbete Nr 48

Lloyd S, Lee J, Clifton A, Elghali L, France C (2012) Recommendations for assessing materials criticality. Proc Inst Civ Eng 165:191–200

Lokanc M, Eggert R, Redlinger M (2015) The availability of indium: the present, medium term, and long term. Technical report, Golden, Colorado, USA, 90 p

Lockington JA, Cook NJ, Ciobanu CL (2014) Trace and minor elements in sphalerite from metamorphosed sulphide deposits. Mineral Petrol 108:873–890

Lombaard AF, Günzel A, Innes J, Krüger TL (1986) The Tsumeb lead-zinc-copper-silver deposit, South West Africa/Namibia. In: Anhaeusser CR, Maske S (eds) Mineral Deposits of Southern Africa, Geological Society of South Africa, Johannesburg, pp 1761–1782

Lueth VW, Megaw PKM, Pingitore NE, Goodell PC (2000) Systematic variation in galena solid-solution compositions at Santa Eulalia, Chihuahua, Mexico. Econ Geol 95:1673–1688

Makovicky E, Karup-Møller S (1994) Exploratory studies on substitution of minor elements in synthetic tetrahedrite. Part I. Substitution by Fe, Zn, Co, Ni, Mn, Cr, V and Pb. Unit-cell parameter changes on substitution and structural role of "Cu^{2+}". N Jb Miner Abh 167: 89–123

Mancheri NA (2015) World trade in rare earths, Chinese export restrictions, and implications. Resour Policy 46:262–271

Márquez-Zavalía MF, Vymazalová A, Galliski MA, Watanabe Y, Murakami H (2020) Indium-bearing paragenesis from the Nueva Esperanza and Restauradora veins, Capillitas mine, Argentina. J Geosci 65:97–109

McFall KA (2016) Critical metals in porphyry copper deposits. M.Sc. thesis. University of Southampton, Southampton, UK, 269 p

Melcher F, Oberthür T, Rammlmair D (2006) Geochemical and mineralogical distribution of germanium in the Khusib Springs Cu-Zn-Pb-Ag sulfide deposit, Otavi Mountain Land, Namibia. Ore Geol Rev 28:32–56

Melcher F, Buchholz P (2014) Germanium. In: Gunn G (ed) Critical Metals Handbook, Chicester, UK, pp 177-203

Mills SJ, Kampf AR, Raudsepp M, Christy AG (2009) The crystal structure of Ga-rich plumbogummite from Tsumeb, Namibia. Mineral Mag 73:837–845

Moëlo Y, Makovicky E, Mozgova NN, Jambor JL, Cook N, Pring A, Paar W, Nickel EH, Graeser S, Karup-Møller S, Balic-Žunic T, Mumme WG, Vurro F, Topa D, Bindi L, Bente K, Shimizu M (2008) Sulfosalt systematics: a review. Report of the sulfosalt sub-committee of the IMA Commission on Ore Mineralogy. Eur J Mineral 20:7–46

Mondillo N, Arfè G, Boni M, Balassone G, Boyce A, Joachimski M, Kang JS, Villa IM (2018a) The Cristal zinc prospect (Amazonas region, northern Peru). Part I: New insights on the sulfide mineralization in the Bongará province. Ore Geol Rev 94:261–276

Mondillo N, Arfè G, Herrington R, Boni M, Wilkinson C, Mormone A (2018b) Germanium enrichment in supergene settings: evidence from the Cristal nonsulfide Zn prospect, Bongará district, northern Peru. Miner Deposita 53:155–169

Monnet A, Abderrahim AA (2018) Report on major trends affecting future demand for critical raw materials

Mordberg LE, Stanley CJ, Germann K (2001) Mineralogy and geochemistry of trace elements in bauxites: the Devonian Schugorsk deposit, Russia. Mineral Mag 65:81–101

Moskalyk RR (2004) Review of germanium processing worldwide. Miner Eng 17:393–402

Moura MA, Botelho NF, Carvalho de Mendonça F (2007) The indium-rich sulfides and rare arsenates of the Sn-In-mineralized Mangabeira A-type granite, central Brazil. Can Mineral 45:485–496

Murakami H, Ishihara S (2013) Trace elements of indium-bearing sphalerite from tin-polymetallic deposits in Bolivia, China and Japan: a femto-second LA-ICPMS study. Ore Geol Rev 53:223–243

Nassar N, Xun S, Fortier S, Schoeberlein D (2016) Assessment of critical minerals: screening methodology and initial application. National Science and Technology Council Executive office of the President of the United States, Washington, 47 p

National Academy of Science (2008) Minerals, critical minerals and the U.S. Economy. National Academies Press, Washington, 245 p

National Research Council (2008) Minerals, critical minerals, and the U.S. Economy. National Academies Press, Washington, 245 p

Oen IS, Kager P, Kieft C (1980) Oscillatory zoning of a discontinuous solid-solution series: sphalerite-stannite. Am Mineral 65:1220–1232

Ohta E (1989) Occurrence and chemistry of Indium-containing minerals from the Toyoha Mine, Hokkaido, Japan. Min Geol 39:355–372

Paradis S (2015) Indium, germanium and gallium in volcanic- and sediment-hosted base-metal sulphide deposits. In: Simandl GJ, Neetz M (eds) Symposium on Strategic and Critical Materials Proceedings, British Columbia Geological Survey Paper, Canada, pp 23–29

Pattrick RAD, Dorling M (1991) The substitution of indium and copper in natural sphalerite: a study using electron microscopy. In: Pagel M, Leroy S (eds) Source, Transport and Deposition of Metals, Balkema, Rotterdam, The Netherlands, pp 223-226

Pattrick RAD, Dorling M, Polya DA (1993) TEM study of indium and copper-bearing growth-banded sphalerite. Can Mineral 31:105–117

Pattrick RAD, Mosselmans JFW, Charnock JM (1998) An x-ray absorption study of doped sphalerites. Eur J Mineral 10:239–249

Pavlova GG, Palessky SV, Borisenko AS, Vladimirov AG, Seifert T, Phan LA (2015) Indium in cassiterite and ores of tin deposits. Ore Geol Rev 66:99–113

Peng Q (2017) Improve strategic minerals supply capacity and promote the rapid development of emerging industries. Land Resour 1:1–3

Picot P, Pierrot R (1963) La roquesite, premier minéral d'indium : CuInS2. Bulletin de la Société française de Minéralogie et de Cristallographie, 86:7–14

Pinto A, Relvas JMRS, Carvalho JRS, Liu Y, Pacheco N, Pinto F, Fonseca R (2014) High-Tech metals in the zinc-rich massive ores of the Neves Corvo deposit: metais de alta

tecnologia nos minérios maciços zincíferos do depósito de Neves Corvo. Comun Geol Espec II 101:825–828

Qi Y (2002) Research on China's mineral resources reserve. Korean Hum Resour Dev Strategy Inst 6:53–54

Renock D, Becker U (2011) A first principles study of coupled substitution in galena. Ore Geol Rev 42:71–83

Reich M, Román N, Barra F, Morata D (2020) Silver-rich chalcopyrite from the active Cerro Pabellón geothermal system, northern Chile. Minerals 10:113–125

Rongguo C, Juan G, Liwen Y, Huy D, Liedtke M (2016) Supply and demand of lithium and gallium (Information Center of Ministry of Land and Resources, Federal Institute for Geosciences and Natural Resources, Hannover, Germany), 52 p

Rottier B, Kouzmanov K, Wälle M, Bendezú R, Fontboté L (2016) Sulfide replacement processes revealed by textural and LA-ICP-MS trace element analyses: example from the early mineralization stages at Cerro de Pasco, Peru. Econ Geol 111:1347–1367

Rottier B, Kouzmanov K, Casanova V, Wälle M, Fontboté L (2018) Cyclic dilution of magmatic metal-rich hypersaline fluids by magmatic low-salinity fluid: a major process generating the giant epithermal polymetallic deposit of Cerro de Pasco, Peru. Econ Geol 113:825–856

Rudnick RL, Gao S (2014) Composition of the continental crust. In: Turekian HD, Holland KK (eds) Treatise on Geochemistry, 2nd edn. Elsevier, Oxford, UK, pp 1-51

Sahlström F, Arribas A, Dirks P, Corral I, Chang Z (2017) Mineralogical distribution of germanium, gallium and indium at the Mt Carlton high-sulfidation epithermal deposit, NE Australia and comparison with similar deposits worldwide. Minerals 7:213–241

Saini-Eidukat B, Melcher F, Lodziak J (2009) Zinc-germanium ores of the Tres Marias mine, Chihuahua, Mexico. Miner Deposita 44:363–370

Schlüter J, Malcherek T, Mihailova B (2014) Galloplumbogummite from Tsumeb, Namibia, a new member of the alunite group with tetravalent charge balance. N Jb Miner Abh 191:301–309

Schmid M (2019) Mitigating supply risks through involvement in rare earth projects: Japan's strategies and what the US can learn. Resour Policy 63:1–10

Schorr S, Wagner G (2005) Structure and phase relations of the Zn2x(CuIn)1−xS2 solid solution series. J Alloy Compd 396:202–207

Schroll E (1999) Indium: element and geochemistry. In: Marshall CP, Fairbridge RW (eds) Geochemistry: Encyclopedia of Earth Science, Springer, Dordrecht, Germany, pp 339–341

Schwarz-Schampera U, Herzig P (2002) Indium: geology, mineralogy, economics. Springer-Verlag, Berlin, 257 p

Schwarz-Schampera U, Terblanche H, Oberthür T (2010) Volcanic-hosted massive sulfide deposits in the Murchison greenstone belt, South Africa. Miner Deposita 45:113–145

Schwarz-Schampera U (2014) Indium. In: Gunn G (ed) Critical Metals Handbook, Chicester, UK, pp 204-229

Seward TM, Henderson CMB, Charnock JM (2000) Indium (III) chloride complexing and solvation in hydrothermal solutions to 350°C: an EXAFS study. Chemical Geol 167: 117–127

Serranti S, Ferrini V, Umberto M, Cabri LJ (2002) Trace-element distribution in cassiterite and sulfides from Rubané and massive ores of the Corvo deposit, Portugal. Can Mineral 40:815–835

Shanks WCP, III Kimball BE, Tolcin AC, Guberman DE (2017) Germanium and indium, chap I. In: Schulz KJ, DeYoung JH, Jr Seal, RR II Bradley DC (eds) Critical mineral resources of the United States Economic and environmental geology and prospects for future supply, U.S. Geological Survey. Professional Paper 1802, pp I1–I26

Shannon RD (1976) Revised effective ionic radii and systematic studies of interatomic distances in halides and chalcogenides. Ac Crystallogr Section A (Foundations) 32:751 – 767

Shimizu T, Morishita Y (2012) Petrography, chemistry, and near-infrared microthermometry of indium-bearing sphalerite from the Toyoha polymetallic deposit, Japan. Econ Geol 107:723–735

Shimizu M, Shikazono N (1985) Iron and zinc partitioning between coexisting stannite and sphalerite: a possible indicator of temperature and sulfur fugacity. Miner Deposita 20:314–320

Sina (2016) China identifies 24 types of minerals as strategic minerals (Accessed 5 February 2019)

Skirrow RG, Huston DL, Mernagh TP, Thorne JP (2013) Critical commodities for a high-tech world: Australia's potential to supply global demand. Geoscience Australia, Canberra, 118 p

Sociedad Nacional de Minería, Petróleo y Energía (2021) https://www.snmpe.org.pe/ (Accessed on 22 October 2021)

Soler P (1987) Variations des teneurs en éléments mineurs (Cd, In, Ge, Ga, Ag, Bi, Se, Hg, Sn) des minerais de Pb-Zn de la province polymétallique des Andes du Pérou Central. Miner Deposita 22:135–143

Song X, Tan H (1996) Geochemical characteristics of the Fankou Pb–Zn deposits, northern Guangdong, South-China. In: Sangster DF (ed) Carbonate-hosted lead–zinc deposits, SEG Spec Publ 4:350–355

Sykes JP, Wright JP, Trench A, Miller P (2016) An assessment of the potential for transformational market growth amongst the critical metals. Appl Earth Sci 125:21–56

Taylor SR, McLennan SM (1995) The geochemical evolution of the continental crust. Rev Geophys 33:241–265

The White House (1974) Critical Imported Commodities. National Security Study Memorandum 197, Washington, United States

Thiele UK (2001) The current status of catalysis and catalyst development for the industrial process of poly(ethylene terephthalate) polycondensation. Int J Polym Mater 50:387–394

Tolcin AC (2017) Indium. U.S. Geological Survey, Mineral Commodity Summaries 2021. Washington DC, United States

Tolcin AC (2021) Germanium. U.S. Geological Survey, Mineral Commodity Summaries 2021. Washington DC, United States

Torró L, Melgarejo J, Gemmrich L, Mollinedo D, Cazorla M, Martínez Á, Pujol-Solà N, Farré-de-Pablo J, Camprubí A, Artiaga D, Torres B, Alfonso P, Arce O (2019a) Spatial and

temporal controls on the distribution of indium in xenothermal vein deposits: the Huari Huari District, Potosí, Bolivia. Minerals 9:304–342

Torró L, Cazorla M, Melgarejo J, Camprubí A, Gemmrich L, Campeny M, Artiaga D, Torres B, Martínez Á, Tarrés M, Mollinedo D, Alfonso P, Arce O (2019b) Indium mineralization in the volcanic dome-hosted Ánimas–Chocaya–Siete Suyos polymetallic deposit, Potosí, Bolivia. Minerals 9:604–646

UK House of Commons (2011) Strategically important metals. Fifth Report of Session 2010–12. House of Commons, London, UK, pp 146

US Public Laws (1939) Strategic and critical materials stockpiling act. Chapter 190, enacted June 7, 1939

USGS (2021) Mineral commodity summaries 2021. U.S. Geological Survey, 200 p

Van Hook HJ (1960) The ternary system Ag_2S-Bi_2S_3-PbS. Econ Geol 55:759–788

Wai CM, Wetherill GW, Wasson JT (1968) The distribution of trace quantities of germanium between metal, silicate and sulfide phases. Geochim Cosmochim Ac 32:1269–1278

Wang R (2009) Rethinking several issues concerning China's strategic mineral exploration work. Geological Bulletin of China 7:817–820

Wang D (2019) The significance of research on critical minerals, determination of mineral resources, resource attributes, progress in prospecting, and main directions. Acta Sin 93:1189–1209

Watanabe M, Koshino K, Myint K, Miyazaki K, Nishido H (1994) Stannite from the Otoge kaolin-pyrophyllite deposits, Yamagata prefectura, NE Japan and its genetical significance. Resour Geol 44:439–444

Watari T, Nansai K, Nakajima K (2020) Review of critical metal dynamics to 2050 for 48 elements. Resour Conserv Recycl 155:104669

Wedepohl HK (1995) The composition of the continental crust. Geochim Cosmochim Acta 59:1217–1232

Wei C, Huang Z, Yan Z, Hu Y, Ye L (2018) Trace element contents in sphalerite from the Nayongzhi Zn-Pb deposit, northwestern Guizhou, China: insights into incorporation mechanisms, metallogenic temperature and ore genesis. Minerals 8:490–513

Wei C, Ye L, Hu Y, Danyushevsky L, Li Z, Huang Z (2019) Distribution and occurrence of Ge and related trace elements in sphalerite from the Lehong carbonate-hosted Zn-Pb deposit, northeastern Yunnan, China: insights from SEM and LA-ICP-MS studies. Ore Geol Rev 115:103175

Wei C, Ye L, Hu Y, Huang Z, Danyushevsky L, Wang H (2021) LA-ICP-MS analyses of trace elements in base metal sulfides from carbonate-hosted Zn-Pb deposits, South China: a case study of the Maoping deposit. Ore Geol Rev 130:103945

Werner TT, Mudd GM, Jowitt SM (2015) Indium: Key issues in assessing mineral resources and long-term supply from recycling. Appl Earth Sci 124:213–226

Werner TT, Mudd GM, Jowitt SM (2017) The world's by-product and critical metal resources part III: a global assessment of indium. Ore Geol Rev 86:939–956

Wilkinson JJ, Eyre SL, Boyce AJ (2005) Ore-forming processes in Irish-type carbonate-hosted Zn-Pb deposits: evidence from mineralogy, chemistry, and isotopic composition of sulfides at the Lisheen Mine. Econ Geol 100:63–86

Wilson J (2019) Character and genesis of indium mineralization, East, Kemptville, Nova Scotia. M.Sc. thesis. University of Windsor, Ontario, Canada, 115 p

Wittmann A (1974) Indium. 49-A Crystal chemistry. In: Wedepoh1 KH (ed) Handbook of geochemistry, Springer–Verlag, Berlin, Germany, vol. II/4, pp 49-A-1 - 49-A-8

Wood SA, Samson IM (2006) The aqueous geochemistry of gallium, germanium, indium and scandium. Ore Geol Rev 28:57–102

Xu J, Cook NJ, Ciobanu CL, Li X, Kontonikas-Charos A, Gilbert S, Lv Y (2020) Indium distribution in sphalerite from sulfide–oxide–silicate skarn assemblages: a case study of the Dulong Zn–Sn–In deposit, Southwest China. Miner Deposita 56:307–324

Xu J, Ciobanu CL, Cook NJ, Slattery A, Li X, Kontonikas-Charos A (2021) Phase relationships in the system ZnS-$CuInS_2$: insights from a nanoscale study of indium-bearing sphalerite. Am Mineral 106:192–205

Ye L, Cook NJ, Ciobanu CL, Yuping L, Qian Z, Tiegeng L, Wei G, Yulong Y, Danyushevsky (2011) Trace and minor elements in sphalerite from base metal deposits in South China: a LA-ICPMS study. Ore Geol Rev 39:188–217

Ye Y, Zhao C (2014) Classification of the importance of minerals in the third round of mineral resources planning. Land Resour 1: 48–49

Yuan G (2010) Establishing China's strategic minerals and protected minerals. China Dev Observ 7:31–33

Yuan B, Zhang C, Yu H, Yang Y, Zhao Y, Zhu C, Ding Q, Zhou Y, Yang J, Xu Y (2018) Element enrichment characteristics: insights from element geochemistry of sphalerite in Daliangzi Pb–Zn deposit, Sichuan, Southwest China. J Geochem Explor 186:187–201

Yudovich YE, Ketris MP (2003) Germanium in coals (in Russian). Komi Scientific Centre UrO Russian Academy of Sciences, Syktyvkar, 204 pp

Zepf V (2020) The dependency of renewable energy technologies on critical resources. In: The Material Basis of Energy Transitions, Elsevier, pp 49–70

Zhai MG, Wu FY, Hu RZ, Jiang SY, Li WC, Wang RC, Wang DH, Qi T, Qin KZ, Wen HJ (2019) Critical mineral resources of China: current views and challenges. China Sci Found 2:106–111

Zhang Z (1980) Mineral resources in Southern Africa and the conflict between the Soviet Union and the United States. World Econ 1:34–39

Zhang X (2002) History and current status of foreign mineral resource reserves. Land Resour 1:1–12

Zhang F, He X, Du Y, Wang Z, Lei X, Fang Y, Hu Y (2013). Thoughts on several important issues of China's strategic new minerals. China Mining Mag 22:7–11

Zhou L, Fan H, Ulrich T (2021) Editorial for special issue "critical metals in hydrothermal ores: Resources, recovery, and challenges." Minerals 11:299–303

CHAPTER II: GEOLOGY, MINERALOGY, AND CASSITERITE GEOCHRONOLOGY OF THE AYAWILCA Zn-Pb-Ag-In-Sn-Cu DEPOSIT, PASCO, PERU

Mineralium Deposita
https://doi.org/10.1007/s00126-021-01066-z

ARTICLE

Geology, mineralogy, and cassiterite geochronology of the Ayawilca Zn-Pb-Ag-In-Sn-Cu deposit, Pasco, Peru

Diego Benites[1] · Lisard Torró[1] · Jean Vallance[1] · Oscar Laurent[2,3] · Patrick Quispe[1] · Silvia Rosas[1] · María Francisca Uzieda[4] · Christopher S. Holm-Denoma[5] · Laura S. Pianowski[5] · Antoni Camprubí[6] · Vanessa Colás[6] · Álvaro Fernández-Baca[7] · Luis Giraldo[7] · Cyril Chelle-Michou[2] · Jorge Sáez[1] · Kalin Kouzmanov[4] · Lluís Fontboté[4]

Received: 5 February 2021 / Accepted: 22 June 2021

Abstract
The Ayawilca deposit in Pasco, Peru, represents the most significant recent base-metal discovery in the central Andes and one of the largest undeveloped In resources globally. As of 2018, it hosts an 11.7 Mt indicated resource grading 6.9% Zn, 0.16% Pb, 15 g/t Ag, and 84 g/t In, an additional 45.0 Mt inferred resource grading 5.6% Zn, 0.23% Pb, 17 g/t Ag, and 67 g/t In, and a separate Sn-Cu-Ag inferred resource of 14.5 Mt grading 0.63% Sn, 0.21% Cu, and 18 g/t Ag. Newly obtained U–Pb dates for cassiterite by LA-ICP-MS (22.77 ± 0.41 and 23.05 ± 2.06 Ma) assign the Ayawilca deposit to the Miocene polymetallic belt of central Peru. The polymetallic mineralization occurs as up to 70-m-thick mantos hosted by carbonate rocks of the Late Triassic to Early Jurassic Pucará Group, and subordinately, as steeply dipping veins hosted by rocks of the Pucará Group and overlying Cretaceous sandstones-siltstones of the Goyllarisquizga Group. Relicts of a distal retrograde magnesian skarn and cassiterite (stage pre-A) were identified in the deepest mantos. The volumetrically most important mineralization at Ayawilca comprises a low-sulfidation assemblage (stage A) with quartz, pyrrhotite, arsenopyrite, chalcopyrite, Fe-rich sphalerite, and traces of stannite and herzenbergite. Stage A sphalerite records progressive Fe depletion, from 33 to 10 mol% FeS, which is compatible with the observed transition from low- to a subsequent intermediate-sulfidation stage (B) marked by the crystallization of abundant pyrite and marcasite. Finally, during a later intermediate-sulfidation stage (C) sphalerite (up to 11 mol% FeS), galena, native bismuth, Cu-Pb-Ag sulfosalts, siderite, Mn-Fe carbonates, kaolinite, dickite, and sericite were deposited. This paragenetic evolution shows striking similarities with that at the Cerro de Pasco Cordilleran-type polymetallic deposit, even if at Ayawilca stage C did not reach high-sulfidation conditions. The occurrence of an early retrograde skarn assemblage suggests that the manto bodies at Ayawilca formed at the transition between distal skarn and skarn-free (Cordilleran-type) carbonate-replacement mineralization. Mineral assemblages define a T-fS_2 evolutionary path close to the pyrrhotite-pyrite boundary. Buffering of hydrothermal fluids by underlying Devonian carbonaceous phyllites of the Excelsior Group imposed highly reduced conditions during stage A mineralization ($\log fO_2 < -30$ atm). The low fO_2 favored efficient Sn mobility during stages pre-A and A, in contrast to other known ore deposits in the polymetallic belt of central Peru, in which the occurrence of Sn minerals is minor. Subsequent cooling, progressive sealing of vein walls, and decreasing buffering potential of the host rocks promoted the shift from low- (stage A) to intermediate-sulfidation (stages B and C) states. LA-ICP-MS analyses reveal significant In contents in Fe-rich sphalerite (up to 1.7 wt%), stannite (up to 1908 ppm), and chalcopyrite (up to 1185 ppm). The highest In content was found in stage A sphalerite that precipitated along with chalcopyrite and stannite, thus pointing to the early, low-sulfidation assemblage as prospective for this *high-tech* metal in similar mineral systems. Indium was likely incorporated into the sphalerite crystal lattice via $Cu^{+} + In^{3+} \leftrightarrow 2\ Zn^{2+}$ and $(Sn, Ge)^{4+} + (Ga, In)^{3+} + (Cu + Ag)^{+} \leftrightarrow 4\ Zn^{2+}$ coupled substitutions. Indium incorporation mechanisms into the stannite and chalcopyrite crystal lattices remain unclear.

Keywords Indium · Critical metals · Central Andes · Cordilleran-type deposits · U–Pb cassiterite geochronology

Editorial handling: B. Lehmann.

Extended author information available on the last page of the article

Published online: 13 September 2021

Introduction

The Ayawilca Zn-Pb-Ag-In-Sn-Cu deposit hosts one of the largest resources among recent base-metal discoveries in central Peru and throughout the Andes. The project is located 40 km northwest of the historic Cerro de Pasco Zn-Ag–Cu mine, and 20 km northeast of the Uchucchacua Ag-Mn mine (Fig. 1). The overall resource at Ayawilca as of November 2018 stands at 11.7 Mt of indicated resources with grades of 6.9% Zn, 0.16% Pb, 15 g/t Ag, and 84 g/t In, equivalent to 983 t of contained In, assuming a 75% metallurgical recovery. Additionally, there are 45.0 Mt of inferred resources with grades of 5.6% Zn, 0.23% Pb, 17 g/t Ag, and 67 g/t In, equivalent to 3003 t of contained In, using the same metallurgical assumptions. The project also hosts a separate Sn-Cu-Ag inferred resource of 14.5 Mt with grades of 0.63% Sn, 0.21% Cu, and 18 g/t Ag (Peralta et al. 2019).

Ayawilca was discovered by Tinka Resources Ltd. in 2012 following a scout drilling program aimed at a district target 2 km south of the Colquipucro sandstone-hosted Ag occurrence, where Tinka had focused its exploration efforts since staking the area in 2005. Zinc-rich mineralization, occurring as replacement bodies (mantos) in a Late Triassic–Early Jurassic carbonate sequence underlying the same gently dipping and unaltered Cretaceous sandstone unit that hosts Colquipucro, was identified and explored over the following years. The main mineralized base metal bodies are blind at Ayawilca. Thin east–west trending, Ag-rich veins with abundant Mn-Fe oxides cropping out over a few hundred meters in the exposed sandstone are the only surface evidence of the deposit. Initial drilling programs defined the West Ayawilca zone, with step-out drilling subsequently finding the Central Ayawilca and East Ayawilca zones. Following ground magnetics, airborne magnetics,

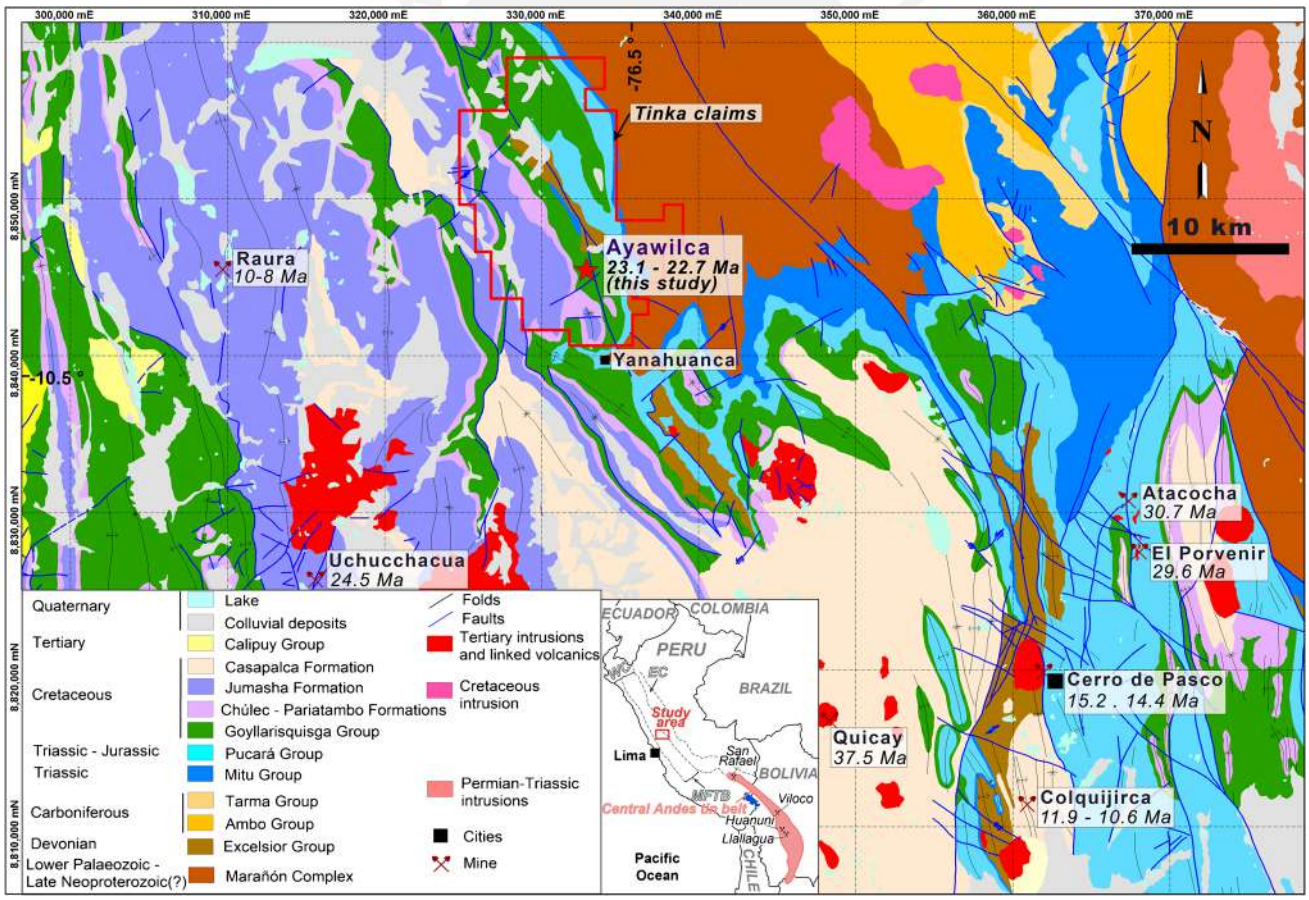

Fig. 1 Simplified geological map (modified from INGEMMET 1996, including data from Rosas et al. 2007, Bissig et al. 2008, Chew et al. 2016, and Spikings et al. 2016) showing the location of the Ayawilca and surrounding polymetallic deposits in central Peru. Approximate radiometric ages taken from summaries by Sillitoe and Perelló (2005) and Bissig et al. (2008) except for the Cerro de Pasco and Colquijirca deposits, which are from Bendezú et al. (2008), Baumgartner et al. (2009), and Rottier et al. (2020). UTM zone 18S. Abbreviations: EC, Eastern Cordillera; MFTB, Marañón fold and thrust belt (MFTB); WC, Western Cordillera

and ground gravity surveys, the South Ayawilca and Zone 3 zones were discovered in 2017 and incorporated into the resource base (Fig. 2).

We show that Ayawilca has strong similarities with Cordilleran polymetallic deposits in central Peru as for example Morococha (Catchpole et al. 2015) and, in particular, Cerro

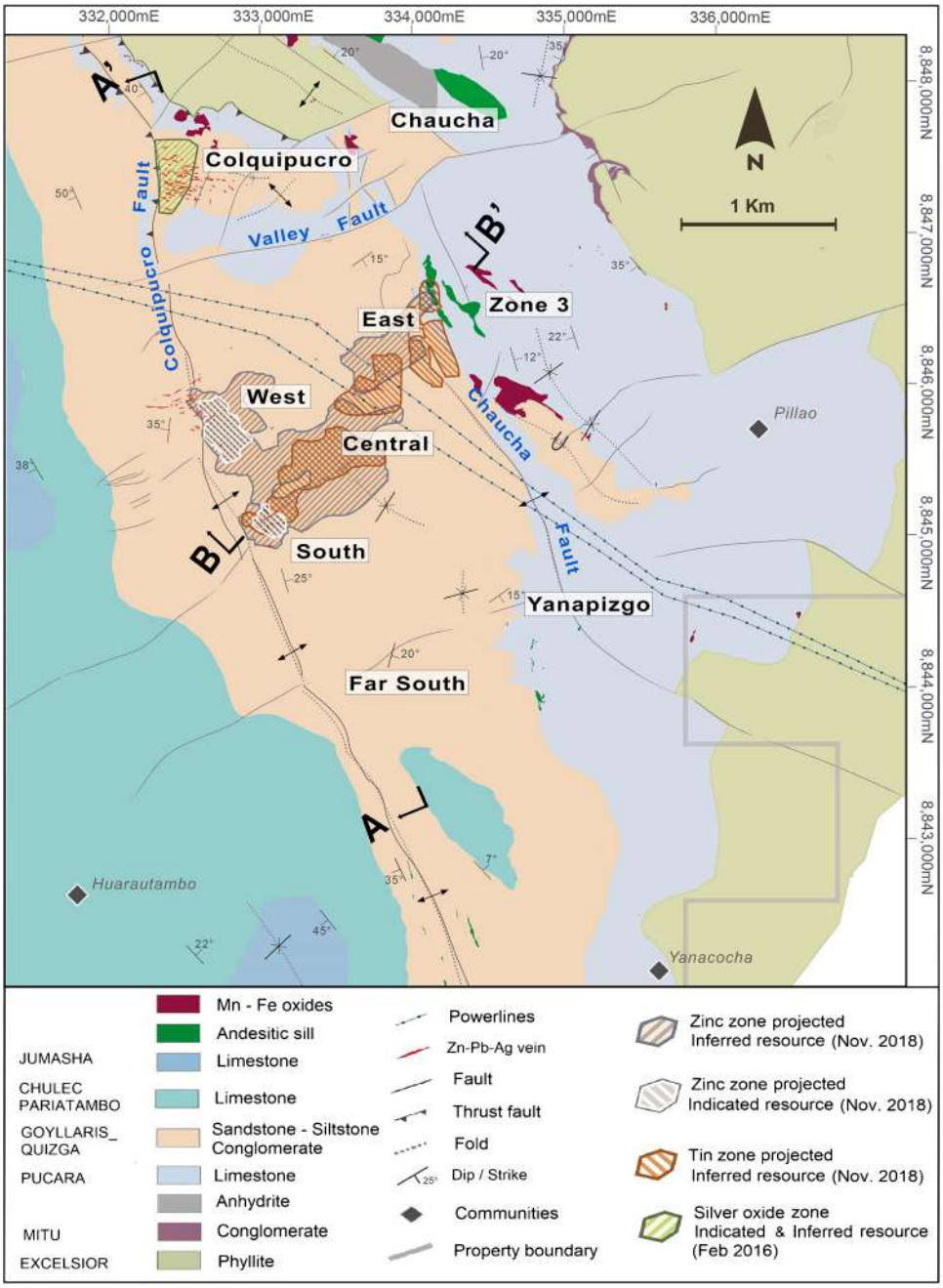

Fig. 2 Geological map of the study area showing the vertical surface projection of Zn, Ag, and Sn resources. A-A' (looking west) and B-B' (looking northwest) cross-sections across the Ayawilca deposit showing the location of the drill holes and metal grades. UTM Zone 18S. The NSR value was based on estimated metallurgical recoveries, assumed metal prices, and smelter terms, which include payable factors, treatment charges, penalties, and refining charges. Metal price assumptions were US$1.15/lb Zn, US$300/kg In, US$15/oz Ag, US$1.00/lb Pb, US$9.00/lb Sn, and US$2.85/lb Cu. Metal recovery assumptions were 90% Zn, 75% In, 60% Ag, 75% Pb, 86% Sn, and 75% Cu. The NSR value for each block was calculated using the following NSR factors: US$15.34 per % Zn, US$4.70 per % Pb, US$0.18 per gram In, and US$0.22 per gram Ag, US$155.21 per % Sn, and US$37.59 per % Cu. The Zn NSR value was calculated using the formula NSR = Zn(%)*US$15.34 + Pb(%)*US$4.70 + In(g/t)*US$0.18 + Ag(g/t)*US$0.22. The Sn NSR value was calculated using the following formula: US$NSR = Sn(%) * US$155.21 + Cu(%) * US$37.59 + Ag(g/t) * US$0.22

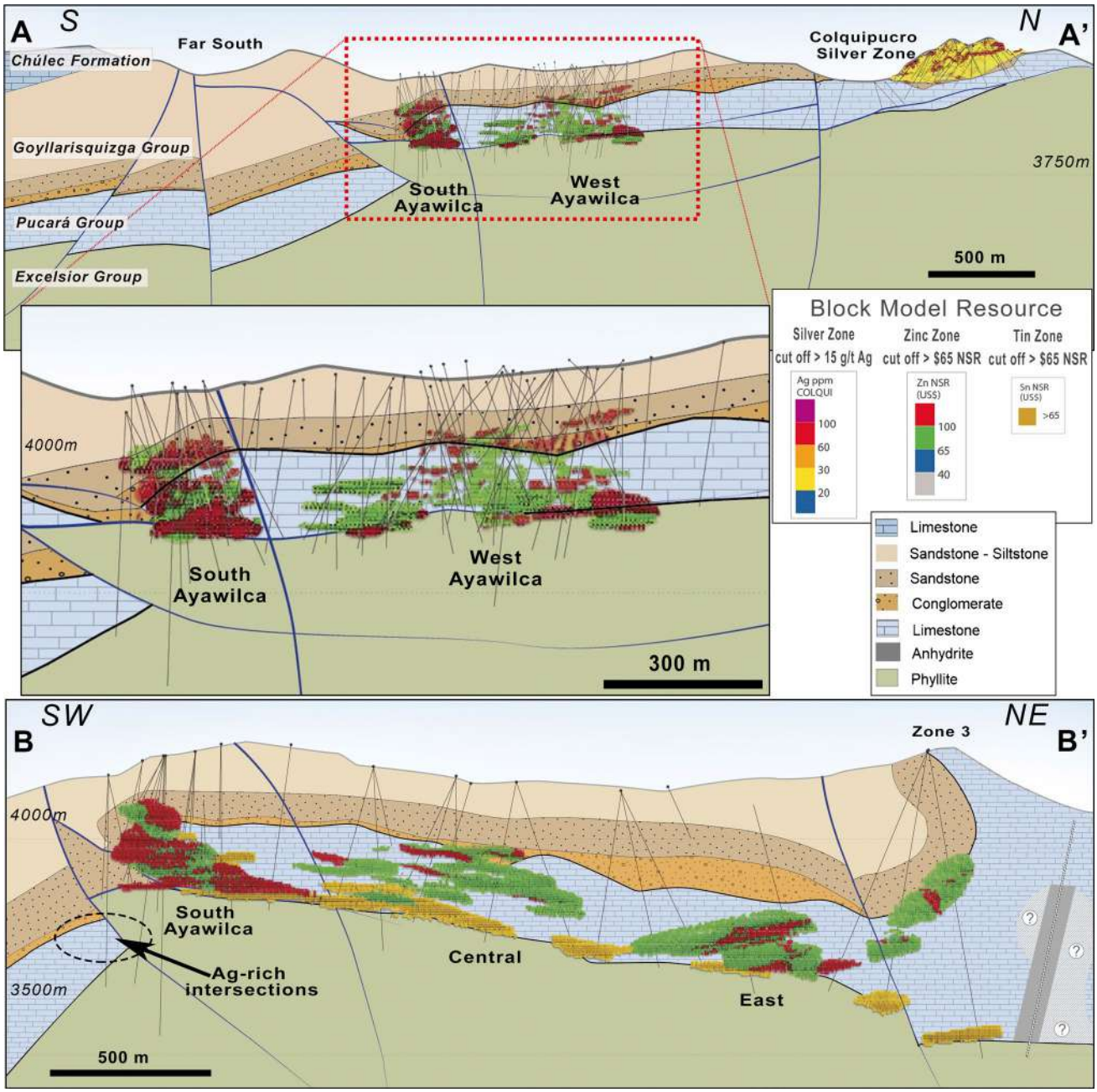

Fig. 2 (continued)

de Pasco (Baumgartner et al. 2008; Rottier et al. 2018). However, the area around Ayawilca was not considered prospective for deposits of this type because it lacked evidence of igneous activity or significant alteration zones, with the exception of that known at Colquipucro.

Indium is a significant component in the current resource at Ayawilca, which stands out as one of the largest undeveloped In resources in the world. Although In may form discrete minerals (e.g., roquesite [$CuInS_2$]), it mostly substitutes into the crystal lattice of sulfides, chiefly in sphalerite (Schwarz-Schampera and Herzig 2002; Cook et al. 2009; Frenzel et al. 2014, 2016a, 2016b; Torró et al. 2019a, 2019b), which explains its strong dependence on Zn production (Nassar et al. 2015). Other important In carriers include stannite (Torró et al. 2019a, 2019b), chalcopyrite (Gaspar 2002; Andersen et al. 2016; George et al. 2016), and cassiterite (Pavlova et al. 2015; Lerouge et al. 2017; Gemmrich et al. 2021).

The aim of this study is to describe the styles of mineralization, mineralogy, and mineral chemistry of the Ayawilca

deposit. Mineral textures are used to establish paragenetic sequences in replacement bodies and veins that serve to contextualize in situ EPMA and LA-ICP-MS trace element analyses of minerals, with special attention to the distribution of In. Additionally, we present the first direct dating of the Ayawilca mineralization, in accordance with which the formation of the deposit is placed within the metallogenic evolution of the central Andes. As a Sn- and In-bearing polymetallic deposit, the discovery, radiometric dating, and classification of the Ayawilca deposit are particularly significant for exploration focused on base and *high-tech* metals in the central Andes and elsewhere.

Regional geology and metallogenic setting

The Ayawilca deposit lies within the eastern part of the Marañón fold and thrust belt (MFTB), near its boundary with the basement high of the Eastern Cordillera (Fig. 1). The 1000-km-long NNW-SSE-trending MFTB constitutes the eastern part of the Western Cordillera of central to northern Peru (Mégard 1984; Benavides-Cáceres 1999; Eude et al. 2015; Pfiffner and Gonzalez 2013; Scherrenberg et al. 2016). It is the host for major ore deposits of Oligocene to Miocene age including Cu ± Mo ± Au porphyry, polymetallic and Cu-Fe skarn, epithermal precious and base metal deposits (e.g., Noble and McKee 1999; Scherrenberg et al. 2016; Fontboté 2018) that belong to "porphyry systems" as described by Sillitoe (2010).

The Marañón Complex (Wilson and Reyes 1964; Dalmayrac et al. 1988) refers historically to all metamorphic rocks in the Eastern Cordillera of Peru. This unit is composed of restricted domains potentially as old as late Neoproterozoic covered by Cambrian to Devonian low- to medium-grade metasedimentary rocks with volcanic intercalations, and is divided into two sub-units (Chew et al. 2007). The older sub-unit underwent metamorphism related to the Ordovician Famatinian orogeny, whereas the younger sub-unit underwent metamorphism related to the Carboniferous Gondwanian (formerly, Eo-Hercynian) orogeny (Chew et al. 2007, 2016; Cardona et al. 2009). The metasedimentary rocks of the Excelsior Group, the tentative Devonian age of which (McLaughlin 1924; Jenks 1951) is supported by osmium isotopic determinations consistent with an Eifelian age (Saintilan et al. 2021), represent the youngest unit of the metamorphic basement in the Eastern Cordillera. The Excelsior Group in central Peru is correlated with the Devonian Cabanillas Group in southern Peru (Rodríguez et al. 2011). Intrusions of I- and S-type granitoids took place during Ordovician, late Carboniferous, Permian, and Triassic magmatic events in the Eastern Cordillera (e.g., Chew et al. 2007, 2016; Mišković et al. 2009).

Carboniferous unmetamorphosed sandstones of the Ambo and Tarma Groups lie discordantly on the Marañón Complex and are unconformably overlain by the Triassic Mitu volcano-sedimentary sequence which includes interbedded alkaline lavas, red siliciclastic rocks, and polymictic conglomerates (McLaughlin 1924; Rosas et al. 2007; Spikings et al. 2016). The Mitu sequence shows large variations in thickness related to extensional faulting indicating deposition in a fault-controlled active rift basin (Rosas et al. 2007; Spikings et al. 2016). Rocks of the Mitu Group are locally absent (as at Ayawilca, see below) and regionally are overlain by the Late Triassic to Early Jurassic carbonate platform rocks of the Pucará Group deposited in the basin formed when the earlier rifts yoked together (Rosas et al. 2007). In central Peru, the Pucará Group is overlain by back-arc Early Cretaceous thick sandstone beds of the Goyllarisquizga Group (Wilson 1963; Scherrenberg et al. 2012). Albian to Maastrichtian sedimentary rocks, also deposited in a back-arc setting, include a transition from marine carbonates (Pariahuanca, Chulec, Pariatambo, and Jumasha Formations) to continental red sandstones and mudstones of the Casapalca formation (Wilson 1963; Jaillard and Arnaud-Vanneau 1993; Mégard et al. 1996; Benavides-Cáceres 1999). Basin inversion with east-vergent thin-skinned tectonics commenced in the Late Cretaceous (Peruvian to later Incaic phases of the Andean orogeny; Mégard 1984; Benavides-Cáceres, 1999; Eude et al. 2015; Scherrenberg et al. 2016) and was followed by west-vergent thick-skinned tectonics mainly from earliest Miocene (Scherrenberg et al. 2016).

The deformed sedimentary sequences were intruded by scattered late Eocene (ca. 40.2 Ma) to late Miocene (5.2 Ma) shallow-level calc-alkaline igneous stocks, mainly of granodioritic to rhyolitic composition (Bissig et al. 2008). Equivalent volcanic rocks occur mainly to the west of the study area. A magmatic lull is recognized in central Peru between 29.3 Ma and late Oligocene/early Miocene depending on the region. Extensive work, including abundant geochronological data, indicates that these shallow-level stocks are linked to porphyry and porphyry-related (in the sense of Sillitoe 2010) precious metal and polymetallic deposits that form a conspicuous NNW-SSE-trending belt in central and northern Peru (Noble and McKee 1999; Bissig et al. 2008; Fontboté 2018 and references therein). Most mineralization is of Miocene age and includes middle to late Miocene world-class deposits and districts as—from south to north—the Toromocho Cu-Mo porphyry deposit and the nearby polymetallic Domo de Yauli and Morococha districts, the polymetallic Colquijirca, Cerro de Pasco, and Antamina deposits, and the Yanacocha high-sulfidation gold deposit (Beuchat et al. 2004; Baumgartner et al. 2008; Bendezú and Fontboté 2009; Longo et al. 2010; Catchpole et al. 2015; Rottier et al. 2018; Mrozek et al. 2020). Middle to late Miocene mineralization

in central Peru coincided with a period of relatively flat subduction and decreasing magmatism subsequent to the subudction of the aseismic Nazca Ridge (Rosenbaum et al. 2005; Bissig et al. 2008; Scherrenberg et al. 2016). The Miocene belt in central and northern Peru is part of the Miocene-early Pliocene porphyry Cu belt recognized Andean wide (Sillitoe and Perelló 2005). In central Peru, the Miocene belt is partly superimposed on an older metallogenic belt of Eocene–Oligocene age that includes the Quicay, Atacocha, Uchucchacua, and Rondoní deposits, which are also parts of porphyry systems (Noble and McKee 1999; Sillitoe 2004; Bissig et al. 2008; Fontboté 2018; Fig. 1).

The Ayawilca deposit occurs in an area where the two metallogenic belts overlap. The lack of intrusive rocks in the area that could provide datable material had previously prevented assignment of the deposit to either the Eocene–Oligocene or Miocene belts.

Geology of the Ayawilca deposit

The Ayawilca Zn-Pb-Ag-In-Sn-Cu deposit lies within mineral concessions that cover an area of ~ 164 km^2 (Fig. 1). The main lithostratigraphic units occurring in the deposit area are the Devonian Excelsior Group, the Triassic-Jurassic Pucará Group, and the Cretaceous Goyllarisquizga Group (Fig. 2).

The Excelsior Group at Ayawilca consists mostly of organic-rich phyllite, composed of fine-grained muscovite and quartz as main minerals, and minor quartzite horizons. The rocks are foliated, locally brecciated, and contain abundant quartz veins. Although Mitu conglomerate-bearing red beds occur in the north of the study area (Fig. 2), at Ayawilca, the Pucará Group limestone overlies directly the Excelsior phyllite. The contact is interpreted to be faulted and is marked by a partly silicified tectonic breccia that consists of shard-like, imbricated quartz clasts derived from the phyllite (Gamarra et al. 2019). The tectonic fabric is parallel to the contact, thus suggesting it is a low-angle shear fault.

The Pucará Group is the main host rock for the mineralization at Ayawilca and ranges typically between 150 and 200 m in thickness. The typical subdivision of the Pucará Group into three units, as commonly described in this part of Peru (see Rosas et al. 2007; Ritterbush et al. 2015), is not recognized at Ayawilca, perhaps because of the hydrothermal alteration that affected the rocks and/or the faulted contact with the underlying Excelsior Group rocks. The identified relict sedimentary facies at Ayawilca are bioclastic wackestones, peloidal packstones, and grapestones. Bivalves and corals are identified in the wackestones. Peloidal packstones include pellets or peloids with a laminar structure. These two facies probably correspond to a subtidal lagoonal environment. The grapestones include millimeter-sized grain lumps (Fig. S1A). A body of massive anhydrite ± gypsum (at least 100-m thick) crops out in the northern part of the study area (Fig. 2). Massive anhydrite ± gypsum has also been intersected by drillholes in zone 3 (e.g., 536.7 m anhydrite ± gypsum intersected in hole A17-73, collar at 334459E 8846615 N). The evaporites cut with discordant brecciated subvertical contacts through the carbonate stratigraphy. The distribution suggests that the evaporites underlie the Pucará carbonate rocks or are interbedded in their lower part, as observed elsewhere (Rosas et al. 2007; Sempere and Acosta 2019), and in places have been subsequently diapirically deformed.

At Ayawilca, the carbonate rocks of the Pucará Group are dominantly dolomitic and display strong brecciation and subordinate chert. The breccias are either monolithic or heterolithic and most likely a product of dissolution due to hydrothermal activity. In the monolithic breccias, both the fragments and matrix are composed of dolomite. The heterolithic breccias are made up of siliceous fragments, predominantly quartz and quartz-arenites, within a dolomitic matrix (Fig. S1B). Pervasive dolomitization is finely to moderately crystalline, locally coarsely crystalline, resulting in a generalized obliteration of primary sedimentary features. The origin of this dolomitization can be diagenetic and/or hydrothermal. Microcrystalline quartz (chert) occurs as nodules that in places also show coarsely crystalline portions.

The Goyllarisquizga Group is empirically subdivided by geologists of Tinka Resources into three distinct clastic sedimentary sequences. The lowermost member, named Lower Goyllar, consists of conglomerates, sedimentary breccias, sandstones, black shales, and siltstones with an overall thickness between 10 and 70 m. Lying conformably above the Lower Goyllar unit is a quartz arenite member named Middle Goyllar. It is 50- to 70-m thick and consists of medium-grained, cross-bedded, and well-sorted quartz arenites. Its contact with the Lower Goyllar unit is gradational, coarsening upwards into thin conglomerate beds that are used as markers to determine the contact. The Upper Goyllar unit lies conformably on the Middle Goyllar unit, and its outcrops are abundant in the study area (Fig. 2). It includes sandstone, siltstone, and mudstone beds that are apparently unaltered (apart from incipient Mn-Fe oxide clots above the zones of mineralization), unmineralized, and undeformed. The Upper Goyllar is approximately 400-m thick in the southern part of the area.

The Ayawilca and Colquipucro deposits are bounded to the west by the NNW-SSE-striking Colquipucro fault (Fig. 2). The Colquipucro fault and other similarly oriented faults are cut by steep NEE-SWW-striking faults with which part of the mineralization is spatially associated with (Fig. 2). North of the NEE-SWW-striking Valle fault, near the Colquipucro Ag mineralization, the Colquipucro fault places the carbonate rocks of the Pucará Group over the

sandstones of the Goyllarisquizga Group; there, the Colquipucro fault shows east-verging thrusting (i.e., the typical vergence of the thin-skinned tectonics along the MFTB; Mégard 1984; Scherrenberg et al. 2016). The vergence of the Colquipucro fault south of the Valle fault could not be determined.

Drilling since 2017 in the western sector of Ayawilca identified several locations where phyllites of the Excelsior Group are thrusted over the carbonate rocks of the Pucará Group along west-verging low-angle faults (Fig. 2, section B-B'). At South Ayawilca, several low-angle thrusts ramp up through the carbonate rocks of the Pucará Group to form a duplex. A moderately inclined and plunging anticline developed in the hanging wall of the roof thrust of the duplex. The core of this anticline is composed of carbonate rocks of the Pucará Group and hosts some of the highest grade and thickest mineralization found at Ayawilca. These west-verging thrust faults project close to the trace of the Colquipucro fault on surface (Fig. 2), but their vergence is at odds with the east vergence observed in this structure north of the Valley Fault. The west-verging faults and the Chaucha fault to the east define a basement high; east of it, the sedimentary sequence appears to be thicker and include the aforementioned thick evaporite unit and forms an overturned syncline (section B-B' in Fig. 2). The west-verging thrusting recognized at South Ayawilca may correspond to the west-verging thick-skinned event described by Scherrenberg et al. (2016).

The mineralization at Ayawilca occurs as replacement mantos and veins in the carbonate rocks of the Pucará Group and, to a lesser extent, in rocks of the Lower Goyllar unit (Fig. 2; Peralta et al. 2019). Quartz-sphalerite and massive sphalerite veins up to 1.3-m thick in the underlying Excelsior phyllites (Fig. S1C) are interpreted as feeders for the mineralized bodies. The sphalerite-bearing mantos in carbonate rocks of the Pucará Group are up to 30-m thick. Tin-copper mineralization occurs mostly within massive, 10- to 70-m-thick pyrrhotite replacement bodies at the base of the Pucará Group, particularly at Central Ayawilca (Fig. S1D), and in places is overprinted by the main Zn mineralization (Fig. S1E-F). Where the Pucará Group rocks are most deformed, particularly near the intersections of major faults and/or folds, the mantos can be stacked, and mineralization can be up to 200-m thick. Mineralization postdates the NNW-SSE-striking thrust faults and is in places affected by NEE-SWW-striking steep normal faults. No intrusive rocks have been found in outcrops nor in drill cores at the Ayawilca deposit. However, 3 km northeast of the East Ayawilca Zone, at about 3300 m.a.s.l., a granodiorite stock showing argillic alteration and pyrite veinlets crops out in an area of 300 x 200 m (Peralta et al. 2019). Minor andesitic dykes and sills in carbonate rocks of the Pucará Group (Fig. 2) are, according to regional comparison, typical for Jurassic and Cretaceous subvolcanic activity unrelated to mineralization.

Sampling and analytical methods

The study is based on 60 representative core samples from mantos and veins in the Ayawilca deposit, which were collected from 24 drill holes. A list of the samples and their locations are provided in Table S1. A detailed description of the analytical methods is available in Appendix S1. A total of 42 thick polished sections were prepared at the QEMSCAN laboratory of the Pontifical Catholic University of Peru (PUCP, Peru) for petrographic study under reflected-light polarizing microscope and SEM–EDS at the Centro de Caracterización de Materiales of the PUCP (CAM-PUCP). Mineralogical determinations, chiefly on hydrothermal alteration products, were carried out by X-ray diffraction (XRD; n = 24) at the CAM-PUCP. Results of XRD analyses are provided in Appendix S2.

Chemical compositions of sulfides, sulfosalts, and oxides were determined by means of electron microprobe (EPMA) and laser-ablation inductively coupled plasma mass spectrometry (LA-ICP-MS). EPMA analysis of sulfides, sulfosalts, and cassiterite was performed at the Centres Científics i Tecnològics of the University of Barcelona (CCiT-UB), and EPMA analysis of magnetite was performed at the Laboratorio Universitario de Petrología of the Instituto de Geofísica, Universidad Nacional Autónoma de México (UNAM). Lower limits of detection (L.O.D.), representative analyses of the different minerals investigated, and the normalization constants used for formula calculations are displayed in Table S2.

LA-ICP-MS analysis of sphalerite, chalcopyrite, and stannite was performed at ETH Zürich (Switzerland) and of magnetite at the Laboratorio de Estudios Isotópicos (LEI) of the Centro de Geociencias, UNAM. The list of analyzed isotopes and corresponding dwell times, the complete data set (content, uncertainties, and L.O.D.), and statistical data are provided in Table S3 (sulfides and sulfosalts) and Table S4 (magnetite). LA-ICP-MS analyses of cassiterite were carried out at ETH Zürich (trace element and U–Pb isotopic compositions; Table S5) and at the Southwest Isotope Research Laboratory of the US Geological Survey (USGS), Denver (U–Pb isotopic compositions; Table S6). Significant effort was made to avoid reporting mixed mineral analyses that result from the presence of nano- and micro-inclusions in the analyzed minerals. To accomplish this, we analyzed areas free of obvious inclusions and, during data processing, only selected smooth, constant signal segments in time-resolved ablation spectra for trace element quantification.

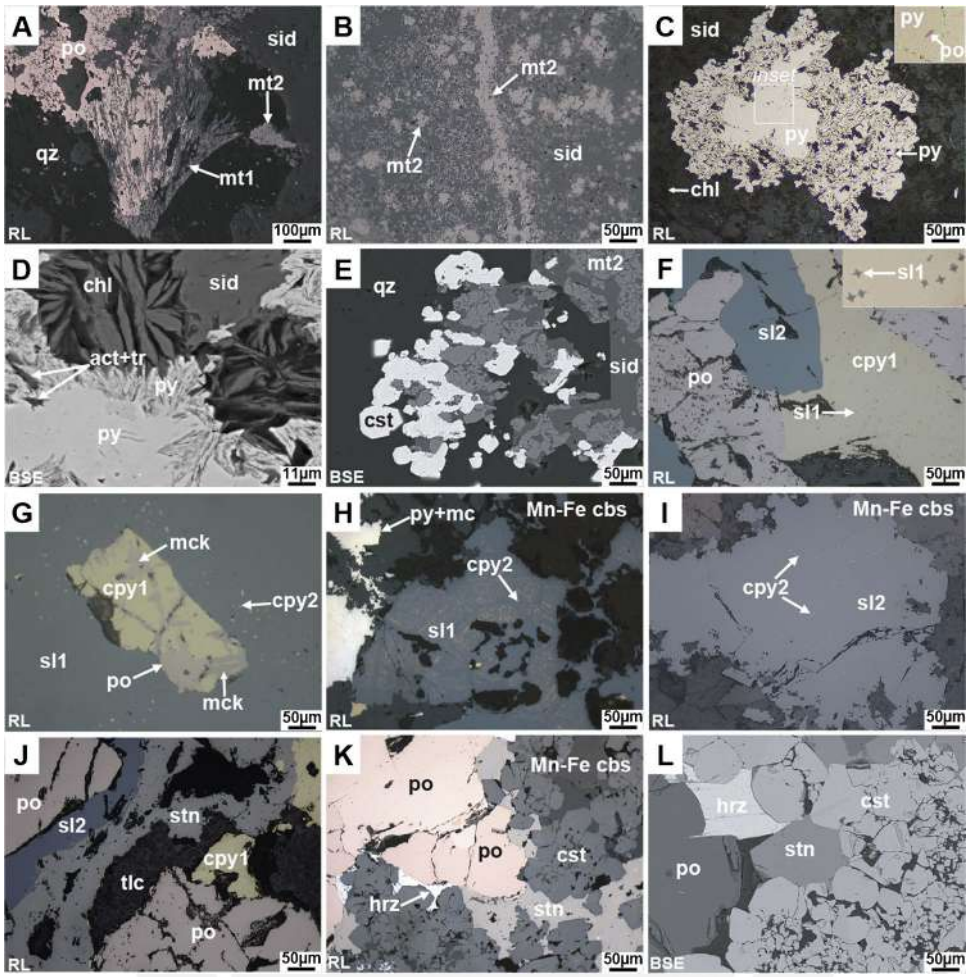

Fig. 3 Photomicrographs of textural features in manto mineralization in the Ayawilca deposit. **A** Magnetite as radial (1st generation) and fine (2nd generation) aggregates pervasively replaced by massive pyrrhotite and Mn-Fe carbonates. **B** Dense dissemination of magnetite (2nd generation) on a Mn-Fe carbonates matrix cut by a magnetite vein (3rd generation). **C**, **D** Zoned coarse pyrite with a massive core hosting small pyrrhotite inclusion, and irregular borders hosting acicular crystals of actinolite-tremolite in part replaced by chlorite. **E** Magnetite aggregates (2nd generation) in quartz matrix partially replaced by subhedral/anhedral cassiterite and siderite. **F** Massive pyrrhotite replaced by chalcopyrite (1st generation) with fine sphalerite-star inclusions (1st generation), and massive, "clean" sphalerite (2nd generation). **G** Chalcopyrite (1st generation) with oriented inclusions of tabular and lamellar mackinawite and irregular grains of pyrrhotite, in sphalerite (1st generation) hosting blebs of chalcopyrite (2nd generation). **H** Sphalerite (1st generation) with fine-grained, oriented chalcopyrite (2nd generation) inclusions, in contact with pyrite and fine-grained marcasite, the assemblage being partially replaced by Mn-Fe carbonates. **I** Sphalerite (2nd generation) aggregates with very fine, low-density dissemination of chalcopyrite blebs (2nd generation). **J** Pyrrhotite and chalcopyrite (1st generation) cut by "clean" sphalerite (2nd generation) and stannite. **K**, **L** Pyrrhotite intergrown with subhedral/euhedral cassiterite aggregates; stannite and herzenbergite occupy interstitial space. **M** Subhedral arsenopyrite crystals replaced by pyrite and marcasite. **N** Massive pyrrhotite partially replaced by an assemblage of fine-grained pyrite, marcasite, and intermediate product, the whole assemblage being replaced by Mn-Fe carbonates. **O** Sphalerite (2nd generation) and arsenopyrite crystals pervasively replaced by pyrite and marcasite. **P** Interstitial sphalerite (1st generation), pyrite, and marcasite within idiomorphic quartz aggregate; sphalerite hosts a fine dissemination of chalcopyrite (2nd generation). **Q** Sphalerite crystal with pyrite-marcasite rims and replaced by Mn-Fe carbonates. **R** Sphalerite (1st generation) with dissemination of chalcopyrite (2nd generation) and replacement of chalcopyrite (3rd generation) and Mn-Fe carbonates. **S** Arsenopyrite crystals with porosity, microfractures, and contacts lined with Fe-poor sphalerite (3rd generation) and Mn-Fe carbonates. **T** Chalcopyrite (1st generation) replaced by sphalerite (2nd generation), tetrahedrite-group minerals and Mn-Fe carbonates. **U** Sphalerite (2nd generation) with polymineral inclusion of argentian tetrahedrite, the latter with relicts of sphalerite (1st generation) with dissemination of chalcopyrite (2nd generation) and pyrrhotite. **V** Sphalerite (2nd generation) with inclusions of chalcopyrite (3rd generation), argentian tetrahedrite and pyrargyrite. **W** Corroded arsenopyrite with galena inclusions. **X** Massive pyrrhotite with secondary porosity lined with native bismuth and bismuthiferous galena. Abbreviations: 1, 2, 3, first, second, and third generations; act-tr, actinolite-tremolite; aspy, arsenopyrite; Bi, native bismuth; Bi_gn, bismuthiferous galena; chl, chlorite; cpy, chalcopyrite; cst, cassiterite; Mn-Fe cbs, Mn-Fe carbonates; gn, galena; hrz, herzenbergite; I.P, intermediate product; mck, mackinawite; mc, marcasite; mt, magnetite; po, pyrrohtite; py, pyrite; pyrg, pyrargyrite; qz, quartz; sid, siderite; sl, sphalerite; stn, stannite; td_Ag, argentian tetrahedrite; tlc, talc; RL, reflected light image; BSE, backscattered electron image

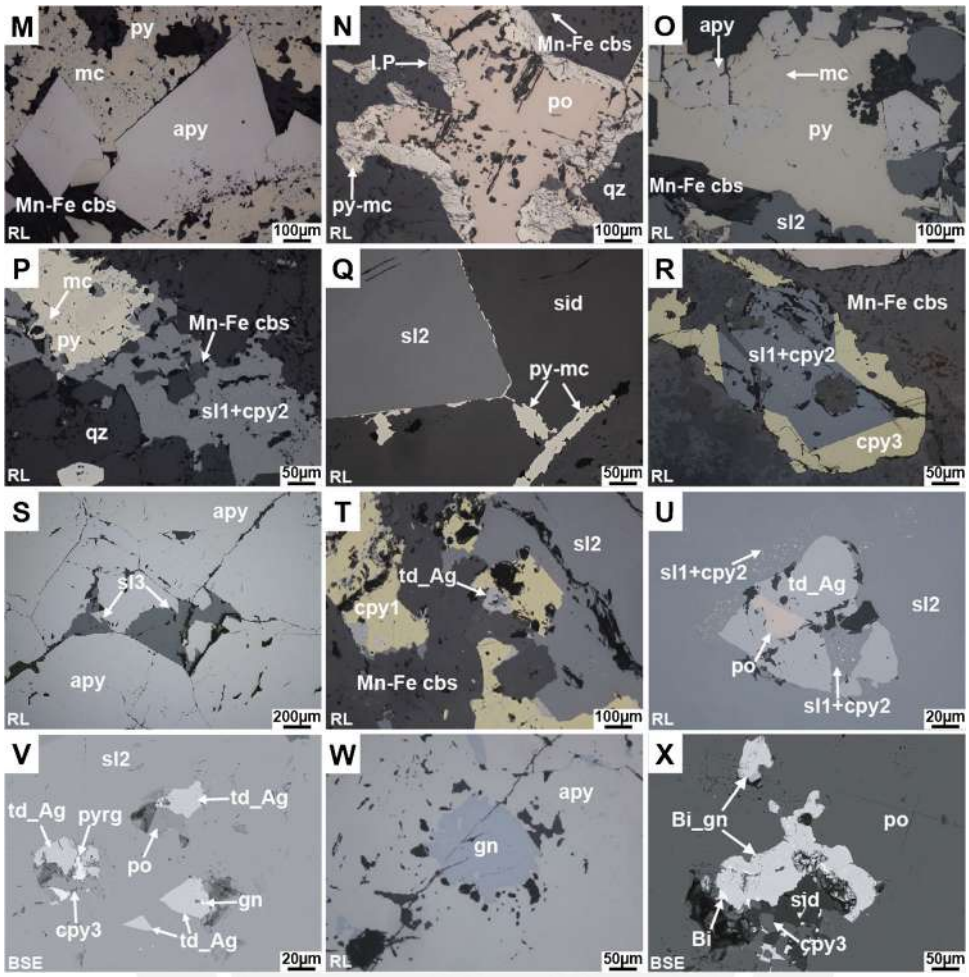

Fig. 3 (continued)

Hydrothermal alteration and mineralization

Mineral assemblages and paragenetic sequences in both mantos and veins define three main stages of evolution (stages A, B, and C; Figs. 3 and 4 and Fig. S2), similar to those recognized by Rottier et al. (2016, 2018) in the Cerro de Pasco deposit, as well as in other Cordilleran-type polymetallic deposits (Fontboté 2020). In addition, relicts of a magnesian retrograde skarn that predated stage A chiefly comprise Mg-siderite + talc + magnetite (Fig. S2A). Cassiterite mineralization, which also predates stage A, is only found in the deepest mantos, close to the contact between rocks of the Pucará and Excelsior Groups. The mineralization formed during stage A is the economically and volumetrically most important at Ayawilca, and is composed of a low-sulfidation assemblage of arsenopyrite, pyrrhotite, chalcopyrite, Fe-rich sphalerite, stannite, and herzenbergite [SnS] (Fig. S2B-E). Stage A minerals are frequently overprinted by coarse pyrite that forms the bulk of stage B (Fig. S2F). Stage C comprises an intermediate-sulfidation assemblage, mainly constituted by sphalerite, chalcopyrite, galena, Cu-Ag sulfosalts, kaolinite, dickite, and carbonates (including siderite and intermediate compositions between rhodochrosite, siderite, and kutnohorite end-members, henceforth referred to as Mn-Fe carbonates). Stage C overprinted the assemblages of both stages A and B (Figs. S2G-I). The paragenetic sequences for mantos and polymetallic veins are summarized in Fig. 5.

Mantos

Hypogene metallic minerals in the mantos at Ayawilca include magnetite, pyrrhotite, arsenopyrite, sphalerite, chalcopyrite, pyrite, marcasite, and lesser amounts of cassiterite, stannite, herzenbergite, mackinawite, tetrahedrite, galena, native bismuth, zoubekite [$AgPb_4Sb_4S_{10}$], stephanite, pyrargyrite, and intermediate product (defined as a transition of pyrrhotite to marcasite and pyrite; Ramdohr 1969).

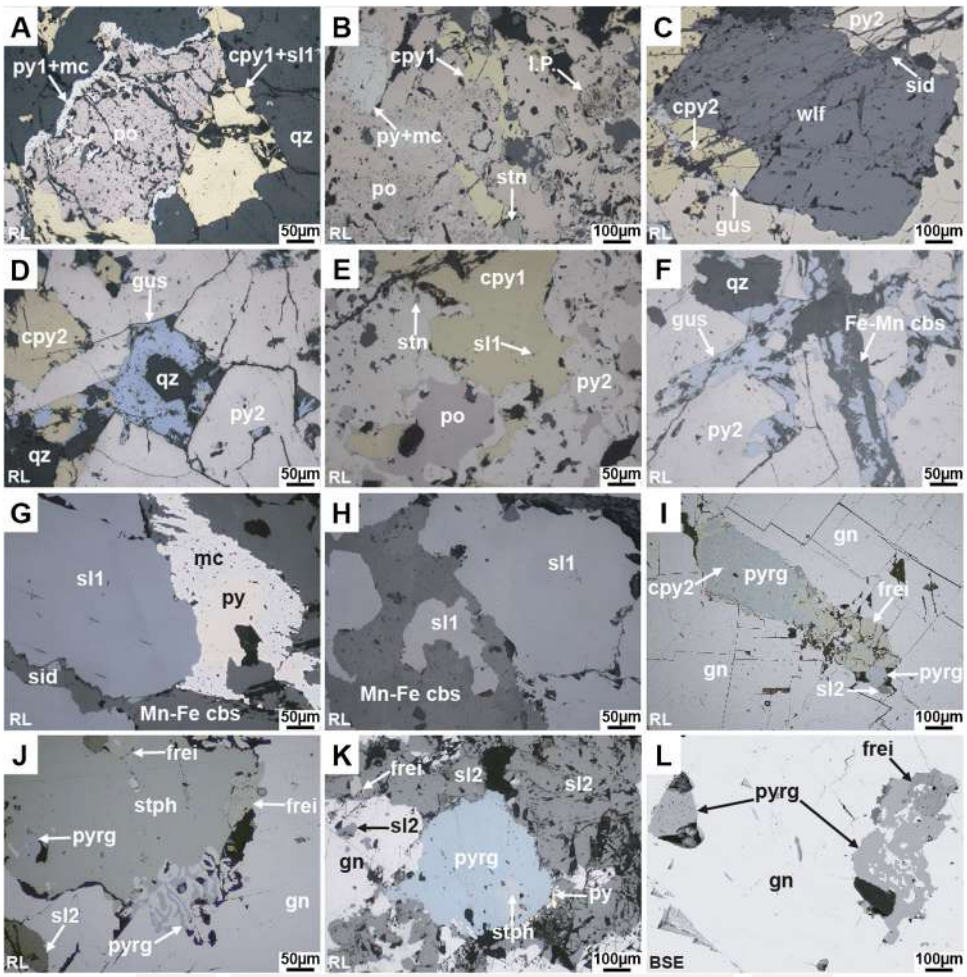

Fig. 4 Photomicrographs of textural features of veins in NE (**A–F**) and NW (**G–L**) Ayawilca deposit. **A** Pyrrhotite in interstices of quartz, replaced by chalcopyrite (1st generation) with fine inclusions of sphalerite "stars" (1st generation) and with pyrite and marcasite rims. **B** Corroded pyrrhotite replaced by a fine-grained assemblage of pyrite, marcasite, and intermediate product. Chalcopyrite (1st generation) and stannite vein pyrrhotite. **C** Medium-grained wolframite within a pyrite aggregate partially replaced by chalcopyrite (2nd generation) and gustavite; the whole assemblage is cut by fine veinlets of siderite. **D** Pyrite aggregates replaced by chalcopyrite (2nd generation) and gustavite. **E** Chalcopyrite (1st generation) with inclusions of sphalerite "stars," and pyrrhotite replaced by pyrite (1st generation). **F** Pyrite vein (2nd generation) with inclusions of quartz and replaced by gustavite. **G–H** Sphalerite (1st generation) replaced by pyrite, marcasite, siderite, and Mn-Fe carbonates. **I** Galena with secondary porosity and microfractures lined with sphalerite (2nd generation), chalcopyrite (3rd generation), freibergite, and pyrargyrite. **J** Stephanite, with inclusions of freibergite and pyrargyrite, is intergrown with galena; note the myrmekitic texture involving galena and pyrargyrite. **K** Galena and finely intergrown pyrargyrite and freibergite line porosity in corroded sphalerite (2nd generation). **L** Secondary porosity in galena is lined with pyrargyrite and freibergite. Abbreviations: 1, 2, 3, first, second, and third generations; cpy, chalcopyrite; Mn-Fe cbs, Mn-Fe carbonates; frei, freibergite; gn, galena; gus, gustative; mc, marcasite; po, pyrrhotite; py, pyrite; pyrg, pyrargyrite; qz, quartz; sid, siderite; sl, sphalerite; stn, stannite; stph, stephanite; td_Ag, argentian tetrahedrite; wlf, wolframite; RL, reflected light image; BSE, backscattered electron image

The deepest mantos are locally enriched in Mg-siderite, magnetite, talc, and cassiterite. Two generations of magnetite have been identified. The first occurs as pseudo-radial aggregates, probably as a replacement of < 600-µm-long acicular amphibole crystals (Fig. 3A). The second generation comprises disseminated octahedral crystals with sizes that range between 800 and 120 µm and < 125-µm-thick stringers (Fig. 3B). Small laths of actinolite–tremolite that were mostly replaced by chlorite occur shielded by pyrrhotite that was, in turn, massively replaced by pyrite (Fig. 3C, D). The amphiboles are interpreted as being part of a magnesian retrograde skarn formed prior to the main stage A sulfide assemblage along with Mg-siderite, magnetite, and talc, as a "pre-A stage" (Fig. 3A-C). Anhedral to subhedral cassiterite crystals up

AYAWILCA MINERALIZATION STYLE - "MANTOS"		STAGE PRE-A	STAGE A (LS)	STAGE B (IS)	STAGE C (IS)
Actinolite-Tremolite	$Ca_2(Mg,Fe)_5Si_8O_{22}(OH)_2$				
Chlorite	$(Fe,Mg,Al,Fe)_6(Si,Al)_4O_{10}(OH,O)_8$				
Quartz	SiO_2				
Apatite	$Ca_5(PO_4)_3F$				
Mg-siderite	$(Fe,Mg)CO_3$				
Talc	$Mg_3Si_4O_{10}(OH)_2$				
Magnetite	$Fe_2O_3.FeO$				
Cassiterite	SnO_2				
Arsenopyrite	FeAsS				
Pyrrhotite	$Fe_{1-x}S$				
Chalcopyrite	$CuFeS_2$				
Fe-rich sphalerite	(Zn,Fe)S				
Mackinawite	$(Fe,Ni)_9S_8$				
Stannite	Cu_2FeSnS_4				
Herzenbergite	SnS				
Pyrite	FeS_2				
I. Product/Marcasite	$Fe_{1-x}S+FeS_2$				
Ag-rich tetrahedrite	$(Cu,Ag)_6[Cu_4(Fe,Zn)_2]Sb_4S_{13}$				
Fe-poor sphalerite	ZnS				
Galena	PbS				
Zoubekite	$AgPb_4Sb_4S_{10}$				
Pyrargyrite/Stephanite	Ag_3SbS_3/Ag_5SbS_4				
Bismuthiferous galena	(Pb,Bi,Ag)S				
Native bismuth	Bi				
Mn-Fe carbonates	$(Mn,Fe)CO_3$				
Siderite	$FeCO_3$				
Dickite	$Al_2(Si_2O_5)(OH)_4$				
Kaolinite	$Al_2(Si_2O_5)(OH)_4$				
Muscovite	$KAl_2(AlSi_3O_{10})(OH)_2$				

AYAWILCA MIN. STYLE - NORTHEAST VEINS		STAGE PRE-A	STAGE A (LS)	STAGE B (IS)	STAGE C (IS)
Quartz	SiO_2				
Pyrrhotite	$Fe_{1-x}S$				
Chalcopyrite	$CuFeS_2$				
Fe-rich sphalerite	(Zn,Fe)S				
Stannite	Cu_2FeSnS_4				
Wolframite	$(Fe,Mn)WO_4$				
Pyrite	FeS_2				
I.Product/Marcasite	$Fe_{1-x}S+FeS_2$				
Galena	PbS				
Gustavite	$PbAgBi_3S_6$				
Native bismuth	Bi				
Mn-Fe carbonates	$(Mn,Fe)CO_3$				
Siderite	$FeCO_3$				

AYAWILCA MIN. STYLE - NORTHWEST VEINS		STAGE PRE-A	STAGE A (LS)	STAGE B (IS)	STAGE C (IS)
Quartz	SiO_2				
Pyrrhotite	$Fe_{1-x}S$				
Arsenopyrite	FeAsS				
Chalcopyrite	$CuFeS_2$				
Fe-rich sphalerite	(Zn,Fe)S				
Pyrite	FeS_2				
Marcasite	FeS_2				
Fe-poor sphalerite	ZnS				
Galena	PbS				
Ag-rich tetrahedrite	$(Cu,Ag)_6[Cu_4(Fe,Zn)_2]Sb_4S_{13}$				
Freibergite	$Ag_6(Cu_4Fe_2)Sb_4S_{12}$ □				
Pyrargyrite	Ag_3SbS_3				
Stephanite	Ag_5SbS_4				
Mn-Fe carbonates	$(Mn,Fe)CO_3$				
Siderite	$FeCO_3$				

Fig. 5 Paragenetic sequence of mantos and polymetallic veins in Ayawilca. Thick bars indicate higher abundance and dashed lines lesser abundance

to 150 µm in size occur as a replacement of or filling interstitial space between magnetite grains (Fig. 3E).

Stage A in mantos comprises early prismatic quartz, massive pyrrhotite, and subhedral arsenopyrite followed by chalcopyrite, Fe-rich sphalerite, stannite, and herzenbergite. Two generations of Fe-rich sphalerite are observed. The first occurs both as star-shaped inclusions (< 4 µm) in massive, first-generation chalcopyrite (Fig. 3F) and as anhedral to subhedral crystals with fine-grained disseminations of second-generation chalcopyrite (Fig. 3G, H). First-generation chalcopyrite occasionally hosts lamellar mackinawite (Fig. 3G). Second-generation sphalerite shows clean surfaces and local, low-density, very fine chalcopyrite disseminations (Fig. 5I). Both Fe-rich sphalerite and first-generation chalcopyrite replaced massive pyrrhotite and were partially replaced, in turn, by rimming stannite (Fig. 3J). Stannite also occurs in the interstices of short, prismatic subhedral cassiterite crystals (< 160 µm). Herzenbergite (< 620 µm) occupies interstitial space between subhedral cassiterite and stannite and corroded pyrrhotite crystals (Fig. 3K, L).

During stage B, pyrite and quartz replaced both the carbonate rocks of the Pucará Group and stage A sulfides, mainly arsenopyrite (Fig. 3M), pyrrhotite (Fig. 3N), and Fe-rich sphalerite (Fig. 3O-Q). In the particular case of pyrrhotite replacement, pyrite is often intergrown with fine-grained marcasite and intermediate product (Fig. 3N).

During stage C, a third generation of chalcopyrite and Fe-poor sphalerite along with galena, and lesser amounts of tetrahedrite, native bismuth, bismuthiferous galena, pyrargyrite, stephanite, and zoubekite are introduced. Third-generation chalcopyrite is observed as a replacement of Fe-rich sphalerite (Fig. 3R). Stage C sphalerite, which shows yellowish-brown internal reflections, occurs locally lining cavities in corroded arsenopyrite crystals (Fig. 3S). Locally, tetrahedrite is observed as a replacement of first-generation chalcopyrite (Fig. 3T). Traces of tetrahedrite (Fig. 3U), pyrargyrite (Fig. 3V), and stephanite typically appear lining fine pores in stage A second-generation sphalerite. Galena occurs lining pores and microfractures in arsenopyrite (Fig. 3W) and sphalerite, and is locally replaced by zoubekite. Native bismuth and bismuthiferous galena occur in secondary pores in pyrrhotite, arsenopyrite, and Fe-rich sphalerite (Fig. 3X).

Veins

Veins in NE Ayawilca (Fig. 2) display similar mineralogy and micro-textural relationships to those ascribed to stages A and B in the mantos. The veins are mainly formed by comb quartz crystals between which available interstitial space is occupied by stage A massive pyrrhotite and first-generation chalcopyrite with star-shaped inclusions of sphalerite (Fig. 4A, B). In contrast to the mantos, prismatic wolframite grains < 1800 µm across occur locally in these veins (Fig. 4C). In some areas, both pyrrhotite and first-generation chalcopyrite were partially replaced by stannite and Fe-rich sphalerite, and the whole assemblage, in turn, by stage B pyrite, intermediate product, and marcasite. Pyrite is also observed forming aggregates of anhedral to subhedral microfractured crystals, with interstices and porosity lined with stage C native bismuth (< 30 µm), galena (< 150 µm), and gustavite [$AgPbBi_3S_6$] (< 350 µm; Fig. 4D-F), and cut by fine veinlets of siderite and Mn-Fe carbonates. A second generation of chalcopyrite (stage C) characterized by absence of mineral inclusions is observed lining microfractures in pyrite and overprinting first-generation chalcopyrite.

Veins in NW Ayawilca (Fig. 2) mainly consist of sphalerite, galena, Ag–Cu sulfosalts, pyrite, and lesser amounts of arsenopyrite, marcasite, pyrrhotite, and chalcopyrite. Two generations of chalcopyrite have been identified: the first occurs as fine disseminations (< 4 µm) on first-generation sphalerite (stage A), and the second forms anhedral crystals (stage C). Stage A sphalerite, which is Fe-rich, presents reddish-brown internal reflections and hosts also small inclusions of pyrrhotite. First-generation sphalerite was replaced by stage B pyrite/marcasite and stage C siderite and Mn-Fe carbonates (Fig. 4G, H). First-generation sphalerite and stage C second-generation chalcopyrite were replaced by, and its porosity lined with galena, Ag–Cu sulfosalts (tetrahedrite, freibergite, stephanite, and pyrargyrite; all < 600 µm across) and a second generation of sphalerite with light yellow internal reflections (Fig. 4I-L). Symplectic intergrowths involving galena, pyrargyrite, and freibergite (Fig. 4J, L) are observed.

Mineral geochemistry

Summaries of the compositions, including minimum, maximum, average, and interquartile range (IQR) values for sphalerite, stannite, and chalcopyrite are reported in Table S3, for magnetite in Table S4, and for cassiterite in Table S5. Additionally, LA-ICP-MS analyses of sphalerite are presented in compiled box-and-whisker plots (Fig. 6 and Appendix S3). Trace elements will be henceforth reported as IQR unless otherwise specified.

Sphalerite

Sphalerite grains from the Ayawilca deposit yield a relatively broad compositional spectrum. In mantos, Fe contents are generally higher in stage A sphalerite, both in the first and second generations (14.1–11.5 wt%), and much lower

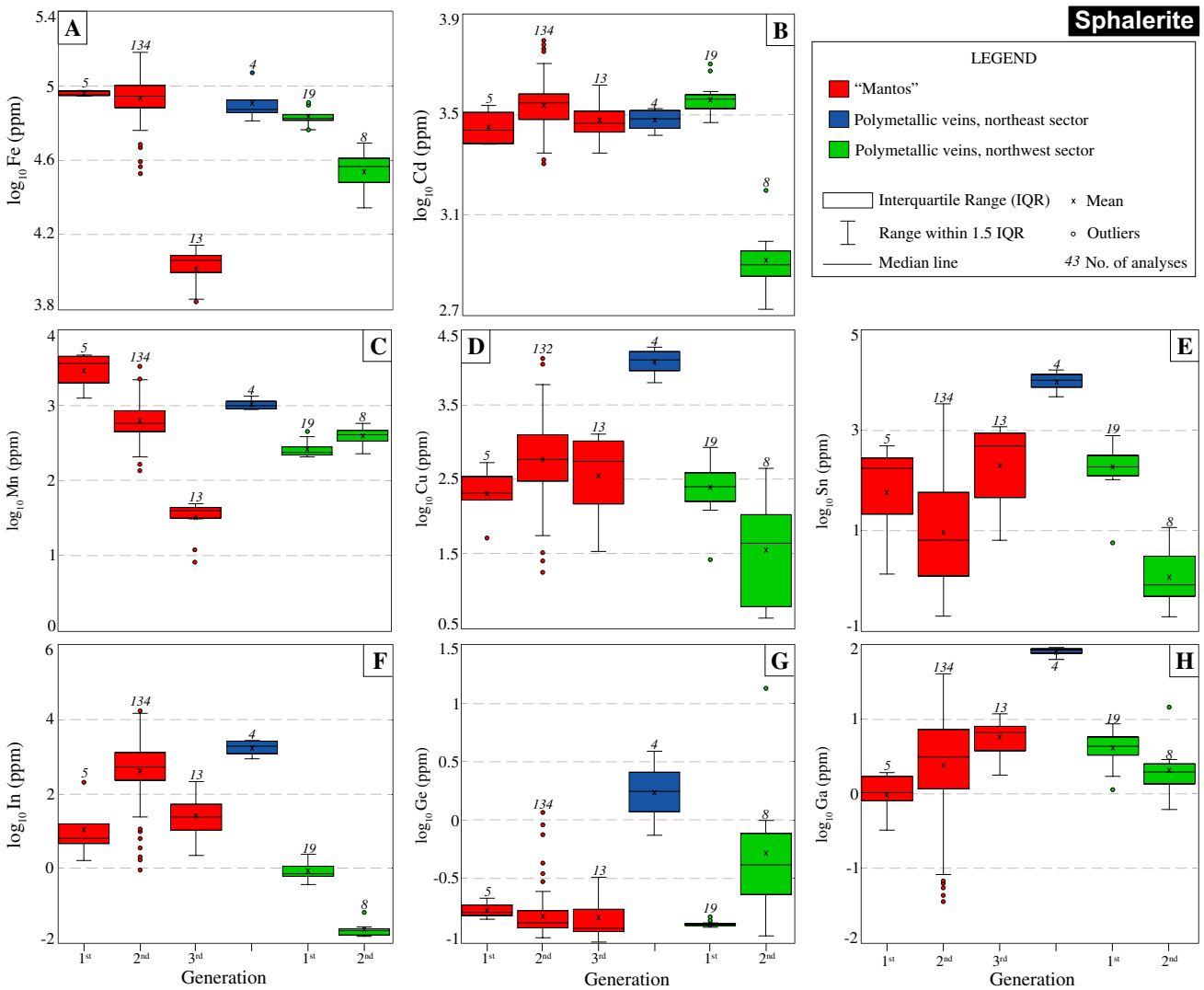

Fig. 6 Selected boxplots of log-transformed element contents in sphalerite from the Ayawilca deposit (LA-ICP-MS data)

in grains of the third generation (stage C; 2.4–2.0 wt%). Iron values are normally higher in sphalerite from NE Ayawilca (10.8–10.3 wt%) than in NW Ayawilca, which records Fe depletion from first (14.4–5.3 wt%, stage A) to second generations (4.7–4.0 wt%, stage C; Fig. 6A). Zinc tends to have a fairly negative correlation with Fe (Fig. 7A), thus pointing to a dominant $Fe^{2+} \leftrightarrow Zn^{2+}$ simple isovalent substitution.

Cadmium values are relatively constant in all analyzed sphalerite grains from mantos (3823–2417 ppm) and veins at the NE sector (3828–2672 ppm; Fig. 6B). In veins from the NW sector, Cd content is much higher in sphalerite grains of the first generation (3818–3329 ppm, stage A) than in those of the second generation (955–698 ppm, stage C). Manganese content in sphalerite from mantos decreases steadily from grains of the first generation (4635–1623 ppm) to those of the second (870–452 ppm, stage A) and third (45–31 ppm, stage C) generations (Fig. 6C). In contrast, sphalerite from veins at NW Ayawilca records a subtle increase in the Mn content from grains of the first (295–218 ppm, stage A) to grains of the second (486–312 ppm, stage C) generations. Cadmium shows a weak negative correlation with Zn (Fig. 7B) and a strong positive correlation with Fe (Fig. 7C). Iron is also positively correlated with Mn (Fig. 7D), thus suggesting more complex isovalent substitution mechanisms of Zn^{2+} for Fe^{2+}, Cd^{2+}, and Mn^{2+} (see Graeser 1969; Cook et al. 2009; Pring et al. 2020).

Copper content in sphalerite from mantos (1273–108 ppm) is higher in grains of the stage A second generation (1273–281 ppm) relative to those of the first (438–108 ppm) and stage C third (1059–127 ppm) generations (Fig. 6D). As for sphalerite in veins, Cu content is higher in grains from the NE sector (18,337–7373 ppm) than

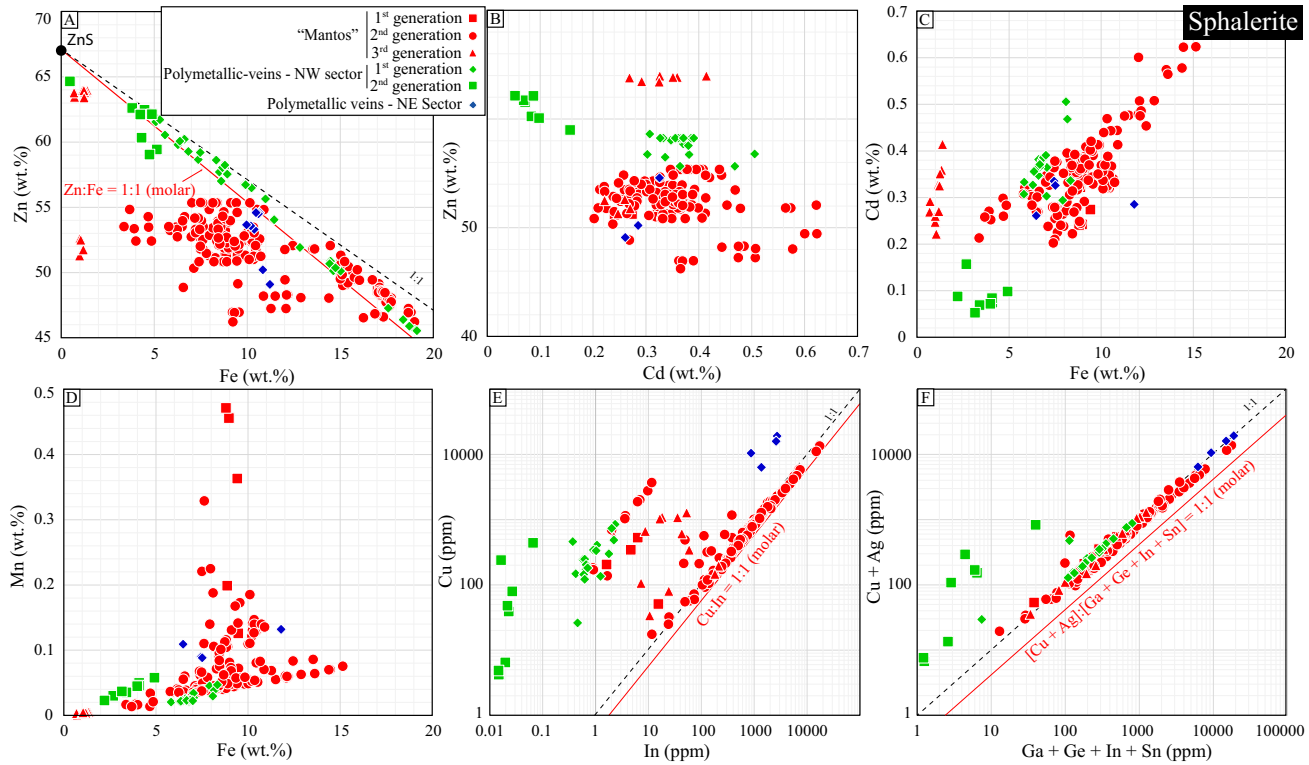

Fig. 7 Correlation between elements in sphalerite from the Ayawilca deposit (LA-ICP-MS data)

in those from the NW sector (408–6 ppm). In veins from the NW sector, there is a drastic depletion in Cu from first- (408–148 ppm, stage A) to second-generation (239–6 ppm, stage C) sphalerite. Copper normally shows very good correlations with other minor and trace elements (e.g., In, Ag, and Sn), thus suggesting that Cu was incorporated within the crystal lattice of sphalerite through coupled substitutions (Fig. 7E, F; further discussed below).

Tin content is markedly variable according to both the mineralization style and the sphalerite generation (Fig. 6E). The highest Sn contents are recorded in sphalerite grains from veins at NE Ayawilca (15,100–5667 ppm). In veins at NW Ayawilca, a trend towards Sn depletion from early (336–125 ppm) to late (3.3–0.48 ppm) sphalerite generations is observed. In contrast, sphalerite grains from mantos show an irregular content, with general depletion in the second generation (59–1.2 ppm, stage A) relative to the first (386–11 ppm, stage A) and third (929–43 ppm, stage C) generations. Silver content is highest in sphalerite from veins at NE Ayawilca (195–110 ppm) and relatively constant in veins at NW Ayawilca (41–2.6 ppm) and mantos (30–3.3 ppm). Much lower are the values of Hg, which increase from the first (1.4–1.1 ppm) to the second (2.1–1.4 ppm, stage A) and third (32–17 ppm, stage C) sphalerite generations in mantos and from the first (3.2–2.6 ppm, stage A) to the second (50–22 ppm, stage C) generations in veins from NW Ayawilca.

Among critical elements (In, Ge, Ga), the highest contents in analyzed sphalerite from Ayawilca are those of In (986–16 ppm, up to 1.7 wt%). In mantos, this element is more abundant in second-generation (1299–227 ppm, stage A) than in first- (109–3.1 ppm, stage A) and third-generation (56–9.6 ppm, stage C) sphalerite (Fig. 6F). Sphalerite from veins at NE Ayawilca yields much higher In contents (2676–993 ppm) than sphalerite from veins at NW Ayawilca (up to 1.2 ppm). In the latter, there is an In depletion trend from first- (1.2–0.6 ppm, stage A) to second-generation (< 0.10 ppm, stage C) sphalerite (Fig. 6F). Germanium contents are systemically low (0.24–0.14 ppm, up to 14 ppm; Fig. 6G) but slightly higher in veins from NE Ayawilca (3.5–0.90 ppm). Gallium values in sphalerite from both mantos and veins are mostly a few ppm but slightly higher in grains from veins at NE Ayawilca (91–69 ppm, up to 92 ppm; Fig. 6H). In mantos, there is a subtle increase in the Ga content from first- (1.8–0.57 ppm) to second- (7.3–1.2 ppm, stage A) and third-generation (8.7–3.7 ppm, stage C) sphalerite. Element correlations and substitution mechanisms of In, Ge, and Ga in sphalerite are addressed in detail in the "Discussion" section.

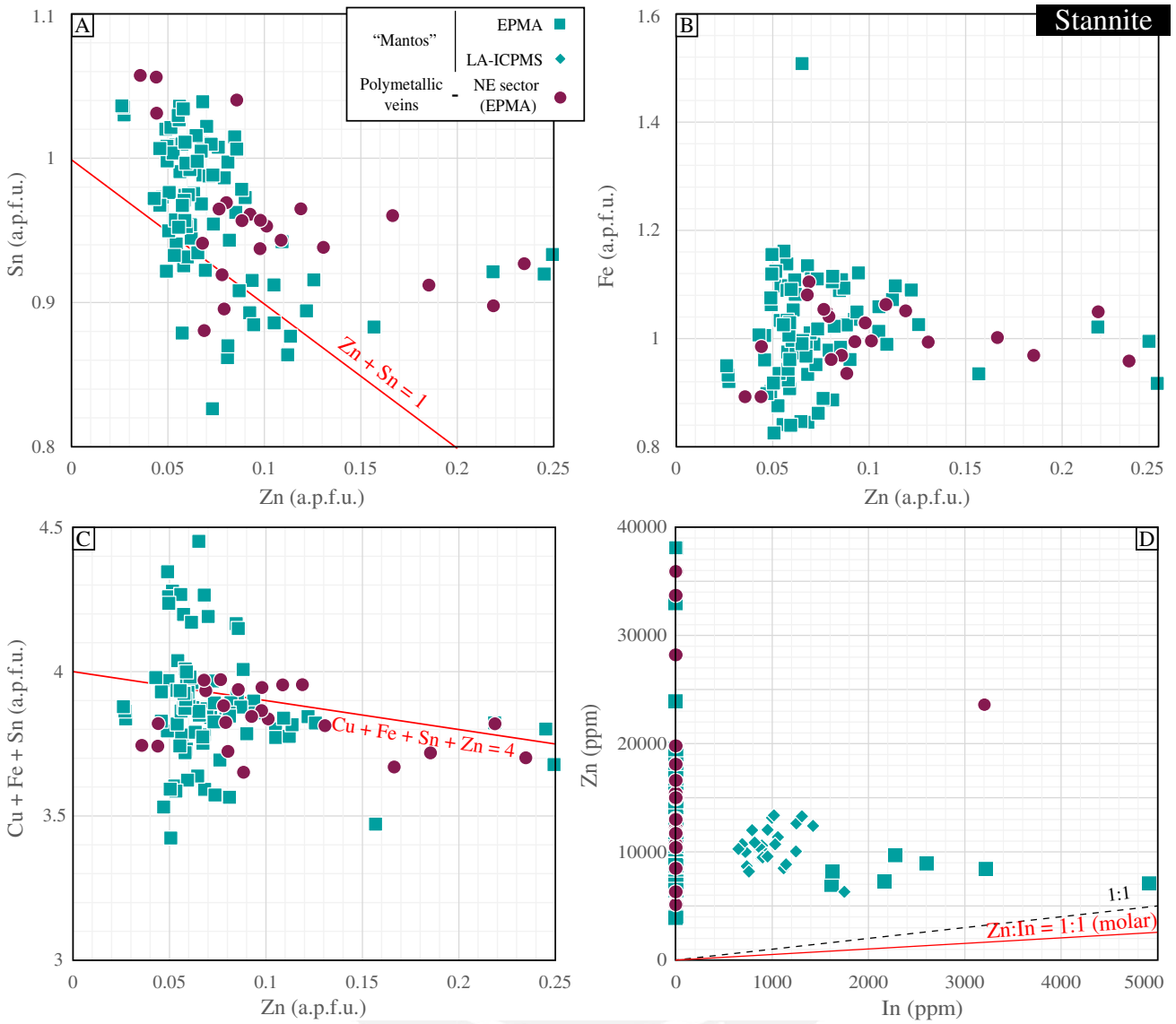

Fig. 8 Correlation between elements in stannite from the Ayawilca deposit (**A**–**C** EPMA data; **D** LA-ICP-MS data)

Stannite group minerals

Our EPMA and LA-ICP-MS datasets for stannite group minerals from the studied mantos reveal a narrow compositional range for Cu (28.9–26.3 wt%), Sn (26.8–25.8 wt%), and Fe (13.8–11.9 wt%), and relatively high Zn (12,025–9315 ppm) and Ag (1623–1360 ppm). Indium content in stannite from mantos is significant (1168–869 ppm; up to 1908 ppm), whereas the contents of Ga and Ge are much lower (both, < 20 ppm). Analyzed stannite grains yield Zn/(Fe + Zn) atomic ratios between 0.03 and 0.24. As Zn tends to have a subtle negative correlation with Sn (Fig. 8A) and does not show a negative correlation with Fe (Fig. 8B), a governing role for the stannite-kësterite solid solution series in the composition of studied stannite is excluded. In contrast, the negative correlation between Zn and Cu + Fe + Sn at Zn + Cu + Fe + Sn ~ 4 a.p.f.u. (Fig. 8C) suggests that the incorporation of Zn can be contextualized within a solid solution between stannite and (Fe-rich) sphalerite (see Oen et al. 1980).

Chalcopyrite

Chalcopyrite grains from mantos and NE Ayawilca veins were analyzed. Iron content is relatively constant (29.9–29.0 wt%) whereas the contents of Sn, Ag, and Cd are considerably higher in vein (4204–3380 ppm Sn, 962–665 ppm Ag, and 31–15 ppm Cd) than in manto (2278–1715 ppm Sn, 402–336 ppm Ag, and 5.8–2.8 ppm Cd) chalcopyrite. Indium values are higher in stage A first-generation

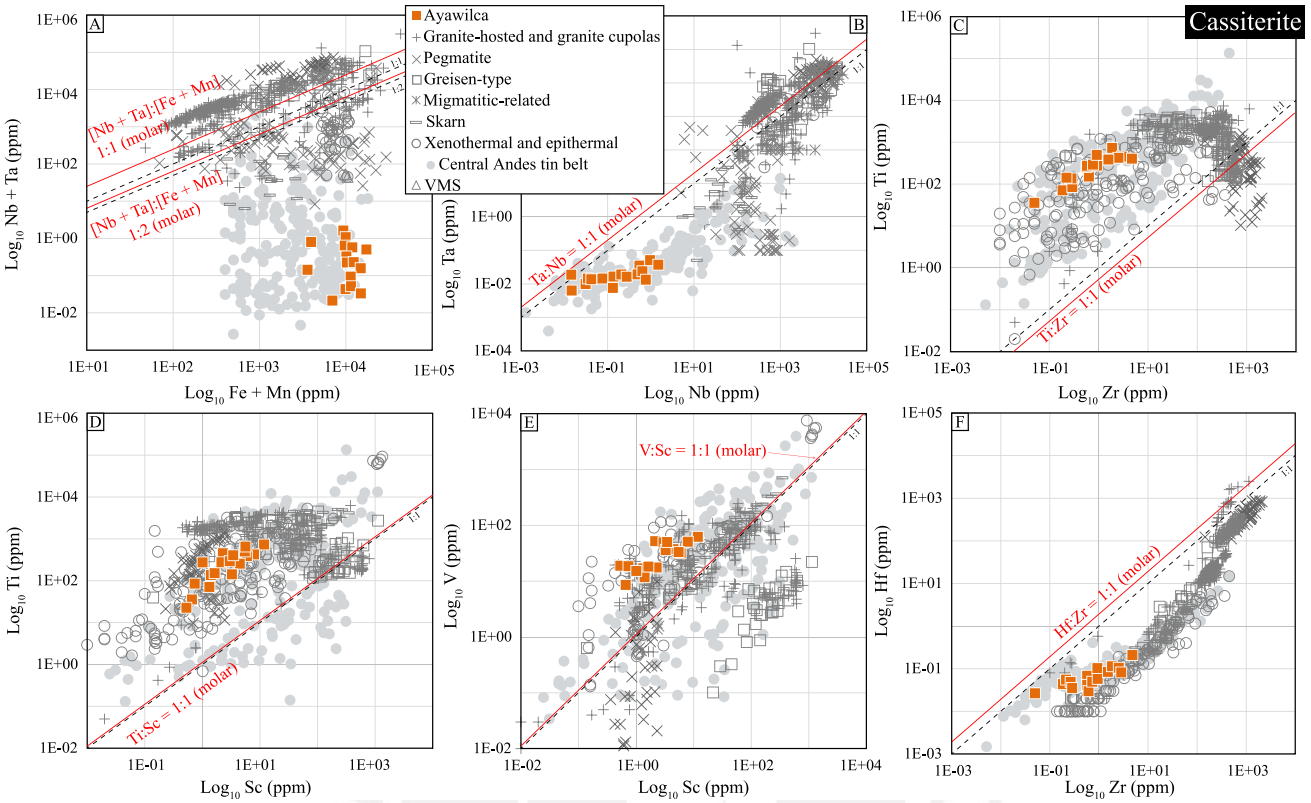

Fig. 9 Correlation binary plots for Ayawilca cassiterite (LA-ICP-MS data). Reference data are shown for comparison (Moore and Howie 1979; Lentz and McAllister 1990; Plimer et al. 1991; Murciego et al. 1997; Serranti et al. 2002; Jiang et al. 2004; Gorelikova et al. (2006); Abdalla et al. 2008; Neiva 2008; Wise and Brown 2011; Pavlova et al. 2015; Lerouge et al. 2017; Nascimento and Souza 2017; Zhang et al. 2017; Guo et al. 2018; Chen et al. 2019; Cheng et al. 2019; Fuchsloch et al. 2019; Hulsbosch and Muchez 2019; Kendall-Langley et al. 2019; Zhao et al. 2019; Zoheir et al. 2019; Mao et al. 2020; Nambaje et al. 2020; Gemmrich et al. 2021)

chalcopyrite from mantos (1078–900 ppm; up to 1185 ppm) than in analyzed chalcopyrite from veins (670–535 ppm). In contrast, Ga content is higher in veins (27–14 ppm) than in mantos (1.9–1.5 ppm). Germanium content is similar in chalcopyrite from both mantos and veins (3.2–0.29 ppm).

Cassiterite

Cassiterite from Ayawilca yields moderate enrichment in Fe (12,300–9350 ppm), W (5032–1670 ppm), Si (925–614 ppm), and Ti (416–111 ppm) relative to Mn (12–2.5 ppm) and HFSE (1.8–0.29 ppm Zr, 0.079–0.041 ppm Hf, 0.62–0.040 ppm Nb, 0.021–0.014 ppm Ta) contents. Other elements with values mostly above their respective lower limits of detection include Al (83–56 ppm), V (50–17 ppm), Sb (84–48 ppm), Ni (24–16 ppm), In (89–47 ppm), and Sc (5.0–1.2 ppm).

In the binary Fe + Mn vs. Nb + Ta diagram, the cassiterite data cluster below both the 1:1 (i.e., $2Sn^{4+} \leftrightarrow (Nb, Ta)^{5+} + (Fe, Mn)^{3+}$ coupled substitution) and 2:1 (i.e., $3\,Sn^{4+} \leftrightarrow 2(Nb,Ta)^{5+} + (Fe,Mn)^{2+}$) ratio lines (Fig. 9A) and yield Nb/Ta atomic ratios between 2 and 113 (Fig. 9B). The analyzed cassiterite shows a fairly positive correlation between Ti and Zr at Ti/Zr atomic ratios between 163 and 1361 (Fig. 9C). Scandium also shows fairly positive correlations with Ti (Ti/Sc atomic ratios between 40 and 255; Fig. 9D) and V (V/Sc atomic ratios between 5 and 31; Fig. 9E). Zirconium and Hf yield a positive correlation in the analyzed cassiterite grains at Zr/Hf atomic ratios between 3 and 74 (Fig. 9F).

Rare-earth-element (REE; La to Lu) contents in cassiterite grains from Ayawilca are relatively homogeneous in all analyzed grains (∑REE between 4.9 and 0.97 ppm). The highest REE contents correspond to Gd (1.2–0.87 ppm) and La (0.33–0.26 ppm), and the lowest to Tm (0.017–0.013 ppm) and Ho (0.021–0.014 ppm). In chondrite-normalized (CN) spider plots (Fig. S3), studied cassiterite grains show roughly parallel patterns with irregular distribution combining concave and convex tetrads.

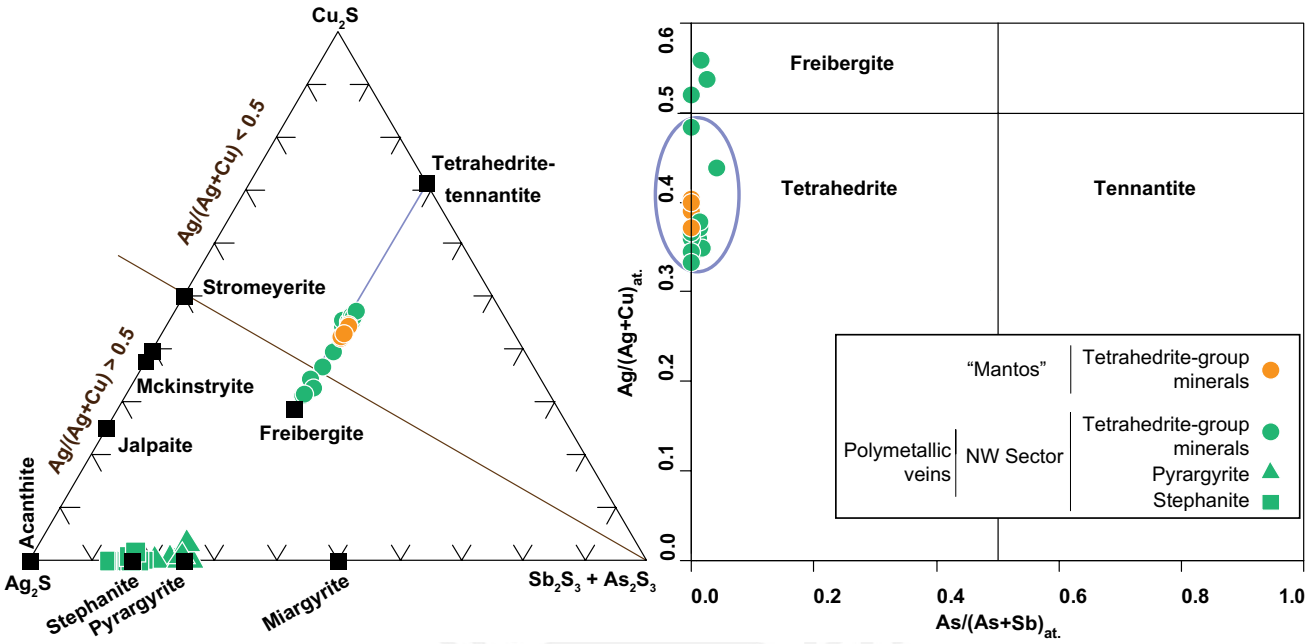

Fig. 10 Plot of the analyzed tetrahedrite-group minerals and Ag–Cu-Sb sulfosalts from the Ayawilca deposit in the Ag_2S vs. $Sb_2S_3 + As_2S_3$ ternary diagram and of the tetrahedrite-group minerals in the $As/(As+Sb)_{at}$ vs. $Ag/(Ag+Cu)_{at}$ binary diagram (right) (EPMA data)

Magnetite

Minor and trace elements analyzed in magnetite include Ti (46–4.7 ppm), V (19–2.9 ppm), Mn (1961–1014 ppm), Al (99–21 ppm), Ca (749–218 ppm), Ni (0.76–0.14 ppm), and Cr (2.6–0.40 ppm). The three generations of magnetite from Ayawilca plot within the field of skarn deposits in discrimination diagrams (e.g., Dupuis and Beaudoin 2011; Nadoll 2011; Nadoll et al. 2014; Meng et al. 2017; Fig. S4).

Other mineral phases

Representative EPMA analyses of pyrrhotite, galena, herzenbergite, and tetrahedrite group minerals are provided in Table S2. Pyrrhotite grains in mantos presented Fe contents in the range between 61.4 and 60.6 wt%, and S contents in the range between 40.4 and 37.3 wt%. The Ag content in galena was relatively low (< d.l. to 1.0 wt%). Herzenbergite

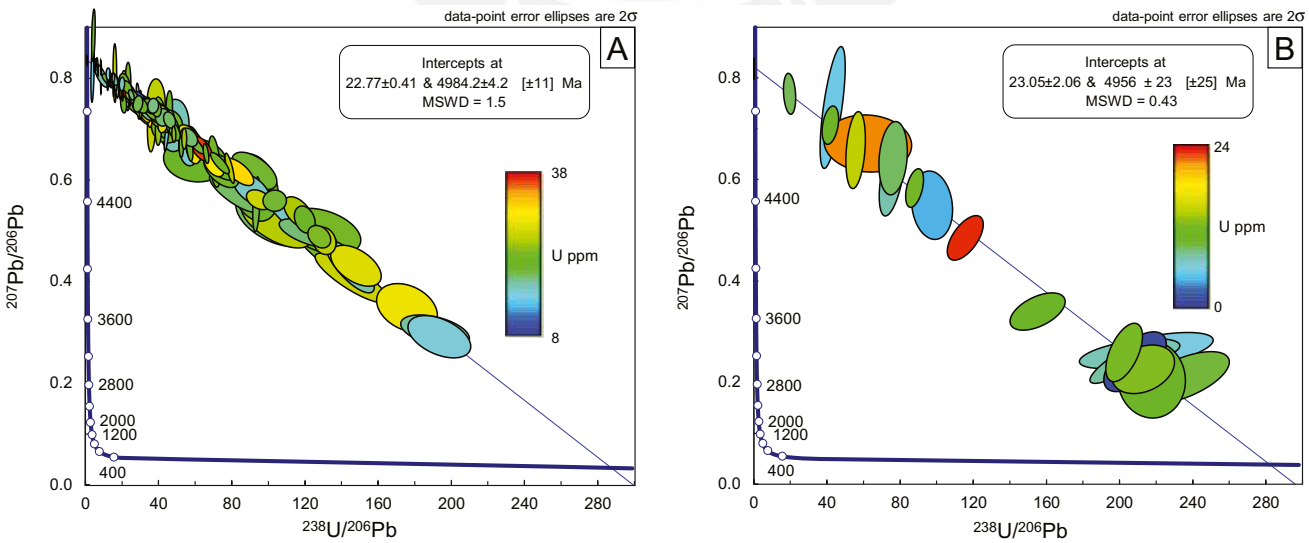

Fig. 11 Tera-Wasserburg (T-W) concordia plots for cassiterite samples from the Ayawilca deposit analyzed at the USGS (**A**) and ETZH (**B**)

yields relatively constant Sn (78.9–74.9 wt%) and S (21.3–19.8 wt%) contents.

Analyzed tetrahedrite group minerals yield As/(As + Sb) atomic proportions < 0.03 (Fig. 10) and generally high Ag content both in mantos (between 22.7 and 20.9 wt%) and in veins located in the NW Ayawilca sector (between 32.1 and 19.6 wt%), with Ag/(Ag + Cu) between 0.33 and 0.56. Accordingly, the analyzed tetrahedrite group minerals are classified as tetrahedrite (*var.* Ag-rich tetrahedrite) and freibergite.

Analyzed Ag sulfosalts include pyrargyrite and stephanite from veins at NW Ayawilca (Fig. 10). Pyrargyrite has Ag contents between 56.4 and 62.9 wt%, Sb contents between 17.6 and 22.4 wt%, and S contents between 16.1 and 17.9 wt%. Stephanite yields Ag values between 63.7 and 72.9 wt%, Sb values between 12.1 and 16.6 wt%, and S values between 11.4 and 16.0 wt%.

U–Pb cassiterite geochronology

U–Pb isotopic analyses of cassiterite grains from the Ayawilca deposits are presented in Tables S5-S6 and illustrated in Fig. 11. Although U–Pb concordant data are missing, spot analyses define isochrons in Tera-Wasserburg (T-W; $^{207}Pb/^{206}Pb$ vs. $^{238}U/^{206}Pb$) diagrams corresponding to mixing lines between the compositions of radiogenic and initial, non-radiogenic Pb in the cassiterite samples. One hundred and twenty spot analyses of cassiterite performed at the USGS laboratory yield a T-W concordia lower intercept date of 22.77 ± 0.41 Ma (2σ; MSWD = 1.5). Twenty spot analyses carried out at the ETHZ laboratory yield a T-W concordia lower intercept date of 23.05 ± 2.06 Ma (2σ; MSWD = 0.43; with matrix effect-related uncertainty propagated—see "Sampling and analytical methods" section for details). The consistency of the two dates (despite different analytical parameters and calibration strategies) supports the notion that the Ayawilca cassiterite crystallized in a single event within the dating uncertainties at ca. 23.1–22.7 Ma and displayed a closed-system behavior with respect to relative U–Pb mobility after formation.

Discussion

Evolution of mineralization conditions

The paragenetic sequences in the polymetallic mantos and veins (Fig. 5) and the chemical compositions of some key minerals are used here to constrain the evolution of mineralization conditions during formation of the Ayawilca deposit. The earliest mineralization stage in the mantos is identified as a likely distal retrograde magnesian skarn (stage pre-A) that includes locally abundant Mg-siderite + talc + magnetite + chlorite and relict actinolite-tremolite. As mentioned above, the trace element composition of the magnetite is characteristic of skarn. The occurrence of skarn assemblages in the deepest mantos at Ayawilca suggests that the studied replacement bodies were formed in a transition zone between a distal skarn and skarn-free Cordilleran-type carbonate-replacement mineralization styles.

Major mineral assemblages in both the mantos and veins record a change from low- (stage A) to intermediate- (stages B and C) sulfidation states, with the paragenetic sequences being broadly equivalent to those of most Cordilleran-type deposits (Fontboté 2018, 2020). However, unlike other Cordilleran-type deposits in the region that contain cassiterite and stannite in trace amounts (e.g., Baumgartner et al. 2008; Bendezú et al. 2009; Catchpole et al. 2012, 2015; Rottier et al. 2016, 2018), Ayawilca hosts a potentially economic Sn resource that includes fairly abundant cassiterite crystallized during stage pre-A, and minor stannite and rare herzenbergite during stage A (Fig. 5). Minor and trace element compositions of cassiterite from Ayawilca are similar to those from xenothermal and epithermal deposits of the Central Andean tin belt in terms of Nb, Ta, Fe, and Mn, and are depleted in Nb + Ta relative to cassiterite from Sn skarns, greisens, migmatites, granite-hosted, and granite cupolas (Fig. 9A, B; references listed in Fig. 9 caption; "xenothermal" is used here in the sense of Imai et al. 1975, as explained in Gemmrich et al. 2021). The contents of Nb and Ta in cassiterite are strongly dependent on temperature so that cassiterite from low-temperature hydrothermal deposits is relatively depleted in these elements (Lerouge et al. 2017; Zhang et al. 2017). On the other hand, cassiterite from Ayawilca shows Ti/Zr (Fig. 9C) and Ti/Sc (Fig. 9D) ratios similar to xenothermal and epithermal deposits, which are normally higher than for those in cassiterite from Sn skarn, greisen, granite-hosted, and granite cupola mineralizations, probably due to the higher mobility of Zr and Sc relative to Ti in the hydrothermal fluids (Taylor 1979; Plimer et al. 1991; Cheng et al. 2019; Gemmrich et al. 2021). Therefore, trace element geochemistry of cassiterite from Ayawilca accords well with a relatively distal position of the manto mineralization relative to a potential causative intrusion.

Cassiterite from Ayawilca is also similar to cassiterite from the Central Andean tin belt in terms of Hf and Zr contents, with Zr/Hf > 1 and mostly higher than cassiterite in greisen, granite-hosted, and granite cupola mineralizations

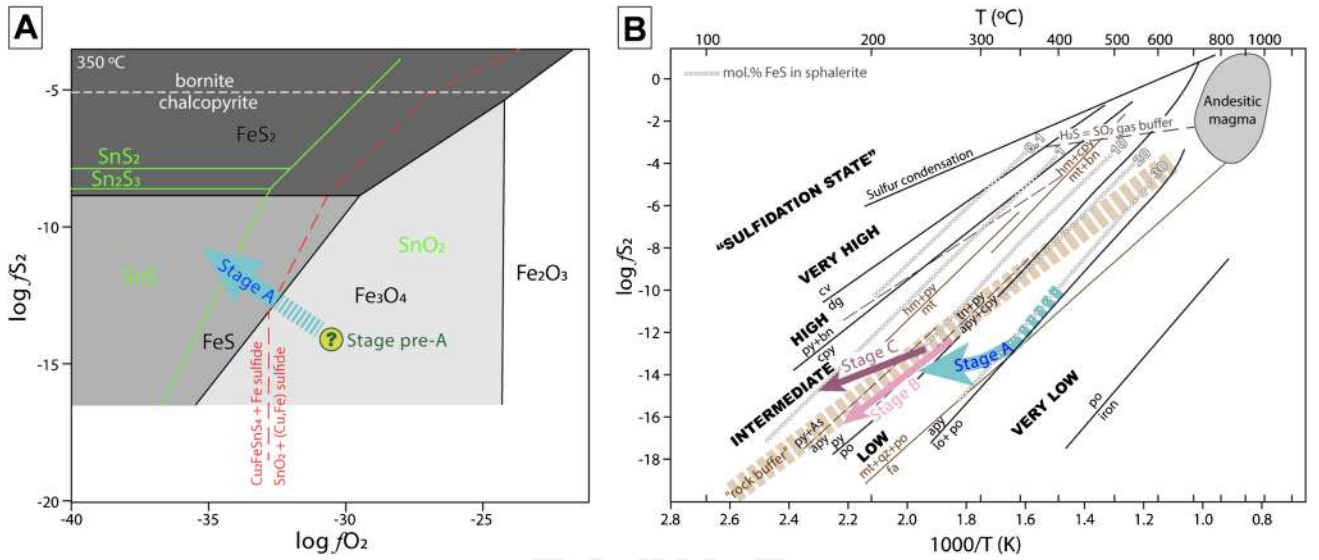

Fig. 12 **A** General fluid path followed by fluids forming stage A in mantos (blue arrow, low sulfidation) in a logfS_2–logfO_2 isothermal (350 °C) diagram. LogfS_2 values inferred from metal-to-sulfur ratios in pyrrhotite (see main text). Position of the blue arrow is only schematic as its origin in the SnO_2 and Fe_3O_4 field does not allow to constrain fS_2. Field boundaries are after Patterson et al. (1981). **B** General fluid path followed by fluids forming stages A (blue arrow, low sulfidation), B (pink arrow, intermediate sulfidation), and C (purple arrow, intermediate sulfidation) in a logfS_2–1000/T diagram (modified from Einaudi et al. 2003). Fluid environment is based on sulfide assemblages and the compositions of sulfide and sulfosalt minerals (see main text), and a preliminary fluid-inclusion study performed by Harlaux (2019). At Ayawilca, the rock-buffer line was probably lower than the one of Giggenbach (1987; shown with a thick, dashed brown line, and based on a fresh andesite) according to the nature of the host rocks, which at Ayawilca include carbonaceous shales and phyllites of the Excelsior Group and carbonates of the Pucará Group. Contours of mol% FeS in sphalerite coexisting with pyrite or pyrrhotite are from Scott and Barnes (1971) and Czamanske (1974). Mineral abbreviations: apy, arsenopyrite; bn, bornite; cpy, chalcopyrite; cv, covellite; dg, digenite; en, enargite; fa, fayalite; fm, famatinite; hm, hematite; lo, löllingite; mt, magnetite; po, pyrrhotite; py, pyrite; qz, quartz

(Fig. 9F). The most likely explanation for this is the preferential mobilization of Zr in B- and F-rich fluids causing fractionation of Zr over Hf in hydrothermal cassiterite (Cheng et al. 2019). However, at Ayawilca, there is a lack of B and F species, which is a significant difference compared with many other Sn(-polymetallic) magmatic-hydrothermal deposits (Pollard et al. 1987; Xiang et al. 2020; Lehmann 2021), including those in the Central Andean tin belt (Kelly and Turneaure 1970; Lehmann et al. 1990, 2000; Cacho et al. 2019; Torres et al. 2019; Harlaux et al. 2020), in which the occurrence of tourmaline + fluorite ± topaz in hydrothermal alteration assemblages is ubiquitous.

The precipitation sequence of cassiterite to stannite to herzenbergite as precipitating Sn phases in the mantos at Ayawilca (Figs. 3K, L and 5) indicates increasingly reducing conditions at relatively low fS_2 in stage pre-A and throughout stage A (Patterson et al. 1981). The occurrence of herzenbergite deserves particular attention. The enhanced solubility of Sn in reduced media (Patterson et al. 1981; Barsukov et al. 1987; Heinrich 1990; Linnen et al. 1995; Lehmann 2021) renders crystallization and preservation of herzenbergite unlikely, hence the global scarcity of localities in which it has been documented. The crystallization of herzenbergite is promoted by exceptionally low fO_2 (~ 10^{-40}–10^{-35} atm) at relatively low fS_2—normally in equilibrium with pyrrhotite—over a wide range of temperature (~ 200–500 °C) and pH (2–10) conditions (Patterson et al. 1981; Smeds 1993 and references therein). Intense chemical buffering of hydrothermal fluids during their interaction with the Excelsior carbonaceous phyllites probably resulted in a significant fO_2 drop to values low enough to stabilize herzenbergite after initial crystallization of cassiterite in the slightly more oxidized sulfur field (Fig. 12A).

A preliminary fluid inclusion study of stage A quartz postdating pyrrhotite yielded homogenization temperatures in the range between 341 and 265 °C (average of 298 ± 22 °C) and salinities between 2.4 and 9.1 wt% NaCl equiv. (Harlaux 2019). If we assume that cassiterite crystallized at higher temperatures than stage A quartz (Fig. 5), a plausible stage A quartz-pyrrhotite and minimum cassiterite crystallization temperatures would be around 350 °C. At 350ºC, atomic metal to sulfur ratios in analyzed pyrrhotite yield log fS_2 in the approximate range between – 13 and – 10 atm (Toulmin and Barton 1964). According to this fS_2 range, herzenbergite would have formed at log fO_2 in the approximate range between – 30 and – 35 atm, which likely

represents the minimum fO_2 value reached by hydrothermal fluids at Ayawilca (Fig. 12A). Sealing of the walls of mineralized structures by quartz along with waning wall-rock buffering capacity favored a progression from low sulfidation (stage A) to higher sulfidation (stages B and C) states as the system cooled (see Baumgartner et al. 2008 and Rottier et al. 2018).

Sphalerite from Ayawilca mantos and veins records a pronounced decrease in the Fe content from the early (stage A) to late (stage C; Fig. 5) generations. The compositions of sphalerite crystallized during stage A in mantos (first generation 30 to 18 mol% FeS, avg. 22 mol% FeS; second-generation 32 to 10 mol% FeS, avg. 22 mol% FeS) and veins at NW Ayawilca (33 to 9 mol% FeS, avg. 19 mol% FeS) and NE Ayawilca (21 to 18 mol% FeS, avg. 19 mol% FeS) accord well with general crystallization in equilibrium with pyrrhotite and beyond the pyrite stability field at about > 21 mol% FeS (Scott and Barnes 1971). FeS values in the range between 19 and 21 mol% suggest co-crystallization in equilibrium with both pyrite and pyrrhotite, and FeS < 19 mol% values suggest crystallization in equilibrium with pyrite and beyond the pyrrhotite stability field. According to these observations, sphalerite records a progressive shift from low- to intermediate-sulfidation states during the transition from stage A to stage B at Ayawilca. At $\log fS_2$ of − 10 atm or lower, sphalerite with 33 mol% FeS would have crystallized at a maximum temperature of ~ 380 °C, and sphalerite with 21 mol% FeS at a maximum temperature of 318 °C (Scott and Barnes 1971). Stage C sphalerite from the mantos (7 to 3 mol% FeS, avg. 4 mol% FeS) and veins (11 to 1 mol% FeS, avg. 8 mol% FeS) yields compositions that indicate crystallization in equilibrium with pyrite and beyond the pyrrhotite stability field.

The composition of co-crystallized sphalerite and stannite (stage A; Fig. 5) yields formation temperatures in the range between 300 and 250 °C according to the Nakamura and Shima (1982) geothermometer. Finally, the composition of tetrahedrite group minerals that crystallized during stage C (Fig. 5) yields crystallization temperatures in the range between 200 and 170 °C for analyzed grains from the mantos and between 300 and 170 °C for analyzed grains from NW Ayawilca veins according to the Sack et al. (2003) geothermometer. However, temperatures < 200 °C are probably unrealistically low for main tetrahedrite crystallization if they are compared with Ti-in-quartz thermobarometry and microthermometric data measured in stage C inclusion fluids in other Cordilleran-type polymetallic deposits (e.g., Catchpole et al. 2015; Rottier et al. 2018, 2021). Possible pathways of fluid evolution leading to the deposition of the sulfides and sulfosalts in the Ayawilca polymetallic mantos and veins are shown on a $\log fS_2$ vs. 1000/T diagram in Fig. 12B.

Mineralogical expression and distribution of indium

In the Ayawilca deposit, In is found within the crystal lattice of some major minerals, and no independent In minerals (e.g., roquesite) were found. This situation is typical of polymetallic deposits in which Zn is a major component and sphalerite fairly abundant (Cook et al. 2011b). According to our dataset, the main In-bearing minerals at Ayawilca are sphalerite (986–16 ppm, up to 1.7 wt%), stannite (1168–809 ppm, up to 1908 ppm), and chalcopyrite (910–537 ppm, up to 1185 ppm).

Sphalerite is volumetrically the most abundant sulfide mineral in both the polymetallic mantos and veins at Ayawilca and therefore represents the main In host at the deposit scale. Effective partitioning of In into sphalerite has been extensively documented (Cook et al. 2009, 2011a, 2011b; Sahlström et al. 2017; Bauer et al. 2019; Carvalho et al. 2018; Torró et al. 2019a, 2019b; Benites et al. 2021). Relatively high In content in Fe-rich sphalerite (avg. 2620 ppm) was reported by Rottier et al. (2016) in the neighboring Cerro de Pasco deposit (Fig. 1). The strong positive correlation between the atomic contents of In and Cu in the studied sphalerite grains that are partly distributed along the 1:1 ratio line (Fig. 7E) points to a $Cu^+ + In^{3+} \leftrightarrow 2\,Zn^{2+}$ coupled substitution (Pattrick et al. 1993; Schwarz-Schampera and Herzig 2002; Cook et al. 2011a, 2011b; 2012; Torró et al. 2019a, b) in the frame of a sphalerite–roquesite solid solution (Oen et al. 1980; Parasyuk et al. 2003; Schorr and Wagner 2005). However, the totality of the analyzed sphalerite from the NE and NW Ayawilca vein systems and part of the analyzed sphalerite from the mantos plot above the Cu:In = 1:1 correlation line, thus denoting higher Cu at a given In content. A similar situation is noticed by others (e.g., Xu et al. 2020) and points to the existence of further coupled substitutions involving Cu. The marked positive correlation between Cu + Ag and Ga + Ge + In + Sn in sphalerite, whose compositions are massively distributed along the 1:1 ratio line (Fig. 7F), supports a $(Sn, Ge)^{4+} + (Ga, In)^{3+} + (Cu + Ag)^+ \leftrightarrow 4\,Zn^{2+}$ coupled substitution (Cook et al. 2009). Therefore, besides Cu, elements such as Ag and Sn also played an important role in the incorporation of In into the sphalerite crystal lattice.

In contrast to sphalerite, the incorporation of In into the stannite crystal lattice is poorly understood. Torró et al. (2019a) suggested, after the study of In-rich stannite grains from the Huari Huari district in the Central Andean tin belt, an $In^{3+} \leftrightarrow (Cu^+ + ½\,Sn^{4+})$ coupled substitution. However, no clear correlation trends that would involve these elements were observed in stannite from Ayawilca. The incorporation of In into the crystal lattice of stannite in the frame of a hypothetical stannite–(In-rich) sphalerite solid solution within the $(Zn,Fe)S–Cu_2FeSnS_4–CuInS_2$ pseudoternary

system described by Oen et al. (1980) is likewise implausible according to the lack of correlation between Zn and In within this mineral at Ayawilca (Fig. 8D).

As observed in stannite, In does not show clear correlation trends with the other analyzed elements in chalcopyrite from Ayawilca. Due to covalent bonding, a substitution mechanism based on element correlation trends and electroneutrality cannot be straightforwardly deduced for chalcopyrite (George et al. 2018). Wittmann (1974) suggested that significant In could be hosted in chalcopyrite (mostly in the Fe site) because it is isostructural with roquesite. The reader is referred to Belissont et al. (2019) and Reich et al. (2020) for previously proposed coupled substitutions in chalcopyrite that involve In.

Although cassiterite may host important In contents (e.g., up to 485 ppm in granites and granite cupolas from the Nghe An deposit, Vietnam, Pavlova et al. 2015; up to 1430 ppm in epithermal deposits from the Central Andean tin belt, Gemmrich et al. 2021), the contents of this *high-tech* metal recorded in cassiterite from Ayawilca are relatively low (89–47 ppm, up to 98 ppm). Lerouge et al. (2019) stated that sulfides (i.e., sphalerite and stannite) with high In contents were often related to In-poor cassiterite, and attributed this fact to a high sulfide/cassiterite partition coefficients. However, as cassiterite crystallized earlier than In-bearing sulfides at Ayawilca (Fig. 5), this hypothesis may not be relevant and may just reflect low concentrations of In in the mineralizing fluids during the crystallization of cassiterite (see Plimer et al. 1991; Gemmrich et al. 2021).

The detailed study of the mineralogy and textures in the Ayawilca deposit poses some temporal constraints on the distribution of In across the paragenetic sequences. The highest contents of In are associated with stage A second-generation sphalerite from the mantos and with stage A sphalerite from the NE Ayawilca veins (a single generation was found there; Figs. 5, 6F). Therefore, high In content in sphalerite from Ayawilca typically correlates with high Fe content, but the opposite is not necessarily true. For example, stage A first-generation sphalerite in the mantos is Fe-rich (as typical of low-sulfidation assemblages) but In poor (Fig. 6A, F). Stage C sphalerite in both the veins from NW Ayawilca and mantos, which formed from late intermediate-sulfidation state fluids (Fig. 5), is systematically In poor (Fig. 6F). Accordingly, low-sulfidation assemblages that contain abundant sphalerite, chalcopyrite, and stannite are the most prospective for In in Cordilleran-type deposits, especially in those with large volumes of low-sulfidation assemblages, as at Ayawilca. Torró et al. (2019a) identified similar temporal trends in the distribution of In in sphalerite from the xenothermal Huari Huari deposit, including In enrichment (up to 9 wt% In) in sphalerite that crystallized during early stages in a low-sulfidation paragenesis in equilibrium with stannite and chalcopyrite. These authors proposed that the co-crystallization of In-rich sphalerite with stannite and chalcopyrite and the strong positive correlation between In and Cu in sphalerite were indicative of a high Cu activity in the hydrothermal fluids, which enabled the incorporation of In into the sphalerite crystal lattice through the substitution mechanisms discussed above.

Regarding the spatial distribution of In content across the deposit, the highest In values in sphalerite from Ayawilca are found at relatively deep levels (e.g., up to 1.7 wt% In at 347.50 m). However, no steady enrichment of In in sphalerite with depth has been noted, and some high In values have been detected in relatively shallow locations as well (e.g., up to 3778 ppm In at 240.10 m; stage A mineralization in mantos). The morphology of the mineralization did not apparently exert any control on In enrichment either: stage A second-generation sphalerite from mantos and sphalerite from the NE Ayawilca veins yield similar In contents (Fig. 6).

The Ayawilca deposit within the metallogenic evolution of the central Andes

Direct U–Pb dating of cassiterite at ca. 23.1–22.7 Ma constrains the age of the Ayawilca deposit as earliest Miocene, suggesting assignment of the Ayawilca deposit to the Miocene polymetallic belt in central Peru. However, it is older than most deposits in this belt, which are mostly mid-Miocene or younger (ca. 15 - 5 Ma—e.g., Domo de Yauli, Morococha, Cerro de Pasco, Colquijirca, Antamina; Beuchat et al. 2004; Baumgartner et al. 2008; Bendezú and Fontboté 2009; Longo et al. 2010; Catchpole et al. 2015; Rottier et al. 2018; Mrozek et al. 2020). Ayawilca appears to be only slightly younger than the late Oligocene Uchucchacua polymetallic deposit (ca. 24.5 Ma; Bissig et al. 2008). The obtained age for the cassiterite of Ayawilca supports the conclusion of the latter authors that potential for polymetallic deposits in central Peru is greater near intrusive rocks of mid to late Miocene age except for an easterly striking broad strip at ~ 10°40′–10°50′S where the late Eocene and Oligocene Uchucchacua (ca. 24.5 Ma), Milpo (now also called El Porvenir–Atachocha (ca. 29.5 Ma)), and Quicay (ca. 37.5 Ma) deposits occur (Bissig et al. 2008). The early Miocene Ayawilca deposit located at 10°43′S occurs in this very transect. Bissig et al. (2008) pointed out that subduction geometry alone cannot account for the observed distribution of mineralization and that specific upper-plate features in this transect should also have exerted a metallogenic control. North of 8°S and still inside the Miocene–early Pliocene porphyry belt of the central Andes (Sillitoe and Perelló 2005), mineralization events bracketed at ca. 22–20 Ma occur in the Cajamarca mining district in northern Peru, including the Michiquillay and Aurora Patricia porphyry Cu-Mo deposits (Laughlin et al. 1968; Noble et al. 2004; Davies 2002;

Davies and Williams 2005; Carlotto et al. 2009; Marinov 2011), which are located ~ 420 km north of Ayawilca. The Malvas and Huinac porphyry districts in the Cordillera Negra (Noble et al. 2004), which are located ~ 150 km northwest of Ayawilca, also fall into this age range.

The discovery of the Ayawilca deposit has important implications for exploration in the central Andes as it hosts a potentially economic Sn resource located ~ 850 km northwest of the northern tip of the Central Andean tin belt (Fig. 1). The obtained U–Pb cassiterite age for Ayawilca overlaps, within analytical error, the age of Sn mineralization in the northern portion of the Central Andean tin belt, including the world-class San Rafael deposit and Santo Domingo and Palca occurrences in southeastern Peru, and the Viloco, Huanuni, and Llallagua deposits in Bolivia (radiometric dates summarized in Gemmrich et al. 2021). In contrast to the Miocene–early Pliocene porphyry belt, in which causative intrusions have "regular" calc-alkaline affinities and belong to the I-type, magnetite series of Ishihara (1981), the causative intrusions in the Central Andean tin belt belong to the S-type, ilmenite series (Sillitoe and Perelló 2005; Fontboté 2018; Lehmann 2021). At Ayawilca, the causative intrusion remains concealed, and therefore, its petrogenetic nature is unknown. Although a relatively reduced magma is required to exsolve tin into comagmatic hydrothermal fluids (tin behaves as an incompatible element in the divalent state; Lehmann 2021), peraluminous, ilmenite-series intrusive rocks of Cenozoic age are apparently absent in the study area and everywhere north of 14°S (i.e., north of the San Rafael tin district; Harlaux et al. 2020 and references therein). The highly reduced nature of the Excelsior carbonaceous phyllites beneath the deposit would have favored effective transport of Sn (Heinrich 1990; Xiang et al. 2020; Lehmann 2021). As a preliminary hypothesis, we surmise that due to the absence of the Mitu Group red beds at Ayawilca (Figs. 1 and 2), in contrast to several other Cordilleran-type polymetallic deposits in the region (e.g., Morococha and Colquijirca), rock buffering of the hydrothermal fluids was particularly intense, facilitating Sn^{2+} transport and an economic accumulation of Sn as cassiterite. However, it should be noted that at Cerro de Pasco, where the available evidence indicates that the Excelsior phyllites strongly buffered the hydrothermal fluid, only minor cassiterite and stannite occur (Baumgartner et al. 2008; Rottier et al. 2016, 2018) and that the tin endowment at Ayawilca is several orders of magnitude higher.

Conclusions

The Ayawilca deposit is one of the most significant recent base-metal discoveries in the central Andes and one of the largest undeveloped In resources worldwide. The mineralization at Ayawilca occurs as 10- to 70-m-thick mantos and subordinate steeply dipping veins. The Sn-dominant resource is hosted by massive pyrrhotite replacement bodies at the base of the Triassic to Early Jurassic carbonate rocks of the Pucará Group, close to and along their contact with underlying Devonian weakly metamorphosed, organic-rich shaly rocks of the Excelsior Group. Zinc mineralization occurs predominantly as Fe-rich sphalerite mantos and veins hosted in rocks of the Pucará Group and, subordinately, in Cretaceous sandstones-siltstones of the Goyllarisquizga Group.

The mineralization at Ayawilca includes relicts of a distal retrograde magnesian skarn composed of Mg-siderite + talc + magnetite + chlorite ± actinolite-tremolite, which along with cassiterite formed prior to the main sulfide mineralization stages (stage pre-A). The volumetrically most important mineralization comprises a low-sulfidation assemblage (stage A) composed of quartz, pyrrhotite, and arsenopyrite, and subsequent chalcopyrite, Fe-rich sphalerite (up to 33 mol% FeS), stannite, and herzenbergite. Pre-A and A stage mineral assemblages are overprinted by an intermediate-sulfidation assemblage (stage B) composed of pyrite, marcasite, and intermediate product. Mineral assemblages from pre-A, A, and B stages are overprinted by a further intermediate-sulfidation assemblage (stage C) composed of sphalerite (up to 11 mol% FeS), galena, native bismuth, Cu-Pb-Ag sulfosalts, chalcopyrite, siderite, Mn-Fe carbonates, kaolinite, dickite, and sericite.

The mineral paragenesis at Ayawilca suggests emplacement of the manto mineralization as a transition between retrograde skarn and Cordilleran-type carbonate-replacement mineralization. A preliminary fluid-inclusion study (Harlaux 2019) points to crystallization of quartz-pyrrhotite in stage A at temperatures as high as ~ 350 °C. The occurrence of herzenbergite [SnS] after cassiterite and stannite suggests increasingly reducing conditions from initial crystallization of cassiterite under slightly more oxidizing conditions in stage pre-A to extremely low $\log fO_2$ values between ~ − 30 and − 35 atm during the crystallization of herzenbergite in stage A, assuming a temperature of 350 °C and a $\log fS_2$ of − 13 to − 10 atm. The composition of Fe-rich sphalerite and stannite that crystallized in equilibrium during stage A suggests that crystallization occurred at temperatures around 300–250 °C.

A significant decrease in fO_2 could have been effectively achieved through intense buffering of hydrothermal fluids by the carbonaceous Excelsior Group during initial stages of the sulfide mineralization. Cooling, progressive sealing of vein walls by quartz, and decreasing redox potential of the host rocks drove the evolution from low-sulfidation (stage A) to intermediate-sulfidation (stages B and C) states of the mineralizing fluids. The reducing

character of the carbonaceous Excelsior Group favored a low oxidation state, thus enhancing Sn mobility.

The main In hosts at Ayawilca are stage A sphalerite, stannite (IQR 1168–809 ppm, up to 1908 ppm), and stages A and C chalcopyrite (IQR 910–537 ppm, up to 1185 ppm). The highest In contents are found in second-generation sphalerite crystallized during stage A (IQR 1299–227 ppm, up to 1.7 wt%). Indium was likely incorporated into the crystal lattice of sphalerite via $Cu^{+} + In^{3+} \leftrightarrow 2\ Zn^{2+}$ and $(Sn, Ge)^{4+} + (Ga, In)^{3+} + (Cu + Ag)^{+} \leftrightarrow 4\ Zn^{2+}$coupled substitutions. The substitution mechanisms of In in the stannite and chalcopyrite crystal lattices remain unclear.

With the obtained LA-ICP-MS U–Pb cassiterite dates (22.77 ± 0.41 and 23.05 ± 2.06 Ma, early Miocene), Ayawilca is older than most deposits in the NNW-SSE-trending polymetallic belt of central Peru, which are mostly mid-Miocene or younger. Within this belt, Ayawilca and the Oligocene Uchucchacua and Milpo-Atacocha deposits appear to be part of an easterly striking broad strip at ~ 10°40′–10°50′S in which slightly older deposits occur. Unlike other deposits in the polymetallic belt of central Peru, in which only minor Sn-bearing minerals have been described, Ayawilca hosts a potentially economic Sn resource, thereby expanding the prospective region for this metal for ~ 850 km northwest from the northernmost tip of the Central Andean tin belt.

Supplementary Information The online version contains supplementary material available at https://doi.org/10.1007/s00126-021-01066-z.

Acknowledgements This study was economically supported by the Peruvian CONCYTEC-FONDECYT-World Bank project 107-2018-FONDECYT-BM-IADT-AV and the Mexican research program CONACYT-Ciencia Básica (A1-S-14574). We thank the staff of Tinka Resources Ltd., particularly to Jorge Gamarra, for help and hospitality during the sampling program. We appreciate the technical support by Xavier Llovet (CCiT-UB) and Carlos Ortega Obregón (LEI-UNAM) during acquisition of EPMA data, and by Pete Tollan (ETH) during acquisition of LA-ICP-MS data. We are grateful to Richard Sillitoe, Andreas Dietrich, Graham Carman (president and CEO of Tinka Resources), and Editor-in-Chief Bernd Lehmann for their constructive comments which significantly improved the manuscript. Any use of trade, firm, or product names is for descriptive purposes only and does not imply endorsement by the U.S. Government.

References

Abdalla HM, Matsueda H, Obeid MA, Takahashi R (2008) Chemistry of cassiterite in rare metal granitoids and the associated rocks in the Eastern Desert. Egypt J Miner Petrol Sci 103:318–326

Andersen JC, Stickland RJ, Rollinson GK, Shail RK (2016) Indium mineralisation in SW England: host parageneses and mineralogical relations. Ore Geol Rev 78:213–238

Barsukov VL, Durasova NA, Kovalenko NI, Ryabchikov ID, Ryzhenko BN (1987) Oxygen fugacity and tin behaviour in melts and fluids. Geol Zbornik-Geot Carpatica 38:723–733

Bauer ME, Burisch M, Ostendorf J, Krause J, Frenzel M, Seifert T, Gutzmer J (2019) Trace element geochemistry of sphalerite in contrasting hydrothermal fluid systems of the Freiberg district, Germany: insights from LA-ICP-MS analysis, near-infrared light microthermometry of sphalerite-hosted fluid inclusions, and sulfur isotope geochemistry. Miner Deposita 54:237–262

Baumgartner R, Fontboté L, Vennemann T (2008) Mineral zoning and geochemistry of epithermal polymetallic Zn-Pb-Ag-Cu-Bi mineralization at Cerro de Pasco, Peru. Econ Geol 103:493–537

Baumgartner R, Fontboté L, Spikings R, Ovtcharova M, Schaltegger U, Schneider J, Page L, Gutjahr M (2009) Bracketing the age of magmatic-hydrothermal activity at the Cerro de Pasco epithermal polymetallic deposit, Central Peru: a U-Pb and $^{40}Ar/^{39}Ar$ study. Econ Geol 104:479–504

Belissont R, Munoz M, Boiron M, Luais B, Mathon O (2019) Germanium crystal chemistry in Cu bearing sulfides from micro-XRF mapping and micro-XANES spectrometry. Minerals 9:227

Benavides-Cáceres V (1999) Orogenic evolution of the Peruvian Andes: the Andean Cycle. Soc Econ Geol Spec Pub 7:61–107

Bendezú R, Fontboté L (2009) Cordilleran epithermal Cu-Zn-Pb-(Au- Ag) mineralization in the Colquijirca district, Central Peru: deposit-scale mineralogical patterns. Econ Geol 104:905–944

Bendezú R, Page L, Spikings R, Pecskay Z, Fontboté L (2008) New $^{40}Ar/^{39}Ar$ alunite ages from the Colquijirca district, Peru: evidence of a long period of magmatic SO_2 degassing during formation of epithermal Au–Ag and Cordilleran polymetallic ores. Miner Deposita 43:777–789

Benites D, Torró L, Vallance J, Laurent O, Valverde PE, Kouzmanov K, Chelle-Michou C, Fontboté L (2021) Distribution of indium, germanium, gallium and other minor and trace elements in polymetallic ores from a porphyry system: the Morococha District, Peru. Ore Geol Rev 136, 104236

Beuchat S, Moritz R, Pettke T (2004) Fluid evolution in the W-Cu–Zn–Pb San Cristobal vein, Peru: fluid inclusion and stable isotope evidence. Chem Geol 210:201–224

Bissig T, Ullrich TD, Tosdal RM, Friedman R, Ebert S (2008) The time-space distribution of Eocene to Miocene magmatism in the central Peruvian polymetallic province and its metallogenetic implications. J S Am Earth Sci 26:16–35

Cacho A, Melgarejo JC, Camprubí A, Torró L, Castillo-Oliver M, Torres B, Artiaga D, Tauler E, Martínez A, Campeny M, Alfonso P, Arce-Burgoa OR (2019) Mineralogy and distribution of critical elements in the Sn-W-Pb-Ag-Zn Huanuni Deposit. Bolivia Minerals 9:753

Cardona A, Cordani UG, Ruiz J, Valencia VA, Armstrong R, Chew D, Nutman A, Sanchez AW (2009) U-Pb zircon geochronology and Nd isotopic signatures of the pre-Mesozoic metamorphic basement of the Eastern Peruvian Andes: growth and provenance of a late Neoproterozoic to Carboniferous accretionary orogen on the northwest margin of Gondwana. J Geol 117:285–305

Carlotto V, Quispe J, Acosta H et al (2009) Geotectonic domains as tool for metallogenetic mapping in Peru. Bol Soc Geol Perú 103:1–89

Carvalho JRS, Relvas JMRS, Pinto AMM, Frenzel M, Krause J, Gutzmer J, Reis T (2018) Indium and selenium distribution in the Neves-Corvo deposit, Iberian Pyrite Belt, Portugal. Mineral Mag 82:S5–S41

Catchpole H, Kouzmanov K, Fontboté L (2012) Copper-excess stannoidite and tennantite-tetrahedrite as proxies for hydrothermal fluid evolution in a zoned Cordilleran base metal district, Morococha, central Peru. Can Mineral 50:719–743

Catchpole H, Kouzmanov K, Putlitz B, Seo J, Fontboté L (2015) Zoned base metal mineralization in a porphyry system: origin and evolution of mineralizing fluids in the Morococha District, Peru. Econ Geol 110:39–71

Chen LL, Ni P, Dai BZ, Li WS, Chi Z, Pan JY (2019) The genetic association between quartz vein- and greisen-type mineralization at the Maoping W-Sn Deposit, Southern Jiangxi, China: insights from zircon and cassiterite U–Pb ages and cassiterite trace element composition. Minerals 9:411

Cheng Y, Spandler C, Kemp A, Mao J, Rusk B, Hu Y, Blake K (2019) Controls on cassiterite (SnO_2) crystallization: evidence from cathodoluminescence, trace-element chemistry, and geochronology at the Gejiu tin district. Am Mineral 104:118–129

Chew DM, Schaltegger U, Košler J, Whitehouse MJ, Gutjahr M, Spikings RA, Mišković A (2007) U-Pb geochronologic evidence for the evolution of the Gondwanan margin of the north-central Andes. Geol Soc Am Bull 119:697–711

Chew DM, Pedemonte G, Corbett E (2016) Proto-Andean evolution of the Eastern Cordillera of Peru. Gondwana Res 35:59–78

Cook NJ, Ciobanu CL, Pring A, Skinner W, Shimizu M, Danyushevsky L, Saini-Eidukat B, Melcher F (2009) Trace and minor elements in sphalerite: a LA-ICP-MS study. Geochim Cosmochim Ac 73:4761–4791

Cook NJ, Ciobanu CL, Williams T (2011) The mineralogy and mineral chemistry of indium in sulphide deposits and implications for mineral processing. Hydrometallurgy 108:226–228

Cook NJ, Sundblad K, Valkama M, Nygård R, Ciobanu CL, Danyushevsky L (2011) Indium mineralisation in A-type granites in southeastern Finland: insights into mineralogy and partitioning between coexisting minerals. Chem Geol 284:62–73

Cook NJ, Ciobanu CL, Brugger J, Etschmann B, Howard DL, de Jonge MD, Ryan C, Paterson D (2012) Determination of the oxidation state of Cu in substituted Cu-In-Fe-bearing sphalerite via μXANES spectroscopy. Am Mineral 97:476–479

Czamanske GK (1974) The FeS content of sphalerite along the chalcopyrite-pyrite-bornite sulfur fugacity buffer. Econ Geol 69:1328–1334

Dalmayrac B, Laubacher G, Marocco R (1988) Caracteres generales de la evolución geológica de los Andes Peruanos. INGEMMET. Boletín, Serie D Estudios Regionales 12, 326 p.

Davies RC (2002) Tectonic, magmatic and metallogenic evolution of the Cajamarca mining district, Northern Peru. Unpublished PhD thesis, James Cook University, Townsville, Australia, 323 p

Davies RC, Williams PJ (2005) The Galeno and Michiquillay porphyry Cu-Au-Mo deposits: geological descriptions and comparison of Miocene porphyry systems in the Cajamarca district, northern Peru. Miner Deposita 40:598–616

Dupuis C, Beaudoin G (2011) Discriminant diagrams for iron oxide trace element fingerprinting of mineral deposit types. Miner Deposita 46:319–335

Einaudi MT, Hedenquist JW, Inan E (2003) Sulfidation state of hydrothermal fluids: the porphyry-epithermal transition and beyond. Soc Economic Geol Geoch Soc Spec Publ 10:285–313

Eude A, Roddaz M, Brichau S, Brusset S, Baby P, Calderon Y, Soula JC (2015) Control of timing of exhumation and deformation in the northern Peruvian Eastern Andean Wedge (5–8 S) as inferred from low temperature thermochronology and balanced cross section. Tectonics 34:715–730

Fontboté L (2018) Ore deposits of the Central Andes. Elements 14:257–261

Fontboté L (2020) Systematic trends in the evolution of porphyry-related Zn-Pb-(Ag) deposits. Abstracts of the Swiss Geoscience Meeting, Zurich, p. 40–41

Frenzel M, Ketris MP, Gutzmer J (2014) On the geological availability of germanium. Miner Deposita 49:471–486

Frenzel M, Hirsch T, Gutzmer J (2016) Gallium, germanium, indium, and other trace and minor elements in sphalerite as a function of deposit type – a meta-analysis. Ore Geol Rev 76:52–78

Frenzel M, Ketris MP, Seifert T, Gutzmer J (2016b) On the current and future availability of gallium. Resour Policy 47:38–50

Fuchsloch W, Nex P, Kinnaird J (2019) The geochemical evolution of Nb-Ta-Sn oxides from pegmatites of the Cape Cross-Uis pegmatite belt, Namibia. Mineral Mag 83:1–56

Gamarra J, Fernández-Baca A, Carman G, Giraldo L, Chaiña R, Carrillo H (2019) New exploration ideas for the Ayawilca zinc-silver-indium-tin property, Central Peru. Proceedings of proEXPLO, Lima 2019. http://www.proexplo.com/2019/docs/programa/L08.pdf. Accessed 7 September 2020

Gaspar OC (2002) Mineralogy and sulfide mineral chemistry of the Neves Corvo ores, Portugal: insight into their genesis. Can Mineral 40:611–636

Gemmrich L, Torró L, Melgarejo JC, Laurent O, Vallance J, Chelle-Michou C, Sempere TPA (2021) Trace element composition and U-Pb ages of cassiterite from the Bolivian tin belt. Miner Deposita, in Press. https://doi.org/10.1007/s00126-020-01030-3

George LL, Cook NJ, Ciobanu CL (2016) Partitioning of trace elements in co-crystallized sphalerite–galena–chalcopyrite hydrothermal ores. Ore Geol Rev 77:97–116

George LL, Cook NJ, Crowe BB, Ciobanu CL (2018) Trace elements in hydrothermal chalcopyrite. Mineral Mag 82:59–88

Giggenbach WF (1987) Redox processes governing the chemistry of fumarolic gas discharges from White Island, New Zealand. Appl Geochem 2:143–161

Gorelikova NV, Tolosana-Delgado R, Pawlowsky-Glahn V, Khanchuk A, Gonevchuk V (2006) Discriminating geodynamical regimes of tin ore formation using trace element composition of cassiterite: the Sikhote'Alin case (Far Eastern Russia). Geol Soc Lond Spec Publ 264:43–57

Graeser S (1969) Minor elements in sphalerite and galena from Binnatal. Contrib Mineral Petrol 24:156–163

Guo J, Zhang RQ, Sun WD, Ling MX, Hu YB, Wu K, Zhang LC (2018) Genesis of tin-dominant polymetallic deposits in the Dachang district, South China: insights from cassiterite U-Pb ages and trace element compositions. Ore Geol Rev 95:863–879

Harlaux M (2019) Fluid inclusion study of the early pyrrhotite mineralization stage from the Ayawilca Zn-In-Ag-Sn deposit. Tinka Resources, internal unpublished report, Peru, p 22

Harlaux M, Kouzmanov K, Gialli S, Laurent O, Rielli A, Dini A, Chauvet A, Menzies A, Kalinaj M, Fontboté L (2020) Tourmaline as a tracer of late-magmatic to hydrothermal fluid evolution: the world-class San Rafael tin (-copper) deposit, Peru. Econ Geol 115:1665–1697

Heinrich CA (1990) The chemistry of hydrothermal tin(-tungsten) ore deposition. Econ Geol 85:457–481

Imai H, Lee MS, Iida K, Fujiki Y, Takenouchi S (1975) Geologic structure and mineralization of xenothermal vein-type deposits in Japan. Econ Geol 70:647–676

Hulsbosch N, Muchez P (2019) Tracing fluid saturation during pegmatite differentiation by studying the fluid inclusion evolution and multiphase cassiterite mineralisation of the Gatumba pegmatite dyke system (NW Rwanda). Lithos 354–355:105285

Ishihara S (1981) The granitoid series and mineralization. In: Skinner BJ (ed) Economic Geology 75th Anniversary Volume, pp 458–484

Jaillard E, Arnaud-Vanneau A (1993) The Cenomanian-Turonian transition on the Peruvian margin. Cretac Res 14:585–605

Jenks WF (1951) Triassic to Tertiary stratigraphy near Cerro de Pasco, Peru. Geol Soc Am Bull 62:202–220

Jiang SY, Yu JM, Lu JJ (2004) Trace and rare-earth element geochemistry in tourmaline and cassiterite from the Yunlong tin deposit, Yunnan, China: implication for migmatitic-hydrothermal fluid evolution and ore genesis. Chem Geol 209:193–213

Jiménez-Franco A, Alfonso P, Canet C, Trujillo J (2018) Mineral chemistry of In-bearing minerals in the Santa Fe mining district, Bolivia. Andean Geol 45:410–432

Kelly WC, Turneaure FS (1970) Mineralogy, paragenesis and geothermometry of the tin and tungsten deposits of the Eastern Andes, Bolivia. Econ Geol 65:609–680

Kendall-Langley L, Kemp A, Grigson J, Hammerli J (2019) U-Pb and reconnaissance Lu-Hf isotope analysis of cassiterite and columbite group minerals from Archean Li-Cs-Ta type pegmatites of Western Australia. Lithos 352–353:105231

Laughlin AW, Damon PE, Watson BN (1968) Potassium argon dates from Toquepala and Michiquillay, Peru. Econ Geol 63:166–168

Lehmann B (2021) Formation of tin ore deposits: a reassessment. Lithos 105756. https://doi.org/10.1016/j.lithos.2020.105756

Lehmann B, Ishihara S, Michel H, Miller J, Rapela C, Sanchez A, Tistl M, Winkelmann L (1990) The Bolivian tin province and regional tin distribution in the Central Andes: a reassessment. Econ Geol 85:1044–1058

Lehmann B, Dietrich A, Heinhorst J, Métrich N, Mosbah M, Palacios C, Schneider HJ, Wallianos A, Webster J, Winkelmann L (2000) Boron in the Bolivian tin belt. Miner Deposita 35:223–232

Lentz D, McAllister A (1990) The petrogenesis of tin- and sulfide mineralization at True Hill, southwestern New Brunswick. Atlant Geol 26:136–155

Lerouge C, Gloaguen E, Wille G, Bailly L (2017) Distribution of In and other rare metals in cassiterite and associated minerals in Sn ± W ore deposits of the western Variscan Belt. Eur J Mineral 29:739–753

Linnen RL, Pichavant M, Holtz F, Burgess S (1995) The effect of fO_2 on the solubility, diffusion, and speciation of tin in haplogranitic melt at 850°C and 2 kbar. Geochim Cosmochim Ac 59:1579–1588

Longo AA, Dilles JH, Grunder AL, Duncan R (2010) Evolution of calc-alkaline volcanism and associated hydrothermal gold deposits at Yanacocha, Peru. Econ Geol 105:1191–1241

Mao W, Zhong H, Yang J, Tang Y, Liu L, Fu Y, Zhang X, Sein K, Soe MA, Li J, Le Z (2020) Combined zircon, molybdenite, and cassiterite geochronology and cassiterite geochemistry of the Kuntabin tin-tungsten deposit in Myanmar. Econ Geol 115:603–625

Marinov D (2011) Re-Os molybdenite geochronology from Michiquillay and Galeno porphyry copper deposits, Cajamarca, Perú. In: Barra F, Reich M, Campos E, Tornos F (eds) Let's Talk Ore Deposits, Proceedings of the 11th Biennial SGA Meeting, Antofagasta, Chile, Universidad Católica del Norte: Antofagasta, Chile pp 113–114

McLaughlin DH (1924) Geology and physiography of the Peruvian Cordillera, Departments of Junin and Lima. Geol Soc Am Bull 35:591–632

Mégard F (1984) The Andean orogenic period and its major structures in central and northern Perú. J Geol Soc Lond 141:893–900

Mégard F, Caldas J, Paredes J, De la Cruz N (1996) Geología de los cuadrángulos de Tarma, La Oroya y Yauyos; Boletín 69; Instituto Geológico Minero y Metalúrgico del Perú: Lima, Peru, Mapas: 23-l, 24-l, 25-l. Scale 1(100):000

Meng Y, Hu R, Huang X, Gao J (2017) Germanium in magnetite: a preliminary review. Acta Geol Sin 91:711–726

Mišković A, Spikings RA, Chew DM, Košler J, Ulianov A, Schaltegger U (2009) Tectonomagmatic evolution of Western Amazonia: geochemical characterization and zircon U-Pb geochronologic constraints from the Peruvian Eastern Cordilleran granitoids. Geol Soc Am Bull 121:1298–1324

Moore F, Howie RA (1979) Geochemistry of some Cornubian cassiterites. Miner Deposita 14:103–107

Mrozek SA, Chang Z, Spandler C, Windle S, Raraz C, Paz A (2020) Classifying skarns and quantifying metasomatism at the Antamina deposit, Peru: insights from whole-rock geochemistry. Econ Geol 115:177–188

Murciego A, Sanchez AG, Dusausoy Y, Pozas JM, Ruck R (1997) Geochemistry and EPR of cassiterites from the Iberian Hercynian Massif. Mineral Mag 61:357–365

Nadoll P (2011) Geochemistry of magnetite from hydrothermal ore deposits and host rocks –case studies from the Proterozoic Belt Supergroup, Cu-Mo-porphyry + skarn and Climax-Mo deposits in the western United States. PhD thesis, The University of Auckland, New Zealand, 313 p

Nadoll P, Angerer T, Mauk JL, French D, Walshe J (2014) The chemistry of hydrothermal magnetite: a review. Ore Geol Rev 61:1–32

Nakamura Y, Shima H (1982) Fe and Zn partitioning between sphalerite and stannite. In: Proceedings of the Joint Meeting of Society of Mining Geologists of Japan; The Japanese Association of Mineralogists, Petrologists and Economic Geologists and the Mineralogical Society of Japan: Sendai, Japan (In Japanese), A-8

Nambaje C, Eggins SM, Yaxley GM, Sajeev K (2020) Micro-characterization of cassiterite by geology, texture and zonation: a case study of the Karagwe Ankole Belt, Rwanda. Ore Geol Rev 124:103609

Nascimento T, Souza V (2017) Mineralogy, stable isotopes ($\delta^{18}O$ and $\delta^{34}S$) and $^{40}Ar^{39}Ar$ geochronology studies on the hydrothermal carapace of the Igarapé Manteiga W-Sn Deposit, Rondônia. Braz J Geol 47:591–613

Nassar NT, Graedel TE, Harper EM (2015) By-product metals are technologically essential but have problematic supply. Sci Adv 1:e1400180

Neiva A (2008) Geochemistry of cassiterite and wolframite from tin and tungsten quartz veins in Portugal. Ore Geol Rev 33:221–238

Noble DC, McKee EH (1999) The Miocene metallogenic belt of central and northern Peru. Soc Econ Geol Spec Publ 7:155–193

Noble DC, Vidal CE, Perelló J, Rodríguez O (2004) Space-time relationships of some porphyry Cu-Au, epithermal Au, and other magmatic-related mineral deposits in Northern Peru. Soc Econ Geol Spec Publ 11:313–318

Oen IS, Kager P, Kieft C (1980) Oscillatory zoning of a discontinuous solid-solution series: sphalerite-stannite. Am Mineral 65:1220–1232

Parasyuk OV, Voronyuk SV, Gulay LD, Davidyuk GY, Halka VO (2003) Phase diagram of the CuInS-ZnS system and some physical properties of solid solutions phases. J Alloy Compd 348:57–64

Patterson DJ, Ohmoto H, Solomon M (1981) Geologic setting and genesis of cassiterite-sulfide mineralization at Renison Bell, Western Tasmania. Econ Geol 76:393–438

Pattrick RAD, Dorling M, Polya DA (1993) TEM study of indium and copper-bearing growth-banded sphalerite. Can Mineral 31:105–117

Pavlova GG, Palessky SV, Borisenko AS, Vladimirov AG, Seifert T, Phan LA (2015) Indium in cassiterite and ores of tin deposits. Ore Geol Rev 66:99–113

Peralta E, Colquhoun W, El Rassi D, Johnston A, Searston S (2019) Technical report on the mineral resource estimate for the Ayawilca property, Department of Pasco, Peru, NI 43-101 Report. 329 p. https://www.tinkaresources.com/site/assets/files/5515/tinka_ayawilca_tr_final.pdf. Accessed 1 Jan 2021

Pfiffner OA, Gonzalez L (2013) Mesozoic-Cenozoic evolution of the western margin of South America: case study of the Peruvian Andes. Geosciences 3:262–310

Plimer IR, Lu J, Kleeman JD (1991) Trace and rare earth elements in cassiterite – sources of components for the tin deposits of the Mole Granite, Australia. Miner Deposita 26:267–274

Pollard PJ, Pichavant M, Charoy B (1987) Contrasting evolution of fluorine- and boron-rich tin systems. Miner Deposita 22:315–321

Pring A, Wade B, McFadden A, Lenehan CE, Cook NJ (2020) Coupled substitutions of minor and trace elements in co-existing sphalerite and wurtzite. Minerals 10:147

Ramdohr P (1969) The ore minerals and their intergrowths, 1st edn. Elsevier, Amsterdam, p 1174

Reich M, Román N, Barra F, Morata D (2020) Silver-rich chalcopyrite from the active Cerro Pabellón geothermal system, northern Chile. Minerals 10:113

Ritterbush K, Rosas S, Corsetti F, Bottjer D, West J (2015) Andean sponges reveal long – term ecosystem shifts following the end – Triassic mass extinction. Palaeogeog Palaeoclimat Palaeocol 420:193–209

Rodríguez R, Cueva E, Carlotto V (2011) Geología del cuadrágulo de Cerro de Pasco. INGEMMET, Carta Geológica Nacional (Boletín N◦ 144 Serie A, escala 1:50,000, 160 p)

Rosas S, Fontboté L, Tankard A (2007) Tectonic evolution and paleogeography of the Mesozoic Pucará Basin, Central Peru. J S Am Earth Sci 24:1–24

Rosenbaum G, Giles D, Saxon M, Betts PG, Weinberg RF, Duboz C (2005) Subduction of the Nazca Ridge and the Inca Plateau: insights into the formation of ore deposits in Peru. Earth Planet Sci Lett 239:18–32

Rottier B, Kouzmanov K, Wälle M, Bendezú R, Fontboté L (2016) Sulfide replacement processes revealed by textural and LA-ICP-MS trace element analyses: example from the early mineralization stages at Cerro de Pasco, Peru. Econ Geol 111:1347–1367

Rottier B, Kouzmanov K, Casanova V, Wälle M, Fontboté L (2018) Cyclic dilution of magmatic metal-rich hypersaline fluids by magmatic low-salinity fluid: a major process generating the giant epithermal polymetallic deposit of Cerro de Pasco, Peru. Econ Geol 113:825–856

Rottier B, Kouzmanov K, Ovtcharova M, Ulianov A, Wälle M, Selby D, Fontboté L (2020) Multiple rejuvenation episodes of a silicic magma reservoir at the origin of the large diatreme-dome complex and porphyry-type mineralization events at Cerro de Pasco (Peru). Lithos 376–377:105766

Rottier B, Kouzmanov K , Casanova V, Bouvier A, Baumgartner LP, Wälle M, Fontboté L (2021) Tracking fluid mixing in epithermal deposits – Insights from in-situ δ18O and trace element composition of hydrothermal quartz from the giant Cerro de Pasco polymetallic deposit Peru. Chemical Geology. https://doi.org/10.1016/j.chemgeo.2021.120277

Sack RO, Lynch JVG, Foit FF (2003) Fahlore as a petrogenetic indicator: Keno Hill Ag-Pb-Zn District, Yukon, Canada. Mineral Mag 67:1023–1038

Sahlström F, Arribas A, Dirks P, Corral I, Chang Z (2017) Mineralogical distribution of germanium, gallium and indium at the Mt Carlton high-sulfidation epithermal deposit, NE Australia and comparison with similar deposits worldwide. Minerals 7:1–213

Saintilan NJ, Sproson AD, Selby D, Rottier B, Casanova V, Creaser RA, Kouzmanov K, Fontboté L, Piecha M, Gereke M, Zambito IVJJ (2021) Osmium isotopic constraints on sulphide formation in the epithermal environment of magmatic-hydrothermal mineral deposits. Chem Geol 564:120053

Scherrenberg AF, Jacay J, Holcombe RJ, Rosenbaum G (2012) Stratigraphic variations across the Marañón Fold-Thrust Belt, Peru: implications for the basin architecture of the West Peruvian Trough. J S Am Earth Sci 38:147–158

Scherrenberg AF, Konh BP, Holcombe RJ, Rosenbaum G (2016) Thermotectonic history of the Marañón Fold-Thrust Belt, Peru: insights into mineralisation in an evolving orogeny. Tectonophysics 667:16–36

Schorr S, Wagner G (2005) Structure and phase relations of the $Zn_{2x}(CuIn)_{1-x}S_2$ solid solution series. J Alloy Compd 396:202–207

Schwarz-Schampera U, Herzig P (2002) Indium: geology, mineralogy, economics. Springer-Verlag, Berlin, p 257

Scott SD, Barnes HL (1971) Sphalerite geothermometry and geobarometry. Econ Geol 66:653–669

Sempere TPA, Acosta J (2019) Extension of the Late Triassic salt into western Peru: implications for Andean tectonics and mineral exploration. Proceedings of proEXPLO, Lima, 2019. http://www.proexplo.com/2019/docs/programa/W03.pdf. Accessed 1 February 2021

Serranti S, Ferrini V, Umberto M, Cabri LJ (2002) Trace-element distribution in cassiterite and sulfides from Rubané and massive ores of the Corvo deposit, Portugal. Can Mineral 40:815–835

Sillitoe RH (2004) Musings on future exploration targets and strategies in the Andes. Soc Econ Geol Spec Publ 11:1–14

Sillitoe RH (2010) Porphyry copper systems. Econ Geol 105:3–41

Sillitoe RH, Perelló J (2005) Andean copper province: tectonomagmatic settings, deposit types, metallogeny, exploration, and discovery. In: Hedenquist JW, Thompson JFH, Goldfarb RJ, Richards JR (eds) Economic Geology 100th Anniversary Volume. Society of Economic Geologists Inc., pp 845–890

Smeds SA (1993) Herzenbergite (SnS) in Proterozoic granite pegmatites in north-central Sweden. Mineral Mag 57:489–494

Spikings R, Reitsma MJ, Boekhout F, Mišković A, Ulianov A, Chiaradia M, Gerdes A, Schaltegger U (2016) Characterisation of Triassic rifting in Peru and implications for the early disassembly of western Pangaea. Gondwana Res 35:124–143

Taylor RG (1979) Geology of tin deposits. Elsevier, The Netherlands, p 556

Torres B, Melgarejo JC, Torró L, Camprubí A, Castillo-Oliver M, Artiaga D, Campeny M, Tauler E, Jiménez-Franco A, Alfonso P, Arce-Burgoa OR (2019) The Poopó polymetallic epithermal deposit, Bolivia: mineralogy, genetic constraints, and distribution of critical elements. Minerals 9:472

Torró L, Melgarejo J, Gemmrich L, Mollinedo D, Cazorla M, Martínez Á, Pujol-Solà N, Farré-de-Pablo J, Camprubí A, Artiaga D, Torres B, Alfonso P, Arce O (2019a) Spatial and temporal controls on the distribution of indium in xenothermal vein deposits: the Huari Huari District, Potosí, Bolivia. Minerals 9:304–340

Torró L, Cazorla M, Melgarejo J, Camprubí A, Gemmrich L, Campeny M, Artiaga D, Torres B, Martínez Á, Tarrés M, Mollinedo D, Alfonso P, Arce O (2019b) Indium mineralization in the volcanic dome-hosted Ánimas–Chocaya–Siete Suyos polymetallic deposit, Potosí, Bolivia. Minerals 9:604–642

Toulmin P, Barton PB (1964) A thermodynamic study of pyrite and pyrrhotite. Geochim Cosmochim Ac 28:641–671

Vermeesch P (2018) IsoplotR: a free and open toolbox for geochronology. Geosci Front 9:1479–1493

Wilson JJ (1963) Cretaceous stratigraphy of central Andes of Peru. Am Assoc Pet Geol Bull 47:1–34

Wilson JJ, Reyes L (1964) Geología del cuadrángulo de Pataz: hoja 16-H. Serie a: Carta Geológica Nacional, Boletín 9:91p

Wise M, Brown C (2011) Chemical composition of coexisting columbite-group minerals and cassiterite from the Black Mountain pegmatite, Maine. Eur J Mineral 23:817–828

Wittmann A (1974) Indium. 49-A crystal chemistry. In: Wedepoh1 KH (ed) Handbook of geochemistry, Berlin, Springer–Verlag, vol. II/4, pp 49-A-1 - 49-A-8

Xiang L, Romer RL, Glodny J, Trumbull RB, Wang R (2020) Li and B isotopic fractionation at the magmatic-hydrothermal transition of highly evolved granites. Lithos 376–377:105753

Xu J, Cook NJ, Ciobanu CL, Li X, Kontonikas-Charos A, Gilbert S, Lv Y (2020) Indium distribution in sphalerite from sulfide–oxide–silicate skarn assemblages: a case study of the Dulong Zn–Sn–In deposit, Southwest China. Miner Deposita 56:307–324

Zhang R, Lu J, Lehmann B, Li C, Li G, Zhang L, Guo J, Sun W (2017) Combined zircon and cassiterite U –Pb dating of the Piaotang granite-related tungsten–tin deposit, southern Jiangxi tungsten district, China. Ore Geol Rev 82:268–284

Zhao Y, Chen S, Huang Y, Zhao J, Xiang T, Chen X (2019) U-Pb ages, O isotope compositions, Raman spectrum, and geochemistry of cassiterites from the Xi'ao copper -tin polymetallic deposit in Gejiu District. Yunnan Province Minerals 9:212

Zoheir B, Lehmann B, Emam A, Radwan A, Zhang R, Bain WM, Steele-MacInnis M, Nolte N (2020) Extreme fractionation and magmatic–hydrothermal transition in the formation of the Abu Dabbab rare-metal granite, Eastern Desert, Egypt, Lithos 352–353:105329

Authors and Affiliations

Diego Benites[1] · Lisard Torró[1] · Jean Vallance[1] · Oscar Laurent[2,3] · Patrick Quispe[1] · Silvia Rosas[1] · María Francisca Uzieda[4] · Christopher S. Holm-Denoma[5] · Laura S. Pianowski[5] · Antoni Camprubí[6] · Vanessa Colás[6] · Álvaro Fernández-Baca[7] · Luis Giraldo[7] · Cyril Chelle-Michou[2] · Jorge Sáez[1] · Kalin Kouzmanov[4] · Lluís Fontboté[4]

✉ Lisard Torró
lisardtorro@hotmail.com

[1] Geological Engineering Program, Faculty of Sciences and Engineering, Pontifical Catholic University of Peru (PUCP), Av. Universitaria 1801, San Miguel, Lima 15088, Peru

[2] ETH Zürich, Department of Earth Sciences, Institute for Geochemistry and Petrology, Zürich, Switzerland

[3] Present Address: CNRS, Géosciences Environnement Toulouse, Observatoire Midi-Pyrénées, 31400 Toulouse, France

[4] Department of Earth Sciences, University of Geneva, CH-1205 Geneva, Switzerland

[5] U.S. Geological Survey, Geology, Geophysics and Geochemistry Science Center, Denver, CO, USA

[6] Instituto de Geología, Universidad Nacional Autónoma de México. Ciudad Universitaria, Coyoacán, CDMX 04510, México

[7] Tinka Resources Limited, Av. Benavides 1579 Of. 306, Miraflores, Lima, Peru

CHAPTER III: DISTRIBUTION OF INDIUM, GERMANIUM, GALLIUM AND OTHER MINOR AND TRACE ELEMENTS IN POLYMETALLIC ORES FROM A PORPHYRY SYSTEM: THE MOROCOCHA DISTRICT, PERU

Ore Geology Reviews 136 (2021) 104236

Contents lists available at ScienceDirect

Ore Geology Reviews

journal homepage: www.elsevier.com/locate/oregeorev

Distribution of indium, germanium, gallium and other minor and trace elements in polymetallic ores from a porphyry system: The Morococha district, Peru

Diego Benites [a], Lisard Torró [a,*], Jean Vallance [a], Oscar Laurent [b], Pablo E. Valverde [a], Kalin Kouzmanov [c], Cyril Chelle-Michou [b], Lluís Fontboté [c]

[a] Geological Engineering Program, Faculty of Sciences and Engineering, Pontifical Catholic University of Peru (PUCP), Av. Universitaria 1801, San Miguel, Lima 15088, Peru
[b] Department of Earth Sciences, ETH Zürich, CH-8092 Zürich, Switzerland
[c] Department of Earth Sciences, University of Geneva, CH-1205 Geneva, Switzerland

ARTICLE INFO

Keywords:
Critical elements
Cordilleran-type
Skarn
Metal zoning

ABSTRACT

We report indium, germanium, gallium, and other minor and trace elements contents in sphalerite, chalcopyrite, galena, and tetrahedrite-tennantite occurring in skarn and skarn-free ("Cordilleran") polymetallic mantos and vein ore bodies in the Miocene porphyry-related Morococha District, Central Peru. Among the investigated minerals, LA-ICP-MS measurements indicate that In and Ga concentrate mostly in sphalerite (Inter-Quartile Range [IQR] 217–2.7 ppm and up to 4608 ppm In; IQR 61–2.0 ppm and up to 2137 ppm Ga) and chalcopyrite (IQR 109–32 ppm and up to 1070 ppm In; IQR 62–1.5 ppm and up to 630 ppm Ga). In coeval generations of sphalerite and chalcopyrite, the contents of In and Ga in sphalerite are at least two times higher than in chalcopyrite. Germanium content is generally low in the four analyzed minerals (IQR 1.2–0.19 ppm), although late Fe-poor sphalerite may yield much higher values (IQR 129–74 ppm).

Certain trace element contents appear to correlate with (i) the evolving characteristics of the hydrothermal fluids during individual mineralization events, and (ii) the location of the studied ore bodies relative to the hydrothermal feeders. The highest In values in sphalerite are found in high-sulfidation assemblages in Cordilleran polymetallic veins and, with lower amounts, in low-sulfidation assemblages in skarn bodies. In intermediate-sulfidation assemblages in Cordilleran mineralization, In content decreases from early to late generations of sphalerite, while that of Ge increases. Spatial trace-element trends in Cordilleran veins and replacement bodies formed during the so-called "Morococha district-scale polymetallic event" include, from porphyry-distal to porphyry-proximal locations: i) In and Cu, and to a lesser extent Ga, enrichment in sphalerite; ii) Se and Hg enrichment and Sn and Ag depletion in chalcopyrite; iii) In enrichment in galena; and iv) Ag depletion in tetrahedrite-tennantite.

Our dataset suggests that In is incorporated in the sphalerite crystal lattice via coupled substitutions involving Cu and subordinately also Sn and Ag. Availability of Cu in the mineralizing fluids is therefore key to In enrichment in sphalerite. Progressive dilution of metal-rich magmatic-hydrothermal fluids and Cu precipitation probably account for the progressive In depletion in distal-to-porphyry Zn-Pb-Ag and Ag-Pb Cordilleran polymetallic mineralization and in late sphalerite generations in intermediate-sulfidation assemblages.

1. Introduction

Porphyry Cu systems host the world's largest resources of Cu and Mo and are important suppliers of Au, Ag, Zn, and Pb. Formed at convergent plate margins and genetically associated with subduction- and post-subduction-related magmatism, these systems host a variety of genetically connected mineralization types (Richards, 2009; Sillitoe, 2010; Lee and Tang, 2020). Indeed, porphyry Cu deposits, which are centered on porphyry intrusions emplaced in the upper 4 km of the crust, may be laterally and vertically associated with skarn and low-, intermediate-,

* Corresponding author.
E-mail address: lisardtorro@hotmail.com (L. Torró).

https://doi.org/10.1016/j.oregeorev.2021.104236
Received 9 December 2020; Received in revised form 16 March 2021; Accepted 13 May 2021
Available online 20 May 2021

and high-sulfidation epithermal polymetallic and precious metal mineralization.

Several technological or *high-tech* elements lacking primary ores may concentrate in porphyry Cu systems. Porphyry Cu (including the subtype Cu-Mo) deposits are major sources of Se, Te, and Re, which are recovered as byproducts, and may occasionally host recoverable amounts of In (John and Taylor, 2016). As for skarn deposits, those of the Au type are typically enriched in Te, whereas those of the Zn, Sn, and W types may host relatively high content of In (Meinert, 2005; Cook et al., 2009; Bauer et al., 2019a; Korges et al., 2020). Polymetallic epithermal deposits may also display positive anomalies of Te, In, Ge, and Ga that, in some cases, can be recovered as byproducts (Cook et al., 2009; Goldfarb et al., 2016; Sahlström et al., 2017; Liu et al., 2019). Frenzel et al. (2017) quantified the contribution of high-temperature carbonate replacement and vein-type deposits to the global supply potential for In in about 25%. Of these potential *high-tech* byproducts, Re is mainly found as ReS_2 in solid solution with molybdenite, whereas Te usually forms a plethora of Au-Ag(-Pd) telluride minerals. The In, Ge, and Ga triad, which is the main focus of the present study, rarely forms own mineral phases but are commonly incorporated in the structure of major sulfides, chiefly sphalerite and chalcopyrite (see Cook et al., 2009, 2011a, 2011b; Cook and Ciobanu, 2015; George et al., 2018 for comprehensive reviews on substitution mechanisms) and, in the case of Ga, also in the structure of Al-rich hydrothermal phases such as hypogene alunite and dickite (Rytuba et al., 2003; Sahlström et al., 2017).

Indium (Reich and Richter, 1863), Ge (Winkler, 1886), and Ga (Le coq de Boisbaudran, 1875) are currently considered of strategic importance and classified as critical to the health of the global economy (Wood and Samson, 2006; Skirrow et al., 2013; European Commission, 2017; Schulz et al., 2017). This is partly explained by their increased use in both modern digital technologies and the so-called green technologies, including solar panels (In, Ge, Ga), optical electronics (In, Ge, Ga), smartphones (In, Ga), and fiber optics applications (Ge) amongst others (Schwarz-Schampera and Herzig, 2002; Guberman, 2015; Jaskula, 2015; Tolcin, 2015). Frenzel et al. (2017) indicate that if the current growth in consumption continues, In could become the most problematic of the three elements in terms of future supply since most of the In contained in concentrate streams is already being extracted.

Recent work on the distribution of high-tech metals in magmatic-hydrothermal systems in the Central Andes has largely focused on xenothermal (cf. Heuschmidt et al., 2002) and epithermal deposits of the Bolivian tin belt, with well-documented conspicuous In enrichments (Schwarz-Schampera and Herzig, 2002; Murakami and Ishihara, 2013; Torró et al., 2019a, 2019b; Gemmrich et al., 2021). In contrast, little research has been conducted on polymetallic deposits associated with porphyry Cu systems in the region. In Peru, a comparative study of high-tech elements in mineral deposits, including those framed in porphyry systems, is limited to the work carried out in zinc concentrates by Soler (1987) that, among other elements, reported contents of some technological elements including Cd, In, Ge, and Ga in several types of polymetallic deposits.

The present contribution documents temporal (through robust paragenetic sequences) and spatial variations in the trace-element compositions of sphalerite, chalcopyrite, galena, and tennantite-tetrahedrite in the world-class Morococha district (Petersen, 1965; Catchpole et al., 2015a, 2015b), Peru, with a special focus on In, Ge, and Ga. In this classical polymetallic district, several Miocene porphyry deposits including the producing Toromocho Cu-Mo porphyry (proven and probable reserves of 1474 Gt at 0.47% Cu, 0.019% Mo, and 6.89 g/t Ag; Chinalco Mining Corporation International, 2015) are associated with skarn and skarn-free ("Cordilleran"), mostly epithermal polymetallic deposits that display high-, intermediate-, and low-sulfidation mineral assemblages. Studied mineralization styles in the present work include Zn-Cu-Ag massive replacement bodies formed adjacent to, and partly overprinting, prograde exoskarn mineralization, and skarn-free Cordilleran mantos and veins spanning from veins cross-cutting the Toromocho Cu-Mo porphyry to more distal carbonate replacement bodies and veins. Minor and selected trace element compositions were determined by laser ablation inductively-coupled plasma mass spectrometry (LA-ICP-MS) with a twofold objective: i) to contextualize, temporally and spatially, the contents of In, Ge, and Ga in the different polymetallic mineralization styles; and ii) to recognize distribution patterns and district-scale zoning. The study of trace element behavior in major sulfides might also be of use to generate more optimal solutions to treat polymetallic concentrates that carry these strategic metals; prime examples of the technological implications of trace-element mineralogy are presented in Cook et al. (2011a) and Frenzel et al. (2019).

2. Geological setting

2.1. Pre-Miocene geology

The Morococha district (11°35′S, 76°20′W) is located in the Western Cordillera of Central Peru ~ 150 km east of Lima at an altitude of 4500 to over 5000 m (Fig. 1). The district belongs to the Eocene and Miocene metallogenic belt of northern and central Peru (Petersen, 1965; Noble and McKee, 1999; Bissig et al., 2008; Fontboté, 2018). The hydrothermal ore deposits of this belt are genetically linked to calc-alkaline magmatism, ranging in age from 40 to 6 Ma. This belt hosts large mineral deposits belonging to the "porphyry system" in the sense of Sillitoe (2010) including porphyry Cu ± Mo ± Au (e.g., Toromocho), polymetallic and copper skarns (e.g., Antamina), epithermal ("Cordilleran") polymetallic deposits (Cerro de Pasco, Colquijirca), and high-sulfidation epithermal gold deposits including Yanacocha.

The Morococha district is located at the northern end of the northwest-trending Yauli Dome (Petersen, 1965; Catchpole et al., 2015a, 2015b; Fig. 1). The dome comprises a core of phyllites with minor limestones, quartzites, and basalts known as the Excelsior Group attributed to the Devonian (Kobe, 1990; Saintilan et al., 2021). The oldest stratigraphic unit cropping out in the Morococha district consists of a ~200-m-thick sequence of interbedded red sandstones and conglomerates covered by a ~500-m-thick pile of andesitic lavas and pyroclastic flows corresponding to the rift-related Mitu Group (Spikings et al., 2016), locally known as "Catalina volcanics" (McLaughlin, 1924; Terrones, 1949; Mégard, 1968). Age determinations (Spikings et al., 2016) and geological constraints (Rosas et al., 2007) indicate a Triassic age for the Mitu Group. The Upper Triassic to Jurassic carbonate rocks of the Pucará Group rest unconformably on the Mitu Group. The Pucará Group is subdivided, from base to top, into the Chambará, Aramachay, and Condorsinga Formations and at Morococha has an average thickness of around 450 m (Terrones, 1949; Rosas et al., 2007). At the base of the Chambará Formation, a lenticular deformed sequence of anhydrite, gypsum, shale, and limestone layers is locally known as the "anhydrite complex". The sulfates are of evaporitic origin with local remobilization due to Miocene magmatic-hydrothermal activity (Haapala, 1953; Kouzmanov et al., 2011). The anhydrite complex is overlain by thick-bedded dolomite and subordinate limestone containing chalcedony lenses and chert nodules with intercalated shale and sandstone beds and a discontinuous ~5-m-thick lava flow, known as the Sacracancha Trachyte. The Aramachay Formation at Morococha differs from the typical black shales lithofacies of deep environment (cf. Rosas et al., 2007) by showing siliceous sponge-dominated on-shelf deposition that indicates shallow water sedimentary facies (Ritterbush et al., 2015). It comprises dolomites, shales, cherts, cherty dolomites, limestones, and intercalated tuffs hardened by sponge spicule silica remobilization which resulted in positive topography as cliffs and crests. The Condorsinga Formation displays similarities with the Chambará Formation including thick-bedded limestones with minor detrital components and chert. At Morococha, the Aramachay and Condorsinga Formations are separated by an up to 38-m-thick basaltic andesite lava flow with within-plate affinity, locally referred to as the "Montero Basalt" (Terrones, 1949; Pérez et al., 2011; Rosas et al., 1996) which constitutes an

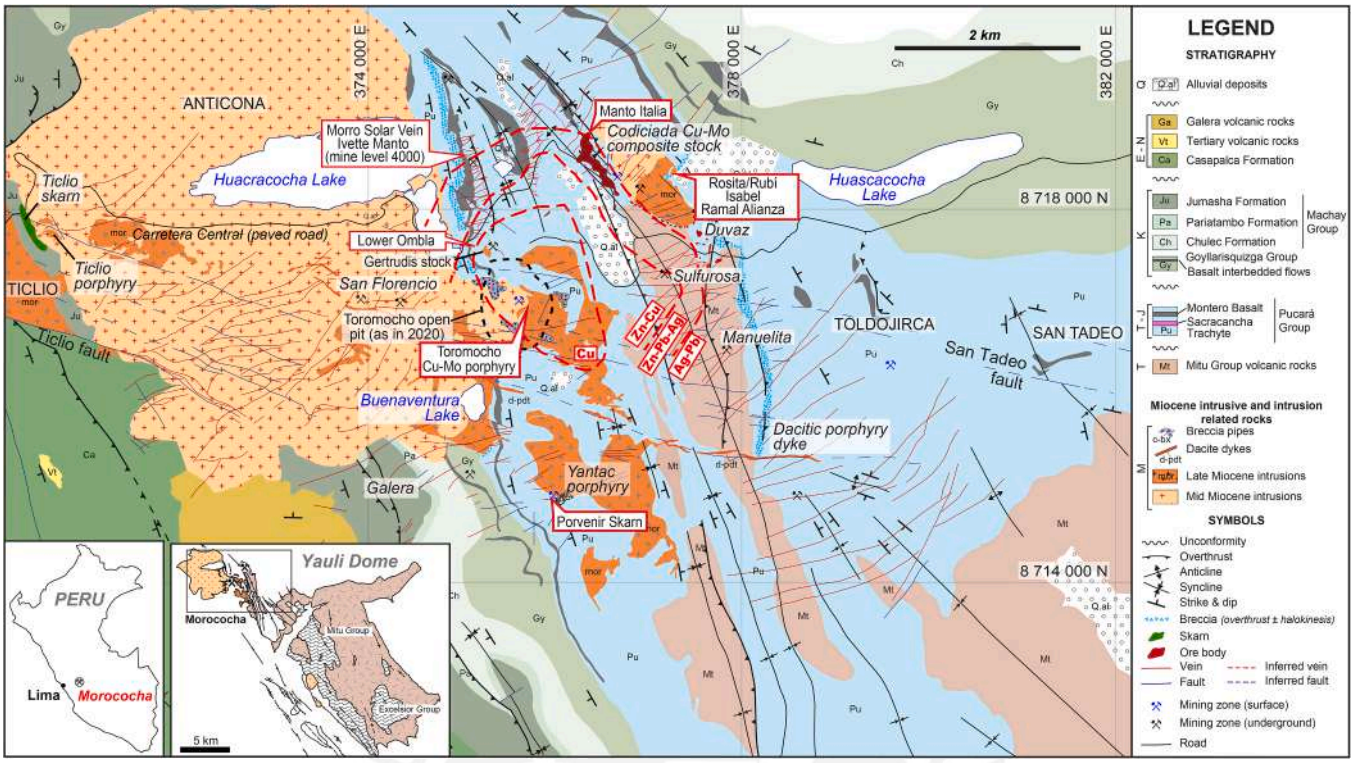

Fig. 1. Regional geologic map of the Morococha mining district (modified from Bendezú et al., 2008).

important marker horizon in the whole Yauli Dome.

The overlying Early Cretaceous Goyllarisquizga Group typically forms the flanks of the Yauli Dome and comprises red conglomerates at the base overlain by interbedded sandstones and limestones intruded by Aptian-Albian mafic sills (Terrones, 1949; Rosas, 1994). The Machay Group rocks, subdivided in Chúlec, Pariatambo, and Jumasha Formations (Lepry, 1981), rest on the Early Cretaceous rocks. Terrones (1949) described limestones, which are locally bituminous, sandstones, and marls (Chúlec Formation), finely-laminated phosphatic black carbonate rocks and lutites (Pariatambo Formation) and dolomitic limestones and limestones, overlain by alternating beds of green to red-colored shales and fossiliferous dolomitic limestone layers (Jumasha Formation). The Jumasha Formation is uncomformably overlain by the Late Cretaceous to Paleocene (?) Casapalca red beds and the Galera pyroclastic flows, of rhyolitic composition, and minor proportions of undifferentiated Tertiary volcanic rocks to the southwest. Most of the folds and thrusts that characterize the Yauli Dome formed during the late Paleocene to Eocene Incaic orogenic phase (Benavides, 1999; Scherrenberg et al., 2016).

2.2. Timing of Miocene magmatic-hydrothermal activity

Mid to Late Miocene magmatic activity in the Morococha District is characterized by a succession of calc-alkaline intrusions emplaced in the afore-described Paleozoic to Cretaceous rocks. Detailed field and geochronological studies (Eyzaguirre et al., 1975; Beuchat, 2003; Kouzmanov et al., 2008; Bendezú et al., 2012; Catchpole et al., 2015a, 2015b) allowed Catchpole et al. (2015a) to propose two main cycles of intrusion during which several successive emplacement episodes of dioritic to granodioritic magma took place. The first cycle corresponds to the emplacement of the Mid-Miocene barren microdioritic Codiciada intrusive in the core of the Morococha anticline at 14.3 Ma, followed by the dioritic Anticona laccolith-like body that crops out largely northwest of the district (Fig. 1). The second cycle corresponds to Late Miocene dioritic, granodioritic, and quartz monzonitic mineralized porphyry stocks emplaced between 9.4 and 7.7 Ma in the Codiciada and Anticona diorites and older rocks, followed by a late NW-SE trending dacitic dike swarm at 7.2 Ma (Fig. 1). The mineralized porphyry intrusions comprise, from NW to SE, the Ticlio, Gertrudis, Codiciada, San Francisco, Toromocho, and Yantac stocks (Fig. 1).

Based on new U-Pb, Re-Os, and $^{40}Ar/^{39}Ar$ geochronological studies and previous data, Catchpole et al. (2015a) proposed a model of multiple hydrothermal mineralization events of porphyry, skarn, and Cordilleran polymetallic deposits and ore showings that formed over a total timespan of 3.5 M.y., centered on three individual magmatic-hydrothermal centers, the oldest being the Codiciada Center (ca. 9.3 Ma), followed by the Ticlio Center (between 8.5 and 7.2 Ma), and the Toromocho Center (between 8.5 and 7.2 Ma). The Toromocho Center occupies the central part of the district, comprises several porphyry intrusions (granodiorite, quartz porphyry, feldspar porphyry, and dacitic porphyry dykes), and was responsible for the formation of the giant Toromocho porphyry Cu-Mo deposit (Kouzmanov et al., 2008).

2.3. Studied polymetallic mineralization styles in the Morococha district

In each of the Morococha centers mentioned above, porphyry and polymetallic mineralization styles have been recognized (Catchpole et al., 2015a, 2015b). The present work focuses, from old to young (all ages from Catchpole et al., 2015b and references therein), on the following polymetallic replacement bodies and veins:

(i) Replacement bodies in "Manto Italia" (Fig. 1), emplaced subsequently to a prograde skarn phase adjacent to the Codiciada stock (ca. 9.3 Ma). Adularia $^{40}Ar/^{39}Ar$ ages (6.0 ± 0.2 Ma and 6.23 ± 0.12 Ma) of crosscutting calcite-adularia veins are interpreted by Catchpole et al. (2015b) to belong to the later hydrothermal event mentioned below under *"iii"*, not to the skarn-related low-sulfidation mineralization at Manto Italia;

(ii) Porvenir skarn (7.2 ± 0.2 Ma; phlogopite $^{40}Ar/^{39}Ar$ ages), adjacent to the Yantac intrusion (ca. 8.8–8.0 Ma; Fig. 1); and

(iii) Massive replacement bodies (mantos) and veins postdating the porphyry mineralization at Toromocho (ca. 6.8 Ma). They include veins overprinting the Toromocho porphyry stock and, from proximal to distal relative to the Toromocho porphyry, the Lower Ombla manto, the Morro Solar vein, the Ivette and Rosita mantos, and the Rubí, Isabel, and Ramal Alianza veins (Table 1).

Economic mineralization in the Manto Italia, Porvenir, and Lower Ombla replacement bodies is interpreted to have developed mainly during the retrograde stage on or adjacent to magnesian serpentine – magnetite ± phlogopite and tremolite – diopside – serpentine – chlorite – talc exoskarns (Catchpole, 2011; Catchpole et al., 2015a, 2015b). The best example of this mineralization style in the Morococha district is Manto Italia, which consists of up to 20-m-thick massive Zn-Pb-Ag-Cu-bearing sulfide bodies (Fig. 1); mineralization comprises abundant pyrrhotite, pyrite, chalcopyrite, Fe-rich sphalerite, and galena, and minor arsenopyrite hosted in the tremolite – serpentine – chlorite – talc core of the body grading to a diopside – andradite outer zone. The low-sulfidation assemblages at Manto Italia and Porvenir described by Catchpole (2011), Catchpole et al. (2015a) and Catchpole et al. (2015b) can be compared to "Stage A" assemblages as described in Cerro de Pasco and other Cordilleran deposits (Rottier et al., 2016, 2018; Fontboté, 2020). Less abundant in these skarn-associated replacement bodies are paragenetically later intermediate-sulfidation assemblages containing pyrite, Fe-moderate sphalerite, tetrahedrite-tennantite, and Mn-Fe carbonates, which are best represented in the studied samples from Lower Ombla (samples from low-sulfidation assembalges from the Lower Ombla skarn were not analyzed).

Extensive steeply dipping NNE- to ENE-trending Cordilleran polymetallic veins emplaced subsequently to the Toromocho porphyry were grouped by Catchpole et al. (2015a) as the "Morococha district-scale polymetallic event" and dated at 5.78 ± 0.10 and 5.72 ± 0.18 Ma ($^{40}Ar/^{39}Ar$ ages). The polymetallic veins overprinting the Toromocho porphyry stock, the Morro Solar, Ramal Alianza, Isabel, and Rubí polymetallic veins as well as the Rosita and Ivette polymetallic bodies belong to this event (Fig. 1). A marked base metal zoning around the Toromocho magmatic-hydrothermal center with a Cu-rich core, a Zn-Cu intermediate zone, and outer Zn-Pb-Ag to Ag-Pb envelopes was early

Table 1
General description of the geological features and locations of the sampled ore bodies and veins in the Morococha district.

ORE BODY/VEIN	Description	Age/Relative age (see text for details)	Evolution stage of analyzed minerals (see text for details)
MANTO ITALIA MASSIVE REPLACEMENT BODY	Polymetallic, low sulfidation mineralization-dominated replacement body in the Chambará Formation, adjacent to the Codiciada composite stock and a relictic magnesian exoskarn. Massive Zn-Pb-Ag-Cu-bearing sulfide bodies are up to 20 m thick and composed of massive pyrrhotite, Fe-rich sphalerite, and chalcopyrite.	Slightly younger than the Codiciada stock (ca. 9.3 Ma; Catchpole et al., 2015b)	A
PORVENIR SKARN	Polymetallic, low-sulfidation assemblage on hydrous skarn in the Chambará Formation. Adjacent to the Yantac intrusion. Magnesian exoskarn of serpentine-magnetite, phlogopite, tremolite, talc, and chlorite cut by dark brown sphalerite with interstitial chalcopyrite and pyrite, and late 5–10-mm-thick calcite veinlets.	7.2 ± 0.2 ($^{40}Ar/^{39}Ar$ in phlogopite; Beuchat, 2003)	A
EPITHERMAL VEINS OVERPRINTING TOROMOCHO PORPHYRY	5–10-cm-wide high-sulfidation epithermal veins composed of chalcopyrite, pyrite, and enargite and lesser proportions of Fe-poor sphalerite overprinting the Toromocho porphyry Cu-Mo mineralization.	Postdating the Toromocho porphyry (<ca. 6.8 Ma, Catchpole et al., 2015b)	C
LOWER OMBLA MASSIVE REPLACEMENT BODY	Polymetallic replacement body in the Chambará Formation, close and along its underlying contact with rocks of the Mitu Group. Adjacent to the Gertrudis stock. Magnesian exoskarn of serpentine-magnetite with interstitial anhydrite and occasional epidote, replaced by massive pyrrhotite, pyrite, brown sphalerite, and chalcopyrite.		C
MORRO SOLAR VEIN	N35°E 75°SE ~ 1-m-thick polymetallic vein located at the limit between the Cu and Cu-Zn zones (Catchpole et al., 2012) NW of the Toromocho magmatic-hydrothermal center. Hosted in the Chambará Formation dolomite and anhydrite. Composed of sphalerite, pyrite, quartz, chalcopyrite, orpiment, and pale pink carbonates. The Morro Solar vein is interpreted as the feeder for the Ivette massive replacement body.		C
IVETTE MASSIVE REPLACEMENT BODY	Polymetallic replacement body located in the Cu-Zn zone (Catchpole et al., 2012) around the Toromocho magmatic-hydrothermal center. Hosted within anhydrite bodies at the base of the Chambara Formation. Brown to yellow sphalerite (late generations with schalenblende texture), galena, and pyrite crystals with interstitial anhydrite, replaced by orpiment and cut by carbonate veinlets. The samples come from the zone in which the Morro Solar vein is in contact with the Ivette body.		C
ROSITA REPLACEMENT BODY/ RUBÍ VEIN	Polymetallic replacement body and vein in the Zn-Pb-Ag zone (Catchpole et al., 2012) around the Toromocho magmatic-hydrothermal center. The Manto is hosted in carbonates of the Pucará Group and the vein cuts Pucará Group carbonates and Catalina volcanics. Pyrite, chalcopyrite, sphalerite, and galena cut by <0.5-mm-wide white to pink carbonates veinlets. Also, sub-rounded yellow sphalerite clasts (1–20 mm) showing jigsaw-fit texture are intergrown with tetrahedrite in carbonate cement.		C
ISABEL VEIN	N45°E-55°SE ~ 1.1-m-thick polymetallic vein in the Zn-Pb-Ag zone (Catchpole et al., 2012) around the Toromocho magmatic-hydrothermal center hosted by Pucará Group carbonates. Sub-rounded sphalerite clasts (1–20 mm) and fine to coarse pyrite grains appear along with white/pale pink carbonate cement.		C
RAMAL ALIANZA VEIN	N45°E-70°SE ~ 0.8-m-thick polymetallic vein in the Zn-Pb-Ag zone (Catchpole et al., 2012) around the Toromocho magmatic-hydrothermal center. Vein cuts Pucará Group carbonates. Breccia formed by pyrite, brown sphalerite, and galena, with pink to beige colloform carbonate cement.		C

recognized (McLaughlin and Graton, 1935; de Pasco and Corporation, 1948; Petersen, 1965; Titley, 1993; Catchpole et al., 2012; Fig. 1). The veins, mainly metric in thickness, have vertical extension reaching more than 1000 m below present-day surface. They crop out at the highest elevations in the district (5100 m) and some of them have been recognized underground at 3700 m.a.s.L. and remain open to depth. The replacement bodies are mainly found within the Pucará carbonate rocks, in particular along thrust faults and at the intersections of veins and lithological contacts.

The studied Cordilleran polymetallic veins and replacement bodies of the Toromocho Center consist mainly of mineral assemblages conforming to those described by Catchpole et al. (2011) and Catchpole et al. (2015b). These authors subdivided the polymetallic mineralization sequence into the following generations. Quartz and pyrite ± hematite were deposited as filling of veins with sericite halos during a barren stage that can be compared to "Stage B" assemblages of Rottier et al. (2016), Rottier et al. (2018) and Fontboté (2020). The subsequent mineral assemblages are comparable to those of "Stage C" described by these authors. They outline several sub-stages including Zn, Pb, Ag, and Cu minerals, chiefly chalcopyrite, Ag-bearing tetrahedrite-tennantite series minerals, Fe-poor sphalerite, and galena, which are commonly postdated by rhodochrosite and quartz with subordinate complex Ca-Mg-Fe-Mn carbonates, and barite. The inner zones tend to show assemblages of high to intermediate sulfidation states, compared to the outer ones (intermediate to low), explaining the large mineralogical variations of this stage and the typically zoned character of the Cordilleran polymetallic veins and bodies.

Massive pyrite bodies occur as replacement of carbonate rocks and develop mainly along the lithological boundary between the Mitu and Pucará Groups, and less frequently along the brecciated contact between porphyry intrusions and carbonate rocks or as sub-vertical pipe-like bodies overprinting overthrust faults. They are predominantly made up of coarse- to fine-grained pyrite with banded texture, the remainder being mainly quartz and subordinate rutile (Catchpole, 2011). Intrusive and volcanic rocks along the contacts of these bodies show sericitic alteration. Although pyrite bodies are generally barren, they are important exploration targets as they, in places, acted as trap for Zn-Pb-Ag-Cu sulfide mineralization, in particular when crosscut by later base metal veins. The Morococha massive pyrite bodies can be compared to the "Stage B" pyrite-quartz body in Cerro de Pasco (Rottier et al., 2016, 2018).

Since mineral assemblages of individual polymetallic ore-bodies and veins at Morococha show characteristics and evolution that can be compared to those observed in Cerro de Pasco and in other porphyry-related polymetallic deposits, we use hereinafter the three-stage terminology proposed by Rottier et al. (2016) and Rottier et al. (2018) and generalized by Fontboté (2020). In a very summarized way, Stage A is characterized by low-sulfidation mineral assemblages bearing pyrrhotite and Fe-rich sphalerite; Stage B consists basically of coarse-grained pyrite and quartz with sericite alteration; Stage C in its inner part may have high-sulfidation assemblages (typically including enargite and Fe-poor sphalerite) but mostly consists of intermediate-sulfidation assemblages including Fe-moderate to Fe-poor sphalerite, tennantite-tetrahedrite and other sulfosalts, and Mn-Fe carbonates. It must be stressed that the mineral assemblages of stages A, B, and C represent steps in the evolution of single events or ore bodies but they do not imply any temporal correlation between different deposits or orebodies that, in addition, at Morococha have been formed in different periods over a time span of 3.5 M.y. The stages recognized in each studied ore body and vein are included in Table 1.

Fluid inclusion and stable and radiogenic isotope studies (Moritz et al., 2001; Ageneau, 2008; Kouzmanov et al., 2011; Catchpole et al., 2011, 2015b) suggest that the Cordilleran polymetallic orebodies at Morococha formed by precipitation from intermediate-density (<5 wt% NaCl equiv.) magmatic fluids during cooling below 400 °C, accompanied by phase separation (CO_2 loss and local salinity increase). Mixing with meteoric waters occurred late in the hydrothermal history of the Morococha district during the post-sulfide carbonate stage of mineralization.

3. Materials and methods

3.1. Sampling

Sampling was conducted on drill cores and mine adits. The study is based on 64 key samples from: i) Stage A low-sulfidation mineral assemblages from the Porvenir and Manto Italia polymetallic replacement bodies; ii) Stage C high-sulfidation veins overprinting the Toromocho porphyry, and iii) Stage C intermediate-sulfidation mineral assemblages from the Lower Ombla, Morro Solar, Ivette, Ramal Alianza, Isabel, and Rosita/Rubí veins and replacement bodies (groups *ii* and *iii* listed in a roughly proximal to distal position relative to the Toromocho porphyry). The main features of the sampled ore bodies and veins are summarized in Table 1. A list of the samples and details on their locations are given in Table S1 in the Supplementary Material. The approximate location of the sampled sites in the geological framework of the Morococha district is shown in Fig. 1. A total of 60 thick polished sections were prepared at the QEMSCAN laboratory of the Pontifical Catholic University of Peru (PUCP) and subsequently studied by optical reflected-light microscopy. A selection of 20 samples was examined on an environmental scanning electron microscope (ESEM) Thermo Fisher Quanta 650 FEI equipment with an EDAX-Octane Pro EDS microanalysis system at Centro de Caracterización de Materiales of the PUCP (CAM-PUCP). The operating conditions were 20 kV accelerating voltage and 5nA beam current in backscattered electron (BSE) imaging mode.

3.2. Electron probe micro analysis (EPMA)

Analyses of the major element composition of sulfide and tetrahedrite-tennantite series minerals were performed using a five-channel JEOL JXA-8230 electron microprobe housed at Centres Científics i Tecnològics of the University of Barcelona (CCiT-UB). The instrument was operated at 20 kV acceleration voltage, 20nA beam current, and with a beam diameter of 5 μm. Analytical standards and emission lines used for analyses were as follows: sphalerite (Zn, and S, Kα), chalcopyrite (Cu, Kα), FeS_2 (Fe, Kα), PbS (Pb, Mα), CdS (Cd, Lβ), GaAs (As, Lβ; Ga, Kα), In_2Se (In, Lβ), Ag (Ag, Lα), Sb (Sb, Lα), Sn (Sn, Lα) and Ge (Ge, Kα). Other measurement parameters, detection limits (d.L.) for each element, representative analyses of the different minerals investigated, and the normalization constants used for formula calculations are reported in Table S2 in Supplementary Material.

3.3. Laser ablation-inductively coupled plasma-mass spectrometry (LA-ICP-MS)

Analyses of sphalerite and chalcopyrite trace element content were carried out at ETH Zürich, Switzerland by laser ablation – inductively coupled plasma – sector field – mass spectrometry (LA-ICP-SF-MS) using a RESOlution S-155 (ASI/Applied Spectra) 193 nm ArF excimer laser system attached to an Element XR (Thermo) sector-field ICP-MS. We used a laser repetition rate of 3 Hz, a spot diameter of 19 μm, and a laser energy density on a sample of ca. 2.5 $J{\cdot}cm^{-2}$. The sample surface was cleaned immediately before each analysis by three pre-ablation pulses. Ablation was performed in a dual-volume, fast-washout S-155 ablation cell (Laurin Technic) fluxed with carrier gas consisting of ca. 0.5 $L{\cdot}min^{-1}$ He and make-up gas consisting of ca. 1 $L{\cdot}min^{-1}$ Ar and 2 $mL{\cdot}min^{-1}$ N_2. The ablated aerosol was homogenized via flushing through a squid device before being introduced in the plasma.

The ICP-MS instrument is equipped with a high capacity (80 $m^3{\cdot}h^{-1}$) interface pump to achieve a detection efficiency (based on U in NIST SRM612 glass) in the range of 2% (Guillong et al., 2020). The instrument was optimized for maximum sensitivity on the entire mass range while

keeping the production of oxides low ($^{248}ThO^+/^{232}Th^+ \leq 0.15\%$) and the U/Th ratio at ca. 1 (on NIST SRM612 glass). The list of analyzed isotopes and corresponding dwell times is provided in Table S3 in Supplementary Material. A total of 68 mass scans (ca. 0.72 s sweep time each) were acquired over ca. 50 s measurement (25 s of background measurement followed by 25 s of sample ablation).

For trace element analyses in galena and tetrahedrite-tennantite, we used a Coherent Compex Pro 102-F 193 nm ArF excimer laser system attached to a NexION 2000 quadrupole ICP-MS. Ablation was performed in a single-volume Plexiglas custom cell fluxed with carrier gas consisting of ca. 1.0 L·min^{-1} He. Make-up gas consisting of ca. 1 L·min^{-1} Ar was admixed downstream of the ablation cell. We have used the same set of ablation parameters as for other sulfide analyses, except for a larger spot diameter (30 μm). The ICP-MS instrument was optimized to fulfill the same requirements as mentioned above, except for a higher oxide production rate (relaxed to $^{248}ThO^+/^{232}Th^+ \leq 0.5\%$) considering the different design of the ablation cell. We have used the same list of elements as above but different dwell times (see details in Table S3 in Supplementary Material). A total of 110 mass scans (ca. 0.59 s sweep time each) were acquired over ca. 65 s measurement (40 s of background measurement followed by 25 s of sample ablation).

The resulting intensities were subsequently processed offline with the standalone version 1.3.2 of the SILLS program (Guillong et al., 2008). The sulfide pressed pellet MASS-1 (former PS-1; Wilson et al., 2002) was used as the primary reference material for trace element quantification and instrumental drift correction using conventional standard-sample bracketing. The contribution of the isobaric ^{115}Sn signal on ^{115}In has been subtracted. The Cu (for chalcopyrite and tetrahedrite-tennantite), Zn (for sphalerite), and Pb (for galena) content obtained by electron microprobe analyses were used as internal

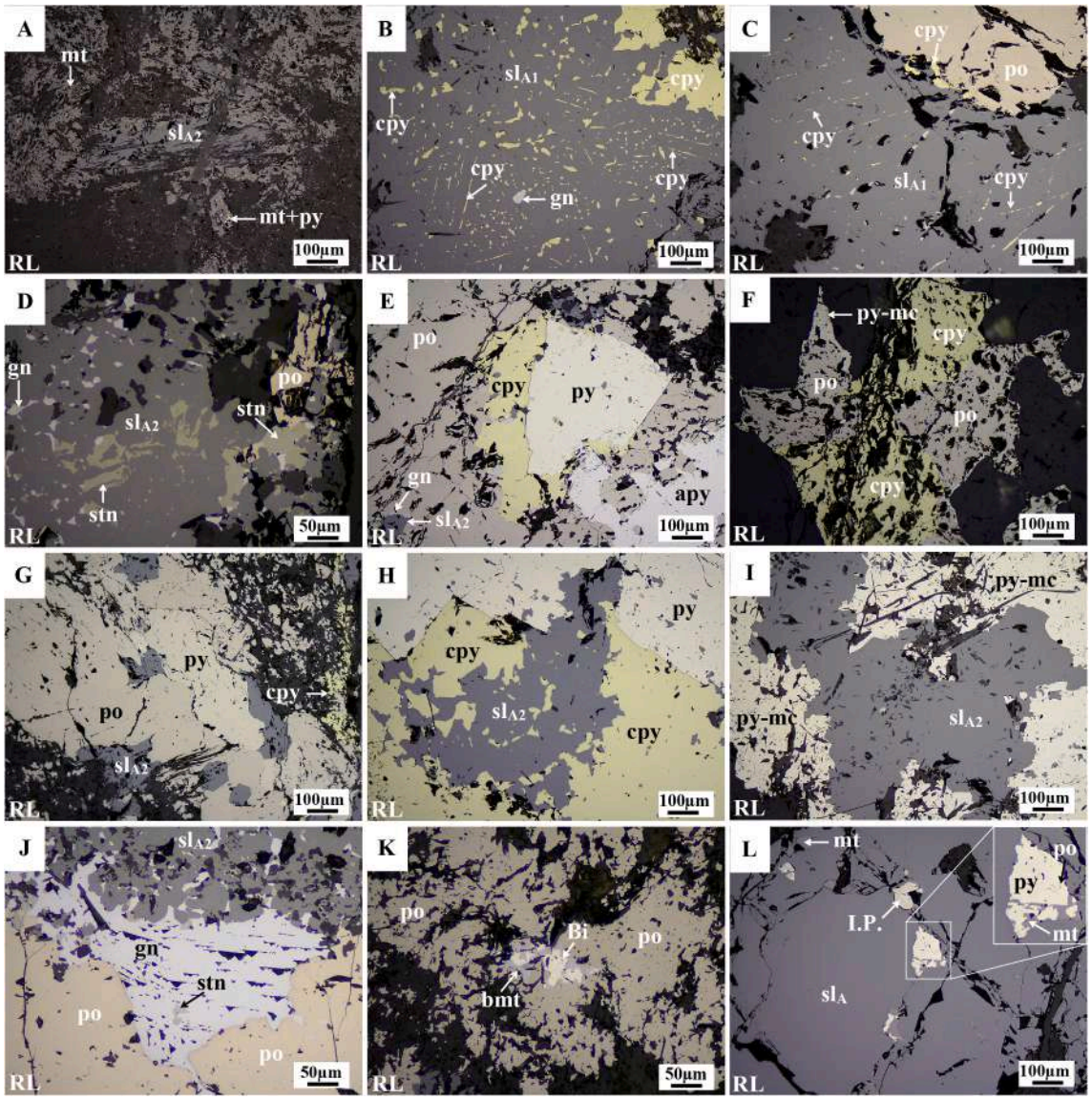

Fig. 2. Photomicrographs of textural features in Manto Italia (A-K) and Porvenir (L). A) Anhedral magnetite replaced by sphalerite (sl_{A2}). B) Sphalerite (sl_{A1}) with dissemination of chalcopyrite and intergrown with massive chalcopyrite. C) Pyrrhotite replaced by sphalerite (sl_{A1}) with chalcopyrite. D) Sphalerite (sl_{A2}) with inclusions of galena and partly replaced by stannite. E) Chalcopyrite as replacement of pyrrhotite, pyrite, and arsenopyrite. F) Massive pyrrhotite replaced by chalcopyrite. G) Pyrrhotite replaced by pyrite, sphalerite (sl_{A2}), and chalcopyrite. H) Chalcopyrite intergrown with sphalerite (sl_{A2}) in contact with anhedral pyrite. I) Massive sphalerite (sl_{A2}) replaced by pyrite and marcasite. J) Galena as replacement of pyrrhotite and sphalerite (sl_{A2}). K) Massive pyrrhotite with inclusions of bismuthinite and native bismuth. L) Magnetite pervasively replaced by sphalerite, with small inclusions of pyrite, intermediate product, and hematite after pyrrhotite. Abbreviations: apy: arsenopyrite; Bi: native bismuth; bmt: bismuthinite; cc: calcite; cpy: chalcopyrite; gn: galena; hm: hematite; I.P.: intermediate product; mt: magnetite; mc: marcasite; po: pyrrhotite; py: pyrite; stn: stannite; sl: sphalerite; RL: reflected light image.

standards for relative sensitivity corrections. The data are reported in Table S4 in Supplementary Material and content statistical data are shown in Tables 2–5.

The analytical reproducibility was checked by repeated measurements of the GSD-1G (Guillong et al., 2005) and NIST SRM610 (Jochum et al., 2011) glass reference materials, and ranges from 10 to 30% relative (2σ) for most elements. The quoted uncertainties for each analysis correspond to the internal (2σ) statistical error and analytical reproducibility propagated by quadratic addition. Accuracy was controlled by repeated measurements of the UQAC-FeS-1 sulfide pressed pellet (unpublished data from D. Savard, UQAC, 2018; see also Baumgartner et al., 2020).

A significant effort was made to report only the content of elements whose variations respond to solid solutions and not to mixed mineral analyses (e.g., presence of nano- and micro-inclusions) by selecting only flat, stable signal intervals in the LA-ICP-MS spectra. The results (reported in Table S4 in Supplementary Material) show that the measurements are accurate within the calculated uncertainties.

4. Mineral assemblages

Petrographic observations are provided below for selected samples hosting the studied minerals in i) Stage A-dominated assemblages of Porvenir and Manto Italia massive replacement bodies, ii) Stage C high-sulfidation assemblages of epithermal veins overprinting the Toromocho porphyry, and iii) Stage C, intermediate-sulfidation dominated assemblages of Lower Ombla, Morro Solar, Ivette, Rosita/Rubí, Isabel, and Ramal Alianza veins and massive replacement bodies. Figs. S1 and S2 illustrate textural and mineral characteristics of selected typical samples of these sites.

4.1. Stage a low-sulfidation assemblages

Manto Italia massive replacement body. The mineralogy and textures of the Manto Italia polymetallic replacement body are described in detail by Catchpole et al. (2015b). In the studied samples, relict magnesian exoskarn is overprinted by an assemblage dominated by pyrrhotite and sphalerite. Relict anhedral magnetite (Fig. 2A) and subhedral prismatic and pseudorhombic crystals of arsenopyrite were partly replaced by massive pyrrhotite, sphalerite, and chalcopyrite. Two generations of sphalerite were distinguished (sl_{A1} and sl_{A2}), both being Fe-rich (between 11.0 and 7.56 wt%; Table 2). The first, sl_{A1}, shows "chalcopyrite disease" (Barton and Bethke, 1987) texture (Fig. 2B-C), whereas the second, sl_{A2}, mostly lacks mineral inclusions (Fig. 2A, G). Chalcopyrite also occurs intergrown with sphalerite (Fig. 2H). Pyrrhotite is replaced by Stage B anhedral aggregates of marcasite and pyrite (Fig. 2F-G, I) and subhedral pyrite (Fig. 2E, H). Locally, minor stannite, native bismuth, and bismuthinite occur as inclusions in pyrrhotite, second-generation sphalerite (sl_{A2}), and galena (Fig. 2D, J-K).

Porvenir massive replacement body. The polymetallic mineralization in this replacement body consists of a low-sulfidation mineral assemblage overprinting a magnesian skarn of serpentinite-magnetite, phlogopite, tremolite, talc, and chlorite (Figs. S1A-B). Magnetite grains are <1.2 mm in size. The skarn assemblage is cut by massive Fe-rich (up to 11.1 wt%; Table 2) sphalerite veins containing also local dissemination of chalcopyrite (<50 μm) and blebs of intermediate product (Ramdohr, 1980) after pyrrhotite and relicts of pyrrhotite as inclusions in pyrite (Fig. 2L). A paragenetic sequence for Porvenir is available in Catchpole (2011).

4.2. Stage C high-sulfidation veins overprinting the Toromocho porphyry mineralization

The studied Cordilleran polymetallic veins overprinting the Toromocho porphyry crosscut a stockwork mineralization of quartz − chalcopyrite ± chalcocite, quartz − pyrite, and quartz − pyrite − molybdenite veinlets occurring in rocks affected by potassic alteration composed primarily of biotite and minor proportions of K-feldspar, and by phyllic alteration, which is dominantly composed of white mica, quartz, and pyrite (Kouzmanov et al., 2008). The ore mineralogy of the studied Cordilleran veins is dominated by Stage B anhedral to subhedral individual crystals and aggregates of pyrite <380 μm in diameter, which are overprinted by a Stage C high-sulfidation assemblage consisting of massive Cu sulfides and sulfosalts and Fe-poor (up to 231 ppm; Table 2) sphalerite replacing or growing along grain boundaries, interstices, and porosity of pyrite (Figs. S1C-D). The main Cu minerals are bornite,

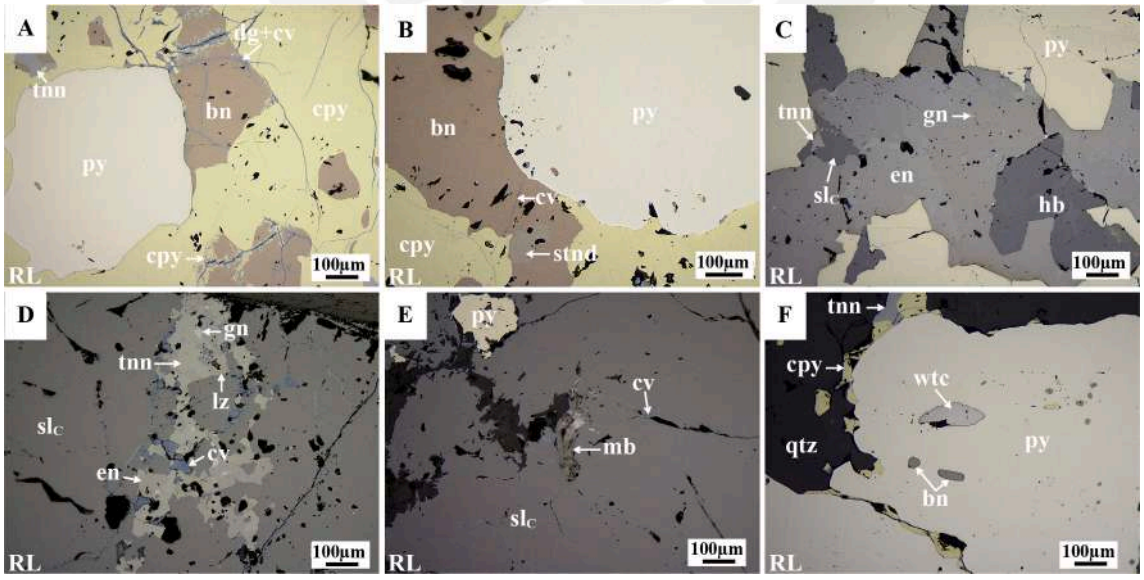

Fig. 3. Photomicrographs of textural features in epithermal veins overprinting the Toromocho porphyry. A) Anhedral pyrite along with massive bornite partly replaced by chalcopyrite along fractures and borders. B) Pyrite replaced by chalcopyrite and bornite, the latter with an inclusion of stannoidite and cut by covellite veinlets. C) Pyrite with hübnerite inclusions replaced by enargite, sphalerite, galena, and tennantite. D) Massive sphalerite cut by tennantite, enargite, luzonite, and covellite. Fine inclusions of galena in both sphalerite and sulfosalts are observed. E) Sphalerite with inclusions of molybdenite and cut by covellite veinlets. F) Chalcopyrite around pyrite grains, which host inclusions of bornite and wittichenite. Abbreviations: bn: bornite; cpy: chalcopyrite; cv: covellite; en: enargite; gn: galena; hb: hübnerite; lz: luzonite; mb: molybdenite; py: pyrite; sl: sphalerite; stnd: stannoidite; tnn: tennantite; wtc: wittichenite; RL: reflected light image.

chalcopyrite (Fig. 3A-B), sub-rounded stannoidite <300 μm in diameter (Fig. 3B), and anhedral enargite (<1050 μm) and tennantite (<900 μm) grains (Fig. 3C-D). The occurrence of chalcopyrite in these veins would point to the occasional passage from high- to intermediate-sulfidation (or vice versa) conditions during vein emplacement. To a lesser extent, covellite (<50 μm), luzonite (<50 μm), and colusite (<100 μm) grains partially replaced enargite (Fig. 3D). Local euhedral to subhedral prismatic hübnerite grains <510 μm long occur as inclusions in quartz and pyrite (Fig. 3C). Scarce galena grains <50 μm in size are present as disseminations in sphalerite, enargite/luzonite, and tennantite (Fig. 3D). Bladed molybdenite crystals <200 μm in length (Fig. 3E) and anhedral grains of wittichenite (<50 μm; Fig. 3F) are found enclosed in sphalerite and pyrite, respectively.

4.3. Stage C intermediate-sulfidation assemblages in Cordilleran veins and replacement bodies

4.3.1. Lower Ombla massive replacement body

(*not to be confused with the classical Ombla ore body – type locality for enargite – which is located topographically at higher levels and comprises a high-sulfidation assemblage; see Catchpole, 2011). In the Lower Ombla ore body (Table 1), magnesian serpentine-magnetite exoskarn with interstitial anhydrite and local epidote is overprinted by low- and intermediate-sulfidation polymetallic assemblages (Figs. S1E–H). Only minerals belonging to intermediate-sulfidation assemblages have been analyzed in this study. Magnetite occurs as microfractured subhedral to anhedral crystals <950 μm in diameter partly replaced by sulfides (Fig. 4A–D). Locally, abundant Stage A massive pyrrhotite is replaced by Stage B pyrite and marcasite. Stage C

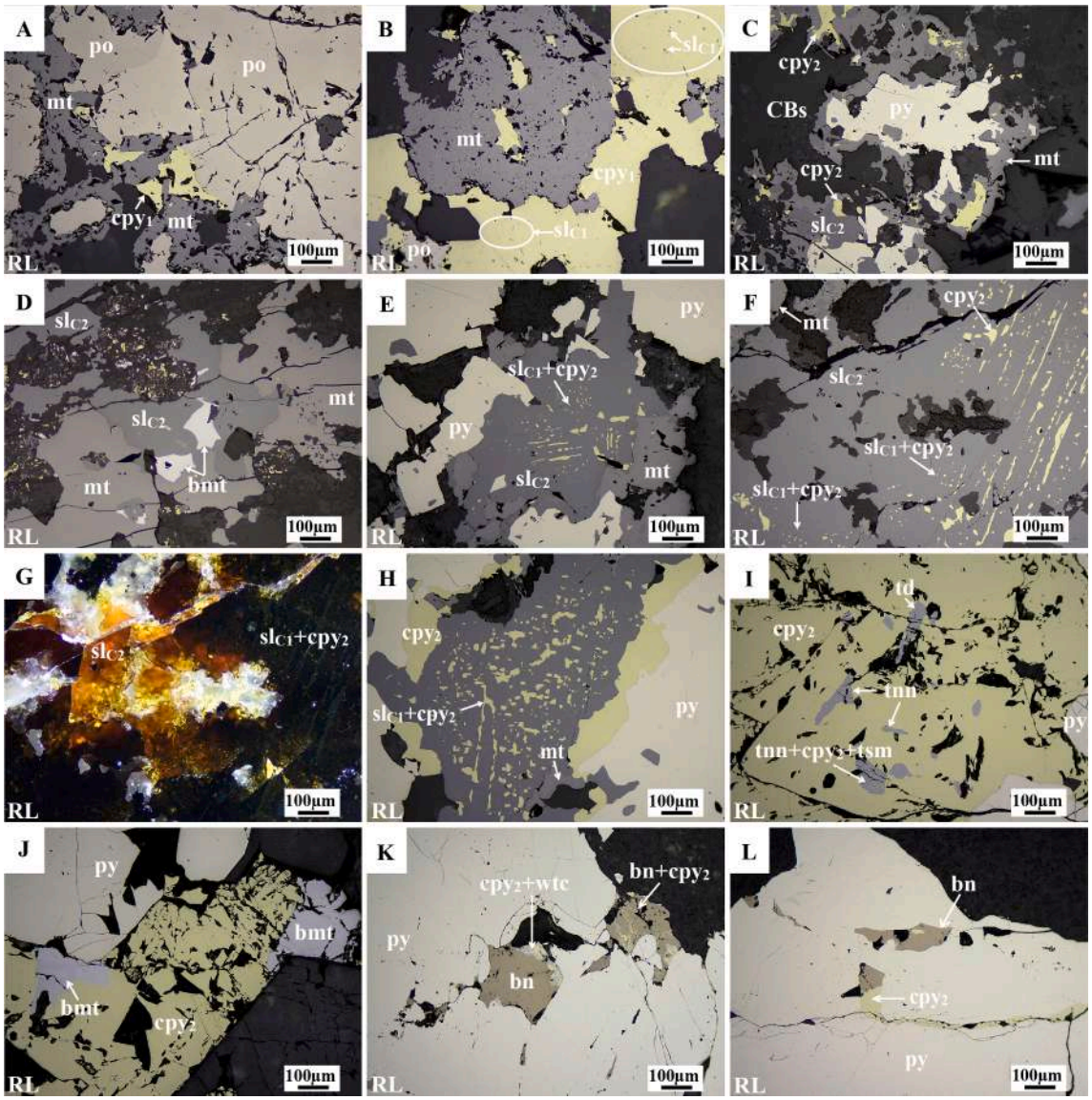

Fig. 4. Photomicrographs of textural features in the Lower Ombla massive replacement body. A-B) Anhedral magnetite replaced by massive pyrrhotite and chalcopyrite (cpy_1) with some star-like inclusions of sphalerite (sl_{C1}). C) Magnetite replaced by pyrite, chalcopyrite (cpy_2), and sphalerite (sl_{C2}). D) Magnetite replaced by sphalerite (sl_{C2}) and bismuthinite. E) Magnetite and pyrite crystals replaced by sphalerite (sl_{C1}) with chalcopyrite as fine disseminations and inclusions (cpy_2). F-G) Parallel and crossed nicols images of sphalerite (sl_{C1}) with "chalcopyrite disease" texture overgrown by sphalerite (sl_{C2}) with clean surfaces. Note that both generations of sphalerite show contrasting internal reflection colors. H) Replacement of pyrite and sphalerite (sl_{C1}) by chalcopyrite (cpy_2). I) Chalcopyrite (cpy_2) with inclusions of tennantite and fine disseminations of tsumoite. J) Pyrite aggregates and chalcopyrite (cpy_2) replaced by bismuthinite. K) Pyrite with cavities lined with bornite, chalcopyrite (cpy_2) and wittichenite. L) Pyrite microfractures filled with chalcopyrite (cpy_2) and bornite. Abbreviations: bmt: bismuthinite; bn: bornite; cpy: chalcopyrite; mt: magnetite; po: pyrrhotite; py: pyrite; sid: siderite; sl: sphalerite; tnn: tennantite; tsm: tsumoite; wtc: wittichenite; RL: reflected light image.

chalcopyrite and Fe-poor (up to 3.59 wt%; Table 2) sphalerite occur as a replacement of pyrrhotite and pyrite along grain boundaries and fractures (Fig. 4E, H). A first generation of sphalerite (sl_{C1}) forms minute (<5μm) star-shaped inclusions in first-generation chalcopyrite (cpy_1) exhibiting transformation twinning (Fig. 4B) as well as massive aggregates with reddish-brown internal reflections and abundant disseminations of chalcopyrite blebs ("chalcopyrite disease" texture; second-generation chalcopyrite – cpy_2; Fig. 4E-F). A second generation of sphalerite (sl_{C2}) occurs as grains without or with only limited "chalcopyrite disease" and shows orange to yellowish-brown internal reflections (Fig. 4D–G). Pyrrhotite, pyrite, and first-generation sphalerite (sl_{C1}) were replaced by second-generation chalcopyrite (cpy_2), which does not show transformation twinning (Fig. 4H). Pyrite aggregates and second-generation chalcopyrite (cpy_2) are intergrown with, and their porosity filled with, bornite (<170 μm), wittichenite (<60 μm), and bismuthinite (<270 μm; Fig. 4J-L). Rare tetrahedrite-tennantite grains <220 μm in diameter with fine dissemination of tsumoite (<60 μm) were found (Fig. 4I).

4.3.2. Rosita, Rubí, Isabel, Ramal Alianza, Morro Solar, and Ivette veins and replacement bodies.

Due to their proximity (Fig. 1) and similarity with respect to the paragenetic sequence of major sulfides and sulfosalts, the other studied replacement bodies and veins have been separated into two groups. The first group comprises the Rosita body and the Rubí vein (both sampled at the same mine level, where both structures intersect each other), and the Ramal Alianza and Isabel veins, all located at the Codiciada Center and hosted in the porphyry stock itself or rocks of the Mitu and Pucará Groups (Table 1). The second group comprises the Morro Solar vein and the Ivette replacement body, both located at the Alapampa zone and

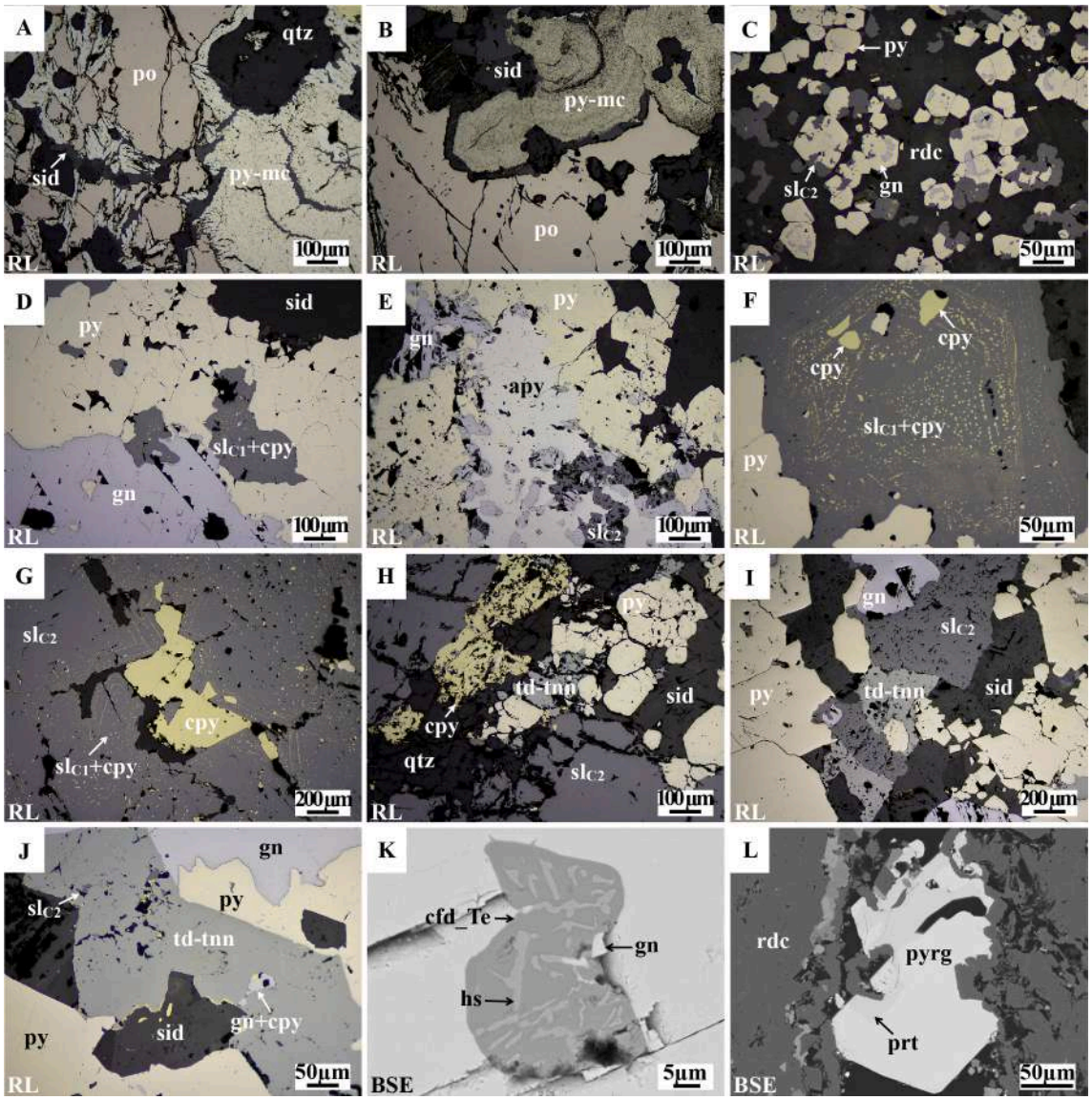

Fig. 5. Photomicrographs of textural features in the Rosita body and Rubí/Isabel/Ramal Alianza veins. A-B) Massive pyrrhotite replaced by pyrite, marcasite, and siderite in a quartz matrix. C) Subhedral pyrite aggregates replaced by sphalerite (sl_{C2}). D) Pyrite replaced by sphalerite (sl_{C1}) with fine chalcopyrite blebs, and galena. E) Pyrite replaced by arsenopyrite, sphalerite (sl_{C2}), and galena. F-G) Sphalerite (sl_{C1}) with disseminations of chalcopyrite, which also fills cavities. H-I) Pyrite aggregates replaced by sphalerite (sl_{C2}), chalcopyrite, and tetrahedrite-tennantite, in a siderite matrix. J) Pyrite replaced by galena and tetrahedrite-tennantite, with inclusions of chalcopyrite, sphalerite (sl_{C2}), and galena. **K)** Galena with inclusions of tellurian canfieldite and hessite. L) Pyrargyrite-proustite crystals in microfracture in rhodochrosite. Abbreviations: apy: arsenopyrite; cpy: chalcopyrite; cfd_Te: tellurian canfieldite; gn: galena; hs: hessite; mc: marcasite; mlc: melnicovite; po: pyrrhotite; prt: proustite; pyrg: pyrargyrite; py: pyrite; qz: quartz; sid: siderite; **sl:** sphalerite; td: tetrahedrite; tnn: tennantite; BSE: backscattered electron scanning electron microscopy image; RL: reflected light image.

hosted in limestones of the Chambará Formation (Pucará Group). The Morro Solar vein is interpreted to be the feeder of the Ivette replacement body.

Rosita replacement body and Rubí, Isabel, and Ramal Alianza veins (Figs. S2D–G). Massive pyrrhotite (Fig. 5A-B) and local arsenopyrite define a low-sulfidation assemblage typical of Stage A. Stage B stands out by the presence of finely intergrown pyrite and marcasite as replacement of pyrrhotite (Fig. 5A-B), as well as pyrite forming subhedral to anhedral micro-fractured crystals <60 μm in size in a matrix of quartz (Fig. 5C). Stage C has been subdivided into the Fe-Cu-Zn-As, Pb, and carbonate sub-stages. The Fe-Cu-Zn-As sub-stage is defined by precipitation of subhedral pyrite with inclusions of hematite (var. specularite), chalcopyrite, and bornite. Porosity and micro-fractures in pyrite grains are lined with sphalerite (up to 7.9 wt% Fe; Table 2), chalcopyrite, and tetrahedrite-tennantite (Fig. 5D-J). Commonly, coarse (5–10 μm) inclusions of chalcopyrite accumulate in the core of first-generation sphalerite (sl_{C1}), whereas fine (<5 μm) chalcopyrite dissemination occurs at the rim (Fig. 5F), thus producing a watermelon-like texture (Barton and Bethke, 1987). A second generation of sphalerite (sl_{C2}) lacks chalcopyrite disseminations. The mineral assemblage of the Pb sub-stage is mainly composed of galena (<500 μm), which partially replaced minerals of the previous Fe-Cu-Zn-As sub-stage. Galena hosts rare inclusions of tellurian canfieldite and hessite (Fig. 5K). The mineral assemblages of the carbonate sub-stage consist essentially of carbonates (mostly rhodochrosite) with local pyrargyrite (<250 μm) and proustite (<50 μm) in micro-fractures (Fig. 5L). Fig. 6 shows a unified paragenetic sequence for the Rosita/Rubí, Isabel, and Ramal Alianza mineralizations.

Morro Solar vein and Ivette replacement body (Figs. S2A–C). The first quartz-pyrite stage (corresponding to Stage B) is primarily composed of quartz and a first generation of pyrite (py_1) that forms subhedral to euhedral individual crystals <650 μm in size (Fig. 7A-B). Stage C is subdivided into the Fe-Cu-As-Sn-Zn, Zn-Pb, and carbonate sub-stages. The Fe-Cu-As-Sn-Zn sub-stage, the most widespread and economically important, is mostly composed of sphalerite, chalcopyrite, tetrahedrite-tennantite, and a second generation of pyrite (py_2) that occurs as micro-fractured subhedral to anhedral crystals <500 μm in size (Fig. 7C). Traces of hübnerite <375 μm long are enclosed in second-generation pyrite (py_2), which also contains small and abundant subrounded inclusions of sulfides, sulfosalts, and tellurides (e.g., cubanite, chalcopyrite, enargite, famatinite – var. stibioluzonite, tennantite – var. tellurian tennantite, hodrusite – Fig. S3F, stannoidite – Fig. S3D, vinciennite – Fig. 7J, S3G, tellurobismuthite – Fig. S3I). First- (py_1) and second- (py_2) generation pyrite grains were replaced along grain boundaries and micro-fractures by massive sphalerite with moderate Fe content (up to 5.79 wt%; Table 2), tetrahedrite-tennantite, chalcopyrite, and galena and show rims of a third generation of distinctly porous and botryoidal pyrite (py_3; Fig. 7H). In this sub-stage, two generations of Fe-poor sphalerite (sl_{C1} and sl_{C2}) were identified: i) first-generation sphalerite (sl_{C1}) shows fine disseminations of chalcopyrite distributed along its crystallographic faces (Fig. 7D-E); ii) second-generation sphalerite (sl_{C2}) shows no or only minor, local "chalcopyrite disease". Sphalerite grains are commonly intergrown with massive chalcopyrite and replaced by tetrahedrite-tennantite and galena (Fig. 7E–G). Locally, second-generation sphalerite (sl_{C2}) was also replaced by stibioluzonite (Fig. S3E) and radial aggregates of orpiment (<150 μm; Fig. S3C) while stannoidite, vinciennite, aikinite, and tsumoite are found as replacement of tetrahedrite-tennantite and galena (Fig. 7I and S3H). Sulfides of the Zn-Pb sub-stage are mainly galena and a third generation of sphalerite (sl_{C3}) forming yellowish-brown to cream-colored colloform layers (var. schalenblende; Ramdohr, 1980; Fig. 7K–L). The mineral assemblage of the carbonate sub-stage consists dominantly of siderite and intermediate

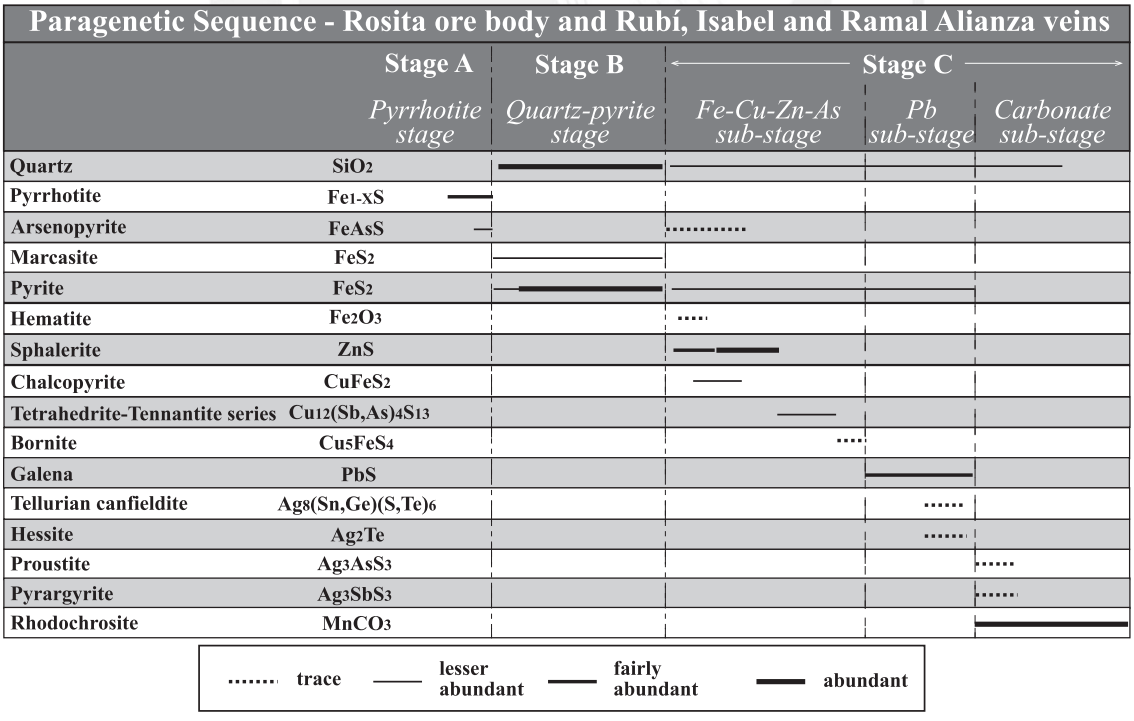

Fig. 6. Paragenetic sequence for the Rosita ore boby and the Rubí, Isabel, and Ramal Alianza veins. Thick bars indicate higher abundances and dashed lines, lesser abundances.

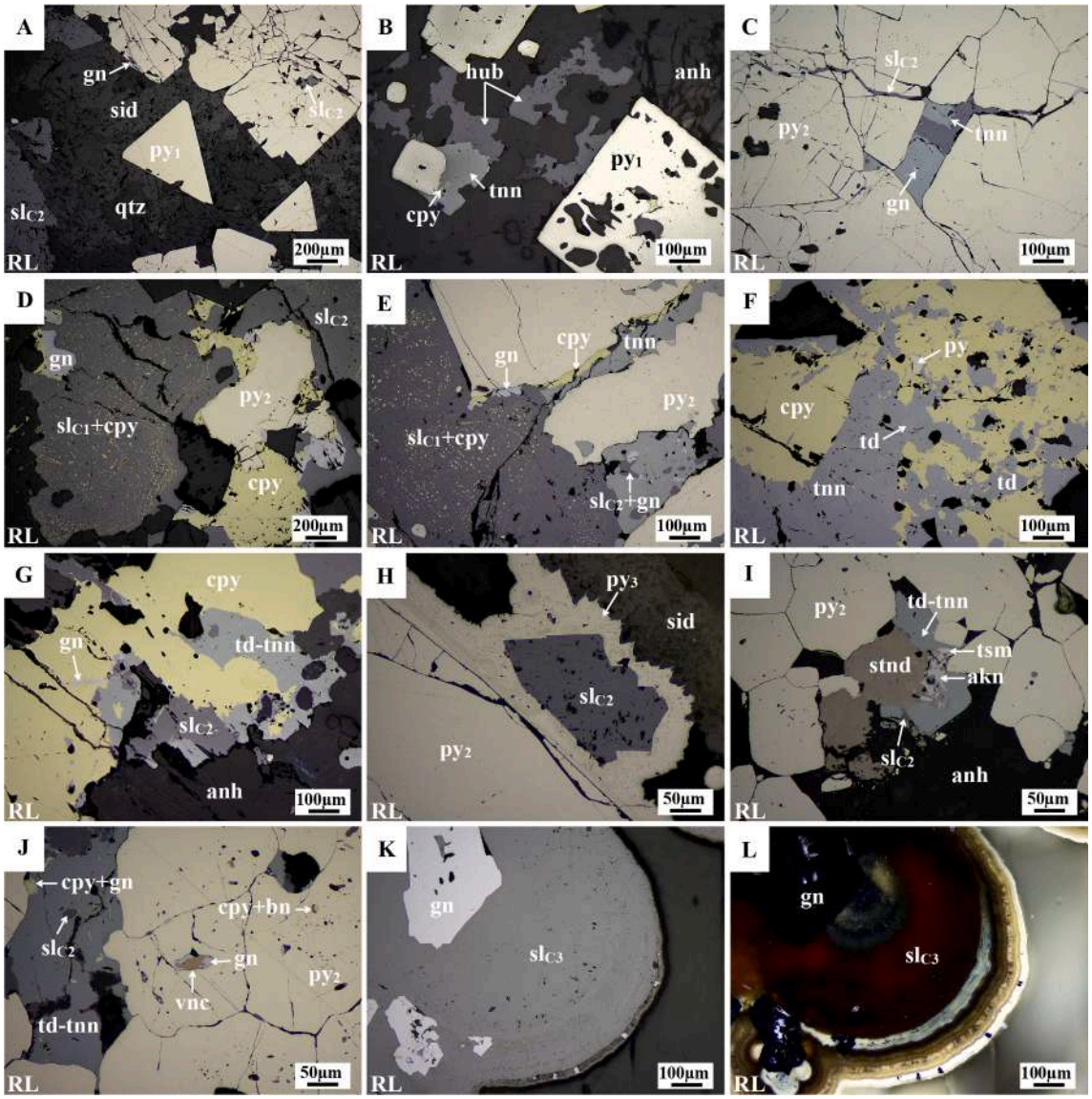

Fig. 7. Photomicrographs of textural features in the Morro Solar vein and Ivette manto. A) Pyrite (py_1) and sphalerite (sl_{C2}) crystals on quartz and siderite matrix. Some pyrite grains present sphalerite inclusions and replacement by galena from its borders. B) Pyrite (py_1) and hübnerite crystals on a siderite and anhydrite matrix, replaced by tennantite with chalcopyrite. C) Micro-fractured pyrite aggregates (py_2) lined with sphalerite (sl_{C2}), tennantite and galena. D-E) Anhedral pyrite (py_2) replaced by sphalerite (sl_{C1}; with fine disseminations of chalcopyrite blebs), galena, sphalerite (sl_{C2}), massive chalcopyrite, and tennantite. F) Massive chalcopyrite replaced by tetrahedrite and tennantite. G) Massive sphalerite (sl_{C2}) replaced by tetrahedrite, tennantite, and chalcopyrite with inclusions of galena. H) Pyrite (py_2) and sphalerite (sl_{C2}) wrapped by botryoidal pyrite (py_3). I-J) Pyrite aggregates (py_2) replaced by stannoidite, tetrahedrite-tennantite, galena, and chalcopyrite, with small inclusions of vinciennite, galena, chalcopyrite, and bornite within an anhydrite matrix. Inclusions of aikinite, tsumoite, and sphalerite (sl_{C2}) in tetrahedrite-tennantite are also observed. K-L) Concentric sphalerite (sl_{C3}) bands intergrown with galena in both parallel and crossed nicols. Abbreviations: akn: aikinite; anh: anhydrite; bornite: bn; cpy: chalcopyrite; gn: galena; hb: hübnerite; py: pyrite; qz: quartz; sid: siderite; sl: sphalerite; stnd: stannoidite; td: tetrahedrite; tnn: tennantite; tsm: tsumoite; vnc: vinciennite; RL: reflected light image.

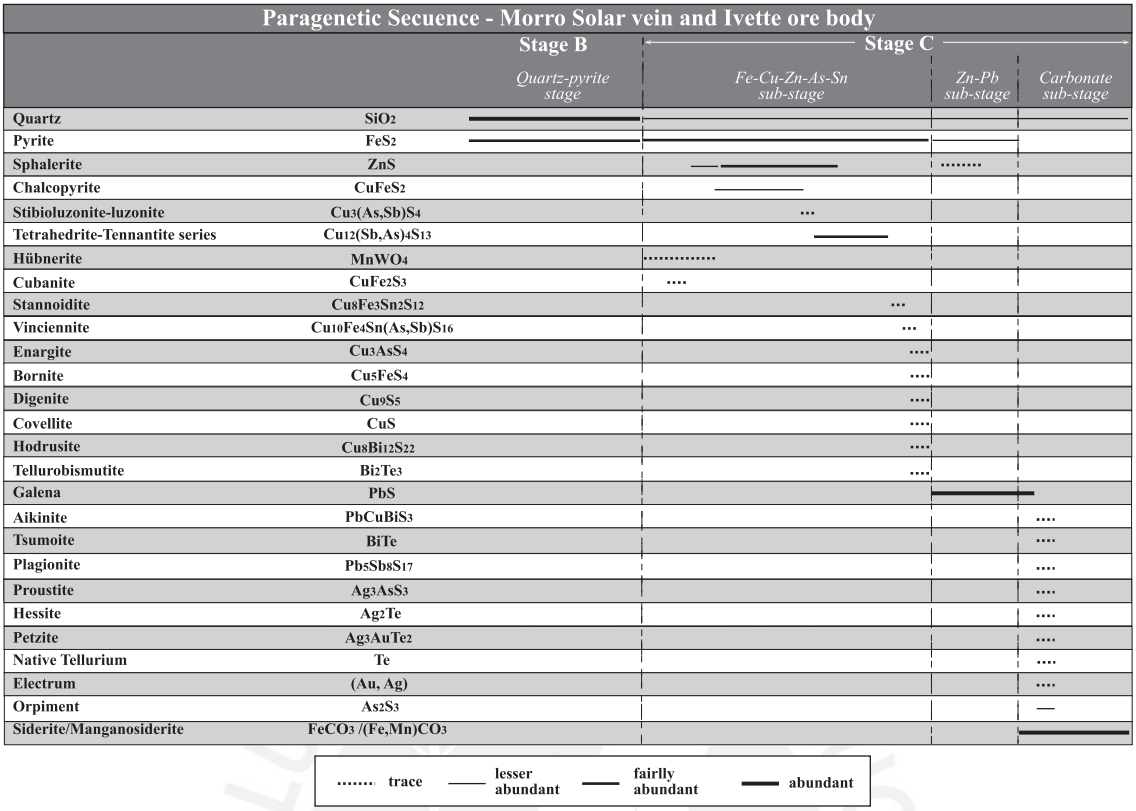

Fig. 8. Paragenetic sequence for the Morro Solar vein and the Ivette replacement body. Thick bars indicate higher abundances and dashed lines, lesser abundances.

members of the siderite-rhodochrosite series (var. manganosiderite), as well as quartz and anhydrite. In places, galena hosts minute inclusions of plagionite (<10 μm), hessite (<65 μm), petzite (<25 μm), and native tellurium (<7 μm; Figs. S3A-B, J-K). Locally, minute crystals of proustite (<3 μm) and electrum (<8 μm) line porosity in siderite and anhydrite (Fig. S3L). Fig. 8 shows a unified paragenetic sequence for both the Morro Solar and Ivette ore bodies.

5. Ore mineral geochemistry

Sphalerite, chalcopyrite, galena, and tetrahedrite-tennantite show, in general, a wide range of major and trace element contents. A summary of the compositions, including minimum, maximum, geometric mean, and interquartile range (IQR) values is reported in Tables 2–5. Content values will be hereinafter reported as the IQR unless otherwise specified. Of the analyzed elements, only Ag, Bi, and Pb in sphalerite, Pb and Bi in chalcopyrite, Mn, Cu, and Zn in galena, and Pb and Tl in tetrahedrite-tennantite present occasionally spiky LA-ICP-MS transient signals and therefore the occurrence of micro and nano-scale solid inclusions cannot be completely ruled out.

5.1. Sphalerite

Sphalerite shows a relatively wide range of Fe content (Table 2). Iron content measured with LA-ICP-MS (up to 79,760 ppm; av. = 17,411 ppm) are broadly comparable with those measured with EPMA (up to 11.1 wt%; av., 1.78 wt%; Table 2); however, Fe-rich sphalerite tends to yield lower values – up to 30% lower – with the second method. The Fe content is generally higher in sphalerite from Stage A low-sulfidation assemblages (Porvenir, 10.3–9.90 wt%; Manto Italia: first generation 10.8–8.42 wt%, and second generation, 10.8–10.1 wt%), and much lower in grains from Stage C high-sulfidation epithermal veins overprinting the Toromocho porphyry (189–85 ppm; Fig. 9A). In sphalerite from the Stage C intermediate-sulfidation assemblages, Fe is highly variable among the different studied ore bodies, in the range between 7.93 wt% and 12 ppm, and there is a pronounced Fe depletion from early to late generations (Table 2, Fig. 9A).

Zinc tends to show a negative correlation with Fe (Fig. 10A) suggesting simple $Fe^{2+} \leftrightarrow Zn^{2+}$ substitution, at least at Fe > ~1 wt% (Cook et al., 2009; Lockington et al., 2014; Wei et al., 2018; Pring et al., 2020). In contrast, Zn and Cd do not show correlation. A positive correlation between Fe and Mn (Fig. 10B) suggests either additional $Fe^{2+} + Mn^{2+} \leftrightarrow 2Zn^{2+}$ substitution (Graeser, 1969; Cook et al., 2009; Pring et al., 2020) or similar controls acting on the concentration of these elements (e.g., temperature: Frenzel et al., 2016). This relationship diverges from the negative correlation between both elements observed by Di Benedetto et al. (2005). Dispersion, however, points to more complex Zn substitution mechanisms involving trace elements, as explained below.

Copper values are generally higher in sphalerite grains from high-sulfidation assemblages overprinting the Toromocho porphyry (3009–1771 ppm Cu) and some intermediate-sulfidation assemblages including Ivette (730–89 ppm Cu), Morro Solar (1099–116 ppm Cu), and Ramal Alianza (536–188 ppm Cu; Fig. 9B). Higher Cd contents (Fig. 9C) are reported in sphalerite grains from intermediate-sulfidation assemblages in Ivette (1st- and 2nd-generation; 4355–2442 ppm), Ramal Alianza (4541–4034 ppm), Isabel (4804–3381 ppm), and Rosita/Rubí (4296–2854 ppm), and in grains from high-sulfidation assemblages overprinting the Toromocho porphyry (4012–3710 ppm). There is a general trend to Cd depletion from early to late sphalerite generations in intermediate-sulfidation assemblages, particularly in Ivette (3rd-generation, 431–80 ppm; Fig. 9C). The As content increases notably in sphalerite from intermediate-sulfidation assemblages, especially in Morro Solar (103–15 ppm) and Ivette (122–19 ppm), relative to sphalerite from high- (0.79–0.33 ppm) and low-sulfidation (e.g., Manto Italia, 0.61–0.30 ppm) assemblages (Fig. 9D). Tin contents are markedly variable in different mineralization style and sphalerite generation

Table 2
Summary of element contents in sphalerite from the Morococha district. Sulfur, Zn, and Fe are given in wt% (EPMA data) and all trace elements, in ppm (LA-ICP-MS data).

Ore-body/vein	Generation		S (wt%)	Zn (wt%)	Fe (wt%)	Fe (ppm)	Mn (ppm)	Cd (ppm)	In (ppm)	Ge (ppm)	Ga (ppm)	Cu (ppm)	Ag (ppm)	Sn (ppm)	Pb (ppm)	Sb (ppm)	Se (ppm)	Mo (ppm)	Co (ppm)	Au (ppm)	Hg (ppm)	Tl (ppm)	Bi (ppm)	As (ppm)
Entire district (n = 382)		MIN.	31.9	52.2	B.D.L.	B.D.L.	B.D.L.	32	B.D.L.	B.D.L.	0.086	B.D.L.	1.3	0.13	B.D.L.	B.D.L.	B.D.L.	B.D.L.	B.D.L.	B.D.L.	1.2	B.D.L.	B.D.L.	B.D.L.
		MAX.	34.7	68.4	11.1	79,760	29,259	5594	4608	701	2137	7110	82	3443	11	247	52	8.1	292	1.5	251	0.81	9.9	1223
		G.M.	33.3	64.4	0.98	3,099	384	2432	23	0.53	12	184	5.2	6.9	0.73	0.41	2.2	0.20	0.62	0.018	12	0.0097	0.091	18
		IQR	33.6-33.0	66.6-63.6	2.39-0.10	21,768-340	2656-130	4010-1766	217-2.7	0.89-0.18	61-2.0	610-74	8.5-2.9	47-0.81	2.7-0.26	2.9-0.040	3.2-1.0	0.36-0.079	1.7-0.15	0.020-0.013	29-4.5	0.015-0.0044	0.70-0.0060	46-8.0
Porvenir (n = 35)	sl_A	MIN.	32.1	54.4	7.86	63,577	3141	1669	163	0.18	0.089	139	2.5	0.15	0.055	B.D.L.	17	0.23	118	B.D.L.	1.2	B.D.L.	0.061	0.37
		MAX.	34.4	56.6	11.1	79,055	15,569	2112	217	0.57	0.27	416	8.8	3.2	4.9	0.29	52	1.6	292	0.051	2.6	0.065	8.5	37
		G.M.	33.4	55.5	9.8	73,939	5478	1852	195	0.35	0.18	174	3.7	0.38	0.50	0.030	38	0.43	232	0.015	1.6	0.0069	0.38	8.7
		IQR	33.9-32.9	55.9-55.0	10.3-9.90	75,486-72,864	8569-3792	2030-1759	209-171	0.44-0.31	0.24-0.14	169-155	4.6-2.9	0.98-0.19	1.0-0.16	0.029-0.027	48-35	0.86-0.27	280-171	0.015-0.013	2.2-1.3	0.012-0.0036	0.69-0.16	33-0.48
Manto Italia (n = 17)	sl_{A1} (n = 4)	MIN.	33.8	52.2	8.42	58,411	2862	1864	19	B.D.L.	6.2	28	3.0	0.18	0.65	B.D.L.	B.D.L.	0.31	0.078	B.D.L.	2.1	B.D.L.	0.0062	0.25
		MAX.	34.3	57.4	11.0	79,760	5711	2558	71	0.23	169	555	12	0.26	1.9	0.88	1.8	0.60	0.39	0.021	4.8	0.0081	0.48	0.56
		G.M.	34.0	56.0	9.29	67,552	4099	2048	39	0.17	46	124	5.9	0.22	1.1	0.21	1.1	0.41	0.14	0.016	3.2	0.0049	0.039	0.37
		IQR	34.1-33.9	57.6-54.4	10.8-8.41	77,008-58,658	5651-3017	2239-1870	68-23	0.20-0.14	160-21	381-42	9.9-3.5	0.24-0.20	1.6-0.86	0.61-0.092	1.5-0.85	0.53-0.31	0.19-0.089	0.018-0.013	4.2-2.4	0.0065-0.0038	0.25-0.058	0.51-0.27
	sl_{A2} (n = 13)	MIN.	33.7	54.4	7.56	56,281	2433	1730	25	B.D.L.	3.3	28	2.8	0.42	0.10	B.D.L.	B.D.L.	0.21	0.19	B.D.L.	2.5	B.D.L.	0.089	0.26
		MAX.	34.7	58.3	11.0	79,411	3312	2157	459	0.89	21	506	15	38	5.9	2.5	12	0.38	1.7	0.020	4.3	0.086	9.9	0.79
		G.M.	34.1	55.3	10.20	70,194	2824	1935	190	0.21	7.7	190	5.9	6.0	0.84	0.27	1.8	0.29	0.42	0.015	3.5	0.0090	0.73	0.46
		IQR	34.2-34.0	55.5-54.7	10.8-10.1	76,403-67,245	3146-2561	2074-1809	324-261	0.23-0.16	11-4.9	293-245	8.7-4.0	15-4.1	1.8-0.44	0.91-0.063	1.9-1.1	0.34-0.26	0.65-0.25	0.017-0.013	4.0-3.3	0.010-0.0044	1.7-0.26	0.61-0.30
Epithermal overprint on Toromocho porphyry (n = 7)	sl_C	MIN.	32.9	66.6	B.D.L.	66	521	3635	145	0.88	646	1002	3.9	0.44	0.54	0.082	1.8	0.12	B.D.L.	B.D.L.	130	0.0087	0.23	B.D.L.
		MAX.	33.4	66.7	B.D.L.	231	5448	4367	1456	4.2	1739	3270	6.7	8.1	3.4	2.1	19	1.3	0.11	0.018	251	0.042	1.2	2.0
		G.M.	33.1	66.1	-	124	2616	3899	775	1.6	959	2124	4.8	1.9	1.6	0.28	6.3	0.36	0.058	0.015	179	0.019	0.46	0.55
		IQR	33.3-32.9	66.4-65.9	-	189-85	4679-2120	4012-3710	1291-726	2.0-1.2	1269-706	3009-1771	5.5-4.2	3.4-1.1	2.6-1.1	0.40-0.13	13-4.3	0.50-0.25	0.066-0.046	0.016-0.013	197-164	0.029-0.013	0.63-0.34	0.79-0.33
Lower Ombla (n = 27)	sl_{C1} (n = 8)	MIN.	33.0	63.0	1.89	13,361	532	1893	45	B.D.L.	0.33	50	1.7	0.20	0.19	B.D.L.	5.3	0.091	B.D.L.	B.D.L.	4.0	B.D.L.	0.94	B.D.L.
		MAX.	33.6	65.3	3.59	27,003	1809	2034	75	0.23	7.3	168	4.0	3.2	3.0	B.D.L.	9.2	0.23	13	0.014	8.4	0.0059	5.5	0.70
		G.M.	33.2	64.3	2.44	19,414	1246	1966	54	0.19	1.9	83	2.6	0.48	0.50	-	7.8	0.17	1.1	0.014	5.4	0.0043	1.5	0.44
		IQR	33.3-33.1	65.0-63.6	3.13-1.97	24,001-16,104	1701-1261	1992-1944	55-48	0.22-0.15	5.7-0.95	94-67	3.3-2.2	0.72-0.22	0.72-0.23	-	8.8-7.2	0.21-0.16	4.7-0.26	-	6.1-4.5	0.0054-0.0036	1.6-1.1	0.54-0.37
	sl_{C2} (n = 19)	MIN.	32.3	63.3	1.68	10,800	499	1872	45	B.D.L.	0.78	51	2.0	0.20	0.10	B.D.L.	5.3	0.090	B.D.L.	B.D.L.	4.2	B.D.L.	0.40	B.D.L.
		MAX.	33.5	65.4	3.24	29,092	1949	2094	77	0.47	6.5	217	13	4.4	1.5	B.D.L.	11	0.26	13	0.053	8.2	0.034	4.2	0.81
		G.M.	33.1	64.1	2.59	17,259	1034	1983	53	0.24	1.9	88	2.9	0.86	0.49	-	8.1	0.15	1.0	0.017	5.7	0.0066	1.6	0.64
		IQR	33.3-33.0	65.0-63.4	3.16-2.08	20,640-13,262	1625-543	2054-1917	53-47	0.32-0.16	4.2-1.0	100-73	3.2-2.3	1.7-0.44	0.80-0.31	-	10-6.9	0.22-0.10	5.9-0.13	0.021-0.013	6.5-4.7	0.0072-0.0045	2.7-1.0	0.55-0.27
Morro Solar (n = 85)	sl_{C2}	MIN.	32.1	64.0	B.D.L.	B.D.L.	B.D.L.	888	B.D.L.	B.D.L.	0.18	B.D.L.	1.3	0.20	B.D.L.	B.D.L.	B.D.L.	B.D.L.	B.D.L.	B.D.L.	13	B.D.L.	B.D.L.	1.2
		MAX.	34.3	67.8	1.06	5666	1974	3994	1804	701	2118	5308	82	426	11	247	5.2	4.4	0.61	1.5	248	0.81	9.7	650
		G.M.	33.3	66.1	0.19	373	24	1565	44	1.1	37	306	5.3	15	0.89	1.7	1.7	0.30	0.14	0.028	56	0.015	0.27	40
		IQR	33.5-32.9	66.6-65.6	0.27-0.04	1202-92	214-1.7	1730-1375	471-8.0	3.4-0.26	191-8.0	1099-116	8.9-2.4	75-2.9	3.0-0.32	16-0.16	2.0-1.3	1.3-0.092	0.17-0.11	0.034-0.018	97-35	0.025-0.0065	1.1-0.043	103-15
Ivette (n = 113)	sl_{C1} (n = 31)	MIN.	32.0	52.6	0.13	340	313	2945	3.2	B.D.L.	0.17	60	1.9	0.72	0.019	B.D.L.	B.D.L.	B.D.L.	B.D.L.	B.D.L.	3.0	B.D.L.	B.D.L.	5.4
		MAX.	34.4	66.9	5.79	36,952	25,763	4727	411	114	2137	3427	24	307	6.7	4.6	15	1.5	6.0	0.018	21	0.067	0.68	769
		G.M.	33.2	64.3	1.36	11,606	1566	4052	52	0.34	34	323	5.9	18	0.39	0.098	1.9	0.14	0.77	0.015	6.3	0.0063	0.012	28
		IQR	33.5-33.0	66.1-63.2	2.79-0.86	22,537-8884	2611-734	4339-3933	104-31	0.34-0.15	64-21	751-145	8.8-3.5	74-3.9	1.0-0.14	0.20-0.032	2.9-1.0	0.27-0.071	3.2-0.19	0.016-0.013	7.6-4.5	0.0059-0.0046	0.023-0.0052	48-6.2
	sl_{C2} (n = 76)	MIN.	32.1	61.1	B.D.L.	19	B.D.L.	952	B.D.L.	B.D.L.	0.086	B.D.L.	1.9	0.13	B.D.L.	B.D.L.	B.D.L.	B.D.L.	B.D.L.	B.D.L.	4.9	B.D.L.	B.D.L.	5.8
		MAX.	34.2	68.4	1.71	8919	29,259	5594	4608	91	979	7110	72	3443	11	196	14	3.1	0.48	0.027	100	0.53	7.4	1223
		G.M.	33.3	66.3	0.21	346	188	2894	12	0.72	27	241	6.3	10	2.0	1.5	1.5	0.24	0.17	0.016	19	0.015	0.10	55
		IQR	33.4-33.1	67.7-65.2	0.38-0.03	2733-83	11,170-1.3	4402-1978	201-0.83	1.6-0.19	72-15	717-66	11-3.0	46-3.2	8.1-0.64	7.7-0.26	2.0-0.92	1.6-0.050	0.19-0.15	0.017-0.013	28-12	0.041-0.0051	0.70-0.013	159-21
	sl_{C3} (n = 6)	MIN.	31.9	64.6	B.D.L.	106	10	32	B.D.L.	38	2.2	11	4.7	0.61	10	1.7	B.D.L.	B.D.L.	B.D.L.	B.D.L.	18	0.10	0.11	-
		MAX.	32.7	67.6	0.22	526	75	896	0.56	215	49	896	69	58	11	5.9	1.0	8.1	0.70	B.D.L.	69	0.34	1.1	-
		G.M.	32.3	66.2	0.042	284	37	160	0.43	98	6.6	57	12	2.9	10	3.6	1.7	0.20	0.24	-	23	0.17	0.24	-
		IQR	32.5-32.1	67.1-65.4	0.07-0.03	468-155	66-33	431-80	0.50-0.39	129-74	8.1-3.6	75-28	11-7.6	13-0.72	10-10	5.0-3.0	1.0-1.0	0.13-0.085	0.22-0.20	-	19-18	0.25-0.11	0.32-0.16	-
Ramal Alianza (n = 18)	sl_{C1}	MIN.	33.5	58.0	2.23	19,702	431	3621	59	B.D.L.	9.6	88	2.2	1.5	B.D.L.	B.D.L.	B.D.L.	0.054	0.28	B.D.L.	1.7	B.D.L.	B.D.L.	9.6
		MAX.	34.5	63.7	7.93	56,941	5603	4915	657	0.36	86	817	12	326	9.0	3.9	3.4	0.45	10	0.015	3.7	0.0037	4.0	46
		G.M.	34.0	61.8	4.60	37,077	1297	4278	242	0.18	36	306	4.8	34	0.20	0.087	1.5	0.14	1.9	0.013	2.7	0.0042	0.080	23
		IQR	34.2-33.8	63.1-61.1	5.43-3.70	44,844-26,652	2867-656	4541-4034	398-157	0.22-0.13	55-28	536-188	5.5-4.2	244-5.1	0.82-0.034	0.19-0.028	2.5-0.84	0.24-0.083	7.4-0.48	0.014-0.012	3.3-2.4	0.0036-0.0035	0.46-0.0089	41-11
Isabel (n = 14)	sl_{C1} (n = 4)	MIN.	32.9	57.0	0.37	15,188	492	4545	67	B.D.L.	9.5	249	3.2	9.1	0.49	B.D.L.	1.1	B.D.L.	0.20	B.D.L.	5.4	B.D.L.	B.D.L.	40
		MAX.	34.0	65.3	1.97	25,352	4955	5318	112	B.D.L.	35	249	25	35.6	7.3	5.4	5.1	0.31	1.6	0.020	7.0	0.034	1.2	56
		G.M.	33.4	63.6	1.29	19,777	1041	4959	81	-	16	249	12	18	5.1	0.86	2.1	0.10	0.44	0.019	6.3	0.010	0.19	46
		IQR	33.6-33.1	65.2-64.2	1.96-0.79	24,740-15,941	1909-528	5150-4820	87-71	-	20-13	-	19-12	29-13	6.9-3.5	2.8-0.75	2.8-1.6	0.16-0.062	0.73-0.26	0.019-0.019	6.7-6.1	0.014-0.0061	0.62-0.24	48-43
	sl_{C2} (n = 10)	MIN.	33.4	66.3	0.19	1519	113	2839	1.2	B.D.L.	0.83	31	1.9	1.79	0.034	B.D.L.	B.D.L.	B.D.L.	B.D.L.	B.D.L.	6.6	B.D.L.	B.D.L.	33
		MAX.	33.9	68.0	0.69	13,719	10,339	4846	277	2.6	174	1115	11	144	8.6	5.7	1.7	0.36	13	B.D.L.	29	0.014	1.4	64
		G.M.	33.7	66.9	0.39	3045	1067	3610	10	0.21	7.2	188	3.2	27	0.43	0.28	1.2	0.12	2.4	-	15	0.0068	0.030	40
		IQR	33.8-33.6	67.8-66.5	0.53-0.24	4464-1900	1879-614	4002-3048	16-5.1	0.18-0.15	26-1.5	540-114	3.7-2.2	95-8.5	1.2-0.089	0.62-0.069	1.2-1.0	0.22-0.062	5.3-2.1	0.017-0.013	19-11	0.011-0.0050	0.067-0.0061	42-36
Rosita/Rubí (n = 66)	sl_{C1} (n = 25)	MIN.	32.2	59.5	0.23	1966	344	2083	0.031	B.D.L.	0.35	13	2.5	0.33	B.D.L.	B.D.L.	B.D.L.	B.D.L.	B.D.L.	B.D.L.	2.4	B.D.L.	B.D.L.	12
		MAX.	34.6	67.0	4.96	30,928	11,704	5525	25	12	429	1021	56	841	11	44	1.1	1.1	1.9	0.37	41	0.078	0.011	95
		G.M.	33.3	64.4	1.12	9,602	1854	3877	0.39	0.41	17	157	12	22.8	0.58	0.57	0.99	0.16	0.42	0.021	11	0.0089	0.0058	30
		IQR	33.5-33.0	65.7-63.7	2.61-0.57	20,173-5,698	2767-1360	4867-3350	1.1-0.054	0.45-0.18	61-10	458-64	19-7.3	235-1.7	2.0-0.20	3.7-0.11	1.1-0.84	0.20-0.11	0.91-0.18	0.021-0.014	22-4.1	0.018-0.0044	0.0061-0.0046	41-17
	sl_{C2} (n = 41)	MIN.	32.6	60.0	0.09	1158	145	2093	B.D.L.	B.D.L.	0.41	4.7	1.7	0.17	0.029	B.D.L.	B.D.L.	B.D.L.	B.D.L.	B.D.L.	4.3	B.D.L.	B.D.L.	11
		MAX.	34.4	67.5	4.75	30,832	4182	5388	6.7	13	136	845	20	124	6.6	19	0.89	0.90	6.0	0.067	33	0.056	0.019	35
		G.M.	33.3	64.5	1.30	10,173	527	3234	0.18	0.42	4.2	29	4.1	4.3	0.49	0.30	0.84	0.069	0.70	0.015	9.5	0.0050	0.0047	30
		IQR	33.6-32.9	65.9-63.1	2.58-0.66	18,102-6657	636-388	3965-2789	0.64-0.031	0.78-0.14	12-1.0	75-8.8	7.2-2.2	18-0.57	1.7-0.11	1.5-0.038	0.89-0.89	0.071-0.048	1.8-0.17	0.014-0.012	12-6.7	0.0048-0.0039	0.0049-0.0041	33-31

G.M.:Geometric means of element content. B.D.L.: below detection limit. EPMA data in wt.%. LA-ICP-MS data in ppm.

G.M.:Geometric means of element content. B.D.L.: below detection limit. EPMA data in wt%. LA-ICP-MS data in ppm.

Table 3
Summary of element contents in chalcopyrite from the Morococha district. Sulfur, Cu, and Fe are given in wt% (EPMA data) and all trace elements, in ppm (LA-ICP-MS data).

Ore-body/vein	Generation		S (wt%)	Cu (wt%)	Fe (wt%)	Fe (ppm)	In (ppm)	Ge (ppm)	Ga (ppm)	Ag (ppm)	Cd (ppm)	Zn (ppm)	Sn (ppm)	Pb (ppm)	Sb (ppm)	Mn (ppm)	Se (ppm)	Mo (ppm)	Co (ppm)	Au (ppm)	Hg (ppm)	Tl (ppm)	Bi (ppm)	As (ppm)
Entire district (n = 42)		MIN.	34.0	33.4	28.5	2,72,294	1.9	B.D.L.	0.18	0.26	B.D.L.	8.1	12	0.15	B.D.L.	B.D.L.	3.0	B.D.L.	B.D.L.	B.D.L.	B.D.L.	B.D.L.	B.D.L.	B.D.L.
		MAX.	35.9	35.2	30.6	3,49,524	1070	20	630	2649	16	1736	1224	7.1	9.5	7.0	112	0.64	18	0.024	0.50	0.45	8.3	5.9
		G.M.	35.1	34.4	29.8	3,08,701	63	1.3	9.3	35	1.2	191	138	1.6	0.22	1.8	12	0.056	0.14	0.013	0.11	0.0078	0.29	0.69
		IQR	35.4-34.9	34.8-34.0	30.0-29.7	322,498-290,072	109-32	3.1-0.68	62-1.5	143-14	5.3-0.23	595-87	360-42	3.3-1.0	0.80-0.068	3.0-1.1	20-6.7	0.066-0.038	0.11-0.052	0.014-0.011	0.13-0.085	0.0085-0.0038	1.3-0.10	1.3-0.40
Manto Italia (n = 3)	cpy	MIN.	35.1	33.9	29.9	2,92,958	7.1	0.22	0.68	1719	1.2	621	27	6.1	0.82	3.9	6.4	0.049	0.06	B.D.L.	B.D.L.	0.13	1.3	0.5
		MAX.	35.3	34.3	30.3	3,39,553	11	1.9	1.3	2649	4.4	1001	46	6.1	3.0	3.9	7.3	0.094	0.31	B.D.L.	B.D.L.	0.45	1.3	1.8
		G.M.	35.2	34.2	30.1	3,22,579	8.3	0.61	1.0	1988	2.8	798	36	6.1	1.8	3.9	6.8	0.067	0.12	-	-	0.27	1.3	1.1
		IQR	35.3-35.1	34.3-34.0	30.2-29.9	338,496-315,198	9.2-7.2	1.2-0.37	1.3-0.95	2187-1722	4.3-2.6	909-719	41-32	6.1-6.1	2.6-1.5	3.9-3.9	7.1-6.6	0.080-0.057	0.21-0.080	-	-	0.41-0.24	1.3-1.3	1.6-0.94
Epithermal overprint on Toromocho Porphyry (n = 7)	cpy	MIN.	35.3	34.7	29.5	3,12,191	64	0.59	2.8	0.26	B.D.L.	8.1	40	0.15	B.D.L.	B.D.L.	20	B.D.L.	B.D.L.	B.D.L.	B.D.L.	0.0064	B.D.L.	B.D.L.
		MAX.	35.7	35.1	30.0	3,49,524	81	3.6	16	2.1	0.20	44	131	0.67	0.17	3.7	30	0.074	0.076	0.012	0.50	0.017	1.3	1.5
		G.M.	35.4	34.8	29.7	3,36,389	73	2.0	8.8	0.71	0.16	23	80	0.25	0.08	1.7	27	0.054	0.051	0.013	0.22	0.0093	0.27	1.1
		IQR	35.6-35.4	34.8-34.7	29.8-29.6	346,492-329,835	77-71	3.0-1.5	11-9.0	1.2-0.39	0.16-0.15	39-16	104-66	0.40-0.16	0.13-0.070	2.1-1.2	29-26	0.067-0.047	0.059-0.042	0.014-0.012	0.30-0.17	0.013-0.0065	0.39-0.21	1.4-1.1
Lower Ombla (n = 8)	cpy_1 (n=4)	MIN.	34.5	34.0	29.9	3,11,941	1.9	0.71	0.18	197	6.3	961	12	1.7	B.D.L.	B.D.L.	106	0.040	12	B.D.L.	B.D.L.	B.D.L.	0.98	0.063
		MAX.	34.9	34.6	30.2	3,30,683	2.4	0.83	0.35	237	9.2	1736	16	2.3	0.077	3.2	112	0.085	18	0.024	0.22	0.0071	1.5	0.096
		G.M.	34.7	34.2	30.1	3,18,830	2.1	0.78	0.27	219	6.6	1147	14	2.1	0.048	2.1	110	0.058	14	0.016	0.13	0.0048	1.3	0.077
		IQR	34.8-34.6	34.4-34.1	30.1-30.0	323,129-312,319	2.3-1.9	0.81-0.75	0.33-0.23	228-215	7.0-5.7	1200-1003	15-13	2.2-2.0	0.071-0.034	1.7-1.2	111-109	0.066-0.052	14-13	0.018-0.014	0.16-0.11	0.0057-0.0039	1.4-1.3	0.090-0.065
	cpy_2 (n=4)	MIN.	34.0	34.3	29.6	3,09,568	19	B.D.L.	0.28	13	0.83	340	23	1.8	B.D.L.	2.2	14	0.043	B.D.L.	0.013	B.D.L.	0.0047	4.5	B.D.L.
		MAX.	35.5	34.7	29.9	3,26,156	31	0.19	0.57	69	1.9	550	31	2.6	B.D.L.	7.0	18	0.32	0.36	0.017	B.D.L.	0.013	8.3	B.D.L.
		G.M.	34.5	34.6	29.7	3,17,348	26	0.18	0.40	21	1.3	417	27	2.2	-	4.1	17	0.12	0.088	0.015	-	0.0072	6.6	-
		IQR	34.6-34.3	34.7-34.5	29.7-29.7	321,347-313,053	30-25	0.19-0.17	0.53-0.29	30-13	1.8-1.0	492-341	30-24	2.5-2.0	-	6.3-2.8	18-17	0.28-0.059	0.15-0.046	0.017-0.014	-	0.0090-0.0055	8.2-5.9	-
Morro Solar (n = 8)	cpy	MIN.	35.0	33.4	30.0	2,92,418	796	0.90	112	40	0.16	75	110	1.9	B.D.L.	B.D.L.	7.3	B.D.L.	B.D.L.	B.D.L.	B.D.L.	0.0050	B.D.L.	B.D.L.
		MAX.	35.6	34.0	30.4	3,23,368	1070	20	630	65	0.35	190	295	7.1	0.35	1.5	11	0.072	0.064	0.018	0.15	0.012	0.38	5.9
		G.M.	35.3	33.8	30.2	3,10,655	917	3.8	234	58	0.23	131	184	4.2	0.092	1.2	8.7	0.051	0.051	0.014	0.10	0.0066	0.12	0.84
		IQR	35.4-35.1	33.9-33.8	30.3-30.1	319,786-301,406	941-891	7.8-1.9	295-160	62-60	0.29-0.18	155-117	257-152	6.1-3.2	0.11-0.053	1.3-1.1	9.3-7.9	0.057-0.045	0.053-0.050	0.015-0.013	0.10-0.091	0.0067-0.0059	0.20-0.093	0.86-0.51
Ivette (n = 9)	cpy	MIN.	34.5	33.9	28.5	2,72,294	33	0.25	2.3	8.2	1.3	48	292	1.0	0.070	B.D.L.	4.8	B.D.L.	B.D.L.	B.D.L.	B.D.L.	B.D.L.	0.010	0.36
		MAX.	35.7	35.2	30.5	3,00,884	93	3.7	77	180	5.6	501	796	4.0	7.4	1.5	9.1	0.64	4.4	0.016	0.10	0.054	1.3	2.5
		G.M.	35.1	34.5	29.6	2,90,839	45	0.92	25	64	2.1	129	434	1.8	0.49	1.1	7.1	0.050	0.14	0.010	0.087	0.0045	0.084	0.94
		IQR	35.3-34.8	34.8-34.2	30.1-29.2	299,126-285,568	40-38	1.4-0.67	63-18	161-42	3.1-1.4	177-83	529-330	2.7-1.1	0.83-0.24	1.3-0.95	8.0-6.5	0.053-0.028	0.11-0.069	0.012-0.0087	0.095-0.079	0.0037-0.0029	0.24-0.020	1.2-0.73
Ramal Alianza (n = 7)	cpy	MIN.	34.7	34.6	29.9	2,64,301	80	0.62	2.1	24	3.2	158	161	0.47	0.28	B.D.L.	3.0	B.D.L.	B.D.L.	B.D.L.	B.D.L.	B.D.L.	0.072	1.1
		MAX.	35.7	34.8	30.5	3,12,988	126	8.1	18	77	16	827	1224	5.5	9.5	5.6	6.7	0.34	B.D.L.	B.D.L.	0.13	0.015	3.6	2.6
		G.M.	35.3	34.7	30.2	2,80,328	102	2.6	8.4	35	9.1	495	676	1.9	1.4	3.4	3.8	0.045	-	-	0.084	0.0051	0.24	1.7
		IQR	35.6-35.2	34.8-34.7	30.4-30.0	287,090-267,292	113-93	3.9-2.0	12-7.7	35-30	14-7.5	665-475	1115-585	4.2-1.1	1.8-1.1	5.2-3.3	4.2-3.1	0.043-0.027	-	-	0.089-0.075	0.0062-0.0031	0.28-0.11	2.2-1.4

G.M.:Geometric means of element content. B.D.L.: below detection limit. EPMA data in wt.%. LA-ICP-MS data in ppm.

Table 4
Summary of element contents in galena from the Morococha district. Sulfur and Pb are given in wt% (EPMA data) and all trace elements, in ppm (LA-ICP-MS data).

Ore-body/vein		S (wt%)	Pb (wt%)	In (ppm)	Ge (ppm)	Ga (ppm)	Ag (ppm)	Sb (ppm)	As (ppm)	Zn (ppm)	Fe (ppm)	Cu (ppm)	Sn (ppm)	Mn (ppm)	Co (ppm)	Se (ppm)	Mo (ppm)	Au (ppm)	Hg (ppm)	Tl (ppm)	Bi (ppm)	Cd (ppm)
Entire district (n = 44)	MIN.	12.0	85.1	B.D.L.	B.D.L.	B.D.L.	272	32	B.D.L.	B.D.L.	B.D.L.	B.D.L.	0.090	B.D.L.	B.D.L.	B.D.L.	B.D.L.	B.D.L.	B.D.L.	0.98	B.D.L.	6.0
	MAX.	13.6	88.9	0.61	2.0	3.6	5712	5124	104	14	12	18	6.7	9.3	0.55	135	0.67	1.1	1.3	4.5	6410	68
	G.M.	13.1	87.4	0.091	0.53	0.056	1277	718	2.8	1.5	7.8	1.8	0.78	2.2	0.29	11	0.28	0.046	0.097	1.9	2.2	28
	IQR	13.2-13.0	88.1-86.9	0.28-0.043	1.2-0.33	0.064-0.043	1477-992	1099-346	9.3-0.57	1.6-1.1	8.5-7.1	2.1-1.2	3.2-0.20	3.6-1.0	0.32-0.27	92-1.4	0.35-0.22	0.048-0.032	0.087-0.077	2.1-1.5	159-0.028	34-24
Manto Italia (n = 4)	MIN.	-	-	0.33	B.D.L.	B.D.L.	4883	4326	B.D.L.	B.D.L.	B.D.L.	3.0	-	6.7	B.D.L.	B.D.L.	B.D.L.	B.D.L.	B.D.L.	3.8	0.022	26
	MAX.	13.5	84.8	0.39	B.D.L.	B.D.L.	5712	5124	B.D.L.	B.D.L.	12	7.4	-	8.1	B.D.L.	B.D.L.	B.D.L.	1.1	B.D.L.	3.9	0.031	36
	G.M.	-	-	0.35	-	-	5230	4663	-	-	8.1	5.2	-	7.5	-	-	-	0.090	-	3.8	0.027	31
	IQR	-	-	0.37-0.33	-	-	5442-4982	4855-4439	-	-	8.7-7.0	6.9-4.3	-	7.8-7.3	-	-	-	0.32-0.036	-	3.8-3.8	0.031-0.023	34-28
Morro Solar (n = 3)	MIN.	12.0	85.7	0.039	B.D.L.	B.D.L.	272	296	0.63	-	B.D.L.	-	0.25	B.D.L.	B.D.L.	B.D.L.	B.D.L.	0.040	0.38	1.2	81	6.0
	MAX.	13.2	88.4	0.61	B.D.L.	B.D.L.	430	1157	104	-	B.D.L.	-	0.74	-	0.55	B.D.L.	B.D.L.	0.33	0.55	1.6	276	8.9
	G.M.	12.8	86.8	0.23	-	-	330	722	13	-	-	-	0.48	-	0.40	-	-	0.16	0.43	1.3	139	7.4
	IQR	13.2-12.9	88.4-86.4	0.56-0.28	-	-	369-290	1127-697	68-17	-	-	-	0.67-0.42	-	0.45-0.35	-	-	0.32-0.17	0.47-0.38	1.4-1.2	198-101	8.2-6.7
Ivette (n = 17)	MIN.	12.8	86.1	B.D.L.	B.D.L.	B.D.L.	480	32	B.D.L.	B.D.L.	B.D.L.	B.D.L.	0.090	0.74	B.D.L.	29	B.D.L.	B.D.L.	B.D.L.	1.3	3.2	16
	MAX.	13.5	88.8	0.10	2.0	3.6	3449	1496	17	3.1	8.6	2.1	6.7	9.3	B.D.L.	135	0.67	0.14	0.089	4.5	6410	68
	G.M.	13.1	87.4	0.053	1.1	0.068	1171	318	2.2	1.4	7.8	1.3	1.2	1.8	-	81	0.28	0.045	0.076	2.0	309	29
	IQR	13.2-13.0	88.2-86.9	0.074-0.039	1.5-0.89	0.068-0.046	1433-981	475-219	9.8-0.43	1.7-0.93	8.7-7.1	1.4-1.1	4.1-0.14	2.5-1.0	-	108-63	0.37-0.22	0.052-0.033	0.085-0.070	2.2-1.7	1600-42	38-20
Rosita/Rubí (n = 20)	MIN.	12.5	85.1	B.D.L.	B.D.L.	B.D.L.	937	737	B.D.L.	B.D.L.	B.D.L.	B.D.L.	0.12	0.52	B.D.L.	B.D.L.	B.D.L.	B.D.L.	B.D.L.	0.98	B.D.L.	24
	MAX.	13.6	88.9	B.D.L.	0.46	0.052	1983	1571	13	14	B.D.L.	18	4.5	5.8	B.D.L.	20	B.D.L.	0.046	1.3	2.4	0.18	41
	G.M.	13.1	87.5	-	0.33	0.045	1270	988	3.9	1.7	-	1.9	0.58	2.3	-	3.7	-	0.034	0.10	1.6	0.041	31
	IQR	13.3-13.0	88.1-87.2	-	0.34-0.32	0.052-0.038	1352-1033	1056-803	6.3-3.2	2.0-1.1	-	2.4-1.2	2.9-0.20	3.5-1.5	-	20-1.3	-	0.039-0.029	0.095-0.079	2.1-1.2	0.090-0.025	33-30

G.M.:Geometric means of element content. B.D.L.: below detection limit. EPMA data in wt.%. LA-ICP-MS data in ppm.

G.M.:Geometric means of element content. B.D.L.: below detection limit. EPMA data in wt%. LA-ICP-MS data in ppm.

Table 5
Summary of element contents in tetrahedrite-group minerals from the Morococha district. Sulfur, Cu, Fe, Sb, As, and Ag are given in wt% (EPMA data) and all trace elements, in ppm (LA-ICP-MS data).

Ore-body/vein		S (wt%)	As (wt%)	Sb (wt%)	Fe (wt%)	Ag (wt%)	Cu (wt%)	Zn (wt%)	In (ppm)	Ge (ppm)	Ga (ppm)	Sn (ppm)	Pb (ppm)	Mn (ppm)	Co (ppm)	Se (ppm)	Mo (ppm)	Au (ppm)	Hg (ppm)	Tl (ppm)	Bi (ppm)	Cd (ppm)
Entire district (n = 12)	MIN.	24.0	3.13	B.D.L.	0.13	B.D.L.	25.9	2.05	0.39	B.D.L.	B.D.L.	B.D.L.	1.1	B.D.L.	B.D.L.	B.D.L.	B.D.L.	B.D.L.	62	B.D.L.	B.D.L.	653
	MAX.	29.0	22.8	24.7	5.92	17.5	44.1	9.15	266	3.3	9.6	24	13	4008	2.0	152	3.2	3.2	446	0.48	66,892	1907
	G.M.	27.2	12.0	5.54	0.58	0.86	40.1	6.99	23	1.2	1.5	1.8	4.2	596	0.36	23	0.70	0.16	147	0.11	359	1236
	IQR	28.2-26.2	21.3-7.54	19.3-0.68	0.99-0.33	1.46-0.18	42.3-39.2	8.12-6.68	44-25	1.9-0.74	3.8-0.65	12-0.42	7.2-2.7	3610-387	0.62-0.27	68-14	0.91-0.34	0.54-0.043	196-94	0.22-0.067	18,786-24	1627-1042
Epithermal overprint on Toromocho porphyry (n = 4)	MIN.	27.8	15.0	1.65	0.13	B.D.L.	42.3	6.43	30	0.64	3.3	B.D.L.	1.1	371	0.22	64	0.29	B.D.L.	169	0.041	17,447	962
	MAX.	28.0	18.1	5.36	0.28	B.D.L.	44.1	9.15	48	1.3	9.6	0.85	8.0	462	0.32	152	0.34	0.046	212	0.087	66,892	1176
	G.M.	27.9	16.5	2.70	0.22	-	43.2	7.39	38	0.89	5.3	0.29	2.9	409	0.28	103	0.32	0.027	188	0.058	36,518	1068
	IQR	27.9-27.9	17.7-15.5	2.78-2.11	0.25-0.25	-	44.0-42.8	7.30-7.10	44-33	1.2-0.65	7.3-3.7	0.43-0.23	6.8-1.2	428-387	0.30-0.27	148-76	0.34-0.30	0.039-0.020	196-180	0.070-0.046	66,842-21,464	1102-1042
Morro Solar (n = 2)	MIN.	25.0	3.56	B.D.L.	0.16	0.17	37.8	6.72	229	0.77	0.31	10	-	B.D.L.	B.D.L.	19	0.67	1.9	402	-	3.9	653
	MAX.	29.0	22.8	24.7	0.87	1.48	42.3	8.37	266	3.3	0.36	17	-	60	B.D.L.	20	1.3	3.2	446	-	31	796
	G.M.	27.5	13.3	3.60	0.41	0.50	40.5	7.91	247	1.6	0.33	13	-	11	-	19	0.94	2.5	424	-	11	721
	IQR	28.8-26.2	22.0-6.65	20.6-0.14	0.55-0.33	1.15-0.22	41.9-39.5	8.25-7.73	257-239	2.7-1.4	0.35-0.32	15-12	-	45-16	-	20-19	1.1-0.83	2.9-2.2	435-413	-	24-11	761-689
Ivette (n = 4)	MIN.	26.1	7.37	B.D.L.	0.63	0.06	38.1	2.05	25	B.D.L.	3.1	1.0	4.2	3529	B.D.L.	13	B.D.L.	B.D.L.	62	B.D.L.	1102	1614
	MAX.	28.7	21.8	19.4	5.92	2.26	43.1	7.57	27	1.8	3.9	24	13	4008	B.D.L.	18	3.2	B.D.L.	102	0.17	1379	1907
	G.M.	27.3	13.2	9.23	1.39	0.91	41.0	5.82	26	1.6	3.5	4.7	6.8	3806	-	15	1.4	-	85	0.12	1225	1691
	IQR	28.2-26.4	20.5-10.1	15.9-1.10	1.89-1.01	1.79-0.66	42.9-39.9	6.94-6.01	26-25	1.9-1.6	3.8-3.4	20-1.1	9.3-5.1	3892-3771	-	16-14	2.7-0.75	-	97-81	0.18-0.079	1323-1127	1703-1622
Rosita/Rubí (n = 2)	MIN.	24.0	3.13	23.8	0.45	2.78	25.9	5.63	0.39	B.D.L.	B.D.L.	0.46	-	1453	B.D.L.	B.D.L.	B.D.L.	0.40	80	0.28	B.D.L.	1318
	MAX.	25.4	3.68	24.2	2.37	17.5	37.1	6.95	1.0	2.1	B.D.L.	5.9	-	2088	B.D.L.	B.D.L.	B.D.L.	0.75	103	0.48	0.27	1734
	G.M.	24.8	3.42	24.0	0.84	7.2	31.7	6.42	0.63	1.1	-	1.7	-	1742	-	-	-	0.55	91	0.37	0.098	1512
	IQR	25.2-24.5	3.57-3.30	24.1-23.9	1.46-0.50	12.65-5.31	35.2-29.6	6.86-6.20	0.84-0.54	1.7-0.99	-	4.6-1.8	-	1929-1612	-	-	-	0.66-0.49	97-86	0.43-0.33	0.21-0.094	1630-1422

G.M.:Geometric means of element content. B.D.L.: below detection limit. EPMA data in wt.%. LA-ICP-MS data in ppm.

G.M.:Geometric means of element content. B.D.L.: below detection limit. EPMA data in wt%. LA-ICP-MS data in ppm.

(Fig. 9E). Tin content is, in general, lower in grains from high-sulfidation (3.4–1.1 ppm) and low-sulfidation (e.g., Porvenir, 0.98–0.19 ppm) assemblages. Except for Lower Ombla (1.2–0.41 ppm), Sn contents are significantly higher in intermediate-sulfidation sphalerite grains from Ivette (47–3.0 ppm), and Morro Solar, Ramal Alianza, Isabel, and Rosita/Rubí (75–2.0 ppm). In low-sulfidation assemblages from Manto Italia, there is a marked Sn enrichment from first- (0.24–0.20 ppm) to second-generation (15–4.1 ppm) sphalerite. In intermediate-sulfidation assemblages, in contrast, there is a trend towards Sn depletion from early to late sphalerite generations. Bismuth contents in sphalerite are systematically low (<10 ppm) with subtle depletion in distal (e.g., Rosita/Rubí, 0.0056–0.0043 ppm) relative to proximal (e.g., Lower Ombla, 2.3–1.0 ppm) intermediate-sulfidation assemblages (Fig. 9F). Bismuth shows both enrichment and depletion trends from early to late sphalerite generations. Selenium content is also generally low. The highest Se contents are recorded in low-sulfidation assemblages from Porvenir (48–35 ppm). In sphalerite from intermediate-sulfidation assemblages (2.1–0.90 ppm), there is Se depletion from proximal to distal mineralized structures (Fig. 9G). Cobalt is distinctly enriched in sphalerite from Porvenir (280–171 ppm), whereas in the rest of the studied structures, Co is typically below 10 ppm. Molybdenum content in the studied sphalerite generations is systematically low (0.36–0.079 ppm) with a slight, steady decrease from high-sulfidation (0.50–0.25 ppm) to distal intermediate-sulfidation (e.g., Rosita/Rubí, 0.17–0.055 ppm; Fig. 9H) mineralization.

The In content in sphalerite is much higher in high-sulfidation assemblages in epithermal veins overprinting the Toromocho porphyry mineralization (1291–726 ppm, up to 1456 ppm) than in the other analyzed sphalerite. In low-sulfidation assemblages, In content is also relatively high (e.g., Porvenir, 209–171 ppm); in Manto Italia, the In content increases from first- (68–23 ppm) to second-generation (324–261 ppm) sphalerite. In intermediate-sulfidation assemblages, sphalerite is particularly enriched in In in Morro Solar (471–8.0 ppm, up to 1804 ppm) and Ramal Alianza (398–157 ppm, up to 657 ppm; Fig. 9I); the In content tends to decrease towards the more distal mineralization at Isabel and Rosita/Rubí (5.3–0.089 ppm). In contrast to sphalerite from Manto Italia, in sphalerite from intermediate-sulfidation assemblages there is a dramatic In depletion from early to late generations.

Germanium values are generally low (0.89–0.18 ppm) and only third-generation, colloform sphalerite grains from Ivette exhibit significantly higher values (129–74 ppm Ge; Fig. 9J). Gallium contents (Fig. 9K) are much higher in sphalerite from high-sulfidation assemblages (1269–706 ppm) and significant in grains from intermediate-

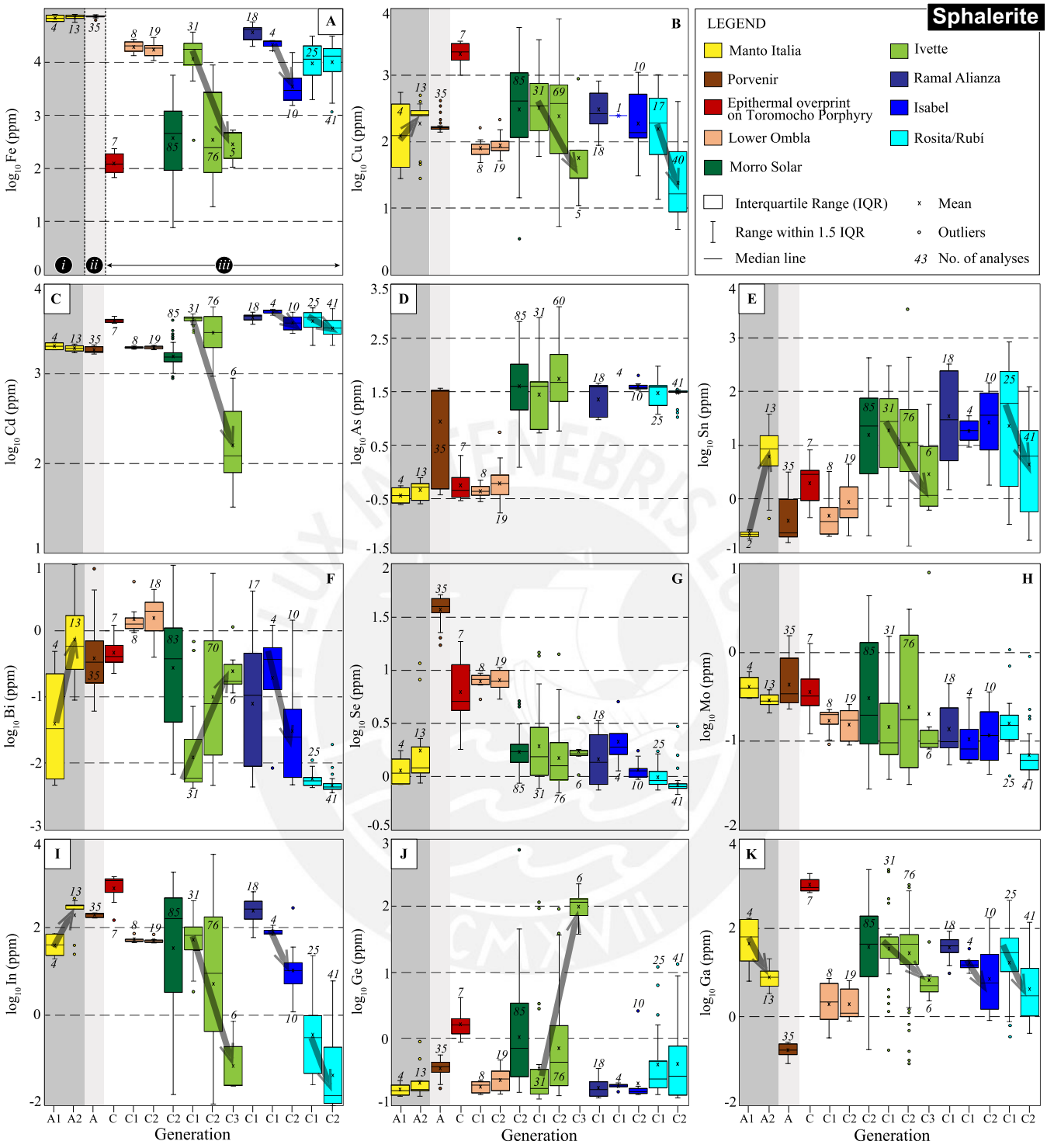

Fig. 9. Selected boxplots of log-transformed element contents in sphalerite (LA-ICP-MS data). Dark gray arrows indicate temporal trends within sites during a same mineralization event. *"i"* (Manto Italia), *"ii"* (Porvenir), and *"iii"* (other sites) refer to the mineralization events described in Section 2.3 ("Studied polymetallic mineralization styles in the Morococha district"). The ordering of the boxplots in *"iii"* follows a roughly proximal to distal position relative to the Toromocho porphyry. Analyzed sphalerite from Manto Italia and Porvenir comes from LS assemblages, that from veins overprinting the Toromocho porphyry from HS assemblages; whereas for the other sites, sphalerite comes from IS assemblages.

sulfidation assemblages in Morro Solar (191–8.0 ppm, up to 2118 ppm). There is a subtle but systematic decrease in the Ga content from early to late sphalerite generations in both low- and intermediate-sulfidation assemblages. Correlations and substitution mechanisms for In, Ge, and Ga in sphalerite are addressed in detail in the Discussion section.

5.2. Chalcopyrite

Tin content in chalcopyrite increases by two orders of magnitude from Lower Ombla (25–14 ppm) to the distal Ramal Alianza (1115–585 ppm; Fig. 11A). Silver in chalcopyrite also displays relatively high (143–14 ppm), though erratic, values at the district scale (Fig. 11B). The

highest Ag content is found in low-sulfidation assemblages in Manto Italia (2187–1722 ppm), followed by intermediate-sulfidation assemblages in Lower Ombla (with higher values in the first [228–215 ppm] than in the third [30–13 ppm] generations). The lowest Ag content is found in chalcopyrite grains from the high-sulfidation assemblages overprinting the Toromocho porphyry (1.2–0.39 ppm). Selenium content is high in chalcopyrite from Lower Ombla, particularly in grains of the first generation (111–109 ppm; Fig. 11C), relative to those of the third generation (18–17 ppm), and progressively decreases towards distal mineralization (e.g., Ramal Alianza, 4.2–3.1 ppm). Mercury shows low values and progressive depletion from high-sulfidation epithermal overprint in the Toromocho porphyry center (0.30–0.17 ppm) to the more distal intermediate-sulfidation mineralization (e.g., Ramal Alianza, <0.13 ppm; Fig. 11D).

A positive correlation between the Zn and Sn content in chalcopyrite is observed (Fig. 11H), although grains from Lower Ombla and Manto Italia seem to deviate from this trend. Noteworthy, Sn contents in chalcopyrite (360–42 ppm) are significantly higher than in sphalerite (47–0.81 ppm). Zinc also correlates positively with Cd (Fig. 11I; see George et al., 2018; Wilson, 2019).

Indium contents are erratic throughout the Morococha chalcopyrite database. Distinctively high In values are recorded in chalcopyrite from intermediate-sulfidation assemblages in Morro Solar (941–891 ppm) and Ramal Alianza (113–93 ppm), followed by chalcopyrite from high-sulfidation assemblages in the Toromocho porphyry center (77–71 ppm). In Lower Ombla, there is a marked increase in the In content from the first (2.3–1.9 ppm) to the third (30–25 ppm) generations of chalcopyrite (Fig. 11E). Germanium contents are systematically low (3.1–0.68 ppm) and show depletion from the first (0.81–0.75 ppm) to the third (0.19–0.17 ppm) generations in Lower Ombla (Fig. 11F). The highest Ga content in chalcopyrite occurs in intermediate-sulfidation assemblages in Morro Solar (295–160 ppm; Fig. 11G).

5.3. Galena

The highest Ag content in galena occurs in low-sulfidation assemblages in Manto Italia (5442–4982 ppm) and, to a lesser extent, in intermediate-sulfidation assemblages in Ivette (1433–981 ppm) and Rosita/Rubí (1352–1033 ppm; Table 4, Fig. 12A). Galena from Morro Solar contains the lowest Ag (369–290 ppm). Silver displays fair positive correlations with Bi and Sb (Fig. 12E-G) that agree with widely described coupled substitutions (e.g., Foord et al., 1988; Sack, 2005; Sack and Ebel, 2006; Sack and Goodell, 2002; Sack and Lichtner, 2009). In Ivette, element correlations suggest coupled substitution of the type $Bi^{3+} + Ag^{+} \leftrightarrow 2Pb^{2+}$ (Fig. 12E-F; Armbruster et al., 2003; Renock and Becker, 2011; George, 2013; George et al., 2015). In Manto Italia and Rosita/Rubí, the strong positive correlation of Ag + Cu + Tl and Bi + Sb (Fig. 12G) suggests $(Ag, Cu, Tl)^{+} + (Bi, Sb)^{3+} \leftrightarrow 2Pb^{2+}$ coupled substitution, as proposed by George et al. (2015).

The In, Ge, and Ga contents in galena from Morococha yield values <3.6 ppm (Fig. 12B-D). In intermediate-sulfidation assemblages, the In content is highest in galena from Morro Solar (0.56–0.28 ppm) and displays a progressive depletion from proximal to distal mineralization.

5.4. Tetrahedrite-tennantite series minerals

Copper content in tetrahedrite-tennantite series minerals tends to decrease from grains in epithermal veins overprinting the Toromocho porphyry mineralization (44.0–43.0 wt%) to distal mineralization (Rosita-Rubí, 35.2–29.6 wt%; Fig. 13A), following an opposite trend to Ag (with the highest values in distal Rosita-Rubí, 12.7–5.3 wt%; Fig. 13B; Table 5) due to the substitution between both elements in the crystal lattice. The Fe and Zn contents show more irregular patterns (Fig. 13C-D). Analyzed grains correspond to tetrahedrite and tennantite, with respective average empirical formulas $(Cu_{8.93}Ag_{0.80})(Zn_{1.70}Fe_{0.23})(Sb_{2.87}As_{1.13})S_{12.66}$ and $(Cu_{9.61}Ag_{0.08})(Zn_{1.51}Fe_{0.33})(As_{3.52}Sb_{0.48})S_{12.68}$. Tetrahedrite-tennantite series minerals from Ramal Alianza and epithermal veins overprinting the Toromocho porphyry classify as tennantite, grains from Morro Solar and Ivette, as both tennantite and tetrahedrite, and grains from Rosita/Rubí, as tetrahedrite.

Tennantite from epithermal veins overprinting the Toromocho porphyry contains the highest Bi content (66842–21464 ppm), which tends to decrease in more distal mineralization (Rosita/Rubí, 0.21–0.094 ppm; Fig. 13E). Selenium shows a similar distribution as Bi, with the highest values recorded in grains from epithermal veins overprinting the Toromocho porphyry mineralization (148–76 ppm) and showing a sustained decrease towards distal mineralization (Fig. 13F). In contrast, the highest Cd contents are found in Ivette and Rosita/Rubí (1709–1616 ppm; Fig. 13G) and the lowest, in Morro Solar (761–689 ppm).

The highest In contents in tetrahedrite-tennantite occur in Morro Solar (257–239 ppm) followed by tetrahedrite-tennantite in epithermal veins from the Toromocho porphyry center (44–33 ppm) and Ivette (26–25 ppm; Fig. 13H). The In content in tetrahedrite-tennantite from Rosita/Rubí is mostly below detection limits. The Ge (1.9–0.74 ppm) and Ga (3.8–0.65 ppm) contents are low and do not show clear trends at the district scale (Fig. 13I-J).

6. Discussion

6.1. Geochemical behavior of In, Ge, and Ga

The studied mineralized structures in the Morococha district do not host independent In, Ge and Ga minerals, but these elements are systematically found in trace amounts in the analyzed minerals (sphalerite, chalcopyrite, galena, and tetrahedrite-tennantite) yet with contrasting values. Indium is more abundant in sphalerite (217–2.7 ppm, up to 4608 ppm) and in chalcopyrite (109–32 ppm, up to 1070 ppm), whereas its content is low in tetrahedrite-tennantite (44–25 ppm, up to 266 ppm) and galena (0.28–0.043 ppm, up to 0.61 ppm). In coeval generations of sphalerite and chalcopyrite, the average In content is at least two times higher in sphalerite than in chalcopyrite (e.g., Ramal Alianza, 398–157 ppm in sphalerite, 113–93 ppm in chalcopyrite). Indium partitioning into sphalerite, and resulting elevated content, are widely documented (Cook et al., 2009, 2011a, 2011b; Sahlström et al., 2017; Bauer et al., 2019a; Frenzel et al., 2019; Torró et al., 2019a, 2019b). At Morococha, Ga also concentrates in sphalerite (61–2.0 ppm, up to 2137 ppm) and chalcopyrite (62–1.5 ppm, up to 630 ppm), and is far lower in tetrahedrite-tennantite (3.8–0.65 ppm, up to 9.6 ppm) and galena (mostly below detection limits, up to 3.6 ppm). The Ge content is systematically very low in all the analyzed minerals (1.2–0.2.0 ppm), except some anomalously high values locally found in late sphalerite (3rd generation in the Ivette Manto, 129–74 ppm). Sphalerite is volumetrically the most abundant component in the studied polymetallic mineralization at Morococha and therefore represents the main host for In and Ga at the district scale. It is noteworthy that sphalerite from the giant Cerro de Pasco Cordilleran deposit in Peru (Rottier et al., 2018) yields broadly equivalent ranges for In (165–17 ppm, up to 1449 ppm), Ga (58–1.7 ppm, up to 423 ppm), and Ge (4.3–3.5 ppm, up to 71 ppm) contents thus suggesting that the presented Morococha sphalerite dataset (Table 2) is likely to be representative of sphalerite compositions in Cordilleran type mineralization in terms of these three elements.

The In and Cu values in the studied sphalerite plot mostly at In:Cu (molar) of 1:1 (Fig. 10C) pointing to a $Cu^{+} + In^{3+} \leftrightarrow 2Zn^{2+}$ coupled substitution. This substitution has been previously identified as the dominant one for the incorporation of In in sphalerite (e.g., Schwarz-Schampera and Herzig, 2002; Cook et al., 2011b, 2012; Torró et al., 2019a, 2019b) and conforms to the solid solution between sphalerite and roquesite [$CuInS_2$] (Parasyuk et al., 2003; Schorr and Wagner, 2005) within the sphalerite – stannite – roquesite pseudoternary system described by Oen et al. (1980). However, there is a set of sphalerite data, which includes part of Ivette, Morro Solar, Isabel, and Rosita/Rubí analyses, that lies above the correlation line in Fig. 10C, thus denoting

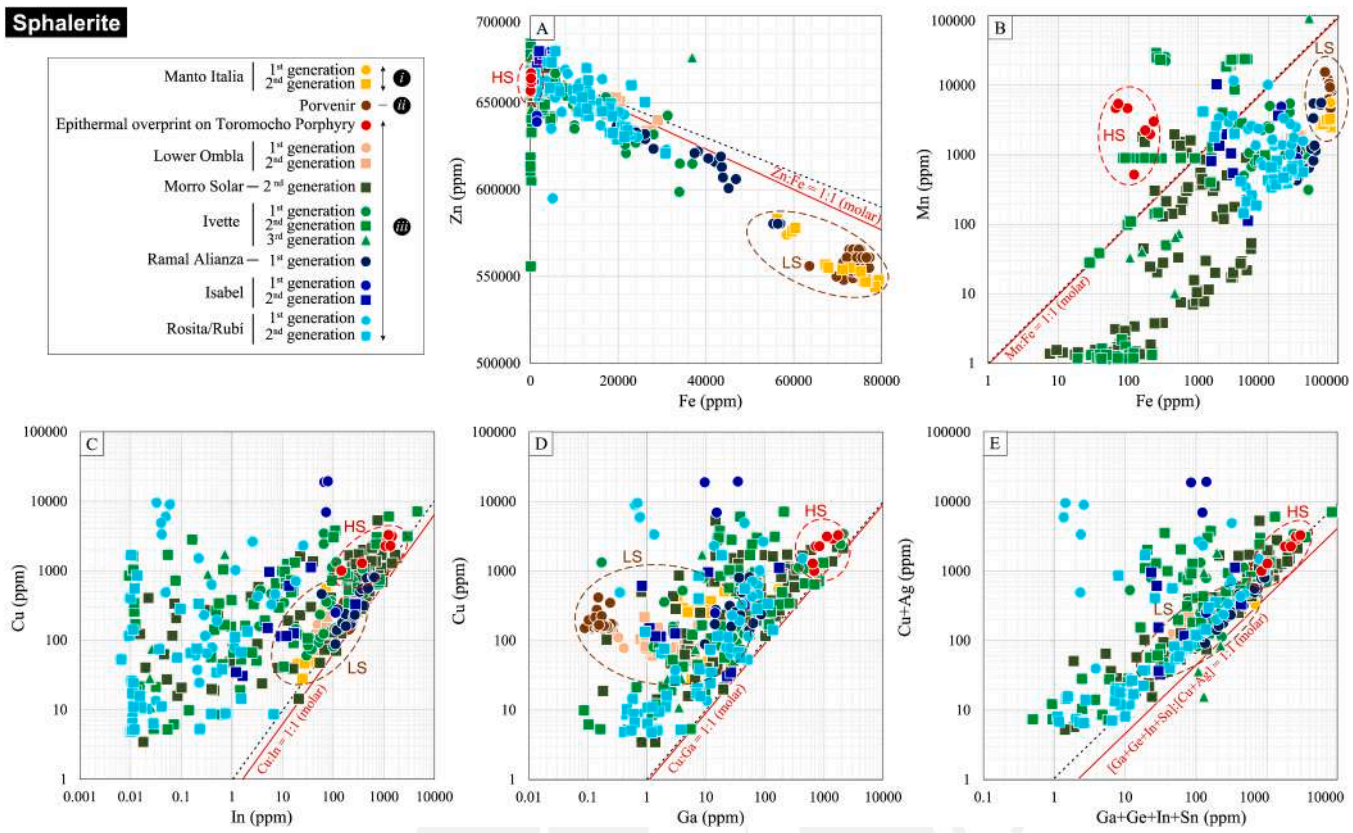

Fig. 10. Correlation between elements in sphalerite from the Morococha district. Black dashed lines indicate ppm ratios and red lines, molar ratios. *"i"*, *"ii"*, and *"iii"* refer to the mineralization events described in Section 2.3 (Studied polymetallic mineralization styles in the Morococha district). Compositional fields for studied sphalerite from skarn bodies are highlighted. Compositional fields for sphalerite in HS (high-sulfidation; epithermal veins overprinting the Toromocho stock) and LS (low-sulfidation; Manto Italia and Porvenir) assemblages are highlighted. The rest of the data correspond to sphalerite from intermediate-sulfidation assemblages.

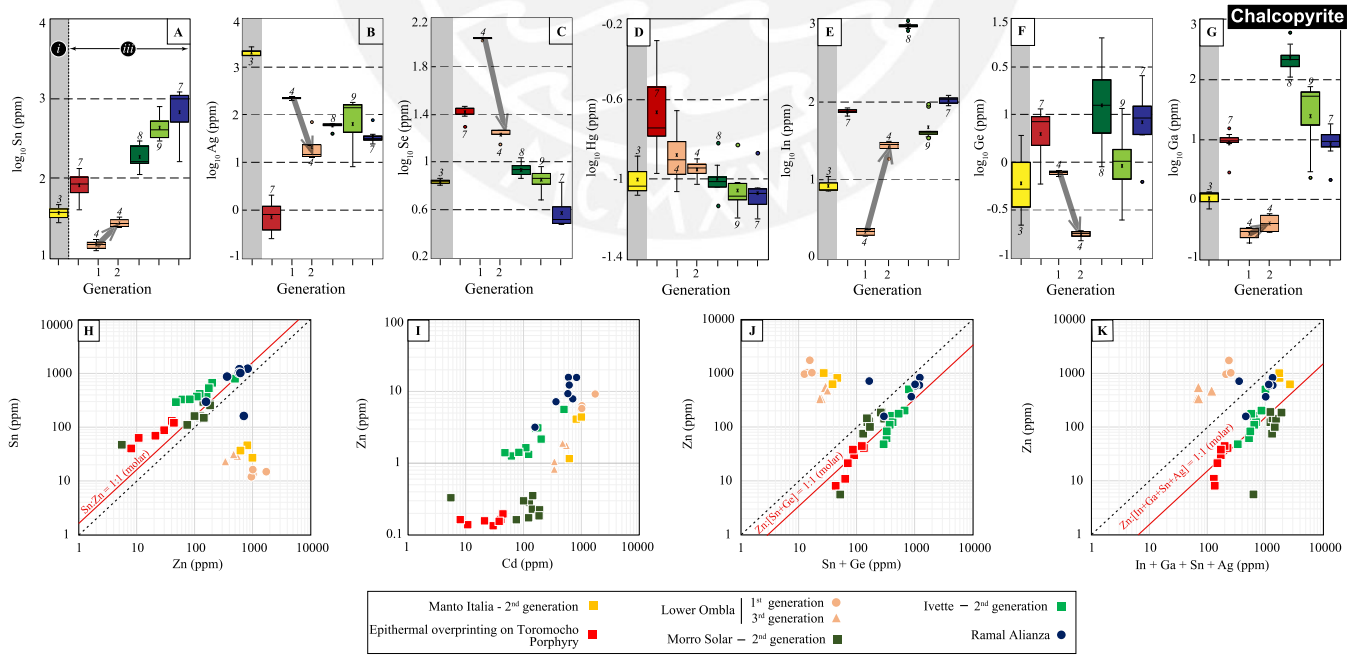

Fig. 11. Selected boxplots of log-transformed element contents (A-G) and correlation between elements (H-K) in chalcopyrite from the Morococha district. In boxplots, legend is as in Fig. 9, dark gray arrows indicate temporal trends within sites, and *"i"* (Manto Italia) and *"iii"* (other sites) refer to the mineralization events described in Section 2.3 ("Studied polymetallic mineralization styles in the Morococha district"). The ordering of the boxplots in *"iii"* follows a roughly proximal to distal position relative to the Toromocho porphyry. In correlation diagrams, black dashed lines indicate ppm ratios and red lines, molar ratios.

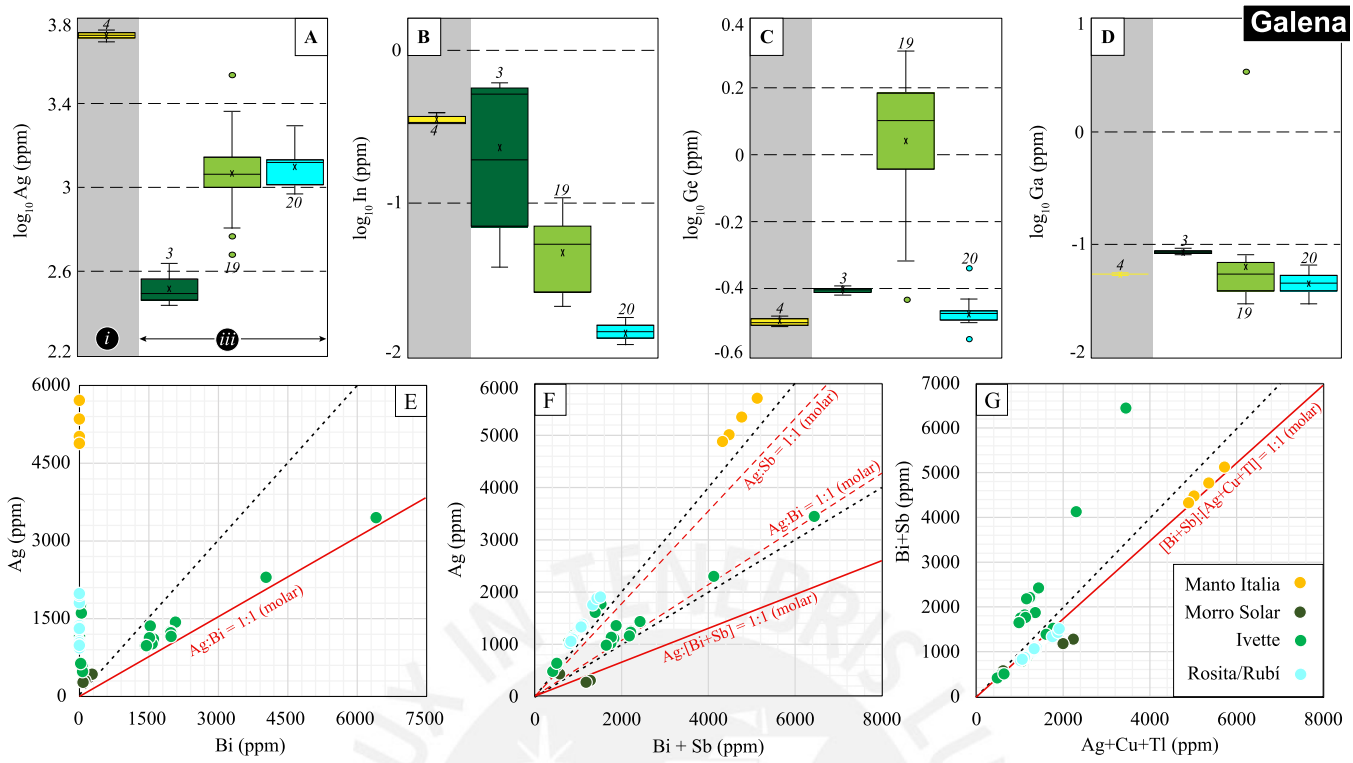

Fig. 12. Selected boxplots of log-transformed element contents (A-D) and correlation between elements (E-G) in galena from the Morococha district. In boxplots, legend is as in Fig. 9, and *"i"* (Manto Italia) and *"iii"* (other sites) refer to the mineralization events described in Section 2.3 ("Studied polymetallic mineralization styles in the Morococha district"). The ordering of the boxplots in *"iii"* follows a roughly proximal to distal position relative to the Toromocho porphyry. In correlation diagrams, black dashed lines indicate ppm ratios and red lines, molar ratios.

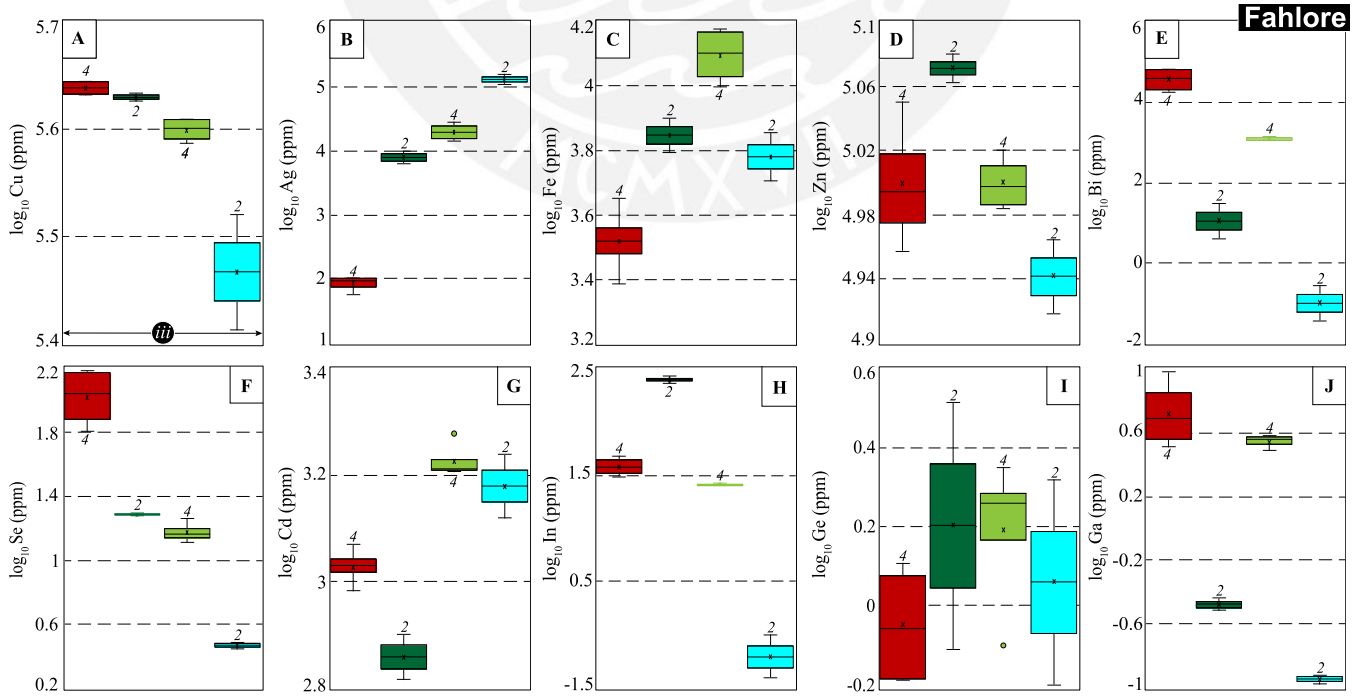

Fig. 13. Selected boxplots of log-transformed element contents in tetrahedrite-tennantite series minerals. Legend as in Fig. 9. *"iii"* refers to the last mineralization event described in Section 2.3 ("Studied polymetallic mineralization styles in the Morococha district"). The ordering of the boxplots follows a roughly proximal to distal position relative to the Toromocho porphyry.

higher Cu at a given In content. A similar situation is noticed by other authors such as Xu et al. (2020) and points to the existence of other coupled substitutions involving Cu, as it is further discussed below.

A positive correlation between Ga and Cu in sphalerite (Fig. 10D) suggests a $Cu^{+} + Ga^{3+} \leftrightarrow 2Zn^{2+}$ coupled substitution (see Johan, 1988; Murakami and Ishihara, 2013; Bonnet et al., 2016; Pring et al., 2020). The distributions of Cu, In, and Ga (Fig. 10 C-D) would indicate that these two substitutions might have operated independently. An additional $(Sn, Ge)^{4+} + (Ga, In)^{3+} + (Cu, Ag)^{+} \leftrightarrow 4Zn^{2+}$ coupled substitution (see Cook et al., 2009) cannot be ruled out either (Fig. 10E), particularly in grains from Porvenir, Manto Italia, and Lower Ombla. According to these observations, the incorporation of In and Ga within the crystal lattice of sphalerite might have involved different substitution schemes in which Cu was always present.

It is noteworthy, however, that the incorporation of In in the sphalerite crystal lattice is decoupled from Fe based on the lack of correlation between the two elements. For instance, the highest In content, recorded in sphalerite from high-sulfidation epithermal veins in the Toromocho porphyry center, occur in Fe-poor sphalerite (189–85 ppm Fe).

Regarding chalcopyrite analyses, there is a positive correlation of both Sn + Ge and In + Ga + Sn + Ag with Zn in grains from the epithermal veins overprinting the Toromocho porphyry mineralization and intermediate-sulfidation assemblages at Ivette, Morro Solar, and Ramal Alianza (Fig. 11J-K). However, since chalcopyrite is not fully ionic, formulating substitutions requires caution. Several authors, including Todd et al. (2003), Mikhlin et al. (2005), Pearce et al. (2006) and Klekovkina et al. (2014), proposed two different valence states for Cu and Fe in chalcopyrite [$Cu^{2+}Fe^{2+}S_2$ vs. $Cu^{+}Fe^{3+}S_2$]. However, other authors (e.g., Li et al., 2013) suggest intermediate valence states. Thus, the incorporation of trace elements within the chalcopyrite lattice is not fully constrained yet. Silver is one of the most widely reported elements that can be incorporated within the chalcopyrite crystal lattice (George et al., 2018), while In, Ga, and Ge can also be incorporated to a lesser extent. Due to the relative good correlation observed between these elements and Zn and Sn (Fig. 11J-K), we suggest that Ag may be introduced in coupled substitutions involving $Cu^{(+)}$, $Ag^{(+)}$, $Zn^{(2+)}$, $In^{(3+)}$, $Ga^{(3+)}$, $Sn^{(4+)}$ and, $Ge^{(2+/4+)}$, as proposed by Belissont et al. (2019) and Reich et al. (2020).

The systematically very low In, Ge, and Ga contents in galena and tetrahedrite-tennantite grains from the Morococha district preclude any possible identification of incorporation mechanisms based upon the correlations between element contents.

6.2. *Sphalerite geothermometry: testing the GGIMFis geothermometer in the Morococha district*

Oftedal (1940) and Warren and Thompson (1945) pioneered the idea that crystallization temperature is closely related to the composition of sphalerite in terms of its minor and trace-elements composition. Wei et al. (2018) suggested that high contents of Fe, Mn, and In, and low contents of Ga and Ge in sphalerite relate to high-temperature deposits. Frenzel et al. (2016) further developed the idea that the composition of sphalerite depends on its crystallization temperature but also on the mineralization style, and by using fluid inclusion microthermometric data established a correlation between the crystallization temperature and sphalerite composition in terms of Ga, Ge, In, Mn, and Fe, referred to as the GGIMFis geothermometer.

The GGIMFis geothermometer has been applied to sphalerite analyzed here (Table 6; Fig. 14) yielding temperatures ranging from approx. 400 °C to below 100 °C. The highest GGIMFis temperatures are recorded in near skarn mineralization including both Stage A (Porvenir: 407 ± 8 °C, 2-sigma error °C; Manto Italia: 334 ± 23 °C in sl_{A1}, and 359 ± 24 °C in sl_{A2}) and Stage C (Lower Ombla: 358 ± 26 °C in sl_{C1}, and 328 ± 25 °C in sl_{C2}) sphalerite grains. In contrast, Stage C sphalerite grains from high-sulfidation assemblages in Cordilleran veins overprinting the Toromocho porphyry yield a much lower GGIMFis temperature of 157 ± 33 °C. Stage C sphalerite grains from Cordilleran intermediate-sulfidation assemblages yield GGIMFis temperatures in the range between 323 ± 39° and 81 ± 26 °C, with a general decrease in the crystallization temperatures from early to late generations (e.g., in Ivette, sl_{C1}, sl_{C2}, and sl_{C3} yield GGIMFis temperatures of 285 ± 81°, 173 ± 194° and 81 ± 26 °C, respectively) and from porphyry-proximal to porphyry-distal position (Table 6).

Available microthermometric data of fluid inclusions in the Morococha district by Catchpole et al. (2011) and Catchpole et al. (2015b) comprise fluid inclusion assemblages in i) quartz from milky quartz veins that cut the San Francisco stock, postdate the Manto Italia and Porvenir skarns and the Toromocho porphyry-type mineralization, and predate the studied Cordilleran mineralization; and ii) Stage C quartz, Fe-poor sphalerite (base-metal sub-stage), and rhodochrosite (carbonate sub-stage) in polymetallic Cordilleran veins. Fluid inclusions in the milky quartz veins, which can be considered representative of latest Toromocho porphyry fluids, yield homogenization temperatures (T_h) of ~420° to 410 °C. This temperature range compares well with the GGIMFis temperature for sphalerite from Porvenir and are higher than GGIMFis temperature for sphalerite from Manto Italia and Lower Ombla (Table 6). Although microthermometric data for fluid inclusions in the studied skarn-associated low-sulfidation assemblages at Porvenir and Manto Italia are unavailable, it can be assumed that they formed at temperatures slightly lower than 400 °C, typical for latest stage porphyry fluids. Therefore, the GGIMFis temperatures between 407° and 334 °C for sphalerite grains from Porvenir and Manto Italia are considered realistic within the large errors of the method.

As for the Cordilleran mineralization post-dating the Toromocho porphyry, primary fluid inclusion assemblages (FIAs) in the early base-metal sub-stage (Stage C) yield T_h in the range between 380° and 340 °C, and FIAs in the late carbonate sub-stage yield T_h in the range between 270° and 230 °C. Taking uncertainties into account, GGIMFis temperatures of sphalerite grains from Ramal Alianza fit the T_h of FIAs in the base-metal sub-stage. On the other hand, GGIMFis temperatures in sphalerite from porphyry-distal Rosita/Rubí match the T_h range of FIAs in the carbonate sub-stage. In contrast, significantly lower GGIMFis temperatures than those obtained by microthermometry, are found in 2nd (sl_{C2}) and 3rd (sl_{C3})-generation sphalerite grains from the Ivette manto and in sphalerite from high-sulfidation assemblages overprinting the Toromocho porphyry stock (Table 6).

6.3. *Spatial and temporal distribution of In, Ge, and Ga in the polymetallic mineralization*

The detailed study of the ore mineralogy and textures in different styles of polymetallic mineralization within the Morococha district reveals some patterns on the distribution of In, Ge, and Ga across the district (i.e., spatial control) and across the paragenetic sequences (i.e., temporal control). A note of caution has to be expressed as not all mineralized bodies studied here belong to a same event nor can be attributed to a same mineralizing center (the reader is referred to Sections 2 and 3.1 for details on the mineralization timing). So, we have studied low-sulfidation Stage A assemblages that have been formed during two mineralizing events significantly separate in time (*"i"* and *"ii"* in Section 3.1). Even for the studied intermediate- and high-sulfidation Stage C assemblages emplaced during the mineralizing event *"iii"* as part of the Morococha district-scale polymetallic event defined by Catchpole et al. (2015b), it cannot be excluded that in part derive from different feeders because they come from "physically" disconnected or independent ore bodies (see Fig. 2b in Catchpole et al., 2015b). Despite these limitations, our observations can serve as a first approximation to the relative variations in the contents of these elements amongst assemblages formed throughout these stages; noteworthy, the GGIMFis geothermometer – which is based on minor and trace element contents in sphalerite – discussed in the previous section

Table 6
Formation temperature of sphalerite according to the GGIMFis geothermometer of Frenzel et al. (2016).

Paragenesis	Site	Generation	N	Mean	Abs error*	1-sigma**	2-sigma
Stage A *(low sulfidation)*	Porvenir	sl_A	35	407	28	4	8
	Manto Italia	sl_{A1}	4	334	26	12	23
		sl_{A2}	13	359	32	12	24
Stage C *(high sulfidation)*	Epithermal overprint on Toromocho Porphyry	sl_C	7	157	29	17	33
Stage C (intermediate sulfidation)	Lower Ombla	sl_{C1}	8	335	32	13	26
		sl_{C2}	19	328	32	12	25
	Morro Solar	sl_{C2}	85	154	142	61	122
	Ivette	sl_{C1}	31	285	56	40	81
		sl_{C2}	76	173	142	97	194
		sl_{C3}	5	81	45	13	26
	Ramal Alianza	sl_{C1}	18	323	39	19	39
	Isabel	sl_{C1}	4	310	20	13	26
		sl_{C2}	10	288	147	52	105
	Rosita/Rubí	sl_{C1}	25	263	57	29	58
		sl_{C2}	41	254	60	34	69

* Relative to the maximum and minimum values of T according to GGIMFis sphalerite geothermometer general formula.
** Relative to mean T values of individual measurements.

yields temperatures that broadly agree with the expected temperature drop from Stage A to Stage C in polymetallic mineralization. On the other hand, the GGIMFis temperatures of the studied Stace C sphalerite indicate a sustained decrease in temperature from porphyry-proximal to porphyry-distal assemblages thus suggesting that the observed trends are likely to be comparable with those in more "continuous" and simpler mineralized structures in other polymetallic districts.

The In content is relatively high in sphalerite from Stage A, low-sulfidation assemblages in polymetallic mineralization overprinting prograde exoskarn assemblages in Porvenir and Manto Italia (Fig. 9I) compared with most sphalerite from intermediate-sulfidation assemblages. However, the highest In content is associated with sphalerite from Stage C, high-sulfidation assemblages in epithermal veins overprinting the causative Toromocho stock. Regarding Stage C sphalerite in intermediate-sulfidation assemblages, the In content is higher in porphyry-proximal Morro Solar (located at the boundary between the Cu and Cu-Zn zones described by Catchpole et al., 2011) than in porphyry-distal Rosita/Rubí mineralization (located at the boundary between the Zn- Pb-Ag and Ag-Pb zones at depth; Fig. 1). Accordingly, the In content in Stage C sphalerite tends to decrease from porphyry-proximal to porphyry-distal zones at the district scale. Unlike In, the distribution patterns of Ge and Ga (Fig. 9J-K) in sphalerite from the different studied mineralized sites do not define clear trends on their spatial distribution. Of the studied minerals, galena is the other phase

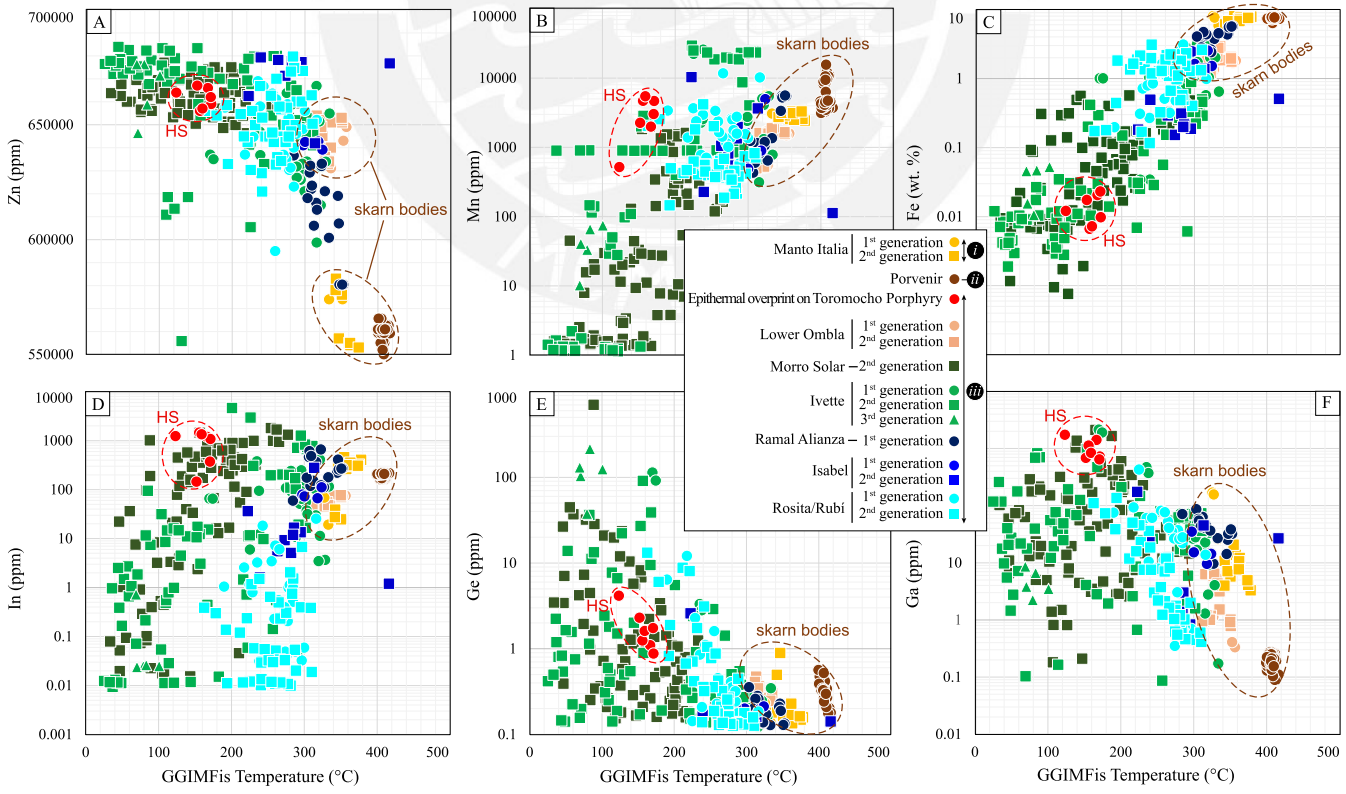

Fig. 14. Correlation between Zn, Mn, Fe, In, Ge, and Ga and GGIMFis T (Frenzel et al., 2016) in sphalerite from the Morococha district. Fields for studied sphalerite from skarn bodies (including low-sulfidation assemblages in Manto Italia and Porvenir, and intermediate-sulfidation assemblages in Lower Ombla) and from high-sulfidation assemblages (HS; epithermal veins overprinting the Toromocho stock) are highlighted. All other analyzed sphalerite comes from intermediate-sulfidation assemblages.

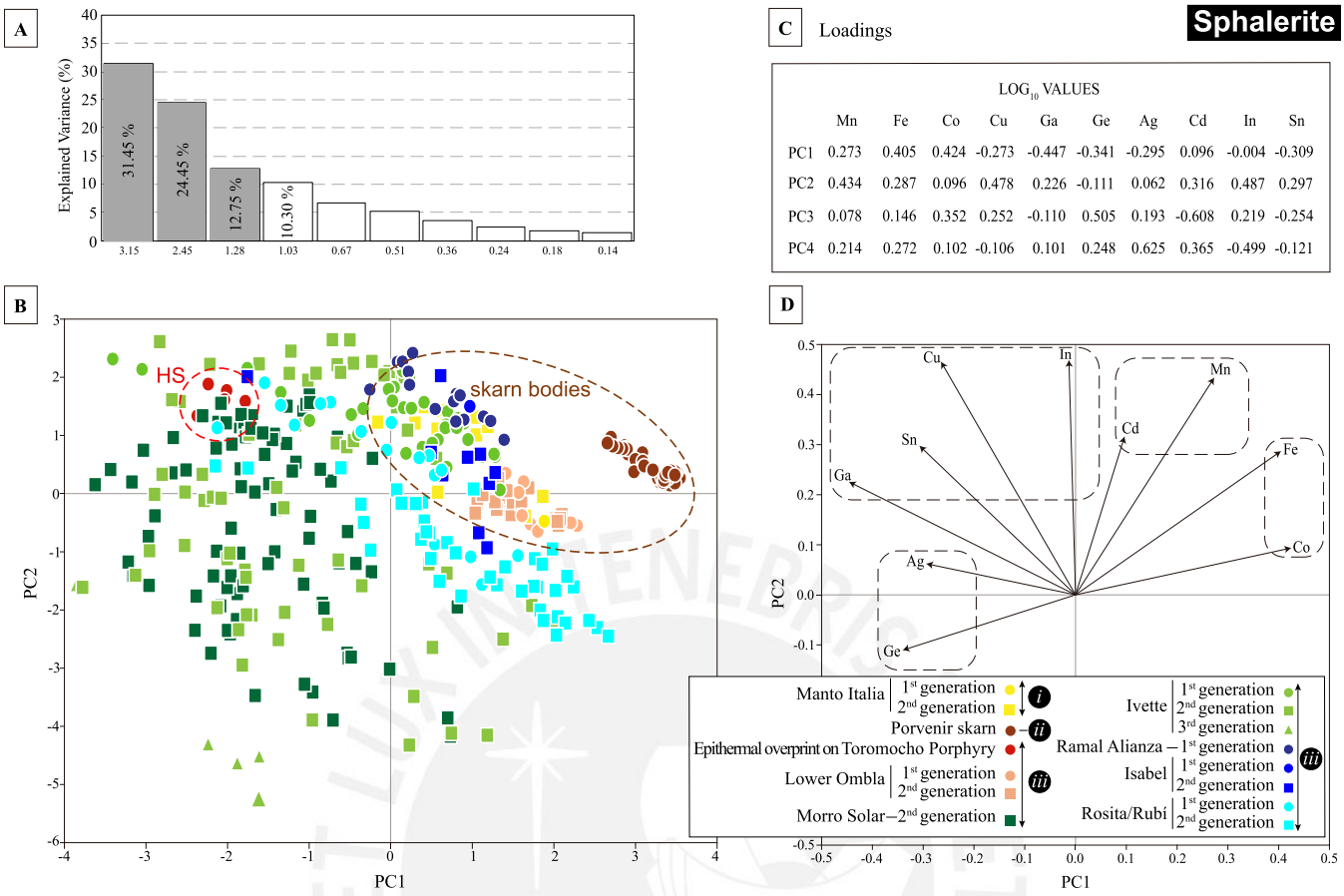

Fig. 15. Principal component analysis (PCA) of the log-transformed LA-ICP-MS data of trace element compositions in sphalerite from the Morococha district. A) Scree plot of the eigenvalues of the correlation matrix, explaining the variance. B) Plot of all data points corresponding to PC1 and PC2 for the trace element composition of sphalerites from all mineralizations. C) Loadings of the principal components (PC1 to PC4, explaining the 78.95% of the variance). D) Loading plots of the PCA showing the elements and framed groups of elements with similar behavior. *"i"*, *"ii"*, and *"iii"* refer to the mineralization events described in Section 2.3 (Studied polymetallic mineralization styles in the Morococha district). Compositional fields for studied sphalerite from skarn bodies (Manto Italia, Porvenir, and Lower Ombla) and from high-sulfidation assemblages (HS; epithermal veins overprinting the Toromocho stock) are highlighted.

that records a consistent depletion in In from porphyry-proximal to porphyry-distal Cordilleran mineralization, albeit at much lower absolute values (Fig. 12B).

The correlation between trace-element contents and mineral position in the paragenetic sequences reflects that comparable high In content in sphalerite may occur in both Stage A (low-sulfidation) and Stage C (high- and intermediate-sulfidation) assemblages. In Stage C Cordilleran assemblages, In-richer sphalerite crystallized during the base-metal substage (Figs. 6 and 8) with early sphalerite generations enriched in In relative to late generations regardless of their location in the district (Fig. 9I). The drastic In depletion recorded in Ivette coincides with an abrupt increase of the Ge content to a maximum of 215 ppm in third-generation sphalerite (Fig. 9J). Gallium only shows limited depletion from early to late sphalerite within Stage C assemblages (Fig. 9K).

Similar trends in the spatial and temporal distributions of In as those described for Stage C sphalerite in Morococha have been recently identified in the sediment-hosted xenothermal Huari Huari and the volcanic dome-hosted epithermal Ánimas-Chocaya-Siete Suyos deposits in the Bolivian tin belt (Torró et al., 2019a, 2019b). In Huari Huari, the highest In contents in sphalerite were found in the vicinity of a dacite stock located at the center of the district and likely genetically related to the mineralization. In the Ánimas-Chocaya-Siete Suyos district, the highest In contents in sphalerite occur in the central area of the dome, where the main feeders of the system are located. In both districts, late generations of sphalerite, which crystallized in an intermediate-sulfidation stage, are systematically depleted in In relative to early generations of sphalerite (which attain up to 9 wt% In). Sahlström et al. (2017) describe a similar trend at the Mt Carlton high-sulfidation epithermal deposit in Australia, with higher In-(Ga) in the intrusion-proximal, Cu-rich zone relative to intrusion-distal (Ag-rich) zone. Therefore, the spatial and temporal patterns in the distribution of In revealed in Morococha are likely representative of intrusion-centered hydrothermal systems.

Yet, the controls behind such system-scale In patterns remain unclear. The work by Shimizu and Morishita (2012) sheds light on this question. This study proposes that fluids at temperatures in excess of 300 °C and enriched in In, Cu and to a lesser extent, in Sn and Ag, favored the crystallization of In-rich sphalerite in the Toyoha polymetallic deposit, and that In was either sourced from metal-rich magmatic fluids (see also Bauer et al., 2019b) or leached from preexisting Cu-rich ores. Intermediate-temperature (>250 °C) saline hydrothermal fluids would also favor the transport of In and Cu as chloride complexes (Seward et al., 2000; Schwarz-Schampera and Herzig, 2002). In summary, there are four main parameters that may apparently enhance In incorporation in sphalerite in hydrothermal systems: i) a sustained or punctual sourcing of In via metal-rich magmatic-hydrothermal fluids or pre-concentration in a Cu-rich ore predating the Zn-rich ore; ii) a relatively high availability of Cu – and of Ag and Sn – in the mineral system that enables the incorporation of In within the sphalerite crystal lattice through coupled substitutions; iii) a relatively

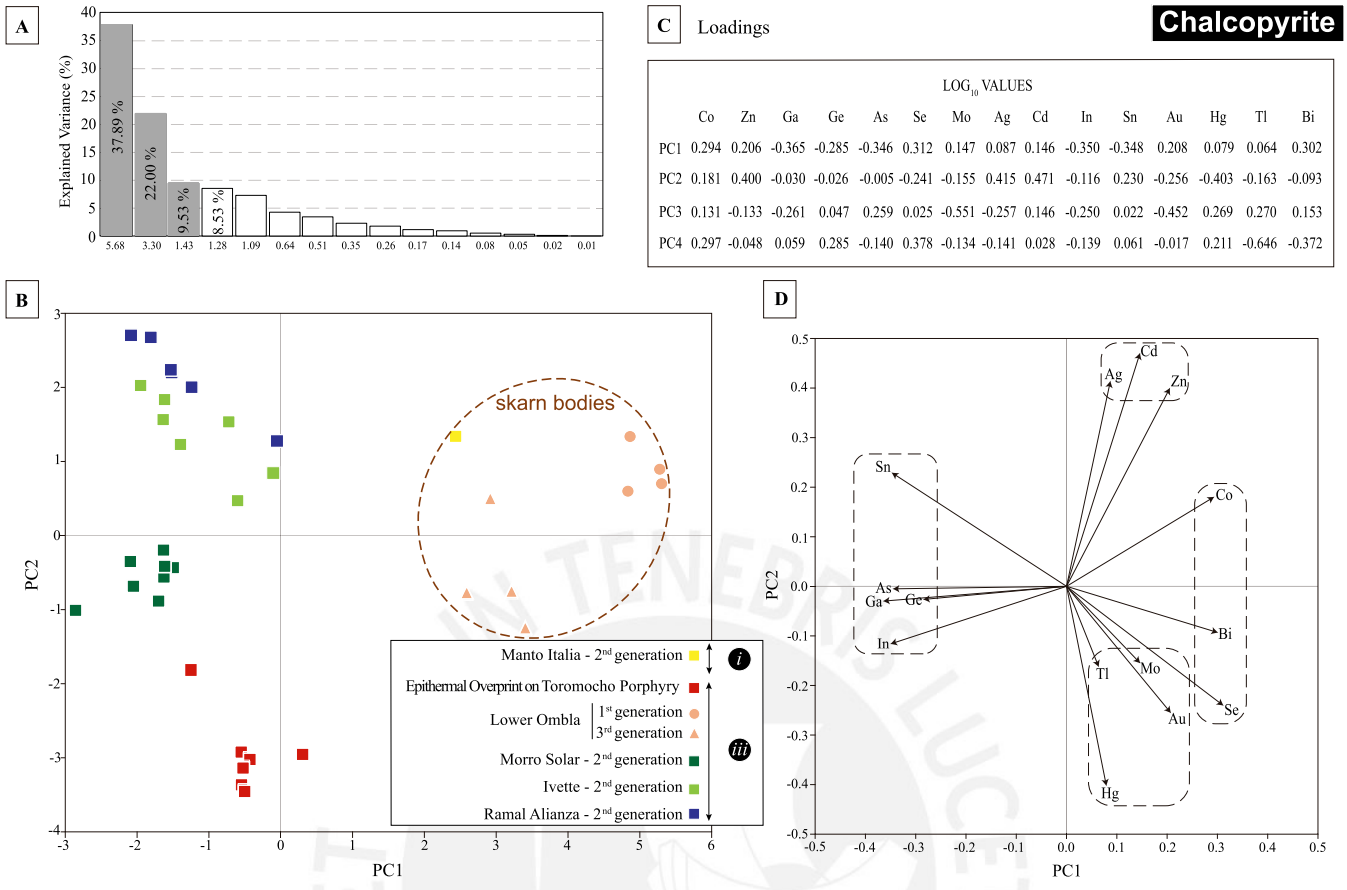

Fig. 16. Principal component analysis (PCA) of the log-transformed LA-ICP-MS data of trace element compositions in chalcopyrite from the Morococha district. A) Scree plot of the eigenvalues of the correlation matrix, explaining the variance. B) Plot of all data points corresponding to PC1 and PC2 for the trace element composition of sphalerites from all mineralizations. C) Loadings of the principal components (PC1 to PC4, explaining the 77.95% of the variance). **D)** Loading plots of the PCA showing the elements and framed groups of elements with similar behavior. *"i"*, *"ii"*, and *"iii"* refer to the mineralization events described in Section 2.3 (Studied polymetallic mineralization styles in the Morococha district). The compositional field for studied sphalerite from skarn bodies (Manto Italia and Lower Ombla) is highlighted.

high temperature of the mineralizing fluid (>250 °C); and iv) availability of Cl to form In (and Cu) chloride complexes.

The fact that the highest In contents are recorded in sphalerite from high-sulfidation assemblages in epithermal veins overprinting the causative Toromocho center (Fig. 9I), precipitated at distinctly low temperature (Table 6), suggests that the impact of temperature was probably secondary to other parameters such as the input of metal-rich magmatic-hydrothermal fluids. The progressive In depletion observed in distal-to-porphyry Zn-Pb-Ag and Ag-Pb Cordilleran mineralization and late generations of sphalerite from Stage C intermediate-sulfidation assemblages – regardless of their location in the district – would reflect crystallization from progressively more diluted fluids. Available fluid inclusion and stable isotope data for the Morococha district define, in addition to cooling, progressive dilution of a hydrothermal fluid of magmatic signature with meteoric water over its late-stage evolution (Catchpole et al., 2011, 2015b). On the other hand, trace-element determinations in inclusion fluids by the same authors revealed general Cu depletion from pre-Cordilleran to Cordilleran base-metal and carbonate stages, due to progressive Cu precipitation. Progressively more diluted and Cu-depleted mineralizing fluids precluded In concentration in late and distal to the porphyry center sphalerite.

6.4. General mineral chemistry trends – a principal component analysis

The principal component analysis (PCA) results of the log-transformed sphalerite trace element dataset are reported in Fig. 15. The first principal component (PC1), which explains a little more than 30% of the total variance (Fig. 15A), includes Fe and Co, characterized by positive signs and similar coefficients (Fig. 15C). PC2 is composed of Mn, Cd, Cu, Ga, In, and Sn. PC3 is a measure of Ge and Ag. PC2 was subdivided into two subgroups composed of Mn and Cd, and Cu, Ga, In, and Sn (Fig. 15D). In this perspective, Cu, In, Sn, and Ga, and to a lesser extent, Ge and Ag, group as a reflection of their positive correlations and paired participation in coupled substitutions.

The results of PCA of the log-transformed chalcopyrite trace element dataset are shown in Fig. 16. PC1 is formed by In, Ge, Ga, As, Sn, Co, Se, Bi, Mo, and Au, representing almost 38% of the variance (Fig. 16A). PC2 is composed of Zn, Cd, and Ag. PC3 is a measure of Hg and Tl. The PC1 vs. PC2 biplot (Fig. 16D) shows four clusters. PC1 was subdivided into three subgroups: a group formed by In, Ge, Ga, As, and Sn, another group composed of Bi, Se, and Co, and a third group constituted by Tl and Mo with PC3s, Mo and Au. Zinc, Cd, and Ag are positively correlated (Fig. 16D). Another positive correlation is between In, Ge, Ga, As, and Sn, highlighting that the incorporation of the three critical metals in the chalcopyrite crystal lattice requires the presence of Sn (especially for Ge), as well as Ag (for In and Ga), to form coupled substitutions. The elements Se, Co, and Bi, are fairly correlated. The most noteworthy example is reflected in the first and second-generation chalcopyrite grains from Lower Ombla with higher Co and Se in the first-generation, supported by the presence of sphalerite "stars" (i.e., high-temperature; Fig. 3B).

PCA for the Morococha sphalerite and chalcopyrite dataset allows for

an overview of the minor and trace-element composition of these two phases throughout the studied polymetallic mineralization in the Morococha porphyry district. Sphalerite grains from the polymetallic mineralization overprinting prograde exoskarn mineralization (i.e., Porvenir, Manto Italia, and Lower Ombla) are particularly enriched in Co and depleted in Ge, Ga, and Ag relative to sphalerite grains from the Cordilleran mineralization, and these elements do not show apparent correlation with In or Cu (Fig. 15B). Chalcopyrite grains from polymetallic mineralization overprinting prograde exoskarn mineralization show also distinctive enrichment in Co and are depleted in Ge, Ga, As, and In (Fig. 16B).

Regarding Stage C sphalerite, grains in high-sulfidation assemblages overprinting the Toromocho stock, and early generations in proximal-to-porphyry, intermediate-sulfidation assemblages are enriched in In and Cu – and to a lesser extent in Ga – relative to early generations in distal-to-porphyry mineralization (see also Fig. 9). Chalcopyrite from high- and intermediate-sulfidation assemblages in Cordilleran mineralization yield, from distal to proximal locations, enrichment in Se and Hg and depletion in Sn and Ag (see also Fig. 11).

7. Conclusions and implications

In this study, systematic trace element determinations have been conducted in sphalerite, chalcopyrite, galena, and tetrahedrite-tennantite from different polymetallic mineralization styles within the Morococha district, Peru. Studied mineralization styles and assemblages include i) low-sulfidation polymetallic assemblages overprinting magnetite-serpentine exoskarn at Manto Italia and Porvenir massive replacement bodies (equivalent to Stage A in Cordilleran-type deposits); ii) high-sulfidation epithermal veins overprinting the causative Toromocho porphyry stock (i.e., Stage C of Cordilleran-type deposits); and iii) skarn and skarn-free intermediate-sulfidation polymetallic mineralization from Cu and Cu-Zn (i.e., proximal to porphyry; Lower Ombla, Morro Solar and Ivette) and Zn-Pb-Ag and Pb-Ag (i.e., distal to porphyry; Ramal Alianza, Isabel, Rosita/Rubí) ore bodies and veins (i.e., Stage C of Cordilleran-type deposits). Detailed petrography and mineral geochemistry in ore samples from these sites reveal some trace-element distribution patterns involving the high-tech metals In, Ge, and Ga across the district and along paragenetic sequences (i.e., stages of mineralization).

Indium is mostly concentrated in sphalerite (217–2.7 ppm, up to 4608 ppm) and chalcopyrite (109–32 ppm, up to 1070 ppm), and much less concentrated in tetrahedrite-tennantite and galena. In coeval generations, the In content in sphalerite is at least 2 times higher than in chalcopyrite. Gallium also concentrates preferentially in sphalerite (61–2.0 ppm, up to 2137 ppm) and in chalcopyrite (62–1.5 ppm, up to 630 ppm), and significantly less in tetrahedrite-tennantite and galena. Germanium is systematically very low in all four investigated minerals (1.2–0.20 ppm) with some anomalous values in sphalerite up to 701 ppm.

The content of the three elements varies significantly across the district and across the generations identified for individual minerals in each mineralized site. The In content is systematically high in sphalerite from Stage A low-sulfidation assemblages in polymetallic skarns. Stage C high-sulfidation assemblages overprinting the Toromocho porphyry host sphalerite with the highest In content. In Stage C intermediate-sulfidation assemblages, sphalerite yields higher In values in proximal-to-porphyry (Cu and Zn-Cu zones) than in distal-to-porphyry (Zn-Pb-Ag and Pb-Ag zones) mineralization. In the same assemblages, the In content also decreases in galena with increasing distances from the hydrothermal center. On the other hand, the In content decreases from early to late generations of Stage C sphalerite, coupled with an increase in the Ge content, with the highest values of this element recorded in late Fe-poor, low-temperature sphalerite forming colloform aggregates.

For Stage C assemblages in Cordilleran mineralization emplaced during the "Morococha district-scale polymetallic event" of Catchpole et al. (2015b) post-dating the porphyry mineralization at Toromocho, trace-element mineral compositions suggests the following trends from porphyry-proximal to porphyry-distal Cordilleran mineralization: i) in sphalerite, In and Cu (and to a lesser extent, Ga) depletion; ii) in chalcopyrite, Se and Hg depletion and Sn and Ag enrichment; complimentarily, iii) in galena, In depletion; and iv) in tetrahedrite-tennantite, Ag enrichment.

The GGIMFis sphalerite geothermometer of Frenzel et al. (2016) has been tested using our Morococha dataset and comparing the obtained temperatures with available fluid inclusion microthermometric data. The GGIMFis geothermometer yields mostly plausible temperature ranges and general temperature decrease from Stage A to Stage C assemblages. In Stage C intermediate-sulfidation assemblages of the "Morococha district-scale polymetatic event", there is a sustained drop in the GGIMFis temperatures from proximal-to-porphyry to distal locations and from early to late sphalerite generations.

The strong positive correlation between In and Cu in sphalerite points to $Cu^{+} + In^{3+} \leftrightarrow 2Zn^{2+}$ coupled substitution as the principal mechanism for the incorporation of In within the crystal lattice. Cationic correlations in sphalerite also support $Cu^{+} + Ga^{3+} \leftrightarrow 2Zn^{2+}$ and probably additional $(Sn, Ge)^{4+} + (Ga, In)^{3+} + (Cu + Ag)^{+} \leftrightarrow 4Zn^{2+}$ coupled substitutions. Copper is involved in all these substitution schemes and hence its availability in the mineral system defines the spatial and temporal distribution of In and Ga in sphalerite. Therefore, our data indicate that a high availability of Cu in metal-rich magmatic-hydrothermal fluids may enhance In enrichment in sphalerite.

Declaration of Competing Interest

The authors declare that they have no known competing financial interests or personal relationships that could have appeared to influence the work reported in this paper.

Acknowledgments

This study was economically supported by the Peruvian CONCYTEC-FONDECYT-World Bank project 107-2018-FONDECYT-BM-IADT-AV, the FONCAI-0023-2019 project granted by the Pontificia Universidad Católica del Perú (PUCP) and a Huiracocha Ph. D grant to D.B. granted by the PUCP. Pan American Silver Corp. provided field and logistical support and access to the mine area. Pan American Silver Corp. Morococha staff is most gratefully acknowledged, particularly Julio Zárate and Rubén Diaz. We appreciate the technical support by Xavier Llovet (CCiT-UB) during the acquisition of EPMA data, and by Peter Tollan (ETHZ) during the acquisition of LA-ICP-MS data. We are grateful to Fredrik Sahlström, Max Frenzel, and Editor-in-Chief Franco Pirajno for their constructive comments which significantly improved the manuscript.

Appendix A. Supplementary data

Supplementary data to this article can be found online at https://doi.org/10.1016/j.oregeorev.2021.104236.

References

Ageneau, M., 2008. Genesis of Ag-rich mineralization in the Buenaventura and Galera veins, Yacumina zone, SW part of the Morococha district, central Peru. M.Sc. thesis. University of Geneva, Geneva, Switzerland, p. 119.

Armbruster, T., Makovicky, E., Berlepsch, P., Sejkora, J., 2003. Crystal structure, cation ordering, and polytypic character of diaphorite, $Pb_2Ag_3Sb_3S_8$, a PbS-based structure. Eur. J. Mineral. 15, 137–146.

Barton, P.B., Bethke, P.M., 1987. Chalcopyrite disease in sphalerite; pathology and epidemiology. Am. Mineral. 72, 451–467.

Bauer, M.E., Seifert, T., Burisch, M., Krause, J., Richter, N., Gutzmer, J., 2019a. Indium-bearing sulfides from the Hämmerlein skarn deposit, Erzgebirge, Germany: Evidence for late-stage diffusion of indium into sphalerite. Miner. Deposita 54, 175–192.

Bauer, M.E., Burisch, M., Ostendorf, J., Krause, J., Frenzel, M., Seifert, T., Gutzmer, J., 2019b. Trace element geochemistry of sphalerite in contrasting hydrothermal fluid systems of the Freiberg district, Germany: insights from LA-ICP-MS analysis, near-

infrared light microthermometry of sphalerite-hosted fluid inclusions, and sulfur isotope geochemistry. Miner. Deposita 54, 237–262.
Baumgartner, R.J., Van Kranendonk, M.J., Pagès, A., Fiorentini, M.L., Wacey, D., Ryan, C., 2020. Accumulation of transition metals and metalloids in sulfidized stromatolites of the 3.48 billion–year–old Dresser Formation, Pilbara Craton. Precambr. Res. 337, 105534.
Belissont, R., Munoz, M., Boiron, M.C., Luais, B., Mathon, O., 2019. Germanium crystal chemistry in Cu bearing sulfides from micro-XRF mapping and micro-XANES spectrometry. Minerals 9, 227.
Benavides, V., 1999. Orogenic evolution of the Peruvian Andes: the Andean Cycle. In: Skinner, B.J. (Ed.), Geology and Ore Deposits of the Central Andes. Society of Economic Geologists Special Publication, pp. 61–107.
Bendezú, A., Catchpole, H., Kouzmanov, K., Fontboté, L., Astorga, C., 2008. Miocene magmatism and related porphyry and polymetallic mineralization in the Morococha district, central Peru. Sociedad Geológica del Perú, XIII Congreso Latinoamericano de Geología, Lima, Peru, September 29–October 3, 2008, Proceedings.
Bendezú, A., Kouzmanov, K., Ovtcharova, M., Spikings, R., Fontboté, L., 2012. Timing of porphyry emplacement in the Miocene Morococha district, central Perú: U-Pb and Ar-Ar geochronological record. In: International Geological Congress, 34th Brisbane, Australia 2012, pp. 1–6.
Beuchat, S., 2003. Geochronological, structural, isotopes and fluid inclusion constraints of the polymetallic Domo de Yauli district, Peru. Terre Environ. 41, 130.
Bissig, T., Ullrich, T., Tosdal, R., Friedman, R., Ebert, S., 2008. The time-space distribution of Eocene to Miocene magmatism in the central Peruvian polymetallic province and its metallogenic implications. J. S. Am. Earth Sci. 26, 16–35.
Bonnet, J., Mosser-Ruck, R., Caumon, M.C., Rouer, O., Andre-Mayer, A.S., Cauzid, J., Peifert, C., 2016. Trace element distribution (Cu, Ga, Ge, Cd and Fe) in sphalerite from the Tennessee MVT deposits, USA, by combined EMPA, LA-ICP-MS, Raman spectroscopy and crystallography. Can. Mineral. 54, 1261–1284.
Catchpole, H., 2011, Porphyry-related polymetallic mineralisation in the Morococha district, central Peru: mineralisation styles, timing and fluid evolution. Ph. D. Thesis, University of Geneva. Terre & Environment, 102, 192 + 86.
Catchpole, H., Kouzmanov, K., Fontboté, L., Guillong, M., Heinrich, C.A., 2011. Fluid evolution in zoned Cordilleran polymetallic veins–- insights from microthermometry and LA-ICP-MS of fluid inclusions. Chem. Geol. 281, 293–304.
Catchpole, H., Kouzmanov, K., Fontboté, L., 2012. Copper-excess stannoidite and tennantite-tetrahedrite as proxies for hydrothermal fluid evolution in a zoned Cordilleran base metal district, Morococha, central Peru. Can. Mineral. 50, 719–743.
Catchpole, H., Kouzmanov, K., Bendezú, A., Ovtcharova, M., Spikings, R., Stein, H., Fontboté, L., 2015a. Timing of porphyry (Cu-Mo) and base metal mineralization (Zn-Pb-Ag-Cu) in a magmatic-hydrothermal system– Morococha district. Peru. Miner. Deposita 50, 895–922.
Catchpole, H., Kouzmanov, K., Putlitz, B., Seo, J., Fontboté, L., 2015b. Zoned base metal mineralization in a porphyry system: Origin and evolution of mineralizing fluids in the Morococha District. Peru. Econ. Geol. 110, 39–71.
de Pasco, C., Corporation, C., 1948. Lead and zinc deposits of the Cerro de Pasco Corporation in central Peru. In: 18th International Geological Congress, Great Britain, Part VII, pp. 154–186.
Chinalco Mining Corporation International, 2015. Annual Report, Lima, pp. 12–35. <https://www1.hkexnews.hk/listedco/listconews/sehk/2016/0428/ltn20160428325.pdf>.
Cook, N.J., Ciobanu, C.L., Pring, A., Skinner, W., Shimizu, M., Danyushevsky, L.V., Saini-Eidukat, B., Melcher, F., 2009. Trace and minor elements in sphalerite: a LA-ICPMS study. Geochim. Cosmochim. Acta 73, 4761–4791.
Cook, N.J., Ciobanu, C., Williams, T., 2011a. The mineralogy and mineral chemistry of indium in sulphide deposits and implications for mineral processing. Hydrometallurgy 108, 226–228.
Cook, N.J., Sundblad, K., Valkama, M., Nygård, R., Ciobanu, C.L., Danyushevsky, L., 2011b. Indium mineralisation in A-type granites in southeastern Finland: insights into mineralogy and partitioning between coexisting minerals. Chem. Geol. 284, 62–73.
Cook, N.J., Ciobanu, C.L., Brugger, J., Etschmann, B., Howard, D.L., de Jonge, M.D., Ryan, C.G., Paterson, D.J., 2012. Determination of the oxidation state of Cu in substituted Cu-In-Fe-bearing sphalerite via μ-XANES spectroscopy. Am. Mineral. 97, 476–479.
Cook, N.J., Ciobanu, C.L., 2015. Mineral hosts for critical metals in hydrothermal ores [ext. abs.]. In: Biennial Meeting of the Society for Geology Applied to Mineral Deposits, 13th, Nancy, France, 2015, Extended Abstracts, pp. 707–710.
Di Benedetto, F., Bernardini, G.P., Costagliola, P., Plant, D., Vaughan, D.J., 2005. Compositional zoning in sphalerite crystals. Am. Mineral. 90, 1384–1392.
European Commission, 2017. Critical Raw Materials. <https://ec.europa.eu/growth/sectors/raw-materials/specific-interest/critical_en>.
Eyzaguirre, V., Montoya, D., Silberman, M., Noble, D., 1975. Age of igneous activity and mineralization, Morococha district, central Peru. Econ. Geol. Bull. Soc. Econ. Geol. 70, 1123–1125.
Fontboté, L., 2018. Ore deposits of the Central Andes. Elements 14, 257–261.
Fontboté, L., 2020. Systematic trends in the evolution of porphyry-related Zn-Pb-(Ag) deposits. Swiss Geoscience Meeting. 18th, Zurich, Switzerland, 2020. Extended Abstracts.
Foord, E.E., Shawe, D.R., Conklin, N.M., 1988. Coexisting galena, PbS and sulfosalts: evidence for multiple episodes of mineralization in the Round Mountain and Manhattan gold districts, Nevada. Can. Mineral. 26, 355–376.
Frenzel, M., Hirsch, T., Gutzmer, J., 2016. Gallium, germanium, indium, and other trace and minor elements in sphalerite as a function of deposit type—a meta-analysis. Ore Geol. Rev. 76, 52–78.
Frenzel, M., Mikolajczak, C., Reuter, M.A., Gutzmer, J., 2017. Quantifying the relative availability of high-tech by-product metals: the cases of gallium, germanium and indium. Resour. Policy 52, 327–335.
Frenzel, M., Bachmann, K., Carvalho, J.R.S., Relvas, J.M.R.S., Pacheco, N., Gutzmer, J., 2019. The geometallurgical assessment of by-products: geochemical proxies for the complex mineralogical deportment of indium at Neves-Corvo, Portugal. Miner. Deposita 54, 959–982.
Gemmrich, L., Torró, L., Melgarejo, J.C., Laurent, O., Vallance, J., Chelle-Michou, C., Sempere, T.P.A., 2021. Trace element composition and U-Pb ages of cassiterite from the Bolivian tin belt. Miner. Deposita (in press).
George, L., 2013. In: Trace and Minor Elements in Galena: A Reconnaissance LA-ICP-MS study: Honours degree in Geology thesis. The University of Adelaide, Adelaide, Australia, p. 133.
George, L., Cook, N.J., Cristiana, L., Wade, B.P., 2015. Trace and minor elements in galena: a reconnaissance LA-ICP-MS study. Am. Mineral. 100, 548–569.
George, L.L., Cook, N.J., Crowe, B.B.P., Ciobanu, C.L., 2018. Trace elements in hydrothermal chalcopyrite. Mineral. Mag. 82, 59–88.
Goldfarb, R.J., Hofstra, A.H., Simmons, S.F., 2016. Critical elements in carlin, epithermal, and orogenic gold deposits. Rev. Econ. Geol. 18, 217–244.
Graeser, S., 1969. Minor elements in sphalerite and galena from Binnatal. Contrib. Mineral. Petr. 24, 156–163.
Guberman, D., 2015. Germanium: U.S. Geological Survey Mineral Commodity Summaries 2015, pp. 64–65. <https://minerals.usgs.gov/minerals/pubs/mcs/2015/mcs2015.pdf>.
Guillong, M., Hametner, K., Reusser, E., Wilson, S.A., Günther, D., 2005. Preliminary Characterisation of New Glass Reference Materials (GSA-1G, GSC-1G, GSD-1G and GSE-1G) by Laser Ablation-Inductively Coupled Plasma-Mass Spectrometry Using 193 nm, 213 nm and 266 nm Wavelengths. Geostand. Geoanal. Res. 29, 315–331.
Guillong, M., Meier, D.L., Allan, M.M., Heinrich, C.A., Yardley, B.W.D., 2008. SILLS: A MATLAB-based program for the reduction of laser ablation ICP-MS data of homogeneous materials and inclusions. In: Sylvester, P. (Ed.), Laser Ablation ICP-MS in the Earth Sciences: Current Practices and Outstanding Issues. Mineralogical Association of Canada, Vancouver, pp. 328–333.
Guillong, M., Wotzlaw, J.F., Looser, N., Laurent, O., 2020. Evaluating the reliability of U-Pb laser ablation inductively coupled plasma mass spectrometry (LA-ICP-MS) carbonate geochronology: matrix issues and a potential calcite validation reference material. Geochronology 2, 155–167. https://doi.org/10.5194/gchron-2-155-2020.
Haapala, P.S., 1953. Morococha anhydrite: Sociedad Geológica Perú. Bulletin 26, 21–32.
Heuschmidt B, La Torre J.B., Angels V.M., Zapata, M.C., 2002. Las áreas prospectivas de Bolivia para yacimientos metalíferos. Boletín del Servicio Nacional de Geología y Minería, 30. ISSN 1023 -7674.
Jaskula, B.W., 2015. Gallium: USGS Mineral Commodity Summaries. January 2015, pp. 58–59.
Jochum, K.P., Weis, U., Stoll, B., Kuzmin, D., Yang, Q., Raczek, I., Jacob, D.E., Stracke, A., Birbaum, K., Frick, D.A., Günther, D., Enzweiler, J., 2011. Determination of reference values for NIST SRM 610–617 glasses following ISO guidelines, Geostand. Geoanal. Res. 35, 397–429.
Johan, Z., 1988. Indium and germanium in the structure of sphalerite: an example of coupled substitution with copper. Miner. Petrol. 39, 211–229.
John, D.A., Taylor, R.D., 2016. By-products of porphyry copper and molybdenum deposits. Rev. Econ. Geol. 18, 137–164.
Klekovkina, V.V., Gainov, R.R., Vagizov, F.G., Dooglav, A.V., Golovanevskiy, V.A., Pen'kov, I.N., 2014. Oxidation and magnetic states of chalcopyrite $CuFeS_2$: a first principles calculation. Opt. Spectrosc+ 116, 885–888.
Kobe, H.W., 1990. Stratabound sulfide occurrences in the Paleozoic of the Yauli Dome, Central Peru. A summary. In: Fontboté, L., Amstutz, G.C., Cardozo, M., Cedillo, E., Frutos, J. (Eds.), Stratabound Ore Deposits in the Andes: Berlin. Springer-Verlag, pp. 113–122.
Korges, M., Weis, P., Lüders, V., Laurent, O., 2020. Sequential evolution of Sn-Zn-In mineralization at the skarn hosted Hämmerlein deposit, Erzgebirge, Germany, from fluid inclusions in ore and gangue minerals. Miner. Deposita 55, 937–952.
Kouzmanov, K., Ovtcharova, M., von Quadt, A., Guillong, M., Spikings, R., Schaltegger, U., Fontboté, L., Rivera, L., 2008. U-Pb and $^{40}Ar/^{39}Ar$ age constraints for the timing of magmatism and mineralization in the giant Toromocho porphyry Cu-Mo deposit, central Peru [ext. abs.]. In: Congreso Latinoamericano de Geología, 13th, Lima, Peru, 2008, Proceedings, p. 6.
Kouzmanov, K., Chiaradia, M., Fontboté, L., Spangenberg, J., 2011. Origin of massive anhydrite bodies in the Morococha district, central Peru: insights from stable (O, S) and radiogenic (Sr, Nd) isotope geochemistry. In: Barra, F., Reich, M., Campos, F., Tornos, F. (Eds.), Biennial Meeting of the Society for Geology Applied to Mineral Deposits, 11th, Antofagasta, Chile, 2011, Extended Abstracts, pp. 405–407.
Le coq de Boisbaudran, P.E., 1875. Caractères chimiques et spectroscopiques d'un nouveau metal, le gallium, découvert dans une blende de la mine de Pierrefitte, vallée d'Argelès (Pyrénées). C. R. Hebdomadaires des Séances de l'Acad. Sci. 81, 493–49.
Lee, C.-T.A., Tang, M., 2020. How to make porphyry copper deposits. Earth Planet. Sc. Lett. 529, 1–11.
Lepry, L.A.J., 1981. The structural geology of the Yauli dome region, Cordillera Occidental, Peru. M.Sc. thesis. University of Arizona, Tucson, United States, p. 100.
Li, Y., Kawashima, N., Li, J., Chandra, A.P., Gerson, A.R., 2013. A review of the structure, and fundamental mechanisms and kinetics of the leaching of chalcopyrite. Adv. Colloid Interface Sci. 197, 1–32.
Liu, W., Cook, N.J., Ciobanu, C.L., Guilbert, S.E., 2019. Trace element substitution and grain-scale compositional heterogeneity in enargite. Ore Geol. Rev. 111, 103004.
Lockington, J.A., Cook, N.J., Ciobanu, C.L., 2014. Trace and minor elements in sphalerite from metamorphosed sulphide deposits. Mineral. Petrol. 108, 873–890.

McLaughlin, D., 1924. The Geology and Physiography of the Peruvian Cordillera, departments of Junin and Lima. GSA Bull. 35, 591–632.
McLaughlin, D.H., Graton, L.C., 1935. Copper in the Cerro de Pasco and Morococha districts. In: International Geological Congress, 16th. Washington, USA. Department of Junin, Peru, pp. 513–544.
Mégard, F., 1968. Geología del cuadrángulo de Huancayo, Servicio de Geología y Minería. Boletín 18, 1–105.
Meinert, L.D., 2005. World skarn deposits. In: Hedenquist, J.W., Thompson, J.F.H., Goldfarb, R.J., Richards, J.P. (Eds.), 100th Anniversary volume: Littleton, Society of Economic Geologists, pp. 299–336.
Mikhlin, Y., Tomashevich, Y., Tauson, V., Vyalikh, D., Molodtsov, S., Szargan, R., 2005. A comparative X-ray absorption near-edge structure study of bornite, Cu_5FeS_4, and chalcopyrite, $CuFeS_2$. J. Electron Spectrosc. 142, 83–88.
Moritz, R., Beuchat, S., Chiaradia, M., Sallier, B., Lisboa, H., Stucky, P., 2001. Zn-Pb mantos and veins at Domo de Yauli, central Peru: Two products of one hydrothermal system with common Pb & S sources, but contrasting fluid inclusion characteristics [ext abs.]. In: Biennial Meeting of the Society for Geology Applied to Mineral Deposits, pp. 173–176.
Murakami, H., Ishihara, S., 2013. Trace elements of indium-bearing sphalerite from tin polymetallic deposits in Bolivia, China and Japan: a femto-second LA-ICPMS study. Ore Geol. Rev. 53, 223–243.
Noble, D., McKee, E., 1999. The Miocene metallogenic belt of central and northern Peru. In: Skinner, B.J. (Ed.), Geology and Ore Deposits of the Central Andes. Society of Economic Geologists Special Publication, pp. 155–193.
Oen, I.S., Kager, P., Kieft, C., 1980. Oscillatory zoning of a discontinuous solid-solution series: Sphalerite-stannite. Am. Mineral. 65, 1220–1232.
Oftedal, I., 1940. Untersuchungen über die Nebenbestandteile von Erzmineralien norwegischer zincblendeführender Vorkommen. Skrift. Norsk Vidensk. Akad. Oslo. Math. Naturv. 8, 1–103.
Parasyuk, O.V., Voronyuk, S.V., Gulay, L.D., Davidyuk, G.Y., Halka, V.O., 2003. Phase diagram in the of the CuInS-ZnS system and some physical properties of solid solutions phases. J. Alloy. Compd. 348, 57–64.
Pearce, C.I., Pattrick, R.A.D., Vaughan, D.J., Henderson, C.M.B., van der Laan, G., 2006. Copper oxidation state in chalcopyrite: Mixed Cu d9 and d10 characteristics. Geochim. Cosmochim. Ac. 70, 4635–4642.
Pérez, J., Kouzmanov, K., Fontboté, L., Astorga, C., 2011. Mineralization, structural, and geochemical characteristics of the Toldojirca prospect and the San Andrés vein, Morococha district, central Peru. In: Society for Geology Applied to Mineral Deposits (SGA) 11th biennial Meeting, pp. 247–249.
Petersen, U., 1965. Regional geology and major ore deposits of Central Perú. Econ. Geol. Bull. Soc. Econ. Geol. 60, 407–476.
Pring, A., Wade, B., McFadden, A., Lenehan, C.E., Cook, N.J., 2020. Coupled substitutions of minor and trace elements in co-existing sphalerite and wurtzite. Minerals 10, 147.
Ramdohr, P., 1980. In: The Ore Minerals and their Intergrowths. Pergamon Press, Berlin, p. 1205.
Renock, D., Becker, U., 2011. A first principles study of coupled substitution in galena. Ore Geol. Rev. 42, 71–83.
Reich, F., Richter, T., 1863. Ueber das Indium. Prakt. Chem. 90, 172–176.
Reich, M., Román, N., Barra, F., Morata, D., 2020. Silver-rich chalcopyrite from the active Cerro Pabellón Geothermal System, northern Chile. Minerals 10, 113.
Richards, J.P., 2009. Post-subduction porphyry Cu–Au and epithermal Au deposits: products of remelting of subduction-modified lithosphere. Geology 37, 247–250.
Ritterbush, K.A., Ibarra, Y., Bottjer, D.J., Corsetti, F.A., Rosas, S., West, A.J., Berelson, W. M., Yager, J.A., 2015. Marine ecological state-shifts following the Triassic Jurassic mass extinction. In: Paleontological Society Papers, pp. 121–136.
Rosas, S., 1994. Facies, diagenetic evolution, and sequence analysis along a SW-NE profile in the southern Pucará basin (Upper Triassic-Lower Jurassic), central Peru. Heidelberger Geowiss. Abh. 80, 337.
Rosas, S., Fontboté, L., Morche, W., 1996. Within-plate volcanism in Upper Triassic to Lower Jurassic Pucará Group carbonates (central Peru) [ext. abs.]. In: International Symposium on Andean Geodynamics (ISAG), 3rd, Saint Malo, France, 1996, Extended Abstracts, pp. 641–644.
Rosas, S., Fontboté, L., Tankard, A., 2007. Tectonic evolution and paleogeography of the Mesozoic Pucará Basin, central Peru. J. S. Am. Earth Sci. 24, 1–24.
Rottier, B., Kouzmanov, K., Wälle, M., Bendezú, R., Fontboté, L., 2016. Sulfide replacement processes revealed by textural an LA-ICP-MS trace element analyses: example from the early mineralization stages at Cerro de Pasco, Peru. Econ. Geol. 111, 1347–1367.
Rottier, B., Kouzmanov, K., Casanova, V., Wälle, M., Fontboté, L., 2018. Cyclic dilution of magmatic metal-rich hypersaline fluids by magmatic low-salinity fluid: A major process generating the giant epithermal polymetallic deposit of Cerro de Pasco, Peru. Econ. Geol. 113, 825–856.
Rytuba, J.J., John, D.A., Foster, A., Ludington, S.D., Kotlyar, B., 2003. Hydrothermal enrichment of gallium in zones of advanced argillic alteration: examples from the Paradise Peak and McDermitt ore deposits, Nevada. In: Bliss, J.D., Moyle, P.R., Long, K.R. (Eds.), Contributions to Industrial-mineral Research. US Department of the Interior, US Geological Survey, p. 16.
Sack, R.O., Goodell, P.C., 2002. Retrograde reactions involving galena and Ag-sulfosalts in a zoned ore deposit, Julcani, Peru. Mineral. Mag. 66, 1043–1062.
Sack, R.O., 2005. Internally consistent database for sulfides and sulfosalts in the system Ag_2S–Cu_2S–ZnS–FeS–Sb_2S_3– As_2S_3. Geochim. Cosmochim. Ac. 69, 1157–1164.
Sack, R.O., Ebel, D.S., 2006. Thermochemistry of sulfide mineral solutions, Sulfide Mineralogy and Geochemistry. Rev. Mineral. Geochem. 61, 265–364.
Sack, R.O., Lichtner, P.C., 2009. Constraining compositions of hydrothermal fluids in equilibrium with polymetallic ore forming sulfide assemblages. Econ. Geol. Bull. Soc. Econ. Geol. 104, 1249–1264.
Sahlström, F., Arribas, A., Dirks, P., Corral, I., Chang, Z., 2017. Mineralogical distribution of germanium, gallium and indium at the Mt Carlton high-sulfidation epithermal deposit, NE Australia and comparison with similar deposits worldwide. Minerals 7, 213.
Saintilan, N.J., Sproson, A.D., Selby, D., Rottier, B., Casanova, V., Creaser, R.A., Kouzmanov, K., Fontboté, L., Piecha, M., Gereke, M., Zambito IV, J.J., 2021. Osmium isotopic constraints on sulphide formation in the epithermal environment of magmatic-hydrothermal mineral deposits. Chem. Geol. 564, 120053.
Savard, D., 2018. UQAC (Université du Québec à Chicoutimi) FeS-1 <https://sulfideslasericpms.wordpress.com/rm-available/>.
Scherrenberg, A.F., Kohn, B.P., Holcombe, R.J., Rosenbaum, G., 2016. Thermotectonic history of the Marañón Fold-Thrust Belt, Peru: insights into mineralization in an evolving orogen. Tectonophysics 667, 16–36.
Schorr, S., Wagner, G., 2005. Structure and phase relations of the Zn[2x](CuIn)[1 − x]S [2] solid solution series. J. Alloy. Compd. 396, 202–207.
Schulz, K.J., DeYoung Jr., J.H., Seal II, R.R., Bradley, D.C., 2017. Critical mineral resources of the United States – economic and environmental geology and prospects for future supply. In: U.S. Geological Survey Professional Paper, p. 797.
Schwarz-Schampera, U., Herzig, P., 2002. In: Indium: Geology, Mineralogy, and Economics. Springer, Heidelberg, p. 216.
Seward, T.M., Henderson, C.M.B., Charnock, J.M., 2000. Indium (III) chloride complexing and solvatation in hydrothermal solutions to 350 °C: An EXAFS study. Chem. Geol. 167, 117–127.
Shimizu, T., Morishita, Y., 2012. Petrography, chemistry, and near-infrared microthermometry of indium-bearing sphalerite from the Toyoha polymetallic deposit, Japan. Econ. Geol. 107, 723–735.
Sillitoe, R.H., 2010. Porphyry Copper Systems. Econ. Geol. Bull. Soc. Econ. Geol. 105, 3–41.
Skirrow, R.G., Huston, D.L., Mernagh, T.P., Thorne, J.P., Dulfer, H., Senior, A.B., 2013. In: Critical Commodities for a High-tech World: Australia's Potential to Supply Global Demand. Geoscience Australia, Canberra, p. 118.
Soler, P., 1987. Variations des teneurs en éléments mineurs (Cd, In, Ge, Ga, Ag, Bi, Se, Hg, Sn) des minerais de Pb-Zn de la province polymetallique des Andes du Pérou Central. Miner. Deposita 22, 135–143.
Spikings, R., Reitsma, M., Boekhout, F., Miskovic, A., Ulianov, A., Chiaradia, M., Schaltegger, U., 2016. Characterisation of Triassic rifting in Peru and implications for the early disassembly of western Pangaea. Gondwana Res. 35, 124–143.
Terrones, A., 1949. La estratigrafía del distrito minero de Morococha. Sociedad Geológica del Perú 2, 1–15.
Titley, S.R., 1993. Characteristics of high-temperature, carbonate-hosted massive sulphide ores in the United States, Mexico and Peru. Geol. Assoc. Can. Spec. Pap. 40, 585–614.
Todd, E.C., Sherman, D.M., Purton, J.A., 2003. Surface oxidation of chalcopyrite ($CuFeS_2$) under ambient atmospheric and aqueous (pH 2–10) conditions: Cu, Fe Land O K-edge X-ray spectroscopy. Geochim. Cosmochim. Acta 67, 2137–2146.
Tolcin, A.C., 2015. Indium: USGS Mineral Commodity Summaries. <https://s3-us-west-2.amazonaws.com/prd-wret/assets/palladium/production/mineral-pubs/mcs/mcs2015.pdf>.
Torró, L., Melgarejo, J., Gemmrich, L., Mollinedo, D., Cazorla, M., Martínez, Á., Pujol-Solà, N., Farré-de-Pablo, J., Camprubí, A., Artiaga, D., Torres, B., Alfonso, P., Arce, O., 2019a. Spatial and temporal controls on the distribution of indium in xenothermal vein deposits: The Huari Huari District, Potosí, Bolivia. Minerals 9, 304–340.
Torró, L., Cazorla, M., Melgarejo, J., Camprubí, A., Gemmrich, L., Campeny, M., Artiaga, D., Torres, B., Martínez, Á., Tarrés, M., Mollinedo, D., Alfonso, P., Arce, O., 2019b. Indium Mineralization in the Volcanic Dome-Hosted Animas–Chocaya–Siete Suyos Polymetallic Deposit, Potosí, Bolivia. Minerals 9, 604–642.
Warren, H.V., Thompson, R.M., 1945. Sphalerites from western Canada. Econ. Geol. Bull. Soc. Econ. Geol. 40, 309–335.
Wei, C., Huang, Z.L., Yan, Z.F., Hu, Y.S., Ye, L., 2018. Trace element contents in sphalerite from the Nayongzhi Zn-Pb Deposit, Northwestern Guizhou, China: insights into incorporation mechanisms, metallogenic temperature and ore genesis. Minerals 8, 490.
Wilson, S.A., Ridley, W.I., Koenig, A.E., 2002. Development of sulfide calibration standards for the laser ablation inductively coupled plasma mass spectrometry technique. J. Anal. Atom. Spectrom. 17, 406–409.
Wilson, J., 2019. Character and Genesis of Indium Mineralization, East, Kemptville, Nova Scotia. M.Sc. thesis. University of Windsor, Ontario, Canada, p. 115.
Winkler, C., 1886. Germanium, Ge, ein neues, nichtmetallisches Element. Deutschen chemischen Gesellschaft 19, 210–211.
Wood, S.A., Samson, I.M., 2006. The aqueous geochemistry of gallium, germanium, indium and scandium. Ore Geol. Rev. 28, 57–102.
Xu, J., Cook, N.J., Ciobanu, C.L., Li, X., Kontonikas-Charos, A., Gilbert, S., Lv, Y., 2020. Indium distribution in sphalerite from sulfide–oxide–silicate skarn assemblages: a case study of the Dulong Zn–Sn–In deposit, Southwest China. Miner. Deposita. https://doi.org/10.1007/s00126-020-00972-y.

CHAPTER IV: TRACE ELEMENT GEOCHEMISTRY OF SPHALERITE AND CHALCOPYRITE IN ARC-HOSTED VMS DEPOSITS

Journal of Geochemical Exploration 232 (2022) 106882

Contents lists available at ScienceDirect

Journal of Geochemical Exploration

journal homepage: www.elsevier.com/locate/gexplo

Trace element geochemistry of sphalerite and chalcopyrite in arc-hosted VMS deposits

Lisard Torró [a,*], Diego Benites [a], Jean Vallance [a], Oscar Laurent [b,e], Brayam A. Ortiz-Benavente [a], Cyril Chelle-Michou [b], Joaquín A. Proenza [c], Lluís Fontboté [d]

[a] Geological Engineering Program, Faculty of Sciences and Engineering, Pontifical Catholic University of Peru (PUCP), Av. Universitaria 1801, San Miguel, Lima 15088, Peru
[b] Department of Earth Sciences, ETH Zürich, CH-8092 Zürich, Switzerland
[c] Departament de Mineralogia, Petrologia i Geologia Aplicada, Universitat de Barcelona (UB), Martí i Franquès s/n, 08028 Barcelona, Spain
[d] Department of Earth Sciences, University of Geneva, CH-1205 Geneva, Switzerland
[e] CNRS, Géosciences Environnement Toulouse, Observatoire Midi-Pyrénées, 31400 Toulouse, France

ARTICLE INFO

Keywords:
Sulfide
LA-ICP-MS
Coupled substitution
Compositional profile
Volcanic arc
Latin America

ABSTRACT

Trace element compositions of sphalerite and chalcopyrite have been investigated for four arc-hosted Cretaceous VMS deposits (María Teresa, Perubar, and Palma in Peru, and Cerro de Maimón in the Dominican Republic) using laser ablation inductively-coupled plasma mass spectrometry. In sphalerite, Fe, Mn, Cd, Hg, Ag, Sb, Se, In, Ge, and Ga are lattice-bound, whereas Sn, Tl, Bi, and Pb occur at least partly as mineral microinclusions. Significant variations in the contents of minor and trace elements are observed in sphalerite grains from individual deposits. A strong negative correlation between Fe (Inter-Quartile Range [IQR] 44,009–18,168 ppm) and Zn indicates a dominant $Fe^{2+} \leftrightarrow Zn^{2+}$ simple isovalent substitution. Regarding potential *high-tech* by-products, the contents of In (IQR 42–1.6 ppm, up to 415 ppm) and Ga (IQR 31–5.9 ppm, up to 96 ppm) in the studied sphalerite are normally much higher than those of Ge (IQR 0.85–0.16 ppm, up to 9.3 ppm). Correlation trends suggest $Cu^{+} + In^{3+} \leftrightarrow 2Zn^{2+}$, $Cu^{+} + Ga^{3+} \leftrightarrow 2Zn^{2+}$, and more complex substitution mechanisms of Zn involving combinations of monovalent (Cu^{+}, Ag^{+}), divalent (Ge^{2+}?), trivalent (In^{3+}, Ga^{3+}, [Sn^{3+}?]), and quadrivalent (Ge^{4+}, Sn^{4+}) cations.

As for chalcopyrite, Zn, Ag, Sn, Cd, Se, In, Ga, and Ge are interpreted to be lattice-bound, whereas Mo, Au, Tl, Sb, Pb, and Bi probably occur as microinclusions. Relative to sphalerite, chalcopyrite is depleted in In (IQR 28–8.4 ppm, up to 49 ppm) and Ga (IQR 8.3–2.9 ppm, up to 24 ppm) and enriched in Ge (IQR 5.9–0.70 ppm, up to 80 ppm). Of the other trace elements, Zn (IQR 426–190 ppm) is the most highly concentrated in the studied chalcopyrite, followed by Ag (IQR 136–23 ppm), Se (IQR 64–22 ppm), Sn (IQR 53–1.3 ppm), and Cd (IQR 12–6.0 ppm). General positive correlation trends between Zn, Cd, In, Ge, and Ga in chalcopyrite suggest varied coupled substitution mechanisms of Fe and Cu with fluctuating valences due to covalent bonding.

Trace-element distribution patterns in sphalerite and chalcopyrite were studied for the zone-refined Sofía-D massive sulfide body in the María Teresa deposit, which comprises a lower lower portion of dominant pyrite sheathed upward by zones of chalcopyrite (Cu zone), sphalerite (Zn zone) and galena + sphalerite ± fahlore ± barite (Pb – Zn – Ag zone). Bottom to top of the sulfide body, sphalerite records progressive depletion in In, Cu, Mn, and Se, and enrichment in Ge. This distribution pattern agrees with increasing crystallization temperatures and/or volatile magmatic influx towards the lower portion of the massive mineralization. Distribution of trace elements in chalcopyrite is rather uneven except for a sustained enrichment in Se towards the basal portion of the sulfide body. The fact that such trends are preserved in spite of extensive recrystallization during thermal metamorphism in parts of the Sofía-D massive sulfide mineralization suggests i) a closed metamorphic system and ii) that element interdiffusion was prominently local. Accordingly, we propose that sphalerite lattice-bound trace elements distribution patterns described in this article can help determine the polarity of massive sulfide bodies in VMS districts in metamorphosed and tectonized terranes.

* Corresponding author.
E-mail address: lisardtorro@hotmail.com (L. Torró).

https://doi.org/10.1016/j.gexplo.2021.106882
Received 14 January 2021; Received in revised form 23 July 2021; Accepted 20 August 2021
Available online 27 August 2021

1. Introduction

Volcanogenic massive sulfide (VMS) deposits are exhalative and/or replacive accumulations of sulfide minerals formed at or near the seafloor where uprising hydrothermal fluids driven and in part generated by synchronous magmatism are entrained with cold seawater or porewaters (Doyle and Allen, 2003; Shanks and Thurston, 2012; Yeats et al., 2014; Tornos et al., 2015). VMS mineralization occurs as sulfide mounds to tabular stratiform bodies, which are often underlain by a stockwork or feeder zone (Galley et al., 2007; Tornos et al., 2015). Their formation responds to the convergence in the time and space of anomalously high thermal gradients and extensional tectonic regimes that promote the circulation of metal-bearing magmatic fluids and/or leaching of metals from the oceanic strata by evolved hydrothermal fluids (Ohmoto, 1996; Tivey, 2007; de Ronde et al., 2011; Piercey, 2011). Such geological features are primarily met in oceanic spreading ridges, arc environments, and rifted continental margins.

Most VMS deposits are preserved in suprasubduction zones either in back-arc, intra-arc, or forearc basins on both oceanic and continental crust (Franklin et al., 1998; Nimis et al., 2003; Herrington et al., 2005; de Ronde et al., 2011; Hollis et al., 2014; Peter et al., 2014; Torró et al., 2016a). In arc-related systems, contrasting water depths in massive sulfide formation exert a major control on the ore and hydrothermal alteration mineral assemblages and the metalliferous contents (Sillitoe et al., 1996; Dubé et al., 2007; Monecke et al., 2014). VMS deposits in back-arc and forearc basins form at water depths typically in the range between 1500 and 3700 m, whereas those in arc volcanoes and arc-related rifts are normally restricted to water depths in the range between 700 and 2000 m. The latter are often associated with elevated magmatic gas contents and boiling of the hydrothermal fluids may occur in shallower arc volcanoes and rifted intra-arc submarine hydrothermal systems (Gemmell et al., 2004; Dubé et al., 2007; Monecke et al., 2014).

VMS deposits are important sources of Cu, Zn, Pb, Au, and Ag (Galley et al., 2007). In addition, a wealth of other metals and metalloids that are potentially economically recoverable as byproducts (e.g., Sn, Co, Ni, In, Ga, Ge, Mo, Re, Se, Te) or deleterious (i.e., harmful or unwanted elements; e.g., Mn, As, Sb, Hg, Tl) may occur in remarkable concentrations in VMS deposits and even determine their economic viability (Benzaazoua et al., 2003; Zaccarini and Garuti, 2008; Koski and Mosier, 2012; Ridley, 2012; Carvalho et al., 2018; Frenzel et al., 2019). Minor and trace elements can either precipitate as native elements or substitute into the crystal lattice of major sulfide minerals (Cook et al., 2009, 2012, 2015; Ye et al., 2011; Ridley, 2012; Murakami and Ishihara, 2013; George et al., 2015, 2018; Benites et al., 2021a, 2021b). The understanding of the mineralogical expression of either potential by-product or deleterious minor and trace elements in a given deposit or mineralization style is essential to predict their metallurgical behavior (e.g., Cook et al., 2011).

This study aims at understanding the mineralogical expression of minor and trace elements in sphalerite and chalcopyrite from arc-related VMS deposits and their distribution across massive sulfide bodies. To do so, we have systematically determined the trace element budget on these ore minerals from four arc-related VMS deposits in the Andes (María Teresa, Perubar, and Palma in Peru) and the Caribbean (Cerro de Maimón in the Dominican Republic). The obtained contents are compared with published data on other VMS deposits worldwide. In addition, a comprehensive set of samples has allowed the study of ore body-scale zoning of certain trace elements in a zone-refined massive sulfide body in the María Teresa deposit. The obtained results are used to assess the incorporation mechanisms of some *high-tech* elements to the crystal lattice of major sulfides (sphalerite and chalcopyrite) and contribute to revealing element distribution patterns across massive sulfide bodies in VMS districts; such patterns can be used to target the most prospective zones of zoned massive sulfide bodies for potential by-products and complementarily also to constrain sulfide body polarity during exploration in tectonized terranes.

2. Geological setting

2.1. Volcanogenic massive sulfide deposits in Peru

2.1.1. General geologic framework

In Peru, several VMS deposits occur along the coastal region and are hosted by rocks of Cretaceous age (Steinmüller et al., 2000; Fontboté, 2019). In northern Peru, the giant Tambogrande deposits represent the largest VMS endowment in this country and probably in South America, and include the TG1 deposit with resources of 109 million metric tons (Mt) grading 1.6% Cu, 1.0% Zn, 0.5 g/t Au, and 22 g/t Ag, plus 16.7 Mt grading 3.5 g/t Au and 64 g/t Ag in oxide ore, and the TG3 deposit with resources of 82 Mt grading 1.0% Cu, 1.4% Zn, 0.8 g/t Au, and 25 g/t Ag (Manhattan Minerals, 2002 in Winter et al., 2010). There, VMS mineralization is hosted by subalkaline (calc-alkaline and tholeiitic) basaltic pillowed and brecciated lavas and lesser amounts of felsic volcanic rocks that filled N and NW-oriented sub-basins in the lower portion of the Lancones basin (Fig. 1; Tegart et al., 2000; Winter et al., 2004, 2010). The formation of the Lancones basin is connected to the break-up of Gondwana and coincided with a period of intense extension and rifting due to trench-rollback (Winter et al., 2010 and their references). Minimum age of massive sulfide formation (and likely synchronous with or slightly postdating massive sulfide formation) is constrained by U—Pb zircon dating of felsic volcaniclastic rocks at 104.8 ± 1.3 to 100.2 ± 0.5 Ma (middle Albian; Winter et al., 2010). The volcanic and sedimentary pile in the Lancones basin was intruded by Late Cretaceous to Tertiary arc-related granitoids of the Coastal Batholith (cf. Pitcher, 1985; Atherton, 1990; Cobbing, 1999; Hildebrand and Whalen, 2014).

In the central coastal segment of Peru, where the deposits studied in this paper are located, VMS mineralizations emplaced in the Huarmey and Cañete basins of the West Peruvian Trough (WPT; Fig. 1) and are now exposed along the Peruvian Western Cordillera to the Coastal region. The opening of the WPT was assigned to an aborted back-arc or true ocean floor extensional marginal basin (e.g., Atherton et al., 1985; Aguirre et al., 1989; Atherton and Aguirre, 1992) and more recently has been interpreted as an intra-arc extensional pull-apart basin (Soler, 1991; Aillard, 1994; Polliand et al., 2005; Polliand, 2006). Stratigraphic relationships in the WPT led Scherrenberg et al. (2012) to delineate i) a western intra-arc basin, which is dominated by igneous rocks and that geographically coincides with the VMS mineralization; and ii) an eastern, deeper back-arc basin in which volcanic rocks overlie continental clastic rocks and marine carbonates. Major basin filling in the WPT occurred from latest Jurassic to Late Cretaceous (Mégard, 1984; Benavides-Cáceres, 1999). The stratigraphy of the WPT (at least in its western portion *sensu* Scherrenberg et al., 2012) is largely composed of a volcano-sedimentary sequence including bimodal mafic-felsic volcanic rocks, limestones, shales, sandstones, and local evaporites that was intruded by the Peruvian Coastal Batholith, which in part is coetaneous with the volcano-sedimentary sequence (Mégard, 1984; Atherton and Aguirre, 1992; Vela, 1997; Benavides-Cáceres, 1999; Polliand et al., 2005, Polliand, 2006; Hildebrand and Whalen, 2014). The stratigraphy of the WPT is complex and includes abrupt lateral facies changes greatly limiting the stratigraphic correlation and age estimates of the sedimentary units. Since the scope of this article is limited to the geochemical composition of some ore minerals in selected VMS deposits, we will not elaborate on the nomenclature of hosting units but will simply conform with 'Casma Group' embracing the Albian-Cenomanian volcano-sedimentary sequence versus the younger 'Upper Cretaceous-Paleocene volcano-sedimentary sequence' (Romero et al., 2008; Cueva et al., 2010; Fontboté, 2019).

From north to south, the most representative VMS mineralization in the Huarmey and Cañete basins are the María Teresa, Aurora Augusta, Perubar, Palma, and Cerro Lindo (Fig. 1). Geochronology has given two groups of ages for these deposits: uppermost Cretaceous and mid-Cretaceous. High-resolution U—Pb zircon geochronology performed by Polliand et al. (2005) on rhyolitic lavas at the bottom and top of

massive ore bodies in Perubar yields dates of 69.71 ± 0.18 and 68.92 ± 0.16 Ma, and on intrusive rocks, dates of 67.91 ± 0.17 and 67.89 ± 0.18 Ma. These dates ascribe the hosting rocks to the Upper Cretaceous-Paleocene volcano-sedimentary sequence and point to largely coeval subsidence, submarine volcanism, and plutonic activity within the Andean magmatic arc during the Late Cretaceous (Polliand et al., 2005; Polliand, 2006). At María Teresa, a date of 68 ± 6 Ma (Rb/Sr in hydrothermal sericite; Romero et al., 2008) points also to VMS mineralization in the latest Cretaceous. In contrast, the Cerro Lindo VMS mineralization is described to be hosted by a volcano-sedimentary sequence whose age has been attributed to the mid-Cretaceous (Casma Group) according to U—Pb zircon dating of host rhyolites at 105.7 ± 0.2 and 106.9 ± 0.2 Ma (Gariepy and Hinostroza, 2013; Votorantim, 2017; Bueno Carreón, 2019; Bueno Carreón and Mendoza Mondragón, 2019). Recent U—Pb zircon dating at 101 Ma of a diorite dike crosscutting the mineralization suggests that the Palma VMS deposit is also mid

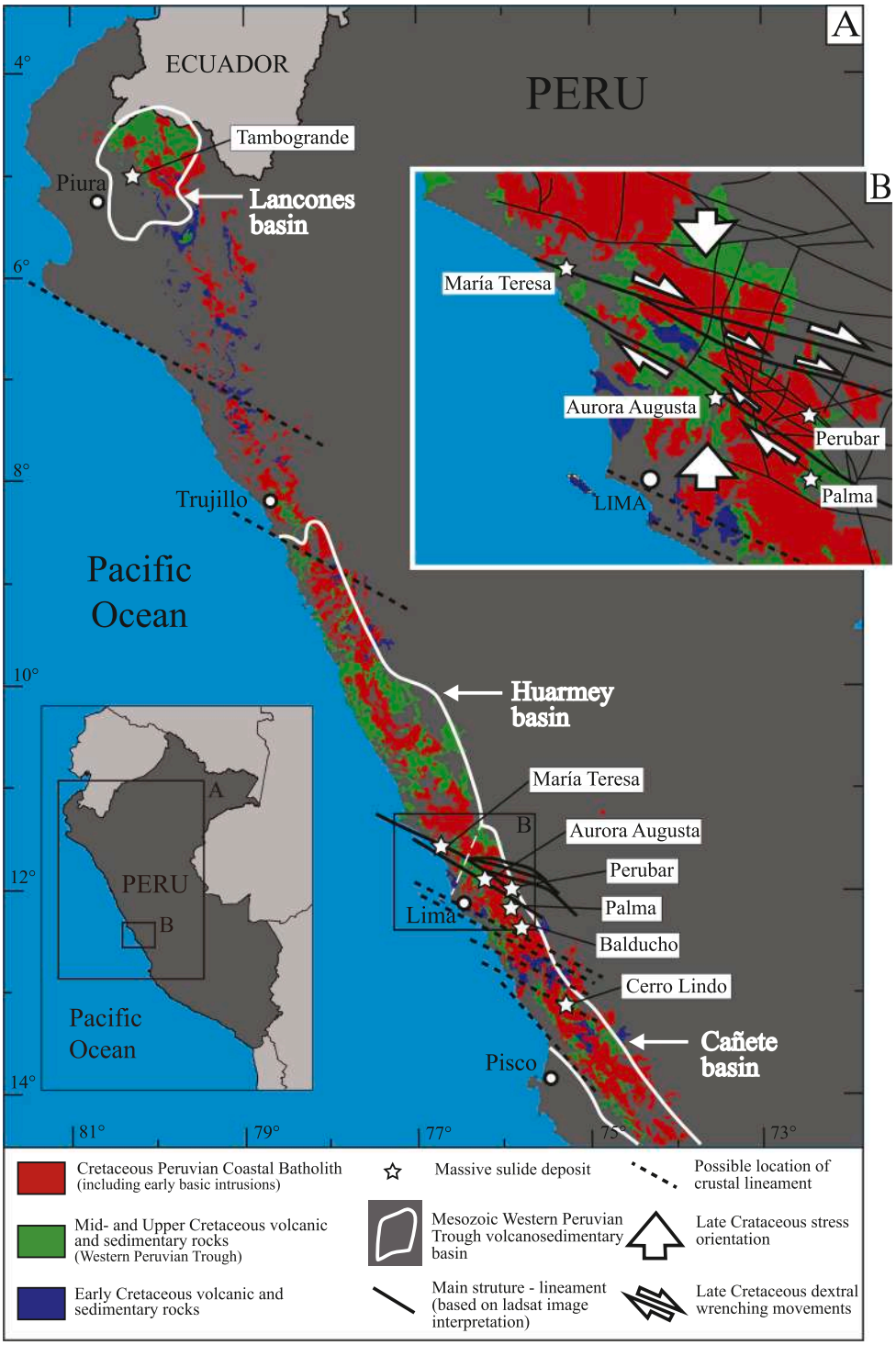

Fig. 1. Geologic map of the Peruvian Coastal Batholith and Mesozoic Western Peruvian Trough (WPT) with related volcano-sedimentary basins hosting massive sulfide deposits. Modified from Polliand et al. (2005). Distribution of the Cretaceous Peruvian Costal Batholith and strata after the digital version of the geological map of Peru (INGEMMET, 2000).

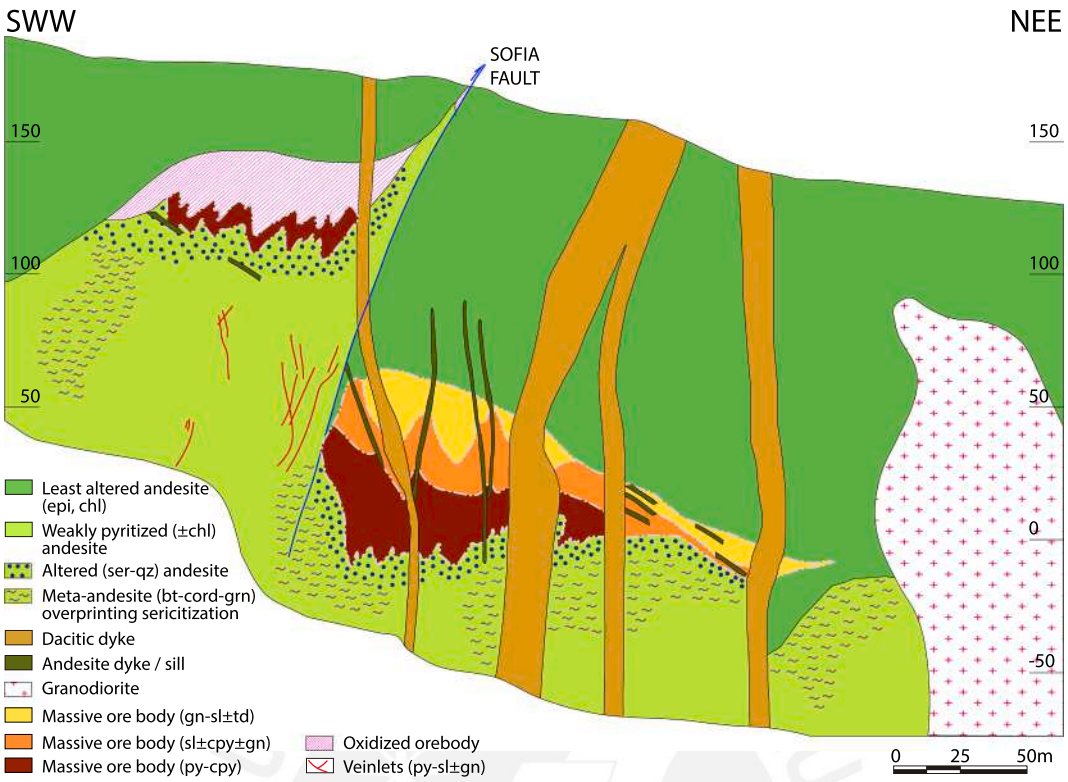

Fig. 2. Representative schematic cross-section across the Sofía D massive sulfide body in the María Teresa VMS deposit, Peru (redrawn from geological documents of the María Teresa Mine geological department as of December 2020).

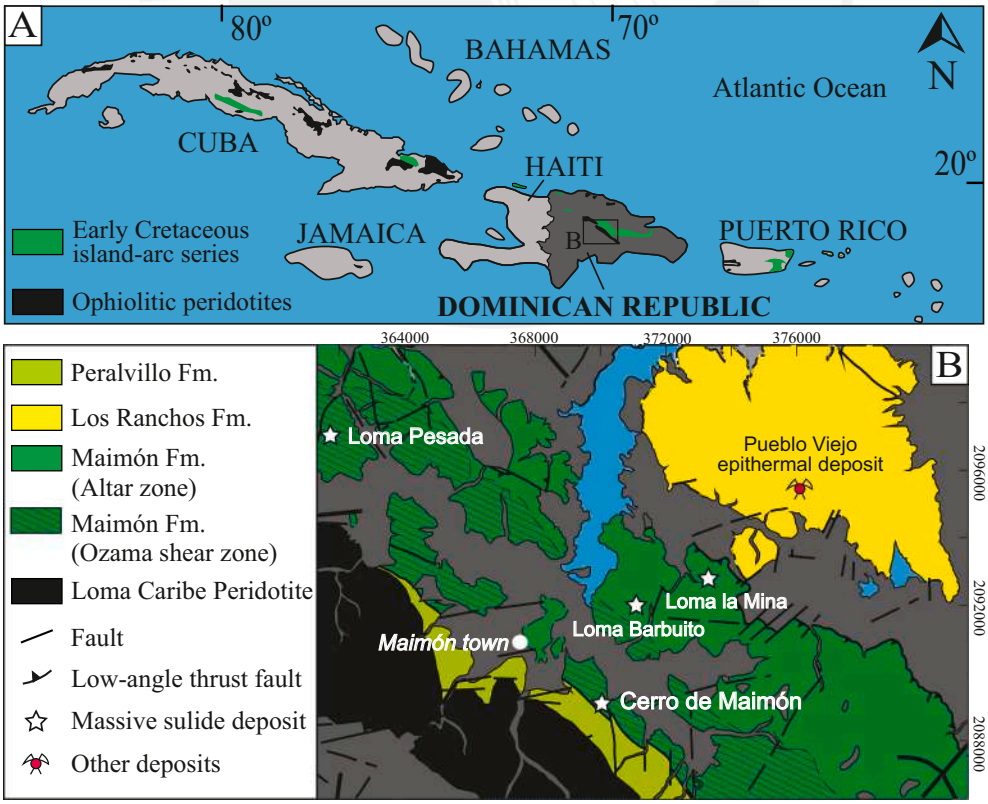

Fig. 3. (A) Geographic location of the Early Cretaceous boninite and island arc tholeiite volcanic series and ophiolitic peridotites along the Greater Antilles. (B) Geological map of the Maimón Formation and surrounding Early Cretaceous arc-related volcanic units (modified from Martín and Draper, 1999).

Table 1
Summary of element contents in sphalerite from the María Teresa, Perubar, Palma, and Cerro de Maimón VMS deposits (LA-ICP-MS data).

Deposit	Sector / Body / Section		Mn (ppm)	Fe (ppm)	Cu (ppm)	Zn (ppm)	Ga (ppm)	Ge (ppm)	As (ppm)	Se (ppm)	Mo (ppm)	Ag (ppm)	Cd (ppm)	In (ppm)	Sn (ppm)*	Sb (ppm)	Hg (ppm)	Tl (ppm)*	Pb (ppm)*	Bi (ppm)*
María Teresa (Peru)	All samples	Min.	107	9772	3.8	569500	1.4	B.D.L.	4.6	B.D.L.	B.D.L.	2.2	4720	0.44	0.14	B.D.L.	98	B.D.L.	0.038	B.D.L.
	(n = 141)	Max.	4998	63534	740	663300	94	2.3	9.3	32	1.6	66	9409	415	20	48	788	19	44	3.5
		GM	1353	29317	96	623168	25	0.51	6.0	6.4	0.16	11	6605**	60	1.2	4.3	392	1.0	6.2	0.44
		SD	1236	13930	106	22726	19	0.56	0.8	9.3	0.19	10	1279	89	2.8	7.2	135	2.1	7.2	0.77
		IQR	2343-326	40675-17122	98-36	641300-608100	32-11	0.65-0.17	6.5-5.5	5.3-1.6	0.20-0.047	12-4.2	7373-5290	68-4.4	0.61-0.25	5.2-0.52	448-326	1.2-0.060	8.7-1.4	0.60-0.0055
	Bubulina / Bubulina 1180	Min.	3139	13000	79	630300	17	B.D.L.	4.7	4.3	0.25	3.2	4720	21	0.30	0.048	664	B.D.L.	0.21	B.D.L.
	(n = 9)	Max.	4998	18702	174	648500	94	0.16	5.8	5.3	0.73	5.2	5044	99	3.2	1.1	788	0.0081	4.3	B.D.L.
		GM	4474	16628	126	640091	51	0.16	5.3	4.8	0.37	4.2	4867	59	1.0	0.28	724	0.0067	1.2	B.D.L.
		SD	550	2135	26	6640	23	-	0.3	0.4	0.15	0.7	118	36	1.0	0.37	35	0.0010	1.7	B.D.L.
		IQR	4747-4492	18088-15614	138-118	643900-633600	68-43	0.16-0.16	5.4-5.1	5.0-4.6	0.36-0.31	4.6-3.8	4964-4804	94-25	1.7-0.35	0.54-0.15	737-704	0.0076-0.0061	4.1-0.62	B.D.L.
	Calera / Sofía-D, all	Min.	107	9772	3.8	569500	1.4	B.D.L.	4.6	B.D.L.	B.D.L.	2.2	4896	0.44	0.14	B.D.L.	98	B.D.L.	0.038	B.D.L.
	samples	Max.	2857	63534	740	663300	70	2.3	9.3	32	1.6	66	9409	415	20	48	677	19	44	3.46
	(n = 132)	GM	716	26558	61	621589	17	0.33	6.0	3.1	0.09	7.9	6613	19	0.48	1.7	349	0.28	3.4	0.04
		SD	939	13984	109	22982	17	0.56	0.8	9.6	0.18	10.6	1235	91	2.86	7.3	107	2.18	7.3	0.77
		IQR	1771-303	40842-17173	87-36	639625-605100	31-11	0.66-0.17	6.5-5.5	5.5-1.5	0.17-0.045	13-4.2	7411-5446	54-4.3	0.58-0.24	5.5-0.65	438-318	1.3-0.084	8.8-1.6	0.60-0.0055
	Calera / Sofía-D / 300	Min.	107	9772	20	569500	3.1	B.D.L.	5.2	B.D.L.	B.D.L.	2.2	4896	3.9	0.14	B.D.L.	98	0.0072	0.038	B.D.L.
	(n = 105)	Max.	2857	63534	740	663300	38	2.3	9.3	32	1.6	66	8051	415	16	48	485	19	33	3.5
		GM	828	25631	66	621999	15	0.37	6.1	3.3	0.11	7.5	6334	33	0.37	2.0	345	0.35	3.9	0.053
		SD	967	14897	120	24203	10	0.60	0.7	10.6	0.19	10.5	967	98	2.19	7.7	97	2.39	6.5	0.801
		IQR	2343-251	42100-15748	90-36	639600-602500	27-10	0.79-0.17	6.4-5.7	5.6-1.5	0.20-0.050	13-3.9	7239-5290	78-12	0.48-0.22	5.9-0.79	438-315	1.7-0.13	9.0-2.0	0.72-0.0057
	Calera / Sofía D / 340	Min.	113	18062	3.8	591600	1.4	B.D.L.	6.7	B.D.L.	B.D.L.	4.1	5592	0.44	0.18	0.10	213	B.D.L.	0.28	B.D.L.
	(n = 10)	Max.	1662	42132	76	642900	38	0.21	7.1	7.1	0.13	9.2	7044	42	1.8	1.1	443	0.32	2.5	0.0051
		GM	468	31839	19	614743	8	0.16	6.9	3.1	0.06	6.9	6198	5	0.46	0.40	300	0.05	0.83	0.0046
		SD	799	9365	35	22717	19	0.04	0.1	2.8	0.05	1.8	656	22	0.45	0.39	105	0.12	0.74	0.0006
		IQR	1646-139	41573-27114	70-5.3	634275-594450	38-1.5	0.19-0.13	7.0-6.9	6.6-1.3	0.11-0.027	8.6-5.7	6899-5632	42-0.56	0.58-0.29	0.87-0.24	409-219	0.17-0.019	1.5-0.48	0.0050-0.0044
	Calera / Sofía D / 500	Min.	320	15296	40	608000	22	0.12	4.9	1.3	0.033	11	8905	1.1	0.34	0.31	329	0.085	3.9	B.D.L.
	(n = 5)	Max.	584	38233	82	645800	59	0.95	5.6	3.7	0.61	46	9409	1.8	2.2	24	677	0.71	44	0.0061
		GM	502	19140	53	637688	28	0.37	5.3	2.1	0.07	24	9121	1.6	0.95	3.3	574	0.23	10	0.0061
		SD	97	8832	15	14717	14	0.31	0.2	0.9	0.23	14	166	0.2	0.71	9.6	130	0.24	15	-
		IQR	557-520	17392-16548	55-47	645150-641800	25-24	0.64-0.29	5.4-5.3	2.4-1.7	0.065-0.038	38-18	9152-9054	1.7-1.6	1.6-0.64	13-1.4	654-620	0.44-0.12	16-6.0	0.0061-0.0061
	Calera / Sofía D / 540	Min.	214	35835	82	608000	58	B.D.L.	4.6	2.1	0.037	5.7	8644	1.0	0.61	0.02	325	0.014	0.10	B.D.L.
	(n = 12)	Max.	357	38973	137	619700	70	1.2	5.4	3.7	0.67	27	9168	1.5	20	11	356	1.2	31	0.011
		GM	322	37824	91	614685	64	0.22	5.0	2.8	0.06	8.9	8877	1.2	3.1	0.9	338	0.14	1.7	0.0069
		SD	36	1036	16	2950	4	0.33	0.3	0.4	0.18	6.2	158	0.2	5.6	4.0	11	0.45	8.6	0.0035
		IQR	339-326	38681-37310	89-84	616125-613700	68-63	0.23-0.16	5.2-4.9	3.0-2.6	0.055-0.042	11-6.5	8951-8784	1.2-1.1	8.4-1.1	3.1-0.28	344-331	0.38-0.052	4.7-0.45	0.0084-0.0053
Perubar (Peru)	All samples	min	667	30747	16	549400	3.4	B.D.L.	4.0	B.D.L.	0.046	1.7	3977	0.0056	0.17	B.D.L.	15	B.D.L.	0.038	B.D.L.
	(n = 50)	max	7639	73876	789	617700	33	0.49	6.1	10	0.55	14	7076	7.1	1.4	5.4	117	1.0	17	0.0037
		GM	2421	51935	35	579909.2969	13	0.17	4.6	3.5	0.19	4.6	5252	1.0	0.27	0.45	44	0.05	1.1	0.0033
		SD	2738	15233	108	24068.28288	11	0.08	0.4	3.0	0.17	2.7	1070	1.8	0.17	1.15	39	0.18	3.3	0.0005
		IQR	5964-907	67570-39965	41-25	600000-551800	30-4.7	0.19-0.15	4.8-4.4	8.2-2.5	0.42-0.089	7.1-3.6	6664.9-4296.6	2.3-0.78	0.31-0.22	1.2-0.18	107-18	0.13-0.025	2.9-0.39	0.0035-0.0031
	Cecilia Sur	Min.	667	30747	20	599800	11	B.D.L.	4.3	B.D.L.	0.046	4.3	5485	0.0056	0.20	B.D.L.	71	0.013	0.038	B.D.L.
	(n = 22)	Max.	1047	42636	789	617700	33	0.19	5.4	4.4	0.20	14	7076	0.82	0.43	4.0	117	1.0	17	B.D.L.
		GM	906	37667	45	605057	25	0.16	4.7	1.7	0.085	6.8	6422	0.10	0.31	0.6	97	0.10	2.5	B.D.L.
		SD	75	3821	160	7381	7	0.03	0.3	1.3	0.031	2.2	518	0.39	0.07	1.1	16	0.23	4.1	B.D.L.
		IQR	939-879	40139-34273	46-36	614400-600000	31-20	0.17-0.14	4.8-4.6	3.2-1.1	0.098-0.071	7.8-5.7	6797-5833	0.75-0.0060	0.35-0.26	1.9-0.23	108-79	0.20-0.047	5.8-1.2	B.D.L.
	Graciela	Min.	6704	59164	23	572900	17	B.D.L.	4.0	3.2	0.39	1.7	4799	1.9	0.17	B.D.L.	37	0.045	0.18	B.D.L.
	(n = 10)	Max.	7639	66451	30	575100	22	0.20	4.7	4.2	0.55	2.8	5135	2.1	0.23	0.59	43	0.17	3.2	B.D.L.
		GM	7267	63460	26	574430	21	0.18	4.3	3.7	0.48	2.0	4983	2.0	0.20	0.13	40	0.076	0.56	B.D.L.
		SD	240	2010	2	699	2	0.01	0.2	0.3	0.04	0.3	89	0.0	0.02	0.20	2	0.043	0.93	B.D.L.
		IQR	7367-7197	64413-62864	27-24	575100-574200	22-21	0.19-0.18	4.3-4.2	4.0-3.5	0.49-0.46	2.1-1.9	5039-4952	2.0-2.0	0.21-0.19	0.27-0.053	41-39	0.10-0.055	1.2-0.22	B.D.L.
	Juanita	Min.	1669	58263	20	557900	4.5	B.D.L.	4.7	2.5	0.12	3.6	3977	6.7	0.19	0.38	15	0.0060	0.63	B.D.L.
	(n = 4)	Max.	1973	64193	126	567000	8.1	0.49	6.1	3.9	0.17	7.4	4388	7.1	1.4	3.0	17	0.49	1.3	B.D.L.
		GM	1801	61300	41	562010	6.5	0.25	5.2	3.1	0.14	4.6	4208	6.9	0.35	0.91	16	0.05	0.83	B.D.L.
		SD	128	2706	49	4813	1.5	0.26	0.6	0.6	0.03	1.8	185	0.2	0.57	1.19	1	0.23	0.31	B.D.L.
		IQR	1856-1736	63248-59558	61-25	565725-557900	7.4-6.4	0.40-0.22	5.4-5.0	3.3-2.9	0.16-0.12	5.2-3.6	4341-4110	7.0-6.9	0.56-0.20	1.4-0.59	17-16	0.18-0.031	1.0-0.64	B.D.L.
	Rímac-D	Min.	5121	66771	16	549400	3.4	B.D.L.	4.4	6.5	0.33	2.5	3996	2.1	0.19	0.14	17	B.D.L.	0.22	B.D.L.
	(n = 14)	Max.	6090	73876	66	552400	4.8	0.22	4.9	10	0.45	10	4436	2.4	0.36	5.4	20	0.12	2.7	0.0037
		GM	5631	71109	27	551092	4.2	0.17	4.6	8.6	0.38	4.4	4235	2.3	0.25	0.47	18	0.011	0.52	0.0033
		SD	325	1984	13	1010	0.5	0.03	0.2	1.1	0.04	2.1	104	0.1	0.04	1.40	1	0.034	0.73	0.0005
		IQR	5915-5408	72557-70501	30-22	551600-550625	4.6-4.0	0.20-0.15	4.8-4.6	9.3-8.3	0.42-0.35	4.1-3.9	4291-4185	2.3-2.2	0.27-0.22	0.75-0.20	19-18	0.028-0.0044	1.0-0.26	0.0035-0.0031
Palma (Peru)	All samples	Min.	2303	28384	5.7	543300	0.61	B.D.L.	3.6	B.D.L.	0.13	1.7	4335	0.0059	0.15	B.D.L.	213	B.D.L.	0.17	B.D.L.
	(n = 37)	Max.	10848	71526	170	625100	3.1	9.3	6.3	1.6	0.69	32	7951	1.6	0.90	28	1215	6.2	140	0.015
		GM	6676	42211	20	591619	1.9	0.6	4.9	0.94	0.44	8.5	5703	0.046	0.30	2.2	603	0.2	14	0.004
		SD	2413	17860	29	31430	0.6	2.6	0.7	0.25	0.15	8.8	1212	0.421	0.16	6.2	316	1.4	42	0.006
		IQR	7751-6734	63423-30015	31-11	619200-557400	2.4-1.9	3.5-0.16	5.3-4.3	1.1-0.8	0.58-0.41	17-3.8	7109-4782	0.22-0.0091	0.41-0.20	7.1-0.78	667-593	1.4-0.020	71-3.9	0.0066-0.0025
	Old mine	Min.	2303	28384	5.7	557400	0.61	B.D.L.	3.6	B.D.L.	0.13	1.7	4335	0.0059	0.15	B.D.L.	213	B.D.L.	0.17	B.D.L.
	(n = 28)	Max.	7751	63423	170	625100	3.1	9.3	6.3	1.6	0.58	32	7293	1.6	0.63	16	667	6.2	140	0.015
		GM	5794	35929	21	605878	1.8	0.9	4.8	1.0	0.39	8	5227	0.0	0.27	2	487	0.3	19	0.005
		SD	1822	12819	33	22214	0.7	2.7	0.84	0.29	0.12	10	848	0.52	0.14	4.1	166	1.5	44	0.007
		IQR	7176-6671	38029-29106	32-12	620375-603350	2.4-1.8	4.6-0.18	5.6-4.0	1.2-0.8	0.47-0.39	18-3.6	5382-4742	0.032-0.0072	0.36-0.18	5.8-0.47	621-504	1.7-0.034	77-4.5	0.0089-0.0025
	Sta Lidia	Min.	9837	64436	8.2	543300	2.0	B.D.L.	4.7	B.D.L.	0.64	3.7	7109	0.13	0.26	1.1	1147	0.0056	1.1	B.D.L.
	(n = 9)	Max.	10848	71526	50	555300	2.9	0.23	5.3	1.1	0.69	23	7951	0.28	0.90	28	1215	0.21	16	0.0037
		GM	10375	69687	17	549369	2.3	0.16	5.1	0.86	0.66	9.3	7481	0.21	0.40	6.1	1169	0.034	5.0	0.0037
		SD	332	2237	14	4919	0.2	0.04	0.2	0.12	0.02	6.7	251	0.06	0.19	8.8	21	0.070	5.1	-
		IQR	10604-10119	71269-68821	44520.0	552500-543300	2.4-2.2	0.19-0.14	5.3-4.9	0.9-0.8	0.67-0.64	16-5.6	7647-7315	0.27-0.17	0.42-0.33	15-3.7	1177-1156	0.11-0.018	10-3.0	0.0037-0.0037
Cerro de Maimón (Dominican Republic)	Cerro de Maimón	Min.	406	B.D.L.	82	650000	70	0.23	3.6	17	B.D.L.	2.6	3413	5.9	0.14	0.026	21	0.036	1.9	0.054
	(n = 17)	Max.	539	643	172	665000	96	6.2	10	67	1.7	21	3905	11	2.5	3.3	30	1.51	30	3.5
		GM	467	371	124	652622	85.2	0.9	4.4	49	0.20	4.4	3684	9.5	0.37	0.15	23.8	0.15	9.9	0.5
		SD	40	193	22	5894	9.0	1.4	1.6	17	0.52	5.3	146	1.3	0.60	0.77	2.9	0.38	8.2	1.0
		IQR	482-446	585-535	138-113	650000-650000	95-78	1.2-0.68	4.4-3.9	61-57	0.30-0.090	4.2-3.1	3829-3574	10-9.5	0.50-0.23	0.26-0.052	26-22	0.23-0.061	17-6.6	1.1-0.33

B.D.L.: Below detection limit; IQR: interquartile range; GM: geometric mean; SD: standard deviation
*Ragged ablation spectra in some analyses indicate that these elements may occur as sub-microinclusions
** According to Zn concentrate analyses, Cd values (LA-ICP-MS data) may be overevaluated by 48-57%

B.D.L.: Below detection limit; IQR: interquartile range; GM: geometric mean; SD: standard deviation.
[a] Ragged ablation spectra in some analyses indicate that these elements may occur as sub-microinclusions.
[b] According to Zn concentrate analyses, Cd values (LA-ICP-MS data) may be overevaluated by 48–57%.

Cretaceous (Choquehuanca, 2020). At Aurora Augusta, hydrothermal sericite yielded inconclusive – both mid- and late Cretaceous – ages (K-Ar; Vidal, 1987).

Hydrothermal alteration in the María Teresa, Perubar, and Palma typically comprises intense sericite ± chlorite in the footwall and epidote + albite + chlorite + carbonates in the hanging wall and 'distal' domains of sulfide bodies (Fontboté, 2019). Sericite alteration is particularly well developed in the María Teresa deposit due to the exclusive igneous nature (i.e., plagioclase-rich) of the host rocks unlike in Perubar and Palma, where the presence of sedimentary rocks in the host sequence distorts the hydrothermal alteration halos. At María Teresa, the identification of a 'prospective horizon' outlined by an intense sericite alteration front has been interpreted as a paleo-horizon in which ascending hydrothermal fluids mixed with seawater in the volcanic pile in the sub-seafloor (Fontboté, 2019; Pichardo et al., 2019). Sulfur and Sr isotope data at Perubar support that mixing between a hydrothermal fluid (dominated by H_2S) and seawater triggered the mineralization (Polliand et al., 1999; Polliand, 2006). The setting of the María Teresa, Palma, and Perubar in a plutono-volcanic arc and the likely involvement of acidic-oxidizing fluids indicated by alteration and ore mineral assemblages are used by Fontboté (2019) to argue for a magmatic origin of the ore-forming hydrothermal fluids.

2.1.2. Geology of the María Teresa deposit

The Zn-Pb-Cu-Ag María Teresa mine is located 11 km NW of Huaral and 85 km N of Lima (Fig. 1) and is owned and operated by Minera Colquisiri SA since 1985. Mineralization at María Teresa (>18 Mt high-grade Zn-Pb-Ag ± Cu ore, Pichardo et al., 2019) occurs as replacement of

Table 2
Summary of element contents in chalcopyrite from the María Teresa and Cerro de Maimón VMS deposits (LA-ICP-MS data).

Deposit	Sector/body/section		Fe (ppm)	Co (ppm)	Ni (ppm)	Cu (ppm)	Zn (ppm)	Ga (ppm)	Ge (ppm)	As (ppm)	Se (ppm)
María Teresa (Peru)	All samples	Min.	264,304	B.D.L.	B.D.L.	340,000	152	0.070	0.18	0.18	10
	(n = 40)	Max.	373,972	0.087	2.2	352,700	647	24	80	1.9	59
		GM	331,188	0.075	1.5	346,217	277	4.0	1.6	0.43	25
		SD	24,272	0.010	0.4	3871	133	6.4	19.4	0.41	13
		IQR	348,538–319,792	0.079–0.070	1.9–1.2	348,300–343,900	425–194	9.2–2.6	4.3–0.66	0.74–0.29	31–19
	Calera/Sofía D/300	Min.	264,304	B.D.L.	B.D.L.	342,000	152	0.070	0.18	0.18	10
	(n = 25)	Max.	373,972	0.087	2.2	352,700	529	24	80	1.9	45
		GM	331,249	0.075	1.4	347,222	263	3.5	1.2	0.45	22
		SD	25,625	0.010	0.4	3155	124	6.8	20.9	0.43	8
		IQR	348,538–319,792	0.079–0.070	1.8–1.2	349,700–345,000	425–192	8.1–2.6	2.2–0.64	0.80–0.29	30–16
	Calera/Sofía D/500	Min.	312,109	B.D.L.	B.D.L.	340,000	276	8.9	7.3	0.25	49
	(n = 4)	Max.	350,244	B.D.L.	1.9	340,000	647	11	12	0.36	59
		GM	330,803	–	1.9	340,000	374	10	9.4	0.30	53
		SD	15,609	–	0.1	–	170	1	2.4	0.05	4
		IQR	336,816–325,247	–	1.9–1.8	340,000–340,000	425–303	10–9.1	11–7.8	0.33–0.28	54–50
Cerro de Maimón (Dominican Republic)	Cerro de Maimón	Min.	270,450	1.2	B.D.L.	346,300	B.D.L.	3.1	4.8	0.36	60
	(n = 11)	Max.	316,435	3.1	2.5	346,300	71	3.9	6.6	2.0	94
		GM	296,657	1.8	1.7	346,300	71	3.4	5.6	0.86	81
		SD	14,668	0.6	0.4	–	–	0.2	0.6	0.54	11
		IQR	307,234–285,613	2.0–1.5	1.9–1.5	346,300–346,300	–	3.6–3.3	6.1–5.3	1.3–0.56	89–79

B.D.L.: Below detection limit; IQR: interquartile range; GM: geometric mean; SD: standard deviation.
aRagged ablation spectra indicate that these elements may occur as sub-microinclusions.

volcanic and subvolcanic rocks that were intruded by a series of sub-vertical, N150E-oriented andesitic and dacitic dykes and, in places, by granodiorite and diorite plutons. Volcanic rocks at María Teresa comprise basaltic andesites and andesites and less abundant rhyodacites which, akin plutonic rocks in the district, show calc-alkaline affinity (Pichardo et al., 2019). Basaltic andesites and andesites show aphanitic, porphyritic textures drawn by plagioclase and amphibole phenocrysts. Amygdaloidal and brecciated textures are also common and, towards the upper section of the sequence, pillow lavas and hyaloclastites occur. Despite that the limit between individual lava flows is mostly blurred, Pichardo et al. (2019) conclude that the locally observed bedding is horizontal to slightly W-dipping. The N160E-oriented El Abra strike-slip fault dismembered and displaced clockwise the mineralization in the 'prospective horizon' so that the Calera sector has been displaced about 500 m to the south in relation to the Mine 2 and Bubulina sectors. In addition, the N140E-oriented Sofía reverse fault has slid the western block on top of the eastern block with an approximate vertical displacement of 90 m (Fig. 2). The mineralization in the María Teresa deposit occurs mostly as N150E-oriented irregular to lenticular massive sulfide bodies and underlying stockwork structures associated with abundant alteration to sericite and quartz (Pichardo et al., 2019). Close to the contact with granodiorite intrusions chiefly to the east of the Calera zone, a mineral assemblage including cordierite and garnet porphyroblasts along with biotite, phlogopite, and tremolite is interpreted as the contact metamorphic product of the hydrothermal sericite alteration (Pichardo et al., 2019). The ore mineral assemblage includes sphalerite, chalcopyrite, tetrahedrite-group minerals, and galena, which occur along with variable proportions of pyrite ± pyrrhotite ± barite. The Sofía-D massive sulfide body is the largest in the deposit (~8 Mt grading 7.1% Zn, 1.37% Cu, 0.64% Pb, 60.3 g/t Ag; Pichardo et al., 2019) and shows clear metal zoning (Fig. 2). Metal zoning, ore mineral assemblages, and textures observed in this ore body are described below. Due to the well-defined metal zoning in Sofía-D, it was selected in this study to trace the distribution of trace elements in sphalerite and chalcopyrite in zone-refined massive sulfide bodies.

2.1.3. Geology of the Perubar deposit

The Zn-Pb-Ba Perubar deposit is located 50 km E of Lima (Fig. 1) and was exploited between 1978 and 2000 with a production of 6 Mt with an average grade of 11.8% Zn and 1.4% Pb (Polliand, 2006). The massive sulfide mineralization is hosted by an uppermost Cretaceous volcano-sedimentary sequence composed of submarine volcanic rocks and pyroclastic deposits of intermediate to felsic composition, intercalated with detrital sediments, volcaniclastic sandstones, tuffaceous mudstones, calcareous volcaniclastics, and limestones. Monzodiorite and monzogranite stocks belonging to the Coastal Batholith intruded in the area <~1 Myr after the mineralizing event causing contact metamorphism at the Perubar deposit (Polliand et al., 1999; see Fig. 3 in Polliand et al., 2005; Polliand, 2006). The hydrothermal alteration of the host rocks comprises a siliceous core in the stockwork zone that grades outward to chlorite + pyrite ± sericite; extensive quartz + sericite developed in the footwall below the sulfide lenses, as well as distal quartz + K-feldspar. The deposit consists of four main massive barite-sulfide ore bodies (Graciela, Juanita, Cecilia Norte, and Cecilia Sur). The Theoriginal (i.e., before tectonic deformation) ore zonation included a stockwork, which is now located north of the deposit, and massive mineralization that comprised pyrite(−magnetite) and pyrite-rich semi-black ores topped by a massive black ore, which graded laterally to banded barite-sulfide ores (Polliand, 2006). The ore included pyrrhotite, pyrite, marcasite, magnetite, sphalerite, galena, barite, and lesser proportions of chalcopyrite, tetrahedrite, and arsenopyrite (Polliand, 2006). In addition, during our survey, tiny amounts of molybdenite and electrum were identified (Fig. S1). Representative photomicrographs of the samples containing the analyzed sphalerite from Perubar are shown in Fig. S1. Polliand (2006) suggests that the conspicuously low proportion of chalcopyrite in the ore mineralization constrains the temperature of the mineralizing fluids <~300 °C.

2.1.4. Geology of the Palma deposit

The Zn—Pb Palma deposit is located 55 km SE of Lima and 15 km south of Perubar (Fig. 1). Ongoing exploration by Volcan Cía. Minera since 2009 has revealed a resource of 14.5 Mt including 9.6 Mt indicated at 5% Zn, 0.7% Pb, and 22 g Ag/t and 4.9 Mt inferred at 6% Zn, 1% Pb, and 21 g Ag/t, all reported with a cut-off of 3.5% Zn (Farfán et al., 2019). The mineralization is hosted in a volcano-sedimentary sequence consisting of sills and NNW-SSE trending dykes of basaltic to andesitic composition and local peperitic textures, organic matter-rich and framboidal-pyrite-bearing pelites, and shallow-water limestones. This sequence is cut by NNW-SSE-oriented felsic dykes. The igneous suite in the district displays calc-alkaline affinity (Farfán et al., 2019). Hydrothermal alteration includes deep, poorly developed sericite alteration and much widespread albite + epidote + chlorite + pyrite alteration The mineralization occurs as stacked massive sulfide bodies roughly parallel to the bedding and replaced chiefly limestone and subordinately pelitic

Mo (ppm)[a]	Ag (ppm)	Cd (ppm)	In (ppm)	Sn (ppm)	Sb (ppm)[a]	Au (ppm)[a]	Hg (ppm)	Tl (ppm)[a]	Pb (ppm)[a]	Bi (ppm)[a]
B.D.L.	3.2	3.5	11	4.3	1.4	B.D.L.	B.D.L.	0.019	1.4	0.0092
0.044	295	15	49	201	31	0.40	3.8	11	82	5.5
0.027	82	8.8	20	43	6.8	0.069	1.1	0.8	7.8	1.0
0.008	67	3.3	12	40	7.3	0.091	1.1	3.0	16.4	1.6
0.034–0.021	150–71	12–6.2	32–12	77–33	12–3.2	0.12–0.039	1.9–0.69	2.4–0.28	12–4.3	2.5–0.54
B.D.L.	3.2	3.5	11	4.3	1.4	B.D.L.	B.D.L.	0.019	1.4	0.0092
0.044	295	15	49	201	31	0.40	3.8	11	82	5.5
0.027	89	9.2	18	42	6.6	0.077	1.0	0.8	8.8	1.0
0.008	68	3.2	11	43	7.4	0.095	0.9	3.2	17.2	1.6
0.035–0.021	166–76	12–8.2	23–12	78–30	10–3.2	0.13–0.041	1.5–0.69	2.4–0.28	14–6.0	2.6–0.86
B.D.L.	44	4.1	34	43	3.6	0.016	0.57	0.62	1.5	0.45
0.033	68	9.6	44	53	17	0.075	3.7	3.4	7.9	2.5
0.025	52	6.6	37	49	7.8	0.036	1.9	1.7	3.6	1.0
0.007	10	2.4	5	4	7.2	0.029	1.5	1.1	3.2	1.0
0.028–0.022	55–48	8.4–5.4	38–34	52–47	16–3.8	0.065–0.020	3.5–1.5	2.5–1.5	7.0–1.9	1.8–0.52
5.4	8.3	B.D.L.	6.7	1.2	0.05	0.015	B.D.L.	0.026	5.1	1.5
250	33	0.59	8.7	1.8	0.34	0.13	0.27	0.42	39	10
40	18	0.45	7.7	1.5	0.16	0.043	0.17	0.078	12	3.8
69	7	0.17	0.6	0.2	0.10	0.034	0.06	0.123	12	3.4
83–23	23–15	0.53–0.41	8.1–7.3	1.6–1.4	0.25–0.10	0.071–0.027	0.21–0.14	0.15–0.042	21–7.1	8.0–2.2

and mafic and intermediate igneous rocks belonging to the lower section of the volcano-sedimentary sequence in the >250-m-thick Palma Unit (see Fig. 3 in Farfán et al., 2019). Stringer and stockwork mineralization are also documented by these authors. Farfán et al. (2019) describe that the mineralogy of the upper semi-massive sulfide bodies comprises mainly pyrite, sphalerite, galena, and barite, with subordinate pyrrhotite and chalcopyrite, while the proportion of these two minerals increases in lower massive sulfide bodies. In addition, minor amounts of arsenopyrite and marcasite were identified during this survey. The samples analyzed in this work come from the upper semi-massive sulfide bodies. Representative microphotographs of samples containing the analyzed sphalerite from Palma are presented in Fig. S2. Ore and host rock have partly undergone contact metamorphism induced by arc plutons (Farfán et al., 2019).

2.2. Geology of the Cerro de Maimón deposit, Dominican Republic

The Cerro de Maimón VMS deposit is located 70 km northwest of Santo Domingo in central Dominican Republic (Fig. 3). It stands as the only VMS deposit currently under production in the Caribbean region. It is owned and operated by Perilya Limited through its subsidiary Corporación Minera Dominicana (CORMIDOM). The Cerro de Maimón massive sulfide body contains 4.8 Mt of proven and probable reserves grading 2.54% copper, 0.96 g/t Au, and 34.9 g/t Ag (Perilya, 2020). VMS mineralization and the metallogenic evolution of the Caribbean Greater Antilles are summarized and discussed by Nelson et al. (2011) and Torró et al. (2018a). The Cerro de Maimón massive sulfide mineralization is hosted by the Aptian Maimón Formation (Fig. 3), which is composed mostly of bimodal mafic-felsic volcanic and volcaniclastic rocks of boninitic and tholeiitic affinities emplaced in the forearc portion of the nascent Caribbean island-arc (Torró et al., 2016a, 2017, 2018b). Massive sulfides and hosting volcanic rocks were deformed and metamorphosed to peak metamorphic conditions in the greenschist/blueschist facies transition (Torró et al., 2016b). The mineralization is composed of pyrite grains with both cataclastic/blow-apart and metablastic welding textures and an interstitial assemblage of chalcopyrite + sphalerite + quartz + tennantite ± galena (paragenetic sequence and photomicrographs available in Fig. 6 in Torró et al., 2016a).

3. Materials and methods

The study is based on 36 ore samples from the María Teresa (n = 24), Palma (n = 4), and Perubar (n = 5) deposits in Peru and the Cerro de Maimón deposit (n = 3) in the Dominican Republic. A list of the samples, their location, and brief textural descriptions are given in Table S1 in the Supplementary material. In the María Teresa deposit, 15 ore samples picked up at different depths along a single drill core (34-18-S) that cut the zone-refined Sofía-D sulfide body (Calera sector) have been used to monitor mineralogical and mineral geochemical variations with depth. A total of 34 thick polished sections were produced at the QEMSCAN laboratory of the Pontificia Universidad Católica del Perú (PUCP) and examined using petrographic and scanning electron (SEM) microscopy. SEM images and major element mineral compositions were acquired on an environmental SEM Thermo Fisher Quanta 650 FEI equipment with an EDAX-Octane Pro EDS microanalysis system at PUCP (Centro de Caracterización de Materiales – CAM-PUCP) and a VEGA II XMU Tescan equipment with a Bruker QUANTAX EDS microanalysis system at BIZALAB at operating conditions of 5 nA and 20 kV accelerating voltage.

Minor and trace element compositions of sphalerite and chalcopyrite were determined by means of electron microprobe (EPMA), at the University of Barcelona, and laser-ablation inductively-coupled plasma mass spectrometry (LA-ICP-MS), at the ETH Zürich, using the same equipment and methodology as described in Benites et al. (2021a). For samples from the María Teresa, Palma, and Perubar deposits, representative EPMA analyses of sphalerite and chalcopyrite are displayed in Table S2 in Supplementary material. For samples from the Cerro de Maimón deposit, representative EPMA analyses of sulfide minerals are provided in Torró et al. (2016a). LA-ICPMS data are reported in Table S3 in Supplementary material. Content statistical data for sphalerite and chalcopyrite are shown in Tables 1–2.

4. Results

4.1. Ore mineral geochemistry

Major and trace element compositions of sphalerite and chalcopyrite show, in general, a wide range of elements at measurable contents. Summaries of their compositions, including minimum, maximum, geometric mean, standard deviation, and interquartile range (IQR) values are displayed in Tables 1 and 2. Content values will be hereinafter reported as IQR unless otherwise specified. Significant effort was made to report only the content of elements whose variations respond to solid solutions and not to mixed mineral analyses by analyzing mineral volumes free of obvious inclusions and by selecting only stable signal intervals in LA-ICP-MS spectra (Fig. S3 in Supplementary material). However, it should be noted that evenly distributed nano-inclusions may

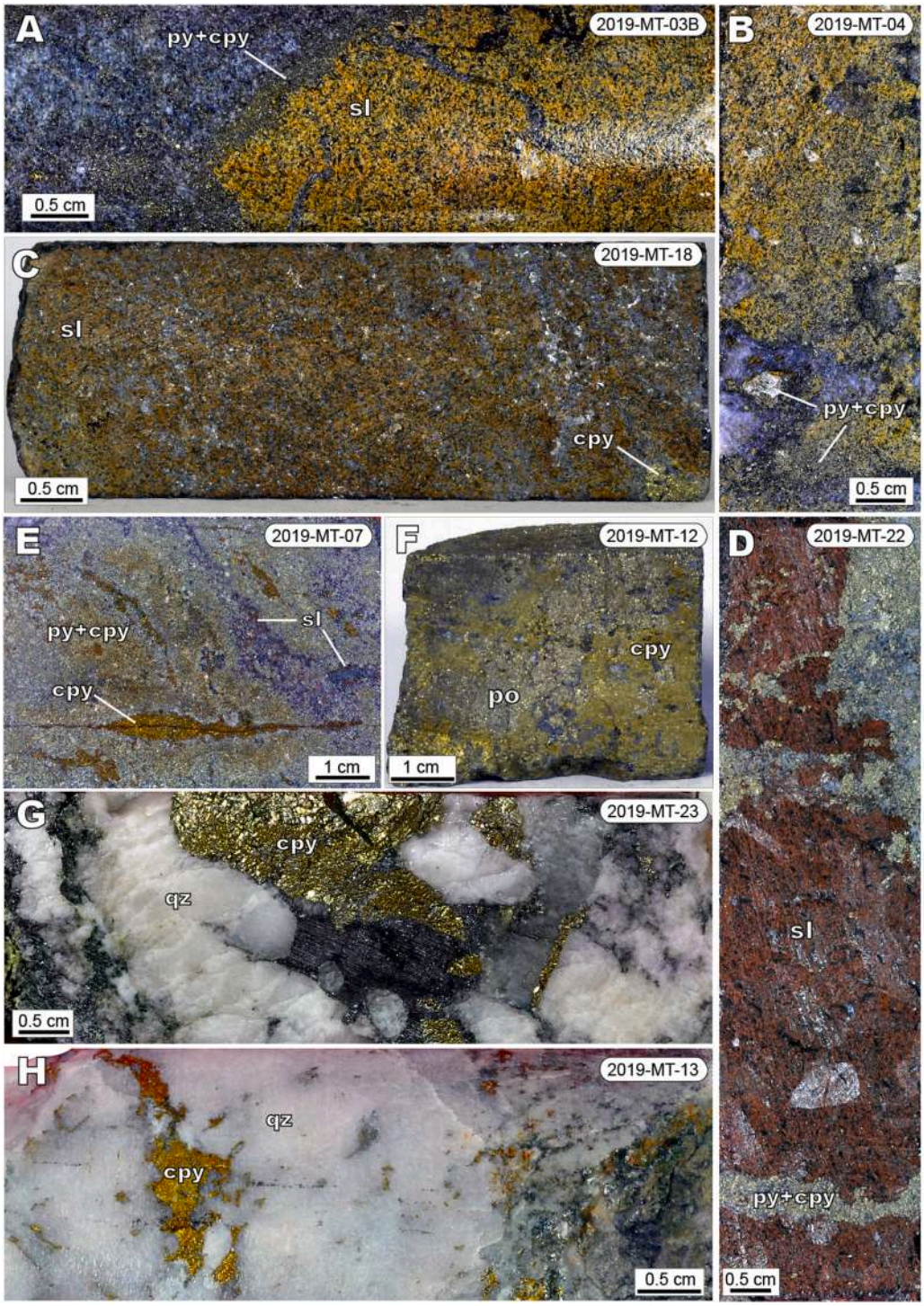

Fig. 4. Drill core photographs of sulfide mineralization from the Sofía-D massive sulfide body in the María Teresa VMS deposit. (A–C) Semi-massive sulfide ore dominated by medium-grained pale-brown sphalerite grains partially replaced by an assemblage of pyrite and chalcopyrite. (D) Massive sulfide ore composed of coarse-grained red-brownish sphalerite grains cut by irregular veinlets of chalcopyrite and pyrite. (E) Dark red, medium-sized sphalerite partially replaced by an assemblage of pyrite and chalcopyrite and the whole assemblage cut by thin, irregular chalcopyrite veinlets. (F) Coarse-grained pyrrhotite and chalcopyrite in a sample picked up close to a contact with a porphyritic andesitic dyke. (G) Silicified volcaniclastic rock with chalcopyrite mineralization along clast contacts. (F) Irregular veinlets of chalcopyrite in a silicified intrusive rock. Key: cpy = chalcopyrite; po = pyrrhotite; py = pyrite; qz = quartz; sl = sphalerite. (For interpretation of the references to color in this figure legend, the reader is referred to the web version of this article.)

also yield flat ablation profiles (e.g., Gregory et al., 2015) and that, therefore, the possibility of mixed mineral analyses cannot be completely discarded due to the relatively low spatial resolution of the used methods.

4.1.1. Sphalerite

Iron, Mn, Cd, Hg, and Cu (Fig. S3 in Supplementary material) yield smooth and constant ablation profiles. Studied sphalerite shows a relatively wide range of Fe contents in samples from the María Teresa deposit (40675–17,122 ppm), which are higher than in samples from the Cerro de Maimón (585–535 ppm) and generally lower than in samples from the Perubar (67570–39,965 ppm) and Palma (63423–30,015 ppm) deposits (Table 1). Manganese also shows a relatively wide range of contents in sphalerite from María Teresa (2343–326 ppm), which overlaps with the composition of grains from Cerro de Maimón (482–446 ppm) and are in general lower than in grains from Perubar (5964–907 ppm) and Palma (7751–6734 ppm). The contents of Cd are constantly high in all analyzed sphalerite samples (7373–5290 ppm in María Teresa, 6665–4297 ppm in Perubar, 7109–4782 ppm in Palma, and 3829–3574 ppm in Cerro de Maimón). Mercury contents are higher in sphalerite from the Palma (667–593 ppm) and María Teresa (448–326 ppm) deposits than in sphalerite from the Perubar (107–18

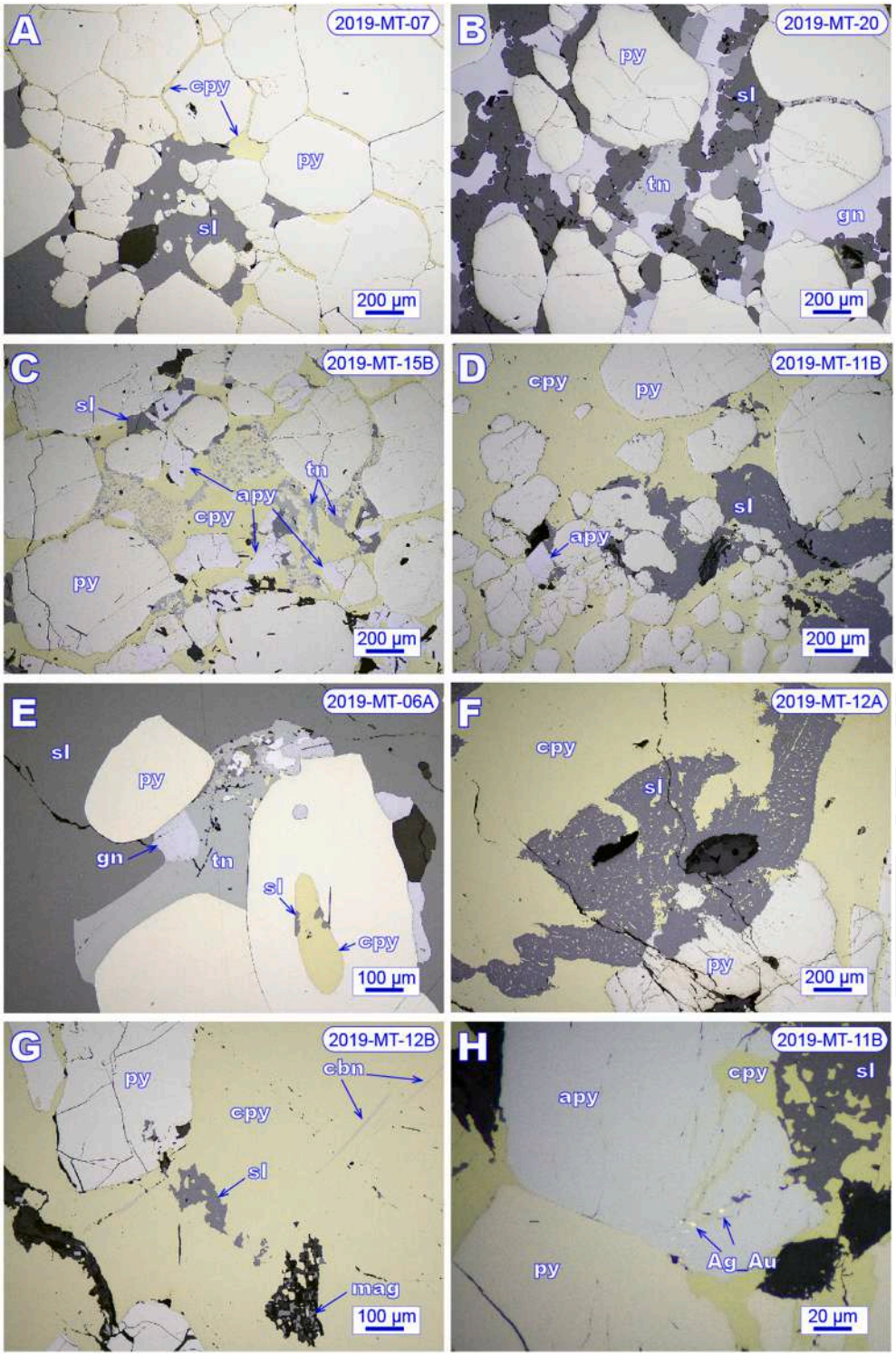

Fig. 5. Photomicrographs (reflected light) of textural features in the samples from the Sofía-D massive sulfide bodies in the María Teresa deposit used for this study. (A) Foam textured pyrite with triple junctions at 120° along with interstitial chalcopyrite and sphalerite. (B) Anhedral roundish and subroundish pyrite grains with irregular fractures are surrounded by an assemblage of sphalerite, galena and tennantite. (C–D) Anhedral, sub-roundish pyrite and subhedral arsenopyrite grains both with internal fractures with interstitial chalcopyrite, sphalerite, and tennantite. (E) Detail of a sphalerite-galena-tennantite intergrowth between roundish pyrite grains; note the general foam texture described by the contacts between all phases. (F) Pervasive replacement of sphalerite by chalcopyrite along borders and as fines disseminations (chalcopyrite disease texture). (G) Detail of chalcopyrite with exsolutions of sharply bounded cubanite laths. (H) Detail of minute inclusions of auriferous silver in chalcopyrite veinlets crosscutting arsenopyrite. Key: apy = arsenopyrite; Ag_Au = auriferous silver; cbn = cubanite; cpy = chalcopyrite; mag = magnetite; po = pyrrhotite; py = pyrite; qz = quartz; sl = sphalerite; tn = tennantite.

ppm) and Cerro de Maimón (26–22 ppm) deposits. The content of Cu is generally higher in sphalerite samples from the Cerro de Maimón (138–113 ppm) and María Teresa (98–36 ppm) deposits than in sphalerite samples from the Perubar (41–25 ppm) and Palma (31–11 ppm) deposits.

At generally lower contents and also showing smooth ablation spectra are Ag, In, Ge, and Ga (Table 1; Fig. S3 in Supplementary material). Silver content ranges mostly overlap in sphalerite grains from the four studied deposits (12–4.2 ppm in María Teresa, 7.1–3.6 ppm in Perubar, 17–3.8 ppm in Palma, and 4.2–3.1 ppm in Cerro de Maimón). The contents of In are in general much higher in sphalerite from the María Teresa deposit (68–4.4 ppm, up to 415 ppm) than in sphalerite from the Cerro Maimón (10–9.5 ppm), Perubar (2.3–0.78 ppm) and Palma (0.22–0.0091 ppm; Table 1) deposits. Gallium contents are higher in sphalerite from the Cerro de Maimón deposit (95–78 ppm, up to 96 ppm) than in sphalerite from the María Teresa (32–11 ppm, up to 94 ppm), Perubar (30–4.7 ppm), and Palma (2.4–1.9 ppm) deposits. Germanium contents are in general very low in analyzed sphalerite grains (0.65–0.17 ppm in María Teresa, 0.19–0.15 ppm in Perubar, 3.5–0.16 ppm in Palma, and 1.2–0.68 ppm in Cerro de Maimón).

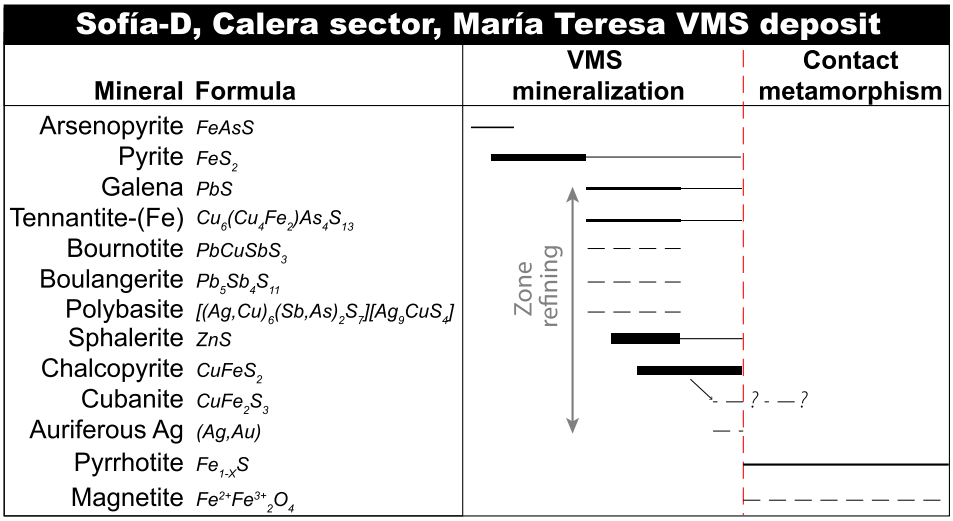

Fig. 6. Paragenetic sequence for the Sofía-D sulfide body in the Calera area, María Teresa VMS deposit. Thick bars indicate higher abundances and dashed lines, lesser abundances.

The content of other elements are in general very low (Pb: 9.3–1.1 ppm; Sb: 3.7–0.31 ppm; Tl: 0.66–0.045; Sn: 0.49–0.23 ppm; Bi: 0.60–0.0055 ppm; detailed results for individual deposits are available in Table 1). Some analyses show slightly ragged ablation spectra (Fig. S1 in Supplementary material).

4.1.2. Chalcopyrite

Chalcopyrite grains from the María Teresa and Cerro de Maimón VMS deposits have been analyzed. Zinc, Ag, Sn, Cd, Se, In, Ge, and Ga show relatively constant ablation profiles (Fig. S3 in Supplementary material). Zinc is the trace element most highly concentrated in studied sphalerite grains; its contents are higher in chalcopyrite from the María Teresa deposit (425–194 ppm) than in chalcopyrite from the Cerro de Maimón deposit (a single analysis >d.l. yields a concentration of 71 ppm; Table 2). Silver, Sn, and Cd are relatively enriched in chalcopyrite grains from the María Teresa deposit (150–71 ppm Ag, 77–33 ppm Sn, 12–6.2 ppm Cd) relative to grains from the Cerro de Maimón deposit (23–15 ppm Ag, 1.6–1.4 ppm Sn, 0.53–0.41 ppm Cd). Selenium is more concentrated in chalcopyrite from the Cerro de Maimón deposit (89–79 ppm) than in chalcopyrite from the María Teresa deposit (31–19 ppm). Indium values are relatively constant in analyzed grains from the studied deposits and are systematically higher in chalcopyrite from María Teresa (32–12 ppm) than in chalcopyrite from Cerro de Maimón (8.1–7.3 ppm). The contents of Ga and Ge are in general lower than those of In (9.2–2.6 ppm Ga and 4.3–0.66 ppm Ge in María Teresa; 3.6–3.3 ppm Ga and 6.1–5.3 ppm Ge in Cerro de Maimón).

Downhole ablation spectra reveal very irregular profiles for Mo and Au and in some samples, slightly irregular profiles for Tl, Sb, and Bi (Fig.

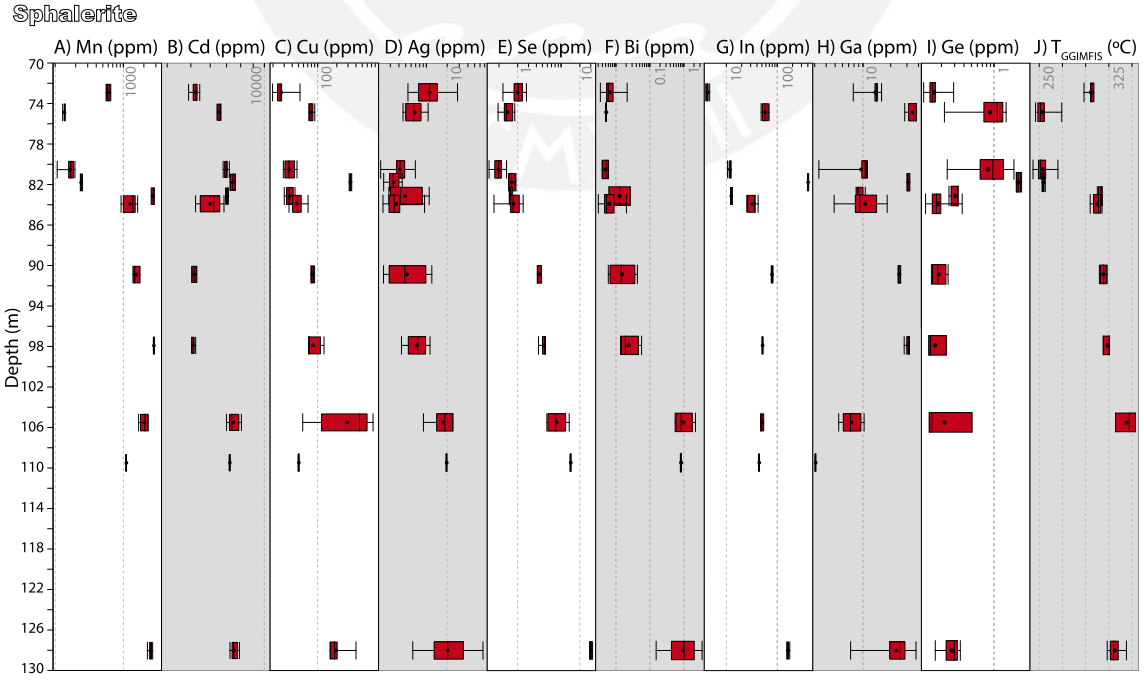

Fig. 7. Boxplots of log-transformed element contents (A-I) and crystallization temperature (J) according to the GGIMFis geothermometer of Frenzel et al. (2016) for sphalerite at different depths along the drill core 34-18-S in the mine section 300 across the Sofía-D massive sulfide body, María Teresa deposit (LA-ICP-MS data). Box-and-whisker plots provide IQR (box), 1.5 IQR (whiskers), median (line), and outliers (circles).

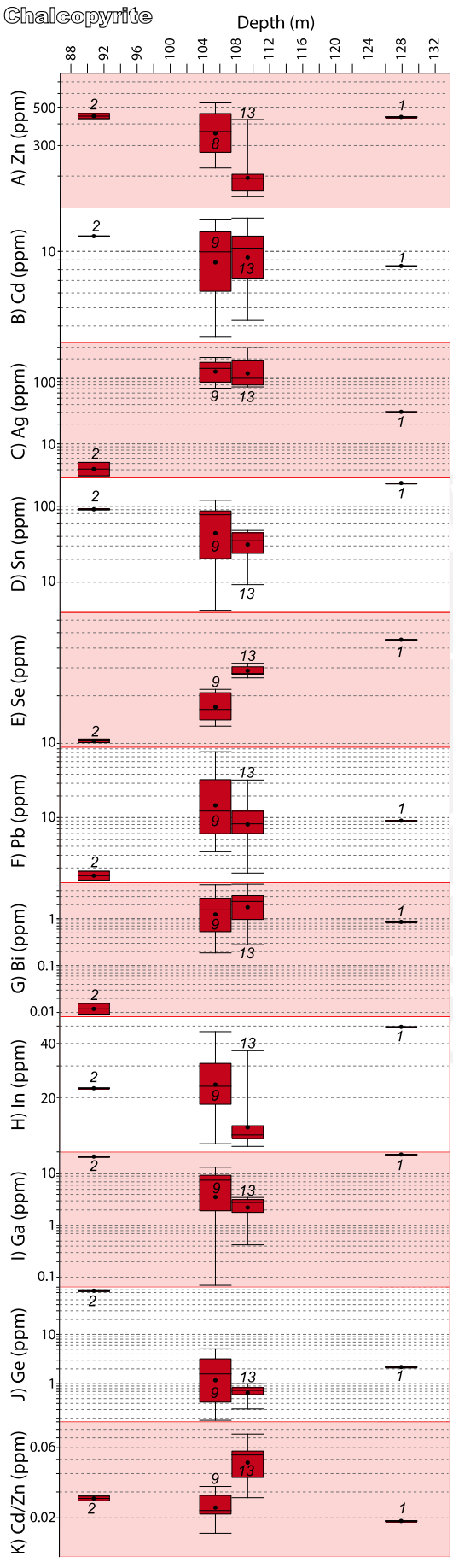

Fig. 8. Boxplots of log-transformed element contents in chalcopyrite at different depths along the drill core 34-18-S in the mine section 300 across the Sofía-D massive sulfide body, Calera sector, María Teresa deposit (LA-ICP-MS data). Box-and-whisker plots provide IQR (box), 1.5 IQR (whiskers), median (line), and outliers (circles).

S3 in Supplementary material). Molybdenum yields relatively erratic contents, which are much higher in analyzed chalcopyrite from Cerro de Maimón (83–23 ppm) than in chalcopyrite from María Teresa (0.034–0.021 ppm, and mostly <d.l.). The contents of Tl (<11 ppm), Sb (<31 ppm), Bi (<10 ppm), and Au (<0.40 ppm) are relatively low (Table 2).

4.2. *Metal zonation, mineralogy and trace-element distribution patterns in the zone-refined Sofía-D body*

The metal zonation in Sofía-D massive sulfide body includes, bottom to top, i) a Cu zone composed dominantly of chalcopyrite and lesser amounts of sphalerite grading downward to massive pyrite; ii) a Zn zone in which sphalerite is the most abundant phase and appears along with lesser amounts of galena and chalcopyrite and minor fahlore; and iii) a Pb – Zn – Ag zone with abundant galena and sphalerite, and lesser proportions of fahlore and barite (Fig. 2). In detail, this zoning is also recognized from the steep feeders outwards.

On the hand sample scale, sphalerite occurs as mm- to cm-sized grains of yellow-pale brown (Fig. 4A–C) and red-brownish (Fig. 4D–E) color. In places, the massive sphalerite aggregates are cut by irregular, chalcopyrite-rich veinlets (Fig. 4A, D–E). In the eastern part of the María Teresa deposit, i.e., close to the granodiorite stock as is the case for the Sofia D ore body, coarse-grained pyrrhotite ± magnetite is observed and, similarly to in Perubar (see Vidal, 1987; Polliand et al., 1999), interpreted as the metamorphic product after pyrite. An example is shown in Fig. 4F coming from a 20-cm-wide band composed of coarse-grained pyrrhotite ± magnetite at the contact with and andesitic dyke. In volcaniclastic rocks in the immediate host of the Sofía-D body, chalcopyrite selectively replaced some of the clasts and the matrix (Fig. 4G). Silicified dykes that cut the Sofía-D body typically contain patches and irregular veinlets of chalcopyrite (Fig. 4H).

Under the petrographic microscope, pyrite grains, which have sizes typically in the range between 100 and 600 μm, draw a variety of textures including anhedral isolated grains with roundish and embayed outlines, aggregates of several grains often with foam equilibrium textures (i.e., contacts at 120°) and, in some cases, internal irregular fractures (Fig. 5A–D). Arsenopyrite is relatively scarce in the studied samples and appears as isolated euhedral and subhedral fractured grains and sizes in the range between 50 and 200 μm (Fig. 5C–D). The other sulfides, fahlore (tennantite-(Fe) ± argentian tetrahedrite), and traces of other sulfosalts such as bournonite, boulangerite, and polybasite (petrographic observations complemented with EDS analyses) occupy interstitial space between, and line porosity and fractures within, pyrite ± arsenopyrite grains (Fig. 5). According to these observations, pyrite and arsenopyrite crystallized early in the paragenetic sequence (Fig. 6) and, in places, underwent thermal re-equilibration connected to dyke and granodiorite intrusions (Pichardo et al., 2019). Internal fractures of pyrite and arsenopyrite (Fig. 5C) also point to fragile deformation, probably due to movements along the Sofía reverse fault (Fig. 2). Sphalerite grains in the Zn zone show clean surfaces (Fig. 5B,E), whereas in the Cu zone they have been pervasively replaced by chalcopyrite and show dense chalcopyrite disease textures (Fig. 5D, F–G). Chalcopyrite floods the interstitial space between pyrite ± arsenopyrite in the Cu zone along with relicts of sphalerite and in places shows sharply bounded exsolutions of cubanite laths up to 150 μm in length (Fig. 5G). Auriferous silver (73 wt% Ag, 27 wt% Au, EDS analysis) has been observed in one sample and appears as minute grains (<2 μm) in fractured arsenopyrite along with chalcopyrite (Fig. 5H).

(caption on next column)

Table 3
Summary of LA-ICP-MS data for sphalerite from subduction-related VMS deposits reported in the literature.

Deposit}	Location}	*ppm*}	Mn}	Fe}	Cu}	Ga}	Ge}	As}	Se}
Vorta	Romania	Max	761	2617	719	363	23	n.a.	1.4
(n = 8)		Min	165	917	131	75	2.7	n.a.	0.82
		GM	485	1844	334	118	8.0	n.a.	1.1
		SD	201	584	193	100	7.2	n.a.	0.18
		IQR	650–424	2404–1524	475–274	171–79	12–5.8	n.a.	1.2–1.0
Eskay Creek	Canada	Max	4744	7112	3483	857	14	1550	4.1
(n = 12)		Min	2296	3880	67	19	0.47	1	1.3
		GM	3206	4814	356	86	1.2	27	2.1
		SD	648	900	1017	228	3.7	435	1.3
		IQR	3437–3113	5284–4316	835–116	123–61	1.4–0.89	196–3.9	3.3–1.5
Zinkgruvan	Sweden	Max	532	33,261	5.1	2.8	1.2	n.a.	1.9
(n = 5)		Min	499	31,735	1.9	1.9	0.82	n.a.	1.9
		GM	513	32,330	3.3	2.2	1.1	n.a.	1.9
		SD	14	737	1.2	0.38	0.15	n.a.	–
		IQR	524–502	33,006–31,751	4.0–3.1	2.4–1.9	1.2–1.1	n.a.	1.9–1.9
Marketorp	Sweden	Max	18,729	119,418	14,368	9.6	13	n.a.	36
(n = 8)		Min	1684	86,959	1414	0.61	1.8	n.a.	29
		GM	2606	96,260	3020	1.5	2.7	n.a.	33
		SD	5930	12,125	4246	3.1	3.7	n.a.	1.8
		IQR	2373–1714	100,257–88,877	3290–2281	1.8–0.87	2.6–1.9	n.a.	34–33
Sauda	Norway	Max	1449	120,205	44	8.6	1.4	n.a.	109
(n = 10)		Min	874	69,576	22	4.1	0.86	n.a.	89
		GM	959	77,585	28	5.5	1.0	n.a.	94
		SD	170	14,797	8.6	1.4	0.16	n.a.	6.0
		IQR	939–903	75,796–72,800	37–23	6.0–4.7	1.1–0.92	n.a.	96–90
Çayeli	NE Turkey	Max	486	182,759	210,618	n.a.	n.a.	7261	62
(n = 40)		Min	0.35	8.0	65	n.a.	n.a.	0.19	0.13
		GM	22	2857	9638	n.a.	n.a.	345	7.1
		SD	102	32,933	41,584	n.a.	n.a.	1874	12
		IQR	83–5.2	16,904–822	35,768–6982	n.a.	n.a.	1693–275	13–5.0
Laochang	S China	Max	4111	154,203	2020	117	15	36	4.0
(n = 30)		Min	2626	121,694	119	2.3	2.1	0.33	0.62
		GM	3040	130,599	211	15	3.8	2.2	1.6
		SD	364	7814	339	24	2.5	9.7	1.1
		IQR	3255–2724	137,135–125,803	254–151	24–8.9	3.9–2.9	4.1–0.93	2.5–1.0

B.D.L.: Below detection limit; n.a.: not analyzed; GM: geometric mean; SD: standard deviation; IQR: interquartile range.

The systematic sampling developed along the drill core 34-18-S from 72.85 to 128 m (Table S1 in the Supplementary material) allows for the assessment of vertical trends in trace-element contents in sphalerite and chalcopyrite. Bottom to top in sphalerite, there is a relatively sustained decrease in the contents of Mn, Cu, Se, Bi, and In and an increase of Ge, and the contents of elements such as Cd and Ga show irregular distributions (Fig. 7A–G). The contents of In significantly decrease from sample 2019-MT-015 (128 m, 167–158 ppm) to sample 2019-MT-001 (72.85 m, 4.4–4.1 ppm), although the maximum contents occur in sample 2019-MT-004 (81.4 m, 409–399 ppm; Fig. 7G). The distribution of Cu contents almost mimics that of In, with a decrease from sample 2019-MT-015 (128 m, 203–160 ppm) to sample 2019-MT-001 (72.85 m, 27–24 ppm), although with maximum contents at intermediate depths in samples 2019-MT-004 (81.4 m, 335–321 ppm) and 2019-MT-011 (105.5 m, 597–115 ppm; Fig. 7C). Germanium contents show a moderately irregular distribution pattern with a general increase in its content from sample 2019-MT-015 (128 m, 0.33–0.23 ppm) to sample 2019-MT-002 (74.6 m, 1.3–0.73 ppm; Fig. 7I). As for chalcopyrite, vertical distribution patterns are mostly irregular (Fig. 8). The most remarkable exception is Se, which content tends to decrease steadily at shallower levels (45 ppm – single value – in sample 2019-MT-015 at 128 m, 31–27 ppm in sample 2019-MT-012 at 109.4 m, 11–10 ppm in sample 2019-MT-007 at 90.5 m; Fig. 8E). An opposite trend is defined by the content of Ge, with general enrichment from deeper (2.2 ppm – single value – in sample 2019-MT-015 at 128 m, 0.84–0.60 ppm in sample 2019-MT-012 at 109.4 m,) to shallower (80–74 ppm in sample 2019-MT-007at 90.5 m) chalcopyrite samples (Fig. 8J). Although probably hosted as sub-microscopic mineral inclusions, the content of Bi in chalcopyrite also shows significant variation and tends to increase with depth (Fig. 8G).

5. Discussion

5.1. Trace-element budget in sphalerite and chalcopyrite from arc-hosted VMS deposits

The minor and trace element contents measured in sphalerite and chalcopyrite from the Palma, Perubar, María Teresa (Perú), and Cerro de Maimón (Dominican Republic) VMS deposits will be compared along the following lines with available data from other VMS deposits, and particularly with those formed in arc systems. We have compared our results with the comprehensive compilation by Monecke et al. (2014) of whole-rock and mineral geochemical data from both active seafloor massive sulfide (SMS) and fossil equivalent deposits emplaced in a variety of tectonic settings worldwide.

Sphalerite from the four investigated deposits yields fairly variable Fe contents (Table 1), the content of the other analyzed trace elements being largely subordinated to that of Fe. The content of Fe in sphalerite samples from the Cerro de Maimón deposit analyzed in this study is particularly low (Table 1); a more complete geochemical dataset based on EPMA analyses on sphalerite samples from this deposit reported by Torró et al. (2016a) indicates average Fe contents of 1.16 wt%. Iron contents in the studied deposits are compatible with sphalerite crystallized in intermediate to high-intermediate sulfidation environments in equilibrium with pyrite (Barton and Toulmin, 1966; Hannington and Scott, 1989). Co-crystallization of fahlore (tennantite and tetrahedrite) along with sphalerite in the studied ore samples is a further indication of intermediate-sulfidation state of the hydrothermal mineralizing fluids. Similar Fe contents to those in the studied Andean VMS deposits are reported in sphalerite samples from the Zinkgruvan, Marketorp, and Sauda VMS deposit (Table 3 and references therein). Iron contents

Mo}	Ag}	Cd}	In}	Sn}	Sb}	Hg}	Tl}	Pb}	Bi}	Reference}
149	21	5088	0.060	0.24	17	n.a.	1.1	3426	0.71	Cook et al. (2009)
8.0	1.4	4169	0.040	0.050	0.040	n.a.	0.010	0.46	0.020	
40	3.7	4734	0.049	0.080	1.1	n.a.	0.034	12	0.16	
50	6.7	337	0.014	0.072	5.7	n.a.	0.50	1201	0.27	
71–20	5.3–2.0	5044–4562	0.055–0.045	0.080–0.055	2.3–0.75	n.a.	0.040–0.010	68–2.1	0.49–0.085	
31	2785	4955	14	31	117,467	n.a.	21	50,955	0.19	Cook et al. (2009)
0.15	6.8	2720	0.10	2.6	5.1	n.a.	0.081	1.2	0.020	
0.63	102	3796	0.29	9.1	1034	n.a.	0.83	467	0.041	
8.7	872	679	3.9	11	33,692	n.a.	7.1	15,639	0.056	
0.77–0.29	575–15	4394–3294	0.45–0.10	19.8–5.2	31,973–33	n.a.	2.3–0.17	17,228–13	0.053–0.028	
n.a.	13	3943	0.32	0.25	4.1	n.a.	n.a.	193	0.15	Cook et al. (2009)
n.a.	4.6	3661	0.26	0.080	0.12	n.a.	n.a.	1.4	0.060	
n.a.	6.0	3811	0.29	0.13	0.54	n.a.	n.a.	8.0	0.094	
n.a.	3.5	126	0.026	0.077	1.7	n.a.	n.a.	84	0.033	
n.a.	6.1–4.6	3933–3718	0.31–0.27	0.21–0.090	1.4–0.24	n.a.	n.a.	15–2.8	0.10–0.080	
0.68	34	3619	28	0.81	0.080	n.a.	0.30	29	74	Cook et al. (2009)
0.11	7.4	2968	25	0.090	0.040	n.a.	0.024	0.81	2.2	
0.27	12	3246	26	0.20	0.057	n.a.	0.072	7.1	13	
0.40	8.8	191	1.1	0.26	0.019	n.a.	0.10	9.6	24	
0.54–0.25	14–8.7	3304–3135	27–26	0.29–0.13	0.070–0.040	n.a.	0.11–0.045	17–6.5	30–4.3	
0.17	5.5	3488	42	1.3	0.10	n.a.	n.a.	n.a.	0.99	Cook et al. (2009)
0.17	2.4	1973	27	0.27	0.010	n.a.	n.a.	n.a.	0.12	
0.17	3.7	2170	29	0.56	0.018	n.a.	n.a.	n.a.	0.31	
–	1.0	455	4.4	0.38	0.035	n.a.	n.a.	n.a.	0.27	
0.17–0.17	4.5–3.1	2117–2031	30–28	0.97–0.38	0.020–0.010	n.a.	n.a.	n.a.	0.47–0.18	
222	450	8957	n.a.	512	3354	n.a.	97	171,820	254	Revan et al. (2014)
0.030	0.80	1051	n.a.	0.43	0.68	n.a.	0.030	8.0	B.D.L.	
5.0	51	3234	n.a.	14	141	n.a.	5.2	727	–	
45	98	1936	n.a.	81	632	n.a.	20	26,976	–	
18–0.99	138–40	3430–2636	n.a.	44–4.4	683–52	n.a.	13–4.9	2123–549	113–6.8	
n.a.	10	9600	566	38	4.1	n.a.	2.6	556	0.050	Ye et al. (2011)
n.a.	4.8	8306	66	2.2	B.D.L.	n.a.	0.0060	0.30	B.D.L.	
n.a.	6.7	8736	184	5.6	–	n.a.	0.19	2.9	–	
n.a.	1.3	240	89	6.9	–	n.a.	0.61	101	–	
n.a.	7.5–5.9	8853–8562	235–164	7.7–3.9	1.6–0.10	n.a.	0.72–0.053	9.2–0.58	0.010–0.010	

similar to those found in sphalerite from the Cerro de Maimón deposit are reported in the Vorta, Eskay Creek, and Çayeli VMS deposits. In contrast, sphalerite from the VMS Laochang deposit (South China) systematically yields higher Fe contents.

The relatively high content of Cd in sphalerite from the studied deposits (Table 1) are comparable with those in sphalerite from other VMS deposits such as Vorta, Eskay Creek, Zinkgruvan, Marketorp, and Laochang, and higher than in Sauda (Table 3). Cadmium contents of several hundreds of parts per million are typical of SMS emplaced in arc settings compared to contents in the range of some tens of parts per million in those emplaced in mid-ocean ridge systems, sphalerite and wurtzite bein the main Cd hosts in VMS deposits according to Monecke et al. (2014). According to our (Table 1) and previous (Table 3) data, Cd in sphalerite from VMS deposits in arc systems typically yields contents of several thousands of parts per million. The content of Hg varies between some tens (Perubar and Cerro de Maimón) and some hundreds (María Teresa and Palma) of parts per million in the studied sphalerite samples; the content of Hg is not provided for sphalerite from other VMS deposits in arc systems in the revised literature. Petersen et al. (2014) reported contents between <0.02 and 7.4 wt% Hg (median = 0.37 wt% Hg; EPMA data) in sphalerite from the Palinuro SMS deposit in the Aeolian arc (transitional arc setting). Monecke et al. (2014) found out that the content of Hg in SMS is higher in mineralization emplaced in arc volcanoes and rifted arcs (some tens of ppm) relative to mineralization emplaced in back-arc spreading centers and mid-ocean ridges; also, that Hg usually shows a strong positive correlation with Sb in mineralized samples from SMS which normally results from the chief concentration of Hg in tetrahedrite and tennantite over other ore minerals. The contents of Sb in the studied sphalerite are mostly in the 1–10 ppm range or below (Table 1), similar to sphalerite from other VMS mineralization such as Vorta, Zinkgruvan, and Laochang, and lower than in Eskay Creek and Çayeli (Table 3). The content of Tl in the studied sphalerite samples is normally below 1 ppm (Table 1), similar to sphalerite from other VMS deposits with the exception of Çayeli, in which the content of Tl is much higher (13–4.9 ppm; Table 3). The contents of Sb and Tl are usually higher in sulfide samples from SMS mineralization emplaced in arc volcanoes and rifted arcs than in SMS mineralization emplaced in back-arc spreading centers and mid-ocean ridges according to data compiled by Monecke et al. (2014).

The studied sphalerite samples yield In contents largely in the range between <1 ppm and some tens of parts per million (Table 1), similar to sphalerite from Vorta, Eskay Creek, Zinggruvan, Marketorp, and Sauda, and lower than in Laochang (Table 3). The measured In contents are also much lower than in sphalerite from the Neves Corvo VMS deposit (up to 2.1 wt%, EPMA data: Carvalho et al., 2018). The contents of Ga in the sphalerite samples analyzed here are largely of the same order of magnitude (from a few ppm to ~100 ppm) as contents reported for sphalerite from other VMS deposits (Table 3), whereas the contents of Ge (mostly <1 ppm) are generally lower than those reported in the literature. The contents of In, Ge, and Ga are mostly indistinguishably low in SMS sulfides irrespective of their tectonic environment of emplacement (Monecke et al., 2014).

In the studied chalcopyrite samples from the Andean VMS deposits, the content of Zn is of some hundreds of parts per million (Table 2), similar to chalcopyrite from Vorta, Sulitjelma, and Kutlular, and lower than in chalcopyrite from Çayeli (Table 4 and references therein); Zn content in sphalerite from the Cerro de Maimón deposit is significantly lower. The contents of Ag are mostly in the range between a few to some hundreds of parts per million in the analyzed chalcopyrite (Table 2), like chalcopyrite from VMS reported in the literature (Table 4). Selenium contents in the studied chalcopyrite samples are of some tens of parts per million (Table 2), and therefore lower than Se contents in chalcopyrite

Table 4
Summary of LA-ICP-MS data for chalcopyrite from subduction-related VMS deposits reported in the literature.

Deposit	Location	*ppm*	Co	Ni	Zn	Ga	Ge	As	Se	Mo	Ag	Cd	In	Sn	Sb	Au	Hg	Tl	Pb	Bi	Reference
Vorta (n = 8)	Romania	Min	12	n.a.	199	0.11	n.a.	2.8	n.a.	n.a.	18	0.48	0.0049	0.19	0.11	0.0080	0.34	0.014	6.1	0.010	George et al. (2018)
		Max	12	n.a.	538	2.2	n.a.	5.8	n.a.	n.a.	92	3.2	0.76	0.79	5.6	0.034	2.6	0.17	53	2.2	
		GM	12	n.a.	391	0.71	n.a.	4.1	n.a.	n.a.	45	1.6	0.044	0.39	2.0	0.021	0.62	0.068	14	0.075	
		SD	–	n.a.	130	0.70	n.a.	1.3	n.a.	n.a.	23	1.0	0.43	0.28	1.8	0.012	0.82	0.061	26	1.3	
		IQR	12–12	n.a.	479–395	1.4–0.49	n.a.	5.2–3.2	n.a.	n.a.	55–41	2.2–1.3	0.39–0.014	0.73–0.23	3.8–2.8	0.033–0.019	0.82–0.38	0.14–0.058	30–7.1	1.1–0.015	
Sulitjelma (n = 120)	Norway	Min	0.016	0.049	97	0.017	n.a.	1.2	4.4	n.a.	5.1	0.79	0.301	0.091	0.025	0.0031	0.051	0.0016	0.071	0.019	George et al. (2018)
		Max	28	5.1	861	19	n.a.	5.3	926	n.a.	331	58	26	75	15	0.76	0.74	3.0	28	11	
		GM	0.8	0.42	381	0.43	n.a.	2.4	101	n.a.	71	10	2.1	4.6	0.7	0.032	0.20	0.015	0.93	0.41	
		SD	3.7	1.3	195	4.1	n.a.	1.1	267	n.a.	95	16	6.1	26	3.7	0.14	0.17	0.50	5.4	2.2	
		IQR	2.6–0.27	1.0–0.20	569–329	2.3–0.098	n.a.	3.4–1.7	202–51	n.a.	201–32	29–3.1	6.7–0.61	51–0.43	2.0–0.18	0.088–0.013	0.32–0.12	0.089–0.0036	1.7–0.37	0.89–0.15	
Çayeli (n = 69)	NE Turkey	Min	0.010	B.D.L.	7.0	n.a.	n.a.	B.D.L.	3.6	0.11	4.0	0.040	n.a.	1.1	B.D.L.	B.D.L.	n.a.	0.010	4.0	0.030	Revan et al. (2014)
		Max	166	200	407,977	n.a.	n.a.	5008	408	290	2549	2194	n.a.	96	3524	25	n.a.	243	244,075	1000	
		GM	0.7	–	1305	n.a.	n.a.	–	62	15	46	12	n.a.	15	–	–	n.a.	1.2	307	35	
		SD	27	–	69,136	n.a.	n.a.	–	124	65	375	366	n.a.	24	–	–	n.a.	38	30,588	217	
		IQR	1.8–0.17	7.0–0.38	30,530–56	n.a.	n.a.	656–5.6	225–17	54–4.6	132–12	163–1.3	n.a.	39–8.4	117–2.2	0.64–0.063	n.a.	14–0.14	1813–43	170–7.0	
Kutlular (n = 9)	NE Turkey	Min	B.D.L.	0.010	70	n.a.	n.a.	1.7	220	0.010	1.1	0.67	n.a.	9.1	0.50	0.030	n.a.	0.020	5.0	16	Revan et al. (2014)
		Max	0.90	0.34	5891	n.a.	n.a.	20	340	2223	45	33	n.a.	31	7.8	1.3	n.a.	6.6	494	1764	
		GM	–	0.037	304	n.a.	n.a.	5.4	281	7.7	6.8	2.7	n.a.	18	1.4	0.17	n.a.	0.21	37	93	
		SD	–	0.14	1885	n.a.	n.a.	5.4	46	795	18	10	n.a.	7.1	2.5	0.48	n.a.	2.5	186	587	
		IQR	0.26–0.010	0.21–0.010	751–98	n.a.	n.a.	7.3–2.8	334–258	265–0.20	7.0–4.14	5.6–0.99	n.a.	22–15	1.4–0.82	0.21–0.090	n.a.	0.59–0.030	55–16	94–50	

B.D.L.: Below detection limit; n.a.: not analyzed; GM: geometric mean; SD: standard deviation; IQR: interquartile range.

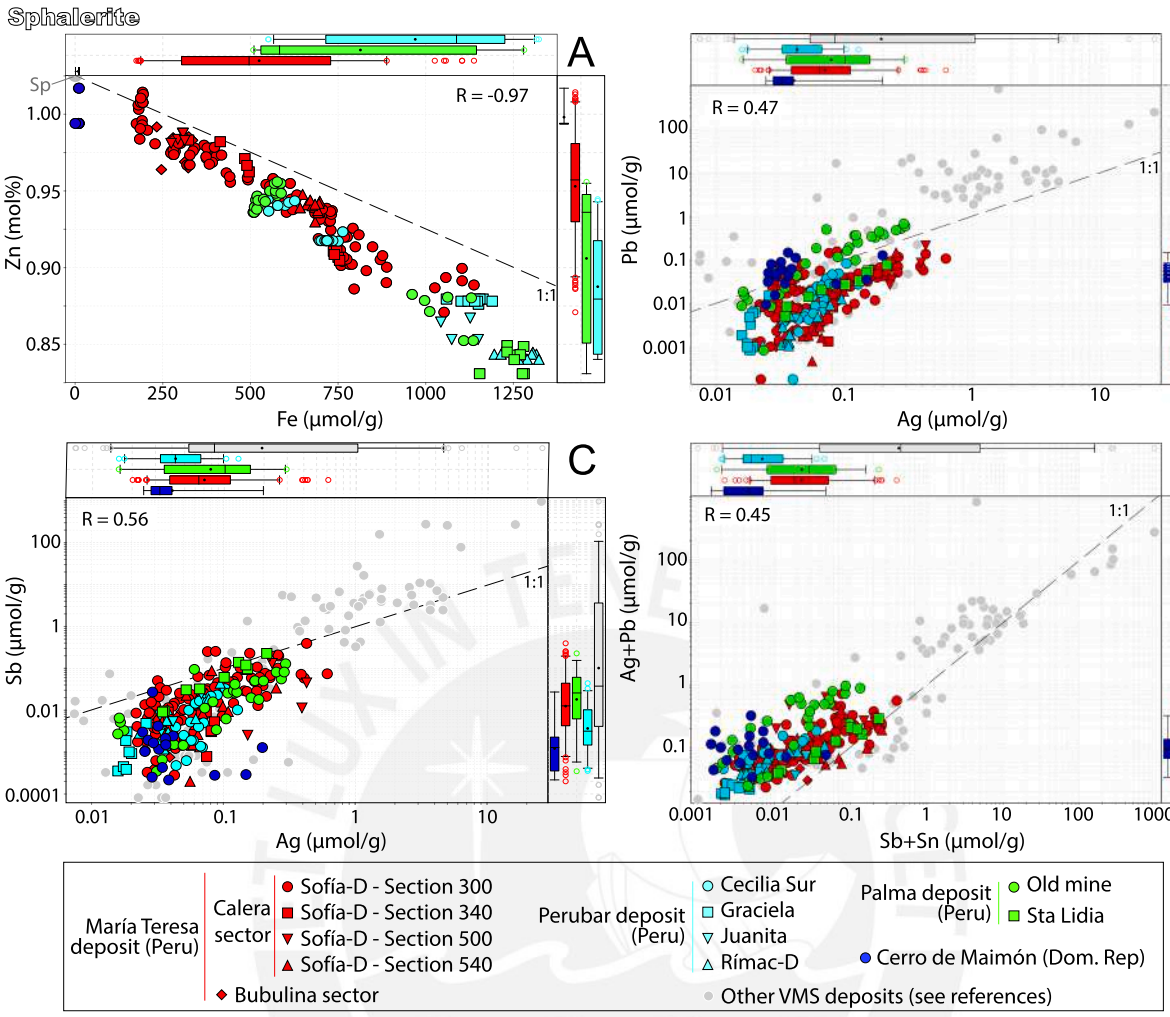

Fig. 9. Binary plots showing inter-element correlations in sphalerite: (A) Fe vs. Zn, (B) Ag vs. Pb, (C) Ag vs. Sb, and (D) Sb+Sn vs. Ag+Pb. Dashed lines represent 1:1 M correlation. Additionally, contents are presented in box-and-whisker plots, which provide IQR (box), 1.5 IQR (whiskers), median (line) and outliers (circles). The composition of sphalerite from other VMS deposits worldwide are shown for comparison (data from Carvalho et al., 2018, Cook et al., 2009, Revan et al., 2014, and Ye et al., 2011).

from other subduction-related VMS deposits, which are mostly in the hundreds of parts per million range (Table 4). According to Monecke et al. (2014), chalcopyrite is the main host of Se in VMS and SMS deposits along with pyrite and, typically, higher Se contents are found in sulfide samples collected in SMS formed in mid-ocean ridges relative to those in subduction related systems. Cadmium shows contents of a few to some tens of parts per million in the analyzed chalcopyrite samples (Table 2), similar to chalcopyrite from other VMS deposits (Table 4); therefore, as expected, Cd contents are much lower in chalcopyrite than in sphalerite from the same deposit (Tables 1 and 3). Similarly, Hg contents in chalcopyrite (up to a few ppm, Table 2) are much lower than in sphalerite (Table 1) from the respective deposits, and similar to or slightly higher than Hg content in chalcopyrite from the Vorta and Sulitjelma VMS deposits (Table 4).

Indium content in analyzed chalcopyrite grains, mostly at the level of tens of parts per million, is only slightly lower than In content in sphalerite grains from the same deposits (Tables 1 and 2), and steadily higher than in chalcopyrite grains from the Vorta and Sulitjelma VMS deposits (Table 4). Germanium content in the analyzed chalcopyrite samples is mostly at the level of some parts per million (Table 2) and usually higher than in sphalerite from the respective deposits (Table 1); Ge content is not provided in reference data for chalcopyrite from other VMS deposits (Table 4). The content of Ga (mostly at the level of a few ppm to some tens of ppm) is lower in chalcopyrite than in sphalerite from the same deposit (Tables 1 and 2); the content of Ga in chalcopyrite from the Vorta and Sulitjelma VMS deposits is systematically lower than in the samples analyzed here (Table 4).

5.2. Correlation trends and substitution mechanisms

5.2.1. Sphalerite

The dataset shows a marked negative correlation trend between Fe and Zn with a slope of ~1 (Fig. 9A) that indicates a dominant $Fe^{2+} \leftrightarrow Zn^{2+}$ simple isovalent substitution. Fair positive correlations between Ag and both Pb (Fig. 9B) and Sb (Fig. 9C) suggest that these three elements likely occur in solid solution in the studied sphalerite samples. Tin is also positively correlated with Ag and the reasonable positive correlation in the Sb + Sn vs. Ag + Pb plot (Fig. 9D) with a slope ~ 1 suggests incorporation of these elements via coupled substitutions of the type $Ag^{+} + Pb^{2+} + (Sn,Sb)^{3+} \leftrightarrow 3Zn^{2+}$ and likely also via independent variations of this scheme (Cook et al., 2009). Nevertheless, the observation of slight ragged downhole ablation spectra for Sn and Pb in a few analyses (e.g., Fig. S3D in Supplementary material) might suggest the local presence of sub-microscopic inclusions of galena and/or Sn—Pb sulfosalts.

The dataset shows a marked correlation trend between Cu and In in samples from María Teresa, particularly in those with the highest In contents, with a slope ~ 1 (Fig. 10A) thus pointing to a $Cu^{+} + In^{3+} \leftrightarrow$

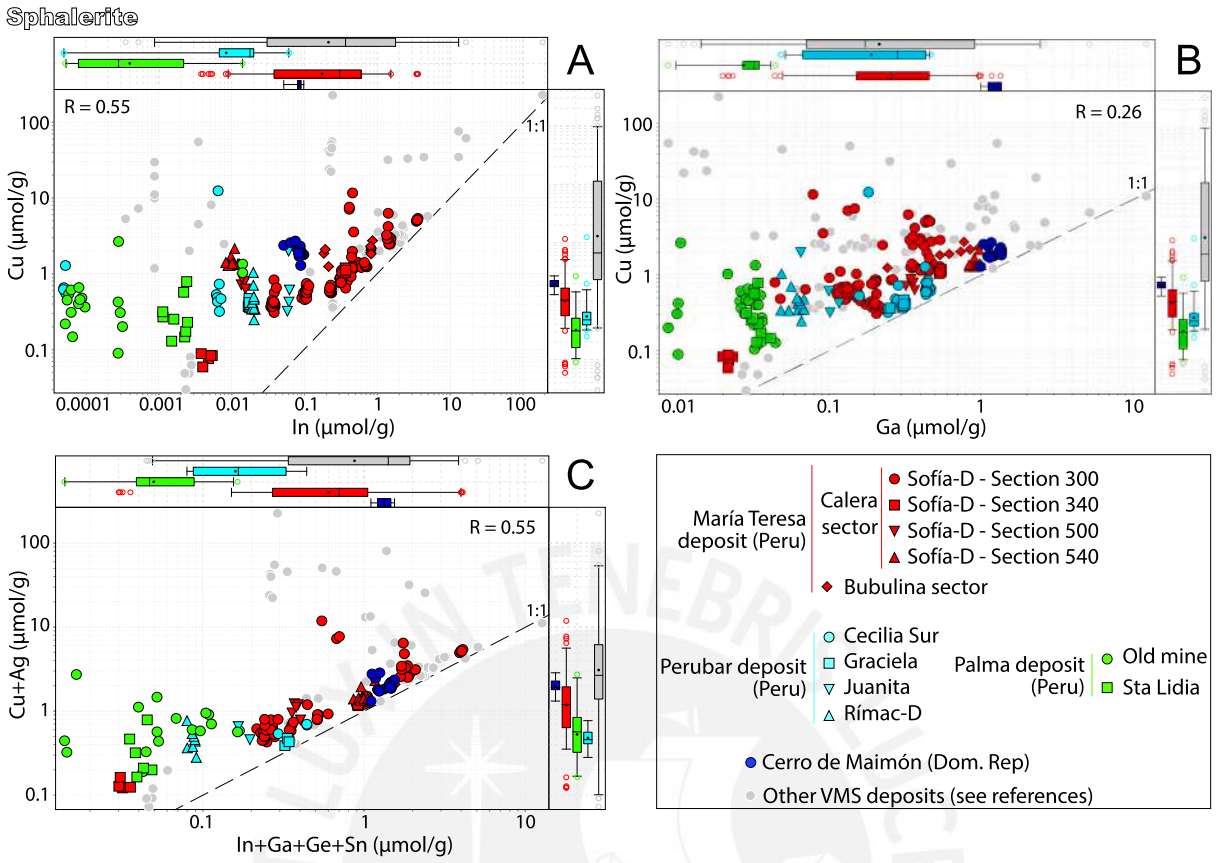

Fig. 10. Binary plots showing inter-element correlations in sphalerite: (A) In vs. Cu, (B) Ga vs. Cu, and (C) Sn+In+Ge+Ga vs. Cu+Ag. Dashed lines represent 1:1 M correlation. Additionally, contents are presented in box-and-whisker plots, which provide IQR (box), 1.5 IQR (whiskers), median (line) and outliers (circles). The composition of sphalerite from other VMS deposits worldwide are shown for comparison (data from Carvalho et al., 2018, Cook et al., 2009, Revan et al., 2014, and Ye et al., 2011).

$2Zn^{2+}$ coupled substitution (Cook et al., 2012; Trofimov et al., 2020; Benites et al., 2021a, 2021b). Gallium yields a fair positive correlation with Cu with some analyses plotting along or close to the 1:1 correlation line (Fig. 10B) suggesting a $Cu^{+} + Ga^{3+} \leftrightarrow 2Zn^{2+}$ coupled substitution. Germanium contents do not show clear correlation trends with the other analyzed elements. The alignment of the analyses in the Sn + In+Ge + Ga vs. Cu + Ag plot (R = 0.55; Fig. 10C) would suggest supplementary complex substitution mechanisms involving combinations of coupled substitutions of trivalent cations (i.e., In, Ga) with monovalent cations (i.e., Cu, Ag) and direct substitution of quadrivalent cations (Sn, Ge) with vacancies for Zn. However, the lacking consensus on the oxidation state of Ge (+2 or + 4) and Sn (+3 or + 4) in sphalerite leaves open the possibility of other substitution schemes (see Cook et al., 2009, 2015; Bellisont et al., 2014). The low content of both Sn and Ge in the studied sphalerite grains and the apparent lack of individual correlation trends with other analyzed elements do not allow to give a definitive conclusion on their incorporation in the crystal lattice.

5.2.2. Chalcopyrite

Unlike sphalerite, chalcopyrite is not a fully ionic mineral but bonding between atoms in its structure is “effectively” covalent with valencies of Fe fluctuating between divalent and trivalent and valencies of Cu, between monovalent and divalent (Donnay et al., 1958; Hall and Stewart, 1973; Li et al., 2013). Therefore, the incorporation mechanism of trace elements in chalcopyrite is far more complex to draw than for sphalerite (see George et al., 2018). Weak to fair positive correlation trends between Zn, Cd, In, Ge, and Ga are observed across our dataset (Fig. 11). George et al. (2018) also noticed the positive correlation between Zn and Cd in chalcopyrite samples from a variety of mineralization styles and argued that systematic variations of Cd:Zn ratio are strongly dependent on crystallization temperature (this question is further addressed in the following section). Our data would suggest that the incorporation of Zn, Cd, In, Ge, and Ga to the structure of chalcopyrite is not completely independent (i.e., simple substitution) but that coupled substitutions involving cations of these elements are likely (see also George et al., 2018 and their references).

5.3. Trace element distribution profiles and conditions of crystallization (and re-crystallization)

Metal and mineral zonation (Fig. 2) and the overprinting and replacement of earlier sulfides (e.g., sphalerite) by minerals that are stable at higher temperature (e.g., chalcopyrite; Figs. 4–6) as described for Sofía-D in the María Teresa deposit denote a thermally intensifying hydrothermal system during the growth of the massive sulfide body; in VMS systems, this process is commonly known as zone refining (Eldridge et al., 1983; Hannington et al., 1998; Grant et al., 2015; Almodóvar et al., 2019). According to the GGIMFIS geothermometer of Frenzel et al. (2016) – which uses the contents of Fe, Mn, In, Ga, and Ge in sphalerite, the analyzed sphalerite from the María Teresa deposit crystallized at temperatures in the range between 320 and 257 °C (IQR). Such a temperature range is in good agreement with a VMS mineralization containing fair abundant chalcopyrite (Hannington et al., 1995; Ohmoto, 1996; Franklin et al., 2005). Assuming that fO_2 and fS_2 were stable during the crystallization of sphalerite (see Hannington and Scott, 1989; Keith et al., 2014) in the Sofía-D sulfide body, sphalerite composition would record a relatively sustained decrease in the crystallization temperature bottom to top (335–327 °C for sample 2019-MT-015 at 128 m

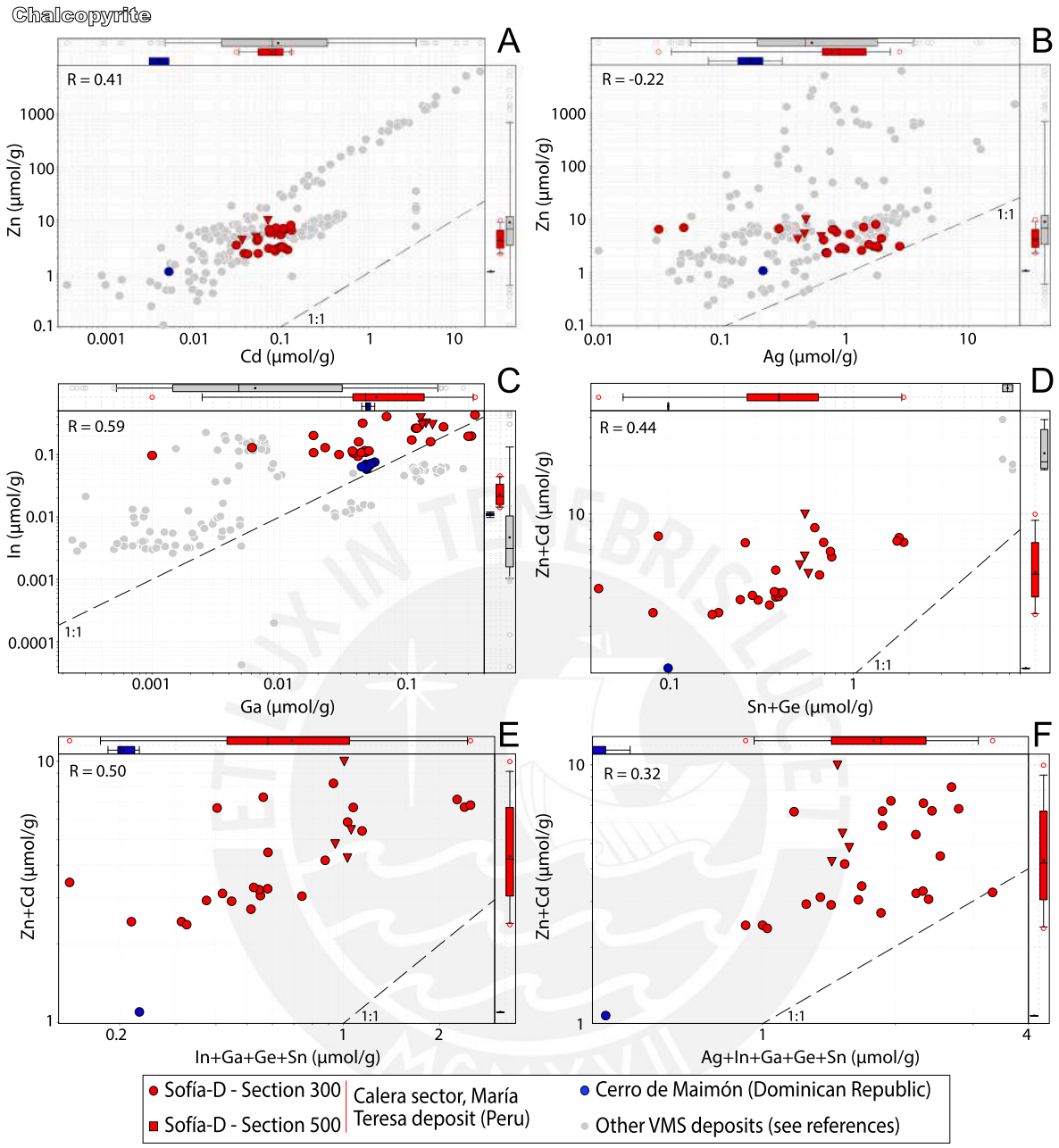

Fig. 11. Binary plots showing inter-element correlations in chalcopyrite: (A) Bi vs. Cu, (B) In vs. Cu, (C) Ga vs. Cu, and (D) Sn+In+Ge+Ga vs. Cu+Ag. Dashed lines represent 1:1 M correlation. Additionally, contents are presented in box-and-whisker plots, which provide IQR (box), 1.5 IQR (whiskers), median (line) and outliers (circles). The composition of sphalerite from other VMS deposits worldwide are shown for comparison (data from Carvalho et al., 2018, George et al., 2018, and Revan et al., 2014).

to 255–249 °C for sample 2019-MT-002 at 74.6 m; Fig. 7J). This decrease in the calculated crystallization temperature is actually a numerical translation of the depletion in In and Mn (directly proportional to the GGIMFIS temperature) and the enrichment in Ge (inversely proportional to the GGIMFIS temperature) bottom to top in sphalerite of the Sofía-D massive sulfide body (Fig. 7). Noteworthy, an increase in the availability of Cu in the mineralizing fluid towards the Cu zone probably also enhanced the incorporation of In to the sphalerite crystal lattice through the coupled substitution mentioned above ($Cu^{+} + In^{3+} \leftrightarrow 2Zn^{2+}$) during zone refining processes.

The Cd:Zn ratio in chalcopyrite is commonly used to trace variations in physicochemical conditions during its crystallization. Higher Cd:Zn ratios are typically ascribed to higher temperatures of crystallization (George et al., 2018). In the Sofía-D sulfide body, chalcopyrite shows rather constant Cd:Zn ratios at different depths and sections (Fig. 8K) suggesting relatively homogeneous physicochemical conditions during the crystallization of this mineral throughout the Cu zone of the mineralized body (Fig. 2). In contrast, the increase of Se contents in chalcopyrite (and sphalerite) with depth would suggest an increase in the temperature and/or magmatic volatile influx (Auclair et al., 1987; Huston et al., 1995; Layton-Matthews et al., 2008; Martin et al., 2019). The concentration of Se, and most trace elements indeed, in the structure of chalcopyrite is distinguishingly strongly influenced by the co-crystallizing phases so that the continuous crystallization of galena during zone refining probably partitioned Se and depleted chalcopyrite in this element (Cook, 1996; Carvalho et al., 2018; George et al., 2018). The progressively increasing abundance of galena towards the upper sections of the Sofía-D body may therefore explain the progressive

depletion of Se in chalcopyrite at shallower levels.

In short, our results suggest that in zone-refined VMS mineralization such as the Sofía-D massive sulfide body in the María Teresa deposit, chalcopyrite and particularly sphalerite register systematic changes in their trace element compositions across the mineralized body. Bottom to top of the sulfide body, observed trends include i) in sphalerite, depletion in In, Cu, Mn, Se, and Bi and enrichment in Ge; and ii) in chalcopyrite, depletion in Se and Bi (the latter probably in microinclusions). Furthermore, these patterns agree with expected physicochemical trends involving decreasing temperatures and influx of hydrothermal fluids with a direct magmatic contribution towards the margins of the sulfide body (Auclair et al., 1987; Huston et al., 1995; Layton-Matthews et al., 2008; Yeats et al., 2014; George et al., 2018; Schmidt et al., 2019; Martin et al., 2019).

Ore mineralization at the Sofía-D massive sulfide body in the María Teresa deposit underwent contact metamorphism connected to nearby granodiorite intrusions (Fig. 2). The identification of key trace-element distribution patterns in sphalerite and chalcopyrite across this body and their reconciliation with expected original trends suggest that contact metamorphism occurred in a closed system and more importantly, that body-scale trace element distribution was largely unaffected. Similarly, Polliand et al. (1999) determined that in the Perubar VMS deposit, sulfur isotope re-equilibration between sulfate-sulfide pairs during contact metamorphism occurred in a closed system and only between adjacent mineral grains. Lockington et al. (2014) found out that the content of lattice-bound trace elements in sphalerite (e.g., Mn, Fe, Cd, Cu, In, Ge, Hg, and Se) from metamorphosed VMS deposits worldwide showed no correlation with the metamorphic grade but were defined primarily by physicochemical conditions during initial deposition; in contrast, the contents of elements that typically occur as micro- and nano-inclusions in sphalerite (e.g., Pb and Bi) decreased with increasing metamorphic grade. Therefore, the use of trace element patterns defined by Mn, In, Ge, and Se in sphalerite, and of Se in chalcopyrite, are likely to reflect primary trends.

6. Conclusions and implications

In this study, systematic trace element determinations have been conducted in sphalerite and chalcopyrite from the Cretaceous arc-related Palma, Perubar, and María Teresa VMS deposits in Peru and the Cerro de Maimón VMS deposits in the Dominican Republic. Sphalerite from the four deposits incorporated Fe, Mn, Cd, Hg, Ag, Sb, Se, In, Ge, and Ga in solid solution. The incorporation of other elements such as Sn, Tl, Bi, and Pb possibly resulted in some cases from microinclusions as suggested by occasional ragged ablation spectra. The contents of minor and trace elements in analyzed sphalerite show significant variations even between samples from any individual deposit. Iron contents (44009–18,168 ppm) correlate negatively with Zn suggesting a dominant $Fe^{2+} \leftrightarrow Zn^{2+}$ simple isovalent substitution. Cadmium (7082–4972 ppm), Mn (4578–140 ppm), and Hg (453–107 ppm) are much concentrated than Pb (9.5–1.1 ppm), Sb (3.7–0.31 ppm), Tl (0.70–0.045 ppm), and Bi (0.60–0.0055 ppm).

Regarding potential *high-tech* by-products in the studied sphalerite grains, In (42–1.6 ppm, up to 415 ppm) and Ga (31–5.9 ppm, up to 96 ppm) contents are mostly higher than Ge contents (0.85–0.16 ppm, up to 9.3 ppm). In samples from the María Teresa deposit, the concentrations of In and Cu yield a positive correlation trend with a slope ~1 corroborating a $Cu^{+} + In^{3+} \leftrightarrow 2Zn^{2+}$ coupled substitution. The dataset also shows a positive correlation trend between Ga and Cu; analyses of sphalerite from the María Teresa, Perubar and Cerro de Maimón deposits lie close to the Ga:Cu 1:1 ratio line thus pointing to a $Cu^{+} + Ga^{3+} \leftrightarrow 2Zn^{2+}$ coupled substitution. Furthermore, the narrow arrangement of most analyses along the 1:1 ratio line in a In + Ga + Ge + Sn vs. Cu + Ag plot suggests the occurrence of additional, more complex substitution mechanisms involving different combinations of monovalent (Cu^{+}, Ag^{+}), divalent (Ge^{2+}?), trivalent (In^{3+}, Ga^{3+}, [Sn^{3+}?]), and quadrivalent (Ge^{4+}, Sn^{4+}) cations.

The trace element composition of chalcopyrite was investigated for the María Teresa and Cerro de Maimón deposits as chalcopyrite is a trace phase in the Palma and Perubar deposits. Trace elements such as Zn, Ag, Sn, Cd, Se, In, Ga, and Ge are present in solid solution as opposed to the likely occurrence of Mo, Au, Tl, Sb, Pb, and Bi in microinclusions. Deleterious elements show low contents (Zn = 426–190 ppm, Se = 64–22 ppm, Sn = 53–1.3 ppm, Cd = 12–6.0 ppm, Tl < 11 ppm, Bi < 10 ppm, Ni < 2.5 ppm, As < 2.0 ppm, Hg < 3.8 ppm) relative to reference maximum contents before charge is incurred *sensu* Fountain (2013). The contents of Ag (136–23 ppm, up to 296 ppm) and Au (<0.40 ppm) are also relatively low. In analyzed chalcopyrite grains, the contents of the potential high-tech by-products In (28–8.4 ppm, up to 49 ppm) and Ga (8.3–2.9 ppm, up to 24 ppm) are lower, and the contents of Ge (5.9–0.70 ppm, up to 80 ppm), higher, than in sphalerite from the respective deposits. General positive correlation trends between Zn, Cd, In, Ge, and Ga in chalcopyrite suggest varied coupled substitution mechanisms of Fe (+2 and +4) and Cu (+1 and +3) with fluctuating valences due to covalent bonding in this mineral.

A comprehensive sampling across the Sofía-D massive sulfide body in the María Teresa deposit revealed significant mineral and trace-element zonation. Mineral zones in Sofía-D include a barren lower part with dominant pyrite sheathed upwards by a Cu zone rich in chalcopyrite that in turn grades to sphalerite ± fahlore ± galena ± chalcopyrite (Zn zone) and galena + sphalerite ± fahlore ± barite (Pb – Zn – Ag zone) carapaces. Strong replacement of early sphalerite by chalcopyrite and the observed metal zonation strongly suggest zone refining. The contents of some trace elements in sphalerite and to a lesser extent in chalcopyrite display systematic vertical distribution patterns. In sphalerite, these include, bottom to top of the sulfide body, depletion in In, Cu, Mn, and Se and enrichment in Ge. This distribution agrees with the expected decrease of the crystallization temperature and/or volatile magmatic influx from the feeders of the massive mineralization. In chalcopyrite, the distributions of trace elements and Sc/Zn ratios are rather uneven except for constant enrichment in Bi (probably present as microinclusions) and Se towards the basal portion of the sulfide body. Unlike sphalerite, the trace element composition of chalcopyrite is strongly dependent on the co-crystallizing phases over physicochemical conditions. Co-crystallization and/or reequilibration of chalcopyrite with galena at shallower levels may therefore account for progressive depletion of Se in chalcopyrite.

The Sofía-D massive sulfide mineralization shows strong textural and mineralogical evidence of recrystallization during thermal metamorphism caused by nearby granodiorite intrusions. The impact of the thermal metamorphism in the absolute trace elements contents in sphalerite and chalcopyrite is unknown. However, the preservation of expected original trace element distribution patterns would suggest a closed metamorphic system and that element interdiffusion was local, probably attaining only contiguous sulfide grains. Accordingly, we propose that the distribution patterns described in this article for lattice-bound trace elements in sphalerite and chalcopyrite may be useful during exploration in order to trace the polarity of massive sulfide bodies in metamorphosed and tectonized terranes.

Supplementary data to this article can be found online at https://doi.org/10.1016/j.gexplo.2021.106882.

CRediT authorship contribution statement

Lisard Torró: Conceptualization, Investigation, Writing – Original Draft, Project Administration, Funding Acquisition

Diego Benites: Methodology, Investigation, Data Curation

Jean Vallance: Methodology, Investigation

Oscar Laurent: Methodology, Validation, Formal Analysis, Data Curation

Brayam A. Ortiz-Benavente: Methodology, Investigation

Cyril Chelle-Michou: Validation, Writing – Review and Editing

Joaquín A. Proenza: Resources, Writing – Review and Editing, Supervision

Lluís Fontboté: Resources, Writing – Review and Editing, Supervision

Declaration of competing interest

The authors declare that they have no known competing financial interests or personal relationships that could have appeared to influence the work reported in this paper.

Acknowledgments

This study was economically supported by the Peruvian CONCYTEC-FONDECYT-World Bank project 107-2018-FONDECYT-BM-IADT-AV, the Spanish projects CGL2015–65824 and PID2019-105625RB-C21, and a Huiracocha Ph. D granted by the PUCP to D.B. Minera Colquisiri provided field and logistical support, access to the mine area, and the documents to prepare Fig. 2; its staff is most gratefully acknowledged, particularly Juan José Herrera, Edgar Pichardo, Thed Mena, and Óscar Chirinos. We also thank Perilya-CORMIDOM for providing specimens from the Cerro de Maimón deposits. The analyzed material from Perubar and Palma was sampled (1998–2000) by Marc Polliand in the frame of his PhD thesis at the University of Geneva. The senior author acknowledges C.E. Nelson for insightful debate on the origin and classification of VMS deposits hosted in Cretaceous arc-related volcanic units in Cuba and the Dominican Republic. We appreciate the technical support by Xavier Llovet (CCiT-UB) during the acquisition of EPMA data, and by Peter Tollan (ETHZ) during the acquisition of LA-ICP-MS data. We are grateful to two anonymous reviewers for their constructive comments.

References

Aguirre, L., Levi, B., Nystrom, J.O., 1989. The link between metamorphism, volcanism and geotectonic setting during the evolution of the Andes. In: Geological Society Special Publications, 43, pp. 223–232.

Aillard, E., 1994. Kimmeridgian to Paleocene tectonic and geodynamic evolution of the Peruvian (and Ecuadorian) margin. In: Salfity, J.A. (Ed.), Cretaceous Tectonics of the Andes. Vieweg, Wiesbaden, pp. 101–167.

Almodóvar, G.R., Yesares, L., Sáez, R., Toscano, M., González, F., Pons, J.M., 2019. Massive sulfide ores in the Iberian Pyrite Belt: mineralogical and textural evolution. Minerals 9, 653.

Atherton, M.P., 1990. The Coastal Batholith of Peru: the product of rapid recycling of 'new' crust formed within rifted continental margin. Geol. J. 25, 337–349.

Atherton, M.P., Aguirre, L., 1992. Thermal and geotectonic setting of cretaceous volcanic rocks near Ica, Peru, in relation to Andean crustal thinning. J. S. Am. Earth Sci. 5, 47–69.

Atherton, M.P., Warden, V., Sanderson, L.M., 1985. The Mesozoic marginal basin of Central Peru: a geochemical study of within- plate-edge volcanism. In: Pitcher, W.S., Atherton, M.P., Cobbing, E.J., Beckinsale, R.D. (Eds.), Magmatism at a Plate Edge; the Peruvian Andes. Blackie, Glasgow, pp. 47–58.

Auclair, G., Fouquet, Y., Bohn, M., 1987. Distribution of selenium in high-temperature hydrothermal sulfide deposits at 13° North, East Pacific rise. Can. Mineral. 25, 577–587.

Barton, P.B., Toulmin, P., 1966. Phase relations involving sphalerite in the Fe-Zn-S system. Econ. Geol. 61, 815–849.

Bellisont, R., Boiron, M.C., Luais, B., Cathelineau, M., 2014. LA-ICP-MS analyses of minor and trace elements and bulk Ge isotopes in zoned Ge-rich sphalerites from the Noailhac – Saint-Salvy deposit (France): Insights into incorporation mechanisms and ore deposition processes. Geochim. Cosmochim. Acta 126, 518–540.

Benavides-Cáceres, V., 1999. Orogenic evolution of the Peruvian Andes: the Andean Cycle. In: Society of Economic Geologists Special Publication, 7, pp. 61–107.

Benites, D., Torró, L., Vallance, J., Laurent, O., Valverde, P.E., Kouzmanov, K., Chelle-Michou, C., Fontboté, L., 2021a. Distribution of indium, germanium, gallium and other minor and trace elements in polymetallic ores from a porphyry system: the Morococha District, Peru. Ore Geol. Rev. 136, 104236.

Benites, D., Torró, L., Vallance, J., Laurent, O., Rosas, S., Uzieda, M.F., Holm-Denoma, C. S., Pianowski, L.S., Camprubí, A., Colás, V., Fernández-Baca, A., Giraldo, L., Chelle-Michou, C., Sáez, J., Kouzmanov, K., Fontboté, L., Quispe, P., 2021. Geology, mineralogy, and cassiterite geochronology of the Ayawilca Zn-Pb-Ag-In-Sn-Cu deposit, Pasco, Peru. Mineral. Deposita. https://doi.org/10.1007/s00126-021-01066-z. June 22, 2021.

Benzaazoua, M., Marion, P., Pinto, A., Migeon, H., Wagner, F.E., 2003. Tin and indium mineralogy within selected samples from the Neves Corvo ore deposit (Portugal): a multidisciplinary study. Miner. Eng. 16, 1291–1302.

Bueno Carreón, J.P., 2019. In: Herramientas de exploración aplicadas a la generación de nuevos targets en el yacimento VMS Cerro Lindo. Proexplo 2019, Lima, Extended Abstracts, pp. 332–340.

Bueno Carreón, J.P., Mendoza Mondragón, M., 2019. In: Caracterización litogeoquímica en el yacimiento VMS - Cerro Lindo y su relación con la mineralización para determinar vectores guías en exploración. Proexplo 2019, Lima, Extended Abstracts, pp. 196–201.

Carvalho, J., Relvas, J., Pinto, A., Frenzel, M., Krause, J., Gutzmer, J., Gonçalves, M., 2018. Indium and selenium distribution in the Neves-Corvo deposit, Iberian Pyrite Belt, Portugal. Mineral. Mag. 82, S5–S41.

Choquehuanca, S., 2020. Petrology, Geochronology and Geochemistry of the Lower Cretaceous in Palma Volcanogenic Massive Sulfide (VMS) Deposit, Central Peru. Master Thesis. China University of Geosciences, Wuhan, 79 p.

Cobbing, E.J., 1999. The Coastal Batholith and other aspects of Andean magmatism in Peru. In: Castro, A., Fernández, C., Vigneresse, J.L. (Eds.), Understanding Granites: Integrating New and Classical Techniques, 168. Geological Society London, Special Publications, pp. 111–122.

Cook, N.J., 1996. Mineralogy of the sulphide deposits at Sulitjelma, northern Norway. Ore Geol. Rev. 11, 303–338.

Cook, N.J., Ciobanu, C.L., Pring, A., Skinner, W., Shimizu, M., Danyushevsky, L.V., Saini-Eidukat, B., Melcher, F., 2009. Trace and minor elements in sphalerite: a LA-ICPMS study. Geochim. Cosmochim. Acta 73, 4761–4791.

Cook, N.J., Ciobanu, C.L., Williams, T., 2011. The mineralogy and mineral chemistry of indium in sulphide deposits and implications for mineral processing. Hydrometallurgy 108, 226–228.

Cook, N.J., Ciobanu, C.L., Brugger, J., Etschmann, B., Howard, D.L., de Jonge, M.D., Ryan, C., Paterson, D., 2012. Determination of the oxidation state of Cu in substituted Cu-In-Fe-bearing sphalerite via mu-XANES spectroscopy. Am. Mineral. 97, 476–479.

Cook, N.J., Etschmann, B., Ciobanu, C.L., Geraki, K., Howard, D.L., Williams, T., Rae, N., Pring, A., Chen, G., Johannessen, B., Brugger, J., 2015. Distribution and substitution mechanism of Ge in a Ge-(Fe)-bearing sphalerite. Minerals 5, 117–132.

Cueva, E., Mamani, M., Rodríguez, R., 2010. In: Magmatismo y geoquímica del volcanismo Albiano Cenomaniano (Grupo Casma) y Maastrichtiano-Daniano entre Pucusana y Chimbote. XV Congreso Peruano de Geología, resúmenes extendidos, 9. Sociedad Geológica de Perú, Peru, pp. 921–924.

Donnay, G., Corliss, L.M., Donnay, J.D.H., Elliott, N., Hastings, J.M., 1958. Symmetry of magnetic structures: magnetic structure of chalcopyrite. Phys. Rev. 112, 1917–1923.

Doyle, M.G., Allen, R.L., 2003. Subsea-floor replacement in volcanic-hosted massive sulfide deposits. Ore Geol. Rev. 23, 183–222.

Dubé, B., Gosselin, P., Mercier-Langevin, P., Hannington, M., Galley, A., 2007. Gold-rich volcanogenic massive sulphide deposits. In: Goodfellow, W.D. (Ed.), Mineral Deposits of Canada: A Synthesis of Major Deposit-Types, District Metallogeny, the Evolution of Geological Provinces, and Exploration Methods: Geological Association of Canada, Mineral Deposits Division, Special Publication No. 5, pp. 75–94.

Eldridge, C.W., Barton, P.B., Ohmoto, H., 1983. Mineral textures and their bearing on formation of the Kuroko orebodies. Econ. Geol. Monogr. 5, 241–281.

Farfán, C., Monge, R., Fontboté, L., 2019. Palma, yacimiento de Zn-Pb tipo VMS en una cuenca intra-arco del Cretácico Superior en Perú central, nuevos avances en exploración para un gran potencial. In: Proceedings of Proexplo 2019, Lima, Extended Abstracts, pp. 209–215.

Fontboté, L., 2019. Volcanogenic Zn-Pb±Cu massive sulfide deposits in the Upper Cretaceous plutono-volcanic arc in central Peru. In: Proceedings of Proexplo 2019, Peru, Extended Abstracts, pp. 45–52.

Fountain, C., 2013. The whys and wherefores of penalty elements in copper concentrates. In: MetPlant: Metallurgical Plant Design and Operating Strategies, 5. Australasian Institute of Mining and Metallurgy, Melbourne, Australia, pp. 502–518.

Franklin, J.M., Hannington, M.D., Jonasson, I.R., Barrie, C.T., 1998. Arc-related volcanogenic massive sulfide deposits Metallogeny of volcanogenic arcs. In: British Columbia Geological Survey, Open-File, p. 32.

Franklin, J.M., Gibson, H.L., Jonasson, I.R., Galley, A.G., 2005. Volcanogenic massive sulfide deposits. In: Economic Geology 100th Anniversary Volume, pp. 523–560.

Frenzel, M.F., Hirsch, T., Gutzmer, J., 2016. Gallium, germanium, indium and other trace and minor elements in sphalerite as a function of the deposit type – a meta-analysis. Ore Geol. Rev. 76, 52–78.

Frenzel, M., Bachmann, K., Carvalho, J.R.S., Relvas, J.M.R.S., Pacheco, N., Gutzmer, J., 2019. The geometallurgical assessment of by-products – geochemical proxies for the complex mineralogical deportment of indium at Neves-Corvo, Portugal. Mineral. Deposita 54, 959–982.

Galley, A.G., Hannington, M.D., Jonasson, I.R., 2007. Volcanogenic massive sulphide deposits. In: Goodfellow, W.D. (Ed.), Mineral Deposits of Canada: A Synthesis of Major Deposit-Types, District Metallogeny, the Evolution of Geological Provinces,

and Exploration Methods, 5. Geological Association of Canada, Mineral Deposits Division, Special Publication, pp. 141–161.
Gariepy, L., Hinostroza, J., 2013. El yacimiento tipo sulfuro masivo volcanogénico Cerro Lindo, Departamento de Ica, Perú. Proexplo, Lima, Extended Abstracts, 23 p.
Gemmell, J.B., Sharpe, R., Jonasson, I.A., Herzig, P.M., 2004. Sulfur isotope evidence for magmatic contributions to submarine and subaerial gold mineralization: Conical Seamount and the Ladolam Gold Deposit, Papua New Guinea. Econ. Geol. 99, 1711–1725.
George, L.L., Cook, N.J., Ciobanu, C.L., Wade, B.P., 2015. Trace and minor elements in galena: a reconnaissance LA-ICP-MS study. Am. Mineral. 100, 548–569.
George, L.L., Cook, N.J., Crowe, B.B.P., Ciobanu, C.L., 2018. Trace elements in hydrothermal chalcopyrite. Mineral. Mag. 82, 59–88.
Grant, H., Layton-Matthews, D., Peter, J.M., 2015. Distribution and controls on silver mineralization in the Hackett River Main Zone, Nunavut, Canada: an Ag- and Pb-enriched Archean volcanogenic massive sulfide deposit. Econ. Geol. 110, 943–982.
Gregory, D.D., Large, R.R., Halpin, J.A., Baturina, E.L., Lyons, T.W., Wu, S., Danyushevsky, L., Sack, P.J., Chappaz, A., Maslennikov, V.V., Bull, S.W., 2015. Trace element content of sedimentary pyrite in black shales. Econ. Geol. 110, 1389–1410.
Hall, S.R., Stewart, J.M., 1973. The crystal structure refinement of chalcopyrite, CuFeS2. Acta Crystallogr. B Struct. Crystallogr. Cryst. Chem. 29, 579–585.
Hannington, M.D., Scott, S.D., 1989. Sulfidation equilibria as guides to gold mineralization in volcanogenic sulfides: evidence from sulfide mineralogy and the composition of sphalerite. Econ. Geol. 84, 1978–1995.
Hannington, M.D., Jonasson, I.R., Herzig, P.M., Petersen, S., 1995. Physical and chemical processes of seafloor mineralization. In: Humphris, S.E., Zierenberg, R.A., Mullineaux, L.S., Thomson, R.E. (Eds.), Seafloor Hydrothermal Systems—Physical, Chemical, Band Geological Interactions, 91. American Geophysical Union Geophysical Monograph, pp. 115–157.
Hannington, M.D., Galley, A.G., Herzig, P.M., Petersen, S., 1998. Comparison of the TAG mound and stock- work complex with Cyprus-type massive sulfide deposits. In: Herzig, P.M., Humphris, S.E., Miller, D.J., Zierenberg, R.A. (Eds.), TAG—Drilling an Active Hydrothermal System on a Sediment-free Slow-spreading Ridge, Site 957: Proceedings of the Ocean Drilling Program, Scientific Results, 158, pp. 389–415.
Herrington, R., Maslennikov, V., Zaykov, V., Seravkin, I., Kosarev, A., Buschmann, B., Orgeval, J.J., Holland, N., Tesalina, S., Nimis, P., Armstrong, R., 2005. 6: classification of VMS deposits: lessons from the uralides. Ore Geol. Rev. 27, 203–237.
Hildebrand, R.S., Whalen, J.B., 2014. Arc and slab-failure magmatism in Cordilleran batholiths I - the cretaceous coastal batholith of Peru and its role in South American orogenesis and Hemispheric subduction flip. Geosci. Can. 41, 255–282.
Hollis, S.P., Roberts, S., Earls, G., Herrington, R., Cooper, M.R., Piercey, S.J., Archibald, S.M., Moloney, M., 2014. Petrochemistry and hydrothermal alteration within the Tyrone igneous complex, Northern Ireland: implications for VMS mineralization in the british and Irish Caledonides. Mineral. Deposita 49, 575–593.
Huston, D.L., Sie, S.H., Suter, G.F., Cooke, D.R., Both, R.A., 1995. Trace elements in sulfide minerals from eastern Australian volcanic-hosted massive sulfide deposits; part I, proton microprobe analyses of pyrite, chalcopyrite, and sphalerite, and part II, selenium levels in pyrite; comparison with delta 34 S values and implications for the source of sulfur in volcanogenic hydrothermal systems. Econ. Geol. 90, 1167–1196.
INGEMMET, 2000. Mapa geológico digitalizadp del Perú (Escala 1:1,000,000). Instituto Geológico, Minero y Metalúrgico, Lima. CD-ROM.
Keith, M., Haase, K.M., Schwarz-Schampera, U., Klemd, R., Petersen, S., Bach, W., 2014. Effect of temperature, sulfur and oxygen fugacity on the composition of sphalerite from submarine hydrothermal vents. Geology 42, 699–702.
Koski, R.A., Mosier, D.L., 2012. Deposit type and associated commodities in volcanogenic massive sulfide occurrence model. In: U.S. Geological Survey Scientific Investigations Report 2010–5070 –C, Chapter 2, 8 p.
Layton-Matthews, D., Peter, J.M., Scott, S.D., Leybourne, M.I., 2008. Distribution, mineralogy, and geochemistry of selenium in felsic volcanic-hosted massive sulfide deposits of the Finlayson Lake District, Yukon Territory, Canada. Econ. Geol. 103, 61–88.
Li, Y., Kawashima, N., Li, J., Chandra, A.P., Gerson, A.R., 2013. A review of the structure, and fundamental mechanisms and kinetics of the leaching of chalcopyrite. Adv. Colloid Interf. Sci. 197, 1–32.
Lockington, J.A., Cook, N.J., Ciobanu, C.L., 2014. Trace and minor elements in sphalerite from metamorphosed sulfide deposits. Mineral. Petrol. 108, 873–890.
Martín, M., Draper, G., 1999. Mapa geológico de la hoja 6172-I (Hatillo) a escala 1:50 000 (SYSMIN, Proyecto C). Consorcio ITGE-PROINTEC-INYPSA. Dirección General de Minería, Santo Domingo.
Martin, A.J., Keith, M., McDonald, I., Haase, K.M., McFall, K.A., Klemd, R., MacLeod, C. J., 2019. Trace element systematics and ore-forming processes in mafic VMS deposits: evidence from the Troodos ophiolite, Cyprus. Ore Geol. Rev. 106, 205–225.
Mégard, F., 1984. The andean orogenic period and its major structures in central and northern Peru. J. Geol. Soc. 141, 893–900.
Monecke, T., Petersen, S., Hannington, M.D., 2014. Constraints on water depth of massive sulfide formation: evidence from modern seafloor hydrothermal systems in arc-related settings. Econ. Geol. 109, 2079–2101.
Murakami, H., Ishihara, S., 2013. Trace elements of indium-bearing sphalerite from tin-polymetallic deposits in Bolivia, China and Japan: a femto-second LA-ICPMS study. Ore Geol. Rev. 53, 223–243.
Nelson, C.E., Proenza, J.A., Lewis, J.F., López-Kramer, J., 2011. The metallogenic evolution of the Greater Antilles. Geol. Acta 9, 229–264.
Nimis, P., Omenetto, P., Tesalina, S.G., Zaykov, V.V., Tartarotti, P., Orgéval, J.-J., 2003. Peculiarities of some mafic–ultramafic-hosted massive sulfide deposits from southern urals – a likely forearc occurrence. In: Eliopoulos, D.G., et al. (Eds.), Mineral Exploration and Sustainable Development. Millpress, Rotterdam, pp. 627–630.
Ohmoto, H., 1996. Formation of volcanogenic massive sulfide deposits: the Kuroko perspective. Ore Geol. Rev. 10, 135–177.
Perilya, 2020. Cerro de Maimón [accessed July 5, 2021].
Peter, J.M., Leybourne, M.I., Scott, S.D., Gorton, M.P., 2014. Geochemical constraints on the tectonic setting of basaltic host rocks to the Windy Craggy Cu-Co-au massive sulphide deposit, northwestern British Columbia. Int. Geol. Rev. 56, 1484–1503.
Petersen, S., Monecke, T., Westhues, A., Hannington, M.D., Gemmell, J.B., Sharpe, R., Peters, M., Strauss, H., Lackschewitz, K., Augustin, N., Gibson, H., Kleeberg, R., 2014. Drilling shallow-water massive sulfides at the Palinuro volcanic complex, Aeolian island arc, Italy. Econ. Geol. 109, 2129–2158.
Pichardo, E., Fontboté, L., Mena, T., Chirinos, O., Halter, W., 2019. El yacimiento de Zn-Pb-Cu-Ag tipo VMS María Teresa, Perú: Geología y exploración. In: Proceedings of Proexplo 2019, Peru, Extended Abstracts, pp. 209–215.
Piercey, S.J., 2011. The setting, style, and role of magmatism in the formation of volcanogenic massive sulfide deposits. Mineral. Deposita 46, 449–471.
Pitcher, W.S., 1985. A multiple and composite batholith. In: Pitcher, W.S., Atherton, M. P., Cobbing, E.J., Beckinsale, R.D. (Eds.), Magmatism at a Plate Edge: The Peruvian Andes. Blackie, Glasgow, pp. 93–101.
141 p Polliand, M., 2006. Genesis, evolution, and tectonic setting of the Upper cretaceous Perubar Ba-Pb-Zn volcanic-hosted massive sulfide deposit, Central Peru. In: Terre & Environment, 60.
Polliand, M., Fontboté, L., Spangenberg, J., 1999. Tracing back sulfur isotope reequilibration due to contact metamorphism: a case study from the Perubar VMS deposit, Central Peru. In: Stanley, C.J., et al. (Eds.), Mineral Deposits: Processes to Processing, 5th Biennial SGA Meeting, London. Balkema, Rotterdam, pp. 967–970.
Polliand, M., Schaltegger, U., Frank, M., Fontboté, L., 2005. Formation of intra-arc volcano-sedimentary basins in the western flank of the central Peruvian Andes during late cretaceous oblique subduction—field evidence and constraints from U-Pb ages and Hf isotopes. Int. J. Earth Sci. 94, 231–242.
Revan, M.K., Genç, Y., Maslennikov, V.V., Maslennikova, S.P., Large, R.R., Danyushevsky, L.V., 2014. Mineralogy and trace-element geochemistry of sulfide minerals in hydrothermal chimneys from the Upper-Cretaceous VMS deposits of the eastern Pontide orogenic belt (NE Turkey). Ore Geol. Rev. 63, 129–149.
Ridley, W.I., 2012. Geochemical characteristics in volcanogenic massive sulfide occurrence model. In: U.S. Geological Survey Scientific Investigations Report 2010–5070 –C, Chap. 14, 18 p.
Romero, D., Quispe, J., Carlotto, V., Tassinari, C., 2008. Los depósitos de la cuenca Maastrichtiano - Daniano: relación con los yacimientos tipo sulfuros masivos volcanogénicos de Pb - Zn - Cu; Perú central. Proceedings of the Congreso Peruano de Geología, 14, Lima (CD – ROM). Sociedad Geológica del Perú, Lima.
de Ronde, C.E.J., Massoth, G.J., Butterfield, D.A., et al., 2011. Submarine hydrothermal activity and gold-rich mineralization at Brothers Volcano, Kermadec Arc, New Zealand. Miner Depos 46, 541–584. https://doi.org/10.1007/s00126-011-0345-8.
Scherrenberg, A.F., Jacay, J., Holcombe, R.J., Rosenbaum, G., 2012. Stratigraphic variations across the Marañón Fold-Thrust Belt, Peru: implications for the basin architecture of the West Peruvian Trough. J. S. Am. Earth Sci. 38, 147–158.
Schmidt, M.A., Leybourne, M.I., Peter, J.M., Petts, D., Layton-Matthews, D., 2019. Fluid inclusion LA-ICP-MS and whole rock geochemical investigation of possible magmatic contributions to the giant Windy Craggy Besshi-type VMS deposit. In: Rogers, N. (Ed.), Targeted Geoscience Initiative: 2018 report of activities, Geological Survey of Canada, Open File 8549, pp. 189–204. https://doi.org/10.4095/313651.
Shanks III, W.C.P., Thurston, R., 2012. Volcanogenic Massive Sulfide Occurrence Model: U.S. Geological Survey Scientific Investigations Report 2010–5070–C.
Sillitoe, R.H., Hannington, M.D., Thompson, J.F.H., 1996. High sulfidation deposits in the volcanogenic massive sulfide environment. Econ. Geol. 91, 204–212.
Soler, P., 1991. In: El volcanismo Casma del Perú Central: cuenca marginal abortada o simple arco volcanico?. VII Congreso Peruano de Geología, Lima, Volumen de Resúmenes Extendidos, Sociedad Geológica de Perú, pp. 659–663.
Steinmüller, K., Chacón Abad, N., Grant, B., 2000. Volcanogenic massive sulfides in Peru. In: Sherlock, R.L., Logan, M.A.V. (Eds.), VMS Deposits of Latin America. Geological Association of Canada, Mineral Deposits Division, 2, pp. 423–437.
Tegart, P., Allen, G., Carstensen, A., 2000. Regional setting, stratigraphy, alteration and mineralization of the Tambo Grande VMS district, Piura department, northern Peru. In: Sherlock, R.L., Logan, M.A.V. (Eds.), VMS Deposits of Latin America. Geological Association of Canada, Mineral Deposits Division, 2, pp. 375–405.
Tivey, M.K., 2007. Generation of seafloor hydrothermal vent fluids and associated mineral deposits. Oceanography 20, 50–65.
Tornos, F., Peter, J.M., Allen, R., Conde, C., 2015. Controls on the sitting and style of volcanogenic massive sulphide deposits. Ore Geol. Rev. 68, 142–163.
Torró, L., Proenza, J.A., Melgarejo, J.C., Alfonso, P., Farré de Pablo, J., Colomer, J.M., García- Casco, A., Gubern, A., Gallardo, E., Cazañas, X., Chávez, C., del Carpio, R., León, P., Nelson, C., Lewis, J.F., 2016a. Mineralogy, geochemistry and sulfur isotope characterization of the Cerro de Maimón (Dominican Republic), San Fernando and Antonio (Cuba): lower cretaceous VMS deposits associated to the subduction initiation of the Proto-Caribbean lithosphere within a fore-arc. Ore Geol. Rev. 72, 794–817.
Torró, L., Garcia-Casco, A., Proenza, J.A., Blanco-Quintero, I.F., Gutiérrez-Alonso, G., Lewis, J.F., 2016b. High-pressure greenschist to blueschist facies transition in the Maimón Formation (Dominican Republic) suggests mid-cretaceous subduction of the early cretaceous Caribbean Arc. Lithos 266–267, 309–331.
Torró, L., Proenza, J.A., Marchesi, C., García-Casco, A., Lewis, J.F., 2017. Petrogenesis of meta-volcanic rocks from the Maimón Formation (Dominican Republic): geochemical record of the nascent Greater Antilles paleo-arc. Lithos 278–281, 255–273.
24 p Torró, L., Proenza, J.A., Espaillat, J., Belén-Manzueta, A.J., Román-Alday, M.C., Amarante, A., González, N., Espinoza, J., Román-Alpiste, M.J., Nelson, C.E., 2018a.

The discovery of the Romero VMS Deposit and its bearing on the metallogenic evolution of Hispaniola during the Cretaceous. Minerals 8, 507.
Torró, L., Proenza, J.A., Rojas-Agramonte, Y., Garcia-Casco, A., Yang, J.-H., Yang, Y.-H., 2018b. Recycling in the subduction factory: Archaean to Permian zircons in the oceanic cretaceous Caribbean island-arc (Hispaniola). Gondwana Res. 54, 23–37.
Trofimov, N.D., Trigub, A.L., Tagirov, B.R., Filimonova, O.N., Evstigneeva, P.V., Chareev, D.A., Kvashnina, K.O., Nickolsky, M.S., 2020. The state of trace elements (In, Cu, Ag) in sphalerite studied by X-Ray absorption spectroscopy of synthetic minerals. Minerals 10, 640.
Vela, C., 1997. In: Nueva concepción estratigráfica de la subcuenca de Lima. IX Congreso Peruano de Geología, Resúmenes Extendidos, Sociedad Geológica de Perú, Peru, pp. 409–412.
Vidal, C.C.E., 1987. Kuroko-type deposits in the Middle-cretaceous marginal basin of Central Peru. Econ. Geol. 82, 1409–1430.
Votorantim, 2017. Cerro Lindo polymetallic mine. In: NI 43-101 Technical Report on Operations, 315 p.
Winter, L.S., Tosdal, R.M., Franklin, J.M., Tegart, P., 2004. A Reconstructed cretaceous depositional setting for giant volcanogenic massive sulfide deposits at Tambogrande, Northwestern Peru. In: Society of Economic Geologists Special Publication, 11, pp. 319–340.
Winter, L.S., Tosdal, R.M., Mortensen, J.K., Franklin, J.M., 2010. Volcanic stratigraphy and geochronology of the cretaceous Lancones Basin, northwestern Peru: position and timing of giant VMS deposits. Econ. Geol. 105, 713–742.
Ye, L., Cook, N.J., Ciobanu, C.L., Yuping, L., Qian, Z., Tiegeng, L., Wei, G., Yulong, Y., Danyushevskiy, L., 2011. Trace and minor elements in sphalerite from base metal deposits in South China: a LA-ICP-MS study. Ore Geol. Rev. 39, 188–217.
Yeats, C.J., Parr, J.M., Binns, R.A., Gemmell, J.B., Scott, S.D., 2014. The SuSu Knolls Hydrothermal Field, Eastern Manus Basin, Papua New Guinea: an active submarine high-sulfidation copper-gold system. Econ. Geol. 109, 2207–2226.
Zaccarini, F., Garuti, G., 2008. Mineralogy and chemical composition of VMS deposits of northern Apennine ophiolites, Italy: evidence for the influence of country rock type on ore composition. Mineral. Petrol. 94, 61–83.

CHAPTER V: TRACE ELEMENT COMPOSITION OF SPHALERITE FROM THE SAN VICENTE AND SHALIPAYCO MISSISSIPPI VALLEY-TYPE DEPOSITS, PERU

Trace element composition of sphalerite from the San Vicente and Shalipayco Mississippi Valley-Type deposits, Peru

Several parts of this chapter have benefited from the input of Lisard Torró[a], Andrea J. Millan-Nuñez[a], Jean Vallance[a], Oscar Laurent[b,*], Cyril Chelle-Michou[b], Silvia Rosas[a], and Lluís Fontboté[c] that should appear a coauthors in a planned publication.

[a] *Geological Engineering Program, Faculty of Sciences and Engineering, Pontifical Catholic University of Peru (PUCP), Av. Universitaria 180, San Miguel, Lima 15088, Peru*

[b] *ETH Zürich, Department of Earth Sciences, Institute for Geochemistry and Petrology, Zürich, Switzerland*

[c] *Department of Earth Sciences, University of Geneva, CH-1205 Geneva, Switzerland*

To be submitted

Corresponding author: Diego Benites, diego.benitesn@gmail.com

Phone: (+51) 6262000 Ext. 5060

[+*] *Present address: CNRS, Géosciences Environnement Toulouse, Observatoire Midi-Pyrénées, 31400 Toulouse, France*

Abstract

Textural and compositional data of sphalerite from the San Vicente and Shalipayco Mississippi Valley-type (MVT) deposits in Peru with focus on germanium and other trace elements are presented. Germanium is a critical raw material in increasing demand for its use in electronic devices and in the manufacture of several digital and environmentally sustainable technologies. Sphalerite in MVT deposits represents an important source of Ge.

In San Vicente, up to seven types of sphalerite, belonging to two subsequent mineralization steps were recognized. In Shalipayco, five types of sphalerite were identified, all assigned to a single ore forming episode. LA-ICP-MS analyses reveal Ge values in sphalerite from San Vicente (Inter-Quartile Range [IQR] = 118-44 ppm), and Shalipayco (IQR = 425-101 ppm) that are similar to those reported for sphalerite from other MVT deposits worldwide. Orange sphalerite from San Vicente of the second mineralization step, which is volumetrically restricted, yielded the highest Ge contents (IQR = 1207-375 ppm, up to 1861 ppm), while in Shalipayco, the highest Ge contents correspond to yellow sphalerite (IQR = 375-267 ppm, up to 1119 ppm). In both deposits, Ge-richest sphalerite crystallized relatively late in the respective paragenetic sequences.

Binary correlations between molar proportions of the analyzed elements suggest that the incorporation of Ge and other trace elements to the sphalerite lattice in San Vicente and Shalipayco were chiefly in the form of coupled substitutions such as $Ge^{4+} + 2Ag^{+} \leftrightarrow 3Zn^{2+}$, $2Cu^{+} + Ge^{4+} \leftrightarrow 3Zn^{2+}$, and $Ge^{4+} + 2(Cu + Ag + Tl)^{+} \leftrightarrow 3Zn^{2+}$. Our data further support that MVT deposits may be attractive for Ge and encourage similar systematic surveys in MVT mineralization worldwide.

Keywords: Critical raw materials, high-tech elements, by-product, Zn-Pb deposits, Andes, mineral color

1. Introduction

Mississippi Valley-type (MVT) Zn-Pb deposits are epigenetic stratabound, and mostly carbonate-(commonly dolostone) hosted occurring mainly in platform sequences, particularly, but not exclusively, in orogenic forelands (Leach et al., 2005, 2010; Ostendorf et al., 2015;

Paradis et al., 2007; Sangster, 1995; Wilkinson, 2014). Although most MVT mineralization formed during contractional events in orogenic zones (Bradley and Leach, 2003; Cathles and Smith, 1983; Leach et al., 2005, 2001), mineralization is typically controlled by extensional faults and fractures that channelized ascending deeply-circulated, high-salinity hydrothermal fluids to reach the deposition site in carbonate rocks (Leach et al., 2010), and in places also in clastic rocks (Kesler, 1994; Saintilan et al., 2016; Fontboté and Saintilan, 2018). The fluids responsible for transporting metals are related to basal brines with salinities between 10 and 30 wt.% NaCl equivalent and temperatures between 50 º and 250 °C (Anderson and Macqueen, 1982; Eisenlohr et al., 1994; Kesler et al., 1995; Leach et al., 2005). In MVT systems, base metals are chiefly transported as chloride complexes, and the main metal sources are basement rocks and/or their detrital erosive products (Leach et al., 2010). However, Saintilan et al. (2019) determined that oil and associated waters can also provide metals in significant quantities. The mineralization processes in MVT systems involve i) sulfide precipitation by the reaction $Me^{+} + H_2S \rightarrow MS + 2H^{+}$ generating acid fluids whereby reduced sulfur frequently is derived by thermochemical sulfate reduction (TSR) mediated by hydrocarbons (Anderson, 2015; Kesler et al., 1994), ii) both dissolution and host rock replacement, and iii) cavity and vein filling (Corbella et al., 2004; Leach and Sangster, 1993).

Main ore minerals in MVT deposits are sphalerite and galena, which occur along with mostly minor amounts of Fe sulfides and Pb-Cu sulfosalts, while gangue is commonly composed of dolomite and in general minor proportions of calcite, quartz, barite, fluorite, and gypsum (Leach et al., 2010; Sangster, 1995). Alteration generally consists of hydrothermal carbonates that occur as a replacement of host carbonates and/or as cement in intergranular porosity and open space-filling (Leach et al., 2005; Wilkinson, 2014). Characteristic textures in these deposits include colloform to botryoidal banding in sphalerite (often referred to as *schalenblende*), replacement (massive sulfides), collapse breccias, “snow-on-the-roof” (sulfides coating the top of crystals or breccia clasts in open spaces; Peace et al., 2003), pseudo-breccias (by selective replacement of host rocks) and zebra textures (Kelka et al., 2017; Leach et al., 2005; Merino and Canals, 2011).

Sphalerite from several MVT deposits is known to host significant Ge contents, and, in general, is particularly enriched in this element in comparison to deposits of magmatic-hydrothermal origin (Bernstein, 1985; Wei et al., 2021; Bauer et al., 2019; Frenzel et al., 2016; Paradis, 2015;

Shanks et al., 2017). Germanium is considered a critical raw material by the European Commission (2020). It is mainly used as a semiconductor in infrared optical devices, a catalyst in plastic production, fiber-optic systems, and in photovoltaic cells (Cook et al., 2015; Höll et al., 2007; Melcher and Buchholz, 2014). Germanium does not form its own deposits but is exploited as a by-product in Zn-rich deposits (e.g., MVT, SEDEX, VMS, Kipushi type; Shanks et al., 2017), mainly from sphalerite, in which it is incorporated under certain crystallization conditions and mostly via coupled substitutions (Belissont et al., 2014; Cook et al., 2009, 2015; Frenzel et al., 2016; Möller and Dulski, 1996). In Peru, sphalerite samples from the Cristal MVT project (Bongará province) have an average Ge content of 142 ppm, with values up to 386 ppm Ge (Mondillo et al., 2018b).

This work aims to present new data on the minor and trace elements composition, with particular attention to Ge, of sphalerite from the San Vicente and Shalipayco MVT deposits through LA-ICP-MS analysis. Petrographic control on point analysis allows for the identification of sphalerite types that are particularly enriched in this element and their contextualization in the paragenetic sequences of the studied deposits. Possible incorporation mechanisms of Ge into the structure of sphalerite are assessed. Additionally, the possible correlation between trace elements contents and crystal color is explored.

2. Geological setting

2.1. The MVT belt in Peru

A MVT metallogenic belt extends along the Eastern Cordillera and Sub-Andean Zone morphotectonic units of Central and Northern Peru and includes the San Vicente, Shalipayco, and Florida Canyon deposits, as well as a dozen of mineral showings (Fig. 1; Carlotto et al., 2009; de Oliveira et al., 2019, 2020; Fontboté, 2018; Fontboté and Gorzawski, 1990; Mondillo et al., 2018a).

MVT mineralization along this belt is hosted by the eastern part of the NNW-trending Pucará basin, at the western margin of the Brazilian Shield (Fig. 1; Benavides-Cáceres, 1999). Rocks of the Pucará Group were deposited on top of Paleozoic units and Triassic syn-rift volcanic and sedimentary rocks of the Mitu Group in a wide carbonate platform during regional subsidence in Upper Triassic to Lower Jurassic times (Kontak et al., 1985; Noble et al., 1978; Rosas et al.,

2007; Spikings et al., 2016). The Pucará Group extends along ~1000 km in a NW-SE direction from central to northern Peru and comprises three distinct formations, which from base to top are Chambará, Aramachay, and Condorsinga (Loughman and Hallam, 1982; Mégard, 1978; Rosas et al., 2007; Szekely and Grose, 1972). The Norian-Rhaetian Chambará Formation is predominantly dolomitic, composed of a thick sequence of dolostones interlayered with dolomitic, dark-gray, and fossiliferous limestones. In the lower part of the sequence, a higher content of detrital material is observed; nodules of chert are common (Rosas and Fontboté, 1995). At San Vicente, a red sandstone unit with anhydrite lenses occurs at the base of the Chambará sequence (Fontboté and Gorzawski, 1990; Moritz et al., 1996). Other macroscopic components include carbonate pseudomorphs after Ca-sulfates and macrofossils (Robson et al., 2017; Rosas et al., 2007). In other places, massive anhydrite/gypsum levels occur also at the base of the Chambará Formation (Baby et al., 2019; Benites et al., 2021; Calderón et al., 2017a, b; Kouzmanov et al., 2011; Ramírez et al., 2022; Rosas and Fontboté,1995; Rosas et al., 2007). Salt tectonics and possible evidences of it have been described by Benites et al. (2021), Berrospi-Rodriguez et al. (2018), de Oliveira et al. (2019, 2020), and Sempere and Cotrina (2018). At Morococha, the anhydrite levels serve as decollement surfaces for thin-skinned overthrust tectonics (Stipetich et al., 2021, 2022). The upper Rhaetian-Sinemurian Aramachay Formation is mostly formed by black argillaceous bituminous limestones and black shales with high organic matter content (Rosas et al., 2007; Szekely and Grose, 1972). Intercalations of andesitic-basaltic flows are also observed in the Chambará and Condorsinga Formations (Muñoz et al., 2000; Rosas et al., 2007; Schaltegger et al., 2008). In the Western Cordillera of Central Peru, abundant material derived from siliceous sponges that would have inhabited shallow platforms has been identified, pointing out that some domains in the Aramachay Formation do not record the typical transgression described by facies along the Altiplano and Eastern Cordillera (Ritterbush et al., 2015; Rosas, 2016). The upper Sinemurian-Toarcian Condorsinga Formation comprises packstone to grainstone limestone with chert, dolomitic limestone with macrofossils, and bioturbated limestone (Rosas and Fontboté, 1995). Compared to the Chambará Formation, the Condorsinga Formation shows lower degrees of dolomitization and lesser chert content (Rosas et al., 2007).

Fig. 1 Morphostructural units of Peru after Basuki et al. (2008), including the location of MVT deposits/districts (yellow stars) in Peru. Topography base image taken from JPL-NASA ©.

Reactivation of pre-Andine structures affecting the Paleozoic basement had an important tectonic control in the genesis of the MVT deposits through the formation of horsts and grabens that controlled the facies of the Pucará sediments, including the development of permeable oolitic bars and structures that served as hydrocarbon traps (Dávila et al., 2000). MVT mineralization along the belt was most probably synchronous with the first overthrusts in the

Sub-Andean region (Badoux et al., 2001; Dávila et al., 2000), which occurred as early as Upper Cretaceous – Paleocene according to Baby et al. (2019), during the Peruvian episode of the Andean orogeny (see Benavides-Cáceres, 1999). This time constraint of the mineralization based on structural features in the San Vicente deposit accords well with Rb-Sr dates on sphalerite from the Florida Canyon MVT deposit at ca. 86-83 Ma (de Oliveira et al., 2020).

2.2. Geology of the San Vicente deposit

The San Vicente deposit (11°14′S, 75°22′W) is located ~300 km east of Lima and sits on the contact between the Eastern Cordillera and the Sub-Andean Zone, at an altitude of 2,030 m (Fig. 1).

In the deposit area, the base of the stratigraphic sequence corresponds to the pre-Devonian (Chew et al., 2016) Maraynioc metamorphic complex (Fig. 2), which is composed of mica schists, amphibolites, and gneisses (Fontboté and Gorzawski, 1990; Mégard, 1987). This unit is overlain by sedimentary rocks of the Pennsylvanian-Early Permian Tarma-Copacabana Group including limestones and subordinate sandstones, black shales, and cherty limestones (Wood et al., 2002). Phyllites of the Excelsior Group, of probable Devonian age (Jenks 1951; McLaughlin 1924; Saintilan et al. 2021), underlie the Mitu Group and have been recognized ~ 15 km southeast of the San Vicente mine (Fig. 2; Davila et al. 2000). Late Permian - Lower Triassic plutonic rocks in the area include the San Ramon granite, dated at 246 ± 10 Ma (Capdevila et al., 1977; recalculated by Lancelot et al., 1978), and the Tarma granodiorite, dated at 240 ± 4 Ma (Gunnesch et al., 1990). Compressive events during the Upper Cretaceous and Tertiary produced low-angle thrusting of the Tarma granodiorite and Precambrian metamorphic basement over rocks of the Mitu and Pucará Groups along the Utcuyacu fault (Davila et al, 2000; Fontboté and Gorzawski, 1990).

Zn-Pb mineralization in San Vicente is hosted by dolomitic rocks of the Pucará Group, which in the central part of the deposit is~ 1,400 m thick. Three ore-bearing dolomitic horizons belonging to the Chambará and Condorsinga Formations are described (Fontboté and Gorzawski, 1990). The Chambará Formation has a thickness around 1200 m in the central part of the deposit and comprises two main ore-bearing dolomitic units known as San Judas and San Vicente

(Fontbote and Gorzawski, 1990; Spangenberg et al., 1999, 1996). The San Judas unit (~280 m thick) is constituted by a fine to very coarsely crystalline dolomite and fairly abundant white sparry dolomite and evaporite pseudomorphs. The San Vicente unit (~ 300 m thick) consists mainly of dolomitized barrier calc-arenites (oolitic packstones to grainstones textures) intercalated with very fine to fine crystalline dolomite deposited in lagoon and tidal flat environments (Fontboté and Gorzawski, 1990). The third ore-bearing dolomitic unit, the Alfonso dolomite (~120 m thick), belongs to the part of the Condorsinga Formation that is not cut by an overthrust and is constituted by medium to very coarse crystalline dolomite with similar characteristics to the San Judas and San Vicente dolomitic units. The Aramachay Formation is represented in San Vicente by the Uncush bituminous limestone (8 to 250 m thick), a hydrocarbon-source rock characterized by its high organic matter content and pyrite dissemination that acted as a seal during the mineralization process atop the San Vicente unit (Dávila et al., 2000; Fontboté and Gorzawski, 1990).

Davila et al. (2000) report an accumulated production until June 1999 of 25 Mt ore with 12% Zn and 1% Pb. In subsequent years the exploited grades have decreased. The San Vicente dolomitic horizon is the main ore host. Stratabound lens-shaped orebodies of the San Vicente mine tend to be stratiform (Fontboté & Gorzawski, 1990), except in the deeper parts of the mine, where they tend to be parallel to fault planes. Most orebodies at San Vicente are hosted in dolomitized oolitic bars, considered former hydrocarbon traps containing sulfur reduced by TSR (Fontboté et al., 1995; Spangenberg, 1995, Spangenberg and Macko, 1998, Spangenberg et al., 1999). The ore is essentially composed of sphalerite and galena, with traces of pyrite-marcasite, chalcopyrite, and sulfosalts. The gangue is mainly constituted by dolomite and calcite (Dávila et al., 2000). Three main types of gangue textures are observed in the San Vicente mine: zebra with dark and white sparry dolomite, breccia with clasts of dark dolomite in a white dolomite cement, and veins filled with white sparry dolomite (Badoux et al., 2001).

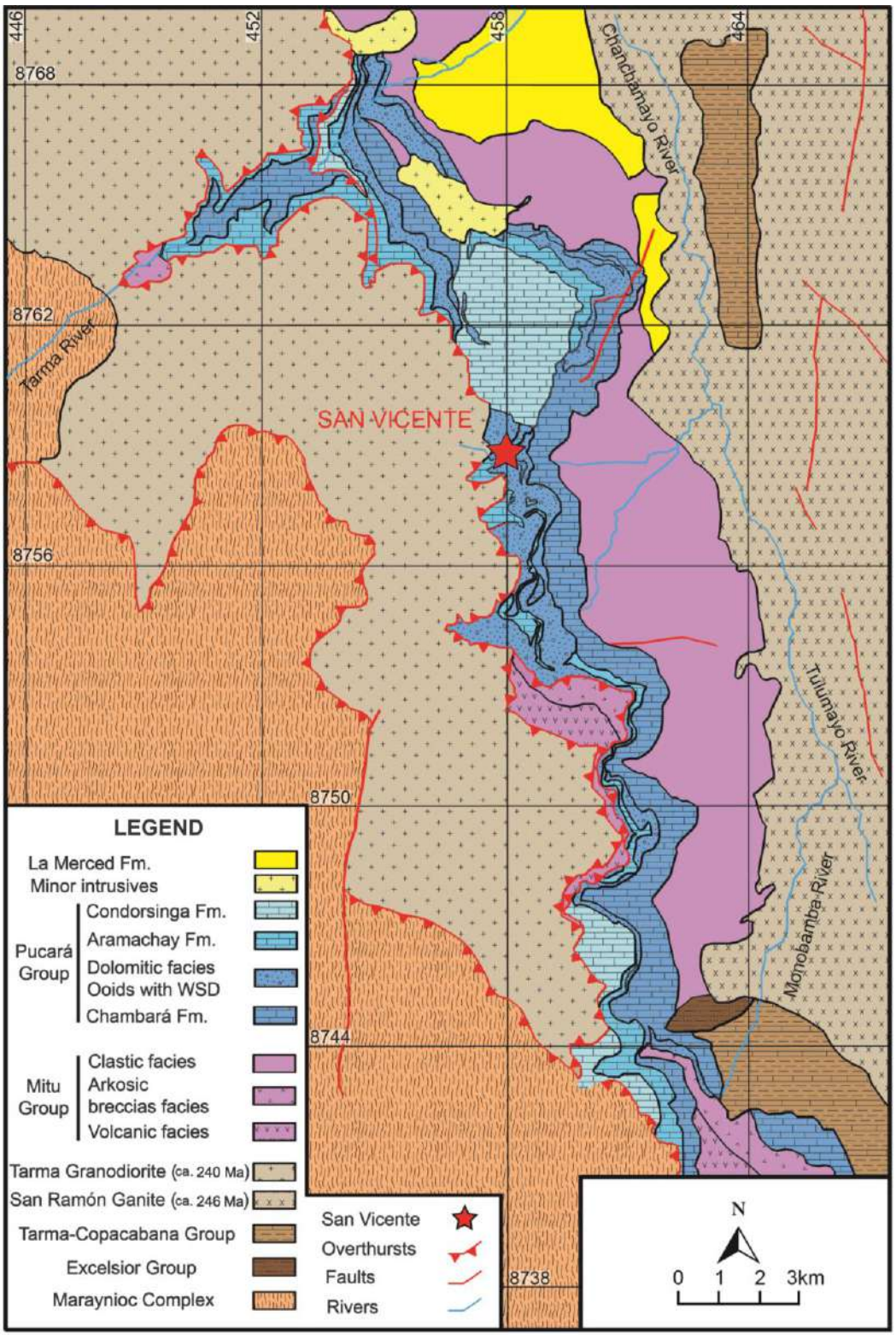

Fig. 2 Geological map of the San Vicente deposit. Modified from Dávila et al. (2000). WSD: white sparry dolomite.

Strontium isotope analyses on carbonates carried out by Fontboté and Gorzawski (1990) and Moritz et al. (1996) showed that a radiogenic Sr-enriched brine interacted with the carbonate

host rock yielding Sr isotopic signatures for the hydrothermal carbonates more radiogenic than those of Lower Jurassic – Upper Triassic seawater. These authors concluded that the basal brine incorporated radiogenic Sr due to interaction with the Brazilian shield rocks, Permo-Triassic intrusions (San Ramón granite), and their erosive products, including detrital series of the Mitu Group. Host-rock O and C isotopic results are in the typical range for lower Jurassic marine carbonates (Fontboté and Gorzawski, 1990), showing lighter values with the advance of hydrothermal interaction. The authors indicate that this trend resulted from a combination of T effects, different fluid/rock interaction ratios, and, in the specific case of C, the incorporation of organic carbon (Fontboté and Gorzawski, 1990; Moritz et al., 1996; Spangenberg et al.,1999).

Fontboté and Gorzawski (1990) and Spangenberg et al. (1999) found a restricted variation of $\delta^{34}S$ in sulfides with enrichment in the heavy isotope related to typical sulfides precipitated from magmatic and magmatic-hydrothermal fluids and attributed this enrichment to the presence of reduced sulfur derived from Triassic/Jurassic seawater sulfate, connate waters, and/or Middle Triassic to Early Jurassic marine evaporites. The presence of hydrocarbons in the carbonate host rock would have provided the redox conditions for sulfate reduction to H_2S and sulfide precipitation. TSR as the main source of reduced sulfur is also indicated by very light carbon isotopes in certain hydrothermal carbonate generations of San Vicente (Spangenberg et al. 1966). Fluid inclusion microthermometry on sparry dolomite yields homogenization temperatures ranging between 115 ° and 162 °C and salinities between 9.5 wt.% and 26 wt.% NaCl equivalent (Mortiz et al., 1996). This temperature range is compatible with sulfur isotope sphalerite-galena geothermometry reported by Schutfort (2001).

2.2. Geology of the Shalipayco deposit

The Shalipayco deposit (10°51′S, 75°58′W) is located ~170 km northeast of Lima and sits on the Central Eastern Cordillera of Peru at an altitude of 4,400 m (Fig. 1). An unconformity separates the Chambará Formation from the underlying Mitu Group (de Oliveira et al., 2021). The ore-hosting Pucará Group limestones at Shalipayco are moderately folded, forming monoclines between 30° and 45° to the southwest (Robson et al., 2017). The NW-SE oriented Ulcumayo-San Rafael fault thrusts the Mitu Group over the Pucará Group, and the Yanacocha-Quilcatacta fault, also NW-SE oriented, thrusts limestones of the Condorsinga Formation upon

themselves (Robson et al., 2017). A cross-sectional structural system is also recognized, including the Eddy, San Teodoro, Virgencita, Pucará, and Santa Inés N-NE and N-NW faults, which could have served as feeding channels for mineralization (Robson et al., 2017; de Oliveira et al., 2021). Geologic maps showing the geology of the Shallipayco deposit are available in Figures 1 and 2 in de Oliveira et al. (2021).

De Oliveira et al. (2021) divided the Chambará Formation, host of the mineralization in Shalipayco, into four members, which from base to top are i) the ~320-m-thick Chambará I Member, which is mainly formed by dark-gray lime mudstone to wackestone with chert clasts and calcite as cavity-filling and veins; ii) the ~120-m-thick Chambará II Member, which is essentially constituted by porous gray dolostone (wackestones) with local mudstone; iii) the ~80-m-thick Chambará III Member, which is composed of beige dolomite boundstones with evaporitic rocks and calcite veins; and iv) the ~130-m-thick Chambará IV Member, which is composed of light gray mudstones with local dolomitization.

The main stratabound and mostly stratiform orebodies in Shalipayco, namely Intermedios and Resurgidora, are largely hosted by the Chambará II and III Members, respectively (Robson et al., 2020; de Oliveira et al., 2020, 2021). The Intermedios level has an average thickness of 8 m (up to 25 m) and extends at least 2 km along strike (de Oliveira et al., 2021). It is located above dark gray mudstones and wackestones and below dark gray sparry fetid dolomites rich in organic matter (Oldham et al., 2017). Approximately 45% of the Zn-Pb mineralization occurs along this horizon and is mainly hosted within porous coarse-grain sparry dolostones. The Resurgidora level has an average thickness of 4 m (up to 11 m) and extends at least 4 km along strike (de Oliveira et al., 2021). It is located between two horizons of coarse-grained, dark, fetid, sparry dolomite rich in organic matter (Oldham et al., 2017) and is mainly hosted in coarse sparry dolostones and evaporite breccias (de Oliveira et al., 2021). Vein mineralization is mainly represented by the Eddy vein (up to 8 m thick), currently considered as one of the potential feeders (Robson et al., 2017; de Oliveira et al., 2021).

The average mineralization grade is 4.9% Zn and 0.5% Pb (Robson et al., 2017), and metallic ore is constituted by sphalerite and galena with lesser amounts of pyrite, marcasite, and Ag sulfosalts (Oldham et al., 2017; Moritz et al., 1996). The main gangue minerals are dolomite, calcite, quartz, and barite.

Strontium isotope signatures evolve from values equivalent to those of Norian seawater in least-altered limestones to increasingly more radiogenic in diagenetic replacement dolomite and, finally, ore-related calcite thus suggesting enhanced interaction with hydrothermal fluids that circulated through basement rocks enriched in radiogenic Sr (de Oliveira et al., 2021; Moritz et al., 1996). As in San Vicente, C and O isotopic values on carbonates from Shallipayco also show a progression from signatures that match the $\delta^{13}C$ and $\delta^{18}O$ of Triassic marine limestones to isotopically lighter signatures along the aforementioned carbonate sequence (de Oliveira et al., 2021; Moritz et al., 1996). Highly negative $\delta^{34}S$ values in sulfides from Shalipayco led de Oliveira et al. (2021) to conclude that in addition to thermochemical sulfate reduction, bacteriogenic sulfate reduction operated previous to ore deposition in Shallipayco.

3. Sampling and analytical methods

Sampling and petrography

A total of 32 sphalerite-rich ore samples were taken from the San Vicente (n = 16) and Shalipayco (n = 16) deposits. In San Vicente, sampling was conducted on drillholes (n =14 samples) and mine adits (n = 2 samples); sampled sites/levels include the Ayala Inferior and Orcopunco zones, the 8909W chamber, and the 630 ramp of the North Zone. In Shalipayco, all samples were picked up from drillholes and come from the Resurgidora and Intermedio levels. The location and name/label of the sampled mine adits and drillholes, and the major mineralogy and hand sample textures are given in Table S1 in the Supplementary Material. A total of 38 thick polished sections were prepared at the QEMSCAN laboratory of the Pontifical Catholic University of Peru (PUCP) for their study under the optical microscope using reflected light. A selection of 5 samples was examined on a Tescan VEGA II XMU SEM equipment with a BRUKER xFlash 6/30 EDS microanalysis system at BIZALAB.SAC. The operating conditions were 20 kV accelerating voltage and 105 μA in backscattered electron (BSE) imaging mode.

Electron Probe Micro Analysis (EPMA)

Mineral chemistry analyses of sphalerite were performed using a five-channel JEOL JXA-8230 electron microprobe equipment housed at Centres Científics i Tecnològics of the University of Barcelona (CCiT-UB). The instrument was operated at 20 kV acceleration voltage, 20 nA beam current, and with a beam diameter of 5 μm. Analytical standards and emission lines used for

analyses were as follows: sphalerite (Zn and S, Kα), chalcopyrite (Cu, Kα), FeS_2 (Fe, Kα), PbS (Pb, Mα), CdS (Cd, Lβ), GaAs (As, Lβ; Ga, Kα), In_2Se (In, Lβ), Ag (Ag, Lα), Sb (Sb, Lα), Sn (Sn, Lα), and Ge (Ge, Kα). The detection limits (d.l.) for each element and representative analyses (values in wt.% and atoms per formula unit - a.p.f.u.) are displayed in Table S2 in Supplementary Material. Sphalerite compositions were normalized to 1 S.

Laser ablation inductively coupled plasma mass spectrometry (LA-ICP-MS)

Analyses of sphalerite trace element content were carried out at ETH Zürich, Switzerland, by laser ablation - inductively coupled plasma - sector field - mass spectrometry (LA-ICP-SF-MS) using a RESOlution S-155 (ASI/Applied Spectra) 193 nm ArF excimer laser system attached to an Element XR (Thermo) sector-field ICP-MS. We used a laser repetition rate of 3 Hz, a spot diameter of 19 µm, and a laser energy density on a sample of ca. 2.5 $J \cdot cm^{-2}$. The sample surface was cleaned before each analysis by three pre-ablation pulses. Ablation was performed in a dual-volume, fast-washout S-155 ablation cell (Laurin Technic) fluxed with carrier gas consisting of ca. 0.5 $L \cdot min^{-1}$ He and make-up gas consisting of ca. 1 $L \cdot min^{-1}$ Ar and 2 $mL \cdot min^{-1}$ N_2. The ablated aerosol was homogenized via flushing through a squid device before being introduced in the plasma.

The ICP-MS instrument is equipped with a high capacity (80 $m^3 \cdot h^{-1}$) interface pump to achieve, in combination with jet sampler and normal H-skimmer cones, a detection efficiency (based on U in NIST SRM612 glass) in the range of 2% (Guillong et al., 2020). The instrument was optimized for maximum sensitivity on the entire mass range while keeping low the production of oxides ($^{248}ThO^+/^{232}Th^+$ ≤0.15%) and the U/Th ratio at ca. 1 (on NIST SRM612 glass). The list of analyzed isotopes and corresponding dwell times is provided in Table S3 in Supplementary Material. A total of 68 mass scans (ca. 0.72 s sweep time each) were acquired over ca. 50 s measurement (25 s of background measurement followed by 25 s of sample ablation).

The resulting intensities were subsequently processed offline with the standalone version 1.3.2 of the SILLS program (Guillong et al., 2008). The sulfide pressed pellet MASS-1 (former PS-1; Wilson et al., 2002) was used as the primary reference material for trace element quantification and instrumental drift correction using conventional standard-sample bracketing. The Zn contents obtained by electron microprobe were used as internal standard for relative sensitivity

corrections. The data are reported in Table S4 in Supplementary Material and content statistical data are shown in Table 1.

The analytical reproducibility was checked by repeated measurements of the GSD-1G (Guillong et al., 2005) and NIST SRM610 (Jochum et al., 2011) glass reference materials, and ranges from 10 to 30% relative (2σ) for most elements. The quoted uncertainties for each analysis correspond to the internal (2σ) statistical error and analytical reproducibility propagated by quadratic addition. Accuracy was controlled by repeated measurements of the UQAC-FeS-1 sulfide pressed pellet (unpublished data from D. Savard, UQAC, 2018; see also Baumgartner et al., 2020). The results (reported in Table S4 in Supplementary Material) show that the measurements are accurate within the calculated uncertainties.

4. Mineralogy and textures

4.1 San Vicente deposit

The mineralization at San Vicente is mainly composed of sphalerite with lesser proportions of galena, pyrite, marcasite, and gratonite [$Pb_9As_4S_{15}$]. Hydrothermal dolomite is the main gangue mineral, whereas hydrothermal calcite and quartz are local. The main textures observed in the studied samples include a) “zebra” texture, with up-to-0.6-cm-wide dolomite bands interlayered with up-to-2-cm-wide lenses of sphalerite displaying a more or less rhythmical pattern (Figs. 3A); b) simple colloform banding (non-rhythmic) of sphalerite and dolomite (Figs. 3F, H, I); c) “snow-on-the-roof” (Fig. 3I); d) hydraulic fluid overpressure breccias with dolomite and sphalerite clasts (Figs. 3D, J-K); and e) replacement between different types of sphalerite and carbonates (Figs. 3B-H).

Three generations of hydrothermal dolomite have been recognized in the studied samples: dark replacement dolomite (DRD), white sparry dolomite 1 (WSD_1), and white sparry dolomite 2 (WSD_2), formed as open space-filling. Hydrothermal calcite appears as fine veins and is generally later than dolomite (see also textural descriptions in Spangenberg et al., 1999).

In general, sphalerite grains show sizes in the range between ~25 μm and <1 mm, and are generally devoid of visible mineral inclusions, except for local dissemination of pyrite/marcasite as described below (Figs. 4A, C). Up to 7 types of sphalerite, grouped into two steps of mineralization, have been differentiated according to their colors (including internal reflection

colors under the petrographic microscope) and textural relationships. Sphalerite formed during the mineralization step 1 (sl_1) accounts for most of the San Vicente ore and includes the black (sl_{1bl}), reddish-brown (sl_{1rb}), yellowish-brown (sl_{1yb}), and yellow (sl_{1y}) types. Sphalerite formed during the mineralization step 2 (sl_2) is volumetrically much restricted and include the orange (sl_{2o}), yellow (sl_{2y}), and white (sl_{2w}, *var.* cleiophane) types. Textural features of the sphalerite types are described below:

- Black sphalerite (sl_{1bl}) occurs mostly along the central part of sphalerite "zebra" bands (Fig. 3A) as well as in the "substrate" of reddish-brown (sl_{1rb}) and yellowish-brown (sl_{1yb}) sphalerite bands (Figs. 3B-C). Under the petrographic microscope, it forms micro- to millimeter-sized subhedral crystals with rectilinear grain boundaries, and does not show internal reflections (Figs. 4A-F).

- Reddish-brown sphalerite (sl_{1rb}) forms anhedral aggregates that have mostly grown on black sphalerite (sl_{1bl}) in "zebra" textural arrangement (Fig. 3A-C, H-I), and is overgrown by yellowish-brown (sl_{1yb}) sphalerite, resulting in a marked gradation of color (Figs. 4C-D, Q-R). It also has been overgrown and replaced by galena along microfractures and grain boundaries (Figs. 3C, H; 4Q-R).

- Yellowish-brown sphalerite (sl_{1yb}) is the volumetrically most abundant sphalerite type in the studied samples and occurs as subhedral grains that grew epitaxially on and locally as replacement of black (sl_{1bl}) and reddish-brown (sl_{1rb}) sphalerite (Figs. 3B-C). In "zebra"-type bands, it appears along sphalerite contacts with WSD_2 (Fig. 3A). It has been replaced by yellow sphalerite (sl_{1y}) and galena, while WSD1 and WSD2 occur as open space-filling (Figs. 4Q-R).

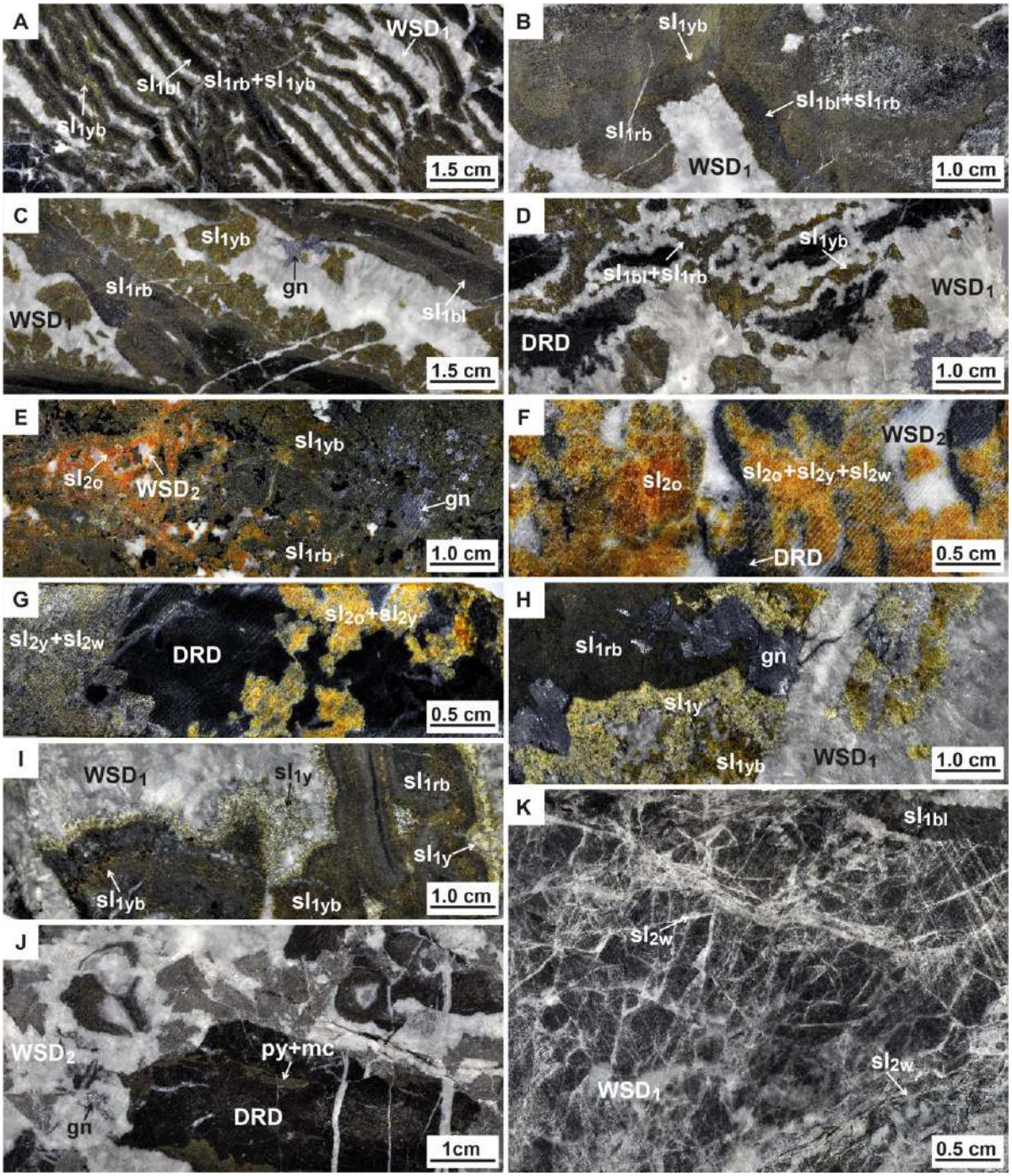

Fig. 3 Hand-sample photographs showing different textures in ore samples from the San Vicente deposit. A) Rock with "zebra"-type texture, composed of black, reddish-brown, and yellowish-brown sphalerite bands. White sparry dolomite 1 occasionally cut and dislocated the sphalerite bands (sample 2019-SV-02). B) Bands of black, reddish-brown, and yellowish-brown sphalerite with white sparry dolomite1 (sample 2019-SV-04). C) Bands of black and reddish-brown sphalerite overgrown by yellowish-brown sphalerite crystals, interspersed with bands of white sparry dolomite 1. Galena has grown perpendicular to sphalerite bands towards white sparry dolomite 1 (sample 2019-SV-11). D) Dark replacement dolomite and clasts of black, reddish-brown, and yellowish-brown sphalerite with white sparry dolomite 1. The rotation and the lateral interruption of sphalerite and dark replacement dolomite bands by white sparry dolomite 1 indicate brecciation (sample 2019-SV-12). E) Aggregates of reddish-brown and yellowish-brown sphalerite with overgrowth by orange and yellow sphalerite, which have occupied open spaces along with galena and white sparry dolomite 2 (sample 2019-SV-15). F) Dark replacement dolomite clasts in breccia with second step orange, yellow and white sphalerite with

cement of white sparry dolomite 2 (sample 2019-SV-13). G) Dark replacement dolomite clasts replaced by yellow and orange sphalerite (sample 2019-SV-14). H) Breccia formed by clasts of reddish-brown colloform sphalerite, overgrown by yellowish-brown and yellow sphalerite, and galena, cemented by white sparry dolomite 1. Note also veinlets of galena that crosscut the white sparry dolomite 1 cement (sample 2019-SV-01). I) Breccia with clasts composed of reddish-brown and yellowish-brown colloform banded growths of sphalerite overgrown by first step yellow sphalerite with "snow-on-the-roof" texture; clasts have been rotated and cemented by white sparry dolomite 1 (sample 2019-SV-03). J) Breccia with clasts of dark replacement dolomite partially replaced by pyrite and marcasite. These clasts have been cemented by white sparry dolomite 2 which in turn contains galena as subhedral cubic grains (sample 2019-SV-10). K) Aggregates of black sphalerite and white sparry dolomite 1 cut by fine veins of white sphalerite (sample 2019-SV-05). Abbreviations: **gn:** galena; **mc:** marcasite; **py:** pyrite; **sl_{1bl}**: first step black sphalerite; **sl_{1rb}**: first step reddish-brown sphalerite; **sl_{1yb}**: first step yellowish-brown sphalerite; **sl_{1y}**: first step yellow sphalerite; **sl_{2o}**: second step orange sphalerite; **sl_{2y}**: second step yellow sphalerite; **sl_{2w}**: second step white sphalerite; **DRD**: dark replacement dolomite; **WSD_1**: white sparry dolomite 1; **WSD_2**: white sparry dolomite 2.

- Yellow sphalerite (sl_{1y}) occurs as subhedral grains that grew epitaxially on and locally replaced reddish-brown sphalerite (sl_{1rd}; Figs. 3H-I; 4C-D) and has been replaced by galena, WSD_1, and WSD_2 (Figs. 3Q-R).

- Orange sphalerite (sl_{2o}) occurs as micro- to millimeter-sized anhedral to subhedral crystals (Figs. 4G-H, O-P), which have grown on reddish-brown (sl_{1rb}) and yellowish-brown (sl_{1yb}) sphalerite types (Fig. 3E) and has replaced DRD and WSD_2 (Fig. 3F). Orange sphalerite (sl_{2o}) is epitaxially overgrowth by yellow (sl_{2y}) and white (sl_{2w}) sphalerite types and replaced by WSD_2 (Figs. 4G-H, O-P).

- Yellow sphalerite (sl_{2y}) forms subhedral aggregates that have passively grown and filled interstices in all aforementioned sphalerite types (Figs. 3F-G 4G-H). It has replaced WSD_1 and has been replaced by galena, WSD_2, and calcite (Figs. 4I-J, M-N).

- White sphalerite (sl_{2w}) has mainly crystallized together with yellow sphalerite (sl_{2y}) as interstitial infill of the other 5 types of sphalerite (Figs. 4A-B, G-H, K-L) and describes "snow-on-the-roof" texture in some samples (Fig. 3I). White sphalerite also occurs as veinlets that crosscut black sphalerite (sl_{1bl}), WSD_1, and WSD_2 (Figs. 3K; 4A-B, K-L). It shows, in addition to white, local light gray to pale-green internal reflections (Figs. 4K-L).

Different textural types of pyrite have been distinguished, all with sizes <400 μm: i) fine disseminations in sl_1 (Figs. 4A-F, Q-R); ii) pseudomorphic pyrite according to disseminated marcasite in DRD (Figs. 3J; 4M-N), and iii) subhedral-euhedral crystals in fractures and cavities of sl_1 (Figs. 4A-B; Q-R). In the studied samples, galena occurs as i) subhedral crystals in WSD_1

and WSD_2 (Figs. 3C, J), often growing epitaxially on sphalerite (Figs. 4Q-R), and ii) in fine veins that cut WSD_1 and WSD_2 (Figs. 3H). Locally, galena has been replaced by anhedral aggregates of gratonite.

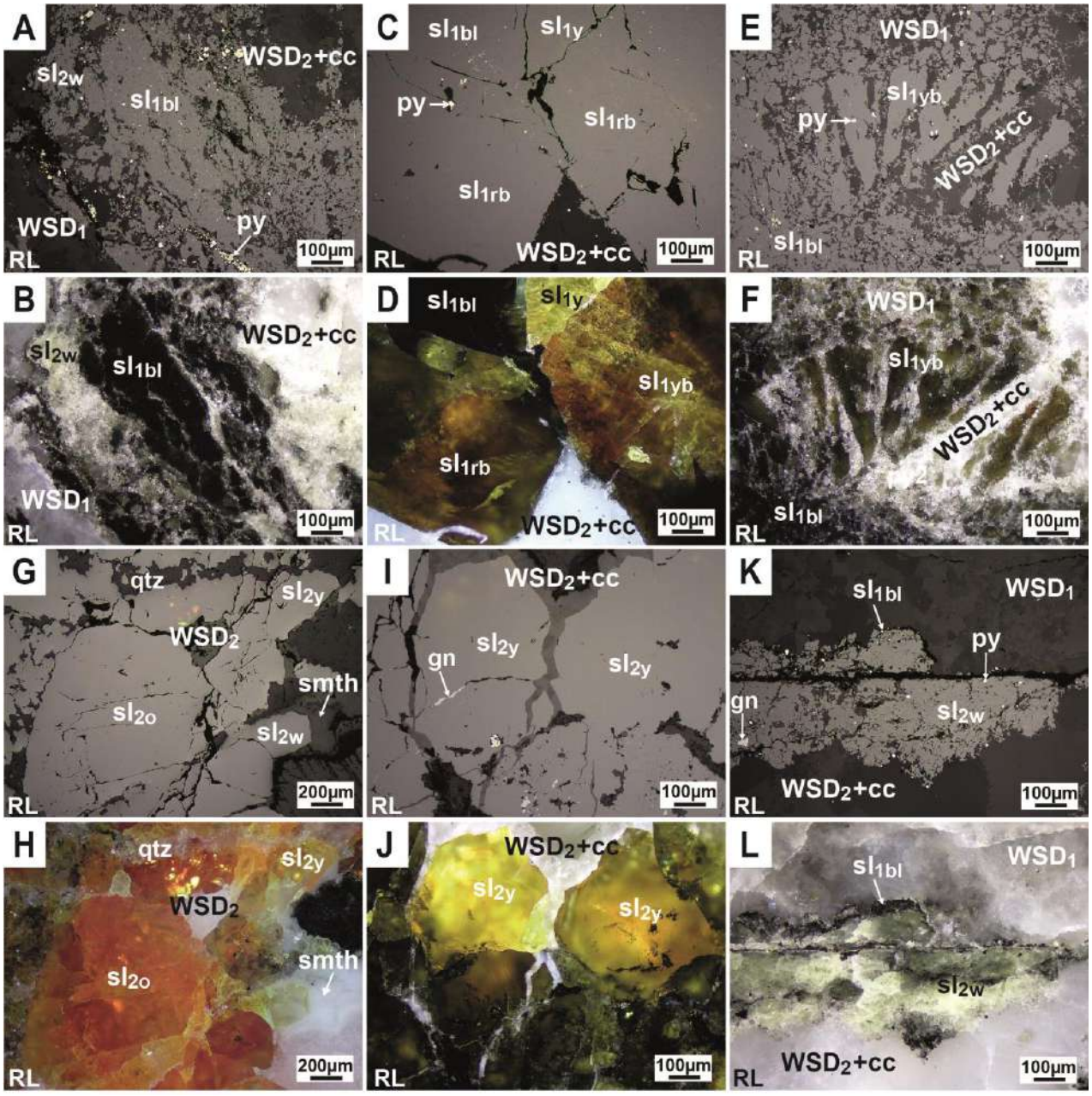

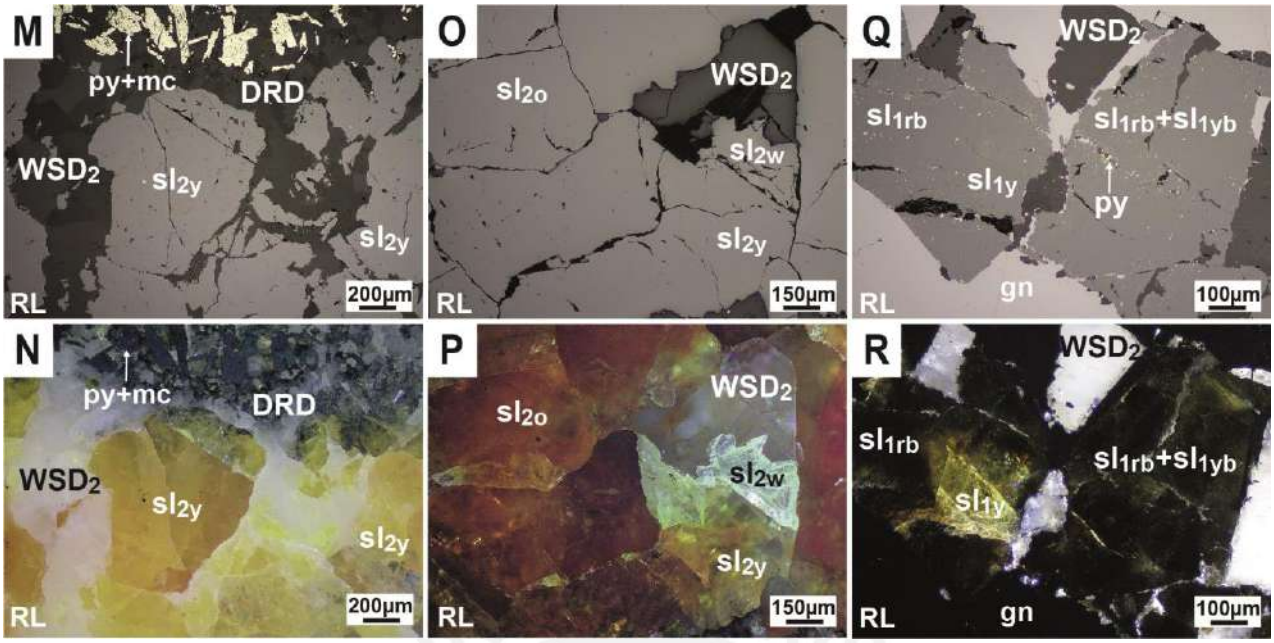

Fig. 4 Photomicrographs of polished sections taken with reflected light without analyzer (A, C, E, G, I, K, M, O, and Q) and in crossed polars (B, D, F, H, J, L, N, P, and R) showing microtextures of ore samples from the Saint Vincent deposit. A-B) Anhedral to subhedral black sphalerite aggregates with white sparry dolomite 1 and 2 and calcite as open space-filling, with fine disseminations of and micro-fractures lined with pyrite. Black sphalerite has been overgrown by white sphalerite. C-D) Subhedral crystals of black and reddish-brown sphalerite; the latter with gradation to first step yellow sphalerite, with fine disseminations and inclusions of pyrite, and replacement by white sparry dolomite 2 and calcite. E-F) Clasts of black and yellowish-brown sphalerite cemented by white sparry dolomite 1 and cut by white sparry dolomite 2 and calcite. G-H) Anhedral to subhedral orange, yellow and white sphalerite crystals with quartz and replaced by white sparry dolomite 2 and smithsonite. I-J) Anhedral yellow sphalerite crystals with white sparry dolomite 2 and calcite as microfractures and open space-filling. Galena occurs in microfractures across sphalerite. K-L) Aggregates of white sparry dolomite 1 and 2 and calcite cut by white to pale-green sphalerite irregular vein, the latter with black sphalerite relicts at its borders. Small inclusions of pyrite and galena in white sphalerite are also noticed. M-N) Dark replacement dolomite with interstitial pyrite and marcasite, and anhedral yellow sphalerite crystals replaced by white sparry dolomite 2. O-P) Anhedral aggregates of orange sphalerite overgrown by yellow and white sphalerite, with white sparry dolomite 2 filling interstitial space. Q-R) Anhedral crystals of reddish-brown and yellowish-brown sphalerite, with microfractures filled by subhedral pyrite. Sphalerite has been replaced by galena. White sparry dolomite 2 as open space-filling. **Abbreviations: cc:** calcite; **gn:** galena; **mc:** marcasite; **py:** pyrite; **qtz:** quartz; **sl_{1bl}**: first step black sphalerite; **sl_{1rb}**: first step reddish-brown sphalerite; **sl_{1yb}**: first step yellowish-brown sphalerite; **sl_{1y}**: first step yellow sphalerite; **s_{l2o}**: second step orange sphalerite; **sl_{2y}**: second step yellow sphalerite; **sl_{2w}**: second step white sphalerite; **smt:** smithsonite; **DRD**: dark replacement dolomite; **WSD_1**: white sparry dolomite 1; **WSD_2**: white sparry dolomite 2.

From the above-described textural relationships, a general paragenetic sequence has been produced (Fig. 5), the deposition sequence being also broadly consistent with petrographic descriptions by Fontboté and Gorzawski (1990).

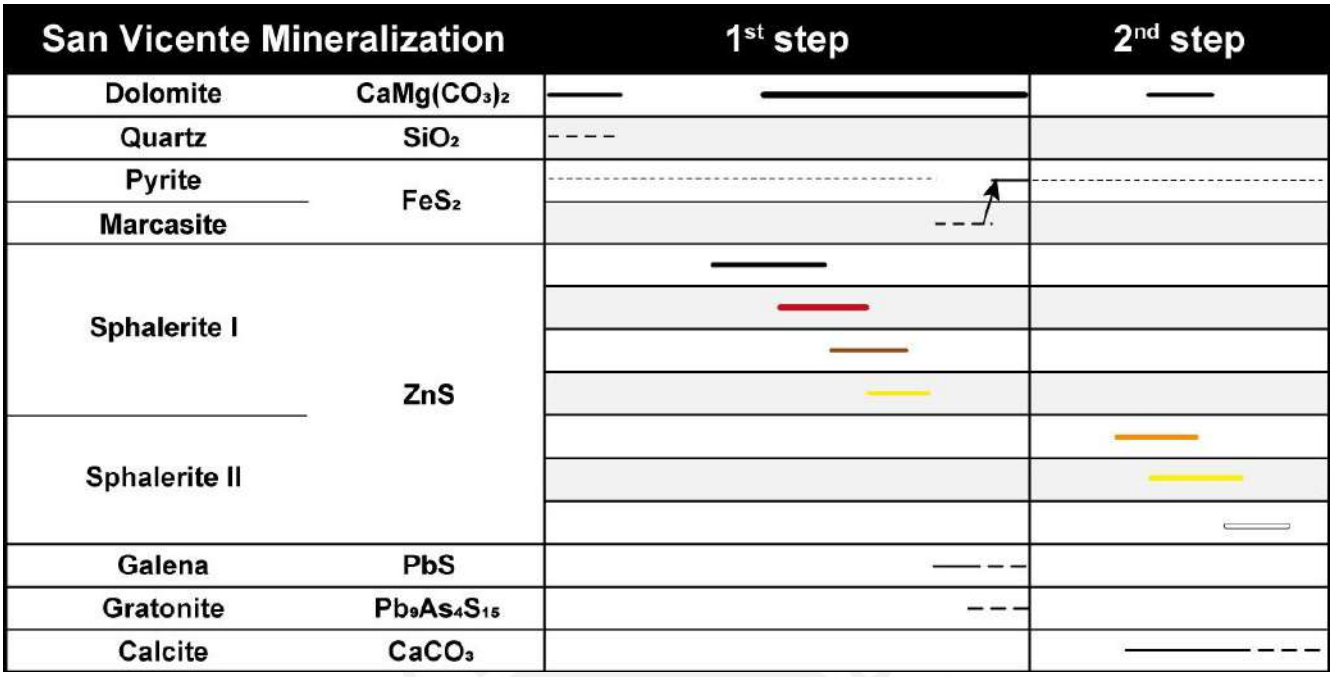

Fig. 5 Paragenetic sequence of The San Vicente deposit. Thick bars indicate higher abundance and dashed lines, lesser abundance. The color of the bars corresponding to sphalerite types are close to those observed in hand samples.

4.2. Shalipayco deposit

Sphalerite constitutes the main ore mineral, and appears along with traces of galena, pyrite, and marcasite. The main gangue mineral is dolomite; other gangue minerals in minor amounts include barite, calcite, and quartz. Two generations of dolomite were recognized: i) white sparry dolomite (WSD_1), which occurs as diagenetic replacement of the host limestone and contains interstitial early sphalerite, and ii) medium-grain white sparry dolomite (WSD_2), which occurs as replacement of late sphalerite. These textural features are consistent with those described by de Oliveira et al. (2021).

Sphalerite grains show sizes between ~20 μm and >1 mm and are largely free of visible inclusions of other sulfides. At the mesoscopic scale, sphalerite occurs a) disseminated in dolomite, b) forming anhedral aggregates and overgrowth bands, sometimes replaced by carbonates, and iii) as infill of collapse breccias. According to de Oliveira et al. (2021), there was a single ore-forming episode at Shallipayco. Following the same criteria as for the discrimination of sphalerite types in San Vicente, up to 5 types of sphalerite were recognized in

the studied samples from Shallipayco: black (sl_{bl}), reddish-brown (sl_{rb}), yellowish-brown (sl_{yb}), yellow (sl_{y}), and white (sl_{w}; *var.* cleiophane). Textural features of the sphalerite types are described below:

- Black sphalerite (sl_{bl}) appears as micro- to millimeter-sized anhedral to subhedral crystals with rectilinear and sub-rounded grain boundaries (Figs. 6A-D). Local secondary porosity (Figs. 6G-H) and absence of internal reflections are also noticed. Some grains have replaced pyrite aggregates and tiny (< 20 µm) prismatic crystals of marcasite (Figs. 6A, C).

- Reddish-brown sphalerite (sl_{rb}) forms anhedral to subhedral grains. It has grown chiefly on black sphalerite (sl_{bl}) and has been overgrown by yellowish-brown sphalerite (sl_{yb}; Figs. 6G-H). It also appears as overgrowth and replacement of subhedral barite crystals (Figs. 6E-F) and has been replaced by WSD_2 (Figs. 6G-H).

- Yellowish-brown sphalerite (sl_{yb}) forms subhedral millimeter crystals. It grew on and locally replaced reddish-brown (sl_{rb}) sphalerite, barite, and quartz (Figs. 6E-F). It has been replaced by WSD_2 (Figs. 6I-J).

- Yellow sphalerite (sl_{y}) appears as anhedral grains that grew on and replaced yellowish-brown sphalerite (sl_{yb}), and has been replaced by WSD_2 (Figs. 6G-L).

- White sphalerite (sl_{w}) forms small anhedral grains and presents colorless internal reflections (Figs. 6K-L). It generally appears as replacement of yellow sphalerite (sl_{y}) and has been replaced by WSD_2.

Two different textural types of pyrite have been observed: i) subhedral to anhedral grains <200 µm in size as void and fracture-filling in WSD_1, partially replaced by black sphalerite (sl_{bl}; Figs. 6A-B) and ii) fine to medium subhedral to euhedral cubic crystals <10 µm, as dissemination and within microfractures in WSD_1 and WSD_2, and at borders of yellowish-brown (sl_{yb}) and yellow (sl_{y}) sphalerite types (Figs. 6E-J). Traces of galena occur as replacement and narrow veinlets that crosscut yellow sphalerite (sl_{y}; Figs. 6I-J).

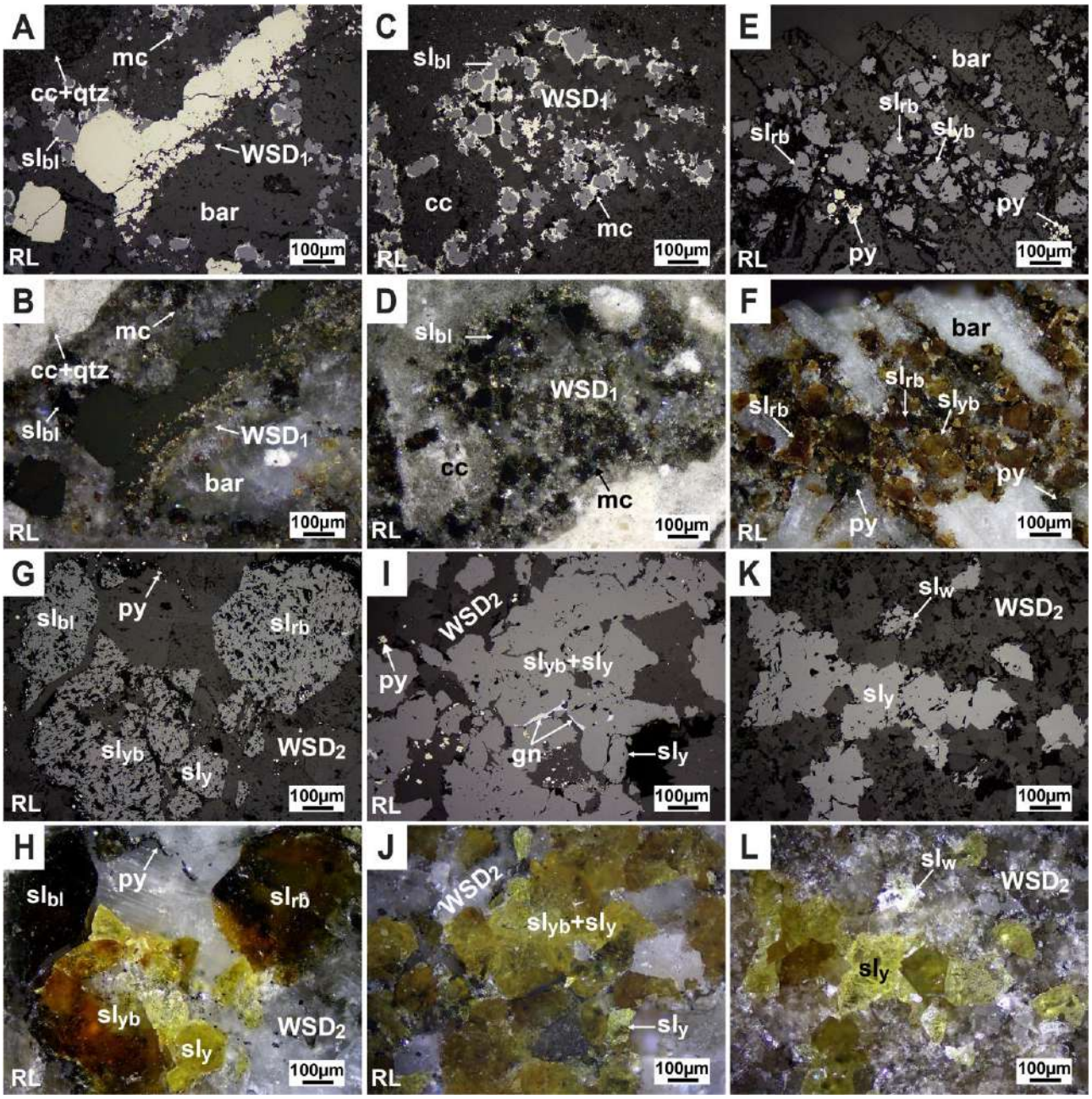

Fig. 6 Photomicrographs of polished sections taken with reflected light without analyzer (A, C, E, G, I, and K) and in crossed polars (B, D, F, H, J, and L) showing microtextures of ore samples from the Shalipayco deposit. A-B; C-D) Micritic calcite with quartz, and subhedral barite replaced by white sparry dolomite 1 and these, in turn, replaced by pyrite and black sphalerite. Small prismatic crystals of marcasite on borders of black sphalerite are also observed. E-F) Prismatic barite crystals with inclusions of pyrite and replaced by aggregates of reddish-brown and yellowish-brown sphalerite. G-H) Anhedral grains of black, reddish-brown, yellowish-brown, yellow, and white sphalerite cut and replaced by white sparry dolomite 2. Pyrite inclusions in both sphalerite and white sparry dolomite 2 are observed I-J) Anhedral yellowish-brown to yellow sphalerite crystals replaced by white sparry dolomite 2 and galena. K-L) Anhedral yellow and white sphalerite with white sparry dolomite 2. **Abbreviations: bar**: barite**; cc**: calcite; **gn**: galena; **mc**: marcasite; **py**: pyrite; **qtz**: quartz; **sl_{bl}**: black sphalerite; **sl_{rb}**: reddish-brown sphalerite; **sl_{yb}**: yellowish-brown sphalerite; **sl_{y}**: yellow sphalerite; **sl_{w}**: white sphalerite; **WSD_1**: white sparry dolomite 1; **WSD_2**: white sparry dolomite 2.

Taking into account the aforementioned petrographic observations as well as textural descriptions carried out by de Oliveira et al. (2021), a paragenetic sequence has been produced (Fig. 7).

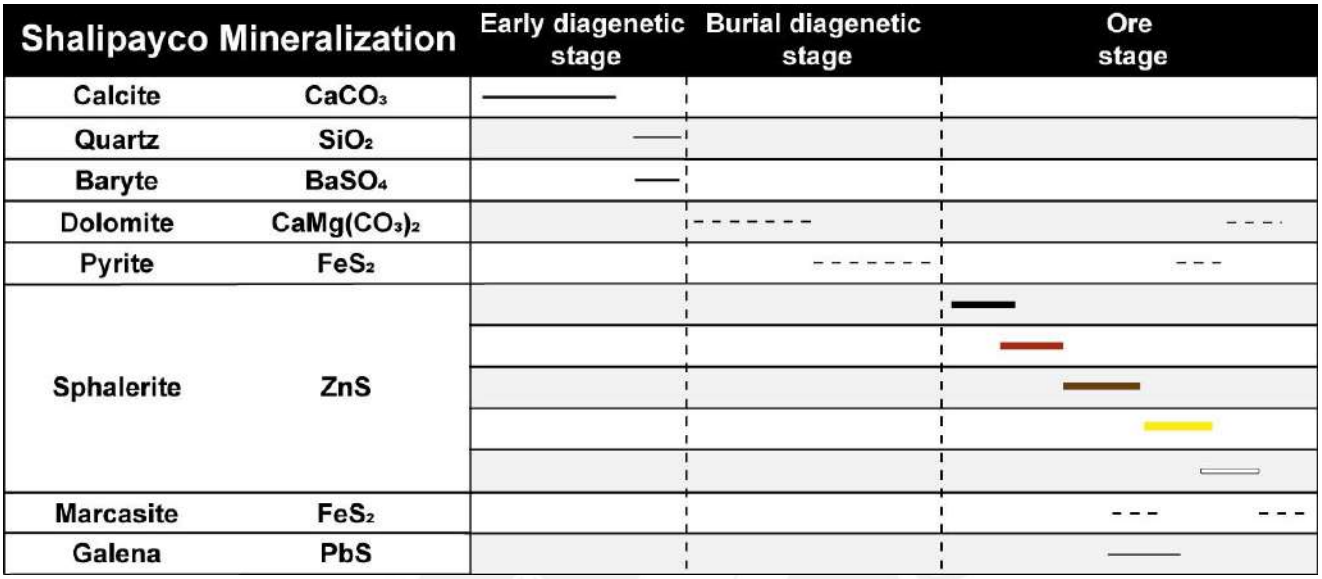

Fig. 7 Paragenetic sequence of the Shalipayco deposit. Thick bars indicate higher abundance and dashed lines, lesser abundances. For sphalerite, color bars correspond to the color of the different types of sphalerite.

5. Sphalerite geochemistry

A summary of sphalerite compositions, including minimum, maximum, average, and interquartile range (IQR) values is presented in Table 1. LA-ICP-MS results are presented in compiled box-and-whisker plots (Fig. 8). In Shalipayco, although up to five types of sphalerite have been identified, only trace element analyses for reddish-brown (sl_{rb}), yellowish-brown (sl_{yb}), and yellow (sl_{y}) sphalerite types were obtained. In addition, EPMA and LA-ICP-MS analyses of sphalerite from the MVT Cristal deposit obtained by Mondillo et al. (2018b) are shown for comparative purposes. A significant effort was made to report only the content of elements whose variations respond to solid solutions and not to mixed mineral analyses (e.g., presence of mineral micro-inclusions) by selecting only flat, stable signal intervals in the LA-ICP-MS spectra. Of the analyzed elements, Sb, As, Sb, Tl, and Pb present occasionally spiky LA-ICP-MS transient signals and, therefore, the occurrence of mineral micro-scale solid inclusions (e.g., galena) is expected.

Sphalerite from the San Vicente and Shalipayco deposits displays a low and narrow range of iron content and a relative wide range of trace element contents. In San Vicente, Fe contents measured with LA-ICP-MS (IQR = 20465-9718 ppm, up to 43271 ppm) are broadly comparable with those measured with EPMA (IQR = 2.4-0.64 wt.%, up to 4.7 wt.%; Table 1). Iron shows a pronounced depletion from first- (sl_1; mostly > 1 wt.%) to second (sl_2; systematically < 125 ppm) mineralization step sphalerite, as well as a gradual decrease within sl_1 sphalerite from sl_{1bl} to sl_{1y} (Fig. 8A). In Shalipayco, Fe content (IQR = 2793-666 ppm, up to 37888 ppm) also decreases from reddish-brown (sl_{rb}) to yellow (sl_y) sphalerite types. Iron values in sphalerite from the Cristal deposit (EPMA data: IQR = 9.95-6.21 wt.%) are higher compared to sphalerite from San Vicente and Shalipayco. Zinc tends to a negative correlation with Fe (Fig. 9), pointing to a dominant $Fe^{2+} \leftrightarrow Zn^{2+}$ simple substitution (Cook et al., 2009; Johan, 1988) when Fe > ~1 wt.%.

Cadmium contents are higher in sphalerite from Cristal (IQR = 5867-2562 ppm), Shalipayco (IQR = 4487- 2741 ppm), and mineralization step 2 (sl_2) of San Vicente (IQR = 5704-3440 ppm) relative to sphalerite from mineralization step 1 (sl_1) of San Vicente (IQR = 1080-489 ppm; Fig. 8B). The content of Mn in sphalerite from San Vicente considerably increases from first (sl_1; IQR = 52-21 ppm) to second (sl_2; IQR = 471-261 ppm) mineralization steps (Fig. 8C). Manganese contents are much lower in sphalerite from Cristal (IQR = 26-9.4 ppm) and Shalipayco than in sphalerite from San Vicente and in Shalipayco tend to decrease from reddish-brown (sl_{rb}) and yellowish-brown (sl_{yb}) (IQR = 7.5-2.2 ppm) to yellow (sl_y; < 3.2 ppm) sphalerite types. Copper content in both San Vicente and Shalipayco is variable among the different analyzed sphalerite types. In San Vicente, Cu (IQR = 335-6.2 ppm; up to 2084 ppm) is noticeable higher in sphalerite from the second mineralization step (sl_2; IQR = 586-33 ppm), particularly in orange sphalerite (sl_{2o}; IQR = 1446-392 ppm), relative to that from the first mineralization step (sl_1; IQR = 6.4-4.5 ppm; Fig 8D). In Shalipayco, Cu values are higher in reddish-brown (sl_{rb}; IQR = 3928-1604 ppm) than in yellowish-brown (sl_{yb}; IQR = 288-13 ppm) and yellow (sl_y; IQR = 164-31 ppm) sphalerite types.

Silver contents in sphalerite from San Vicente (IQR = 18-4.9 ppm; up to 3029 ppm) are also higher in the second mineralization step (sl_2; IQR = 627-15 ppm) compared to the first mineralization step (sl_1; IQR = 11-4.3 ppm) and is particularly high in orange sphalerite (sl_{2o}; IQR = 1335-414 ppm; Fig 8E). Sphalerite from Shalipayco (IQR = 508-56 ppm; up to 1600 ppm

Ag) shows gradual Ag enrichment from reddish-brown (sl_{rb}; IQR = 320-26 ppm) to yellowish-brown (sl_{yb}; IQR = 511-63 ppm) to yellow (sl_{y}; IQR = 574-300 ppm) sphalerite types. Silver values in Cristal are low (IQR = 77-3.4 ppm). Tin contents in sphalerite from San Vicente and Shalipayco are low but markedly variable (Fig. 8F). In general, Sn values in sphalerite from San Vicente are lower in grains from the first (sl_{1}; IQR = 0.55-0.21 ppm) than in grains from the second mineralization step (sl_{2}; IQR = 1.1-0.32 ppm) and reaches maximum contents in orange sphalerite (sl_{2o}; IQR = 4.3-0.34 ppm, up to 17 ppm). The Hg content is considerably higher in sphalerite from Shalipayco (IQR = 313-58 ppm) compared to sphalerite from San Vicente (IQR = 4.4-3.2 ppm; Fig. 8G). In Shalipayco, there is Hg depletion from reddish-brown (sl_{rb}; IQR = 451-50 ppm) to yellow (sl_{y}; IQR = 81-50 ppm) sphalerite types whereas in San Vicente there is progressive Hg enrichment from early (sl_{1bl}; IQR = 3.9-3.1 ppm) to late (sl_{2w}; IQR = 8.5-8.4 ppm) sphalerite.

As for critical elements, sphalerite from San Vincente shows significantly higher Ge contents in grains from the second mineralization step (sl_{2}; IQR = 580-60 ppm), particularly in orange (sl_{2o}; IQR = 1207-375 ppm, up to 1861 ppm) and yellow (sl_{2y}; IQR = 269-130 ppm, up to 1096 ppm) sphalerite types relative to sphalerite from the first mineralization step (sl_{1}; IQR = 91-44 ppm); white sphalerite (sl_{2w}) yields, however, the lowest Ge values (IQR = 0.69-0.16 ppm, up to 2.1 ppm) among analyzed sphalerite (Fig. 8H). In Shalipayco, the highest Ge values are registered in yellow sphalerite (sl_{y}; IQR = 375-267 ppm, up to 1119ppm). Sphalerite from the Cristal deposit also yields significant Ge contents (IQR = 231-31 ppm, up to 386 ppm). Gallium content reaches maximum values in sphalerite from the second mineralization step in San Vicente (sl_{2}; IQR = 93-15 ppm), particularly in orange sphalerite (sl_{2o}; IQR = 200-12 ppm, up to 997 ppm; Fig. 8I). In Shalipayco and Crystal, Ga values are mostly of some ppm. Indium contents in San Vicente, Shalipayco, and Crystal deposits are systematically low, mostly at the sub-ppm level (Fig. 8J).

Table 1. Summary of element contents in sphalerite from the San Vicente, Shalipayco, and Cristal deposits. EPMA data are given in wt.% and LA-ICP-MS data, in ppm. Data for the Crystal deposit are from Mondillo et al. (2018b). B.D.L.= below detection limit. EPMA. Data in wt.%. LA-ICP-MS data in ppm.

Ore-body/vein	Generation		S (wt%)	Zn (wt%)	Fe (wt%)	Fe (ppm)	Mn (ppm)	Cd (ppm)	In (ppm)	Ge (ppm)	Ga (ppm)	Cu (ppm)	Ag (ppm)	Sn (ppm)	Pb (ppm)	Sb (ppm)	Se (ppm)	Mo (ppm)	Co (ppm)	Au (ppm)	Hg (ppm)	Tl (ppm)	Bi (ppm)	As (ppm)
San Vicente	All analyses (n = 155)	MIN.	32.2	61.7	B.D.L.	B.D.L.	3.0	185	B.D.L.	B.D.L.	0.038	B.D.L.	1.8	0.13	0.098	B.D.L.	B.D.L.	B.D.L.	B.D.L.	B.D.L.	1.9	B.D.L.	B.D.L.	2.6
		MAX.	34.0	67.9	4.7	43271	1161	9924	18	1861	997	2084	3029	17	8.3	2.3	2.0	1.5	68	0.016	9.1	9.6	0.023	439
		Av.	33.2	65.3	1.6	15353	122	1778	1.1	149	27	313	117	0.81	3.1	0.45	1.1	0.064	17	0.012	4.0	1.9	0.0070	35
		IQR	33.4-32.9	66.4-64.3	2.4-0.64	20465-9718	97-23	1974-535	0.41-0.016	118-44	13-0.25	335-6.2	18-4.9	0.65-0.25	5.0-0.23	0.44-0.035	1.3-0.85	0.052-0.029	25-0.32	0.013-0.010	4.4-3.2	2.5-0.50	0.0086-0.0046	21-4.8
	sl_1 (n = 118)	MIN.	32.2	61.7	0.25	3000	3.0	185	B.D.L.	14	0.038	B.D.L.	1.8	0.13	-	B.D.L.	B.D.L.	B.D.L.	B.D.L.	B.D.L.	1.9	0.036	B.D.L.	2.6
		MAX.	34.0	67.5	4.7	43271	172	3784	0.66	180	80	10	39	7.7	-	2.3	2.0	1.5	68	0.016	8.6	7.0	0.023	439
		Av.	33.2	65.0	2.0	17038	39	840	0.056	71	4.4	5.9	8.8	0.55	-	0.30	1.1	0.071	17	0.012	3.5	1.4	0.0076	41
		IQR	33.4-32.9	66.4-64.3	2.4-0.64	20663-10680	52-21	1080-489	0.060-0.012	91-44	4.4-0.18	6.4-4.5	11-4.3	0.55-0.21	-	0.063-0.035	1.3-0.85	0.041-0.029	25-0.31	0.014-0.011	3.9-3.1	1.6-0.52	0.0088-0.0043	27-6.3
	sl_{1bl} (n = 34)	MIN.	32.5	61.7	0.25	9774	7.4	311	B.D.L.	19	0.064	B.D.L.	1.9	0.19	-	B.D.L.	B.D.L.	B.D.L.	B.D.L.	B.D.L.	2.4	0.26	B.D.L.	2.6
		MAX.	33.9	67.5	4.7	43271	172	3784	0.66	180	80	7.8	29	7.7	-	2.3	2.0	1.5	61	0.0096	8.6	3.3	0.023	167
		Av.	33.3	64.6	2.2	22066	47	762	0.087	79	7.0	6.1	8.5	0.90	-	0.61	1.4	0.14	14	-	3.7	1.1	0.0088	21
		IQR	33.6-33.0	65.9-63.8	2.4-1.5	25831-16671	63-25	899-495	0.071-0.017	105-54	7.1-0.23	6.8-5.3	11-4.4	0.83-0.27	-	0.64-0.039	1.6-1.1	0.050-0.029	24-0.25	-	4.0-2.9	1.2-0.66	0.011-0.0047	22-6.4
	sl_{1rb} (n = 27)	MIN.	32.8	62.2	0.58	8342	8.9	185	B.D.L.	31	0.038	B.D.L.	1.8	0.14	-	B.D.L.	B.D.L.	B.D.L.	B.D.L.	B.D.L.	1.9	0.23	B.D.L.	3.0
		MAX.	33.8	67.1	4.2	32945	77	1430	0.21	168	48	6.4	21	2.2	-	0.063	1.4	0.068	32	0.013	5.4	3.1	0.020	183
		Av.	33.3	64.6	2.3	19531	39	727	0.049	71	3.4	5.3	6.0	0.43	-	0.049	0.95	0.035	12	0.013	3.2	0.91	0.0066	26
		IQR	33.5-33.0	65.4-63.9	2.7-1.5	22035-15116	54-23	897-503	0.043-0.013	90-43	2.8-0.069	5.8-5.0	6.4-2.7	0.43-0.20	-	0.056-0.042	1.1-0.82	0.034-0.029	19-0.38	0.013-0.012	3.5-2.4	1.3-0.41	0.0054-0.0040	23-8.7
	sl_{1yb} (n = 57)	MIN.	32.4	63.1	0.37	3000	3.0	247	B.D.L.	14	0.044	B.D.L.	2.4	0.13	-	B.D.L.	B.D.L.	B.D.L.	B.D.L.	B.D.L.	2.1	0.036	B.D.L.	3.1
		MAX.	33.9	67.3	3.6	38867	97	2458	0.23	167	27	10	39	2.0	-	0.059	1.3	0.085	68	0.011	5.7	7.0	0.019	439
		Av.	33.1	65.0	1.8	13278	38	912	0.039	63	3.4	6.4	9.3	0.42	-	0.046	1.0	0.039	18	-	3.5	1.6	0.0076	54
		IQR	33.2-32.9	65.5-64.3	2.4-1.2	16839-9473	47-18	1447-456	0.046-0.011	83-42	3.2-0.47	8.8-4.0	10-5.0	0.42-0.23	-	0.052-0.040	1.1-0.85	0.041-0.029	36-0.32	-	3.9-3.2	2.5-0.43	0.0088-0.0048	38-5.0
	sl_{1y} (n = 37)	MIN.	32.6	63.8	1.2	6309	6.3	531	B.D.L.	37	0.049	B.D.L.	2.6	0.14	-	B.D.L.	B.D.L.	B.D.L.	B.D.L.	B.D.L.	2.1	0.34	B.D.L.	3.3
		MAX.	33.4	65.9	2.4	16235	68	1598	0.067	144	16	4.5	22	0.84	-	0.035	B.D.L.	0.039	56	0.016	5.7	4.3	0.0084	237
		Av.	32.9	65.1	1.8	11281	20	1039	0.030	78	2.5	4.5	14	0.30	-	0.305	-	0.031	30	-	3.7	2.1	0.0057	79
		IQR	33.0-32.7	65.4-64.9	2.0-1.5	13656-8621	23-11	1383-731	0.054-0.0087	104-46	1.3-0.16	-	20-7.2	0.28-0.16	-	-	-	0.036-0.027	48-6.5	-	4.3-3.1	2.9-1.3	0.0070-0.0040	145-7.5
	sl_2 (n = 37)	MIN.	32.4	65.6	B.D.L.	B.D.L.	139	1363	B.D.L.	B.D.L.	0.21	B.D.L.	5.8	0.19	0.098	B.D.L.	B.D.L.	B.D.L.	B.D.L.	B.D.L.	3.5	B.D.L.	B.D.L.	3.0
		MAX.	33.5	67.9	B.D.L.	122	1161	9924	18	1861	997	2084	3029	17	8.3	1.8	1.7	0.21	0.79	0.0087	9.1	9.6	0.010	173
		Av.	33.0	66.5	-	57	391	4772	3.4	403	100	442	463	1.7	3.1	0.67	1.2	0.053	-	-	5.7	3.9	0.0062	15
		IQR	33.4-32.9	66.3-64.3	-	88-29	471-261	5704-3440	4.6-0.45	580-60	93-15	586-33	627-15	1.1-0.32	5.0-2.3	1.1-0.14	1.4-1.0	0.055-0.037	-	-	6.2-4.5	7.2-0.29	0.068-0.048	8.5-3.6
	sl_{2a} (n = 13)	MIN.	32.7	66.2	B.D.L.	B.D.L.	139	3489	0.0084	0.18	0.21	55	15	0.29	0.098	B.D.L.	B.D.L.	B.D.L.	B.D.L.	B.D.L.	4.1	0.0093	B.D.L.	3.7
		MAX.	33.4	67.6	B.D.L.	B.D.L.	683	8253	18	1861	997	2084	3029	17	5.0	1.8	1.7	0.080	B.D.L.	B.D.L.	9.1	9.6	0.0055	173
		Av.	33.0	66.8	-	-	379	5577	5.9	747	172	890	990	3.2	1.4	0.98	1.5	0.049	-	-	5.5	3.6	0.0048	28
		IQR	33.0-32.8	67.0-66.6	-	-	524-266	7180-4281	8.2-2.2	1207-375	200-12	1446-392	1335-414	4.3-0.34	1.4-0.13	1.4-0.49	1.6-1.3	0.054-0.040	-	-	5.8-4.5	5.4-0.22	0.0051-0.0044	18-6.0
	sl_{2y} (n =19)	MIN.	32.7	65.8	B.D.L.	B.D.L.	146	1363	B.D.L.	6.7	0.76	B.D.L.	5.8	0.19	0.26	B.D.L.	B.D.L.	B.D.L.	B.D.L.	B.D.L.	3.5	0.020	B.D.L.	3.0
		MAX.	33.5	67.9	B.D.L.	122	1161	9924	8.6	1096	306	1150	1959	2.7	4.9	0.071	1.4	0.10	0.79	B.D.L.	7.3	9.2	0.010	82
		Av.	33.1	66.3	-	57	392	4308	1.2	252	43	168	217	0.88	2.6	0.052	1.2	0.047	-	-	4.9	4.9	0.0068	9.1
		IQR	33.3-33.0	66.7-65.8	-	88-29	375-244	5307-3120	0.94-0.21	269-130	49-15	206-15	69-13	1.0-0.37	3.7-1.4	0.061-0.043	1.3-1.0	0.054-0.030	-	-	5.2-4.4	7.9-1.8	0.0076-0.0058	5.1-3.4
	sl_{2v} (n = 5)	MIN.	33.0	67.4	B.D.L.	B.D.L.	273	3817	3.8	B.D.L.	92	96	14	0.22	1.5	B.D.L.	B.D.L.	B.D.L.	B.D.L.	B.D.L.	8.4	B.D.L.	B.D.L.	3.8
		MAX.	33.0	67.4	B.D.L.	B.D.L.	593	4805	5.8	2.1	195	206	46	1.4	8.3	B.D.L.	1.1	0.21	B.D.L.	0.0087	8.9	0.15	0.0047	4.8
		Av.	33.0	67.4	-	-	423	4441	4.6	0.65	130	137	28	0.53	5.1	-	1.0	0.10	-	-	8.6	0.049	-	4.1
		IQR	-	-	-	-	486-381	4727-4356	5.0-3.9	0.69-0.16	171-93	172-96	30-22	0.44-0.28	6.8-3.5	-	1.0-1.0	0.13-0.044	-	-	8.5-8.4	0.055-0.010	-	4.0-3.8
Shalipayco	All analyses (n = 50)	MIN.	-	-	-	181	B.D.L.	1501	B.D.L.	2.7	B.D.L.	B.D.L.	5.6	0.15	0.067	0.070	B.D.L.	B.D.L.	B.D.L.	B.D.L.	3.0	0.011	B.D.L.	4.0
		MAX.	-	-	-	37888	14	7687	2.6	1119	32	5090	1600	4.3	11	412	1.4	0.51	29	0.015	780	6.7	0.0059	93
		Av.	-	-	-	4893	5.9	3898	0.34	316	4.5	456	362	0.39	6.5	103	0.96	0.074	11	0.013	203	1.6	0.0042	20
		IQR	-	-	-	2793-666	7.5-2.2	4487-2741	0.17-0.021	425-101	2.9-0.081	405-14	508-56	0.26-0.19	9.2-3.8	100-7.5	1.1-0.75	0.062-0.029	19-0.53	0.014-0.012	313-58	2.0-0.39	0.0048-0.0035	22-7.6
	sl_{rb} (n = 13)	MIN.	-	-	-	384	B.D.L.	1501	B.D.L.	4.5	0.032	B.D.L.	12	0.16	4.4	5.7	B.D.L.	B.D.L.	B.D.L.	B.D.L.	8.7	0.037	B.D.L.	4.0
		MAX.	-	-	-	37888	14	7687	1.2	731	1.3	5090	512	0.30	9.2	412	1.0	0.18	18	B.D.L.	780	6.7	0.0050	63
		Av.	-	-	-	11193	10	3943	0.59	254	0.47	2766	192	0.24	6.9	95	0.86	0.063	3.4	-	315	2.0	-	18
		IQR	-	-	-	18937-820	14-7.1	4936-2295	0.87-0.31	384-52	1.0-0.062	3928-1604	320-26	0.26-0.20	9.2-4.6	133-10	0.90-0.79	0.044-0.030	0.57-0.41	-	451-50	2.2-0.98	-	20-7.1
	sl_{yb} (n = 30)	MIN.	-	-	-	181	B.D.L.	2426	B.D.L.	2.7	B.D.L.	B.D.L.	5.6	0.15	0.067	0.070	B.D.L.	B.D.L.	B.D.L.	B.D.L.	3.0	0.011	B.D.L.	5.0
		MAX.	-	-	-	22783	7.9	7048	2.6	966	32	1347	1600	0.52	11	407	1.4	0.51	29	0.015	772	5.5	0.0059	93
		Av.	-	-	-	3151	4.4	4094	0.31	321	4.6	286	389	0.23	6.5	82	1.1	0.087	20	-	180	1.4	0.0042	23
		IQR	-	-	-	1760-786	6.7-2.0	4639-3396	0.12-0.011	468-71	3.1-0.081	288-13	511-63	0.25-0.18	10-2.6	105-11	1.2-0.86	0.064-0.031	24-15	-	272-74	1.6-0.25	0.0045-0.0036	26-7.7
	sl_y (n =7)	MIN.	-	-	-	424	B.D.L.	2134	B.D.L.	156	0.073	B.D.L.	176	0.18	3.8	3.8	B.D.L.	B.D.L.	B.D.L.	B.D.L.	46	0.34	B.D.L.	7.3
		MAX.	-	-	-	882	3.2	4058	0.57	1119	31	549	1469	4.3	9.2	45	0.74	0.030	B.D.L.	0.0012	301	3.8	0.0034	14
		Av.	-	-	-	659	-	2977	0.28	409	11	178	562	1.4	6.1	14	-	0.029	-	-	95	1.4	-	9.2
		IQR	-	-	-	746-573	-	3474-2343	0.38-0.13	375-267	21-0.17	164-31	574-300	2.3-0.20	7.2-4.6	15-5.6	-	0.029-0.028	-	-	81-50	1.9-0.52	-	10-7.7
Cristal (n = 20) Mondillo et al. 2018b		MIN.	32.7	54.4	5.30	-	7.6	1939	B.D.L.	0.25	B.D.L.	40	1.2	0.61	0.066	B.D.L.	-	-	129	-	-	-	-	-
		MAX.	33.7	61.9	12.90	-	40	8429	37	386	6.6	229	134	2.1	22	0.84	-	-	242	-	-	-	-	-
		Av.	33.3	58.2	8.20	-	19	4600	3.2	142	1.3	112	38	1.0	8.1	0.31	-	-	190	-	-	-	-	-
		IQR	33.5-33.1	59.9-56.3	9.95-6.21	-	26-9.4	5867-2562	0.51-0.010	231-31	1.8-0.051	182-53	77-3.4	1.0-0.83	12-3.3	0.47-0.13	-	-	231-160	-	-	-	-	-

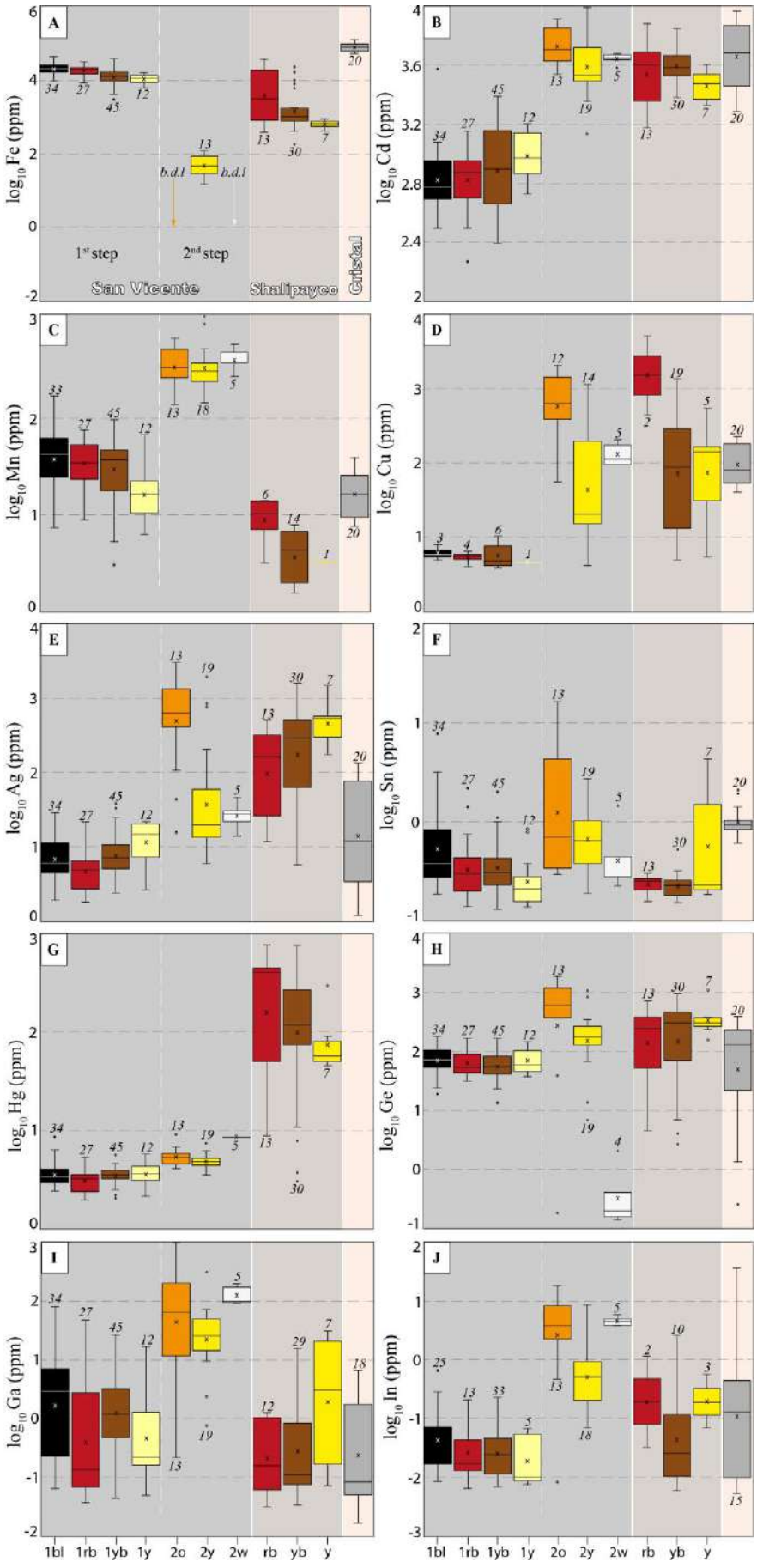
A
B
C
D
E
F
G
H
I
J
log10 Fe (ppm)
log10 Cd (ppm)
log10 Mn (ppm)
log10 Cu (ppm)
log10 Ag (ppm)
log10 Sn (ppm)
log10 Hg (ppm)
log10 Ge (ppm)
log10 Ga (ppm)
log10 In (ppm)
b.d.l
b.d.l
1st step
2nd step
San Vicente
Shalipayco
Cristal
1bl 1rb 1yb 1y 2o 2y 2w rb yb y

Fig. 8 Boxplot of LA - ICP - MS data for selected minor and trace elements in sphalerite from the San Vicente, Shalipayco, and Crystal deposits: a) iron, b) cadmium, c) manganese, d) copper, e) silver, f) tin, g) mercury, h) germanium, i) gallium, and j) indium. Analyses are plotted in parts per million (ppm) on a vertical logarithmic scale. The maximum, median, and minimum concentrations are indicated, as well as the number of analyses above the detection limit for each element (displayed up or below the boxes). Analyses with "spiky profiles" in Table S2, attributed to inclusions, were not plotted. Data for the Crystal deposit are from Mondillo et al. (2018b).

6. Discussion

6.1. Enrichment and incorporation mechanisms of Ge in sphalerite

In San Vicente, sphalerite deposited during the first mineralization step, which is the volumetrically most abundant, yields Ge contents (Table 1) similar to sphalerite from other MVT deposits in Peru (Cristal MVT deposit, IQR = 231-31 ppm; Mondillo et al., 2018b) and worldwide (Paradis, 2015; Shanks et al., 2018). Germanium is remarkably higher in orange sphalerite (sl_{2o}, IQR = 1207 – 375 ppm, up to 1861 ppm; Fig. 8) formed at the beginning of the second mineralization step in San Vicente (Fig. 5), of smaller volume and local distribution. In Shalipayco, yellow sphalerite (sl_y) registered the highest Ge contents in this deposit (IQR = 375-267 ppm, up to 1119 ppm). These values are comparable with those obtained in Ge-rich sphalerite from the Tres Marías deposit in Mexico (average = 960 ppm, up to 3200 ppm; Saini-Eidukat et al., 2009) that for some authors is a MVT deposit and for others is of magmatic affiliation (see discussion in Ostendorf et al., 2017) and the Saint Salvy vein-like deposit (up to 2600 ppm of Ge; Belissont et al., 2014). Germanium enrichment in sphalerite from the Shalipayco deposit represents a further argument for the classification of this deposit as MVT versus a carbonate-replacement deposit in a porphyry Cu system (see de Oliveira et al., 2021). Relative significant Ga content is also hosted in orange sphalerite from San Vicente (sl_{2o}; IQR = 200-12 ppm, up to 997 ppm), while in sphalerite from Shalipayco and Crystal deposits is systematically low. Indium content in sphalerite from San Vicente and Shalipayco, as expected in MVT deposits (Cook et al., 2009; Ye et al., 2016, 2011; Yuan et al., 2018), is systematically low (mostly < 1 ppm).

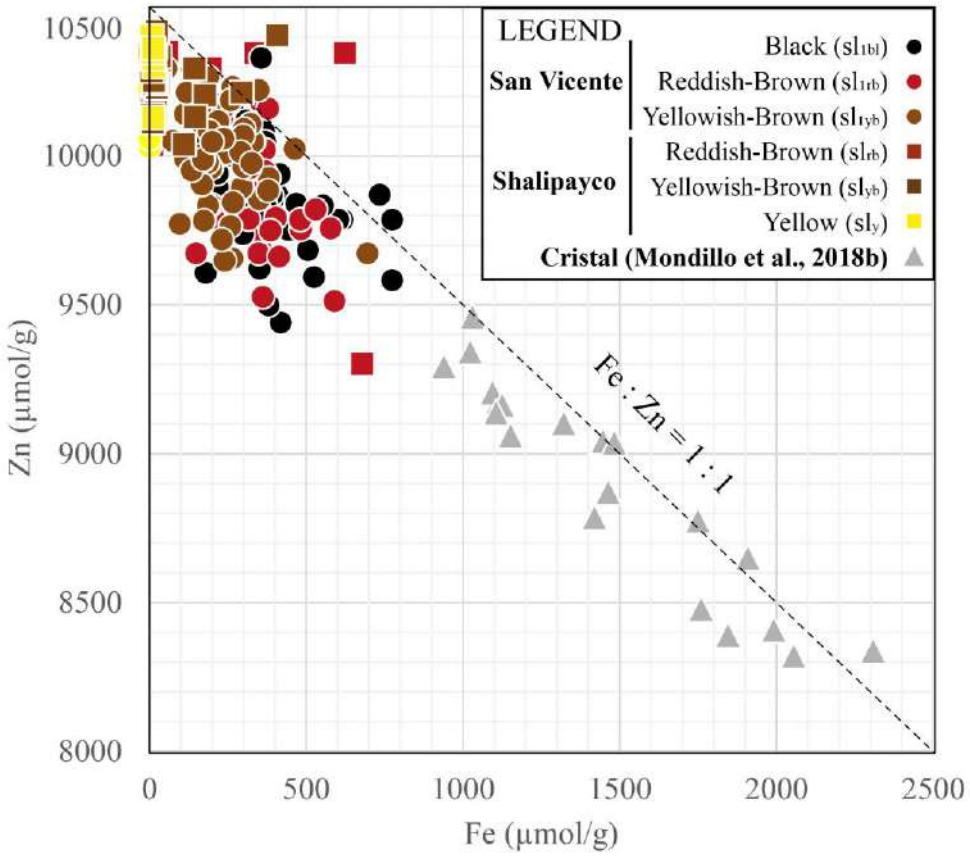

Fig. 9 Binary Fe vs Zn correlation plot for analyzed sphalerite from the San Vicente, Shalipayco, and Crystal deposits. Data for the Crystal deposit are from Mondillo et al. (2018b).

In order to determine possible incorporation mechanisms of Ge and other trace elements into the sphalerite structure, elemental content (represented as µmol/g) correlation diagrams have been developed (Fig. 10). A positive correlation between the molar contents of Ge and Cu is only observed for some step 2 yellow (sl_{2y}) and orange (sl_{2o}) sphalerite types in San Vicente (Fig. 10A), suggesting a $3Zn^{2+} \leftrightarrow 2Cu^{+} + Ge^{4+}$ coupled substitution, which has been previously described in other deposits (Cave et al., 2020; Belissont, 2016; Belissont et al., 2016; Bonnet et al., 2016; Wei et al., 2019). A positive correlation occurs between Ge and Ag in part lying along the ~1:2 ratio line (Fig. 10B); it is mainly noticed for yellowish-brown (sl_{yb}) and yellow (sl_{y}) sphalerite from Shalipayco and in second-mineralization-step yellow (sl_{2y}) sphalerite from San Vicente, suggesting a $3Zn^{2+} \leftrightarrow Ge^{4+} + 2Ag^{+}$ coupled substitution (previously proposed by Belissont et al., 2014 and Cook et al., 2009). Positive correlation between the molar contents of Ge and Tl in San Vicente and Shalipayco (Fig. 10C) is observed.

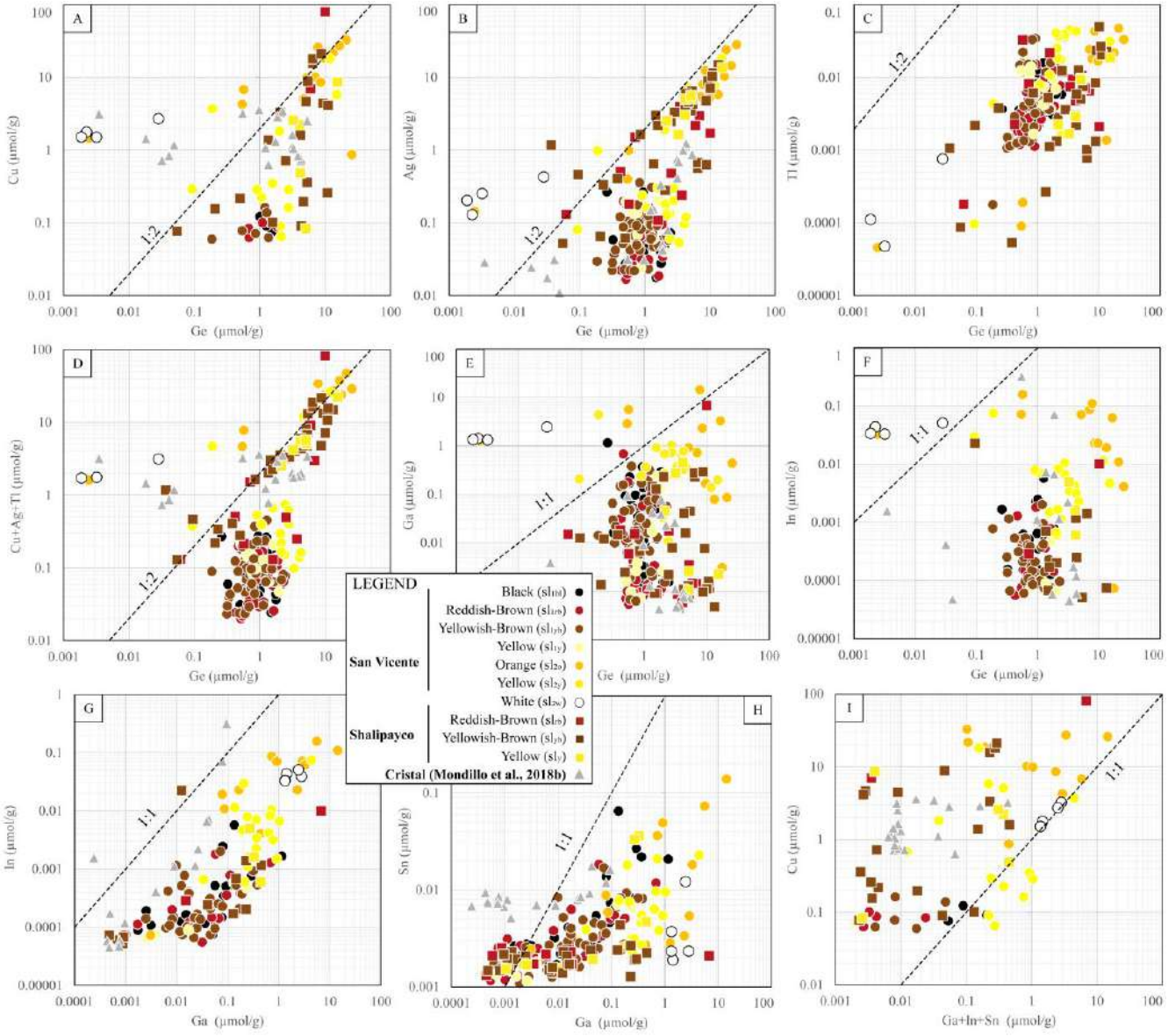

Fig. 10 Binary correlation plots for trace elements in sphalerite from San Vicente, Shalipayco, and Crystal deposits. Data for the Crystal deposit are from Mondillo et al. (2018b).

The aforementioned correlations indicates that incorporation of Ge in studied sphalerite took place with the entry of monovalent cations such as Cu, Ag, and Tl (Fig. 10D), and that combinations of these coupled substitution schemes (i.e., $Ge^{4+} + 2(Cu + Ag + Tl)^{+} \leftrightarrow 3Zn^{2+}$) are plausible. In contrast, Ge content shows no correlation with Ga or In contents (Figs. 10E, F), suggesting independent substitution mechanisms regarding these two elements. Although with certain dispersion, positive correlations between the molar contents of Ga and In (Fig. 10G) and of Ga and Sn are noticed (Fig. 10H), suggesting that these elements could be incorporated in conjunction via coupled substitutions. Some analyses show indeed a positive correlation

between Cu and Ga + In + Sn at ~1:1 (Fig. 10l), especially in second-mineralization-step white (sl_{2w}) and some yellow (sl_{2y}) sphalerite from San Vicente, thus suggesting a $Cu^{+} + (Ga, In)^{3+} + Sn^{4+} \leftrightarrow 4Zn^{2+}$ coupled substitution. However, there is a set of data, which includes part of the analyzed sphalerite from San Vicente, Shalipayco, and Cristal that lies far above the Cu: Ga + In + Sn = 1:1 correlation line, pointing to higher Cu at a given Ga + In + Sn content, probably due to the fact that Cu is also involved in coupled substitutions for the incorporation of Ge, which is much abundant in the analyzed sphalerite.

6.2. Color of sphalerite vs. element composition

The most common names used to refer to sphalerite varieties according to crystal color include i) cleiophane (Palache et al., 1944), characterized by transparency and by white color or being colorless, ii) ruby blende (Dana, 1892), with red shades, and iii) marmatite (Boussingault, 1830), highlighted by its black color and opacity (sphalerite with reddish-dark to brown shades may also be considered as marmatite). Other less commonly used variety names for sphalerite include iv) golden sphalerite, with yellow to orange shades, and v) green sphalerite, among others.

Iron is often hosted in the sphalerite crystal lattice (Di Benedetto et al., 2005), and it is considered the most ubiquitous impurity element in this mineral. For many years, there has been a consensus that sphalerite colors are directly and essentially dependent on the Fe content, substituting Zn at different proportions (Awadh, 2009; Cook et al., 2009; Knorsch et al., 2020; Li and Barnes, 2019). Unfortunately, this principle is not always fulfilled, as observed particularly in Fe-poor sphalerite (< 2-3 wt.% Fe; see Roedder and Dwornik, 1968).

In varietal names (e.g., cleiophane, ruby blende, and marmatite), no scientific criteria to associate them with specific percentages of Fe are established. For example, each author can determine if it is considered marmatite with very different amounts of Fe or sometimes simply because of the color since it does not follow crystal-chemical or structural criteria that allow it to have a well-defined composition. Furthermore, dark or black sphalerite has always been called marmatite, regardless of the Fe content, which can be highly variable. The only record of a proposal to catalog Fe-rich sphalerite as marmatite was given by Ramdohr (1980), who suggested that Fe should be equal to or greater than 10 wt.%. In the analyzed sphalerite samples from San Vicente and Shalipayco, black sphalerite does not exceed 5 wt.% Fe. Thus,

variety names define descriptive (i.e., color) or compositional characteristics and have a mere descriptive value, not systematic in terms of composition.

The ore petrographic study in San Vicente and Shalipayco reveals a wide variety of colors in sphalerite (Fig. 8) that can be correlated with the paragenetic evolution of the mineralization (Figs. 5 and 7). In general, it is observed that the decrease in Fe content in San Vicente sphalerite types is not continuous, showing an abrupt depletion from sl_1 (including the black, reddish-brown, yellowish-brown, and yellow types) to sl_2 (including orange, yellow, and white types). This observation suggests that other element contents could control sphalerite color.

Black sphalerite is often related to higher Fe content (Craig and Vaughan, 1994; Katsev et al., 2001). However, values of this element do not necessarily have to be high to produce such color, as occurs in sphalerite from San Vicente (sl_{1bl}, IQR = 2.6-1.7 wt.% Fe) and other MVT deposits (Bradbury, 1961; Jolly and Heyl, 1964; Roedder and Dwornik, 1968), with content even lower than those registered in this study. Reddish-brown sphalerite in San Vicente (sl_{1rb}) and Shalipayco (sl_{rb}) also presents low Fe contents (IQR = 21247-10881 ppm). However, the significant Cd, Cu, Hg, Ge, and Ag values suggest that some of these elements could have an impact in crystal colors. Sapalski and Gómez (1992) determined that red sphalerite from the Áliva MVT mine in Santander, Spain, coincides with high Ge and Hg contents, whereas Sanabria and García-Álvarez (2005) correlated this color tone with high Cd, Cu, and Hg contents. Yellowish-brown sphalerite identified both in San Vicente (sl_{1yb}) and Shalipayco (sl_{yb}) may be considered an intermediate color tone between reddish-brown and yellow. As for yellow sphalerite, Kelley et al. (2004) suggest correlation with relatively high As and Hg contents. Yellow sphalerite from the first mineralization step at San Vicente (sl_{1y}) yields the highest As content (IQR = 145-7.5 ppm; Table 1) among analyzed sphalerite; however, yellow sphalerite from Shallipayco (sl_y; IQR = 5.1-3.4 ppm) and from the second mineralization step at San Vicente (sl_{2y}; IQR = 5.1-3.4 ppm) yields much lower As values and therefore we do not observe a systematic correlation between the yellow color and As contents in the studied samples. On the other hand, Hg contents are not comparatively high in analyzed yellow sphalerite from both deposits compared to the other sphalerite types (Fig. 8G). Yellow cyclic growth bands of sphalerite have been corelated with higher Ge, Cu, and Pb contents in the North German Basin (Knorsch et al. 2020). However, yellow sphalerite has also been explained according to its absorption elements. Slack et al. (1967, 1966) suggested that the absorption band of Fe^{2+} and

Zn^{2+} (blue), added with the absorption of small amounts of Co^{2+} (red), compound the yellow color. Nevertheless, it does not seem possible due to the very low Co contents registered in sphalerite from both studied deposits, mostly below its lower limit of detection. Orange sphalerite from San Vicente (sl_{2o}) displays relatively high contents of Cu, Ge, Ag, and Cd (Fig. 8); high Cd is also reported in orange sphalerite from Áliva (Gómez-Fernández et al., 2000). Finally, white sphalerite would be mainly related to very low Fe contents (Ramdohr, 1980). White sphalerite occasionally shows pale green internal reflections that, in principle, would be linked to Co trace contents (Hofmann and Henn, 1985; Rager et al., 1996).

The above observations suggest possible relationship between some sphalerite colors and different contents of certain trace elements. However, it is still challenging to affirm which element or combination of elements and under which oxidation states could directly influence crystal colors since not enough evidence has been found yet. Unfortunately, we are not far from the conclusions raised by Roedder and Dwornik (1968) that “the true coloring mechanism is not known”.

7. Conclusions

LA-ICP-MS analyses on sphalerite have been performed after a thorough petrographic study of ore samples from the San Vicente and Shalipayco MVT deposits in Peru, which has allowed correlation between trace element contents and sphalerite types. Up to 7 types of sphalerite in San Vicente crystallized during two mineralization steps have been identified. In Shalipayco, 5 types of sphalerite attributed to a single ore-forming episode were recognized.

In the analyzed samples, all types of sphalerite show significant Ge contents (IQR = 118-44 ppm), as it is typical in MVT mineralization. The Ge content in San Vicente is significantly higher in sphalerite crystallized during the second mineralization step – which is volumetrically minor compared to sphalerite from the first mineralization step – particularly in orange (IQR = 1207 – 375 ppm, up to 1861 ppm) and yellow (IQR = 269-130 ppm, up to 1096ppm) sphalerite types. In Shalipayco, the highest Ge values are found in yellow sphalerite (IQR = 375-267 ppm, up to 1119 ppm). Germanium-richest sphalerite types from both deposits crystallized relatively late in the respective paragenetic sequences. According to these values, some paragenetically late sphalerite types from San Vicente and Shalipayco are among the most enriched in this element globally. Correlations between molar contents suggest incorporation of Ge into the sphalerite

crystal lattice coupled with monovalent cations through substitution schemes such as Ge^{4+} + $2Cu^{+} \leftrightarrow 3Zn^{2+}$, $Ge^{4+} + 2Ag^{+} \leftrightarrow 3Zn^{2+}$, and $Ge^{4+} + 2(Cu + Ag + Tl)^{+} \leftrightarrow 3Zn^{2+}$.

The targeting of light-colored sphalerite crystals, some of which yield the highest Ge values, may preliminarily constitute a guideline for future explorations in this critical element during the evaluation of an MVT mineralization. However, a clear association between sphalerite color and minor and trace element contents has not yet been stablished.

Acknowledgements

This study was economically supported by the Peruvian CONCYTEC-FONDECYT-World Bank project 107-2018-FONDECYT-BM-IADT-AV managed through the PROCIENCIA agency. We want to thank the staff of SIMSA - Unidad Minera San Vicente for the help and hospitality during sampling tasks and the Minera Nexa Resources for providing samples from the Shalipayco deposit. We thank Joan Carles Melgarejo (University of Barcelona) for the scientific discussion on sphalerite color. We appreciate the technical support by Xavier Llovet (CCiT-UB) during the acquisition of EPMA data and by Pete Tollan (ETH) during the acquisition of LA-ICP-MS data. Finally, we also would like to thank Alejandro Vargas (BIZALAB.SAC) for the SEM analyses.

References

Anderson, G.M., 2015. Kerogen as a source of sulfur in MVT deposits. Economic Geology, 110, 837–840. https://doi.org/10.2113/econgeo.110.3.837

Anderson, G.M., Macqueen, R.W., 1982. Ore deposit models. Mississippi Valley-type lead-zinc deposits. Geoscience Canada, 9, 108–117.

Awadh, S.M., 2009. Iron content variations in sphalerite and their effects on reflectance and internal reflections under reflected light. Arabian Journal of Geoscience, 2, 139–142. https://doi.org/10.1007/s12517-008-0023-z

Baby, P., Calderón, Y., Hurtado, C., Louterbach, M., Espurt, N., Brusset, S., Roddaz, M., Brichau, S., Eude, A., Calvès, G., 2019. The Peruvian Sub-Andean foreland basin

system: structural overview, geochronologic constraints, and unexplored plays. In: Zamora, G., McClay, K.R., Ramos, V.A. (Eds.), Memoir 117: Petroleum Basins and Hydrocarbon Potential of the Andes of Peru and Bolivia. American Association of Petroleum Geologists Special Volumes, 117, 87–116.

Badoux, V., Moritz, R., Fontboté, L., 2001. The Mississippi Valley-type Zn-Pb deposit of San Vicente, Central Peru: an Andean syntectonic deposit. Mineral deposits at the beginning of the 21th Century. In: Proceedings of the Joint 6th Biennial SGA-SEG Meeting. Krakow, Poland, 191–195.

Basuki, N.I., Taylor, B.E., Spooner, E.T.C., 2008. Sulfur isotope evidence for thermochemical reduction of dissolved sulfate in Mississippi Valley-type zinc-lead mineralization, Bongará area, Northern Peru. Economic Geology, 103, 783–799. https://doi.org/10.2113/gsecongeo.103.4.783

Bauer, M.E., Burisch, M., Ostendorf, J., Krause, J., Frenzel, M., Seifert, T., Gutzmer, J., 2019. Trace element geochemistry of sphalerite in contrasting hydrothermal fluid systems of the Freiberg district, Germany: insights from LA-ICP-MS analysis, near-infrared light microthermometry of sphalerite-hosted fluid inclusions, and sulfur isotope geochemistry. Mineralium Deposita, 54, 237–262. https://doi.org/10.1007/s00126-018-0850-0

Baumgartner, R.J., Van Kranendonk, M.J., Pagès, A., Fiorentini, M.L., Wacey, D., Ryan, C., 2020. Accumulation of transition metals and metalloids in sulfidized stromatolites of the 3.48 billion–year–old Dresser Formation, Pilbara Craton. Precambrian Research, 337, 105534. https://doi.org/10.1016/j.precamres.2019.105534

Belissont, R., Boiron, M.C., Luais, B., Cathelineau, M., 2014. LA-ICP-MS analyses of minor

and trace elements and bulk Ge isotopes in zoned Ge-rich sphalerites from the Noailhac - Saint-Salvy deposit (France): insights into incorporation mechanisms and ore deposition processes. Geochimica et Cosmochimica Acta, 126, 518–540. https://doi.org/10.1016/j.gca.2013.10.052

Belissont, R., 2016. Germanium and related elements in sulphide minerals: crystal chemistry, incorporation and isotope fractionation. Ph.D. thesis, Université de Lorraine.

Belissont, R., Muñoz, M., Boiron, M.C., Luais, B., Mathon, O., 2016. Distribution and oxidation state of Ge, Cu and Fe in sphalerite by μ-XRF and K-edge μ-XANES: insights into Ge incorporation, partitioning and isotopic fractionation. Geochimica et Cosmochimica Acta, 177, 298–314. https://doi.org/10.1016/j.gca.2016.01.001

Benavides-Cáceres, V., 1999. Orogenic evolution of the Peruvian Andes: the Andean cycle. In: Skinner, B.J. (Ed.), Geology and Mineral Deposits of the Central Andes. Society of Economic Geologists Special Publication, 7, 61–107.

Benites, D., Torró, L., Vallance, J., Laurent, O., Quispe, P., Rosas, S., Uzieda, M.F., Holm-Denomad, H., Pianoski, L.S., Camprubí, A., Colás, V., Fernández-Baca, A., Giraldo, L., Chelle-Michou, C., Sáez, J., Kouzmanov, K., Fontboté, L., 2021. Geology, mineralogy, and cassiterite geochronology of the Ayawilca Zn-Pb-Ag-In-Sn-Cu deposit, Pasco, Peru. Mineralium Deposita, *in press*. https://doi.org/10.1007/s00126-021-01066-z,

Bernstein, L.R., 1985. Germanium geochemistry and mineralogy. Geochimica et Cosmochima Acta, 49, 2409–2422. https://doi.org/10.1016/0016-7037(85)90241-8

Berrospi-Rodríguez, R., Fiestas, J., Alvarado, A., Leach, D., Sempere, T., 2018. Role of Jurassic salt tectonics in the structural shaping of MVT Pb-Zn deposits and hydrocarbon

traps in Peru, and implications for exploration. In: SEG Conference. Keystone, Colorado, United States.

Bonnet, J., Mosser-Ruck, R., Caumon, M.C., Rouer, O., Andre-Mayer, A.S., Cauzid, J., Peiffert, C., 2016. Trace element distribution (Cu, Ga, Ge, Cd, and Fe) in sphalerite from the Tennessee MVT deposits, USA, by combined EMPA, LA-ICP-MS, Raman spectroscopy, and crystallography. Canadian Mineralogist, 54, 1261–1284. https://doi.org/10.3749/canmin.1500104

Boussingault, J.B., 1830. Analyse de la blende noire de Marmato, province de Popayán. Annales de Chimie et de Physique, 42, 312–316.

Bradbury, J.C., 1961. Mineralogy and the question of zoning, Northwestern Illinois zinc-lead district. Economic Geology, 56, 132–148. https://doi.org/10.2113/gsecongeo.56.1.132

Bradley, D.C., Leach, D.L., 2003. Tectonic controls of Mississippi Valley-type lead-zinc mineralization in orogenic forelands. Mineralium Deposita, 38, 652–667. https://doi.org/10.1007/s00126-003-0355-2

Calderón, Y., Baby, P., Hurtado, C., Brusset, S., 2017a. Thrust tectonics in the Andean retro-foreland basin of Northern Peru: Permian inheritances and petroleum implications. Marine and Petroleum Geology, 82, 238–250. https://doi.org/10.1016/j.marpetgeo.2017.02.009

Calderón, Y., Vela, Y., Hurtado, C., Bolaños, R., Baby, P., Eude, A., Roddaz, M., Brusset, S., Calvès, G., 2017b. Petroleum systems restoration of the Huallaga—Marañón Andean retroforeland basin, Peru. In: AbuAli, M.A., Moretti, I., Bolås, H.M.N. (Eds.), Memoir 114: Petroleum Systems Analysis—Case Studies. American Association of Petroleum

Geologists Special Volumes, 95–116.

Capdevila, R., Mégard, F., Paredes, J., Vidal, P., 1977. Le batholite de San Ramón, Cordillére Orientale du Pérou central. Geologische Rundschau, 66, 434–446. https://doi.org/10.1007/BF01989586

Carlotto, V., Quispe, J., Acosta, H., Rodríguez, R., Romero, D., Cerpa, L., Mamani, M., Díaz-Martínez, E., Navarro, P., Jaimes, F., 2009. Dominios geotectónicos y metalogénesis del Perú. Boletín de la Sociedad Geológica del Perú, 103, 1–89.

Cathles, L.M., Smith, A.T., 1983. Thermal constraints on the formation of Mississippi Valley-type lead- zinc deposits and their implications for episodic basin dewatering and deposit genesis. Economic Geology, 78, 983–1002. https://doi.org/10.2113/gsecongeo.78.5.983

Cave, B., Lilly, R., Hong, W., 2020. The effect of co-crystallising sulphides and precipitation mechanisms on sphalerite. Geochemistry: a case study from the Hilton Zn-Pb (Ag) deposit, Australia. Minerals, 10, 797. https://doi.org/10.3390/min10090797

Chew, D.M., Pedemonte, G., and Corbett, E., 2016. Proto-Andean evolution of the Eastern Cordillera of Peru. Gondwana Research, 35, 59–78. doi: 10.1016/j.gr.2016.03.016

Cook, N.J., Ciobanu, C.L., Pring, A., Skinner, W., Shimizu, M., Danyushevsky, L., Saini-Eidukat, B., Melcher, F., 2009. Trace and minor elements in sphalerite: a LA-ICPMS study. Geochimica et Cosmochimica Acta, 73, 4761–4791. https://doi.org/10.1016/j.gca.2009.05.045

Cook, N.J., Etschmann, B., Ciobanu, C.L., Geraki, K., Howard, D.L., Williams, T., Rae, N., Pring, A., Chen, G., Johannessen, B., Brugger, J., 2015. Distribution and substitution

mechanism of Ge in a Ge-(Fe)-bearing sphalerite. Minerals, 5, 117–132. https://doi.org/10.3390/min5020117

Corbella, M., Ayora, C., Cardellach, E., 2004. Hydrothermal mixing, carbonate dissolution and sulfide precipitation in Mississippi Valley-type deposits. Mineralium Deposita, 39, 344–357.

Craig, J.R., Vaughan, D.J., 1994. Ore Microscopy and Ore Petrography. John Wiley & Sons Ltd, New York.

Dana, E.S., 1892. System of mineralogy. John Wiley & Sons Ltd, New York.

Dávila, D., Febres, O., Fontboté, L., Oldham, L., 2000. Exploración y geología del yacimiento San Vicente. In: Yacimientos minerales peruanos. Instituto Ingenieros de Minas del Perú, 1, 305–328.

de Oliveira, S.B., Leach, D.L., Juliani, C., Monteiro, L.V.S., Johnson, C.A., 2019. The Zn–Pb mineralization of Florida Canyon, an evaporite-related Mississippi Valley-type deposit in the Bongará district, Northern Peru. Economic Geology, 114, 1621–1647. https://doi.org/10.5382/econgeo.4690

de Oliveira, S.B., Juliani, C., Monteiro, L.V.S., Tassinari, C.C.G., 2020. Structural control and timing of evaporite-related Mississippi Valley-type Zn–Pb deposits in Pucará Group, Northern Central Peru. Journal of South American Earth Science, 103, 102736. https://doi.org/10.1016/j.jsames.2020.102736

de Oliveira, S.B., Johnson, C.A., Juliani, C., Monteiro, L.V.S., Leach, D.L., Caran, M.G.N., 2021. Geology and genesis of the Shalipayco evaporite-related Mississippi Valley-type

Zn–Pb deposit, Central Peru: 3D geological modeling and C–O–S–Sr isotope constraints. Mineralium Deposita, 56, 1543–1563. https://doi.org/10.1007/s00126-020-01029-w

Di Benedetto, F., Bernardini, G.P., Costagliola, P., Plant, D., Vaughan, D.J., 2005. Compositional zoning in sphalerite crystals. American Mineralogist, 90, 1384–1392. https://doi.org/10.2138/am.2005.1754

Eisenlohr, B.N., Tompkins, L.A., Cathles, L.M., Barley, M.E., Groves, D.I., 1994. Mississippi Valley-type deposits: products of brine expulsion by eustatically induced hydrocarbon generation? An example from Northwestern Australia. Geology, 22, 315–318. https://doi.org/10.1130/0091-7613(1994)022<0315:MVTDPO>2.3.CO;2

European Commission, 2020. Communication from the Commission to the European Parliament, the Council, the European Economic and Social Committee and the Committee of the Region.

Fontboté, L., Gorzawski, H., 1990. Genesis of the Mississippi Valley-type Zn-Pb deposit of San Vicente, Central Peru; geologic and isotopic (Sr, O, C, S, Pb) evidence. Economic Geology, 85, 1402–1437. https://doi.org/10.2113/gsecongeo.85.7.1402

Fontboté, L., Spangenberg, J., Oldham, L., Dávila, D., Febres, O., 1995. The Mississippi Valley-type zinc-lead mine of San Vicente, Eastern Pucará basin, Peru. International Field Conference on Carbonate Hosted Lead-Zinc Deposits. Extended Abstracts, 83–86.

Fontboté, L., 2018. Ore deposits of the Central Andes. Elements, 14, 257–261. https://doi.org/10.2138/gselements.14.4.257

Fontboté, L., Saintilan, N.J., 2018. Reply to discussion of “A refined genetic model for the Laisvall and Vassbo Mississippi Valley-type sandstone-hosted deposits, Sweden: constraints from paragenetic studies, organic geochemistry, and S, C, N, and Sr isotope data” by D. Sangster. Mineralium Deposita, 53, 295–297. https://doi: 10.1007/s00126-017-0785-x

Frenzel, M., Hirsch, T., Gutzmer, J., 2016. Gallium, germanium, indium, and other trace and minor elements in sphalerite as a function of deposit type — A meta -analysis. Ore Geology Reviews, 76, 52–78. https://doi.org/10.1016/j.oregeorev.2015.12.017

Gómez-Fernández, F., Both, R.A., Mangas, J., Arribas, A., 2000. Metallogenesis of Zn-Pb carbonate-hosted mineralization in the southeastern region of the Picos de Europa (Central Northern Spain) Province: geologic, fluid inclusion, and stable isotope studies. Economic Geology, 95, 19–40. https://doi.org/10.2113/gsecongeo.95.1.19

Guillong, M., Hametner, K., Reusser, E., Wilson, S.A., Günther, D., 2005. Preliminary characterisation of new glass reference materials (GSA-1G, GSC-1G, GSD-1G and GSE-1G) by laser ablation-inductively coupled plasma-mass spectrometry using 193 nm, 213 nm and 266 nm wavelengths. Geostandards and Geoanalytical Research, 29, 315–331. https://doi.org/10.1111/j.1751-908x.2005.tb00903.x

Guillong, M., Meier, D.L., Allan, M.M., Heinrich, C.A., Yardley, B.W.D., 2008. SILLS: a matlab-based program for the reduction of Laser Ablation ICP–MS data of homogeneous materials and inclusions. In: Sylvester P. (Ed.), Laser Ablation ICP-MS in the Earth Sciences: Current Practices and Outstanding Issues. Mineralogical Association of Canada Short Course, 40, 328–333.

Guillong, M., Wotzlaw, J.F., Looser, N., Laurent, O., 2020. New analytical and data evaluation protocols to improve the reliability of U-Pb LA-ICP-MS carbonate dating. Geochronology https://doi.org/10.5194/gchron-2019-20

Gunnesch, K.A., Baumann, A., Gunnesch, M., 1990. Lead isotope variations across the Central Peruvian Andes. Economic Geology, 85, 1384–1401. https://doi.org/10.2113/gsecongeo.85.7.1384

Hofmann, C., Henn, U., 1985. Green sphalerite from Zaire. Journal of Gemmology, 19, 416–418.

Höll, R., Kling, M., Schroll, E., 2007. Metallogenesis of germanium - a review. Ore Geology Reviews, 30, 145–180. https://doi.org/10.1016/j.oregeorev.2005.07.034

Jenks, W.F., 1951. Triassic to Tertiary stratigraphy near Cerro de Pasco, Peru. Geological Society of America Bulletin, 62, 202 – 220. https://doi.org/10.1130/0016-7606(1951)62[202:TTTSNC]2.0.CO;2

Jochum, K.P., Weis, U., Stoll, B., Kuzmin, D., Yang, Q., Raczek, I., Jacob, D.E., Stracke, A., Birbaum, K., Frick, D.A., Günther, D., Enzweiler, J., 2011. Determination of reference values for NIST SRM 610-617 glasses following ISO guidelines. Geostandards Geoanalytical Research, 35, 397–429. https://doi.org/10.1111/j.1751-908X.2011.00120.x

Johan, Z., 1988. Indium and germanium in the structure of sphalerite: an example of coupled substitution with Copper. Mineralogy and Petrology, 39, 211–229. https://doi.org/10.1007/BF01163036

Jolly, J.L., Heyl, A.V., 1964. Mineral paragenesis and zoning in the Central Kentucky Mineral

district. Economic Geology, 59, 596–624. https://doi.org/10.2113/gsecongeo.59.4.596

Katsev, S., L'Heureux, I., Fowler, A., 2001. Mechanism and duration of banding in Mississippi Valley-type sphalerite. Geophysical Research Letters, 28, 4643 -4646. https://doi.org/10.1029/2001GL013080

Kelka, U., Veveakis, M., Koehn, D., Beaudoin, N., 2017. Zebra rocks: compaction waves create ore deposits. Scientifc Reports, 7, 14260. https://doi.org/10.1038/s41598-017-14541-3

Kelley, K.D., Leach, D.L., Johnson, C.A., Clark, J.L., Fayek, M., Slack, J.F., Anderson, V.M., Ayuso, R.A., Ridley, W.I., 2004. Textural, compositional, and sulfur isotope variations of sulfide minerals in the Red Dog Zn-Pb-Ag deposits, Brooks Range, Alaska: implications for ore formation. Economic Geology, 99, 1509–1532. https://doi.org/10.2113/99.7.1509

Kesler, S.E., 1994. Mississippi Valley-type deposits in continental margin basins: lessons from the Appalachian-Caledonian Orogen. In: Fontboté, L., Boni, M. (Eds.), Sediment-hosted Zn-Pb ores. Springer, Berlin, 90–102. https://doi.org/10.1007/978-3-662-03054-7

Kesler, S.E., Jones, H.D., Furman, F.C., Sassen, R., Anderson, W.H., Kyle, J.R., 1994. Role of crude oil in the genesis of Mississippi Valley-type deposits: evidence from the Cincinnati arch. Geology, 22, 609–612. https://doi.org/10.1130/0091-7613(1994)022<0609:ROCOIT>2.3.CO;2

Kesler, S.E., Appold, M.S., Martini, A.M., Walter, L.M., Huston, T.J., Kyle, J.R., 1995. Na-Cl-Br systematics of mineralizing brines in Mississippi Valley-type deposits. Geology, 23, 641–644. https://doi.org/10.1130/0091-7613(1995)023%3C0641:NCBSOM%3E2.3.CO;2

Knorsch, M., Nadoll, P., Klemd, R., 2020. Trace elements and textures of hydrothermal

sphalerite and pyrite in Upper Permian (Zechstein) carbonates of the North German Basin. Journal of Geochemical Exploration, 209, 106416. https://doi.org/10.1016/j.gexplo.2019.106416

Kontak, D.J., Clark, A.H., Farrar, E., Strong, D.F., 1985. The rift associated Permo-Triassic magmatism of the Eastern Cordillera: a precursor of the Andean orogeny. In: Atherton, W.S., Pitcher, M.P., Cobbing, E.J., Beckinsale, R.D. (Eds.), Magmatism at a plate edge. The Peruvian Andes, Wiley, New York, 36–44.

Kouzmanov, K., Chiaradia, M., Fontbote, L., Spangenberg, J., 2011. Origin of massive anhydrite bodies in the Morococha district, central Peru: insights from stable (O, S) and radiogenic (Sr, Nd) isotope geochemistry. Proceedings of the SGA 11th Biennial Meeting: Antofagasta, Chile, 405–407.

Lancelot, J.R., Laubacher, G., Marocco, R., Renaud, U., 1978. U/Pb radiochronology of two granitic plutons from the Eastern Cordillera (Peru) - extent of Permian magmatic activity and consequences. Geologische Rundschau 67, 236–243. https://doi.org/10.1007/BF01803263

Leach, D.L., Sangster, D.F., 1993. Mississippi Valley type lead-zinc deposits. Geological Association of Canada, 40, 289–314.

Leach, D.L., Bradley, D., Lewchuk, M.T., Symons, D.T.A., De Marsily, G., Brannon, J., 2001. Mississippi Valley-type lead-zinc deposits through geological time: implications from recent age-dating research. Mineralium Deposita, 36, 711–740. https://doi.org/10.1007/s001260100208

Leach, D.L., Sangster, D.F., Kelley, K.D., Large, R.R., Garven, G., Allen, C.R., Gutzmer, J.,

Walters, S., 2005. Sediment-hosted lead-zinc deposits: a global perspective. Economic Geology, 100, 561–607. https://doi.org/10.5382/AV100.18

Leach, D.L., Taylor, R.D., Fey, D.L., Diehl, S.F., Saltus, R.W., 2010. A deposit model for Mississippi Valley-type lead-zinc ores. In: chapter A of mineral deposit models for resource assessment. U.S Geological Survey Scientific Investigations Report 2010–5070–A. https://doi.org/10.3133/sir20105070A

Li, M., Barnes, H.L., 2019. Orbitally forced sphalerite growth in the Upper Mississippi Valley district. Geochemical Perspective Letters, 12, 18–22. https://doi.org/10.7185/geochemlet.1929

Li, Z., Ye, L., Hu, Y., Wei, C., Huang, Z., Yang, Y., Danyushevsky, L., 2020. Trace elements in sulfides from the Maozu Pb-Zn deposit, Yunnan Province, China: implications for trace-element incorporation mechanisms and ore genesis. American Mineralogist, 105, 1734–1751. https://doi.org/10.2138/am-2020-6950

Loughman, D.L., Hallam, A., 1982. A facies analysis of the Pucará Group (Norian to Toarcian carbonates, organic-rich shale and phosphate) of Central and Northern Peru. Sedimentary Geology, 32, 161–194. https://doi.org/10.1016/0037-0738(82)90049-5

McLaughlin, D.H., 1924. Geology and physiography of the Peruvian Cordillera, Departments of Junin and Lima. Geological Society of America Bulletin, 35, 591–632. https://doi.org/10.1130/GSAB-35-591

Mégard, F., 1978. Etude géologique des Andes du Pérou Central, contribution à l'étude géologique des Andes. Office de la Recherche Scientifique et Technique. Institut français d'études andines, Paris. https://doi.org/10.4000/books.ifea.1450

Mégard, F., 1984. The Andean orogenic period and its major structures in Central and Northern Peru. Journal of the Geological Society, 141, 893–900. https://doi.org/10.1144/gsjgs.141.5.0893

Mégard, F., 1987. Structure and evolution of the Peruvian Andes. In: Schaer, J.P., Rodgers, J. (Eds.), The Anatomy of Mountain Ranges. Princeton University, Princeton, New Jersey, United States,179–210.

Melcher, F., Buchholz, P., 2014. Germanium. In: Gunn, G. (Ed.), Critical Metals Handbook, 177–203. https://doi.org/10.1002/9781118755341.ch8

Merino, E., Canals, A., 2011. Self-accelerating dolomite-for-calcite replacement: self-organized dynamics of burial dolomitization and associated mineralization. American Journal of Science, 311, 573–607. https://doi.org/10.2475/07.2011.01

Möller, P., Dulski, P., 1996. Germanium and gallium distribution in sphalerite: a key to the genesis of sediment-hosted sulphide mineralizations. Zeitschrift für Geologische Wissenschaften, 24, 527–538.

Mondillo, N., Arfè, G., Boni, M., Balassone, G., Boyce, A., Joachimski, M., Kang, J.S., Villa, I.M., 2018a. The Cristal Zinc prospect (Amazonas region, Northern Peru). Part I: new insights on the sulfide mineralization in the Bongará province. Ore Geology Reviews, 94, 261–276. https://doi.org/10.1016/j.oregeorev.2018.01.021

Mondillo, N., Arfè, G., Herrington, R., Boni, M., Wilkinson, C., Mormone, A., 2018b. Germanium enrichment in supergene settings: evidence from the Cristal nonsulfide Zn prospect, Bongará district, Northern Peru. Mineralium Deposita, 53, 155–169. https://doi.org/10.1007/s00126-017-0781-1

Moritz, R., Fontboté, L., Spangenberg, J., Rosas, S., Sharp, Z., Fontignie, D., 1996. Sr, C and O isotope systematics in the Pucará basin, Central Peru. Mineralium Deposita, 31, 147–162. https://doi.org/10.1007/BF00204023

Muñoz, C., Farfán, C., López, G., Rosas, S., 2000. Vulcanismo asociado a los carbonatos del Grupo Pucará (Triásico Superior – Liásico) en el área de Shalipayco, Junín – Perú Central. Resúmenes X Congreso Peruano de Geología. Sociedad Geológica del Perú, Publicación Especial, 2, 42.

Noble, D.C., Silberman, M.L., Megard, F., Bowman, H.P., 1978. Comendite (peralkaline rhyolite) and basalt in the Mitu Group, Peru: evidence for Permian-Triassic lithospheric extension in the Central Andes. US Geological Survey. Journal of Research, 6, 453–457.

Oldham, L., Dávila, D., Flores, W., Mamani, W., Minaya, J., Cano, P., 2017. Reporte annual de exploraciones. Proyecto Shalipayco. Propietary Report.

Ostendorf, J., Henjes-Kunst, F., Mondillo, N., Boni, M., Schneider, J., Gutzmer, J., 2015. Formation of Mississippi Valley-type deposits linked to hydrocarbon generation in extensional tectonic settings: Evidence from the Jabali Zn-Pb-(Ag) deposit (Yemen). Geology, 43, 1055–1058. https://doi.org/10.1130/G37112.1

Palache, C., Berman, H., Frondel, C., 1944. The system of mineralogy of James Dwight Dana and Edward Salisbury Dana Yale University 1837-1892, Volume I: Elements, Sulfides, Sulfosalts, Oxides. John Wiley and Sons, New York.

Paradis, S., Hannigan, P., Dewing, K., 2007. Mssissippi Valley-type lead-zinc deposits. In: Goodfellow, W.D. (Ed.), Mineral Deposits of Canada: A Synthesis of Major Deposit-Types, District Metallogeny, the Evolution of Geological Provinces, and Exploration

Methods. Geological Association of Canada, Mineral Deposits Division, Special Publication, 5, 185–203.

Paradis, S., 2015. Indium, germanium and gallium in volcanic- and sediment-hosted base-metal sulphide deposits. In: Simandl, G.J., Neetz, M. (Eds.), Symposium on Strategic and Critical Materials Proceedings, November 13-14, 2015, Victoria, British Columbia. British Columbia Geological Survey Paper 2015-3, 23–29.

Peace, W.M., Wallace, M.W., Holdstock, M.P., Ashton, J.H., 2003. Ore textures within the U lens of the Navan Zn-Pb deposit, Ireland. Mineralium Deposita, 38, 568–584. https://doi.org/10.1007/s00126-002-0340-1

Rager, H., Amthauer, G., Bernroider, M., Schürmann, K., 1996. Colour, crystal chemistry, and mineral association of a green sphalerite from Steinperf, Dill syncline, FRG. European Journal of Mineralogy, 8, 1191–1198. https://doi.org/10.1127/ejm/8/5/1191

Ramdohr, P., 1980. The ore minerals and their intergrowths. Pergamon Press, Oxford.

Ramírez, J., Torró, L., Quispe, P., Benites, D., Vallance, J., Rosas, S., Guzmán, L., Fernández-Baca, A., Spangenberg, J.E., Vennemann, T., Chiaradia, M., Kouzmanov, K., Fontboté, L., 2022. Isotopic signatures of sulfides (S) and anhydrite (S, O, Sr) from the Ayawilca polymetallic deposit, Pasco, Peru. In: Proceedings of the 16th Biennial SGA Meeting, submitted.

Ritterbush, K.A., Rosas, S., Corsetti, F.A., Bottjer, D.J., West, A.J., 2015. Andean sponges reveal long-term benthic ecosystem shifts following the end-Triassic mass extinction. Palaeogeography, Palaeoclimatology, Palaeoecology, 420, 193–209. https://doi.org/10.1016/j.palaeo.2014.12.002

Robson, D., Carlsson, J., Altman, K., Theben, S., 2017. Technical report on the preliminary economic assessment of the Shalipayco project, Junín Region, Peru.

Roedder, E., Dwornik, E.J., 1968. Sphalerite color banding. Lack of correlation with iron content, Pine Point, Northwest Territories, Canada. The American Mineralogist, 53, 1523–1529.

Rosas, S., Fontboté, L., 1995. Evolución sedimentológica del Grupo Pucará (Triásico Superior – Jurásico Inferior) en un perfil SW-NE en el Centro del Perú. Volumen Jubilar Alberto Benavides, Sociedad Geológica del Perú, 279–309.

Rosas, S., Fontboté, L., Tankard, A., 2007. Tectonic evolution and paleogeography of the Mesozoic Pucará basin, Central Peru. Journal of South American Earth Sciences, 24, 1–24. https://doi.org/10.1016/j.jsames.2007.03.002

Rosas, S., 2016. Profundización sedimentaria solo en la parte de la cuenca Pucará (Perú Central) durante el Hetangiano Sinemuriano. In: XVIII Congreso Peruano de Geología. Sociedad Geológica del Perú, 1–4.

Saini-Eidukat, B., Melcher, F., Lodziak, J., 2009. Zinc-germanium ores of the Tres Marias mine, Chihuahua, Mexico. Mineralium Deposita, 44, 363–370. https://doi.org/10.1007/s00126-008-0222-2

Saintilan, N.J., Spangenberg, J.E., Chiaradia, M., Chelle-Michou, C., Stephens, M.B., Fontboté, L., 2019. Petroleum as source and carrier of metals in epigenetic sediment-hosted mineralization. Scientific Reports, 9, 1–8. https://doi.org/10.1038/s41598-019-44770-7

Saintilan, N.J., Spangenberg, J.E., Samankassou, E., Kouzmanov, K., Chiaradia, M., Stephens, M.B., Fontboté, L., 2016. A refined genetic model for the Laisvall and Vassbo Mississippi Valley-type sandstone-hosted deposits, Sweden: constraints from paragenetic studies, organic geochemistry, and S, C, N and Sr isotope data. Mineralium Deposita, 51, 639–664. https://doi.org/10.1007/s00126-015-0627-7

Saintilan, N.J., Sproson, A.D., Selby, D., Rottier, B., Casanova, V., Creaser, R.A., Kouzmanov, K., Fontboté, L., Piecha, M., Gereke, M., Zambito IV, J.J., 2021. Osmium isotopic constraints on sulphide formation in the epithermal environment of magmatic-hydrothermal mineral deposits. Chemical Geology, 564,120053. https://doi.org/10.1016/j.chemgeo.2020.120053

Sanabria, R., García-Álvarez, J.R., 2005. Les sphalérites d'Aliva, Picos de Europa (Espagne). Le Règne Minéral, 63, 6–27.

Sangster, D.F., 1995. Mississippi Valley-type lead-zinc. In: Eckstrand, O.R., Sinclair, W.D., Thorpe, R.I. (Eds.), Geology of Canadian Mineral Deposit Types. Geological Survey of Canada, Geology of Canada, 8, 253–261. https://doi.org/10.1130/DNAG-GNA-P1.253

Sapalski, C., Gómez, F., 1992. Estudio de la esfalerita de la mina de Ávila, Santander. Boletín del Instituto Gemológico Español, 34, 28–39.

Schaltegger, U., Guex, J., Bartolini, A., Schoene, B., Ovtcharova, M., 2008. Precise U–Pb age constraints for end-Triassic mass extinction, its correlation to volcanism and Hettangian post-extinction recovery. Earth and Planetary Science Letters, 267, 266–275. https://doi.org/10.1016/j.epsl.2007.11.031

Schutfort, 2001. The genesis of the San Vicente lead-zinc rhythmites deposit, Peru - a

petrologic, geochemical, and sulfur isotope study. Master of Science thesis, Oregon State University.

Sempere, T.P.A., Cotrina, J., 2018. An overlooked giant salt basin in Peru. In: 9th INGEPET, Lima, paper GEO-EX-TS-10-N, 18 p.

Shanks III, W.C.P., Kimball, B.E., Tolcin, A.C., Guberman, D.E., 2017. Germanium and indium. In: Schulz, K.J., DeYoung, J.H., Seal II, R.R., and Bradley, D.C. Critical mineral resources of the United States—Economic and environmental geology and prospects for future supply: US Geological Survey Professional Paper, 1802 I1–I27.

Slack, G.A., Ham, F.S., Chrenko, R.M., 1966. Optical absorption of tetrahedral Fe^{2+} ($3d^6$) in cubic ZnS, CdTe, and $MgAl_2O_4$. Physical Review, 152, 376–402. https://doi.org/10.1103/PhysRev.152.376

Slack, G.A., Roberts, S., Ham, F.S., 1967. Far-infrared optical absorption of Fe^{2+} in ZnS. Physical Review, 155, 170–177. https://doi.org/10.1103/PhysRev.155.170

Spangenberg, J.E., 1995. Geochemical (elemental and isotopic) constraints on the genesis of the Mississippi Valley-type zinc-lead deposit of San Vicente, Central Peru. Ph.D. thesis, Université de Genève. 10.13097/archive-ouverte/unige:98591

Spangenberg, J.E., Fontboté, L., Sharp, Z.D., Hunziker, J., 1996. Carbon and oxygen isotope study of hydrothermal carbonates in the zinc-lead deposits of the San Vicente district, Central Peru: a quantitative modeling on mixing processes and CO_2 degassing. Chemical Geology, 133, 289–315. https://doi.org/10.1016/S0009-2541(96)00106-4

Spangenberg, J.E., Macko, S.A., 1998. Organic geochemistry of the San Vicente zinc-lead

district, eastern Pucará Basin, Peru. Chemical Geology, 146, 1–23. https://doi.org/10.1016/S0009-2541(97)00158-7

Spangenberg, J.E., Fontboté, L., Macko, S.A., 1999. An evaluation of the inorganic and organic geochemistry of the San Vicente Mississippi Valley-type zinc-lead district, Central Peru; implications for ore fluid composition, mixing processes, and sulfate reduction. Economic Geology, 94, 1067–1092. https://doi.org/10.2113/gsecongeo.94.7.1067

Spikings, R., Reitsma, M.J., Boekhout, F., Mišković, A., Ulianov, A., Chiaradia, M., Gerdes, A., Schaltegger, U., 2016. Characterisation of Triassic rifting in Peru and implications for the early disassembly of western Pangaea. Gondwana Research, 35, 124–143. https://doi.org/10.1016/j.gr.2016.02.008

Stipetich, S., Zorrilla, A., Valencia, E., Zárate, J., Valverde, P., Benites, D., Torró, L., Vallance, J., 2021. Halocinesis y mineralizaciones polimetálicas de origen magmático-hidrotermal: el caso del distrito de Morococha. In: proExplo Conference. Lima, Peru.

Stipetich, S., Vallance, J., Torró, L., Rosas, S., Benites, D., Valverde, P., Spangenberg, J.E., Vennemann, T., Kouzmanov, K., Chiaradia, M., Fontboté, L., Zorrilla, A., Valencia, E., Zarate, J., Díaz, R., Huamantalla, J., 2022. Role of massive anhydrite bodies in the Cordilleran-type polymetallic mineralization of Morococha district, Peru: 3D geological modeling and S-O-Sr isotope constraints. In: Proceedings of the 16th Biennial SGA Meeting, submitted.

Szekely, T.S., Grose, L.T., 1972. Stratigraphy of the carbonate, black shale, and phosphate of the Pucará Group (Upper Triassic-Lower Jurassic), Central Andes, Peru. Geological Society of America Bulletin, 83, 407– 428.

https://doi.org/10.1130/0016-7606(1972)83[407:SOTCBS]2.0.CO;2

Wei, C., Ye, L., Hu, Y., Danyushevskiy, L., Li, Z., Huang, Z., 2019. Distribution and occurrence of Ge and related trace elements in sphalerite from the Lehong carbonate-hosted Zn-Pb deposit, Northeastern Yunnan, China: insights from SEM and LA-ICP-MS studies. Ore Geology Reviews, 115, 103175. https://doi.org/10.1016/j.oregeorev.2019.103175

Wei, C., Ye, L., Hu, Y., Huang, Z., Danyushevsky, L., Wang, H., 2021. LA-ICP-MS analyses of trace elements in base metal sulfides from carbonate-hosted Zn-Pb deposits, South China: A case study of the Maoping deposit. Ore Geology Reviews, 130, 103945 https://doi.org/10.1016/j.oregeorev.2020.103945

Wilkinson, J.J., 2014. Sediment-hosted zinc-lead mineralization. In: Holland, H., Turekian, K. (Eds.), Treatise on Geochemistry, 13, 219–249. https://doi.org/10.1016/B978-0-08-095975-7.01109-8

Wilson, S.A., Ridley, W.I., Koenig, A.E., 2002. Development of sulfide calibration standards for the laser ablation inductively-coupled plasma mass spectrometry technique. Journal of Analytical Atomic Spectrometry, 17, 406–409. https://doi.org/10.1039/b108787h

Wood, G.D., Groves, J.R., Wahlman, G.P., Brenckle, P.L., Alemán, A.M., 2002. The paleogeographic and biostratigraphic significance of fusulinacean and smaller foraminifers, and palynomorphs from the Copacabana Formation (Pennsylvanian-Permian), Madre de Dios Basin, Peru. In: Hills, L.V., Henderson, C.M., Bamber, E.W. (Eds.), Carboniferous and Permien of the World. Canadian Society of Petroleum Geologist, Memoirs, 19, 630 – 664.

Ye, L., Cook, N.J., Ciobanu, C.L., Yuping, L., Qian, Z., Tiegeng, L., Wei, G., Yulong, Y.,

Danyushevskiy, L., 2011. Trace and minor elements in sphalerite from base metal deposits in South China: A LA-ICPMS study. Ore Geology Reviews, 39, 188–217. https://doi.org/10.1016/j.oregeorev.2011.03.001

Ye, L., Li, Z., Hu, Y., Huang, Z., Zhou, J., Fan, H., Danyushevsky, L.V., 2016. Trace elements in sulfide from the Tianbaoshan Pb-Zn deposit, Sichuan province, China: a LA-ICPMS study. Acta Petrologica Sinica, 32, 3377–3393.

Yuan, B., Zhang, C., Yu, H., Yang, Y., Zhao, Y., Zhu, C., Ding, Q., Zhou, Y., Yang, J., Xu, Y., 2018. Element enrichment characteristics: insights from element geochemistry of sphalerite in Daliangzi Pb-Zn deposit, Sichuan, Southwest China. Journal of Geochemical Exploration, 186, 187–201. https://doi.org/10.1016/j.gexplo.2017.12.014

ET LUX IN TENEBRIS LUCET
MCMXVII

TABLE S1: LIST OF SAMPLES AND THEIR LOCATION

SAMPLE	DEPOSIT	UTM E	UTM N	LONGITUDE	LATITUDE	DRILLHOLE	MEASURED DEPTH
2019-SV-01	San Vicente	456758	8758781	-75.396135	-11.228002	4630	492.25-492.35
2019-SV-02	San Vicente	456758	8758781	-75.396135	-11.228002	4630	491.60-491.80
2019-SV-03	San Vicente	456758	8758781	-75.396135	-11.228002	4630	497.00-497.05
2019-SV-04	San Vicente	456758	8758781	-75.396135	-11.228002	4630	492.85-492.95
2019-SV-05	San Vicente	456758	8758781	-75.396135	-11.228002	4630	439.35-439.45
2019-SV-06	San Vicente	457233	8761509	-75.39175	-11.203337	4635	166.80-166.95
2019-SV-07	San Vicente	457233	8761509	-75.39175	-11.203337	4635	159.80-159.90
2019-SV-08	San Vicente	457233	8761509	-75.39175	-11.203337	4635	158.40-158.50
2019-SV-09	San Vicente	457233	8761509	-75.39175	-11.203337	4635	149.35-149.55

SAMPLE	DEPOSIT	UTM E	UTM N	LONGITUDE	LATITUDE	DRILLHOLE	MEASURED DEPTH
2019-SV-10	San Vicente	457233	8761509	-75.39175	-11.203337	4635	157.50-157.60
2019-SV-11	San Vicente	456758	8758910	-75.396133	-11.226835	4670	480.10-480.25
2019-SV-12	San Vicente	456758	8758910	-75.396133	-11.226835	4670	480.80-480.95
2019-SV-13	San Vicente	4578287	8758775	-75.386333	-11.228069	4714	-
2019-SV-14	San Vicente	4578287	8758775	-75.386333	-11.228069	4714	-
2019-SV-15	San Vicente	-	-	-	-	Gallery	-
2019-SV-16	San Vicente	-	-	-	-	Gallery	-
TP-1524437	Shalipayco	392923.63	8800668.07	-75.979616	-10.847881	SH-76	110.5 - 110.59
SH-104-TP-1526158	Shalipayco	392712.16	8800630.69	-75.981551	-10.848213	SH-104	229.25 - 229.34
SH-212-TP-1548884	Shalipayco	391987.39	8802288.77	-75.988132	-10.833198	SH-212	179.55 - 179.65
SH-59-TP-1521040	Shalipayco	392796.29	8800531.43	-75.980785	-10.849113	SH-59	210.1 - 210.2
SH-157-TP-1539052	Shalipayco	392744.76	8800531.89	-75.981256	-10.849107	SH-157	250.5 - 251.5
SH-227-TP-1549036	Shalipayco	392942	8800584	-75.97945	-10.848642	SH-227	153 - 153.7

SAMPLE	DEPOSIT	UTM E	UTM N	LONGITUDE	LATITUDE	DRILLHOLE	MEASURED DEPTH
PESHA000004 PEDC0000173	Shalipayco	394498.88	8799241.52	-75.965247	-10.860826	PESHD000001	79.7 - 79.8
SH-120-TP-1528304	Shalipayco	392738.04	8800650.45	-75.981314	-10.848035	SH-120	129.45 - 129.54
SH-167-TP-154465	Shalipayco	392274.63	8801430.17	-75.98553	-10.840971	SH-167	136.6 - 136.69
SH-31-TP-1511385	Shalipayco	392184.95	8801171.39	-75.986358	-10.843308	SH-31	365 - 365.1
SH-187-TP-1542565	Shalipayco	393246.44	8799807.1	-75.976688	-10.855676	SH-187	248.7 - 248.79
SH-191-TP-1542927	Shalipayco	393506.21	8799598.32	-75.974318	-10.857571	SH-191	205.9 - 206
SH-84-TP-1525057	Shalipayco	392769.43	8800615.97	-75.981028	-10.848348	SH-84	191.9 - 191.99
SH-233-TP-1549582	Shalipayco	393149.92	8800386.26	-75.977554	-10.850436	PESHDD0233	102.6 - 102.69
SH-192-TP-1543077	Shalipayco	392406	8801076	-75.984339	-10.844177	SH-192	184.2 - 185.4
SH-231-TP-1549473	Shalipayco	393084.86	8800325.11	-75.978151	-10.850987	PESHDD0231	139.45 - 139.54

SAMPLE	ORE BODY - VEIN/ZONE/LEVEL	MINERALS
2019-SV-01	Ayala Inferior, Horizonte San Vicente, N Zone, Chamber 782 W, Gallery 690	sl, gn, dol
2019-SV-02	Ayala Inferior, Horizonte San Vicente, N Zone, Chamber 782 W, Gallery 690	sl
2019-SV-03	Ayala Inferior, Horizonte San Vicente, N Zone , Chamber 782 W, Gallery 690	sl
2019-SV-04	Ayala Inferior, Horizonte San Vicente, N Zone , Chamber 782 W, Gallery 690	sl, dol, py
2019-SV-05	Ayala Inferior, Horizonte San Vicente, N Zone, Chamber 782 W, Gallery 690	sl, dol
2019-SV-06	Orcopunco Zone, Galley 1275N, Level 1739	sl, dol
2019-SV-07	Orcopunco Zone, Gallery 1275N, Level 1739	sl, dol
2019-SV-08	Orcopunco Zone, Gallery 1275N, Level 1739	sl, dol
2019-SV-09	Orcopunco Zone, Gallery 1275N, Level 1739	sl, dol, cc

SAMPLE	ORE BODY - VEIN/ZONE/LEVEL	MINERALS
2019-SV-10	Orcopunco Zone, Gallery 1275N, Level 1739	sl, py, gn, dol
2019-SV-11	N Zone, Chamber 8909W, Gallery 690, Level 1529	sl, gn, dol
2019-SV-12	N Zone, Chamber 8909W, Gallery 690, Level 1529	sl, dol, gn
2019-SV-13	N Zone, Ramp 630, Level 1475	sl, dol
2019-SV-14	N Zone, Ramp 630, Level 1475	sl
2019-SV-15	Ayala inferior, Pit 632	sl, dol
2019-SV-16	Frente 8093, horizonte San Vicente, Manto IIIS	sl, dol
TP-1524437	Manto Intermedio; Elevation 4244	sl, py
SH-104-TP-1526158	Manto Intermedio; Elevation 4099	sl
SH-212-TP-1548884	Manto Intermedio; Elevation4300	sl
SH-59-TP-1521040	Manto Intermedio; Elevation 4123	sl
SH-157-TP-1539052	Manto Intermedio; Elevation 4100	sl, py
SH-227-TP-1549036	Manto Resurgidora; Elevation 4329	sl

SAMPLE	ORE BODY - VEIN/ZONE/LEVEL	MINERALS
PESHA000004 PEDC0000173	Manto Resurgidora; Elevation 4425	sl, gn
SH-120-TP-1528304	Manto Resurgidora; Elevation 4201	sl, gn
SH-167-TP-154465	Manto Intermedio; Elevation 4247	ef, py
SH-31-TP-1511385	Manto Intermedio; Elevation 4053	sl, gn, py
SH-187-TP-1542565	Manto Intermedio; Elevation 4093	sl
SH-191-TP-1542927	Manto Resurgidora; Elevation 4154	sl, gn
SH-84-TP-1525057	Manto Intermedio; Elevation 4144	sl
SH-233-TP-1549582	Manto Intermedio	sl, gn
SH-192-TP-1543077	Manto Resurgidora; Elevation 4333	sl, gn, py
SH-231-TP-1549473	Manto Intermedio; Elevation 4198	sl

SAMPLE	DESCRIPTION
2019-SV-01	Sphaleirte+galena breccia. Banding of reddish-brown and yellowish-brown sphalerite. Fine sphalerite grains, from brown to yellowish color occur in galena groundmass. Galena postdates filling and replacing. Above this assemblage, medium grain, interstitial light yellow sphalerite also occur. Postdating, dolomite intergrown with brown sphalerite is noticed.
2019-SV-02	Zebra-bands with yellowish-brown sphalerite.
2019-SV-03	Colloform fine sphalerite. Internal bands or sphalerite are of reddish-brown and yellowh-brown colors, followed by reddish-brown bands, then by yellowish-brown sphalerite and finally by sphalerite of yellow and white colors.
2019-SV-04	Colloform bands of coarse-grained sphalerite are observed. The central part of the sphalerite is of black and reddish-brown color intergrown with gray dolomite, grading to colloform zones with 8 to 10mm of thickness, ending in yellowish-brown sphalerite. Pyrite within dolomite is also observed.
2019-SV-05	White sphalerite forms thin veinlets, less than 1mm in thickness. Brecciated black sphalerite+grey dolomite cemented by white dolomite. White sphalerite veinlets seems to have cut the whole assemblage.
2019-SV-06	Brecciation. Sphalerite (black, reddish-brown and yellowish-brown) occurs previous to brecciation. Clasts are cemented by dolomite. Late dolomite veinlets (<1mm in thickness) cut this assemblage.
2019-SV-07	Coarse black, reddish-brown and yellowish-brown sphalerite. Yellowish tone increases with grain size, forming rims. Clasts within the dolomite cement.
2019-SV-08	Clasts of black, reddish-brown, yellowish-brown and yellow sphalerite cemented by gray and white dolomite.
2019-SV-09	Sphalerite in limestone enriched in organic matter, dark. In the inner parts of the clasts, reddish-brown sphalerite is observed, and in the external part, finer and yellowish to greenish-grey sphalerite (this sphalerite is brecciated and filled with vein dolomite).

SAMPLE	DESCRIPTION
2019-SV-10	The sample is constituted by black dolomite with calcite fragments (rich in organic matter) enriched in pyrite. Brecciated fragments of black dolomite+calcite with replacement and cut by veinlets of very fine-grained pyrite, cemented by gray dolomite is observed. Gray dolomite cut by thin veinlets (<1mm in thickness) of white to pale-grey sphalerite. Gray Cement has been brecciated and cemented again by white dolomite and lesser amounts of galena. Finally, veinlets of white dolomite cut the whole assemblage (including the clasts). At least three generations of dolomite are identified.
2019-SV-11	Brecciated bands. Black, reddish-brown and yellowish-brown fine-grained sphalerite (have replaced clasts and concentrates along the clasts' outlines). Lead-grey coarse crystals of dolomite (cement) grade to white dolomite (this dolomite cements gray dolomite). Galena with gray dolomite lines voids and forms veinlets, suggesting that is later than the white dolomite.
2019-SV-12	Similar to sample 2019-SV-11. Black dolomite cemented by black and brown spahalerite. The cement is constituted by pale grey dolomite grading to white dolomite. Galena grains occur in gray dolomite.
2019-SV-13	Black dolomite replaced by orange and yellow sphalerite; the latter showing in sections an intense color. Sphalerite forms clusters of 2-4mm-sized grains. White dolomite cements this assemblage.
2019-SV-14	Black dolomite replaced by orange and yellow sphalerite; the latter showing in sections an intense color. Sphalerite forms clusters of 2-4mm-sized grains. White dolomite cements this assemblage.
2019-SV-15	Orange to yellow sphalerite with white dolomite and calcite. Some sectors show reddish-brown and yellowish sphalerite.
2019-SV-16	Zebra bands constituted by gray and white dolomite, sphalerite (black, reddish-brown, and yellowish-brown), and calcite with galena.
TP-1524437	Disseminated galena <1%. Dolomite; metadolomite.
SH-104-TP-1526158	Scarce veins and pseudomorphs of calcite; disseminated sphalerite. Dolomite; metadolomite.
SH-212-TP-1548884	Dolomite; metadolomite.
SH-59-TP-1521040	Pseudo-breccia. Calcite in karst cavities, sphalerite disseminated in fractures, crackle breccia. Dolomite; metadolomite.
SH-157-TP-1539052	Few pseudomorphs of calcite, stylolites, disseminated sphalerite, pyrite with patch texture. Dolomite; metadolomite.
SH-227-TP-1549036	Intraformational breccia. Evaporitic. Sphalerite as matrix. Dolomite; metadolomite.

SAMPLE	DESCRIPTION
PESHA000004 PEDC0000173	Dolomite; metadolomite.
SH-120-TP-1528304	Breccia. Clasts of mudstone dolomite, sulffide and calcite matrix, karstic cavities, massive sphalerite and veinlets; veinlets of galena (<1%). Evaporite.
SH-167-TP-154465	Veinlets and pseudomorphs of calcite, karstic cavities, fractures, sphalerite veinles and disseminated (<1%), pyrite with patchy texture (<1%). Dolomite; metadolomite.
SH-31-TP-1511385	Veinlets of calcite, massive sphalerite (40%); massive galena. Dolomite; metadolomite.
SH-187-TP-1542565	Scarce veinlets and pseudomorphs of csalcite, sphalerite as dissemination and veinllets. Dolomite; metadolomite.
SH-191-TP-1542927	Veinlets of baryte and calcite, pseudomorphs of calcite, bitumen-filled stylolites, disseminated sphalerite, patchy galena (<1%). Dolomite; metadolomite.
SH-84-TP-1525057	Breccia. Veinlets of calcite, stylolites, disseminated sphalerite (4%). Dolomite; metadolomite.
SH-233-TP-1549582	Scarce veinlets of calcite, bitumen-filled stylolites and pyrite (<1%), massive sphalerite disseminated, massive galena with patchy texture. Dolomite; metadolomite.
SH-192-TP-1543077	Homolitic. Veinlets and pseudomorphs of calcite, sphalerite (7%), patchy galena (<1%), fracture pyrite (<1%). Dolomite; metadolomite.
SH-231-TP-1549473	Evaporitic breccia horizons, few veinlets and pseudomorphs of calcite, bitumen-filled stylolites, disseminated sphalerite (also as veins). Dolomite; metadolomite.

TABLE S2: REPRESENTATIVE EPMA ANALYSES OF SPHALERITE IN THE SAN VICENTE DEPOSIT

	Sample	SV-07	SV-07	SV-07	SV-07	SV-08A	SV-08A	SV-08A	SV-08B	SV-08B
	Color	Black	Black	Black	Black	Black	Black	Black	Black	Black
Detection limit	wt.%	SV-07-circulo A-ef-004	SV-07-circulo B-ef-003	SV-07-circulo C-ef-002	SV-07-circulo C-ef-003	SV-08A-circulo A-ef-004	SV-08A-circulo C-ef-002	SV-08A-circulo C-ef-003	SV-08B-circulo A-ef-002	SV-08B-circulo B-ef-001
0.12	Sb	B.D.L	B.D.L	B.D.L	B.D.L	B.D.L	B.D.L	B.D.L	B.D.L	B.D.L
0.15	In	B.D.L	B.D.L	B.D.L	B.D.L	B.D.L	B.D.L	B.D.L	B.D.L	B.D.L
0.07	S	32.92	33.16	32.73	33.32	33.82	33.35	33.85	32.74	33.03
0.18	Pb	B.D.L	0.29	0.19	B.D.L	0.30	B.D.L	0.23	B.D.L	B.D.L
0.44	As	B.D.L	B.D.L	B.D.L	B.D.L	B.D.L	B.D.L	B.D.L	B.D.L	B.D.L
0.23	Ga	B.D.L	B.D.L	B.D.L	B.D.L	B.D.L	B.D.L	B.D.L	B.D.L	B.D.L
0.10	Ge	B.D.L	B.D.L	B.D.L	B.D.L	B.D.L	B.D.L	B.D.L	B.D.L	B.D.L
0.07	Zn	65.68	65.40	66.49	66.10	64.68	61.72	62.90	64.99	64.51
0.06	Cu	B.D.L	B.D.L	B.D.L	B.D.L	B.D.L	B.D.L	B.D.L	B.D.L	B.D.L
0.05	Fe	1.87	2.01	1.10	1.36	1.53	4.26	3.13	1.37	1.96
0.06	Cd	B.D.L	B.D.L	B.D.L	B.D.L	B.D.L	B.D.L	B.D.L	B.D.L	B.D.L
0.05	Ag	B.D.L	B.D.L	B.D.L	B.D.L	B.D.L	B.D.L	B.D.L	B.D.L	B.D.L
0.05	Sn	B.D.L	B.D.L	B.D.L	B.D.L	B.D.L	B.D.L	B.D.L	B.D.L	B.D.L
	SUM	100.47	100.86	100.51	100.78	100.33	99.33	100.11	99.10	99.50
	apfu									
	Sb	-	-	-	-	-	-	-	-	-
	In	-	-	-	-	-	-	-	-	-
	S	1.00	1.00	1.00	1.00	1.00	1.00	1.00	1.00	1.00
	Pb	-	-	-	-	-	-	-	-	-
	As	-	-	-	-	-	-	-	-	-
	Ga	-	-	-	-	-	-	-	-	-
	Ge	-	-	-	-	-	-	-	-	-
	Zn	0.98	0.97	1.00	0.97	0.94	0.91	0.91	0.97	0.96
	Cu	-	-	-	-	-	-	-	-	-
	Fe	0.03	0.03	0.02	0.02	0.03	0.07	0.05	0.02	0.03
	Cd	-	-	-	-	-	-	-	-	-
	Ag	-	-	-	-	-	-	-	-	-
	Sn	-	-	-	-	-	-	-	-	-

B.D.L.: below detection limit. a.p.f.u.: atoms per formula unit.

	Sample	SV-08B	SV-09	SV-09	SV-11A	SV-11B	SV-11B	SV-11C	SV-12A	SV-12A
	Color	Black	Black	Black	Black	Black	Black	Black	Black	Black
Detection limit	wt.%	SV-08B-circulo D-ef-003	SV-09-circulo A-ef-003	SV-09-circulo C-ef-001	SV-11A-circulo B-ef-001	SV-11B-circulo D-ef-001	SV-11B-circulo D-ef-003	SV-11C-circulo C-ef-001	SV-12A-circulo A-ef-001	SV-12A-circulo B-ef-001
0.12	Sb	B.D.L	B.D.L	B.D.L	B.D.L	B.D.L	B.D.L	B.D.L	B.D.L	B.D.L
0.15	In	B.D.L	B.D.L	B.D.L	B.D.L	B.D.L	B.D.L	B.D.L	B.D.L	B.D.L
0.07	S	32.86	32.99	33.39	33.40	33.06	33.26	33.39	33.26	33.68
0.18	Pb	B.D.L	B.D.L	B.D.L	B.D.L	B.D.L	B.D.L	B.D.L	B.D.L	B.D.L
0.44	As	B.D.L	B.D.L	B.D.L	B.D.L	B.D.L	B.D.L	B.D.L	B.D.L	B.D.L
0.23	Ga	B.D.L	B.D.L	B.D.L	B.D.L	B.D.L	B.D.L	B.D.L	B.D.L	B.D.L
0.10	Ge	B.D.L	B.D.L	B.D.L	B.D.L	0.15	B.D.L	B.D.L	B.D.L	B.D.L
0.07	Zn	64.10	65.97	67.53	65.85	64.33	63.98	63.75	65.91	62.81
0.06	Cu	B.D.L	B.D.L	B.D.L	B.D.L	B.D.L	B.D.L	B.D.L	B.D.L	B.D.L
0.05	Fe	2.38	1.66	0.25	1.46	2.08	2.18	2.08	1.30	4.50
0.06	Cd	0.15	B.D.L	B.D.L	B.D.L	B.D.L	B.D.L	B.D.L	B.D.L	B.D.L
0.05	Ag	B.D.L	B.D.L	B.D.L	B.D.L	B.D.L	B.D.L	B.D.L	B.D.L	B.D.L
0.05	Sn	B.D.L	B.D.L	B.D.L	B.D.L	B.D.L	B.D.L	B.D.L	B.D.L	B.D.L
	SUM	99.49	100.62	100.17	100.71	99.62	99.42	99.22	100.47	100.99
	apfu									
	Sb	-	-	-	-	-	-	-	-	-
	In	-	-	-	-	-	-	-	-	-
	S	1.00	1.00	1.00	1.00	1.00	1.00	1.00	1.00	1.00
	Pb	-	-	-	-	-	-	-	-	-
	As	-	-	-	-	-	-	-	-	-
	Ga	-	-	-	-	-	-	-	-	-
	Ge	-	-	-	-	-	-	-	-	-
	Zn	0.96	0.98	0.99	0.97	0.95	0.94	0.94	0.97	0.91
	Cu	-	-	-	-	-	-	-	-	-
	Fe	0.04	0.03	-	0.03	0.04	0.04	0.04	0.02	0.08
	Cd	-	-	-	-	-	-	-	-	-
	Ag	-	-	-	-	-	-	-	-	-
	Sn	-	-	-	-	-	-	-	-	-

B.D.L.: below detection limit. a.p

	Sample	SV-16	SV-16	SV-16	SV-06A	SV-06B	SV-07	SV-08A	SV-08A	SV-08A
	Color	Black	Black	Black	R. Brown	R. Brown	R. Brown	R. Brown	R. Brown	R. Brown
Detection limit	wt.%	SV-16-circulo A-ef-001	SV-16-circulo A-ef-002	SV-16-circulo B-ef-001	SV-06A-circulo C-ef-001	SV-06B-circulo A-ef-002	SV-07-circulo B-ef-001	SV-08A-circulo A-ef-002	SV-08A-circulo A-ef-003	SV-08A-circulo C-ef-001
0.12	Sb	B.D.L	B.D.L	0.15	B.D.L	B.D.L	B.D.L	B.D.L	B.D.L	B.D.L
0.15	In	B.D.L	B.D.L	0.20	B.D.L	B.D.L	B.D.L	B.D.L	B.D.L	B.D.L
0.07	S	33.94	33.62	33.69	33.39	32.96	32.92	33.61	33.81	33.60
0.18	Pb	0.21	B.D.L	B.D.L	B.D.L	B.D.L	0.21	B.D.L	B.D.L	B.D.L
0.44	As	B.D.L	B.D.L	B.D.L	B.D.L	B.D.L	B.D.L	B.D.L	B.D.L	B.D.L
0.23	Ga	B.D.L	B.D.L	B.D.L	B.D.L	B.D.L	B.D.L	B.D.L	B.D.L	B.D.L
0.10	Ge	B.D.L	B.D.L	B.D.L	B.D.L	B.D.L	B.D.L	B.D.L	B.D.L	B.D.L
0.07	Zn	62.10	64.53	63.66	65.51	65.36	67.10	63.77	64.02	62.19
0.06	Cu	B.D.L	B.D.L	B.D.L	B.D.L	B.D.L	B.D.L	B.D.L	B.D.L	B.D.L
0.05	Fe	4.70	2.00	2.88	2.04	2.57	0.58	2.89	2.62	4.16
0.06	Cd	B.D.L	B.D.L	B.D.L	B.D.L	B.D.L	B.D.L	B.D.L	B.D.L	B.D.L
0.05	Ag	B.D.L	B.D.L	B.D.L	B.D.L	B.D.L	B.D.L	B.D.L	B.D.L	B.D.L
0.05	Sn	B.D.L	B.D.L	B.D.L	B.D.L	B.D.L	B.D.L	B.D.L	B.D.L	B.D.L
	SUM	100.95	100.15	100.58	100.94	100.89	100.81	100.27	100.45	99.95
	apfu									
	Sb	-	-	-	-	-	-	-	-	-
	In	-	-	-	-	-	-	-	-	-
	S	1.00	1.00	1.00	1.00	1.00	1.00	1.00	1.00	1.00
	Pb	-	-	-	-	-	-	-	-	-
	As	-	-	-	-	-	-	-	-	-
	Ga	-	-	-	-	-	-	-	-	-
	Ge	-	-	-	-	-	-	-	-	-
	Zn	0.90	0.94	0.93	0.96	0.97	1.00	0.93	0.93	0.91
	Cu	-	-	-	-	-	-	-	-	-
	Fe	0.08	0.03	0.05	0.04	0.04	0.01	0.05	0.04	0.07
	Cd	-	-	-	-	-	-	-	-	-
	Ag	-	-	-	-	-	-	-	-	-
	Sn	-	-	-	-	-	-	-	-	-

B.D.L.: below detection limit. a.p

	Sample	SV-11A	SV-11A	SV-11A	SV-11A	SV-11B	SV-11B	SV-11B	SV-11B	SV-11B
	Color	R. Brown	R. Brown	R. Brown	R. Brown	R. Brown	R. Brown	R. Brown	R. Brown	R. Brown
Detection limit	wt.%	SV-11A-circulo B-ef-002	SV-11A-circulo B-ef-004	SV-11A-circulo C-ef-001	SV-11A-circulo C-ef-002	SV-11B-circulo A-ef-001	SV-11B-circulo A-ef-002	SV-11B-circulo A-ef-003	SV-11B-circulo A-ef-004	SV-11B-circulo C-ef-001
0.12	Sb	B.D.L	B.D.L	B.D.L	B.D.L	B.D.L	B.D.L	B.D.L	B.D.L	0.14
0.15	In	B.D.L	B.D.L	B.D.L	B.D.L	B.D.L	B.D.L	B.D.L	B.D.L	B.D.L
0.07	S	33.02	32.83	33.31	33.39	33.02	33.44	33.10	33.05	32.82
0.18	Pb	B.D.L	B.D.L	B.D.L	B.D.L	B.D.L	0.22	B.D.L	B.D.L	B.D.L
0.44	As	B.D.L	B.D.L	B.D.L	B.D.L	B.D.L	B.D.L	B.D.L	B.D.L	B.D.L
0.23	Ga	B.D.L	B.D.L	B.D.L	B.D.L	B.D.L	B.D.L	B.D.L	B.D.L	B.D.L
0.10	Ge	B.D.L	B.D.L	B.D.L	B.D.L	0.13	B.D.L	B.D.L	B.D.L	B.D.L
0.07	Zn	64.68	66.00	66.42	65.05	64.86	64.21	63.74	63.24	63.98
0.06	Cu	B.D.L	B.D.L	B.D.L	B.D.L	B.D.L	B.D.L	B.D.L	B.D.L	B.D.L
0.05	Fe	2.58	1.39	1.09	2.56	1.35	2.25	2.67	3.09	2.12
0.06	Cd	B.D.L	B.D.L	B.D.L	B.D.L	B.D.L	B.D.L	B.D.L	B.D.L	B.D.L
0.05	Ag	B.D.L	B.D.L	B.D.L	B.D.L	B.D.L	B.D.L	B.D.L	B.D.L	B.D.L
0.05	Sn	B.D.L	B.D.L	B.D.L	B.D.L	B.D.L	B.D.L	B.D.L	B.D.L	B.D.L
	SUM	100.28	100.22	100.82	101.00	99.36	100.12	99.51	99.38	99.06
	apfu									
	Sb	-	-	-	-	-	-	-	-	-
	In	-	-	-	-	-	-	-	-	-
	S	1.00	1.00	1.00	1.00	1.00	1.00	1.00	1.00	1.00
	Pb	-	-	-	-	-	-	-	-	-
	As	-	-	-	-	-	-	-	-	-
	Ga	-	-	-	-	-	-	-	-	-
	Ge	-	-	-	-	-	-	-	-	-
	Zn	0.96	0.99	0.98	0.96	0.96	0.94	0.94	0.94	0.96
	Cu	-	-	-	-	-	-	-	-	-
	Fe	0.04	0.02	0.02	0.04	0.02	0.04	0.05	0.05	0.04
	Cd	-	-	-	-	-	-	-	-	-
	Ag	-	-	-	-	-	-	-	-	-
	Sn	-	-	-	-	-	-	-	-	-

B.D.L.: below detection limit. a.p

	Sample	SV-11B	SV-11C	SV-12A	SV-16	SV-16	SV-02	SV-04	SV-04	SV-04
	Color	R. Brown	R. Brown	R. Brown	R. Brown	R. Brown	Y. Brown	Y. Brown	Y. Brown	Y. Brown
Detection limit	wt.%	SV-11B-circulo D-ef-002	SV-11C-circulo B-ef-002	SV-12A-circulo D-ef-002	SV-16-circulo D-ef-001	SV-16-circulo D-ef-002	SV-02-circulo C-ef-001	SV-04-circulo B-ef-001	SV-04-circulo B-ef-002	SV-04-circulo B-ef-003
0.12	Sb	B.D.L	B.D.L	B.D.L	B.D.L	B.D.L	B.D.L	B.D.L	B.D.L	B.D.L
0.15	In	B.D.L	B.D.L	B.D.L	B.D.L	B.D.L	B.D.L	B.D.L	B.D.L	B.D.L
0.07	S	33.12	32.97	33.39	33.55	33.60	33.16	32.93	32.64	33.05
0.18	Pb	0.21	0.35	B.D.L	B.D.L	B.D.L	B.D.L	B.D.L	0.30	B.D.L
0.44	As	B.D.L	B.D.L	B.D.L	B.D.L	B.D.L	B.D.L	B.D.L	B.D.L	B.D.L
0.23	Ga	B.D.L	B.D.L	B.D.L	B.D.L	B.D.L	B.D.L	B.D.L	B.D.L	B.D.L
0.10	Ge	B.D.L	B.D.L	B.D.L	B.D.L	B.D.L	B.D.L	B.D.L	B.D.L	B.D.L
0.07	Zn	63.79	64.58	63.99	63.99	65.68	64.43	66.09	65.67	63.08
0.06	Cu	B.D.L	B.D.L	B.D.L	B.D.L	B.D.L	B.D.L	B.D.L	B.D.L	B.D.L
0.05	Fe	2.32	1.54	3.26	2.99	1.50	2.42	0.64	0.99	3.18
0.06	Cd	B.D.L	B.D.L	B.D.L	B.D.L	B.D.L	B.D.L	0.09	0.12	0.11
0.05	Ag	B.D.L	B.D.L	B.D.L	B.D.L	B.D.L	B.D.L	0.05	B.D.L	B.D.L
0.05	Sn	B.D.L	B.D.L	B.D.L	B.D.L	B.D.L	B.D.L	B.D.L	B.D.L	B.D.L
	SUM	99.44	99.44	100.64	100.53	100.78	100.01	99.80	99.72	99.42
	apfu									
	Sb	-	-	-	-	-	-	-	-	-
	In	-	-	-	-	-	-	-	-	-
	S	1.00	1.00	1.00	1.00	1.00	1.00	1.00	1.00	1.00
	Pb	-	-	-	-	-	-	-	-	-
	As	-	-	-	-	-	-	-	-	-
	Ga	-	-	-	-	-	-	-	-	-
	Ge	-	-	-	-	-	-	-	-	-
	Zn	0.94	0.96	0.94	0.94	0.96	0.95	0.98	0.99	0.94
	Cu	-	-	-	-	-	-	-	-	-
	Fe	0.04	0.03	0.06	0.05	0.03	0.04	0.01	0.02	0.06
	Cd	-	-	-	-	-	-	-	-	-
	Ag	-	-	-	-	-	-	-	-	-
	Sn	-	-	-	-	-	-	-	-	-

B.D.L.: below detection limit. a.p

	Sample	SV-04	SV-04	SV-07	SV-07	SV-07	SV-08A	SV-08A	SV-08A	SV-08B
	Color	Y. Brown	Y. Brown	Y. Brown	Y. Brown	Y. Brown	Y. Brown	Y. Brown	Y. Brown	Y. Brown
Detection limit	wt.%	SV-04-circulo C-ef-002	SV-04-circulo C-ef-003	SV-07-circulo A-ef-002	SV-07-circulo A-ef-003	SV-07-circulo C-ef-001	SV-08A-circulo D-ef-001	SV-08A-circulo D-ef-002	SV-08A-circulo D-ef-003	SV-08B-circulo A-ef-001
0.12	Sb	B.D.L	B.D.L	B.D.L	B.D.L	B.D.L	B.D.L	B.D.L	B.D.L	B.D.L
0.15	In	B.D.L	B.D.L	B.D.L	B.D.L	B.D.L	B.D.L	B.D.L	B.D.L	B.D.L
0.07	S	32.67	32.44	32.90	33.24	33.03	33.47	33.58	33.92	33.15
0.18	Pb	0.19	B.D.L	0.19	B.D.L	B.D.L	B.D.L	0.38	B.D.L	B.D.L
0.44	As	B.D.L	B.D.L	B.D.L	B.D.L	B.D.L	B.D.L	B.D.L	B.D.L	B.D.L
0.23	Ga	B.D.L	B.D.L	B.D.L	B.D.L	B.D.L	B.D.L	B.D.L	B.D.L	B.D.L
0.10	Ge	B.D.L	B.D.L	B.D.L	B.D.L	B.D.L	B.D.L	B.D.L	B.D.L	B.D.L
0.07	Zn	64.31	65.40	65.68	66.77	67.30	64.69	65.11	64.01	65.23
0.06	Cu	B.D.L	B.D.L	B.D.L	B.D.L	B.D.L	B.D.L	B.D.L	B.D.L	B.D.L
0.05	Fe	2.44	1.28	1.87	0.91	0.37	1.55	1.30	2.61	1.13
0.06	Cd	0.10	0.07	B.D.L	0.08	0.09	B.D.L	B.D.L	B.D.L	B.D.L
0.05	Ag	0.05	B.D.L	B.D.L	B.D.L	B.D.L	B.D.L	B.D.L	B.D.L	B.D.L
0.05	Sn	B.D.L	B.D.L	B.D.L	B.D.L	B.D.L	B.D.L	B.D.L	B.D.L	B.D.L
	SUM	99.76	99.19	100.64	101.00	100.79	99.71	100.37	100.54	99.51
	apfu									
	Sb	-	-	-	-	-	-	-	-	-
	In	-	-	-	-	-	-	-	-	-
	S	1.00	1.00	1.00	1.00	1.00	1.00	1.00	1.00	1.00
	Pb	-	-	-	-	-	-	-	-	-
	As	-	-	-	-	-	-	-	-	-
	Ga	-	-	-	-	-	-	-	-	-
	Ge	-	-	-	-	-	-	-	-	-
	Zn	0.97	0.99	0.98	0.99	1.00	0.95	0.95	0.93	0.96
	Cu	-	-	-	-	-	-	-	-	-
	Fe	0.04	0.02	0.03	0.02	0.01	0.03	0.02	0.04	0.02
	Cd	-	-	-	-	-	-	-	-	-
	Ag	-	-	-	-	-	-	-	-	-
	Sn	-	-	-	-	-	-	-	-	-

B.D.L.: below detection limit. a.p

	Sample	SV-08B	SV-08B	SV-08B	SV-08B	SV-08B	SV-08B	SV-08B	SV-09	SV-11A
	Color	Y. Brown	Y. Brown	Y. Brown	Y. Brown	Y. Brown	Y. Brown	Y. Brown	Y. Brown	Y. Brown
Detection limit	wt.%	SV-08B-circulo C-ef-002	SV-08B-circulo C-ef-003	SV-08B-circulo D-ef-002	SV-08B-circulo D-ef-004	SV-08B-circulo E-ef-001	SV-08B-circulo E-ef-003	SV-08B-circulo E-ef-004	SV-09-circulo A-ef-001	SV-11A-circulo C-ef-003
0.12	Sb	B.D.L	B.D.L	B.D.L	B.D.L	B.D.L	B.D.L	B.D.L	B.D.L	B.D.L
0.15	In	B.D.L	B.D.L	B.D.L	B.D.L	B.D.L	B.D.L	B.D.L	B.D.L	B.D.L
0.07	S	32.94	32.99	32.88	32.70	33.19	32.85	32.97	32.98	33.40
0.18	Pb	0.43	B.D.L	0.24	B.D.L	0.24	B.D.L	B.D.L	0.28	B.D.L
0.44	As	B.D.L	B.D.L	B.D.L	B.D.L	B.D.L	B.D.L	B.D.L	B.D.L	B.D.L
0.23	Ga	B.D.L	B.D.L	B.D.L	B.D.L	B.D.L	B.D.L	B.D.L	B.D.L	B.D.L
0.10	Ge	B.D.L	B.D.L	B.D.L	B.D.L	B.D.L	B.D.L	B.D.L	B.D.L	B.D.L
0.07	Zn	65.28	64.36	64.29	63.96	64.75	65.30	65.71	65.11	65.14
0.06	Cu	B.D.L	B.D.L	B.D.L	B.D.L	B.D.L	B.D.L	B.D.L	B.D.L	B.D.L
0.05	Fe	1.35	2.08	1.86	2.55	1.45	1.05	0.56	2.13	2.44
0.06	Cd	B.D.L	B.D.L	B.D.L	B.D.L	0.08	B.D.L	0.06	B.D.L	B.D.L
0.05	Ag	B.D.L	B.D.L	B.D.L	B.D.L	B.D.L	B.D.L	B.D.L	B.D.L	B.D.L
0.05	Sn	B.D.L	B.D.L	B.D.L	B.D.L	B.D.L	B.D.L	B.D.L	B.D.L	B.D.L
	SUM	100.00	99.43	99.27	99.21	99.72	99.20	99.31	100.50	100.98
	apfu									
	Sb	-	-	-	-	-	-	-	-	-
	In	-	-	-	-	-	-	-	-	-
	S	1.00	1.00	1.00	1.00	1.00	1.00	1.00	1.00	1.00
	Pb	-	-	-	-	-	-	-	-	-
	As	-	-	-	-	-	-	-	-	-
	Ga	-	-	-	-	-	-	-	-	-
	Ge	-	-	-	-	-	-	-	-	-
	Zn	0.97	0.96	0.96	0.96	0.96	0.97	0.98	0.97	0.96
	Cu	-	-	-	-	-	-	-	-	-
	Fe	0.02	0.04	0.03	0.04	0.03	0.02	0.01	0.04	0.04
	Cd	-	-	-	-	-	-	-	-	-
	Ag	-	-	-	-	-	-	-	-	-
	Sn	-	-	-	-	-	-	-	-	-

B.D.L.: below detection limit. a.p

	Sample	SV-11B	SV-12B	SV-12B	SV-16	SV-16	SV-04	SV-04	SV-04	SV-08B
	Color	Y. Brown	Y. Brown	Y. Brown	Y. Brown	Y. Brown	Yellow (sl_1)	Yellow (sl_1)	Yellow (sl_1)	Yellow (sl_1)
Detection limit	wt.%	SV-11B-circulo B-ef-002	SV-12B-circulo A-ef-001	SV-12B-circulo A-ef-002	SV-16-circulo E-ef-002	SV-16-circulo E-ef-003	SV-04-circulo A-ef-001	SV-04-circulo D-ef-001	SV-04-circulo D-ef-003	SV-08B-circulo E-ef-002
0.12	Sb	B.D.L	B.D.L	B.D.L	B.D.L	0.22	B.D.L	B.D.L	B.D.L	B.D.L
0.15	In	B.D.L	B.D.L	B.D.L	B.D.L	B.D.L	B.D.L	B.D.L	B.D.L	B.D.L
0.07	S	32.98	32.82	32.87	33.34	33.46	32.58	32.74	32.69	32.80
0.18	Pb	B.D.L	0.22	0.43	0.50	B.D.L	0.25	0.24	0.22	B.D.L
0.44	As	B.D.L	B.D.L	B.D.L	B.D.L	B.D.L	B.D.L	B.D.L	B.D.L	B.D.L
0.23	Ga	B.D.L	B.D.L	B.D.L	B.D.L	B.D.L	B.D.L	B.D.L	B.D.L	B.D.L
0.10	Ge	B.D.L	B.D.L	B.D.L	B.D.L	B.D.L	B.D.L	B.D.L	B.D.L	B.D.L
0.07	Zn	64.27	65.22	65.69	63.54	63.89	63.84	64.89	65.37	65.06
0.06	Cu	B.D.L	B.D.L	B.D.L	B.D.L	B.D.L	B.D.L	B.D.L	B.D.L	B.D.L
0.05	Fe	2.07	2.10	1.39	3.56	2.88	2.44	1.95	1.63	1.17
0.06	Cd	B.D.L	B.D.L	B.D.L	B.D.L	B.D.L	B.D.L	0.07	0.07	B.D.L
0.05	Ag	B.D.L	B.D.L	B.D.L	B.D.L	B.D.L	B.D.L	B.D.L	B.D.L	B.D.L
0.05	Sn	B.D.L	B.D.L	B.D.L	B.D.L	B.D.L	B.D.L	B.D.L	B.D.L	B.D.L
	SUM	99.32	100.36	100.38	100.94	100.45	99.11	99.89	99.98	99.03
	apfu									
	Sb	-	-	-	-	-	-	-	-	-
	In	-	-	-	-	-	-	-	-	-
	S	1.00	1.00	1.00	1.00	1.00	1.00	1.00	1.00	1.00
	Pb	-	-	-	-	-	-	-	-	-
	As	-	-	-	-	-	-	-	-	-
	Ga	-	-	-	-	-	-	-	-	-
	Ge	-	-	-	-	-	-	-	-	-
	Zn	0.96	0.97	0.98	0.93	0.94	0.96	0.97	0.98	0.97
	Cu	-	-	-	-	-	-	-	-	-
	Fe	0.04	0.04	0.02	0.06	0.05	0.04	0.03	0.03	0.02
	Cd	-	-	-	-	-	-	-	-	-
	Ag	-	-	-	-	-	-	-	-	-
	Sn	-	-	-	-	-	-	-	-	-

B.D.L.: below detection limit. a.p

	Sample	SV-11A	SV-11A	SV-15B	SV-15B	SV-15B	SV-15B	SV-15A	SV-15A	SV-15A
	Color	Yellow (sl_1)	Yellow (sl_1)	Orange	Orange	Orange	Orange	Orange	Orange	Orange
Detection limit	wt.%	SV-11A-circulo B-ef-003	SV-11A-circulo C-ef-004	SV-15B-circulo A-ef-001	SV-15B-circulo A-ef-002	SV-15B-circulo B-ef-002	SV-15B-circulo C-ef-002	SV-15A-circulo B-ef-002	SV-15A-circulo B-ef-003	SV-15A-circulo D-ef-001
0.12	Sb	B.D.L	B.D.L	B.D.L	0.17	B.D.L	B.D.L	B.D.L	B.D.L	B.D.L
0.15	In	B.D.L	B.D.L	B.D.L	B.D.L	B.D.L	0.16	B.D.L	B.D.L	B.D.L
0.07	S	33.38	33.08	32.83	32.73	33.06	33.00	32.97	32.94	32.81
0.18	Pb	B.D.L	B.D.L	B.D.L	B.D.L	B.D.L	0.19	B.D.L	B.D.L	B.D.L
0.44	As	B.D.L	B.D.L	B.D.L	B.D.L	B.D.L	B.D.L	0.52	B.D.L	B.D.L
0.23	Ga	B.D.L	B.D.L	B.D.L	B.D.L	B.D.L	B.D.L	B.D.L	B.D.L	B.D.L
0.10	Ge	B.D.L	B.D.L	B.D.L	B.D.L	B.D.L	B.D.L	0.19	B.D.L	B.D.L
0.07	Zn	65.93	65.46	67.06	67.05	67.62	66.29	66.24	66.57	66.67
0.06	Cu	B.D.L	B.D.L	B.D.L	B.D.L	B.D.L	0.25	B.D.L	0.27	B.D.L
0.05	Fe	1.43	1.97	B.D.L	B.D.L	B.D.L	B.D.L	B.D.L	B.D.L	B.D.L
0.06	Cd	B.D.L	B.D.L	0.32	0.32	0.20	0.40	0.48	0.32	0.69
0.05	Ag	B.D.L	B.D.L	B.D.L	B.D.L	B.D.L	0.09	0.42	0.16	B.D.L
0.05	Sn	B.D.L	B.D.L	B.D.L	B.D.L	B.D.L	B.D.L	B.D.L	B.D.L	B.D.L
	SUM	100.74	100.51	100.21	100.27	100.88	100.37	100.81	100.26	100.17
	apfu									
	Sb	-	-	-	-	-	-	-	-	-
	In	-	-	-	-	-	-	-	-	-
	S	1.00	1.00	1.00	1.00	1.00	1.00	1.00	1.00	1.00
	Pb	-	-	-	-	-	-	-	-	-
	As	-	-	-	-	-	-	0.01	-	-
	Ga	-	-	-	-	-	-	-	-	-
	Ge	-	-	-	-	-	-	-	-	-
	Zn	0.97	0.97	1.00	1.00	1.00	0.99	0.99	0.99	1.00
	Cu	-	-	-	-	-	-	-	-	-
	Fe	0.02	0.03	-	-	-	-	-	-	-
	Cd	-	-	-	-	-	-	-	-	0.01
	Ag	-	-	-	-	-	-	-	-	-
	Sn	-	-	-	-	-	-	-	-	-

B.D.L.: below detection limit. a.p

	Sample	SV-15A	SV-15A	SV-15A	SV-15A	SV-07	SV-13	SV-13	SV-13	SV-13
	Color	Orange	Orange	Orange	Orange	Yellow-sl$_2$	Yellow-sl$_2$	Yellow-sl$_2$	Yellow-sl$_2$	Yellow-sl$_2$
Detection limit	wt.%	SV-15A-circulo D-ef-002	SV-15A-circulo D-ef-003	SV-15A-circulo E-ef-001	SV-15A-circulo E-ef-003	SV-07-circulo A-ef-001	SV-13-circulo A-ef-001	SV-13-circulo A-ef-002	SV-13-circulo B-ef-001	SV-13-circulo B-ef-002
0.12	Sb	B.D.L	B.D.L	B.D.L	B.D.L	B.D.L	B.D.L	B.D.L	B.D.L	B.D.L
0.15	In	B.D.L	B.D.L	B.D.L	B.D.L	B.D.L	B.D.L	B.D.L	B.D.L	B.D.L
0.07	S	32.73	33.35	32.96	33.28	32.95	32.70	33.39	32.97	32.88
0.18	Pb	0.54	B.D.L	0.21	B.D.L	B.D.L	0.22	B.D.L	B.D.L	B.D.L
0.44	As	B.D.L	B.D.L	B.D.L	B.D.L	B.D.L	B.D.L	B.D.L	B.D.L	B.D.L
0.23	Ga	B.D.L	B.D.L	B.D.L	B.D.L	B.D.L	B.D.L	B.D.L	B.D.L	B.D.L
0.10	Ge	B.D.L	B.D.L	B.D.L	0.15	B.D.L	B.D.L	B.D.L	B.D.L	B.D.L
0.07	Zn	66.69	66.85	66.65	66.82	67.92	66.08	65.81	65.84	66.09
0.06	Cu	B.D.L	0.18	0.11	0.20	B.D.L	B.D.L	B.D.L	B.D.L	B.D.L
0.05	Fe	B.D.L	B.D.L	B.D.L	B.D.L	B.D.L	B.D.L	B.D.L	B.D.L	B.D.L
0.06	Cd	0.56	0.20	0.20	0.26	B.D.L	0.26	0.18	0.22	0.28
0.05	Ag	B.D.L	0.06	0.05	0.15	B.D.L	B.D.L	B.D.L	B.D.L	B.D.L
0.05	Sn	B.D.L	B.D.L	B.D.L	B.D.L	B.D.L	B.D.L	B.D.L	B.D.L	B.D.L
	SUM	100.52	100.65	100.18	100.86	100.87	99.26	99.38	99.03	99.25
	apfu									
	Sb	-	-	-	-	-	-	-	-	-
	In	-	-	-	-	-	-	-	-	-
	S	1.00	1.00	1.00	1.00	1.00	1.00	1.00	1.00	1.00
	Pb	-	-	-	-	-	-	-	-	-
	As	-	-	-	-	-	-	-	-	-
	Ga	-	-	-	-	-	-	-	-	-
	Ge	-	-	-	-	-	-	-	-	-
	Zn	1.00	0.98	0.99	0.98	1.01	0.99	0.97	0.98	0.99
	Cu	-	-	-	-	-	-	-	-	-
	Fe	-	-	-	-	-	-	-	-	-
	Cd	-	-	-	-	-	-	-	-	-
	Ag	-	-	-	-	-	-	-	-	-
	Sn	-	-	-	-	-	-	-	-	-

B.D.L.: below detection limit. a.p

	Sample	SV-13	SV-13	SV-14	SV-14	SV-14	SV-14	SV-15B	SV-15A	SV-15A
	Color	Yellow-sl_2	Yellow-sl_2	Yellow-sl_2	Yellow-sl_2	Yellow-sl_2	Yellow-sl_2	Yellow-sl_2	Yellow-sl_2	Yellow-sl_2
Detection limit	wt.%	SV-13-circulo C-ef-001	SV-13-circulo C-ef-002	SV-14-circulo A-ef-002	SV-14-circulo B-ef-001	SV-14-circulo C-ef-001	SV-14-circulo C-ef-002	SV-15B-circulo C-ef-001	SV-15A-circulo A-ef-001	SV-15A-circulo B-ef-001
0.12	Sb	B.D.L	B.D.L	B.D.L	B.D.L	B.D.L	B.D.L	B.D.L	B.D.L	B.D.L
0.15	In	B.D.L	B.D.L	B.D.L	B.D.L	B.D.L	B.D.L	B.D.L	B.D.L	B.D.L
0.07	S	33.07	33.40	33.12	33.27	33.49	33.04	33.25	32.78	33.30
0.18	Pb	0.22	B.D.L	B.D.L	B.D.L	0.24	0.36	B.D.L	0.50	0.29
0.44	As	B.D.L	B.D.L	B.D.L	B.D.L	B.D.L	B.D.L	B.D.L	B.D.L	B.D.L
0.23	Ga	B.D.L	B.D.L	B.D.L	B.D.L	B.D.L	B.D.L	B.D.L	B.D.L	B.D.L
0.10	Ge	B.D.L	B.D.L	B.D.L	B.D.L	B.D.L	B.D.L	B.D.L	B.D.L	B.D.L
0.07	Zn	66.06	67.04	66.05	65.80	65.81	65.75	67.40	66.70	66.37
0.06	Cu	B.D.L	B.D.L	B.D.L	B.D.L	B.D.L	B.D.L	B.D.L	B.D.L	B.D.L
0.05	Fe	B.D.L	B.D.L	B.D.L	B.D.L	B.D.L	B.D.L	B.D.L	B.D.L	B.D.L
0.06	Cd	0.20	0.18	0.17	0.22	0.22	0.23	0.27	0.49	0.37
0.05	Ag	B.D.L	B.D.L	B.D.L	B.D.L	B.D.L	B.D.L	B.D.L	B.D.L	0.29
0.05	Sn	B.D.L	B.D.L	B.D.L	B.D.L	B.D.L	B.D.L	B.D.L	B.D.L	B.D.L
	SUM	99.56	100.62	99.34	99.29	99.76	99.39	100.92	100.47	100.63
	apfu									
	Sb	-	-	-	-	-	-	-	-	-
	In	-	-	-	-	-	-	-	-	-
	S	1.00	1.00	1.00	1.00	1.00	1.00	1.00	1.00	1.00
	Pb	-	-	-	-	-	-	-	-	-
	As	-	-	-	-	-	-	-	-	-
	Ga	-	-	-	-	-	-	-	-	-
	Ge	-	-	-	-	-	-	-	-	-
	Zn	0.98	0.98	0.98	0.97	0.96	0.98	0.99	1.00	0.98
	Cu	-	-	-	-	-	-	-	-	-
	Fe	-	-	-	-	-	-	-	-	-
	Cd	-	-	-	-	-	-	-	-	-
	Ag	-	-	-	-	-	-	-	-	-
	Sn	-	-	-	-	-	-	-	-	-

B.D.L.: below detection limit. a.p

	Sample	SV-15A	SV-15A	SV-15B
	Color	Yellow-sl$_2$	Yellow-sl$_2$	White
Detection limit	wt.%	SV-15A-circulo C-ef	SV-15A-circulo E-ef-002	SV-15B-circulo B-ef-001
0.12	Sb	B.D.L	B.D.L	B.D.L
0.15	In	0.26	B.D.L	B.D.L
0.07	S	32.95	33.20	33.04
0.18	Pb	B.D.L	B.D.L	B.D.L
0.44	As	B.D.L	B.D.L	B.D.L
0.23	Ga	B.D.L	B.D.L	B.D.L
0.10	Ge	B.D.L	B.D.L	B.D.L
0.07	Zn	66.86	66.45	67.35
0.06	Cu	B.D.L	0.29	B.D.L
0.05	Fe	B.D.L	B.D.L	B.D.L
0.06	Cd	0.70	0.25	0.19
0.05	Ag	B.D.L	0.12	B.D.L
0.05	Sn	B.D.L	B.D.L	B.D.L
	SUM	100.76	100.31	100.58
	apfu			
	Sb	-	-	-
	In	-	-	-
	S	1.00	1.00	1.00
	Pb	-	-	-
	As	-	-	-
	Ga	-	-	-
	Ge	-	-	-
	Zn	1.00	0.98	1.00
	Cu	-	-	-
	Fe	-	-	-
	Cd	0.01	-	-
	Ag	-	-	-
	Sn	-	-	-

B.D.L.: below detection limit. a.p

TABLE S3: LA-ICP-MS TRACE ELEMENT ANALYSES ON SPHALERITE-METADATA.

LA-ICP-MS trace element analyses on sphalerite - Metadata

Laboratory and Sample Preparation	
Laboratory name	Dept. of Earth Science, Institute for Geochemistry and Petrology - ETH Zurich
Sample type/mineral	Natural sulfide
Sample preparation	Sample fragments in 1-inch epoxy mounts
Imaging	Conventional optical microscopy + SEM-EDS
Laser ablation system	
Make, Model and type	ASI (Resonetics) RESOolution S-155
Ablation cell and volume	Laurin Technic, dual-volume S-155 ablation cell, effective volume *ca*. 1 cm^3
Laser wavelength (nm)	193 nm
Pulse width (ns)	25 ns
Fluence (J cm^{-2})	ca. 2.5 J cm^{-2}
Repetition rate (Hz)	3 Hz
Ablation duration	25 s
Spot diameter (μm)	19 μm
Sampling mode / pattern	Static spot ablation
Carrier gas	100% He in the cell, Ar make-up gas combined in ablation funnel
Cell carrier gas flow (l min^{-1})	0.5 l min^{-1}
ICP-MS Instrument	
Make, Model and type	Thermo Element XR, Sector-field single collector ICP-MS
Sample introduction	Direct
RF power (W)	1275 to 1455 W (tuned daily)
Make-up gas flow (l min^{-1})	ca. 0.89 to 0.92 l min^{-1} Ar (tuned daily) + 0.002 l min^{-1} N_2
Detection system	Triple (pulse counting, analog, Faraday), cross calibrated daily
Masses measured (amu)	33, 34, 53, 55, 57, 59, 62, 65, 66, 71, 74, 75, 77, 95, 107, 111, 115, 118, 121, 125, 182, 197, 202, 205, 208, 209
Integration time per peak/dwell times (ms)	25 ms except at amu 33, 34, 53, 55, 59, 62, 65 and 66 (11 ms)
Total integration time per output data point (s)	0.719 s
Dead time (ns)	22

Typical oxide rate ($^{248}ThO^{+}/^{232}Th^{+}$)	0.15%
Typical doubly charged rate (Ba^{++}/Ba^{+})	3.50%
Data Processing	
Gas blank	25 s
Calibration strategy	Mass-1 used as primary reference material for trace element quantification; sulfide pressed power UQAC-FeS-1 and silicate glasses GSD-1G and NIST SRM610 as secondaries/validation.
Reference Material info	Mass-1 (Wilson et al., 2002) UQAC-FeS-1 (unpublished data from D. Savard, UQAC, 2018; see also Baumgartner et al., 2020) GSD-1G (Guillong et al., 2005) NIST SRM610 (Jochum et al., 2011)
Data processing package used / Correction for LIEF	SILLS standalone v. 1.3.2 (Guillong et al., 2008)
Internal standard for trace element quantification	Measured Zn concentrations with EPMA

Baumgartner, R.J., et al. (2020). Accumulation of transition metals and metalloids in sulfidized stromatolites of the 3.48 billion–year–old Dresser Formation, Pilbara Craton. Precambrian Research 337, 105534.

Guillong, M., et al. (2005). Preliminary Characterisation of New Glass Reference Materials (GSA-1G, GSC-1G, GSD-1G and GSE-1G) by Laser Ablation-Inductively Coupled Plasma-Mass Spectrometry Using 193 nm, 213 nm and 266 nm Wavelengths. Geostandards and Geoanalytical Research 29(3), 315-331

Guillong, M., et al. (2008). SILLS: A Matlab-based program for the reduction of laser ablation ICP-MS data of homogeneous materials and inclusions. In: Laser Ablation ICP-MS in the Earth Sciences: Current Practices and Outstanding Issues (ed. Sylvester, P.) 328–333 (Mineralogical Association of Canada, 2008).

Jochum, K.P., et al. (2011). Determination of reference values for NIST SRM 610-617 glasses following ISO guidelines. Geostandards and Geoanalytical Research 35, 397–429.

Université du Québec à Chicoutimi (2018): FeS-1 data. Available from: https://sulfideslasericpms.wordpress.com/rm-available/

Wilson, S.A., Ridley, W.I., Koenig, A.E. (2002). Development of sulfide calibration standards for the laser ablation inductively coupled plasma mass spectrometry technique. Journal of Analytical Atomic Spectrometry 17, 406-409.

TABLE S4: LA-ICP-MS TRACE ELEMENT ANALYSES ON SPHALERITE AND REFERENCE MATERIALS

Label	Mineral	Color	Deposit	Sample
UQAC-FeS-1 - 1				
GSD-1G - 1				
NIST610 - 1				
2019-SV-02-Circulo A-ef - 1	sl	Yellow (sl_{1y})	San Vicente	2019-SV-02
2019-SV-02-Circulo A-ef - 2	sl	Yellowish brown (sl_{1yb})	San Vicente	2019-SV-02
2019-SV-02-Circulo A-ef - 3	sl	Yellowish brown (sl_{1yb})	San Vicente	2019-SV-02
2019-SV-02-Circulo B-ef - 1	sl	Yellow (sl_{1y})	San Vicente	2019-SV-02
2019-SV-02-Circulo B-ef - 2	sl	Yellow (sl_{1y})	San Vicente	2019-SV-02
2019-SV-02-Circulo B-ef - 3	sl	Yellow (sl_{1y})	San Vicente	2019-SV-02
2019-SV-02-Circulo C-ef - 1	sl	Yellowish brown (sl_{1yb})	San Vicente	2019-SV-02
2019-SV-04-Circulo A-ef - 1	sl	Yellow (sl_{1y})	San Vicente	2019-SV-04
2019-SV-04-Circulo A-ef - 2	sl	Yellowish brown (sl_{1yb})	San Vicente	2019-SV-04
2019-SV-04-Circulo B-ef - 1	sl	Yellowish brown (sl_{1yb})	San Vicente	2019-SV-04
2019-SV-04-Circulo B-ef - 2	sl	Yellowish brown (sl_{1yb})	San Vicente	2019-SV-04
2019-SV-04-Circulo B-ef - 3	sl	Yellowish brown (sl_{1yb})	San Vicente	2019-SV-04
2019-SV-04-Circulo C-ef - 2	sl	Yellowish brown (sl_{1yb})	San Vicente	2019-SV-04
2019-SV-04-Circulo C-ef - 3	sl	Yellowish brown (sl_{1yb})	San Vicente	2019-SV-04
2019-SV-04-Circulo D-ef - 1	sl	Yellowish brown (sl_{1yb})	San Vicente	2019-SV-04
2019-SV-04-Circulo D-ef - 3	sl	Yellow (sl_{1y})	San Vicente	2019-SV-04
2019-SV-06A-Circulo A-ef - 1	sl	Yellowish brown (sl_{1yb})	San Vicente	2019-SV-06A
2019-SV-06A-Circulo A-ef - 2	sl	Yellowish brown (sl_{1yb})	San Vicente	2019-SV-06A
2019-SV-06A-Circulo A-ef - 3	sl	Yellowish brown (sl_{1yb})	San Vicente	2019-SV-06A
UQAC-FeS-1 - 2				
GSD-1G - 2				
NIST610 - 2				
2019-SV-06A-Circulo B-ef - 3	sl	Black (sl_{1bl})	San Vicente	2019-SV-06A
2019-SV-06A-Circulo B-ef - 4	sl	Black (sl_{1bl})	San Vicente	2019-SV-06A
2019-SV-06A-Circulo C-ef - 1	sl	Reddish Brown ($sl1_{rb}$)	San Vicente	2019-SV-06A
2019-SV-06A-Circulo C-ef - 2	sl	Reddish Brown ($sl1_{rb}$)	San Vicente	2019-SV-06A
2019-SV-06A-Circulo C-ef - 3	sl	Black (sl_{1bl})	San Vicente	2019-SV-06A
2019-SV-06B-Circulo A-ef - 1	sl	Yellow (sl_{1y})	San Vicente	2019-SV-06B
2019-SV-06B-Circulo A-ef - 2	sl	Reddish Brown ($sl1_{rb}$)	San Vicente	2019-SV-06B
2019-SV-06B-Circulo A-ef - 3	sl	Yellowish brown (sl_{1yb})	San Vicente	2019-SV-06B

Label	Mineral	Color	Deposit	Sample
2019-SV-06B-Circulo A-ef - 4	sl	Yellowish brown (sl_{1yb})	San Vicente	2019-SV-06B
2019-SV-06B-Circulo B-ef - 1	sl	Reddish Brown ($sl1_{rb}$)	San Vicente	2019-SV-06B
2019-SV-06B-Circulo B-ef - 2	sl	Yellow (sl_{1y})	San Vicente	2019-SV-06B
2019-SV-06B-Circulo B-ef - 3	sl	Yellowish brown (sl_{1yb})	San Vicente	2019-SV-06B
2019-SV-06B-Circulo C-ef - 2	sl	Yellowish brown (sl_{1yb})	San Vicente	2019-SV-06B
2019-SV-06B-Circulo C-ef - 3	sl	Yellowish brown (sl_{1yb})	San Vicente	2019-SV-06B
2019-SV-07-Circulo A-ef - 1	sl	Yellow ($sl2_{y}$)	San Vicente	2019-SV-07
2019-SV-07-Circulo A-ef - 2	sl	Yellowish brown (sl_{1yb})	San Vicente	2019-SV-07
2019-SV-07-Circulo A-ef - 3	sl	Yellowish brown (sl_{1yb})	San Vicente	2019-SV-07
2019-SV-07-Circulo A-ef - 4	sl	Black (sl_{1bl})	San Vicente	2019-SV-07
2019-SV-07-Circulo B-ef - 1	sl	Reddish Brown ($sl1_{rb}$)	San Vicente	2019-SV-07
2019-SV-07-Circulo B-ef - 2	sl	Black (sl_{1bl})	San Vicente	2019-SV-07
2019-SV-07-Circulo B-ef - 3	sl	Black (sl_{1bl})	San Vicente	2019-SV-07
2019-SV-07-Circulo B-ef - 4	sl	Reddish Brown ($sl1_{rb}$)	San Vicente	2019-SV-07
2019-SV-07-Circulo C-ef - 1	sl	Yellowish brown (sl_{1yb})	San Vicente	2019-SV-07
2019-SV-07-Circulo C-ef - 2	sl	Black (sl_{1bl})	San Vicente	2019-SV-07
2019-SV-07-Circulo C-ef - 3	sl	Black (sl_{1bl})	San Vicente	2019-SV-07
UQAC-FeS-1 - 3				
GSD-1G - 3				
NIST610 - 3				
2019-SV-08A-Circulo A-ef - 2	sl	Reddish Brown ($sl1_{rb}$)	San Vicente	2019-SV-08A
2019-SV-08A-Circulo A-ef - 3	sl	Reddish Brown ($sl1_{rb}$)	San Vicente	2019-SV-08A
2019-SV-08A-Circulo A-ef - 4	sl	Black (sl_{1bl})	San Vicente	2019-SV-08A
2019-SV-08A-Circulo C-ef - 1	sl	Reddish Brown ($sl1_{rb}$)	San Vicente	2019-SV-08A
2019-SV-08A-Circulo C-ef - 2	sl	Black (sl_{1bl})	San Vicente	2019-SV-08A
2019-SV-08A-Circulo C-ef - 3	sl	Black (sl_{1bl})	San Vicente	2019-SV-08A
2019-SV-08A-Circulo D-ef - 1	sl	Yellowish brown (sl_{1yb})	San Vicente	2019-SV-08A
2019-SV-08A-Circulo D-ef - 2	sl	Yellowish brown (sl_{1yb})	San Vicente	2019-SV-08A
2019-SV-08A-Circulo D-ef - 3	sl	Yellowish brown (sl_{1yb})	San Vicente	2019-SV-08A
2019-SV-08B-Circulo A-ef - 1	sl	Yellowish brown (sl_{1yb})	San Vicente	2019-SV-08B
2019-SV-08B-Circulo A-ef - 2	sl	Black (sl_{1bl})	San Vicente	2019-SV-08B
2019-SV-08B-Circulo B-ef - 1	sl	Black (sl_{1bl})	San Vicente	2019-SV-08B

Label	Mineral	Color	Deposit	Sample
2019-SV-08B-Circulo B-ef - 3	sl	Black (sl_{1bl})	San Vicente	2019-SV-08B
2019-SV-08B-Circulo C-ef - 2	sl	Yellowish brown (sl_{1yb})	San Vicente	2019-SV-08B
2019-SV-08B-Circulo C-ef - 3	sl	Yellowish brown (sl_{1yb})	San Vicente	2019-SV-08B
2019-SV-08B-Circulo D-ef - 1	sl	Yellowish brown (sl_{1yb})	San Vicente	2019-SV-08B
2019-SV-08B-Circulo D-ef - 2	sl	Yellowish brown (sl_{1yb})	San Vicente	2019-SV-08B
2019-SV-08B-Circulo D-ef - 3	sl	Black (sl_{1bl})	San Vicente	2019-SV-08B
2019-SV-08B-Circulo D-ef - 4	sl	Yellowish brown (sl_{1yb})	San Vicente	2019-SV-08B
2019-SV-08B-Circulo E-ef - 1	sl	Yellowish brown (sl_{1yb})	San Vicente	2019-SV-08B
2019-SV-08B-Circulo E-ef - 2	sl	Yellow (sl_{1y})	San Vicente	2019-SV-08B
UQAC-FeS-1 - 4				
GSD-1G - 4				
NIST610 - 4				
2019-SV-08B-Circulo E-ef - 3	sl	Yellowish brown (sl_{1yb})	San Vicente	2019-SV-08B
2019-SV-08B-Circulo E-ef - 4	sl	Yellowish brown (sl_{1yb})	San Vicente	2019-SV-08B
2019-SV-09-Circulo A-ef - 1	sl	Yellowish brown (sl_{1yb})	San Vicente	2019-SV-09
2019-SV-09-Circulo A-ef - 2	sl	Yellow (sl_{1y})	San Vicente	2019-SV-09
2019-SV-09-Circulo A-ef - 3	sl	Black (sl_{1bl})	San Vicente	2019-SV-09
2019-SV-09-Circulo A-ef - 4	sl	Yellowish brown (sl_{1yb})	San Vicente	2019-SV-09
2019-SV-09-Circulo B-ef - 1	sl	Yellowish brown (sl_{1yb})	San Vicente	2019-SV-09
2019-SV-09-Circulo B-ef - 2	sl	Yellowish brown (sl_{1yb})	San Vicente	2019-SV-09
2019-SV-09-Circulo B-ef - 3	sl	Black (sl_{1bl})	San Vicente	2019-SV-09
2019-SV-09-Circulo B-ef - 4	sl	Yellowish brown (sl_{1yb})	San Vicente	2019-SV-09
2019-SV-09-Circulo C-ef - 1	sl	Black (sl_{1bl})	San Vicente	2019-SV-09
2019-SV-09-Circulo C-ef - 3	sl	Black (sl_{1bl})	San Vicente	2019-SV-09
2019-SV-011A-Circulo B-ef - 1	sl	Black (sl_{1bl})	San Vicente	2019-SV-11A
2019-SV-011A-Circulo B-ef - 2	sl	Reddish Brown (sl_{1rb})	San Vicente	2019-SV-11A
2019-SV-011A-Circulo B-ef - 3	sl	Yellow (sl_{1y})	San Vicente	2019-SV-11A
2019-SV-011A-Circulo B-ef - 4	sl	Reddish Brown (sl_{1rb})	San Vicente	2019-SV-11A
2019-SV-011A-Circulo C-ef - 1	sl	Reddish Brown (sl_{1rb})	San Vicente	2019-SV-11A
2019-SV-011A-Circulo C-ef - 2	sl	Reddish Brown (sl_{1rb})	San Vicente	2019-SV-11A
2019-SV-011A-Circulo C-ef - 3	sl	Yellowish brown (sl_{1yb})	San Vicente	2019-SV-11A
2019-SV-011A-Circulo C-ef - 4	sl	Yellow (sl_{1y})	San Vicente	2019-SV-11A

Label	Mineral	Color	Deposit	Sample
2019-SV-011B-Circulo A-ef - 1	sl	Reddish Brown (sl_{1rb})	San Vicente	2019-SV-11B
2019-SV-011B-Circulo A-ef - 2	sl	Reddish Brown (sl_{1rb})	San Vicente	2019-SV-11B
2019-SV-011B-Circulo A-ef - 3	sl	Reddish Brown (sl_{1rb})	San Vicente	2019-SV-11B
2019-SV-011B-Circulo A-ef - 4	sl	Reddish Brown (sl_{1rb})	San Vicente	2019-SV-11B
2019-SV-011B-Circulo A-ef - 5	sl	Reddish Brown (sl_{1rb})	San Vicente	2019-SV-11B
UQAC-FeS-1 - 5				
GSD-1G - 5				
NIST610 - 5				
2019-SV-011B-Circulo B-ef - 2	sl	Yellowish brown (sl_{1yb})	San Vicente	2019-SV-11B
2019-SV-011B-Circulo C-ef - 1	sl	Reddish Brown (sl_{1rb})	San Vicente	2019-SV-11B
2019-SV-011B-Circulo C-ef - 2	sl	Black (sl_{1bl})	San Vicente	2019-SV-11B
2019-SV-011B-Circulo C-ef - 3	sl	Black (sl_{1bl})	San Vicente	2019-SV-11B
2019-SV-011B-Circulo D-ef - 1	sl	Black (sl_{1bl})	San Vicente	2019-SV-11B
2019-SV-011B-Circulo D-ef - 2	sl	Reddish Brown (sl_{1rb})	San Vicente	2019-SV-11B
2019-SV-011B-Circulo D-ef - 3	sl	Black (sl_{1bl})	San Vicente	2019-SV-11B
2019-SV-011C-Circulo A-ef - 1	sl	Black (sl_{1bl})	San Vicente	2019-SV-11C
2019-SV-011C-Circulo B-ef - 2	sl	Reddish Brown (sl_{1rb})	San Vicente	2019-SV-11C
2019-SV-011C-Circulo C-ef - 1	sl	Black (sl_{1bl})	San Vicente	2019-SV-11C
2019-SV-011C-Circulo C-ef - 2	sl	Reddish Brown (sl_{1rb})	San Vicente	2019-SV-11C
2019-SV-012A-Circulo A-ef - 1	sl	Black (sl_{1bl})	San Vicente	2019-SV-12A
2019-SV-012A-Circulo A-ef - 2	sl	Black (sl_{1bl})	San Vicente	2019-SV-12A
2019-SV-012A-Circulo B-ef - 1	sl	Black (sl_{1bl})	San Vicente	2019-SV-12A
2019-SV-012A-Circulo C-ef - 1	sl	Black (sl_{1bl})	San Vicente	2019-SV-12A
2019-SV-012A-Circulo C-ef - 2	sl	Reddish Brown (sl_{1rb})	San Vicente	2019-SV-12A
2019-SV-012A-Circulo D-ef - 1	sl	Yellowish brown (sl_{1yb})	San Vicente	2019-SV-12A
2019-SV-012A-Circulo D-ef - 2	sl	Reddish Brown (sl_{1rb})	San Vicente	2019-SV-12A
2019-SV-012B-Circulo A-ef - 1	sl	Yellowish brown (sl_{1yb})	San Vicente	2019-SV-12B
2019-SV-012B-Circulo A-ef - 2	sl	Yellowish brown (sl_{1yb})	San Vicente	2019-SV-12B
2019-SV-012B-Circulo B-ef - 1	sl	Reddish Brown (sl_{1rb})	San Vicente	2019-SV-12B
2019-SV-012B-Circulo B-ef - 2	sl	Black (sl_{1bl})	San Vicente	2019-SV-12B
NIST610 - 6				
GSD-1G - 6				
UQAC-FeS-1 - 6				

Label	Mineral	Color	Deposit	Sample
UQAC-FeS-1 - 1				
GSD-1G - 1				
NIST610 - 1				
2019-SV-013-Circulo A-ef - 1	sl	Yellow (sl_{2y})	San Vicente	2019-SV-13
2019-SV-013-Circulo A-ef - 2	sl	Yellow (sl_{2y})	San Vicente	2019-SV-13
2019-SV-013-Circulo B-ef - 1	sl	Yellow (sl_{2y})	San Vicente	2019-SV-13
2019-SV-013-Circulo B-ef - 2	sl	Yellow (sl_{2y})	San Vicente	2019-SV-13
2019-SV-013-Circulo C-ef - 1	sl	Yellow (sl_{2y})	San Vicente	2019-SV-13
2019-SV-013-Circulo C-ef - 2	sl	Yellow (sl_{2y})	San Vicente	2019-SV-13
2019-SV-014-Circulo A-ef - 1	sl	Yellow (sl_{2y})	San Vicente	2019-SV-14
2019-SV-014-Circulo A-ef - 2	sl	Yellow (sl_{2y})	San Vicente	2019-SV-14
2019-SV-014-Circulo B-ef - 1	sl	Yellow (sl_{2y})	San Vicente	2019-SV-14
2019-SV-014-Circulo B-ef - 2	sl	Yellow (sl_{2y})	San Vicente	2019-SV-14
2019-SV-014-Circulo C-ef - 1	sl	Yellow (sl_{2y})	San Vicente	2019-SV-14
2019-SV-014-Circulo C-ef - 2	sl	Yellow (sl_{2y})	San Vicente	2019-SV-14
2019-SV-015A-Circulo A-ef - 1	sl	Yellow (sl_{2y})	San Vicente	2019-SV-15A
2019-SV-015A-Circulo A-ef - 2	sl	Yellow (sl_{2y})	San Vicente	2019-SV-15A
2019-SV-015A-Circulo B-ef - 1	sl	Yellow (sl_{2y})	San Vicente	2019-SV-15A
2019-SV-015A-Circulo B-ef - 2	sl	Orange (sl_{2o})	San Vicente	2019-SV-15A
2019-SV-015A-Circulo B-ef - 3	sl	Orange (sl_{2o})	San Vicente	2019-SV-15A
2019-SV-015A-Circulo C-ef - 1	sl	Yellow (sl_{2y})	San Vicente	2019-SV-15A
2019-SV-015A-Circulo D-ef - 1	sl	Orange (sl_{2o})	San Vicente	2019-SV-15A
2019-SV-015A-Circulo D-ef - 2	sl	Orange (sl_{2o})	San Vicente	2019-SV-15A
2019-SV-015A-Circulo D-ef - 3	sl	Orange (sl_{2o})	San Vicente	2019-SV-15A
2019-SV-015A-Circulo E-ef - 1	sl	Orange (sl_{2o})	San Vicente	2019-SV-15A
2019-SV-015A-Circulo E-ef - 2	sl	Yellow (sl_{2y})	San Vicente	2019-SV-15A
2019-SV-015A-Circulo E-ef - 3	sl	Orange (sl_{2o})	San Vicente	2019-SV-15A
2019-SV-015B-Circulo A-ef - 1	sl	Orange (sl_{2o})	San Vicente	2019-SV-15B
2019-SV-015B-Circulo A-ef - 2	sl	Orange (sl_{2o})	San Vicente	2019-SV-15B
UQAC-FeS-1 - 2				
GSD-1G - 2				
NIST610 - 2				
2019-SV-015B-Circulo A-ef - 3	sl	Orange (sl_{2o})	San Vicente	2019-SV-15B

Label	Mineral	Color	Deposit	Sample
2019-SV-015B-Circulo B-ef- 1	sl	White (sl_{2w})	San Vicente	2019-SV-15B
2019-SV-015B-Circulo B-ef - 2	sl	White (sl_{2w})	San Vicente	2019-SV-15B
2019-SV-015B-Circulo B-ef - 3	sl	White (sl_{2w})	San Vicente	2019-SV-15B
2019-SV-015B-Circulo B-ef - 4	sl	White (sl_{2w})	San Vicente	2019-SV-15B
2019-SV-015B-Circulo B-ef- 5	sl	White (sl_{2w})	San Vicente	2019-SV-15B
2019-SV-015B-Circulo B-ef-2 - 1	sl	Orange (sl_{2o})	San Vicente	2019-SV-15B
2019-SV-015B-Circulo C-ef - 1	sl	Yellow (sl_{2y})	San Vicente	2019-SV-15B
2019-SV-015B-Circulo C-ef - 2	sl	Orange (sl_{2o})	San Vicente	2019-SV-15B
2019-SV-015B-Circulo C-ef - 3	sl	Orange (sl_{2o})	San Vicente	2019-SV-15B
2019-SV-016-Circulo A-ef - 1	sl	Black (sl_{1bl})	San Vicente	2019-SV-16
2019-SV-016-Circulo A-ef - 2	sl	Black (sl_{1bl})	San Vicente	2019-SV-16
2019-SV-016-Circulo B-ef - 1	sl	Black (sl_{1bl})	San Vicente	2019-SV-16
2019-SV-016-Circulo D-ef - 1	sl	Reddish Brown (sl_{1rb})	San Vicente	2019-SV-16
2019-SV-016-Circulo D-ef - 1	sl	Reddish Brown (sl_{1rb})	San Vicente	2019-SV-16
2019-SV-016-Circulo E-ef - 2	sl	Yellowish brown (sl_{1yb})	San Vicente	2019-SV-16
2019-SV-016-Circulo E-ef - 3	sl	Yellowish brown (sl_{1yb})	San Vicente	2019-SV-16
2019-SH-31-Circulo A-ef - 1	sl	Yellowish brown (sl_{yb})	Shalipayco	2019-SH-231
2019-SH-31-Circulo A-ef - 2	sl	Yellowish brown (sl_{yb})	Shalipayco	2019-SH-231
2019-SH-31-Circulo A-ef - 3	sl	Yellowish brown (sl_{yb})	Shalipayco	2019-SH-231
2019-SH-31-Circulo A-ef - 4	sl	Yellowish brown (sl_{yb})	Shalipayco	2019-SH-231
2019-SH-31-Circulo B-ef - 1	sl	Yellowish brown (sl_{yb})	Shalipayco	2019-SH-231
2019-SH-31-Circulo B-ef - 2	sl	Yellowish brown (sl_{yb})	Shalipayco	2019-SH-231
2019-SH-31-Circulo B-ef - 3	sl	Yellowish brown (sl_{yb})	Shalipayco	2019-SH-231
2019-SH-31-Circulo C-ef - 1	sl	Yellow (sl_{y})	Shalipayco	2019-SH-231
UQAC-FeS-1 - 3 GSD-1G - 3 NIST610 - 3				
2019-SH-31-Circulo C-ef - 2	sl	Yellowish brown (sl_{yb})	Shalipayco	2019-SH-231
2019-SH-31-Circulo C-ef - 3	sl	Yellowish brown (sl_{yb})	Shalipayco	2019-SH-231
2019-SH-31-Circulo C-ef - 4	sl	Yellowish brown (sl_{yb})	Shalipayco	2019-SH-231
2019-SH-120-Circulo A-ef - 1	sl	Reddish Brown (sl_{rb})	Shalipayco	2019-SH-120
2019-SH-120-Circulo A-ef - 2	sl	Reddish Brown (sl_{rb})	Shalipayco	2019-SH-120

Label	Mineral	Color	Deposit	Sample
2019-SH-120-Circulo A-ef - 3	sl	Reddish Brown (sl_{rb})	Shalipayco	2019-SH-120
2019-SH-120-Circulo B-ef - 1	sl	Reddish Brown (sl_{rb})	Shalipayco	2019-SH-120
2019-SH-120-Circulo B-ef - 2	sl	Reddish Brown (sl_{rb})	Shalipayco	2019-SH-120
2019-SH-120-Circulo B-ef - 3	sl	Reddish Brown (sl_{rb})	Shalipayco	2019-SH-120
2019-SH-167-Circulo A-ef - 1	sl	Reddish Brown (sl_{rb})	Shalipayco	2019-SH-167
2019-SH-167-Circulo A-ef - 2	sl	Reddish Brown (sl_{rb})	Shalipayco	2019-SH-167
2019-SH-167-Circulo A-ef - 3	sl	Yellowish brown (sl_{yb})	Shalipayco	2019-SH-167
2019-SH-167-Circulo A-ef - 4	sl	Yellowish brown (sl_{yb})	Shalipayco	2019-SH-167
2019-SH-167-Circulo B-ef - 1	sl	Yellowish brown (sl_{yb})	Shalipayco	2019-SH-167
2019-SH-167-Circulo B-ef - 2	sl	Yellowish brown (sl_{yb})	Shalipayco	2019-SH-167
2019-SH-167-Circulo B-ef - 3	sl	Yellowish brown (sl_{yb})	Shalipayco	2019-SH-167
2019-SH-167-Circulo B-ef - 4	sl	Yellowish brown (sl_{yb})	Shalipayco	2019-SH-167
2019-SH-167-Circulo C-ef - 1	sl	Reddish Brown (sl_{rb})	Shalipayco	2019-SH-167
2019-SH-167-Circulo C-ef - 2	sl	Reddish Brown (sl_{rb})	Shalipayco	2019-SH-167
2019-SH-167-Circulo C-ef - 3	sl	Reddish Brown (sl_{rb})	Shalipayco	2019-SH-167
2019-SH-167-Circulo C-ef - 4	sl	Reddish Brown (sl_{rb})	Shalipayco	2019-SH-167
2019-SH-187-Circulo A-ef - 1	sl	Yellowish brown (sl_{yb})	Shalipayco	2019-SH-187
2019-SH-187-Circulo A-ef - 2	sl	Yellowish brown (sl_{yb})	Shalipayco	2019-SH-187
2019-SH-187-Circulo A-ef - 3	sl	Yellowish brown (sl_{yb})	Shalipayco	2019-SH-187
2019-SH-187-Circulo A-ef - 4	sl	Yellowish brown (sl_{yb})	Shalipayco	2019-SH-187
2019-SH-187-Circulo C-ef - 1	sl	Yellowish brown (sl_{yb})	Shalipayco	2019-SH-187
2019-SH-187-Circulo C-ef - 2	sl	Yellowish brown (sl_{yb})	Shalipayco	2019-SH-187
UQAC-FeS-1 - 4				
GSD-1G - 4				
NIST610 - 4				
2019-SH-187-Circulo C-ef - 3	sl	Reddish Brown (sl_{rb})	Shalipayco	2019-SH-187
2019-SH-212-Circulo A-ef - 1	sl	Yellowish brown (sl_{yb})	Shalipayco	2019-SH-212
2019-SH-212-Circulo A-ef - 2	sl	Yellow (sl_{y})	Shalipayco	2019-SH-212
2019-SH-212-Circulo A-ef - 3	sl	Yellowish brown (sl_{yb})	Shalipayco	2019-SH-212
2019-SH-212-Circulo A-ef - 4	sl	Yellow (sl_{2y})	Shalipayco	2019-SH-212
2019-SH-212-Circulo B-ef - 1	sl	Yellowish brown (sl_{yb})	Shalipayco	2019-SH-212
2019-SH-212-Circulo B-ef - 2	sl	Yellow (sl_{y})	Shalipayco	2019-SH-212

Label	Mineral	Color	Deposit	Sample
2019-SH-212-Circulo B-ef - 3	sl	Yellow (sl_y)	Shalipayco	2019-SH-212
2019-SH-212-Circulo B-ef - 4	sl	Yellow (sl_y)	Shalipayco	2019-SH-212
SH-227-Circulo B-ef - 1	sl	Yellowish brown (sl_{yb})	Shalipayco	2019-SH-227
SH-227-Circulo B-ef - 2	sl	Yellowish brown (sl_{yb})	Shalipayco	2019-SH-227
SH-227-Circulo B-ef - 3	sl	Yellowish brown (sl_{yb})	Shalipayco	2019-SH-227
SH-227-Circulo A-ef - 1	sl	Yellow (sl_y)	Shalipayco	2019-SH-227
SH-227-Circulo A-ef - 2	sl	Yellowish brown (sl_{yb})	Shalipayco	2019-SH-227
SH-227-Circulo A-ef - 3	sl	Yellowish brown (sl_{yb})	Shalipayco	2019-SH-227
NIST610 - 5				
GSD-1G - 5				
UQAC-FeS-1 - 5				

*Values in red color have been discarded in plots and text since they represent spurious values (spicky time vs. intensity signal and mine

Label	Vein/Body	District	S33	S34
UQAC-FeS-1 - 1			538432.2	528165
GSD-1G - 1			15803.82	13750.74
NIST610 - 1			15739.72	18896.6
2019-SV-02-Circulo A-ef - 1	Ayala Inferior, Horizonte San Vicente, Zona N, Camara 782 W, Galería 690	San Vicente	509163	503345
2019-SV-02-Circulo A-ef - 2	Ayala Inferior, Horizonte San Vicente, Zona N, Camara 782 W, Galería 690	San Vicente	504851	502448
2019-SV-02-Circulo A-ef - 3	Ayala Inferior, Horizonte San Vicente, Zona N, Camara 782 W, Galería 690	San Vicente	526692	522316
2019-SV-02-Circulo B-ef - 1	Ayala Inferior, Horizonte San Vicente, Zona N, Camara 782 W, Galería 690	San Vicente	506811	510101
2019-SV-02-Circulo B-ef - 2	Ayala Inferior, Horizonte San Vicente, Zona N, Camara 782 W, Galería 690	San Vicente	515587	508038
2019-SV-02-Circulo B-ef - 3	Ayala Inferior, Horizonte San Vicente, Zona N, Camara 782 W, Galería 690	San Vicente	499312	491379
2019-SV-02-Circulo C-ef - 1	Ayala Inferior, Horizonte San Vicente, Zona N, Camara 782 W, Galería 690	San Vicente	525595	515460
2019-SV-04-Circulo A-ef - 1	Ayala Inferior, Horizonte San Vicente, Zona N, Camara 782 W, Galería 690	San Vicente	496927	495823
2019-SV-04-Circulo A-ef - 2	Ayala Inferior, Horizonte San Vicente, Zona N, Camara 782 W, Galería 690	San Vicente	502751	494709
2019-SV-04-Circulo B-ef - 1	Ayala Inferior, Horizonte San Vicente, Zona N, Camara 782 W, Galería 690	San Vicente	522383	511457
2019-SV-04-Circulo B-ef - 2	Ayala Inferior, Horizonte San Vicente, Zona N, Camara 782 W, Galería 690	San Vicente	523359	517936
2019-SV-04-Circulo B-ef - 3	Ayala Inferior, Horizonte San Vicente, Zona N, Camara 782 W, Galería 690	San Vicente	504173	500361
2019-SV-04-Circulo C-ef - 2	Ayala Inferior, Horizonte San Vicente, Zona N, Camara 782 W, Galería 690	San Vicente	517194	513210
2019-SV-04-Circulo C-ef - 3	Ayala Inferior, Horizonte San Vicente, Zona N, Camara 782 W, Galería 690	San Vicente	529905	527507
2019-SV-04-Circulo D-ef - 1	Ayala Inferior, Horizonte San Vicente, Zona N, Camara 782 W, Galería 690	San Vicente	526908	522437
2019-SV-04-Circulo D-ef - 3	Ayala Inferior, Horizonte San Vicente, Zona N, Camara 782 W, Galería 690	San Vicente	526657	534287
2019-SV-06A-Circulo A-ef - 1	Zona Orcopunco, Galería 1275N, Cota 1739	San Vicente	532062	526135
2019-SV-06A-Circulo A-ef - 2	Zona Orcopunco, Galería 1275N, Cota 1739	San Vicente	529054	522385
2019-SV-06A-Circulo A-ef - 3	Zona Orcopunco, Galería 1275N, Cota 1739	San Vicente	543546	537952
UQAC-FeS-1 - 2			612380.9	571511.5
GSD-1G - 2			32996.25	32948.84
NIST610 - 2			19310.34	21247.41
2019-SV-06A-Circulo B-ef - 3	Zona Orcopunco, Galería 1275N, Cota 1739	San Vicente	534292	536330
2019-SV-06A-Circulo B-ef - 4	Zona Orcopunco, Galería 1275N, Cota 1739	San Vicente	520364	522758
2019-SV-06A-Circulo C-ef - 1	Zona Orcopunco, Galería 1275N, Cota 1739	San Vicente	539941	545455
2019-SV-06A-Circulo C-ef - 2	Zona Orcopunco, Galería 1275N, Cota 1739	San Vicente	548803	555850
2019-SV-06A-Circulo C-ef - 3	Zona Orcopunco, Galería 1275N, Cota 1739	San Vicente	531498	534851
2019-SV-06B-Circulo A-ef - 1	Zona Orcopunco, Galería 1275N, Cota 1739	San Vicente	520865	532625
2019-SV-06B-Circulo A-ef - 2	Zona Orcopunco, Galería 1275N, Cota 1739	San Vicente	519231	526528
2019-SV-06B-Circulo A-ef - 3	Zona Orcopunco, Galería 1275N, Cota 1739	San Vicente	524866	534736

Label	Vein/Body	District	S33	S34
2019-SV-06B-Circulo A-ef - 4	Zona Orcopunco, Galería 1275N, Cota 1739	San Vicente	518739	529298
2019-SV-06B-Circulo B-ef - 1	Zona Orcopunco, Galería 1275N, Cota 1739	San Vicente	515064	530584
2019-SV-06B-Circulo B-ef - 2	Zona Orcopunco, Galería 1275N, Cota 1739	San Vicente	539737	566384
2019-SV-06B-Circulo B-ef - 3	Zona Orcopunco, Galería 1275N, Cota 1739	San Vicente	521474	534919
2019-SV-06B-Circulo C-ef - 2	Zona Orcopunco, Galería 1275N, Cota 1739	San Vicente	514607	531699
2019-SV-06B-Circulo C-ef - 3	Zona Orcopunco, Galería 1275N, Cota 1739	San Vicente	526823	537882
2019-SV-07-Circulo A-ef - 1	Zona Orcopunco, Galería 1275N, Cota 1739	San Vicente	509072	525489
2019-SV-07-Circulo A-ef - 2	Zona Orcopunco, Galería 1275N, Cota 1739	San Vicente	505530	518020
2019-SV-07-Circulo A-ef - 3	Zona Orcopunco, Galería 1275N, Cota 1739	San Vicente	511590	530676
2019-SV-07-Circulo A-ef - 4	Zona Orcopunco, Galería 1275N, Cota 1739	San Vicente	510522	531552
2019-SV-07-Circulo B-ef - 1	Zona Orcopunco, Galería 1275N, Cota 1739	San Vicente	518524	528220
2019-SV-07-Circulo B-ef - 2	Zona Orcopunco, Galería 1275N, Cota 1739	San Vicente	496015	515820
2019-SV-07-Circulo B-ef - 3	Zona Orcopunco, Galería 1275N, Cota 1739	San Vicente	502759	516682
2019-SV-07-Circulo B-ef - 4	Zona Orcopunco, Galería 1275N, Cota 1739	San Vicente	504310	536972
2019-SV-07-Circulo C-ef - 1	Zona Orcopunco, Galería 1275N, Cota 1739	San Vicente	502116	520923
2019-SV-07-Circulo C-ef - 2	Zona Orcopunco, Galería 1275N, Cota 1739	San Vicente	495312	508920
2019-SV-07-Circulo C-ef - 3	Zona Orcopunco, Galería 1275N, Cota 1739	San Vicente	482051	502760
UQAC-FeS-1 - 3			528431	546987.2
GSD-1G - 3			13397.66	15187.46
NIST610 - 3			18271.39	19835.34
2019-SV-08A-Circulo A-ef - 2	Zona Orcopunco, Galería 1275N, Cota 1739	San Vicente	494058	508018
2019-SV-08A-Circulo A-ef - 3	Zona Orcopunco, Galería 1275N, Cota 1739	San Vicente	487201	497609
2019-SV-08A-Circulo A-ef - 4	Zona Orcopunco, Galería 1275N, Cota 1739	San Vicente	493102	503785
2019-SV-08A-Circulo C-ef - 1	Zona Orcopunco, Galería 1275N, Cota 1739	San Vicente	490259	500810
2019-SV-08A-Circulo C-ef - 2	Zona Orcopunco, Galería 1275N, Cota 1739	San Vicente	479378	493611
2019-SV-08A-Circulo C-ef - 3	Zona Orcopunco, Galería 1275N, Cota 1739	San Vicente	494435	507129
2019-SV-08A-Circulo D-ef - 1	Zona Orcopunco, Galería 1275N, Cota 1739	San Vicente	485429	487621
2019-SV-08A-Circulo D-ef - 2	Zona Orcopunco, Galería 1275N, Cota 1739	San Vicente	494222	506294
2019-SV-08A-Circulo D-ef - 3	Zona Orcopunco, Galería 1275N, Cota 1739	San Vicente	492300	502494
2019-SV-08B-Circulo A-ef - 1	Zona Orcopunco, Galería 1275N, Cota 1739	San Vicente	506582	518442
2019-SV-08B-Circulo A-ef - 2	Zona Orcopunco, Galería 1275N, Cota 1739	San Vicente	487418	505670
2019-SV-08B-Circulo B-ef - 1	Zona Orcopunco, Galería 1275N, Cota 1739	San Vicente	491347	510507

Label	Vein/Body	District	S33	S34
2019-SV-08B-Circulo B-ef - 3	Zona Orcopunco, Galería 1275N, Cota 1739	San Vicente	486307	504379
2019-SV-08B-Circulo C-ef - 2	Zona Orcopunco, Galería 1275N, Cota 1739	San Vicente	492560	500063
2019-SV-08B-Circulo C-ef - 3	Zona Orcopunco, Galería 1275N, Cota 1739	San Vicente	479610	497708
2019-SV-08B-Circulo D-ef - 1	Zona Orcopunco, Galería 1275N, Cota 1739	San Vicente	490393	500927
2019-SV-08B-Circulo D-ef - 2	Zona Orcopunco, Galería 1275N, Cota 1739	San Vicente	484558	488504
2019-SV-08B-Circulo D-ef - 3	Zona Orcopunco, Galería 1275N, Cota 1739	San Vicente	483631	487517
2019-SV-08B-Circulo D-ef - 4	Zona Orcopunco, Galería 1275N, Cota 1739	San Vicente	485069	488068
2019-SV-08B-Circulo E-ef - 1	Zona Orcopunco, Galería 1275N, Cota 1739	San Vicente	489605	498043
2019-SV-08B-Circulo E-ef - 2	Zona Orcopunco, Galería 1275N, Cota 1739	San Vicente	499080	505757
UQAC-FeS-1 - 4			496937	500088.3
GSD-1G - 4			14636.68	16091.97
NIST610 - 4			19005.66	18667.56
2019-SV-08B-Circulo E-ef - 3	Zona Orcopunco, Galería 1275N, Cota 1739	San Vicente	497562	494398
2019-SV-08B-Circulo E-ef - 4	Zona Orcopunco, Galería 1275N, Cota 1739	San Vicente	483678	497098
2019-SV-09-Circulo A-ef - 1	Zona Orcopunco, Galería 1275N, Cota 1739	San Vicente	485875	493017
2019-SV-09-Circulo A-ef - 2	Zona Orcopunco, Galería 1275N, Cota 1739	San Vicente	483230	498650
2019-SV-09-Circulo A-ef - 3	Zona Orcopunco, Galería 1275N, Cota 1739	San Vicente	488476	487776
2019-SV-09-Circulo A-ef - 4	Zona Orcopunco, Galería 1275N, Cota 1739	San Vicente	492274	503650
2019-SV-09-Circulo B-ef - 1	Zona Orcopunco, Galería 1275N, Cota 1739	San Vicente	485012	496222
2019-SV-09-Circulo B-ef - 2	Zona Orcopunco, Galería 1275N, Cota 1739	San Vicente	488340	492304
2019-SV-09-Circulo B-ef - 3	Zona Orcopunco, Galería 1275N, Cota 1739	San Vicente	473024	476699
2019-SV-09-Circulo B-ef - 4	Zona Orcopunco, Galería 1275N, Cota 1739	San Vicente	482690	502524
2019-SV-09-Circulo C-ef - 1	Zona Orcopunco, Galería 1275N, Cota 1739	San Vicente	533259	534278
2019-SV-09-Circulo C-ef - 3	Zona Orcopunco, Galería 1275N, Cota 1739	San Vicente	486826	496607
2019-SV-011A-Circulo B-ef - 1	Zona N, Cámara 8909W,Galería 690, Cota 1529	San Vicente	468956	478059
2019-SV-011A-Circulo B-ef - 2	Zona N, Cámara 8909W,Galería 690, Cota 1529	San Vicente	468850	475595
2019-SV-011A-Circulo B-ef - 3	Zona N, Cámara 8909W,Galería 690, Cota 1529	San Vicente	473391	480083
2019-SV-011A-Circulo B-ef - 4	Zona N, Cámara 8909W,Galería 690, Cota 1529	San Vicente	473287	481347
2019-SV-011A-Circulo C-ef - 1	Zona N, Cámara 8909W,Galería 690, Cota 1529	San Vicente	483472	484993
2019-SV-011A-Circulo C-ef - 2	Zona N, Cámara 8909W,Galería 690, Cota 1529	San Vicente	465535	465401
2019-SV-011A-Circulo C-ef - 3	Zona N, Cámara 8909W,Galería 690, Cota 1529	San Vicente	465528	470480
2019-SV-011A-Circulo C-ef - 4	Zona N, Cámara 8909W,Galería 690, Cota 1529	San Vicente	461716	459093

Label	Vein/Body	District	S33	S34
2019-SV-011B-Circulo A-ef - 1	Zona N, Cámara 8909W,Galería 690, Cota 1529	San Vicente	457589	467382
2019-SV-011B-Circulo A-ef - 2	Zona N, Cámara 8909W,Galería 690, Cota 1529	San Vicente	451827	455000
2019-SV-011B-Circulo A-ef - 3	Zona N, Cámara 8909W,Galería 690, Cota 1529	San Vicente	445194	457382
2019-SV-011B-Circulo A-ef - 4	Zona N, Cámara 8909W,Galería 690, Cota 1529	San Vicente	439591	452140
2019-SV-011B-Circulo A-ef - 5	Zona Orcopunco, Galería 1275N, Cota 1739	San Vicente	436843	439784
UQAC-FeS-1 - 5			324327.7	309397.3
GSD-1G - 5			22020.74	23092.27
NIST610 - 5			24622.08	23180.2
2019-SV-011B-Circulo B-ef - 2	Zona N, Cámara 8909W,Galería 690, Cota 1529	San Vicente	630020	633932
2019-SV-011B-Circulo C-ef - 1	Zona N, Cámara 8909W,Galería 690, Cota 1529	San Vicente	621261	635337
2019-SV-011B-Circulo C-ef - 2	Zona N, Cámara 8909W,Galería 690, Cota 1529	San Vicente	634848	636124
2019-SV-011B-Circulo C-ef - 3	Zona N, Cámara 8909W,Galería 690, Cota 1529	San Vicente	622295	629089
2019-SV-011B-Circulo D-ef - 1	Zona N, Cámara 8909W,Galería 690, Cota 1529	San Vicente	606790	614137
2019-SV-011B-Circulo D-ef - 2	Zona N, Cámara 8909W,Galería 690, Cota 1529	San Vicente	605328	610641
2019-SV-011B-Circulo D-ef - 3	Zona N, Cámara 8909W,Galería 690, Cota 1529	San Vicente	605500	606963
2019-SV-011C-Circulo A-ef - 1	Zona N, Cámara 8909W,Galería 690, Cota 1529	San Vicente	586793	589582
2019-SV-011C-Circulo B-ef - 2	Zona N, Cámara 8909W,Galería 690, Cota 1529	San Vicente	585120	586410
2019-SV-011C-Circulo C-ef - 1	Zona N, Cámara 8909W,Galería 690, Cota 1529	San Vicente	578564	572861
2019-SV-011C-Circulo C-ef - 2	Zona N, Cámara 8909W,Galería 690, Cota 1529	San Vicente	560563	561469
2019-SV-012A-Circulo A-ef - 1	Zona N, Cámara 8909W,Galería 690, Cota 1529	San Vicente	593817	605178
2019-SV-012A-Circulo A-ef - 2	Zona N, Cámara 8909W,Galería 690, Cota 1529	San Vicente	558925	550604
2019-SV-012A-Circulo B-ef - 1	Zona N, Cámara 8909W,Galería 690, Cota 1529	San Vicente	544487	546013
2019-SV-012A-Circulo C-ef - 1	Zona N, Cámara 8909W,Galería 690, Cota 1529	San Vicente	547596	551931
2019-SV-012A-Circulo C-ef - 2	Zona N, Cámara 8909W,Galería 690, Cota 1529	San Vicente	542058	546525
2019-SV-012A-Circulo D-ef - 1	Zona N, Cámara 8909W,Galería 690, Cota 1529	San Vicente	540550	539672
2019-SV-012A-Circulo D-ef - 2	Zona N, Cámara 8909W,Galería 690, Cota 1529	San Vicente	522643	516757
2019-SV-012B-Circulo A-ef - 1	Zona N, Cámara 8909W,Galería 690, Cota 1529	San Vicente	544381	543602
2019-SV-012B-Circulo A-ef - 2	Zona N, Cámara 8909W,Galería 690, Cota 1529	San Vicente	529552	530207
2019-SV-012B-Circulo B-ef - 1	Zona N, Cámara 8909W,Galería 690, Cota 1529	San Vicente	534599	533563
2019-SV-012B-Circulo B-ef - 2	Zona N, Cámara 8909W,Galería 690, Cota 1529	San Vicente	521343	518157
NIST610 - 6			17968.35	15274.15
GSD-1G - 6			18796.15	21172.81
UQAC-FeS-1 - 6			488671.1	489469.2

Label	Vein/Body	District	S33	S34
UQAC-FeS-1 - 1			523134.2	530138
GSD-1G - 1			14975.42	16630.26
NIST610 - 1			18868.16	17947.57
2019-SV-013-Circulo A-ef - 1	Zona N, Rampa 630, Cota 1475	San Vicente	467845	480191
2019-SV-013-Circulo A-ef - 2	Zona N, Rampa 630, Cota 1475	San Vicente	479263	494890
2019-SV-013-Circulo B-ef - 1	Zona N, Rampa 630, Cota 1475	San Vicente	493898	502594
2019-SV-013-Circulo B-ef - 2	Zona N, Rampa 630, Cota 1475	San Vicente	506952	518888
2019-SV-013-Circulo C-ef - 1	Zona N, Rampa 630, Cota 1475	San Vicente	502713	508769
2019-SV-013-Circulo C-ef - 2	Zona N, Rampa 630, Cota 1475	San Vicente	510056	522821
2019-SV-014-Circulo A-ef - 1	Zona N, Rampa 630, Cota 1475	San Vicente	504471	512937
2019-SV-014-Circulo A-ef - 2	Zona N, Rampa 630, Cota 1476	San Vicente	507642	516449
2019-SV-014-Circulo B-ef - 1	Zona N, Rampa 630, Cota 1477	San Vicente	513815	517911
2019-SV-014-Circulo B-ef - 2	Zona N, Rampa 630, Cota 1478	San Vicente	507996	517158
2019-SV-014-Circulo C-ef - 1	Zona N, Rampa 630, Cota 1479	San Vicente	508377	511758
2019-SV-014-Circulo C-ef - 2	Zona N, Rampa 630, Cota 1480	San Vicente	514575	522173
2019-SV-015A-Circulo A-ef - 1	Ayala inferior, Tajo 632	San Vicente	529827	548927
2019-SV-015A-Circulo A-ef - 2	Ayala inferior, Tajo 632	San Vicente	510639	523031
2019-SV-015A-Circulo B-ef - 1	Ayala inferior, Tajo 632	San Vicente	529145	532065
2019-SV-015A-Circulo B-ef - 2	Ayala inferior, Tajo 632	San Vicente	522313	527085
2019-SV-015A-Circulo B-ef - 3	Ayala inferior, Tajo 632	San Vicente	522029	527263
2019-SV-015A-Circulo C-ef - 1	Ayala inferior, Tajo 632	San Vicente	543157	545725
2019-SV-015A-Circulo D-ef - 1	Ayala inferior, Tajo 632	San Vicente	553795	541355
2019-SV-015A-Circulo D-ef - 2	Ayala inferior, Tajo 632	San Vicente	544656	547599
2019-SV-015A-Circulo D-ef - 3	Ayala inferior, Tajo 632	San Vicente	551334	549569
2019-SV-015A-Circulo E-ef - 1	Ayala inferior, Tajo 632	San Vicente	534114	538236
2019-SV-015A-Circulo E-ef - 2	Ayala inferior, Tajo 632	San Vicente	553942	550292
2019-SV-015A-Circulo E-ef - 3	Ayala inferior, Tajo 632	San Vicente	554578	547179
2019-SV-015B-Circulo A-ef - 1	Ayala inferior, Tajo 632	San Vicente	548806	548713
2019-SV-015B-Circulo A-ef - 2	Ayala inferior, Tajo 632	San Vicente	564991	563657
UQAC-FeS-1 - 2			602736.4	597684.3
GSD-1G - 2			10093.24	10898.2
NIST610 - 2			22740.31	23574.43
2019-SV-015B-Circulo A-ef - 3	Ayala inferior, Tajo 632	San Vicente	551368	552011

Label	Vein/Body	District	S33	S34
2019-SV-015B-Circulo B-ef- 1	Ayala inferior, Tajo 632	San Vicente	566202	558334
2019-SV-015B-Circulo B-ef - 2	Ayala inferior, Tajo 632	San Vicente	565007	552771
2019-SV-015B-Circulo B-ef - 3	Ayala inferior, Tajo 632	San Vicente	555488	552506
2019-SV-015B-Circulo B-ef - 4	Ayala inferior, Tajo 632	San Vicente	558492	555358
2019-SV-015B-Circulo B-ef- 5	Ayala inferior, Tajo 632	San Vicente	552477	545230
2019-SV-015B-Circulo B-ef-2 - 1	Ayala inferior, Tajo 632	San Vicente	543066	536151
2019-SV-015B-Circulo C-ef - 1	Ayala inferior, Tajo 632	San Vicente	557932	550233
2019-SV-015B-Circulo C-ef - 2	Ayala inferior, Tajo 632	San Vicente	524843	521936
2019-SV-015B-Circulo C-ef - 3	Ayala inferior, Tajo 632	San Vicente	535849	535608
2019-SV-016-Circulo A-ef - 1	Frente 8093, horizonte San Viente, Manto IIIS	San Vicente	513331	513072
2019-SV-016-Circulo A-ef - 2	Frente 8093, horizonte San Viente, Manto IIIS	San Vicente	611096	618537
2019-SV-016-Circulo B-ef - 1	Frente 8093, horizonte San Viente, Manto IIIS	San Vicente	518579	513373
2019-SV-016-Circulo D-ef - 1	Frente 8093, horizonte San Viente, Manto IIIS	San Vicente	511493	502578
2019-SV-016-Circulo D-ef - 1	Frente 8093, horizonte San Viente, Manto IIIS	San Vicente	527079	511272
2019-SV-016-Circulo E-ef - 2	Frente 8093, horizonte San Viente, Manto IIIS	San Vicente	503335	497855
2019-SV-016-Circulo E-ef - 3	Frente 8093, horizonte San Viente, Manto IIIS	San Vicente	493976	493276
2019-SH-31-Circulo A-ef - 1	Shalipayco	Shalipayco	522373	517059
2019-SH-31-Circulo A-ef - 2	Shalipayco	Shalipayco	521212	506551
2019-SH-31-Circulo A-ef - 3	Shalipayco	Shalipayco	551268	524697
2019-SH-31-Circulo A-ef - 4	Shalipayco	Shalipayco	517520	506901
2019-SH-31-Circulo B-ef - 1	Shalipayco	Shalipayco	517109	502532
2019-SH-31-Circulo B-ef - 2	Shalipayco	Shalipayco	517993	509338
2019-SH-31-Circulo B-ef - 3	Shalipayco	Shalipayco	514096	496513
2019-SH-31-Circulo C-ef - 1	Shalipayco	Shalipayco	513583	500571
UQAC-FeS-1 - 3			583197.8	563288
GSD-1G - 3			10813.84	12823.81
NIST610 - 3			19128.31	15096.74
2019-SH-31-Circulo C-ef - 2	Shalipayco	Shalipayco	505778	495064
2019-SH-31-Circulo C-ef - 3	Shalipayco	Shalipayco	504542	493622
2019-SH-31-Circulo C-ef - 4	Shalipayco	Shalipayco	510760	496830
2019-SH-120-Circulo A-ef - 1	Shalipayco	Shalipayco	472870	462890
2019-SH-120-Circulo A-ef - 2	Shalipayco	Shalipayco	527762	505512

Label	Vein/Body	District	S33	S34
2019-SH-120-Circulo A-ef - 3	Shalipayco	Shalipayco	474722	458845
2019-SH-120-Circulo B-ef - 1	Shalipayco	Shalipayco	512379	504638
2019-SH-120-Circulo B-ef - 2	Shalipayco	Shalipayco	486742	477001
2019-SH-120-Circulo B-ef - 3	Shalipayco	Shalipayco	506961	497894
2019-SH-167-Circulo A-ef - 1	Shalipayco	Shalipayco	496807	489441
2019-SH-167-Circulo A-ef - 2	Shalipayco	Shalipayco	498489	483899
2019-SH-167-Circulo A-ef - 3	Shalipayco	Shalipayco	514731	496271
2019-SH-167-Circulo A-ef - 4	Shalipayco	Shalipayco	515951	505035
2019-SH-167-Circulo B-ef - 1	Shalipayco	Shalipayco	497784	490676
2019-SH-167-Circulo B-ef - 2	Shalipayco	Shalipayco	497698	484303
2019-SH-167-Circulo B-ef - 3	Shalipayco	Shalipayco	493480	478248
2019-SH-167-Circulo B-ef - 4	Shalipayco	Shalipayco	516717	509026
2019-SH-167-Circulo C-ef - 1	Shalipayco	Shalipayco	498230	483897
2019-SH-167-Circulo C-ef - 2	Shalipayco	Shalipayco	507802	490515
2019-SH-167-Circulo C-ef - 3	Shalipayco	Shalipayco	515310	491891
2019-SH-167-Circulo C-ef - 4	Shalipayco	Shalipayco	500639	482271
2019-SH-187-Circulo A-ef - 1	Shalipayco	Shalipayco	508949	491132
2019-SH-187-Circulo A-ef - 2	Shalipayco	Shalipayco	525244	504936
2019-SH-187-Circulo A-ef - 3	Shalipayco	Shalipayco	523801	503887
2019-SH-187-Circulo A-ef - 4	Shalipayco	Shalipayco	542018	517893
2019-SH-187-Circulo C-ef - 1	Shalipayco	Shalipayco	527664	500036
2019-SH-187-Circulo C-ef - 2	Shalipayco	Shalipayco	524520	508291
UQAC-FeS-1 - 4			545548.4	536113.1
GSD-1G - 4			20031.58	18624.72
NIST610 - 4			15815.29	17311.08
2019-SH-187-Circulo C-ef - 3	Shalipayco	Shalipayco	511699	497084
2019-SH-212-Circulo A-ef - 1	Shalipayco	Shalipayco	515128	500792
2019-SH-212-Circulo A-ef - 2	Shalipayco	Shalipayco	508512	499687
2019-SH-212-Circulo A-ef - 3	Shalipayco	Shalipayco	521342	510308
2019-SH-212-Circulo A-ef - 4	Shalipayco	Shalipayco	511828	496012
2019-SH-212-Circulo B-ef - 1	Shalipayco	Shalipayco	514520	497696
2019-SH-212-Circulo B-ef - 2	Shalipayco	Shalipayco	518493	499475

Label	Vein/Body	District	S33	S34
2019-SH-212-Circulo B-ef - 3	Shalipayco	Shalipayco	514492	502333
2019-SH-212-Circulo B-ef - 4	Shalipayco	Shalipayco	516667	503491
SH-227-Circulo B-ef - 1	Shalipayco	Shalipayco	506230	492982
SH-227-Circulo B-ef - 2	Shalipayco	Shalipayco	511129	497362
SH-227-Circulo B-ef - 3	Shalipayco	Shalipayco	506276	488686
SH-227-Circulo A-ef - 1	Shalipayco	Shalipayco	503380	488446
SH-227-Circulo A-ef - 2	Shalipayco	Shalipayco	505612	487946
SH-227-Circulo A-ef - 3	Shalipayco	Shalipayco	507904	491810
NIST610 - 5			18329.06	19330.37
GSD-1G - 5			14144.58	13640.39
UQAC-FeS-1 - 5			567554.3	555449.3

*Values in red color have been discarded in pyral micro-inclusions)

Label	Cr53	Mn55	Fe57	Co59	Ni62	Cu65	Zn66	Ga71	Ge74
UQAC-FeS-1 - 1	52.88666	2.8141967	9176.595	25.60561	740.2362	1032.47	9.135784	0.151528	0.144315
GSD-1G - 1	1.332003	4.3872367	1479.241	0.822165	3.562085	4.22294	13.90696	0.561048	0.554312
NIST610 - 1	6.34974	13.320812	23.23421	8.978228	12.22641	16.3542	19.31699	8.652373	7.22233
2019-SV-02-Circulo A-ef - 1	<0.5	8.7	7767	50.7	2.0	<3	668400	0.185	44
2019-SV-02-Circulo A-ef - 2	<0.59	5.2	7563	53	<1.7	<4.0	672800	0.132	43.5
2019-SV-02-Circulo A-ef - 3	<0.7	8.4	6755	44.3	9.0	<4.7	662800	0.20	45.9
2019-SV-02-Circulo B-ef - 1	<0.7	6.3	6309	45	<1.9	<4	663000	0.183	54.7
2019-SV-02-Circulo B-ef - 2	<0.55	13	14818	56	<1.4	<3.4	668900	0.112	37.5
2019-SV-02-Circulo B-ef - 3	<0.79	11.1	8905	40.7	2.58	<4.9	668900	0.54	46.3
2019-SV-02-Circulo C-ef - 1	<0.5	41	19557	55.2	31.0	<3.4	644300	0.399	60.5
2019-SV-04-Circulo A-ef - 1	<0.5	68	14440	46.2	<1	<3	638400	0.07	44.6
2019-SV-04-Circulo A-ef - 2	<0.5	61	14775	43.3	<1.1	<3	631300	0.569	66.8
2019-SV-04-Circulo B-ef - 1	<0.5	69.5	9395	36.1	2.8	<3	660900	3.20	41.8
2019-SV-04-Circulo B-ef - 2	<0.56	91.5	16867	36.4	<1.5	<3.4	656700	1.754	56.6
2019-SV-04-Circulo B-ef - 3	<0.5	55.9	13399	38.0	<1.5	<3	630800	1.553	59.2
2019-SV-04-Circulo C-ef - 2	<0.5	11.4	11006	60.3	<1.2	<3.3	643100	0.433	45.7
2019-SV-04-Circulo C-ef - 3	<0.6	18	9473	51.8	<1.7	<3.8	654000	0.507	51.0
2019-SV-04-Circulo D-ef - 1	<0.58	20.6	21269	68.4	<1.4	4.9	648900	0.439	39.1
2019-SV-04-Circulo D-ef - 3	<0.8	11.5	12198	55.9	<2	<4.6	653700	0.267	56
2019-SV-06A-Circulo A-ef - 1	<0.58	97.4	18475	<0.12	<1.2	<3.4	656900	1.12	82.4
2019-SV-06A-Circulo A-ef - 2	<0.5	39.2	21184	0.24	<1.2	<3	646200	3.33	43
2019-SV-06A-Circulo A-ef - 3	<0.6	66.9	12996	0.146	<1.6	<3.8	662200	5.0	86.0
UQAC-FeS-1 - 2	230.3014	49.093255	450000	542.3167	18138.33	16515.1	187.2174	6.640685	3.653154
GSD-1G - 2	50.1922	445.4654	198397.7	77.29785	106.518	74.172	54	91.74612	60.41369
NIST610 - 2	258.407	494.40329	436.9147	421.6049	438.1947	413.44	460	369.0023	331.7695
2019-SV-06A-Circulo B-ef - 3	<0.5	25.6	22788	<0.12	<1.3	<3	645200	5.38	44.6
2019-SV-06A-Circulo B-ef - 4	<0.50	20	12547	0.207	1.2	5	642500	3.48	113
2019-SV-06A-Circulo C-ef - 1	<0.56	32.9	20568	<0.11	<1	<3	655100	2.21	31.3
2019-SV-06A-Circulo C-ef - 2	<0.55	74.9	19687	0.21	<1.2	<3	665900	6.65	96
2019-SV-06A-Circulo C-ef - 3	<0.5	72	23232	0.161	<1.4	<3.3	649800	6.68	52.9
2019-SV-06B-Circulo A-ef - 1	<0.5	21.3	13395	0.407	<1.3	<3	654400	1.573	93.3
2019-SV-06B-Circulo A-ef - 2	<0.5	35.3	17475	0.30	<1.5	<3	653600	0.087	51
2019-SV-06B-Circulo A-ef - 3	<0.5	27.6	10483	0.5	<1.2	4.0	671100	0.143	99

Label	Cr53	Mn55	Fe57	Co59	Ni62	Cu65	Zn66	Ga71	Ge74
2019-SV-06B-Circulo A-ef - 4	<0.55	41	8430	0.39	<1.3	<3.3	667300	1.276	59.7
2019-SV-06B-Circulo B-ef - 1	<0.5	26.4	11074	0.378	<1.2	<3	665500	4.69	133
2019-SV-06B-Circulo B-ef - 2	<0.8	26.9	10927	0.32	<2	<4.7	663700	9.04	134.3
2019-SV-06B-Circulo B-ef - 3	<0.56	46.9	13289	0.3	<1.5	<3.5	664500	0.91	118.4
2019-SV-06B-Circulo C-ef - 2	<0.5	21.6	18010	0.26	<1.3	<3	660800	0.98	53.8
2019-SV-06B-Circulo C-ef - 3	<0.5	47.3	19463	0.41	<1.4	<3.5	668300	13.29	82.9
2019-SV-07-Circulo A-ef - 1	<0.56	<1.2	88	0.79	<1.4	43.1	679200	0.756	177.2
2019-SV-07-Circulo A-ef - 2	<0.5	14	5641	<0.1	<1.3	3.8	656800	0.99	13.5
2019-SV-07-Circulo A-ef - 3	<0.55	25.5	6682	<0.12	<1.3	10.3	667700	0.46	87.5
2019-SV-07-Circulo A-ef - 4	<0.5	15.4	16731	0.26	<1.3	<3.6	656800	3.94	95.0
2019-SV-07-Circulo B-ef - 1	<0.55	9	10035	0.16	<1.6	<3.7	671000	0.77	37.2
2019-SV-07-Circulo B-ef - 2	<0.5	62.8	28218	<0.12	<1.3	<3.6	633100	15.8	43.0
2019-SV-07-Circulo B-ef - 3	<0.50	84	14381	0.28	<1.4	<3.5	654000	7.27	108.8
2019-SV-07-Circulo B-ef - 4	<0.80	75.9	12757	0.24	<2.5	<5	654000	7.8	118.5
2019-SV-07-Circulo C-ef - 1	<0.55	49.2	3000	<0.12	<1.4	8.8	673000	3.21	93
2019-SV-07-Circulo C-ef - 2	<0.58	24.6	10122	<0.13	<1.4	<4	664900	1.11	23.6
2019-SV-07-Circulo C-ef - 3	<0.7	19.5	17762	0.24	<2.4	<4.5	661000	20.4	136
UQAC-FeS-1 - 3	155.9461	56.98858	450000	608.5333	23109.81	24712.4	235.118	7.343608	4.35218
GSD-1G - 3	23.04803	203.68713	93666.03	37.43371	52.13262	37.7686	54	40.4424	29.47212
NIST610 - 3	280.5663	536.33975	527.3399	479.9545	515.3398	523.445	460	394.8329	389.0118
2019-SV-08A-Circulo A-ef - 2	<0.57	19.6	26958	0.14	<1.3	<3.8	637700	47.6	34.1
2019-SV-08A-Circulo A-ef - 3	<0.5	48	22527	<0.13	<1.2	<3.7	640200	3.39	45.3
2019-SV-08A-Circulo A-ef - 4	<0.5	70.1	12157	0.18	<1.6	<3.8	646800	8.3	128.6
2019-SV-08A-Circulo C-ef - 1	<0.5	70	32945	0.15	<1.4	<3.7	621900	12.47	40.3
2019-SV-08A-Circulo C-ef - 2	<0.48	72	23364	<0.11	<1.3	<3.5	617200	11.82	42
2019-SV-08A-Circulo C-ef - 3	<0.5	95.9	19599	<0.13	<1.5	<3.8	629000	25.5	69
2019-SV-08A-Circulo D-ef - 1	<0.69	41.2	16459	<0.17	<2.2	<4.8	646900	0.867	39
2019-SV-08A-Circulo D-ef - 2	<0.5	45.2	11005	<0.12	<1.3	<3.7	651100	1.75	79.2
2019-SV-08A-Circulo D-ef - 3	<0.5	37.7	9742	<0.12	<1.4	<3.7	640100	0.81	60.5
2019-SV-08B-Circulo A-ef - 1	<0.58	42.1	10443	<0.12	<1.4	<3.9	652300	0.688	24.72
2019-SV-08B-Circulo A-ef - 2	<0.56	7.37	12135	0.17	<1.1	<3.6	649900	0.088	59.5
2019-SV-08B-Circulo B-ef - 1	<0.56	68.8	21780	<0.12	<1.4	<3.7	645100	6.46	36.6

Label	Cr53	Mn55	Fe57	Co59	Ni62	Cu65	Zn66	Ga71	Ge74
2019-SV-08B-Circulo B-ef - 3	<0.55	32	20666	0.38	<1.3	<3.6	643000	9.4	71.5
2019-SV-08B-Circulo C-ef - 2	<0.56	25.3	9531	0.61	<1.1	<3.6	652800	3.14	35.32
2019-SV-08B-Circulo C-ef - 3	<0.58	12.9	14899	0.50	<1.4	<3.9	643600	26	46.0
2019-SV-08B-Circulo D-ef - 1	<0.56	17.8	6305	0.484	<1.4	<3.7	653200	4.54	22.9
2019-SV-08B-Circulo D-ef - 2	<0.5	15.2	10414	0.40	<1.1	<3.5	642900	11.81	66.1
2019-SV-08B-Circulo D-ef - 3	<0.5	38.3	17677	0.13	<1.2	<3.4	641000	80	19.07
2019-SV-08B-Circulo D-ef - 4	<0.59	25.9	9695	0.264	<1.7	<3.9	639600	22	90.0
2019-SV-08B-Circulo E-ef - 1	<0.6	37.5	9329	0.20	<1.5	<4.0	647500	2.03	23.28
2019-SV-08B-Circulo E-ef - 2	<0.6	9.0	7539	0.51	<1.5	<4	650600	16.6	118.2
UQAC-FeS-1 - 4	114.6563	41.434134	450000	644.3346	21389.16	20382.7	293.3749	7.454148	3.579143
GSD-1G - 4	28.30052	242.01409	115729.7	43.35622	51.55381	36.8457	54	53.16769	36.7216
NIST610 - 4	279.5605	513.67716	503.1805	459.985	443.9472	490.237	460	412.6533	377.7192
2019-SV-08B-Circulo E-ef - 3	<0.58	81.5	9556	0.278	<1.5	<4	653000	10.22	30.5
2019-SV-08B-Circulo E-ef - 4	<0.5	3.0	4179	0.66	<1.6	<3.7	657100	10.93	33.8
2019-SV-09-Circulo A-ef - 1	<0.5	23.8	17824	<0.13	<1.5	<3.8	651100	1.518	25.62
2019-SV-09-Circulo A-ef - 2	<0.55	21.0	12254	<0.13	<1.2	<3.8	661400	1.185	99
2019-SV-09-Circulo A-ef - 3	<0.5	8.0	14889	<0.13	<1.4	<3.7	663500	0.65	75
2019-SV-09-Circulo A-ef - 4	<0.55	20.8	16839	<0.13	<1.4	<4	659700	1.06	33.5
2019-SV-09-Circulo B-ef - 1	<0.58	17.2	25873	0.31	<1.7	<4	655300	5.51	111.5
2019-SV-09-Circulo B-ef - 2	<0.5	15	16697	0.26	<1.3	<3.7	658200	2.262	63.3
2019-SV-09-Circulo B-ef - 3	<0.50	52	19584	0.26	<1.3	<3.7	641800	3.58	50.7
2019-SV-09-Circulo B-ef - 4	<0.6	47.1	14490	0.23	<1.6	<4	666000	3.90	167
2019-SV-09-Circulo C-ef - 1	<0.8	81.4	19930	0.34	<1.9	8	675300	5.8	73.3
2019-SV-09-Circulo C-ef - 3	<0.5	31.6	17251	0.15	<1.5	<4	661500	2.50	58.71
2019-SV-011A-Circulo B-ef - 1	0.65	35.6	9774	12.10	<1.2	<3.9	658500	0.122	73.9
2019-SV-011A-Circulo B-ef - 2	0.6	55.9	18998	9.84	<1.3	<3.9	646800	0.049	37.34
2019-SV-011A-Circulo B-ef - 3	<0.5	24.4	10581	12.50	<1.3	<4	659300	0.18	144
2019-SV-011A-Circulo B-ef - 4	<0.5	19	10598	14.6	<1.5	5.5	660000	0.078	136.73
2019-SV-011A-Circulo C-ef - 1	<0.47	35.5	21149	13.76	1	<3.9	664200	0.038	41.54
2019-SV-011A-Circulo C-ef - 2	<0.48	23.8	20536	20	2.4	<3.9	650500	0.056	71
2019-SV-011A-Circulo C-ef - 3	<0.49	27.4	16762	14.33	<1.3	<3.9	651400	0.047	43.4
2019-SV-011A-Circulo C-ef - 4	<0.49	21.9	16235	17.3	<1.6	4.5	654600	0.049	62.7

Label	Cr53	Mn55	Fe57	Co59	Ni62	Cu65	Zn66	Ga71	Ge74
2019-SV-011B-Circulo A-ef - 1	<0.5	16.4	20997	19.6	<1.4	<4.0	648600	0.068	65.0
2019-SV-011B-Circulo A-ef - 2	<0.5	27.7	12378	16.3	<1.3	<3.9	642100	0.120	54.5
2019-SV-011B-Circulo A-ef - 3	<0.47	36.5	21542	15.4	<1.3	<3.6	637400	0.070	39.5
2019-SV-011B-Circulo A-ef - 4	<0.50	21	19422	18.8	<1.4	<3.9	632400	0.095	83.2
2019-SV-011B-Circulo A-ef - 5	<0.44	23.3	8342	8.40	<1.1	4.0	632400	0.065	50.1
UQAC-FeS-1 - 5	104.6514	56.066686	450000	623.9683	23210.02	25078.6	202.0064	8.356587	3.08921
GSD-1G - 5	54.18762	555.51139	237681.3	95.60799	124.622	90.9753	54	105.3535	54.99707
NIST610 - 5	516.5189	1090.9991	958.5543	939.2713	971.0945	1091.09	460	778.5419	538.5263
2019-SV-011B-Circulo B-ef - 2	<1	57.0	38867	19.3	<2.8	<8	632400	0.175	94
2019-SV-011B-Circulo C-ef - 1	<1	32.3	26853	13.4	<3	<8	639800	0.136	168
2019-SV-011B-Circulo C-ef - 2	<1	58.6	43271	12.34	2.4	<8	639800	0.176	132.3
2019-SV-011B-Circulo C-ef - 3	<0.9	48.8	34371	6.56	<2.5	<7.9	639800	0.842	117
2019-SV-011B-Circulo D-ef - 1	<0.89	26	26178	37.23	<2	<7	643300	0.109	180
2019-SV-011B-Circulo D-ef - 2	<0.90	38.6	32314	31.79	2.5	<7	637900	0.237	106.2
2019-SV-011B-Circulo D-ef - 3	<0.9	46.4	33635	30.17	<2.8	<7	639800	0.153	69.8
2019-SV-011C-Circulo A-ef - 1	<0.8	23.9	29301	23	<2	<6	627200	0.064	127
2019-SV-011C-Circulo B-ef - 2	<0.8	51.2	19512	12.4	<1.9	<6	645800	0.062	119.0
2019-SV-011C-Circulo C-ef - 1	<0.8	28.4	24788	9.47	<1.9	<6	637500	0.106	145
2019-SV-011C-Circulo C-ef - 2	<0.77	34.9	23086	9.24	<2	6	631700	0.08	80.3
2019-SV-012A-Circulo A-ef - 1	<1	172	20395	23.38	3.1	<6.9	659100	5.6	73
2019-SV-012A-Circulo A-ef - 2	<0.8	49.6	43217	35.39	<1.9	<5.5	626500	0.229	72.4
2019-SV-012A-Circulo B-ef - 1	<0.8	22.9	10057	32	<2.2	<5.9	628100	0.22	62
2019-SV-012A-Circulo C-ef - 1	<0.7	50.1	30904	20.2	<1.8	<5	642900	0.60	42.5
2019-SV-012A-Circulo C-ef - 2	<0.69	76.6	29582	15.7	1.59	<5	642000	0.29	48.3
2019-SV-012A-Circulo D-ef - 1	<0.67	97	13196	18.8	<1.6	<4.8	657600	1.21	49.8
2019-SV-012A-Circulo D-ef - 2	<0.68	68	17684	15.77	<1.9	5.3	639900	1.22	49.7
2019-SV-012B-Circulo A-ef - 1	<0.67	87.6	18177	17.8	<1.8	<4.8	652200	1.21	55
2019-SV-012B-Circulo A-ef - 2	<0.68	43.6	11178	20	<1.6	<4.9	656900	0.472	90
2019-SV-012B-Circulo B-ef - 1	<0.7	23.5	18594	19.1	<1.8	<4.8	656900	0.569	52.0
2019-SV-012B-Circulo B-ef - 2	<0.57	16	20655	20.4	<1.6	<4	656900	1.07	69.5
NIST610 - 6	289.6845	557.36846	534.3429	482.8888	467.7386	508.19	460	435.3613	395.5273
GSD-1G - 6	42.84857	359.36907	165962.5	63.44418	88.06567	73.0237	54	75.73304	52.34225
UQAC-FeS-1 - 6	125.0926	49.871955	450000	571.4442	19726.54	21193.8	2120.543	9.375303	4.082012

Label	Cr53	Mn55	Fe57	Co59	Ni62	Cu65	Zn66	Ga71	Ge74
UQAC-FeS-1 - 1	123.182	53.446609	450000	586.9617	22311.04	19395.7	268.2121	6.724461	3.331698
GSD-1G - 1	32.8616	232.50754	126760.7	47.10993	99.59971	61.0622	54	61.99411	38.59284
NIST610 - 1	313.3354	454.29378	501.5828	449.097	471.4937	490.156	460	438.4335	359.617
2019-SV-013-Circulo A-ef - 1	<0.5	174	41	<0.09	<1.2	14.3	660800	25	78
2019-SV-013-Circulo A-ef - 2	<0.56	239	56	<0.1	<1.2	6	658100	14.94	150
2019-SV-013-Circulo B-ef - 1	<0.56	368	92	<0.10	<1.4	<3.5	658400	44.3	294.2
2019-SV-013-Circulo B-ef - 2	<0.56	243	68	<0.099	<1.3	22.2	660900	63.9	115
2019-SV-013-Circulo C-ef - 1	<0.5	247.8	107	<0.1	<1.3	<3.4	660600	25.62	243
2019-SV-013-Circulo C-ef - 2	<0.6	311	122	<0.11	<1.6	<3.8	670400	54	310
2019-SV-014-Circulo A-ef - 1	<0.56	278	25	<0.1	<1.5	<3.5	658700	17.2	175.8
2019-SV-014-Circulo A-ef - 2	<0.5	209	20	<0.1	<1.1	18.2	660500	16.82	65.8
2019-SV-014-Circulo B-ef - 1	<0.68	318	33	<0.13	<1.7	18.1	658000	72	201.6
2019-SV-014-Circulo B-ef - 2	<0.5	308	47	<0.10	<1.5	4.1	655800	18.6	154.9
2019-SV-014-Circulo C-ef - 1	<0.5	376	15	<0.10	<1.2	10.3	658100	50.5	201
2019-SV-014-Circulo C-ef - 2	<0.59	336	29	<0.12	<1.6	<3.8	657500	47.4	156.4
2019-SV-015A-Circulo A-ef - 1	<1	371	<19	<0.19	<2.9	236	667700	306	13.7
2019-SV-015A-Circulo A-ef - 2	<0.58	967	<10	<0.10	<1.5	324	667700	25.4	342
2019-SV-015A-Circulo B-ef - 1	<0.8	466	<15	<0.16	<2.0	370	663700	13.70	1096
2019-SV-015A-Circulo B-ef - 2	<0.57	614	<10	<0.10	<1.5	<3.5	662400	0.214	1284
2019-SV-015A-Circulo B-ef - 3	<0.58	365	<10	<0.12	<1.5	640	665700	50.48	514
2019-SV-015A-Circulo C-ef - 1	<0.8	1161	<14	<0.14	<1.7	116	668600	2.3	146
2019-SV-015A-Circulo D-ef - 1	<0.9	683	<17	<0.18	<2.5	546	666700	161.41	620.7
2019-SV-015A-Circulo D-ef - 2	<0.56	340	<11	<0.10	<1.2	55	666900	30.68	1861
2019-SV-015A-Circulo D-ef - 3	<0.7	187	<13	<0.14	<1.6	433	668500	388.97	41.4
2019-SV-015A-Circulo E-ef - 1	<0.68	271.2	57	<0.13	<1.6	626	666500	63.83	375
2019-SV-015A-Circulo E-ef - 2	<0.57	533	<11	<0.12	<1.4	1149	664500	9.6	855
2019-SV-015A-Circulo E-ef - 3	<0.5	425	<10	<0.12	<1.4	1651	668200	997	566
2019-SV-015B-Circulo A-ef - 1	<0.57	204.4	<11	<0.12	<1.4	1378	670600	5.47	967
2019-SV-015B-Circulo A-ef - 2	<0.6	266	<13	<0.14	<1.6	93	670500	87.5	0.2
UQAC-FeS-1 - 2	111.8505	60.279685	450000	647.3859	21693.91	21380.1	199.4724	7.093936	3.830459
GSD-1G - 2	20.24036	219.80271	90688.52	36.6927	52.10989	36.1978	54	42.08765	28.82466
NIST610 - 2	296.7203	638.15206	535.7013	509.4492	513.189	547.256	460	442.4164	406.4576
2019-SV-015B-Circulo A-ef - 3	<0.5	524	<10	<0.11	<1.5	2084	670500	5.99	1534

Label	Cr53	Mn55	Fe57	Co59	Ni62	Cu65	Zn66	Ga71	Ge74
2019-SV-015B-Circulo B-ef- 1	0.61	593	<11	<0.13	<1.5	206	673500	195.4	<0.14
2019-SV-015B-Circulo B-ef - 2	<0.7	273	<13	<0.15	<1.7	112	676200	99	0.16
2019-SV-015B-Circulo B-ef - 3	<0.59	381.2	<11	<0.13	<1.4	96	676200	93.0	0.136
2019-SV-015B-Circulo B-ef - 4	<0.5	381.7	<11	<0.12	<1.6	96	676200	92.3	0.23
2019-SV-015B-Circulo B-ef- 5	<0.6	486.4	<12	<0.15	<1.4	172	676200	170.8	2.05
2019-SV-015B-Circulo B-ef-2 - 1	<0.55	139.1	<10	<0.11	<1.4	271	676200	200	39.3
2019-SV-015B-Circulo C-ef - 1	<0.77	145.7	<15	<0.18	<2	19	674000	14.4	6.7
2019-SV-015B-Circulo C-ef - 2	<0.57	614	<11	<0.13	<1.4	1730	662900	228	1207
2019-SV-015B-Circulo C-ef - 3	<0.56	287	<11	<0.12	<1.5	1171	662900	11.6	702
2019-SV-016-Circulo A-ef - 1	<0.49	42.8	21206	26.3	17.4	<3.6	621000	0.235	67.7
2019-SV-016-Circulo A-ef - 2	2.48	281	41021	61	403	5.8	645300	9.38	91
2019-SV-016-Circulo B-ef - 1	<0.47	55.6	16651	24.0	<1.3	<3.7	636600	0.78	71
2019-SV-016-Circulo D-ef - 1	0.5	64.4	20197	24.2	<1.4	<3.9	622800	4.03	68.8
2019-SV-016-Circulo D-ef - 1	<0.7	20.6	11533	24.99	<2	<5.5	639900	0.052	62.4
2019-SV-016-Circulo E-ef - 2	<0.49	22.1	12906	24.4	<1.2	<3.7	635400	0.044	54.0
2019-SV-016-Circulo E-ef - 3	<0.47	7.4	5426	33.4	<1.4	<3.6	638900	0.106	156.0
2019-SH-31-Circulo A-ef - 1	<0.7	<1.7	1820	<0.19	<2.0	294	671900	0.090	371
2019-SH-31-Circulo A-ef - 2	<0.5	7.5	622	<0.13	<1.7	10	674700	0.094	15.00
2019-SH-31-Circulo A-ef - 3	<0.79	6.2	1032	<0.21	<2	46	678600	0.15	181
2019-SH-31-Circulo A-ef - 4	<0.48	1.7	1049	<0.12	<1.4	22.8	669200	0.061	386
2019-SH-31-Circulo B-ef - 1	<0.49	8	952	<0.13	<1.5	13.9	671300	0.171	36.4
2019-SH-31-Circulo B-ef - 2	<0.46	<1.2	1583	<0.14	<1.3	282	669500	0.530	672
2019-SH-31-Circulo B-ef - 3	<0.50	<1.1	792	<0.14	<1.2	<3.9	664800	0.034	966
2019-SH-31-Circulo C-ef - 1	<0.55	3.2	882	<0.14	<1.4	549	673400	0.157	1119
UQAC-FeS-1 - 3	103.4631	122.13569	450000	641.5517	21279.2	21720.7	380.9975	8.03013	4.020606
GSD-1G - 3	23.29813	225.78652	95028.81	39.42172	49.97425	35.4855	54	42.23386	31.08821
NIST610 - 3	247.2887	523.42685	456.6081	458.7314	418.4793	460.128	460	364.5189	355.9176
2019-SH-31-Circulo C-ef - 2	<0.48	6.9	914	<0.12	<1.2	262	675900	0.081	810
2019-SH-31-Circulo C-ef - 3	<0.5	1.9	1821	<0.14	<1.3	561	675600	3.09	397
2019-SH-31-Circulo C-ef - 4	<0.5	<1.2	1200	<0.13	<1.4	<4	669800	0.076	309.7
2019-SH-120-Circulo A-ef - 1	<0.5	6.9	15130	0.15	<1.5	<4.0	643300	1.3	30.5
2019-SH-120-Circulo A-ef - 2	<0.5	14.2	34859	0.416	<1.5	<4	676400	0.062	115.1

Label	Cr53	Mn55	Fe57	Co59	Ni62	Cu65	Zn66	Ga71	Ge74
2019-SH-120-Circulo A-ef - 3	<0.47	13.55	37888	0.56	<1.5	<3.7	608100	0.032	268.8
2019-SH-120-Circulo B-ef - 1	<0.6	<1.4	3116	<0.16	<1.7	<4.8	676600	1.036	4.5
2019-SH-120-Circulo B-ef - 2	<0.48	7.79	19665	0.57	<1.1	<3.9	635900	1.21	182.8
2019-SH-120-Circulo B-ef - 3	<0.5	13.9	18937	0.41	<1.4	<3.8	676400	0.412	41.8
2019-SH-167-Circulo A-ef - 1	<0.49	3.2	1642	<0.13	<1.4	<3.9	665800	0.061	249
2019-SH-167-Circulo A-ef - 2	<0.49	<1.1	1129	<0.12	<1.3	<3.7	661000	0.041	301.0
2019-SH-167-Circulo A-ef - 3	<0.5	<1.2	917	<0.13	<1.6	5.8	668900	2.83	316
2019-SH-167-Circulo A-ef - 4	<0.6	<1.4	784	<0.16	<1.4	16.4	667500	0.110	787
2019-SH-167-Circulo B-ef - 1	<0.6	<1.4	666	<0.16	<1.8	210	662900	16	149.6
2019-SH-167-Circulo B-ef - 2	<0.5	<1.2	801	<0.14	<1.4	999	665000	16	468
2019-SH-167-Circulo B-ef - 3	<0.45	<1	181	<0.12	<1.4	<3.7	664300	0.078	734
2019-SH-167-Circulo B-ef - 4	<0.6	<1.4	412	<0.15	<1.7	<4.8	672400	0.067	636
2019-SH-167-Circulo C-ef - 1	0.60	<1	523	<0.12	<1.3	5090	656200	475	731
2019-SH-167-Circulo C-ef - 2	<0.49	<1.1	384	<0.12	<1.3	<3.9	668200	0.099	503
2019-SH-167-Circulo C-ef - 3	<0.5	<1.1	437	<0.13	<1.3	<4	669600	0.24	384
2019-SH-167-Circulo C-ef - 4	<0.48	<1	820	<0.12	<1.3	442	658300	0.102	434
2019-SH-187-Circulo A-ef - 1	<0.48	2.2	6146	18.74	<1.2	<4	656300	0.064	107.1
2019-SH-187-Circulo A-ef - 2	<0.49	3.5	16416	18.73	<1.2	<4	667700	0.47	62.1
2019-SH-187-Circulo A-ef - 3	<0.5	1.8	9881	25.8	<1.4	4.9	667100	0.057	3.98
2019-SH-187-Circulo A-ef - 4	<0.5	6.99	22783	28.50	<1.6	<4.5	680300	0.84	16.7
2019-SH-187-Circulo C-ef - 1	<0.5	5.7	8139	13.85	<1.6	<4.7	662400	0.866	6.89
2019-SH-187-Circulo C-ef - 2	<0.5	5.23	8035	11.18	<1.8	<4.5	673000	<0.028	2.67
UQAC-FeS-1 - 4	120.0227	47.87097	450000	634.4066	19817.84	20780	348.912	6.879568	3.676419
GSD-1G - 4	34.75231	327.53554	148457.7	60.95998	70.15312	85.5666	54	67.49458	50.27629
NIST610 - 4	248.2735	493.2516	454.1601	433.6292	432.5408	452.124	460	362.3102	357.1513
2019-SH-187-Circulo C-ef - 3	<0.5	<1.1	10975	18.38	<1.1	<4	673000	1.05	52
2019-SH-212-Circulo A-ef - 1	<0.5	<1.1	1003	<0.14	<1.6	88	678000	10.1	98.7
2019-SH-212-Circulo A-ef - 2	0.75	<1.1	706	<0.13	<1.3	141	675100	23.1	296.9
2019-SH-212-Circulo A-ef - 3	<0.55	2.2	1082	<0.15	<1.7	<4.5	677600	1.01	27.5
2019-SH-212-Circulo A-ef - 4	<0.5	<1.1	786	<0.14	<1	31	676900	31.3	303.7
2019-SH-212-Circulo B-ef - 1	0.52	1.5	1360	<0.14	<1.4	6.4	681200	9.0	114.1
2019-SH-212-Circulo B-ef - 2	<0.49	<1.1	486	<0.14	<1.3	<4	676500	0.18	379

Label	Cr53	Mn55	Fe57	Co59	Ni62	Cu65	Zn66	Ga71	Ge74
2019-SH-212-Circulo B-ef - 3	<0.49	<1.1	424	<0.13	<1.1	5.3	680100	0.073	370.1
2019-SH-212-Circulo B-ef - 4	<0.69	<1.5	666	<0.19	<1.8	163.7	677400	19	236.1
SH-227-Circulo B-ef - 1	<0.5	<1.1	577	<0.14	<1.5	<3.9	663800	0.54	206.6
SH-227-Circulo B-ef - 2	<0.56	<1.2	1376	<0.13	<1.4	101	664500	31.8	303.9
SH-227-Circulo B-ef - 3	<0.49	<1.1	642	<0.14	<1.4	1149	661100	19.07	467
SH-227-Circulo A-ef - 1	<0.59	<1.2	659	<0.16	<1.7	<4.4	662200	3.1	156
SH-227-Circulo A-ef - 2	<0.5	<1.1	1077	<0.14	<1.3	12.5	663400	1.12	337
SH-227-Circulo A-ef - 3	<0.50	<1.2	479	<0.14	1.32	1347	662800	20.39	640
NIST610 - 5	276.5904	518.29265	470.204	447.4788	403.8361	457.982	460	381.9822	369.7353
GSD-1G - 5	21.74948	188.62877	82873.84	33.90529	42.05886	32.7807	54	38.4335	26.86038
UQAC-FeS-1 - 5	272.0094	48.120414	450000	621.8323	19301.5	21130.2	334.7638	6.286415	3.754833

*Values in red color have been discarded in pl

Label	As75	Se77	Mo95	Ag107	Cd111	In115	Sn118	Sb121	Au197
UQAC-FeS-1 - 1	15.64776	8.376115	2.034644	14.02986	0.294177	0.216205	27.89223	2.08314	4.157365
GSD-1G - 1	0.763058	1.349364	0.62651	0.443252	1.06667	0.515381	0.652756	0.582989	0.10941
NIST610 - 1	8.151548	4.036654	10.68101	6.496054	10.24087	8.883037	9.651772	7.8195	0.592399
2019-SV-02-Circulo A-ef - 1	94.5	<0.8	0.039	20.1	1339	<0.0059	0.184	0.035	<0.011
2019-SV-02-Circulo A-ef - 2	300	<0.9	<0.024	12.48	1452	<0.0066	0.129	<0.03	<0.013
2019-SV-02-Circulo A-ef - 3	94.6	<1.1	0.041	17.93	1447	<0.0079	0.151	<0.039	<0.015
2019-SV-02-Circulo B-ef - 1	145	<1.1	<0.03	15	1567	<0.008	0.14	<0.037	<0.014
2019-SV-02-Circulo B-ef - 2	160.1	<0.8	0.029	21.1	1514	<0.005	0.152	<0.03	<0.009
2019-SV-02-Circulo B-ef - 3	106	<1.2	<0.035	14.7	1165	<0.008	0.149	<0.04	<0.018
2019-SV-02-Circulo C-ef - 1	204	<0.8	0.06	38.5	546	<0.005	0.212	<0.030	<0.010
2019-SV-04-Circulo A-ef - 1	237.1	<0.80	<0.02	16	750	<0.0049	0.20	<0.025	<0.009
2019-SV-04-Circulo A-ef - 2	439	<0.8	0.032	9.32	2458	0.0158	0.164	<0.03	<0.010
2019-SV-04-Circulo B-ef - 1	160	<0.78	<0.022	9.23	1672	0.0241	0.265	<0.028	<0.0099
2019-SV-04-Circulo B-ef - 2	218.4	<0.79	0.025	19.1	2065	0.019	0.191	<0.028	<0.0089
2019-SV-04-Circulo B-ef - 3	288	0.85	0.035	10.8	1882	0.017	0.231	<0.028	<0.01
2019-SV-04-Circulo C-ef - 2	149.5	<0.7	<0.02	6.1	1542	0.0111	0.176	<0.029	<0.01
2019-SV-04-Circulo C-ef - 3	194.7	1.13	<0.024	7.07	1461	0.0124	0.166	<0.03	<0.01
2019-SV-04-Circulo D-ef - 1	95	0.87	0.037	11.39	1825	<0.006	0.206	<0.03	<0.01
2019-SV-04-Circulo D-ef - 3	146	<1	<0.034	7.38	1254	0.0087	0.21	<0.035	<0.013
2019-SV-06A-Circulo A-ef - 1	19.4	1.3	<0.024	2.51	361	0.0118	0.31	<0.024	<0.01
2019-SV-06A-Circulo A-ef - 2	12.6	0.78	0.029	4.58	456	0.029	0.54	<0.026	<0.0088
2019-SV-06A-Circulo A-ef - 3	6.28	<0.9	<0.028	10.39	541	0.231	1.99	<0.03	<0.011
UQAC-FeS-1 - 2	1232.862	291.7344	64.26705	154.6102	3.328823	8.119333	223.5068	62.98757	83.92735
GSD-1G - 2	79.18835	5.271958	81.17586	46.7958	70.50298	69.90523	66.09404	64.8211	8.770472
NIST610 - 2	335.8675	112.9471	459.4515	262.2432	375.9367	381.5086	403.0839	342.7117	21.28529
2019-SV-06A-Circulo B-ef - 3	6.0	<0.67	0.023	8.25	558	0.0169	0.41	<0.027	<0.01
2019-SV-06A-Circulo B-ef - 4	5.06	<0.67	<0.023	11.06	553	0.0085	0.323	<0.024	<0.009
2019-SV-06A-Circulo C-ef - 1	8.67	<0.77	<0.025	2.41	536	0.006	0.246	<0.026	<0.0088
2019-SV-06A-Circulo C-ef - 2	10.10	0.79	0.036	7.68	519	0.0409	0.60	<0.029	<0.008
2019-SV-06A-Circulo C-ef - 3	6.5	<0.7	<0.025	4.72	704	0.060	0.870001	<0.025	<0.009
2019-SV-06B-Circulo A-ef - 1	7.7	<0.8	0.023	12.21	560	<0.0058	0.37	<0.025	<0.0089
2019-SV-06B-Circulo A-ef - 2	17.41	<0.7	0.027	3.81	476	<0.006	0.194	<0.026	<0.0089
2019-SV-06B-Circulo A-ef - 3	13.25	<0.8	<0.02	5.07	247	<0.0059	0.238	<0.027	<0.010

Label	As75	Se77	Mo95	Ag107	Cd111	In115	Sn118	Sb121	Au197
2019-SV-06B-Circulo A-ef - 4	12.1	<0.7	<0.027	5.00	488	0.011	0.36	<0.028	<0.0090
2019-SV-06B-Circulo B-ef - 1	14.3	<0.8	<0.026	10.22	635	0.016	0.40	<0.029	<0.010
2019-SV-06B-Circulo B-ef - 2	12.28	<1.1	0.036	21.53	724	0.067	0.84	<0.036	<0.016
2019-SV-06B-Circulo B-ef - 3	27.1	<0.7	<0.025	5.19	517	0.0085	0.28	<0.028	<0.01
2019-SV-06B-Circulo C-ef - 2	3.33	<0.7	<0.026	5.54	479	<0.0059	0.28	<0.025	<0.009
2019-SV-06B-Circulo C-ef - 3	8.40	0.9	0.085	13.41	501	0.0428	1.10	0.059	<0.012
2019-SV-07-Circulo A-ef - 1	3.02	<0.77	<0.025	6.53	1363	<0.006	0.185	<0.029	<0.01
2019-SV-07-Circulo A-ef - 2	3.39	<0.7	<0.02	3.19	786	0.089	0.285	<0.023	<0.0099
2019-SV-07-Circulo A-ef - 3	3.61	<0.7	0.036	7.41	873	<0.006	0.195	<0.027	<0.011
2019-SV-07-Circulo A-ef - 4	3.99	<0.78	<0.023	16.75	576	0.060	0.376	<0.026	<0.01
2019-SV-07-Circulo B-ef - 1	2.99	<0.78	<0.025	19.46	841	<0.006	0.305	<0.026	<0.012
2019-SV-07-Circulo B-ef - 2	15.68	0.84	0.026	2.65	1099	0.0506	0.99	<0.023	<0.01
2019-SV-07-Circulo B-ef - 3	18.4	<0.77	0.040	1.9	484	0.059604	0.62	<0.025	<0.01
2019-SV-07-Circulo B-ef - 4	19.9	<1	<0.036	2.00	487	0.0894	0.651	<0.038	<0.0178
2019-SV-07-Circulo C-ef - 1	3.1	<0.9	<0.023	33.2	1565	0.0085	0.248	<0.030	<0.011
2019-SV-07-Circulo C-ef - 2	5.40	<0.9	<0.025	6.29	737	0.0178	0.36	<0.034	<0.013
2019-SV-07-Circulo C-ef - 3	3.51	<1.0	<0.03	11.35	618	0.088	3.2	<0.038	<0.014
UQAC-FeS-1 - 3	1130.6	356.4009	71.24512	183.9683	3.535594	8.027226	175.2142	68.49074	66.80561
GSD-1G - 3	38.65984	3.172694	39.45399	24.19009	34.7999	30.52282	31.4365	32.40323	4.957274
NIST610 - 3	378.3828	143.6545	540.1051	326.8969	451.366	400.523	469.5465	410.0916	28.18284
2019-SV-08A-Circulo A-ef - 2	3.38	<0.8	<0.024	21.34	1252	0.147	1.39	<0.029	<0.01
2019-SV-08A-Circulo A-ef - 3	6.98	<0.8	<0.030	5.02	1229	0.0170	0.384	<0.026	<0.01
2019-SV-08A-Circulo A-ef - 4	9.66	<0.7	<0.027	2.99	538	0.068	0.772	<0.027	<0.01
2019-SV-08A-Circulo C-ef - 1	8.25	<0.78	<0.025	2.40	1430	0.043	0.60	<0.024	0.0118
2019-SV-08A-Circulo C-ef - 2	11.4	<0.7	<0.028	2.95	1174	0.0713	0.99	<0.027	<0.01
2019-SV-08A-Circulo C-ef - 3	10.7	<0.78	<0.027	28.5	1103	0.262	2.59	0.09	<0.01
2019-SV-08A-Circulo D-ef - 1	4.86	<1	<0.036	11.4	874	0.059	0.62	<0.037	<0.014
2019-SV-08A-Circulo D-ef - 2	6.36	<0.8	0.029	8.9	421	0.0111	0.334	<0.024	<0.01
2019-SV-08A-Circulo D-ef - 3	4.76	<0.77	<0.030	4.55	410	0.0097	0.31	<0.024	<0.01
2019-SV-08B-Circulo A-ef - 1	4.90	0.94	0.050	4.04	453	0.132	0.99	0.034	0.011
2019-SV-08B-Circulo A-ef - 2	2.62	<0.77	0.028	6.49	400	<0.0068	0.185	<0.029	<0.01
2019-SV-08B-Circulo B-ef - 1	11.54	<0.8	0.032	2.95	820	0.058	0.548	<0.026	<0.011

Label	As75	Se77	Mo95	Ag107	Cd111	In115	Sn118	Sb121	Au197
2019-SV-08B-Circulo B-ef - 3	11.8	<0.69	<0.027	12.76	730	0.074	0.855	<0.025	<0.01
2019-SV-08B-Circulo C-ef - 2	9.10	<0.7	<0.027	2.45	388	0.036	0.39	<0.03	<0.01
2019-SV-08B-Circulo C-ef - 3	6.1	<0.8	<0.030	10.48	841	0.062	0.964	<0.029	<0.011
2019-SV-08B-Circulo D-ef - 1	5.62	<0.8	<0.025	2.39	699	0.0289	0.52	<0.030	<0.011
2019-SV-08B-Circulo D-ef - 2	5.2	<0.67	0.029	24.8	1603	0.0240	0.326	<0.023	<0.01
2019-SV-08B-Circulo D-ef - 3	3.66	<0.7	0.025	28.8	3784	0.191	2.46	0.029	<0.01
2019-SV-08B-Circulo D-ef - 4	8.43	<0.8	0.042	10.1	1245	0.107	0.976	<0.026	<0.01
2019-SV-08B-Circulo E-ef - 1	13.41	<0.8	<0.03	3.06	892	0.0157	0.58	<0.028	<0.012
2019-SV-08B-Circulo E-ef - 2	4.55	<0.80	<0.03	22	1598	0.054	0.78	<0.035	0.0156
UQAC-FeS-1 - 4	1042.967	285.8987	61.73389	129.6804	2.834	8.295058	128.1273	59.10203	42.64957
GSD-1G - 4	45.98544	<2.4168	47.3333	25.8012	38.17101	38.10782	36.60701	38.31842	5.632504
NIST610 - 4	367.2671	130.9859	519.1977	276.7738	392.6756	394.7918	432.8365	389.6019	26.182
2019-SV-08B-Circulo E-ef - 3	6.85	<0.8	0.039	13	1151	0.0610	1.0	<0.03	<0.012
2019-SV-08B-Circulo E-ef - 4	3.22	<0.8	<0.025	9.40	1564	<0.008	0.289	<0.029	<0.01
2019-SV-09-Circulo A-ef - 1	4.37	<0.70	0.039	4.55	1267	0.0076	0.228	<0.029	<0.011
2019-SV-09-Circulo A-ef - 2	3.33	<0.7	<0.023	6.5	737	0.010	0.21	<0.028	<0.009
2019-SV-09-Circulo A-ef - 3	2.74	<0.7	<0.028	10.72	1202	<0.006	0.201	<0.026	<0.009
2019-SV-09-Circulo A-ef - 4	3.86	1.3	0.029	5.56	854	<0.0080	0.351	<0.03	<0.011
2019-SV-09-Circulo B-ef - 1	4.57	1.0	<0.030	10.0	428	0.0263	0.42	<0.025	<0.012
2019-SV-09-Circulo B-ef - 2	5.10	<0.78	<0.026	8.83	436	<0.006	0.316	<0.027	<0.01
2019-SV-09-Circulo B-ef - 3	22.74	<0.7	<0.027	2.98	493	0.0156	0.64	<0.029	<0.009
2019-SV-09-Circulo B-ef - 4	14.35	<0.77	<0.03	6.88	312.3	0.0110	0.29	<0.028	<0.012
2019-SV-09-Circulo C-ef - 1	29.1	<1	<0.036	6.37	435	0.040	0.70	0.04	<0.014
2019-SV-09-Circulo C-ef - 3	17.58	<0.8	0.032	4.84	503	0.013	0.319	<0.029	<0.0099
2019-SV-011A-Circulo B-ef - 1	27.8	<0.7	0.030	2.68	500	0.0102	0.26	<0.025	<0.01
2019-SV-011A-Circulo B-ef - 2	34.20	0.9	<0.03	1.8	974	<0.0069	0.16	<0.028	<0.009
2019-SV-011A-Circulo B-ef - 3	22.52	<0.70	<0.02	4.33	733	0.0075	0.249	<0.029	<0.01
2019-SV-011A-Circulo B-ef - 4	13.0	1.1	<0.026	3.68	759	<0.008	0.4	<0.025	<0.01
2019-SV-011A-Circulo C-ef - 1	11.79	<0.69	0.032	2.17	753	<0.0068	0.14	<0.027	<0.0099
2019-SV-011A-Circulo C-ef - 2	8.76	0.84	0.029	2.92	598	<0.0067	0.164	<0.026	<0.01
2019-SV-011A-Circulo C-ef - 3	8.8	0.77	0.027	2.39	660	0.007	0.203	<0.024	<0.011
2019-SV-011A-Circulo C-ef - 4	6.83	<0.7	<0.033	2.58	531	<0.007	0.157	<0.026	<0.009

Label	As75	Se77	Mo95	Ag107	Cd111	In115	Sn118	Sb121	Au197
2019-SV-011B-Circulo A-ef - 1	4.28	<0.7	<0.026	3.42	746	<0.0069	0.191	<0.026	<0.01
2019-SV-011B-Circulo A-ef - 2	40.9	<0.67	<0.03	4.9	603	0.013	0.155	<0.023	<0.01
2019-SV-011B-Circulo A-ef - 3	14.48	<0.6	0.032	2.14	784	0.0086	0.141	<0.025	<0.0089
2019-SV-011B-Circulo A-ef - 4	9.28	0.64	0.026	3.36	770	<0.008	0.20	<0.027	0.014
2019-SV-011B-Circulo A-ef - 5	7.40	<0.68	<0.026	2.7	312	0.0085	0.200	<0.026	<0.009
UQAC-FeS-1 - 5	1711.58	312.1825	67.05655	183.3035	1.306282	10.96342	249.1165	58.84062	49.85817
GSD-1G - 5	95.10574	<5.0243	105.9139	66.21846	26.98725	82.74367	81.13969	85.60959	11.92857
NIST610 - 5	727.4665	254.008	1067.916	664.0603	270.1126	811.3845	916.2169	801.7901	50.74639
2019-SV-011B-Circulo B-ef - 2	16.0	<1.4	<0.05	6.83	529	0.016	0.31	<0.055	<0.020
2019-SV-011B-Circulo C-ef - 1	12.21	1.4	0.07	6.15	342	<0.014	0.31	<0.05	<0.018
2019-SV-011B-Circulo C-ef - 2	14.4	<1.5	<0.05	6.25	433	0.022	0.33	<0.058	<0.02
2019-SV-011B-Circulo C-ef - 3	16.8	1.7	0.07	5.29	328	0.014	0.30	<0.05	<0.02
2019-SV-011B-Circulo D-ef - 1	12.78	1.4	0.101	7.79	428	<0.013	0.216	<0.05	<0.019
2019-SV-011B-Circulo D-ef - 2	19.3	<1	<0.057	6.07	550	<0.012	0.25	<0.05	<0.017
2019-SV-011B-Circulo D-ef - 3	26.2	<1.2	<0.058	5.76	574	<0.013	0.237	<0.04	<0.019
2019-SV-011C-Circulo A-ef - 1	7.2	<1	0.041	4.34	639	<0.012	0.21	<0.045	<0.015
2019-SV-011C-Circulo B-ef - 2	25.92	<1	<0.040	5.29	405	<0.012	0.292	<0.04	<0.016
2019-SV-011C-Circulo C-ef - 1	12.54	<1.00	0.044	5.26	435	<0.012	0.311	<0.04	<0.016
2019-SV-011C-Circulo C-ef - 2	20.2	<1.0	<0.04	6.73	468	<0.009	0.26	<0.040	<0.015
2019-SV-012A-Circulo A-ef - 1	98	<1.3	0.07	5.26	683	0.28	1.6	<0.05	<0.02
2019-SV-012A-Circulo A-ef - 2	21.8	<1.0	<0.04	4.78	606	<0.01	0.247	<0.036	<0.015
2019-SV-012A-Circulo B-ef - 1	21.5	1.96	0.044	13.22	311	0.0124	0.31	<0.04	<0.016
2019-SV-012A-Circulo C-ef - 1	36	<1.0	<0.039	5.14	995	0.0172	0.377	<0.036	<0.016
2019-SV-012A-Circulo C-ef - 2	69.4	<0.88	<0.034	2.73	939	<0.01	0.296	<0.035	<0.015
2019-SV-012A-Circulo D-ef - 1	121	<0.9	<0.03	2.37	474	0.046	0.41	<0.03	<0.011
2019-SV-012A-Circulo D-ef - 2	87	1.1	<0.035	5.41	940	0.0138	0.75	<0.03	<0.014
2019-SV-012B-Circulo A-ef - 1	133.3	<0.88	<0.038	5.30	831	0.044	0.48	<0.03	<0.012
2019-SV-012B-Circulo A-ef - 2	20.9	<0.8	0.054	6.5	861	0.05	0.319	<0.036	<0.013
2019-SV-012B-Circulo B-ef - 1	19.0	<0.80	<0.04	5.08	855	0.023	0.451	<0.035	<0.014
2019-SV-012B-Circulo B-ef - 2	9.3	<0.68	<0.03	4.25	925	0.019	0.49	<0.03	<0.011
NIST610 - 6	400.3539	125.1356	566.7159	313.263	383.4905	421.6459	477.2934	422.5012	28.6039
GSD-1G - 6	67.09355	<2.8213	71.04072	41.01644	53.45628	54.82998	54.18367	56.32884	8.704088
UQAC-FeS-1 - 6	1285.788	274.6333	63.35688	170.1975	11.10758	11.56519	157.6363	97.75629	67.64232

Label	As75	Se77	Mo95	Ag107	Cd111	In115	Sn118	Sb121	Au197
UQAC-FeS-1 - 1	1320.131	307.3634	68.82949	178.1721	3.689023	7.647332	199.2362	157.7683	49.3254
GSD-1G - 1	58.92731	4.207901	53.46739	31.38152	49.33155	43.86563	42.57759	41.61257	6.030818
NIST610 - 1	376.9409	128.794	532.5742	296.3454	435	415.6885	452.3741	377.2033	25.10695
2019-SV-013-Circulo A-ef - 1	3.30	<0.8	0.022	17.28	3407	0.811	0.545	<0.029	<0.009
2019-SV-013-Circulo A-ef - 2	3.5	<0.9	0.040	19.6	3069	0.0691	0.89	<0.026	<0.01
2019-SV-013-Circulo B-ef - 1	5.04	<0.9	0.046	10.4	4212	0.483	0.75	<0.027	<0.009
2019-SV-013-Circulo B-ef - 2	3.36	<0.90	0.026	32.7	4026	0.172	0.65	<0.029	<0.009
2019-SV-013-Circulo C-ef - 1	4.67	<0.78	0.03	5.78	3170	0.39	0.65	<0.028	<0.009
2019-SV-013-Circulo C-ef - 2	5.11	<0.88	0.04	12.85	3255	0.36	0.45	<0.027	<0.01
2019-SV-014-Circulo A-ef - 1	3.4	1.0	0.052	14.4	2274	0.1280	0.27	<0.027	<0.009
2019-SV-014-Circulo A-ef - 2	3.22	<0.8	0.031	25.58	3364	0.91	0.375	<0.027	<0.009
2019-SV-014-Circulo B-ef - 1	3.48	1.2	0.040	32.1	3058	0.77	1.12	<0.035	<0.012
2019-SV-014-Circulo B-ef - 2	3.43	<0.79	0.059	14.8	2920	0.189	0.37	<0.029	<0.009
2019-SV-014-Circulo C-ef - 1	3.91	<0.8	0.028	21.94	3440	1.201	2.48	0.033	<0.008
2019-SV-014-Circulo C-ef - 2	3.65	1.0	<0.025	13.8	3645	0.950	1.14	<0.030	<0.0089
2019-SV-015A-Circulo A-ef - 1	5.82	<1.7	0.07	105.6	5965	8.6	2.7	<0.05	<0.017
2019-SV-015A-Circulo A-ef - 2	139.8	<0.9	0.101	761	7783	0.26	0.321	<0.027	<0.010
2019-SV-015A-Circulo B-ef - 1	12.2	<1.3	0.045	1959	6361	0.54	2.14	<0.04	<0.014
2019-SV-015A-Circulo B-ef - 2	10.70	<0.9	0.039	2585	7192	0.0084	0.29	<0.027	<0.009
2019-SV-015A-Circulo B-ef - 3	6.04	<0.9	<0.025	590	5704	9.96	4.3	<0.026	<0.009
2019-SV-015A-Circulo C-ef - 1	82.1	<1.2	0.073	205	9924	0.076	0.46	<0.040	<0.012
2019-SV-015A-Circulo D-ef - 1	17.6	<1.5	<0.04	1335	6254	2.640	0.40	<0.048	<0.014
2019-SV-015A-Circulo D-ef - 2	6.56	<0.9	0.044	3029	4281	0.469	0.321	<0.030	<0.008
2019-SV-015A-Circulo D-ef - 3	3.7	1.69	<0.027	107	3888	18.06	8.67	<0.034	<0.011
2019-SV-015A-Circulo E-ef - 1	12.8	<1.1	0.072	414	4230	8.13	5.84	0.53	<0.011
2019-SV-015A-Circulo E-ef - 2	11.1	<0.9	0.053	847	5632	1.3	0.92	0.071	<0.009
2019-SV-015A-Circulo E-ef - 3	7.81	1.43	0.080	867	5126	12.53	16.5	<0.026	<0.007
2019-SV-015B-Circulo A-ef - 1	6.15	<0.8	0.028	627.4	4641	2.21	1.04	0.351	<0.008
2019-SV-015B-Circulo A-ef - 2	3.9	<1	0.044	15.4	4697	3.750	0.34	<0.029	<0.011
UQAC-FeS-1 - 2	1435.681	352.0323	70.36667	221.5742	2.547243	7.455243	176.2674	56.49376	66.90521
GSD-1G - 2	45.65126	2.936631	38.88364	23.91635	36.16809	30.09857	30.75554	30.89301	3.652923
NIST610 - 2	410.7554	150.2683	569.1629	336.1174	454.5162	426.1859	499.0557	429.705	22.91118
2019-SV-015B-Circulo A-ef - 3	85	<0.9	0.032	1563	8253	1.241426	0.70	<0.03	<0.0090

Label	As75	Se77	Mo95	Ag107	Cd111	In115	Sn118	Sb121	Au197
2019-SV-015B-Circulo B-ef- 1	3.83	1.05	<0.03	30.1	4805	4.493872	0.277	<0.03	<0.009
2019-SV-015B-Circulo B-ef - 2	4.0	<1.1	<0.03	14	3817	4.994189	0.223	<0.036	<0.01
2019-SV-015B-Circulo B-ef - 3	3.96	<1.0	0.052	21.9	4497	3.85458	0.44	<0.027	<0.009
2019-SV-015B-Circulo B-ef - 4	3.8	1.00	0.04	27.2	4356	3.762377	0.28	<0.03	0.0087
2019-SV-015B-Circulo B-ef- 5	4.8	<1.0	0.21	46.1	4727	5.822238	1.44	<0.03	<0.01
2019-SV-015B-Circulo B-ef-2 - 1	3.79	<0.90	0.055	43.2	3489	8.189949	0.64	<0.024	<0.008
2019-SV-015B-Circulo C-ef - 1	3.52	1.4	<0.036	8.74	4982	3.383163	0.324	<0.045	<0.011
2019-SV-015B-Circulo C-ef - 2	20.4	1.22	0.05	1121	7569	7.159863	2.15	1.24	<0.01
2019-SV-015B-Circulo C-ef - 3	173	<0.9	0.044	568	7180	2.621556	0.31	1.795	<0.009
2019-SV-016-Circulo A-ef - 1	64.3	1.0	<0.024	13.8	534	<0.0059	0.256	<0.027	<0.008
2019-SV-016-Circulo A-ef - 2	389	1.3	1.54	16.9	990	0.655	7.72	2.27	0.0096
2019-SV-016-Circulo B-ef - 1	167	<0.8	0.030	16.6	1023	<0.0057	0.259	<0.028	<0.007
2019-SV-016-Circulo D-ef - 1	182.8	<0.8	0.03	15.2	1241	0.207	2.18	0.06	<0.01
2019-SV-016-Circulo D-ef - 1	28.4	<1.1	<0.04	7.04	185.0	<0.008	0.299	0.036	<0.010
2019-SV-016-Circulo E-ef - 2	49.4	1.06	0.021	9.88	408	<0.007	0.203	<0.024	<0.008
2019-SV-016-Circulo E-ef - 3	7.7	<0.7	<0.02	7.06	290	<0.0059	0.27	<0.023	<0.01
2019-SH-31-Circulo A-ef - 1	23.86	1.12	<0.038	376	5824	<0.01	0.19	92.80	<0.011
2019-SH-31-Circulo A-ef - 2	83.6	<0.8	0.065	7.0	4309	<0.0068	0.27	292.45	<0.008
2019-SH-31-Circulo A-ef - 3	26	<1.2	0.081	267	2425	<0.01	0.24	62.14	<0.01
2019-SH-31-Circulo A-ef - 4	5.03	<0.77	<0.027	695	4402	0.006	0.18	7.41	<0.006
2019-SH-31-Circulo B-ef - 1	158.7	<0.79	0.5	6.7	3836	<0.0069	0.246	407	<0.0066
2019-SH-31-Circulo B-ef - 2	32.84	<0.8	<0.027	954	4685	<0.0077	0.169	129.34	<0.006
2019-SH-31-Circulo B-ef - 3	8.17	<0.8	<0.025	1600	3061	0.008	0.17	22.18	<0.006
2019-SH-31-Circulo C-ef - 1	13.6	<0.8	<0.024	1469	3010	<0.0089	0.207	44.66	<0.007
UQAC-FeS-1 - 3	1006.286	288.869	61.17564	160.55	4.653993	9.427526	148.4842	50.69865	26.57877
GSD-1G - 3	46.109	3.361733	40.72351	25.28046	37.15404	32.53051	32.63123	32.91574	3.093279
NIST610 - 3	346.6366	121.3367	487.8669	293.4119	399.1513	368.9715	422.5711	362.4977	16.35111
2019-SH-31-Circulo C-ef - 2	15.35	<0.7	0.036	1248	3385	<0.0068	0.179	51.3	<0.0060
2019-SH-31-Circulo C-ef - 3	40	<0.77	0.062	466	4781	<0.0069	0.241	151	<0.008
2019-SH-31-Circulo C-ef - 4	6.5	<0.78	<0.027	648.4	6274	<0.0068	0.21	10.6	<0.008
2019-SH-120-Circulo A-ef - 1	8.04	<0.8	<0.026	54.4	2481	<0.006	0.203	50.16	<0.007
2019-SH-120-Circulo A-ef - 2	35	<0.8	0.027	11.7	2295	<0.007	0.179	188	<0.0079

Label	As75	Se77	Mo95	Ag107	Cd111	In115	Sn118	Sb121	Au197
2019-SH-120-Circulo A-ef - 3	8.13	1.02	0.044	25.9	1501	<0.0056	0.156	129.77	<0.0068
2019-SH-120-Circulo B-ef - 1	4.18	<0.9	<0.037	14.1	2532	<0.0077	0.285	6.28	<0.009
2019-SH-120-Circulo B-ef - 2	14.50	<0.77	<0.026	51.8	2090	<0.0067	0.272	143.56	<0.0069
2019-SH-120-Circulo B-ef - 3	38.4	<0.68	<0.025	19.6	1710	<0.006	0.256	412	<0.008
2019-SH-167-Circulo A-ef - 1	13.20	<0.7	<0.024	431	7687	<0.0060	0.299	53	<0.0066
2019-SH-167-Circulo A-ef - 2	3.97	<0.7	0.030	478	4327	<0.007	0.250	5.74	<0.007
2019-SH-167-Circulo A-ef - 3	5.36	<0.8	0.034	462	4502	0.0281	0.28	12.27	<0.009
2019-SH-167-Circulo A-ef - 4	17.4	<0.88	<0.034	1119	3907	<0.0078	0.23	51.66	<0.01
2019-SH-167-Circulo B-ef - 1	9.25	<0.90	<0.037	30.2	2634	0.023	0.316	20.4	<0.0099
2019-SH-167-Circulo B-ef - 2	45.3	<0.7	<0.026	60.9	3428	0.16	0.151	150	<0.008
2019-SH-167-Circulo B-ef - 3	18.2	1.16	<0.023	763	7048	<0.006	0.232	80.79	<0.008
2019-SH-167-Circulo B-ef - 4	5.55	<0.89	<0.029	517	5969	<0.008	0.256	7.5	0.015
2019-SH-167-Circulo C-ef - 1	896	0.8	0.033	184.9	4032	1.15	0.25	2238	<0.0078
2019-SH-167-Circulo C-ef - 2	5.42	0.9	<0.029	320	7265	<0.0059	0.26	6.66	<0.0078
2019-SH-167-Circulo C-ef - 3	7.7	<0.69	<0.027	512	4936	<0.007	0.20	11.48	<0.009
2019-SH-167-Circulo C-ef - 4	12.58	0.80	<0.027	235	4443	<0.006	0.25	37.1	<0.008
2019-SH-187-Circulo A-ef - 1	18.2	<0.7	<0.029	323	2434	0.0078	0.184	75	<0.0090
2019-SH-187-Circulo A-ef - 2	28.5	1.3	0.023	177	4179	<0.007	0.178	108.53	<0.009
2019-SH-187-Circulo A-ef - 3	5.0	0.99	0.029	5.62	3346	<0.0068	0.174	1.17	<0.009
2019-SH-187-Circulo A-ef - 4	20.98	<0.8	<0.023	36.27	3310	<0.008	0.17	31.29	<0.01
2019-SH-187-Circulo C-ef - 1	18.3	<0.79	0.029	50	3504	2.58	0.27	5.6	<0.01
2019-SH-187-Circulo C-ef - 2	8.3	1.4	<0.028	126.2	3494	<0.0080	0.15	14.62	<0.01
UQAC-FeS-1 - 4	1071.611	321.3558	69.861	159.9763	3.321618	8.47636	154.6069	75.22749	57.10342
GSD-1G - 4	77.72129	<3.7448	68.96516	39.96474	61.12798	50.51281	50.80636	52.88702	6.670429
NIST610 - 4	366.3415	133.8269	509.0149	291.147	427.2041	368.6879	429.5884	377.3628	22.52701
2019-SH-187-Circulo C-ef - 3	62	<0.77	0.180	163	5957	0.033	0.20	100	<0.01
2019-SH-212-Circulo A-ef - 1	7.7	<0.8	<0.027	70.2	3788	0.079	0.517	5.49	<0.009
2019-SH-212-Circulo A-ef - 2	7.81	<0.78	<0.03	326	2134	0.186	4.29	8.25	<0.009
2019-SH-212-Circulo A-ef - 3	6.10	<0.8	<0.029	44	4820	<0.009	0.24	0.070	<0.01
2019-SH-212-Circulo A-ef - 4	12.43	<0.7	0.030	540	2505	0.069	0.557	21.7	0.012
2019-SH-212-Circulo B-ef - 1	14.0	<0.7	0.033	234	5029	0.0195	0.3	22	<0.008
2019-SH-212-Circulo B-ef - 2	7.50	<0.7	<0.026	545	4058	<0.008	0.200	8.32	<0.009

Label	As75	Se77	Mo95	Ag107	Cd111	In115	Sn118	Sb121	Au197
2019-SH-212-Circulo B-ef - 3	7.31	0.74	0.028	604	3400	<0.0067	0.182	5.7	<0.01
2019-SH-212-Circulo B-ef - 4	8.02	<1	<0.04	176	2180	0.57	3.9	5.51	<0.014
SH-227-Circulo B-ef - 1	7.30	0.7	<0.028	356	3652	<0.0077	0.19	4.16	<0.01
SH-227-Circulo B-ef - 2	12.3	<0.7	<0.03	389	4057	0.133	0.265	23.95	<0.01
SH-227-Circulo B-ef - 3	77.0	<0.68	<0.024	73	3829	<0.007	0.22	273	<0.008
SH-227-Circulo A-ef - 1	7.8	<0.80	<0.03	274	3548	<0.009	0.23	3.87	<0.011
SH-227-Circulo A-ef - 2	12.67	0.68	<0.027	495	4270	<0.006	0.202	29.1	<0.009
SH-227-Circulo A-ef - 3	92.9	<0.7	0.062	68	2651	<0.008	0.230	309	<0.0089
NIST610 - 5	387.2298	120.8146	490.3499	294.8799	411.6166	394.4532	430.5995	379.7253	21.59888
GSD-1G - 5	44.38529	<1.7783	34.91097	21.68173	32.89558	29.09856	28.63407	29.27008	3.560179
UQAC-FeS-1 - 5	1272.715	283.7661	61.14817	163.3301	3.174129	7.792146	151.888	74.68137	53.63961

*Values in red color have been discarded in pl

Label	Hg202	Tl205	Pb208	Bi209	2σ uncertainty >	S33	S34	Cr53	Mn55
UQAC-FeS-1 - 1	4.858323	0.013916	1.457488	1.674368		11619.06	11352.73	52.88666	2.814197
GSD-1G - 1	<0.22629	0.025522	0.706017	0.526506		2250.944	1227.299	1.332003	4.387237
NIST610 - 1	0.138133	1.519864	11.09988	9.317545		2736.625	1531.434	6.34974	13.32081
2019-SV-02-Circulo A-ef - 1	5.73	2.38	418	<0.0045		14381	12147	<0.5	1.1
2019-SV-02-Circulo A-ef - 2	4.14	3.36	2084	0.0193		21772	21670	<0.59	1.4
2019-SV-02-Circulo A-ef - 3	5.66	2.71	456	<0.005		11189	9302	<0.7	1.5
2019-SV-02-Circulo B-ef - 1	4.79	3.02	641	<0.005		19226	20940	<0.7	1.6
2019-SV-02-Circulo B-ef - 2	3.46	3.00	714	0.0084		13810	14692	<0.55	1
2019-SV-02-Circulo B-ef - 3	2.52	2.55	540	<0.007		17737	20940	<0.79	1.2
2019-SV-02-Circulo C-ef - 1	3.50	3.034	551	0.0088		14428	13257	<0.5	2
2019-SV-04-Circulo A-ef - 1	3.35	4.28	690	0.007		15317	14237	<0.5	4
2019-SV-04-Circulo A-ef - 2	3.43	7.0	1103	0.0058		14554	13169	<0.5	3
2019-SV-04-Circulo B-ef - 1	3.65	4.5	675	0.0066		13451	12975	<0.5	2.9
2019-SV-04-Circulo B-ef - 2	3.16	6.6	980	0.007		14854	14253	<0.56	4.6
2019-SV-04-Circulo B-ef - 3	3.13	6.8	915	<0.0038		13873	13128	<0.5	2.4
2019-SV-04-Circulo C-ef - 2	3.31	2.46	527	<0.0037		16850	14785	<0.5	1.2
2019-SV-04-Circulo C-ef - 3	4.21	3.08	706	<0.0047		12171	10444	<0.6	1
2019-SV-04-Circulo D-ef - 1	2.50	2.54	518	<0.004		18439	14523	<0.58	1.3
2019-SV-04-Circulo D-ef - 3	4.12	2.9	478	<0.0047		10318	8867	<0.8	1.1
2019-SV-06A-Circulo A-ef - 1	3.48	1.493	490	0.0041		14059	13680	<0.58	3.9
2019-SV-06A-Circulo A-ef - 2	3.35	0.821	148	<0.0034		15408	14552	<0.5	2.5
2019-SV-06A-Circulo A-ef - 3	4.12	1.330	150	<0.004		19775	17551	<0.6	4.8
UQAC-FeS-1 - 2	88.49832	0.213333	88.18664	127.2886		11287.52	7164.307	29.8147	2.33755
GSD-1G - 2	<0.5353	1.788556	94.42064	70.48838		6817.574	3883.234	3.02094	7.705075
NIST610 - 2	<0.22995	66.78783	433.1019	397.3177		2854.58	1818.243	7.456039	11.92255
2019-SV-06A-Circulo B-ef - 3	3.58	0.489	75.1	<0.004		15909	13509	<0.5	1.3
2019-SV-06A-Circulo B-ef - 4	3.57	0.884	75	<0.0037		13329	11799	<0.50	1
2019-SV-06A-Circulo C-ef - 1	3.27	0.41	90.6	<0.003		13356	12807	<0.56	1.4
2019-SV-06A-Circulo C-ef - 2	3.37	2.07	130.9	<0.0034		14009	12677	<0.55	4.4
2019-SV-06A-Circulo C-ef - 3	3.97	0.85	95	<0.0038		16377	15959	<0.5	4
2019-SV-06B-Circulo A-ef - 1	3.56	1.518	74.6	0.0039		15973	15001	<0.5	1.6
2019-SV-06B-Circulo A-ef - 2	3.07	0.823	379	<0.0037		14093	13008	<0.5	1.6
2019-SV-06B-Circulo A-ef - 3	3.32	2.401	298	<0.003		14955	14299	<0.5	0.9

Label	Hg202	Tl205	Pb208	Bi209	2σ uncertainty >	S33	S34	Cr53	Mn55
2019-SV-06B-Circulo A-ef - 4	3.58	0.862	1195	0.005		14399	13858	<0.55	1
2019-SV-06B-Circulo B-ef - 1	3.40	2.50	164.3	<0.0029		12611	11049	<0.5	1.7
2019-SV-06B-Circulo B-ef - 2	4.40	1.92	109	<0.0045		12181	13832	<0.8	1.9
2019-SV-06B-Circulo B-ef - 3	3.33	3.246	285.4	0.0038		18087	16435	<0.56	3.0
2019-SV-06B-Circulo C-ef - 2	3.38	0.269536	25.4	<0.003		12440	11801	<0.5	2.3
2019-SV-06B-Circulo C-ef - 3	3.16	0.929	86.9	<0.0038		16219	15751	<0.5	2.3
2019-SV-07-Circulo A-ef - 1	3.51	0.325	4.89	<0.0037		15110	14942	<0.56	<1.2
2019-SV-07-Circulo A-ef - 2	3.93	0.036	20.74	<0.0037		14077	12600	<0.5	1
2019-SV-07-Circulo A-ef - 3	3.87	1.00	181	<0.0033		15504	14731	<0.55	2.2
2019-SV-07-Circulo A-ef - 4	3.43	0.67	34.7	<0.0033		17445	15745	<0.5	1.2
2019-SV-07-Circulo B-ef - 1	3.88	0.244	29.8	<0.0039		17690	14280	<0.55	1
2019-SV-07-Circulo B-ef - 2	3.67	0.73	312.1	0.0071		12314	11064	<0.5	3.0
2019-SV-07-Circulo B-ef - 3	3.28	1.344	2210	0.0148		11959	11107	<0.50	3
2019-SV-07-Circulo B-ef - 4	5.40	1.443	2484	0.0197		5863	7735	<0.80	2.6
2019-SV-07-Circulo C-ef - 1	4.0	0.89	158	<0.003		18305	18268	<0.55	3.8
2019-SV-07-Circulo C-ef - 2	2.87	0.30	64	<0.0034		9851	11854	<0.58	1.2
2019-SV-07-Circulo C-ef - 3	2.84	1.2	41.1	<0.005		15292	13363	<0.7	1.3
UQAC-FeS-1 - 3	58.91661	0.234542	89.39764	127.1556		12717.88	14695.79	10.83359	3.515829
GSD-1G - 3	<0.28363	0.852424	49.94503	34.25721		3245.487	1600.902	1.107181	4.715723
NIST610 - 3	<0.28087	72.80856	541.0458	468.8936		3280.122	1982.255	6.073441	11.97732
2019-SV-08A-Circulo A-ef - 2	3.38	0.374	79.3	<0.0033		15216	14191	<0.57	1.8
2019-SV-08A-Circulo A-ef - 3	3.15	0.566	409	0.0040		11188	11062	<0.5	2
2019-SV-08A-Circulo A-ef - 4	2.84	1.766	1323	0.0126		12043	12009	<0.5	2.8
2019-SV-08A-Circulo C-ef - 1	3.54	0.518	362.1	0.0029		12965	12655	<0.5	3
2019-SV-08A-Circulo C-ef - 2	2.6	0.62	415.6	<0.0034		13488	12613	<0.48	3
2019-SV-08A-Circulo C-ef - 3	2.85	1.658999	504	0.0046		13793	14563	<0.5	1.6
2019-SV-08A-Circulo D-ef - 1	2.05	0.50	160.5	<0.004		18946	14208	<0.69	1.6
2019-SV-08A-Circulo D-ef - 2	2.73	0.682	1757	0.0108		12694	11947	<0.5	1.5
2019-SV-08A-Circulo D-ef - 3	3.0	0.403	1488	0.010396		14265	13038	<0.5	1.5
2019-SV-08B-Circulo A-ef - 1	3.21	0.306	80.9	<0.0038		14019	14165	<0.58	8.9
2019-SV-08B-Circulo A-ef - 2	3.12	0.258	19.00	<0.0033		13029	12353	<0.56	0.89
2019-SV-08B-Circulo B-ef - 1	3.14	0.729	121.2	<0.003		14381	14199	<0.56	2.3

Label	Hg202	Tl205	Pb208	Bi209	2σ uncertainty >	S33	S34	Cr53	Mn55
2019-SV-08B-Circulo B-ef - 3	3.16	0.933	616	0.0049		12167	12268	<0.55	2
2019-SV-08B-Circulo C-ef - 2	3.07	0.267	1049	0.0088		14425	13314	<0.56	1.1
2019-SV-08B-Circulo C-ef - 3	3.30	0.414	55.7	<0.0034		11755	11099	<0.58	0.9
2019-SV-08B-Circulo D-ef - 1	3.62	0.219	576	0.0056		14978	14539	<0.56	1.4
2019-SV-08B-Circulo D-ef - 2	3.91	0.654	85.5	<0.003		11653	10596	<0.5	1.2
2019-SV-08B-Circulo D-ef - 3	8.59	0.748	113.9	<0.0034		14998	13906	<0.5	2.4
2019-SV-08B-Circulo D-ef - 4	4.32	0.961	116	<0.003		19891	17703	<0.59	1.2
2019-SV-08B-Circulo E-ef - 1	3.60	0.305	161.1	<0.0035		15648	14079	<0.6	1.8
2019-SV-08B-Circulo E-ef - 2	4.27	0.754	60.0	<0.003		13211	10786	<0.6	1.3
UQAC-FeS-1 - 4	29.76147	0.226224	84.18787	104.5932		8472.074	11205.14	7.143192	1.706424
GSD-1G - 4	<0.3004	1.031229	59.853	39.9531		3135.089	1999.041	1.658457	5.406654
NIST610 - 4	<0.25657	75.91247	521.0936	436.852		2613.641	1529.975	6.332067	12.89135
2019-SV-08B-Circulo E-ef - 3	3.92	0.59	97.7	0.009		19784	18914	<0.58	4.4
2019-SV-08B-Circulo E-ef - 4	3.52	0.462	41.0	<0.0035		14566	14136	<0.5	0.9
2019-SV-09-Circulo A-ef - 1	4.26	0.2313	62.9	<0.0034		15087	12727	<0.5	1.5
2019-SV-09-Circulo A-ef - 2	3.7	0.804	53.9	<0.0034		12823	12247	<0.55	1.0
2019-SV-09-Circulo A-ef - 3	4.86	0.436	23.0	<0.0033		15379	14678	<0.5	1.3
2019-SV-09-Circulo A-ef - 4	3.97	0.255	51.5	<0.0038		14942	13109	<0.55	1.4
2019-SV-09-Circulo B-ef - 1	2.85	0.74	38.6	<0.0038		15262	16063	<0.58	5.6
2019-SV-09-Circulo B-ef - 2	3.02	0.426	39.2	<0.003		13745	13110	<0.5	1
2019-SV-09-Circulo B-ef - 3	2.74	0.975	270	0.0041		12068	10172	<0.50	2
2019-SV-09-Circulo B-ef - 4	3.4	3.449	315	0.0049		14307	12828	<0.6	1.7
2019-SV-09-Circulo C-ef - 1	4.24	2.31	272	<0.005		15521	15349	<0.8	3.4
2019-SV-09-Circulo C-ef - 3	3.19	0.972	140.4	<0.0035		15819	14650	<0.5	2.3
2019-SV-011A-Circulo B-ef - 1	2.52	1.21	417	0.0040		15024	13740	0.28	1.3
2019-SV-011A-Circulo B-ef - 2	2.17	0.645	238.7	<0.0028		12245	11318	0.6	2.9
2019-SV-011A-Circulo B-ef - 3	2.43	1.407	180	0.0040		13215	12263	<0.5	1.4
2019-SV-011A-Circulo B-ef - 4	2.67	0.821	126.1	<0.0036		12888	12514	<0.5	1
2019-SV-011A-Circulo C-ef - 1	2.07	0.329	85.9	<0.0034		12360	11796	<0.47	2.3
2019-SV-011A-Circulo C-ef - 2	2.1	0.421	64	<0.0035		12357	10880	<0.48	1.2
2019-SV-011A-Circulo C-ef - 3	2.18	0.276	67.9	0.0037		13004	11180	<0.49	1.6
2019-SV-011A-Circulo C-ef - 4	2.12	0.34	50.0	<0.0039		12023	10461	<0.49	1.5

Label	Hg202	Tl205	Pb208	Bi209	2σ uncertainty >	S33	S34	Cr53	Mn55
2019-SV-011B-Circulo A-ef - 1	2.01	0.230	25.65	<0.0036		13807	13849	<0.5	1.2
2019-SV-011B-Circulo A-ef - 2	2.30	0.589	165.6	0.0055		15277	14008	<0.5	1.5
2019-SV-011B-Circulo A-ef - 3	2.04	0.367	106	<0.0028		11097	10995	<0.47	1.5
2019-SV-011B-Circulo A-ef - 4	1.94	0.544	85.8	<0.003		11105	9425	<0.50	2
2019-SV-011B-Circulo A-ef - 5	2.46	0.364	756	<0.0036		12279	11328	<0.44	1.6
UQAC-FeS-1 - 5	20.80673	0.229083	18.46811	130.657		7853.16	8026.154	4.656369	3.226585
GSD-1G - 5	<0.66821	2.1503	24.68684	92.74184		4681.138	2960.324	2.763852	14.4446
NIST610 - 5	<0.53314	145.0636	207.6911	955.4681		3246.232	1936.163	12.55245	30.22951
2019-SV-011B-Circulo B-ef - 2	4.63	0.86	41.5	<0.006		16543	15561	<1	5.5
2019-SV-011B-Circulo C-ef - 1	4.73	1.576	24.6	<0.007		17903	16736	<1	2.3
2019-SV-011B-Circulo C-ef - 2	4.45	1.158	46	<0.007		22946	22298	<1	4.6
2019-SV-011B-Circulo C-ef - 3	4.0	1.12	45.7	<0.0067		19764	19279	<0.9	2.8
2019-SV-011B-Circulo D-ef - 1	4.29	1.194	22.43	<0.0056		17767	16298	<0.89	2
2019-SV-011B-Circulo D-ef - 2	3.93	0.728	38.88	<0.007		19319	17935	<0.90	2.7
2019-SV-011B-Circulo D-ef - 3	3.69	0.639	41.21	0.006		19066	16644	<0.9	2.9
2019-SV-011C-Circulo A-ef - 1	4.00	0.630	12.98	<0.006		16619	16082	<0.8	2.2
2019-SV-011C-Circulo B-ef - 2	3.98	1.338	114.0	0.0050		15796	15268	<0.8	2.1
2019-SV-011C-Circulo C-ef - 1	3.7	1.211	47.5	<0.0060		17904	14884	<0.8	2.0
2019-SV-011C-Circulo C-ef - 2	3.55	0.758	58.2	<0.0046		15500	12799	<0.77	2.2
2019-SV-012A-Circulo A-ef - 1	4.36	2.3	347	<0.006		21997	21523	<1	6
2019-SV-012A-Circulo A-ef - 2	2.64	0.915	37.8	<0.0039		15262	13295	<0.8	2.9
2019-SV-012A-Circulo B-ef - 1	4.42	0.65	26.6	<0.0056		12106	11504	<0.8	1.6
2019-SV-012A-Circulo C-ef - 1	3.19	0.76	71	<0.005		17193	17074	<0.7	3.4
2019-SV-012A-Circulo C-ef - 2	3.11	1.28	160.6	<0.0044		17058	16392	<0.69	3.7
2019-SV-012A-Circulo D-ef - 1	3.26	1.456	1111	0.0147		14381	12091	<0.67	4
2019-SV-012A-Circulo D-ef - 2	3.01	1.53	207	0.0040		15112	14536	<0.68	5
2019-SV-012B-Circulo A-ef - 1	3.59	2.344	338.4	0.0055		14332	13086	<0.67	2.3
2019-SV-012B-Circulo A-ef - 2	3.65	0.87	48.7	<0.0036		15471	13156	<0.68	2.9
2019-SV-012B-Circulo B-ef - 1	3.22	0.563	60.8	<0.0046		14015	13042	<0.7	2.6
2019-SV-012B-Circulo B-ef - 2	2.4	0.478	51.6	<0.003		14534	12390	<0.57	1
NIST610 - 6	<0.28146	78.62593	440.5117	472.157		3438.942	1441.233	6.675343	14.27253
GSD-1G - 6	<0.43091	1.518338	73.5531	58.6088		3960.157	2288.105	1.788182	9.729531
UQAC-FeS-1 - 6	22.96028	0.277929	87.69799	120.4218		21586.13	20707.84	10.21342	2.90751

Label	Hg202	Tl205	Pb208	Bi209	2σ uncertainty >	S33	S34	Cr53	Mn55
UQAC-FeS-1 - 1	29.61332	0.251832	91.30904	123.469		14743.22	12547.92	11.39763	4.56727
GSD-1G - 1	<0.41272	1.280688	66.99994	44.31748		4729.081	2696.384	2.200107	6.489686
NIST610 - 1	0.403006	79.52767	532.4584	443.7793		3214.381	1957.922	8.472573	12.55053
2019-SV-013-Circulo A-ef - 1	5.20	1.6	117	<0.004		12307	11263	<0.5	14
2019-SV-013-Circulo A-ef - 2	4.74	5.12	314	<0.0039		12766	11771	<0.56	10
2019-SV-013-Circulo B-ef - 1	5.16	8.86	1345	0.0072		13006	11820	<0.56	15
2019-SV-013-Circulo B-ef - 2	4.54	2.19	117	<0.0037		14668	14367	<0.56	14
2019-SV-013-Circulo C-ef - 1	4.89	9.2	1193	0.0087		13121	13841	<0.5	9.9
2019-SV-013-Circulo C-ef - 2	4.76	8.82	1186.997	0.0103		19170	18862	<0.6	17
2019-SV-014-Circulo A-ef - 1	4.13	3.6	817	0.0064		13818	13598	<0.56	15
2019-SV-014-Circulo A-ef - 2	4.30	1.25	123	<0.0038		13126	12610	<0.5	10
2019-SV-014-Circulo B-ef - 1	5.19	7.4	695	0.0061		13910	12615	<0.68	12
2019-SV-014-Circulo B-ef - 2	4.13	3.73	634	0.005		14115	13965	<0.5	13
2019-SV-014-Circulo C-ef - 1	4.38	7.98	738	0.005		13595	13497	<0.5	14
2019-SV-014-Circulo C-ef - 2	4.75	7.55	730	0.006098		12726	12029	<0.59	12
2019-SV-015A-Circulo A-ef - 1	7.33	0.887	48.8	<0.0066		6880	7850	<1	11
2019-SV-015A-Circulo A-ef - 2	6.16	25	319	<0.0039		17214	16460	<0.58	40
2019-SV-015A-Circulo B-ef - 1	4.41	6.4	1092	<0.0060		30114	27641	<0.8	33
2019-SV-015A-Circulo B-ef - 2	4.05	4.45	14.18	0.004		17301	16008	<0.57	24
2019-SV-015A-Circulo B-ef - 3	5.74	4.9	33.6	<0.004		18839	17373	<0.58	20
2019-SV-015A-Circulo C-ef - 1	5.08	8.28	162	<0.0049		9525	11031	<0.8	31
2019-SV-015A-Circulo D-ef - 1	6.24	8.82	277	<0.006		9295	6573	<0.9	18
2019-SV-015A-Circulo D-ef - 2	5.54	6.77	12.6	<0.0035		15051	13555	<0.56	14
2019-SV-015A-Circulo D-ef - 3	6.81	0.0388	0.137	<0.004		9790	10567	<0.7	5
2019-SV-015A-Circulo E-ef - 1	4.54	1.63	31.2	<0.0047		13338	14312	<0.68	7.8
2019-SV-015A-Circulo E-ef - 2	4.8	4.22	20.7	<0.004		18176	15685	<0.57	48
2019-SV-015A-Circulo E-ef - 3	5.85	3.7	49	<0.003		14318	12600	<0.5	20
2019-SV-015B-Circulo A-ef - 1	5.29	0.279	5.0	<0.0034		14514	13426	<0.57	4.9
2019-SV-015B-Circulo A-ef - 2	9.13	0.009	0.098	<0.0044		13343	12820	<0.6	8
UQAC-FeS-1 - 2	32.98033	0.259305	101.6607	130.7737		16633.01	15435.32	6.677651	3.564268
GSD-1G - 2	<0.30102	0.808363	47.55847	32.52283		3960.84	1952.246	1.291358	5.059887
NIST610 - 2	0.397328	76.1518	554.5864	477.5372		4190.736	2718.842	9.117533	16.37566
2019-SV-015B-Circulo A-ef - 3	4.32	9.64	171.6	<0.0040		15153	14519	<0.5	21

Label	Hg202	Tl205	Pb208	Bi209	2σ uncertainty >	S33	S34	Cr53	Mn55
2019-SV-015B-Circulo B-ef- 1	8.43	0.010	4.24	<0.0036		18239	17584	0.33	10
2019-SV-015B-Circulo B-ef - 2	8.93	<0.005	1.45	<0.0046		22718	20680	<0.7	6.7
2019-SV-015B-Circulo B-ef - 3	8.50	0.0227	6.3	<0.0038		15727	15561	<0.59	7.7
2019-SV-015B-Circulo B-ef - 4	8.54	0.0097	8.29	<0.0035		15823	16150	<0.5	6.6
2019-SV-015B-Circulo B-ef- 5	8.35	0.15	76	0.005		25268	22837	<0.6	5.9
2019-SV-015B-Circulo B-ef-2 - 1	5.17	0.018	0.216	<0.003		16671	16191	<0.55	4.9
2019-SV-015B-Circulo C-ef - 1	6.07	0.0196	0.263	<0.004		11368	7721	<0.77	4.7
2019-SV-015B-Circulo C-ef - 2	5.11	14.9	84	0.0055		16933	16662	<0.57	30
2019-SV-015B-Circulo C-ef - 3	4.11	3.44	42.48	<0.003		16983	16359	<0.56	15
2019-SV-016-Circulo A-ef - 1	3.15	1.205	207.9	<0.0033		15980	14284	<0.49	2.7
2019-SV-016-Circulo A-ef - 2	6.35	3.25	845	0.0229		14073	16953	0.50	23
2019-SV-016-Circulo B-ef - 1	3.19	2.60	850	0.0069		15438	14456	<0.47	3.4
2019-SV-016-Circulo D-ef - 1	3.24	3.1	785	0.005		16495	14899	0.3	2.8
2019-SV-016-Circulo D-ef - 1	4.64	0.419	200	<0.0037		12008	11101	<0.7	1.6
2019-SV-016-Circulo E-ef - 2	3.28	0.955	220	0.0045		13165	13353	<0.49	1.4
2019-SV-016-Circulo E-ef - 3	3.50	0.57	95.7	<0.0029		13374	11912	<0.47	1.1
2019-SH-31-Circulo A-ef - 1	771.5	1.023	65.1	<0.004		10264	8839	<0.7	<1.7
2019-SH-31-Circulo A-ef - 2	3.0	21.5	423	0.005903		14607	14890	<0.5	1.2
2019-SH-31-Circulo A-ef - 3	66	2.52	68.6	<0.0055		13355	10919	<0.79	2.4
2019-SH-31-Circulo A-ef - 4	233.4	1.49	10.40	<0.003		14293	13486	<0.48	0.8
2019-SH-31-Circulo B-ef - 1	3.68	34.8	609	0.0045		13573	13565	<0.49	1
2019-SH-31-Circulo B-ef - 2	442	4.78	92.3	<0.003		11705	11652	<0.46	<1.2
2019-SH-31-Circulo B-ef - 3	187.5	4.62	35.4	<0.0037		11812	10458	<0.50	<1.1
2019-SH-31-Circulo C-ef - 1	301	3.78	43.1	0.0034		17798	17118	<0.55	0.9
UQAC-FeS-1 - 3	33.96819	0.229455	78.08301	109.7734		22565.27	20401.45	6.826187	15.44808
GSD-1G - 3	<0.36257	0.756775	47.76685	34.35047		3827.602	1683.272	1.526448	4.864131
NIST610 - 3	<0.3258	60.12805	455.0436	408.1587		2901.324	1882.812	6.18101	12.75221
2019-SH-31-Circulo C-ef - 2	327.5	4.15	50.2	<0.0037		12609	11981	<0.48	2.5
2019-SH-31-Circulo C-ef - 3	486	1.54	80	<0.0033		12831	10398	<0.5	1.0
2019-SH-31-Circulo C-ef - 4	316.0	0.45	11.70	<0.0035		13801	14431	<0.5	<1.2
2019-SH-120-Circulo A-ef - 1	411	0.464	40.9	<0.0030		10517	10580	<0.5	1.0
2019-SH-120-Circulo A-ef - 2	561.9	4.46	189	<0.003		16546	15234	<0.5	1.6

Label	Hg202	Tl205	Pb208	Bi209	2σ uncertainty >	S33	S34	Cr53	Mn55
2019-SH-120-Circulo A-ef - 3	184	1.928	53.4	<0.0029		11951	10638	<0.47	0.89
2019-SH-120-Circulo B-ef - 1	655	0.037	4.4	<0.0045		10458	9008	<0.6	<1.4
2019-SH-120-Circulo B-ef - 2	408	2.427	140	<0.003		16153	15084	<0.48	0.89
2019-SH-120-Circulo B-ef - 3	451	6.7	349.5	0.0050		13456	11736	<0.5	1.4
2019-SH-167-Circulo A-ef - 1	50.1	1.53	57.92	<0.0030		14131	11041	<0.49	0.8
2019-SH-167-Circulo A-ef - 2	41.61	0.975	4.69	<0.0029		12712	11997	<0.49	<1.1
2019-SH-167-Circulo A-ef - 3	24.44	1.202	10.89	0.0036		13911	12356	<0.5	<1.2
2019-SH-167-Circulo A-ef - 4	112.2	5.46	54.3	<0.0047		15319	13857	<0.6	<1.4
2019-SH-167-Circulo B-ef - 1	117.0	0.271	8.94	<0.0039		12014	10605	<0.6	<1.4
2019-SH-167-Circulo B-ef - 2	81.0	0.159	56	0.0036		14365	12164	<0.5	<1.2
2019-SH-167-Circulo B-ef - 3	7.8	10.1	68	<0.0029		13742	12163	<0.45	<1
2019-SH-167-Circulo B-ef - 4	10.84	1.72	10.94	<0.0050		10309	11369	<0.6	<1.4
2019-SH-167-Circulo C-ef - 1	419.6	0.431	226.6	<0.003		13288	11938	0.26	<1
2019-SH-167-Circulo C-ef - 2	12.05	1.333	9.21	<0.0035		14678	13639	<0.49	<1.1
2019-SH-167-Circulo C-ef - 3	8.74	2.16	9.2	<0.0030		16087	14434	<0.5	<1.1
2019-SH-167-Circulo C-ef - 4	113	1.442	15.44	<0.0029		13959	12634	<0.48	<1
2019-SH-187-Circulo A-ef - 1	73.7	1.072	56.5	<0.0033		15367	14192	<0.48	0.9
2019-SH-187-Circulo A-ef - 2	303	1.25	67	<0.0029		15121	13987	<0.49	0.8
2019-SH-187-Circulo A-ef - 3	146	0.0177	1.854	<0.004		13975	13546	<0.5	0.9
2019-SH-187-Circulo A-ef - 4	179.0	0.77	52.7	0.0031		14656	14328	<0.5	0.89
2019-SH-187-Circulo C-ef - 1	121	0.445	18.2	<0.0035		18625	16915	<0.5	0.7
2019-SH-187-Circulo C-ef - 2	93.1	0.216	35.44	<0.0036		15989	14299	<0.5	0.89
UQAC-FeS-1 - 4	67.87174	0.226343	81.03374	110.6245		11017.17	11052.31	9.602294	1.771052
GSD-1G - 4	<0.60405	1.446826	75.87552	57.07206		5573.241	3567.008	1.959759	8.463572
NIST610 - 4	<0.33224	67.96041	458.9545	435.8086		3106.676	1737.279	5.686705	11.27349
2019-SH-187-Circulo C-ef - 3	780	1.66	75	<0.004		16139	15227	<0.5	<1.1
2019-SH-212-Circulo A-ef - 1	158.6	0.054	2.618	<0.0036		13963	13706	<0.5	<1.1
2019-SH-212-Circulo A-ef - 2	57	0.589	6.54	<0.0035		14855	14434	0.28	<1.1
2019-SH-212-Circulo A-ef - 3	59.4	0.011	0.07	<0.0037		12284	12852	<0.55	0.9
2019-SH-212-Circulo A-ef - 4	45.5	0.591	9.21	<0.003		14744	13089	<0.5	<1.1
2019-SH-212-Circulo B-ef - 1	92.4	0.229	9.5	<0.0036		15745	14402	0.36	0.6
2019-SH-212-Circulo B-ef - 2	49	1.960	14.68	<0.0034		15120	12858	<0.49	<1.1

Label	Hg202	Tl205	Pb208	Bi209	2σ uncertainty >	S33	S34	Cr53	Mn55
2019-SH-212-Circulo B-ef - 3	52.15	1.917	11.35	<0.0035		14518	12880	<0.49	<1.1
2019-SH-212-Circulo B-ef - 4	71	0.343	3.78	<0.005		9344	9372	<0.69	<1.5
SH-227-Circulo B-ef - 1	91.4	0.736	3.5	<0.0029		11753	11106	<0.5	<1.1
SH-227-Circulo B-ef - 2	285	0.61	12.5	<0.004		16899	14176	<0.56	<1.2
SH-227-Circulo B-ef - 3	319	0.207	95	<0.003		14825	13222	<0.49	<1.1
SH-227-Circulo A-ef - 1	91.0	0.457	4.82	<0.0040		12024	11390	<0.59	<1.2
SH-227-Circulo A-ef - 2	77	2.574	32.78	<0.0028		13686	12953	<0.5	<1.1
SH-227-Circulo A-ef - 3	221.6	0.270	79.3	<0.004		14054	13227	<0.50	<1.2
NIST610 - 5	<0.39841	71.72125	476.6675	422.8939		2872.023	1379.946	6.052768	11.63008
GSD-1G - 5	<0.33073	0.824923	42.94114	30.6042		3096.203	1317.917	1.277506	5.051459
UQAC-FeS-1 - 5	52.37054	0.24631	85.60151	109.528		12180.39	12672.93	134.3352	3.120798

*Values in red color have been discarded in pl

Label	Fe57	Co59	Ni62	Cu65	Zn66	Ga71	Ge74	As75	Se77
UQAC-FeS-1 - 1	9176.595	25.60561	740.2362	1032.472	9.135784	0.151528	0.144315	15.64776	8.376115
GSD-1G - 1	1479.241	0.822165	3.562085	4.22294	13.90696	0.561048	0.554312	0.763058	1.349364
NIST610 - 1	23.23421	8.978228	12.22641	16.35417	19.31699	8.652373	7.22233	8.151548	4.036654
2019-SV-02-Circulo A-ef - 1	247	2.2	0.9	<3	19968	0.022	1	2.3	<0.8
2019-SV-02-Circulo A-ef - 2	209	2	<1.7	<4.0	31950	0.026	2.4	13	<0.9
2019-SV-02-Circulo A-ef - 3	112	1.0	1.5	<4.7	15437	0.02	0.9	1.9	<1.1
2019-SV-02-Circulo B-ef - 1	503	2	<1.9	<4	28300	0.024	1.8	8	<1.1
2019-SV-02-Circulo B-ef - 2	1012	3	<1.4	<3.4	20829	0.019	0.9	7.9	<0.8
2019-SV-02-Circulo B-ef - 3	422	1.8	0.90	<4.9	29504	0.06	2.3	5	<1.2
2019-SV-02-Circulo C-ef - 1	565	2.4	2.6	<3.4	20872	0.034	2.2	5	<0.8
2019-SV-04-Circulo A-ef - 1	565	1.9	<1	<3	20455	0.01	0.8	8.9	<0.80
2019-SV-04-Circulo A-ef - 2	826	1.9	<1.1	<3	20868	0.049	1.3	20	<0.8
2019-SV-04-Circulo B-ef - 1	547	4.8	1.1	<3	19176	0.13	1.7	10	<0.78
2019-SV-04-Circulo B-ef - 2	761	1.7	<1.5	<3.4	19583	0.078	2.0	7.9	<0.79
2019-SV-04-Circulo B-ef - 3	572	2.3	<1.5	<3	18408	0.049	1.8	12	0.36
2019-SV-04-Circulo C-ef - 2	360	2.9	<1.2	<3.3	22132	0.027	1.2	4.7	<0.7
2019-SV-04-Circulo C-ef - 3	121	0.8	<1.7	<3.8	17354	0.036	1.6	5.7	0.47
2019-SV-04-Circulo D-ef - 1	1120	4.7	<1.4	3.0	22739	0.037	0.6	5	0.47
2019-SV-04-Circulo D-ef - 3	161	2.0	<2	<4.6	13599	0.037	1	10	<1
2019-SV-06A-Circulo A-ef - 1	707	<0.12	<1.2	<3.4	22064	0.08	1.8	0.4	0.5
2019-SV-06A-Circulo A-ef - 2	838	0.08	<1.2	<3	19038	0.16	1	0.3	0.36
2019-SV-06A-Circulo A-ef - 3	587	0.068	<1.6	<3.8	22999	0.7	2.9	0.34	<0.9
UQAC-FeS-1 - 2	11049.05	21.14574	678.3773	875.1593	10.5385	0.26374	0.176276	32.86075	6.513465
GSD-1G - 2	2761.457	1.367372	9.503228	14.9983	35.88739	1.440568	1.294963	1.762937	2.65268
NIST610 - 2	25.63832	10.23215	13.77788	12.69061	22.59551	8.238833	7.109951	7.031396	4.314485
2019-SV-06A-Circulo B-ef - 3	858	<0.12	<1.3	<3	18530	0.15	0.7	0.2	<0.67
2019-SV-06A-Circulo B-ef - 4	434	0.058	0.8	2	19229	0.34	3	0.25	<0.67
2019-SV-06A-Circulo C-ef - 1	899	<0.11	<1	<3	16350	0.09	0.8	0.35	<0.77
2019-SV-06A-Circulo C-ef - 2	737	0.07	<1.2	<3	20084	0.18	3	0.48	0.49
2019-SV-06A-Circulo C-ef - 3	1143	0.068	<1.4	<3.3	21228	0.58	2.6	0.4	<0.7
2019-SV-06B-Circulo A-ef - 1	663	0.078	<1.3	<3	22631	0.056	2.6	0.2	<0.8
2019-SV-06B-Circulo A-ef - 2	777	0.08	<1.5	<3	18918	0.014	1	0.49	<0.7
2019-SV-06B-Circulo A-ef - 3	201	0.2	<1.2	2.7	23136	0.018	1	0.57	<0.8

Label	Fe57	Co59	Ni62	Cu65	Zn66	Ga71	Ge74	As75	Se77
2019-SV-06B-Circulo A-ef - 4	243	0.09	<1.3	<3.3	21282	0.070	1.4	0.3	<0.7
2019-SV-06B-Circulo B-ef - 1	431	0.077	<1.2	<3	18353	0.55	3	0.4	<0.8
2019-SV-06B-Circulo B-ef - 2	974	0.12	<2	<4.7	15214	0.17	2.7	0.36	<1.1
2019-SV-06B-Circulo B-ef - 3	561	0.1	<1.5	<3.5	22865	0.05	2.2	0.8	<0.7
2019-SV-06B-Circulo C-ef - 2	641	0.06	<1.3	<3	19105	0.12	1.4	0.17	<0.7
2019-SV-06B-Circulo C-ef - 3	792	0.08	<1.4	<3.5	22947	0.56	2.7	0.55	0.5
2019-SV-07-Circulo A-ef - 1	8.8	0.12	<1.4	3.9	24762	0.035	3.5	0.17	<0.77
2019-SV-07-Circulo A-ef - 2	223	<0.1	<1.3	2.5	21243	0.14	0.3	0.20	<0.7
2019-SV-07-Circulo A-ef - 3	277	<0.12	<1.3	2.9	23179	0.05	2.8	0.19	<0.7
2019-SV-07-Circulo A-ef - 4	729	0.07	<1.3	<3.6	25299	0.26	2.8	0.23	<0.78
2019-SV-07-Circulo B-ef - 1	479	0.10	<1.6	<3.7	24090	0.13	1.0	0.17	<0.78
2019-SV-07-Circulo B-ef - 2	871	<0.12	<1.3	<3.6	12752	0.5	0.8	0.39	0.45
2019-SV-07-Circulo B-ef - 3	487	0.09	<1.4	<3.5	16183	0.23	2.3	0.4	<0.77
2019-SV-07-Circulo B-ef - 4	214	0.10	<2.5	<5	9138	0.2	1.4	0.4	<1
2019-SV-07-Circulo C-ef - 1	134	<0.13	<1.4	2.7	23596	0.10	3	0.2	<0.9
2019-SV-07-Circulo C-ef - 2	945	<0.14	<1.4	<4	17656	0.05	0.5	0.25	<0.9
2019-SV-07-Circulo C-ef - 3	568	0.09	<2.4	<4.5	15232	1.2	10	0.18	<1.0
UQAC-FeS-1 - 3	15228.29	19.18743	888.3649	1434.441	17.94393	0.152933	0.252363	26.3109	9.969044
GSD-1G - 3	1334.784	0.723642	4.31295	7.320501	13.40667	0.583213	0.553804	0.800522	1.429713
NIST610 - 3	27.92954	9.762774	15.21305	17.6072	22.16386	7.721659	6.504519	7.276977	4.574664
2019-SV-08A-Circulo A-ef - 2	1096	0.08	<1.3	<3.8	20219	1.2	0.8	0.17	<0.8
2019-SV-08A-Circulo A-ef - 3	683	<0.13	<1.2	<3.7	18638	0.13	1.2	0.27	<0.8
2019-SV-08A-Circulo A-ef - 4	430	0.07	<1.6	<3.8	18366	0.2	3.0	0.26	<0.7
2019-SV-08A-Circulo C-ef - 1	1240	0.08	<1.4	<3.7	16868	0.44	1.3	0.25	<0.78
2019-SV-08A-Circulo C-ef - 2	849	<0.11	<1.3	<3.5	20310	0.50	1	0.3	<0.7
2019-SV-08A-Circulo C-ef - 3	525	<0.13	<1.5	<3.8	20635	0.5	4	0.4	<0.78
2019-SV-08A-Circulo D-ef - 1	427	<0.17	<2.2	<4.8	16950	0.045	2	0.20	<1
2019-SV-08A-Circulo D-ef - 2	447	<0.12	<1.3	<3.7	16179	0.14	1.5	0.16	<0.8
2019-SV-08A-Circulo D-ef - 3	549	<0.12	<1.4	<3.7	17945	0.12	1.3	0.18	<0.77
2019-SV-08B-Circulo A-ef - 1	506	<0.12	<1.4	<3.9	22367	0.070	0.69	0.18	0.44
2019-SV-08B-Circulo A-ef - 2	489	0.06	<1.1	<3.6	20498	0.016	2.7	0.17	<0.77
2019-SV-08B-Circulo B-ef - 1	804	<0.12	<1.4	<3.7	20651	0.24	0.9	0.39	<0.8

Label	Fe57	Co59	Ni62	Cu65	Zn66	Ga71	Ge74	As75	Se77
2019-SV-08B-Circulo B-ef - 3	1030	0.09	<1.3	<3.6	19065	0.1	2.5	0.5	<0.69
2019-SV-08B-Circulo C-ef - 2	315	0.12	<1.1	<3.6	20888	0.36	0.79	0.24	<0.7
2019-SV-08B-Circulo C-ef - 3	590	0.09	<1.4	<3.9	17484	2	2.2	0.2	<0.8
2019-SV-08B-Circulo D-ef - 1	275	0.078	<1.4	<3.7	24245	0.68	0.6	0.23	<0.8
2019-SV-08B-Circulo D-ef - 2	298	0.10	<1.1	<3.5	18169	0.46	1.6	0.2	<0.67
2019-SV-08B-Circulo D-ef - 3	801	0.06	<1.2	<3.4	19785	4	0.59	0.18	<0.7
2019-SV-08B-Circulo D-ef - 4	373	0.079	<1.7	<3.9	27452	2	6.7	0.28	<0.8
2019-SV-08B-Circulo E-ef - 1	383	0.08	<1.5	<4.0	22479	0.26	0.99	0.35	<0.8
2019-SV-08B-Circulo E-ef - 2	97	0.10	<1.5	<4	19737	0.9	8.9	0.18	<0.80
UQAC-FeS-1 - 4	13428.15	15.7297	491.0497	781.3674	19.27034	0.216554	0.13782	25.28694	5.002699
GSD-1G - 4	1717.925	0.890631	4.652763	9.794936	17.4798	0.771683	0.680931	1.147554	<2.4168
NIST610 - 4	31.60653	11.18751	13.74392	16.48585	18.33897	9.288091	7.590729	7.514947	4.731475
2019-SV-08B-Circulo E-ef - 3	798	0.089	<1.5	<4	30762	0.55	1.6	0.36	<0.8
2019-SV-08B-Circulo E-ef - 4	198	0.09	<1.6	<3.7	22142	0.36	0.9	0.18	<0.8
2019-SV-09-Circulo A-ef - 1	684	<0.13	<1.5	<3.8	20777	0.049	0.45	0.17	<0.70
2019-SV-09-Circulo A-ef - 2	548	<0.13	<1.2	<3.8	22207	0.045	4	0.14	<0.7
2019-SV-09-Circulo A-ef - 3	639	<0.13	<1.4	<3.7	22892	0.09	2	0.17	<0.7
2019-SV-09-Circulo A-ef - 4	499	<0.13	<1.4	<4	19578	0.19	2.0	0.16	0.5
2019-SV-09-Circulo B-ef - 1	3288	0.09	<1.7	<4	24642	0.23	6.7	0.34	0.6
2019-SV-09-Circulo B-ef - 2	826	0.09	<1.3	<3.7	21688	0.068	1.2	0.29	<0.78
2019-SV-09-Circulo B-ef - 3	624	0.07	<1.3	<3.7	16763	0.14	1.2	0.55	<0.7
2019-SV-09-Circulo B-ef - 4	460	0.09	<1.6	<4	23154	0.08	2	0.39	<0.77
2019-SV-09-Circulo C-ef - 1	3379	0.15	<1.9	5	23096	0.2	2.0	1.4	<1
2019-SV-09-Circulo C-ef - 3	894	0.09	<1.5	<4	21507	0.07	0.89	0.68	<0.8
2019-SV-011A-Circulo B-ef - 1	356	0.57	<1.2	<3.9	20948	0.019	1.6	0.5	<0.7
2019-SV-011A-Circulo B-ef - 2	675	0.39	<1.3	<3.9	18696	0.017	0.79	0.69	0.4
2019-SV-011A-Circulo B-ef - 3	420	0.47	<1.3	<4	21022	0.02	4	0.49	<0.70
2019-SV-011A-Circulo B-ef - 4	378	0.6	<1.5	3.4	19261	0.019	5.83	0.4	0.4
2019-SV-011A-Circulo C-ef - 1	725	0.47	1	<3.9	19179	0.014	1.11	0.69	<0.69
2019-SV-011A-Circulo C-ef - 2	764	1	0.7	<3.9	20591	0.014	3	0.26	0.47
2019-SV-011A-Circulo C-ef - 3	687	0.70	<1.3	<3.9	18542	0.017	1.7	0.3	0.49
2019-SV-011A-Circulo C-ef - 4	562	0.8	<1.6	3.6	18683	0.016	2.5	0.24	<0.7

Label	Fe57	Co59	Ni62	Cu65	Zn66	Ga71	Ge74	As75	Se77
2019-SV-011B-Circulo A-ef - 1	879	0.9	<1.4	<4.0	22116	0.013	2.4	0.15	<0.7
2019-SV-011B-Circulo A-ef - 2	553	0.7	<1.3	<3.9	24200	0.024	2.3	4.7	<0.67
2019-SV-011B-Circulo A-ef - 3	772	0.8	<1.3	<3.6	19094	0.019	1.2	0.47	<0.6
2019-SV-011B-Circulo A-ef - 4	894	1.0	<1.4	<3.9	16726	0.015	3.8	0.29	0.38
2019-SV-011B-Circulo A-ef - 5	267	0.36	<1.1	2.4	17974	0.017	0.5	0.25	<0.68
UQAC-FeS-1 - 5	15817.22	29.19519	760.0036	1109.691	51.29674	0.392754	0.131559	320.4056	5.303749
GSD-1G - 5	4851.113	2.657242	10.27958	22.98315	14.01184	1.857136	1.276409	2.864108	<5.0243
NIST610 - 5	55.19298	18.65216	34.34852	42.49232	18.98835	16.26713	10.56401	15.48748	9.052466
2019-SV-011B-Circulo B-ef - 2	1109	0.7	<2.8	<8	17623	0.038	3	0.5	<1.4
2019-SV-011B-Circulo C-ef - 1	1335	0.6	<3	<8	19385	0.028	4	0.49	0.9
2019-SV-011B-Circulo C-ef - 2	2291	0.68	1.5	<8	26431	0.037	4.7	0.7	<1.5
2019-SV-011B-Circulo C-ef - 3	1226	0.45	<2.5	<7.9	22125	0.057	4	0.4	0.7
2019-SV-011B-Circulo D-ef - 1	993	1.32	<2	<7	19018	0.019	3	0.55	0.7
2019-SV-011B-Circulo D-ef - 2	1210	1.46	1.2	<7	19297	0.033	3.8	0.7	<1
2019-SV-011B-Circulo D-ef - 3	1302	1.32	<2.8	<7	19918	0.030	1.9	0.7	<1.2
2019-SV-011C-Circulo A-ef - 1	1063	1	<2	<6	18944	0.028	3	0.4	<1
2019-SV-011C-Circulo B-ef - 2	824	0.5	<1.9	<6	18415	0.029	1.2	0.68	<1
2019-SV-011C-Circulo C-ef - 1	995	0.58	<1.9	<6	19694	0.024	5	0.34	<1.00
2019-SV-011C-Circulo C-ef - 2	623	0.39	<2	5	20026	0.03	1.8	0.8	<1.0
2019-SV-012A-Circulo A-ef - 1	2051	1.51	1.5	<6.9	25813	0.4	4	2	<1.3
2019-SV-012A-Circulo A-ef - 2	1554	1.44	<1.9	<5.5	19380	0.029	1.2	0.4	<1.0
2019-SV-012A-Circulo B-ef - 1	335	2	<2.2	<5.9	15996	0.03	2	0.6	0.67
2019-SV-012A-Circulo C-ef - 1	1204	0.7	<1.8	<5	23268	0.04	1.4	2	<1.0
2019-SV-012A-Circulo C-ef - 2	1355	0.8	0.89	<5	21901	0.03	1.3	1.6	<0.88
2019-SV-012A-Circulo D-ef - 1	462	0.7	<1.6	<4.8	18422	0.06	1.2	3	<0.9
2019-SV-012A-Circulo D-ef - 2	1217	0.99	<1.9	3.9	22188	0.13	3.5	5	0.5
2019-SV-012B-Circulo A-ef - 1	826	0.8	<1.8	<4.8	18385	0.11	1	1.5	<0.88
2019-SV-012B-Circulo A-ef - 2	379	1	<1.6	<4.9	26125	0.067	2	0.8	<0.8
2019-SV-012B-Circulo B-ef - 1	1245	0.8	<1.8	<4.8	17844	0.057	1.7	1.0	<0.80
2019-SV-012B-Circulo B-ef - 2	461	1.0	<1.6	<4	20783	0.14	1.3	0.5	<0.68
NIST610 - 6	37.01564	9.522038	17.99024	18.63212	23.32481	9.232878	7.263986	8.251367	4.161153
GSD-1G - 6	3230.173	1.490674	7.73967	13.20538	19.91524	1.171524	1.120077	1.373941	<2.8213
UQAC-FeS-1 - 6	17069.78	21.97603	561.6494	1528.642	557.5988	0.460363	0.187564	88.21632	9.707774

Label	Fe57	Co59	Ni62	Cu65	Zn66	Ga71	Ge74	As75	Se77
UQAC-FeS-1 - 1	9204.463	30.33012	1154.136	1119.344	20.85004	0.201074	0.124433	91.85272	7.903792
GSD-1G - 1	2319.755	0.840834	17.89632	10.85152	15.79203	1.068898	0.809316	1.232505	2.413383
NIST610 - 1	35.81667	10.24884	15.47068	17.5361	25.25976	10.20595	7.806743	9.239602	5.079943
2019-SV-013-Circulo A-ef - 1	9	<0.09	<1.2	3.4	23605	1	3	0.16	<0.8
2019-SV-013-Circulo A-ef - 2	7	<0.1	<1.2	2	19924	0.22	5	0.2	<0.9
2019-SV-013-Circulo B-ef - 1	8	<0.10	<1.4	<3.5	18317	1.5	6.9	0.24	<0.9
2019-SV-013-Circulo B-ef - 2	10	<0.099	<1.3	2.7	20742	1.8	3	0.19	<0.90
2019-SV-013-Circulo C-ef - 1	12	<0.1	<1.3	<3.4	20756	0.88	5	0.19	<0.78
2019-SV-013-Circulo C-ef - 2	10	<0.11	<1.6	<3.8	28400	2	14	0.28	<0.88
2019-SV-014-Circulo A-ef - 1	7	<0.1	<1.5	<3.5	20701	0.8	6.8	0.2	0.5
2019-SV-014-Circulo A-ef - 2	12	<0.1	<1.1	2.7	17330	0.38	3.4	0.18	<0.8
2019-SV-014-Circulo B-ef - 1	12	<0.13	<1.7	3.7	19606	3	5.9	0.24	0.7
2019-SV-014-Circulo B-ef - 2	11	<0.10	<1.5	2.5	20264	0.4	5.5	0.18	<0.79
2019-SV-014-Circulo C-ef - 1	11	<0.10	<1.2	2.4	18516	2.2	5	0.18	<0.8
2019-SV-014-Circulo C-ef - 2	8	<0.12	<1.6	<3.8	18483	1.8	6.6	0.23	0.5
2019-SV-015A-Circulo A-ef - 1	<18	<0.19	<2.9	30	7824	29	1.2	0.24	<1.7
2019-SV-015A-Circulo A-ef - 2	<10	<0.10	<1.5	15	25309	0.7	9	4.6	<0.9
2019-SV-015A-Circulo B-ef - 1	<14	<0.16	<2.0	39	45269	0.88	45	0.9	<1.3
2019-SV-015A-Circulo B-ef - 2	<10	<0.10	<1.5	<3.5	23291	0.019	38	0.37	<0.9
2019-SV-015A-Circulo B-ef - 3	<10	<0.12	<1.5	41	26985	5.50	18	0.36	<0.9
2019-SV-015A-Circulo C-ef - 1	<13	<0.14	<1.7	12	14570	0.2	10	3.3	<1.2
2019-SV-015A-Circulo D-ef - 1	<16	<0.18	<2.5	10	9624	1.87	6.0	0.7	<1.5
2019-SV-015A-Circulo D-ef - 2	<10	<0.10	<1.2	4.4	20268	1.61	31	0.27	<0.9
2019-SV-015A-Circulo D-ef - 3	<12	<0.14	<1.6	12	14421	3.39	3.9	0.2	0.58
2019-SV-015A-Circulo E-ef - 1	12	<0.13	<1.6	40	13175	3.81	19	0.6	<1.1
2019-SV-015A-Circulo E-ef - 2	<10	<0.12	<1.4	136	20779	1.0	84	0.5	<0.9
2019-SV-015A-Circulo E-ef - 3	<10	<0.12	<1.4	89	20526	37	30	0.28	0.57
2019-SV-015B-Circulo A-ef - 1	<10	<0.12	<1.4	61	19530	0.39	19	0.15	<0.8
2019-SV-015B-Circulo A-ef - 2	<12	<0.14	<1.6	6	16047	3.4	0.1	0.2	<1
UQAC-FeS-1 - 2	10386.65	28.55935	953.7766	1102.562	13.76568	0.174829	0.156128	61.16074	7.564802
GSD-1G - 2	1864.038	0.925421	4.111557	7.007909	16.41005	0.942833	0.717247	1.171	1.779343
NIST610 - 2	35.33958	10.95715	17.87073	18.82781	21.983	9.629965	8.31544	8.079663	5.522789
2019-SV-015B-Circulo A-ef - 3	<10	<0.11	<1.5	51	21703	0.13	14	2	<0.9

Label	Fe57	Co59	Ni62	Cu65	Zn66	Ga71	Ge74	As75	Se77
2019-SV-015B-Circulo B-ef- 1	<11	<0.13	<1.5	8	25957	6.6	<0.14	0.24	0.56
2019-SV-015B-Circulo B-ef - 2	<13	<0.15	<1.7	12	31027	9	0.10	0.3	<1.1
2019-SV-015B-Circulo B-ef - 3	<11	<0.13	<1.4	6	24862	3.6	0.068	0.27	<1.0
2019-SV-015B-Circulo B-ef - 4	<11	<0.12	<1.6	6	22398	3.9	0.07	0.2	0.47
2019-SV-015B-Circulo B-ef- 5	<12	<0.15	<1.4	11	34282	11.0	0.11	0.3	<1.0
2019-SV-015B-Circulo B-ef-2 - 1	<10	<0.11	<1.4	13	21929	14	5.6	0.18	<0.90
2019-SV-015B-Circulo C-ef - 1	<15	<0.18	<2	4	13475	0.9	0.9	0.23	0.7
2019-SV-015B-Circulo C-ef - 2	<11	<0.13	<1.4	72	24151	11	21	0.9	0.49
2019-SV-015B-Circulo C-ef - 3	<11	<0.12	<1.5	63	23440	1.4	23	3	<0.9
2019-SV-016-Circulo A-ef - 1	1845	1.6	1.9	<3.6	20882	0.024	1.3	3.6	0.5
2019-SV-016-Circulo A-ef - 2	2731	3	30	3.9	16923	0.28	6	16	0.6
2019-SV-016-Circulo B-ef - 1	610	0.8	<1.3	<3.7	19763	0.12	1	5	<0.8
2019-SV-016-Circulo D-ef - 1	1166	1.1	<1.4	<3.9	20037	0.16	1.5	3.5	<0.8
2019-SV-016-Circulo D-ef - 1	281	0.46	<2	<5.5	10708	0.025	1.3	2.2	<1.1
2019-SV-016-Circulo E-ef - 2	228	0.9	<1.2	<3.7	19665	0.017	1.0	0.9	0.40
2019-SV-016-Circulo E-ef - 3	258	1.2	<1.4	<3.6	19104	0.014	3.9	0.4	<0.7
2019-SH-31-Circulo A-ef - 1	38	<0.19	<2.0	20	9781	0.029	12	0.68	0.58
2019-SH-31-Circulo A-ef - 2	39	<0.13	<1.7	3	22286	0.016	0.25	3.7	<0.8
2019-SH-31-Circulo A-ef - 3	96	<0.21	<2	10	15145	0.03	10	3	<1.2
2019-SH-31-Circulo A-ef - 4	33	<0.12	<1.4	3.4	20220	0.014	8	0.17	<0.77
2019-SH-31-Circulo B-ef - 1	50	<0.13	<1.5	3.6	21395	0.023	2.9	7.7	<0.79
2019-SH-31-Circulo B-ef - 2	35	<0.14	<1.3	20	19719	0.049	46	0.48	<0.8
2019-SH-31-Circulo B-ef - 3	32	<0.14	<1.2	<3.9	18444	0.016	23	0.24	<0.8
2019-SH-31-Circulo C-ef - 1	72	<0.14	<1.4	162	25949	0.040	49	1.5	<0.8
UQAC-FeS-1 - 3	17655.46	27.33123	852.9502	1116.203	24.56854	0.581423	0.331805	43.62086	12.46578
GSD-1G - 3	1680.229	0.938817	5.13828	9.576449	15.19016	0.716312	0.684445	0.909036	1.391346
NIST610 - 3	28.91834	9.895178	12.15717	14.69426	20.45496	7.377988	6.781553	7.003176	5.150611
2019-SH-31-Circulo C-ef - 2	42	<0.12	<1.2	25	16651	0.018	26	0.45	<0.7
2019-SH-31-Circulo C-ef - 3	104	<0.14	<1.3	58	18950	0.23	28	2	<0.77
2019-SH-31-Circulo C-ef - 4	49	<0.13	<1.4	<4	20433	0.017	3.7	0.3	<0.78
2019-SH-120-Circulo A-ef - 1	720	0.09	<1.5	<4.0	19185	0.1	0.6	0.25	<0.8
2019-SH-120-Circulo A-ef - 2	1616	0.080	<1.5	<4	22659	0.016	9.0	3	<0.8

Label	Fe57	Co59	Ni62	Cu65	Zn66	Ga71	Ge74	As75	Se77
2019-SH-120-Circulo A-ef - 3	1363	0.07	<1.5	<3.7	15793	0.014	2.8	0.24	0.50
2019-SH-120-Circulo B-ef - 1	128	<0.16	<1.7	<4.8	15859	0.077	0.2	0.25	<0.9
2019-SH-120-Circulo B-ef - 2	883	0.09	<1.1	<3.9	23475	0.11	4.8	0.36	<0.77
2019-SH-120-Circulo B-ef - 3	579	0.07	<1.4	<3.8	21149	0.066	1.6	1.2	<0.68
2019-SH-167-Circulo A-ef - 1	86	<0.13	<1.4	<3.9	20237	0.019	13	0.25	<0.7
2019-SH-167-Circulo A-ef - 2	66	<0.12	<1.3	<3.7	20720	0.013	5.8	0.19	<0.7
2019-SH-167-Circulo A-ef - 3	18	<0.13	<1.6	2.6	19188	0.44	5	0.17	<0.8
2019-SH-167-Circulo A-ef - 4	32	<0.16	<1.4	6.7	21843	0.019	26	0.6	<0.88
2019-SH-167-Circulo B-ef - 1	21	<0.16	<1.8	9	13963	1	2.3	0.36	<0.90
2019-SH-167-Circulo B-ef - 2	48	<0.14	<1.4	56	21112	2	13	3.4	<0.7
2019-SH-167-Circulo B-ef - 3	14	<0.12	<1.4	<3.7	19537	0.019	27	1.6	0.34
2019-SH-167-Circulo B-ef - 4	17	<0.15	<1.7	<4.8	16911	0.026	18	0.24	<0.89
2019-SH-167-Circulo C-ef - 1	25	<0.12	<1.3	81	18080	48	7	18	0.3
2019-SH-167-Circulo C-ef - 2	19	<0.12	<1.3	<3.9	21601	0.018	15	0.24	0.4
2019-SH-167-Circulo C-ef - 3	23	<0.13	<1.3	<4	23957	0.04	15	0.6	<0.69
2019-SH-167-Circulo C-ef - 4	43	<0.12	<1.3	10	21151	0.014	8	0.27	0.47
2019-SH-187-Circulo A-ef - 1	258	1.00	<1.2	<4	20287	0.015	3.4	0.6	<0.7
2019-SH-187-Circulo A-ef - 2	507	0.68	<1.2	<4	18515	0.03	1.8	1.4	0.5
2019-SH-187-Circulo A-ef - 3	317	0.9	<1.4	3.3	19873	0.020	0.16	0.2	0.48
2019-SH-187-Circulo A-ef - 4	846	1.28	<1.6	<4.5	21685	0.05	0.4	0.48	<0.8
2019-SH-187-Circulo C-ef - 1	115	0.79	<1.6	<4.7	26304	0.099	0.35	0.8	<0.79
2019-SH-187-Circulo C-ef - 2	520	0.56	<1.8	<4.5	22013	<0.028	0.25	0.5	0.4
UQAC-FeS-1 - 4	11421.96	22.67809	616.9848	505.4945	56.62795	0.179124	0.145604	24.05629	8.244997
GSD-1G - 4	2083.438	1.456427	7.432486	14.13808	23.80908	1.022214	0.963211	1.500286	<3.7448
NIST610 - 4	30.78407	8.00183	12.04784	16.78958	20.02805	7.279351	6.707307	7.68235	3.939967
2019-SH-187-Circulo C-ef - 3	552	1.24	<1.1	<4	24208	0.11	7	12	<0.77
2019-SH-212-Circulo A-ef - 1	51	<0.14	<1.6	5	20888	1.2	1.6	0.3	<0.8
2019-SH-212-Circulo A-ef - 2	36	<0.13	<1.3	5	22432	1.3	3.4	0.30	<0.78
2019-SH-212-Circulo A-ef - 3	23	<0.15	<1.7	<4.5	17810	0.09	2.8	0.30	<0.8
2019-SH-212-Circulo A-ef - 4	49	<0.14	<1	5	21185	1.8	4.9	0.38	<0.7
2019-SH-212-Circulo B-ef - 1	65	<0.14	<1.4	3.5	22383	1.3	8.0	0.9	<0.7
2019-SH-212-Circulo B-ef - 2	16	<0.14	<1.3	<4	20340	0.03	10	0.28	<0.7

Label	Fe57	Co59	Ni62	Cu65	Zn66	Ga71	Ge74	As75	Se77
2019-SH-212-Circulo B-ef - 3	24	<0.13	<1.1	3.4	20568	0.016	6.7	0.28	0.37
2019-SH-212-Circulo B-ef - 4	28	<0.19	<1.8	8.8	13911	1	7.7	0.29	<1
SH-227-Circulo B-ef - 1	27	<0.14	<1.5	<3.9	18127	0.08	4.6	0.29	0.4
SH-227-Circulo B-ef - 2	54	<0.13	<1.4	16	21647	2.9	5.6	0.9	<0.7
SH-227-Circulo B-ef - 3	34	<0.14	<1.4	56	19901	0.49	16	2.7	<0.68
SH-227-Circulo A-ef - 1	20	<0.16	<1.7	<4.4	18301	1.4	5.6	0.4	<0.80
SH-227-Circulo A-ef - 2	57	<0.14	<1.3	3.4	21093	0.06	5	0.26	0.35
SH-227-Circulo A-ef - 3	26	<0.14	0.69	57	20298	0.77	19	2.6	<0.7
NIST610 - 5	29.9914	8.359282	12.41556	15.55143	21.0529	6.746355	6.385708	6.575511	4.200597
GSD-1G - 5	1407.57	0.725097	4.018774	8.314741	15.39813	0.555811	0.4789	0.909196	<1.7783
UQAC-FeS-1 - 5	10013.37	23.88622	597.6152	1143.5	41.56612	0.178818	0.145627	26.52213	4.795986

*Values in red color have been discarded in pl

Label	Mo95	Ag107	Cd111	In115	Sn118	Sb121	Au197	Hg202	Tl205
UQAC-FeS-1 - 1	2.034644	14.02986	0.294177	0.216205	27.89223	2.08314	4.157365	4.85832	0.013916
GSD-1G - 1	0.62651	0.443252	1.06667	0.515381	0.652756	0.582989	0.10941	<0.22629	0.025522
NIST610 - 1	10.68101	6.496054	10.24087	8.883037	9.651772	7.8195	0.592399	0.13813	1.519864
2019-SV-02-Circulo A-ef - 1	0.016	0.6	47	<0.0059	0.036	0.018	<0.011	0.17	0.05
2019-SV-02-Circulo A-ef - 2	<0.024	0.88	76	<0.0066	0.038	<0.03	<0.013	0.25	0.22
2019-SV-02-Circulo A-ef - 3	0.020	0.24	31	<0.0079	0.049	<0.039	<0.015	0.15	0.05
2019-SV-02-Circulo B-ef - 1	<0.03	1	80	<0.008	0.05	<0.037	<0.014	0.19	0.12
2019-SV-02-Circulo B-ef - 2	0.010	1.6	73	<0.005	0.035	<0.03	<0.009	0.18	0.09
2019-SV-02-Circulo B-ef - 3	<0.035	0.4	33	<0.008	0.035	<0.04	<0.018	0.27	0.07
2019-SV-02-Circulo C-ef - 1	0.02	1.8	25	<0.005	0.039	<0.030	<0.010	0.16	0.055
2019-SV-04-Circulo A-ef - 1	<0.02	1	28	<0.0049	0.03	<0.025	<0.009	0.16	0.15
2019-SV-04-Circulo A-ef - 2	0.012	0.49	106	0.0044	0.034	<0.03	<0.010	0.15	0.4
2019-SV-04-Circulo B-ef - 1	<0.022	0.44	43	0.0046	0.037	<0.028	<0.0099	0.16	0.2
2019-SV-04-Circulo B-ef - 2	0.012	0.9	62	0.004	0.038	<0.028	<0.0089	0.12	0.2
2019-SV-04-Circulo B-ef - 3	0.015	0.4	50	0.004	0.039	<0.028	<0.01	0.13	0.2
2019-SV-04-Circulo C-ef - 2	<0.02	0.2	51	0.0039	0.034	<0.029	<0.01	0.13	0.07
2019-SV-04-Circulo C-ef - 3	<0.024	0.18	35	0.0044	0.035	<0.03	<0.01	0.14	0.12
2019-SV-04-Circulo D-ef - 1	0.015	0.59	73	<0.006	0.036	<0.03	<0.01	0.18	0.05
2019-SV-04-Circulo D-ef - 3	<0.034	0.23	22	0.0040	0.04	<0.035	<0.013	0.09	0.1
2019-SV-06A-Circulo A-ef - 1	<0.024	0.13	11	0.0037	0.04	<0.024	<0.01	0.16	0.045
2019-SV-06A-Circulo A-ef - 2	0.009	0.18	15	0.005	0.04	<0.026	<0.0088	0.14	0.029
2019-SV-06A-Circulo A-ef - 3	<0.028	0.28	25	0.022	0.26	<0.03	<0.011	0.18	0.060
UQAC-FeS-1 - 2	1.858652	5.675365	0.30908	0.396806	35.08226	3.31537	14.78012	35.0863	0.019235
GSD-1G - 2	1.298731	0.793572	2.157177	0.855173	1.152371	1.207089	0.224189	<0.5353	0.061465
NIST610 - 2	9.841262	5.677947	9.312914	8.073066	8.196093	6.981237	0.569229	<0.22995	1.483941
2019-SV-06A-Circulo B-ef - 3	0.017	0.34	15	0.0045	0.04	<0.027	<0.01	0.12	0.015
2019-SV-06A-Circulo B-ef - 4	<0.023	0.26	18	0.0039	0.044	<0.024	<0.009	0.14	0.035
2019-SV-06A-Circulo C-ef - 1	<0.025	0.12	18	0.003	0.030	<0.026	<0.0088	0.14	0.02
2019-SV-06A-Circulo C-ef - 2	0.010	0.25	14	0.0055	0.05	<0.029	<0.008	0.12	0.11
2019-SV-06A-Circulo C-ef - 3	<0.025	0.33	16	0.009	0.09	<0.025	<0.009	0.11	0.05
2019-SV-06B-Circulo A-ef - 1	0.016	0.49	20	<0.0058	0.05	<0.025	<0.0089	0.15	0.049
2019-SV-06B-Circulo A-ef - 2	0.016	0.19	18	<0.006	0.029	<0.026	<0.0089	0.15	0.025
2019-SV-06B-Circulo A-ef - 3	<0.02	0.19	4	<0.0059	0.036	<0.027	<0.010	0.13	0.037

Label	Mo95	Ag107	Cd111	In115	Sn118	Sb121	Au197	Hg202	Tl205
2019-SV-06B-Circulo A-ef - 4	<0.027	0.17	12	0.004	0.04	<0.028	<0.0090	0.16	0.039
2019-SV-06B-Circulo B-ef - 1	<0.026	0.45	16	0.004	0.05	<0.029	<0.010	0.14	0.09
2019-SV-06B-Circulo B-ef - 2	0.017	0.38	19	0.006	0.06	<0.036	<0.016	0.19	0.05
2019-SV-06B-Circulo B-ef - 3	<0.025	0.23	19	0.0030	0.04	<0.028	<0.01	0.17	0.080
2019-SV-06B-Circulo C-ef - 2	<0.026	0.26	13	<0.0059	0.04	<0.025	<0.009	0.15	0.019
2019-SV-06B-Circulo C-ef - 3	0.023	0.67	19	0.0068	0.06	0.019	<0.012	0.13	0.038
2019-SV-07-Circulo A-ef - 1	<0.025	0.27	41	<0.006	0.027	<0.029	<0.01	0.14	0.029
2019-SV-07-Circulo A-ef - 2	<0.02	0.17	31	0.014	0.044	<0.023	<0.0099	0.16	0.005
2019-SV-07-Circulo A-ef - 3	0.015	0.30	28	<0.006	0.044	<0.027	<0.011	0.15	0.04
2019-SV-07-Circulo A-ef - 4	<0.023	0.79	22	0.010	0.047	<0.026	<0.01	0.15	0.03
2019-SV-07-Circulo B-ef - 1	<0.025	0.99	35	<0.006	0.037	<0.026	<0.012	0.16	0.013
2019-SV-07-Circulo B-ef - 2	0.016	0.14	29	0.0067	0.08	<0.023	<0.01	0.14	0.02
2019-SV-07-Circulo B-ef - 3	0.017	0.1	11	0.0057	0.05	<0.025	<0.01	0.12	0.040
2019-SV-07-Circulo B-ef - 4	<0.036	0.12	7	0.0099	0.057	<0.038	<0.0178	0.15	0.029
2019-SV-07-Circulo C-ef - 1	<0.023	1.6	61	0.0039	0.036	<0.030	<0.011	0.2	0.04
2019-SV-07-Circulo C-ef - 2	<0.025	0.24	15	0.0057	0.08	<0.034	<0.013	0.16	0.02
2019-SV-07-Circulo C-ef - 3	<0.03	0.45	14	0.015	0.4	<0.038	<0.014	0.08	0.1
UQAC-FeS-1 - 3	3.163919	4.315229	0.307409	0.31936	13.8964	4.146882	6.533043	5.18321	0.013725
GSD-1G - 3	0.647215	0.449167	1.029125	0.491188	0.37678	0.473342	0.099918	<0.28363	0.020397
NIST610 - 3	11.43383	7.06639	10.96516	8.463757	8.989517	8.114233	0.527856	<0.28087	1.451943
2019-SV-08A-Circulo A-ef - 2	<0.024	0.78	45	0.010	0.066	<0.029	<0.01	0.09	0.015
2019-SV-08A-Circulo A-ef - 3	<0.030	0.38	19	0.0048	0.037	<0.026	<0.01	0.11	0.025
2019-SV-08A-Circulo A-ef - 4	<0.027	0.18	15	0.010	0.055	<0.027	<0.01	0.12	0.046
2019-SV-08A-Circulo C-ef - 1	<0.025	0.12	36	0.007	0.05	<0.024	0.0059	0.09	0.020
2019-SV-08A-Circulo C-ef - 2	<0.028	0.18	29	0.0068	0.06	<0.027	<0.01	0.1	0.02
2019-SV-08A-Circulo C-ef - 3	<0.027	0.5	23	0.014	0.28	0.02	<0.01	0.12	0.068
2019-SV-08A-Circulo D-ef - 1	<0.036	0.5	21	0.009	0.05	<0.037	<0.014	0.16	0.02
2019-SV-08A-Circulo D-ef - 2	0.016	0.6	11	0.0037	0.044	<0.024	<0.01	0.09	0.017
2019-SV-08A-Circulo D-ef - 3	<0.030	0.45	19	0.0039	0.04	<0.024	<0.01	0.1	0.013
2019-SV-08B-Circulo A-ef - 1	0.019	0.18	13	0.015	0.08	0.019	0.008	0.19	0.013
2019-SV-08B-Circulo A-ef - 2	0.018	0.29	13	<0.0068	0.046	<0.029	<0.01	0.15	0.019
2019-SV-08B-Circulo B-ef - 1	0.016	0.16	22	0.008	0.048	<0.026	<0.011	0.13	0.034

Label	Mo95	Ag107	Cd111	In115	Sn118	Sb121	Au197	Hg202	Tl205
2019-SV-08B-Circulo B-ef - 3	<0.027	0.50	19	0.006	0.048	<0.025	<0.01	0.11	0.038
2019-SV-08B-Circulo C-ef - 2	<0.027	0.16	18	0.008	0.05	<0.03	<0.01	0.11	0.011
2019-SV-08B-Circulo C-ef - 3	<0.030	0.44	21	0.008	0.099	<0.029	<0.011	0.12	0.016
2019-SV-08B-Circulo D-ef - 1	<0.025	0.18	35	0.0068	0.08	<0.030	<0.011	0.11	0.019
2019-SV-08B-Circulo D-ef - 2	0.011	1.1	36	0.0078	0.039	<0.023	<0.01	0.16	0.036
2019-SV-08B-Circulo D-ef - 3	0.013	1.8	116	0.015	0.12	0.016	<0.01	0.13	0.038
2019-SV-08B-Circulo D-ef - 4	0.012	1.4	63	0.017	0.068	<0.026	<0.01	0.14	0.046
2019-SV-08B-Circulo E-ef - 1	<0.03	0.34	41	0.0079	0.14	<0.028	<0.012	0.11	0.023
2019-SV-08B-Circulo E-ef - 2	<0.03	1	62	0.008	0.06	<0.035	0.007	0.12	0.025
UQAC-FeS-1 - 4	1.447571	3.826152	0.256068	0.232994	4.662159	3.144165	3.305032	3.14746	0.010304
GSD-1G - 4	0.990209	0.466212	1.244202	0.519193	0.635472	0.746155	0.126284	<0.3004	0.041687
NIST610 - 4	11.26277	6.052608	10.05967	8.950036	9.070512	8.289811	0.659055	<0.25657	1.834626
2019-SV-08B-Circulo E-ef - 3	0.017	1	55	0.0077	0.1	<0.03	<0.012	0.12	0.03
2019-SV-08B-Circulo E-ef - 4	<0.025	0.55	49	<0.008	0.035	<0.029	<0.01	0.13	0.022
2019-SV-09-Circulo A-ef - 1	0.015	0.19	38	0.0038	0.029	<0.029	<0.011	0.12	0.0088
2019-SV-09-Circulo A-ef - 2	<0.023	0.3	31	0.004	0.04	<0.028	<0.009	0.1	0.038
2019-SV-09-Circulo A-ef - 3	<0.028	0.58	40	<0.006	0.039	<0.026	<0.009	0.13	0.015
2019-SV-09-Circulo A-ef - 4	0.019	0.36	18	<0.0080	0.057	<0.03	<0.011	0.13	0.025
2019-SV-09-Circulo B-ef - 1	<0.030	0.5	12	0.0058	0.05	<0.025	<0.012	0.12	0.03
2019-SV-09-Circulo B-ef - 2	<0.026	0.50	15	<0.006	0.033	<0.027	<0.01	0.13	0.015
2019-SV-09-Circulo B-ef - 3	<0.027	0.14	14	0.0047	0.13	<0.029	<0.009	0.12	0.034
2019-SV-09-Circulo B-ef - 4	<0.03	0.19	7.7	0.0046	0.03	<0.028	<0.012	0.1	0.058
2019-SV-09-Circulo C-ef - 1	<0.036	0.27	16	0.006	0.09	0.03	<0.014	0.17	0.15
2019-SV-09-Circulo C-ef - 3	0.017	0.19	20	0.005	0.038	<0.029	<0.0099	0.15	0.029
2019-SV-011A-Circulo B-ef - 1	0.016	0.13	15	0.0044	0.03	<0.025	<0.01	0.1	0.03
2019-SV-011A-Circulo B-ef - 2	<0.03	0.1	29	<0.0069	0.03	<0.028	<0.009	0.11	0.020
2019-SV-011A-Circulo B-ef - 3	<0.02	0.23	22	0.0045	0.044	<0.029	<0.01	0.12	0.048
2019-SV-011A-Circulo B-ef - 4	<0.026	0.17	23	<0.008	0.2	<0.025	<0.01	0.13	0.014
2019-SV-011A-Circulo C-ef - 1	0.016	0.13	22	<0.0068	0.03	<0.027	<0.0099	0.12	0.016
2019-SV-011A-Circulo C-ef - 2	0.016	0.16	11	<0.0067	0.036	<0.026	<0.01	0.1	0.026
2019-SV-011A-Circulo C-ef - 3	0.018	0.12	19	0.004	0.033	<0.024	<0.011	0.12	0.013
2019-SV-011A-Circulo C-ef - 4	<0.033	0.13	14	<0.007	0.036	<0.026	<0.009	0.12	0.02

Label	Mo95	Ag107	Cd111	In115	Sn118	Sb121	Au197	Hg202	Tl205
2019-SV-011B-Circulo A-ef - 1	<0.026	0.20	28	<0.0069	0.039	<0.026	<0.01	0.12	0.012
2019-SV-011B-Circulo A-ef - 2	<0.03	0.3	21	0.005	0.038	<0.023	<0.01	0.16	0.028
2019-SV-011B-Circulo A-ef - 3	0.015	0.14	14	0.0034	0.039	<0.025	<0.0089	0.12	0.019
2019-SV-011B-Circulo A-ef - 4	0.015	0.14	20	<0.008	0.03	<0.027	0.006	0.16	0.020
2019-SV-011B-Circulo A-ef - 5	<0.026	0.1	7	0.0047	0.038	<0.026	<0.009	0.12	0.012
UQAC-FeS-1 - 5	3.069522	4.839643	0.366365	0.695857	28.28483	2.117847	7.47359	2.06685	0.020788
GSD-1G - 5	2.508319	1.688757	1.008975	1.625282	1.81061	1.961563	0.341066	<0.66821	0.078648
NIST610 - 5	23.11974	14.96291	7.317074	19.32244	20.60792	16.94805	1.226614	<0.53314	3.60448
2019-SV-011B-Circulo B-ef - 2	<0.05	0.40	13	0.009	0.05	<0.055	<0.020	0.19	0.04
2019-SV-011B-Circulo C-ef - 1	0.03	0.26	11	<0.014	0.07	<0.05	<0.018	0.27	0.057
2019-SV-011B-Circulo C-ef - 2	<0.05	0.35	21	0.009	0.08	<0.058	<0.02	0.22	0.056
2019-SV-011B-Circulo C-ef - 3	0.04	0.38	11	0.007	0.06	<0.05	<0.02	0.2	0.05
2019-SV-011B-Circulo D-ef - 1	0.026	0.37	13	<0.013	0.078	<0.05	<0.019	0.22	0.046
2019-SV-011B-Circulo D-ef - 2	<0.057	0.33	17	<0.012	0.07	<0.05	<0.017	0.18	0.027
2019-SV-011B-Circulo D-ef - 3	<0.058	0.30	16	<0.013	0.067	<0.04	<0.019	0.24	0.034
2019-SV-011C-Circulo A-ef - 1	0.023	0.27	19	<0.012	0.05	<0.045	<0.015	0.19	0.033
2019-SV-011C-Circulo B-ef - 2	<0.040	0.34	15	<0.012	0.060	<0.04	<0.016	0.19	0.040
2019-SV-011C-Circulo C-ef - 1	0.024	0.36	13	<0.012	0.058	<0.04	<0.016	0.2	0.068
2019-SV-011C-Circulo C-ef - 2	<0.04	0.22	11	<0.009	0.05	<0.040	<0.015	0.16	0.028
2019-SV-012A-Circulo A-ef - 1	0.03	0.67	37	0.03	0.2	<0.05	<0.02	0.28	0.1
2019-SV-012A-Circulo A-ef - 2	<0.04	0.26	17	<0.01	0.058	<0.036	<0.015	0.15	0.024
2019-SV-012A-Circulo B-ef - 1	0.027	0.35	7	0.0078	0.07	<0.04	<0.016	0.15	0.03
2019-SV-012A-Circulo C-ef - 1	<0.039	0.30	35	0.0078	0.057	<0.036	<0.016	0.17	0.05
2019-SV-012A-Circulo C-ef - 2	<0.034	0.34	28	<0.01	0.048	<0.035	<0.015	0.16	0.04
2019-SV-012A-Circulo D-ef - 1	<0.03	0.15	13	0.006	0.05	<0.03	<0.011	0.18	0.055
2019-SV-012A-Circulo D-ef - 2	<0.035	0.48	31	0.0058	0.09	<0.03	<0.014	0.20	0.09
2019-SV-012B-Circulo A-ef - 1	<0.038	0.35	28	0.009	0.06	<0.03	<0.012	0.17	0.028
2019-SV-012B-Circulo A-ef - 2	0.016	0.3	24	0.01	0.045	<0.036	<0.013	0.13	0.04
2019-SV-012B-Circulo B-ef - 1	<0.04	0.22	29	0.007	0.049	<0.035	<0.014	0.17	0.034
2019-SV-012B-Circulo B-ef - 2	<0.03	0.20	17	0.005	0.05	<0.03	<0.011	0.1	0.028
NIST610 - 6	11.57549	6.581151	9.795272	8.341962	9.640916	8.56519	0.594067	<0.28146	1.852525
GSD-1G - 6	1.178128	1.077491	1.487528	0.974538	1.166477	1.452418	0.183711	<0.43091	0.054812
UQAC-FeS-1 - 6	2.729553	8.358141	2.578509	1.172627	12.73653	18.57566	8.104764	1.98886	0.022722

Label	Mo95	Ag107	Cd111	In115	Sn118	Sb121	Au197	Hg202	Tl205
UQAC-FeS-1 - 1	2.240505	6.739849	0.297503	0.246041	38.8457	72.76453	3.80608	2.09931	0.009979
GSD-1G - 1	1.151167	0.777905	1.461629	0.718792	0.808353	0.876807	0.151572	<0.41272	0.04439
NIST610 - 1	12.08351	6.897238	13.26998	9.634853	10.17994	8.589796	0.601978	0.1915	2.039463
2019-SV-013-Circulo A-ef - 1	0.012	0.99	78	0.056	0.060	<0.029	<0.009	0.13	0.1
2019-SV-013-Circulo A-ef - 2	0.012	0.7	91	0.0058	0.05	<0.026	<0.01	0.12	0.23
2019-SV-013-Circulo B-ef - 1	0.014	0.3	132	0.029	0.08	<0.027	<0.009	0.11	0.29
2019-SV-013-Circulo B-ef - 2	0.015	1.6	116	0.014	0.08	<0.029	<0.009	0.11	0.09
2019-SV-013-Circulo C-ef - 1	0.02	0.17	94	0.02	0.07	<0.028	<0.009	0.13	0.2
2019-SV-013-Circulo C-ef - 2	0.02	0.70	114	0.014	0.05	<0.027	<0.01	0.14	0.49
2019-SV-014-Circulo A-ef - 1	0.015	0.5	63	0.0088	0.03	<0.027	<0.009	0.11	0.2
2019-SV-014-Circulo A-ef - 2	0.013	0.60	89	0.03	0.049	<0.027	<0.009	0.12	0.09
2019-SV-014-Circulo B-ef - 1	0.013	1.3	98	0.04	0.08	<0.035	<0.012	0.12	0.3
2019-SV-014-Circulo B-ef - 2	0.018	0.4	82	0.007	0.05	<0.029	<0.009	0.12	0.15
2019-SV-014-Circulo C-ef - 1	0.015	0.59	105	0.067	0.15	0.016	<0.008	0.12	0.28
2019-SV-014-Circulo C-ef - 2	<0.025	0.5	103	0.030	0.09	<0.030	<0.0089	0.13	0.27
2019-SV-015A-Circulo A-ef - 1	0.03	4.9	104	0.3	0.2	<0.05	<0.017	0.27	0.067
2019-SV-015A-Circulo A-ef - 2	0.018	30	257	0.01	0.048	<0.027	<0.010	0.15	1
2019-SV-015A-Circulo B-ef - 1	0.029	89	387	0.09	0.26	<0.04	<0.014	0.18	0.6
2019-SV-015A-Circulo B-ef - 2	0.013	120	260	0.0037	0.04	<0.027	<0.009	0.15	0.17
2019-SV-015A-Circulo B-ef - 3	<0.025	32	236	0.67	0.3	<0.026	<0.009	0.15	0.3
2019-SV-015A-Circulo C-ef - 1	0.029	14	117	0.009	0.06	<0.040	<0.012	0.12	0.34
2019-SV-015A-Circulo D-ef - 1	<0.04	19	123	0.049	0.08	<0.048	<0.014	0.17	0.28
2019-SV-015A-Circulo D-ef - 2	0.017	94	130	0.028	0.047	<0.030	<0.008	0.14	0.20
2019-SV-015A-Circulo D-ef - 3	<0.027	6	77	0.27	0.22	<0.034	<0.011	0.18	0.0056
2019-SV-015A-Circulo E-ef - 1	0.023	27	117	0.28	0.47	0.06	<0.011	0.13	0.38
2019-SV-015A-Circulo E-ef - 2	0.017	80	42	0.1	0.08	0.020	<0.009	0.2	0.40
2019-SV-015A-Circulo E-ef - 3	0.019	54	141	0.18	0.9	<0.026	<0.007	0.15	0.2
2019-SV-015B-Circulo A-ef - 1	0.016	6.6	86	0.20	0.09	0.033	<0.008	0.16	0.024
2019-SV-015B-Circulo A-ef - 2	0.016	0.5	118	0.086	0.05	<0.029	<0.011	0.19	0.004
UQAC-FeS-1 - 2	2.616771	10.47973	0.312842	0.241956	16.50305	2.348538	13.65748	2.79159	0.019498
GSD-1G - 2	0.713531	0.697677	1.405925	0.51498	0.588327	0.742466	0.118151	<0.30102	0.032066
NIST610 - 2	12.21451	7.733947	14.24196	9.840331	11.66729	10.03322	0.49337	0.25142	1.81058
2019-SV-015B-Circulo A-ef - 3	0.016	38	247	0.093	0.07	<0.03	<0.0090	0.15	0.39

Label	Mo95	Ag107	Cd111	In115	Sn118	Sb121	Au197	Hg202	Tl205
2019-SV-015B-Circulo B-ef- 1	<0.03	0.5	134	0.085	0.046	<0.03	<0.009	0.22	0.003
2019-SV-015B-Circulo B-ef - 2	<0.03	1	96	0.6	0.058	<0.036	<0.01	0.23	<0.005
2019-SV-015B-Circulo B-ef - 3	0.017	0.5	95	0.15	0.06	<0.027	<0.009	0.17	0.0039
2019-SV-015B-Circulo B-ef - 4	0.02	0.9	83	0.17	0.04	<0.03	0.0047	0.17	0.0033
2019-SV-015B-Circulo B-ef- 5	0.18	1.3	169	0.24	0.08	<0.03	<0.01	0.26	0.01
2019-SV-015B-Circulo B-ef-2 - 1	0.018	1.3	94	0.48	0.05	<0.024	<0.008	0.14	0.003
2019-SV-015B-Circulo C-ef - 1	<0.036	0.50	104	0.16	0.059	<0.045	<0.011	0.15	0.0044
2019-SV-015B-Circulo C-ef - 2	0.02	27	262	0.36	0.11	0.09	<0.01	0.20	0.5
2019-SV-015B-Circulo C-ef - 3	0.018	18	165	0.3	0.06	0.069	<0.009	0.18	0.23
2019-SV-016-Circulo A-ef - 1	<0.024	1.1	33	<0.0059	0.049	<0.027	<0.008	0.15	0.024
2019-SV-016-Circulo A-ef - 2	0.16	0.8	37	0.029	0.38	0.14	0.0059	0.19	0.14
2019-SV-016-Circulo B-ef - 1	0.013	0.6	35	<0.0057	0.039	<0.028	<0.007	0.17	0.11
2019-SV-016-Circulo D-ef - 1	0.02	0.7	51	0.008	0.07	0.02	<0.01	0.18	0.1
2019-SV-016-Circulo D-ef - 1	<0.04	0.38	3.9	<0.008	0.058	0.023	<0.010	0.15	0.034
2019-SV-016-Circulo E-ef - 2	0.012	0.33	10	<0.007	0.038	<0.024	<0.008	0.14	0.037
2019-SV-016-Circulo E-ef - 3	<0.02	0.34	7	<0.0059	0.04	<0.023	<0.01	0.15	0.02
2019-SH-31-Circulo A-ef - 1	<0.038	18	85	<0.01	0.04	2.44	<0.011	7.0	0.036
2019-SH-31-Circulo A-ef - 2	0.026	0.4	156	<0.0068	0.05	6.96	<0.008	0.2	0.6
2019-SH-31-Circulo A-ef - 3	0.049	10	50	<0.01	0.06	3.50	<0.01	3	0.22
2019-SH-31-Circulo A-ef - 4	<0.027	20	44	0.003	0.04	0.29	<0.006	3.4	0.06
2019-SH-31-Circulo B-ef - 1	0.1	0.3	57	<0.0069	0.039	8	<0.0066	0.12	1.3
2019-SH-31-Circulo B-ef - 2	<0.027	45	85	<0.0077	0.034	2.45	<0.006	14	0.38
2019-SH-31-Circulo B-ef - 3	<0.025	51	81	0.004	0.04	0.55	<0.006	4.4	0.14
2019-SH-31-Circulo C-ef - 1	<0.024	73	98	<0.0089	0.037	5.84	<0.007	16	0.07
UQAC-FeS-1 - 3	2.575894	9.254506	0.544373	0.571943	15.02088	3.727127	2.375857	0.77194	0.018067
GSD-1G - 3	0.968074	0.586585	1.706886	0.520477	0.767026	0.514156	0.06893	<0.36257	0.024524
NIST610 - 3	10.11738	6.102613	9.14134	7.44561	8.586962	6.855603	0.338846	<0.3258	1.262764
2019-SH-31-Circulo C-ef - 2	0.014	31	63	<0.0068	0.029	1.55	<0.0060	5.7	0.09
2019-SH-31-Circulo C-ef - 3	0.022	23	298	<0.0069	0.048	9	<0.008	39	0.14
2019-SH-31-Circulo C-ef - 4	<0.027	7.9	244	<0.0068	0.04	0.2	<0.008	6.8	0.02
2019-SH-120-Circulo A-ef - 1	<0.026	2.3	91	<0.006	0.038	2.86	<0.007	12	0.020
2019-SH-120-Circulo A-ef - 2	0.019	1.4	32	<0.007	0.049	23	<0.0079	8.9	0.58

Label	Mo95	Ag107	Cd111	In115	Sn118	Sb121	Au197	Hg202	Tl205
2019-SH-120-Circulo A-ef - 3	0.018	1.6	42	<0.0056	0.035	1.58	<0.0068	3	0.033
2019-SH-120-Circulo B-ef - 1	<0.037	0.6	69	<0.0077	0.060	0.22	<0.009	14	0.006
2019-SH-120-Circulo B-ef - 2	<0.026	2.2	94	<0.0067	0.048	4.71	<0.0069	15	0.090
2019-SH-120-Circulo B-ef - 3	<0.025	0.6	64	<0.006	0.038	9	<0.008	9	0.2
2019-SH-167-Circulo A-ef - 1	<0.024	12	298	<0.0060	0.036	1	<0.0066	2.4	0.12
2019-SH-167-Circulo A-ef - 2	0.014	14	142	<0.007	0.044	0.12	<0.007	0.35	0.026
2019-SH-167-Circulo A-ef - 3	0.013	10	143	0.0050	0.05	0.34	<0.009	0.68	0.029
2019-SH-167-Circulo A-ef - 4	<0.034	37	164	<0.0078	0.05	2.73	<0.01	4.5	0.22
2019-SH-167-Circulo B-ef - 1	<0.037	1.3	21	0.012	0.055	0.8	<0.0099	2.8	0.022
2019-SH-167-Circulo B-ef - 2	<0.026	3.3	236	0.07	0.044	13	<0.008	3.7	0.011
2019-SH-167-Circulo B-ef - 3	<0.023	32	308	<0.006	0.036	6.76	<0.008	0.2	0.5
2019-SH-167-Circulo B-ef - 4	<0.029	20	133	<0.008	0.047	0.3	0.005	0.18	0.11
2019-SH-167-Circulo C-ef - 1	0.020	4.6	125	0.15	0.05	41	<0.0078	6.7	0.015
2019-SH-167-Circulo C-ef - 2	<0.029	15	216	<0.0059	0.06	0.17	<0.0078	0.23	0.037
2019-SH-167-Circulo C-ef - 3	<0.027	25	176	<0.007	0.04	0.78	<0.009	0.12	0.13
2019-SH-167-Circulo C-ef - 4	<0.027	14	142	<0.006	0.04	0.4	<0.008	2	0.038
2019-SH-187-Circulo A-ef - 1	<0.029	13	57	0.0039	0.036	3	<0.0090	2.0	0.029
2019-SH-187-Circulo A-ef - 2	0.013	14	160	<0.007	0.046	6.80	<0.009	8	0.08
2019-SH-187-Circulo A-ef - 3	0.014	0.20	105	<0.0068	0.037	0.05	<0.009	3	0.0035
2019-SH-187-Circulo A-ef - 4	<0.023	0.58	124	<0.008	0.04	0.46	<0.01	2.5	0.02
2019-SH-187-Circulo C-ef - 1	0.017	7	71	0.26	0.04	0.3	<0.01	4	0.047
2019-SH-187-Circulo C-ef - 2	<0.028	3.7	197	<0.0080	0.04	0.27	<0.01	5.6	0.022
UQAC-FeS-1 - 4	2.117415	3.801788	0.39337	0.161322	6.361102	7.945869	6.241368	12.8103	0.01342
GSD-1G - 4	0.980112	1.031803	2.153705	0.702909	0.762966	0.943569	0.189843	<0.60405	0.050557
NIST610 - 4	9.564136	5.74415	10.42983	7.013099	8.931058	7.53934	0.461949	<0.33224	1.33173
2019-SH-187-Circulo C-ef - 3	0.080	23	65	0.012	0.04	9	<0.01	23	0.17
2019-SH-212-Circulo A-ef - 1	<0.027	3.9	72	0.014	0.089	0.12	<0.009	2.8	0.006
2019-SH-212-Circulo A-ef - 2	<0.03	10	52	0.015	0.25	0.28	<0.009	1	0.019
2019-SH-212-Circulo A-ef - 3	<0.029	5	35	<0.009	0.04	0.025	<0.01	1.5	0.003
2019-SH-212-Circulo A-ef - 4	0.015	11	85	0.008	0.056	0.4	0.006	2.4	0.014
2019-SH-212-Circulo B-ef - 1	0.015	22	218	0.0066	0.04	2	<0.008	1.5	0.026
2019-SH-212-Circulo B-ef - 2	<0.026	21	69	<0.008	0.039	0.19	<0.009	2	0.079

Label	Mo95	Ag107	Cd111	In115	Sn118	Sb121	Au197	Hg202	Tl205
2019-SH-212-Circulo B-ef - 3	0.016	14	95	<0.0067	0.037	0.1	<0.01	0.55	0.025
2019-SH-212-Circulo B-ef - 4	<0.04	6	60	0.03	0.5	0.22	<0.014	3	0.019
SH-227-Circulo B-ef - 1	<0.028	12	95	<0.0077	0.04	0.13	<0.01	2.4	0.027
SH-227-Circulo B-ef - 2	<0.03	6	186	0.035	0.045	2.44	<0.01	14	0.02
SH-227-Circulo B-ef - 3	<0.024	4	130	<0.007	0.04	10	<0.008	9	0.018
SH-227-Circulo A-ef - 1	<0.03	18	125	<0.009	0.04	0.24	<0.011	4.5	0.025
SH-227-Circulo A-ef - 2	<0.027	10	176	<0.006	0.039	0.6	<0.009	4	0.055
SH-227-Circulo A-ef - 3	0.023	3	84	<0.008	0.035	8	<0.0089	4.7	0.015
NIST610 - 5	8.29728	5.274236	10.17649	7.478902	7.899182	5.989187	0.367081	<0.39841	1.4471
GSD-1G - 5	0.488241	0.507888	1.123886	0.42962	0.600561	0.489873	0.082974	<0.33073	0.028817
UQAC-FeS-1 - 5	2.134744	6.123181	0.390839	0.212998	7.763209	10.79297	8.023234	9.9724	0.015879

*Values in red color have been discarded in pl

Label	Pb208	Bi209	L.O.D. >	S33	S34	Cr53	Mn55	Fe57	Co59
UQAC-FeS-1 - 1	1.457488	1.674368		1713.175	781.4451	0.534416	1.193419	8.921029	0.11383
GSD-1G - 1	0.706017	0.526506		3974.816	1791.713	1.218626	2.668888	19.57379	0.254192
NIST610 - 1	11.09988	9.317545		4364.907	1973.945	1.344577	2.991276	22.21269	0.306707
2019-SV-02-Circulo A-ef - 1	6	<0.0045		1635	745	0.5	1.1	9	0.11
2019-SV-02-Circulo A-ef - 2	105	0.0049		1974	884	0.59	1.4	10	0.1
2019-SV-02-Circulo A-ef - 3	8	<0.005		2310	1042	0.7	1.6	12	0.15
2019-SV-02-Circulo B-ef - 1	43	<0.005		2185	985	0.7	1.5	12	0.2
2019-SV-02-Circulo B-ef - 2	35	0.0024		1717	782	0.55	1	9	0.1
2019-SV-02-Circulo B-ef - 3	27	<0.007		2504	1129	0.79	1.7	13	0.18
2019-SV-02-Circulo C-ef - 1	13	0.0027		1719	775	0.5	1	9	0.12
2019-SV-04-Circulo A-ef - 1	26	0.002		1682	754	0.5	1	9	0.11
2019-SV-04-Circulo A-ef - 2	70	0.0029		1679	758	0.5	1	9	0.11
2019-SV-04-Circulo B-ef - 1	25	0.0028		1722	784	0.5	1.2	9	0.11
2019-SV-04-Circulo B-ef - 2	33	0.003		1820	826	0.56	1.2	10	0.12
2019-SV-04-Circulo B-ef - 3	36	<0.0038		1652	750	0.5	1.1	9	0.10
2019-SV-04-Circulo C-ef - 2	17	<0.0037		1790	817	0.5	1.2	9	0.11
2019-SV-04-Circulo C-ef - 3	28	<0.0047		2098	960	0.6	1	11	0.1
2019-SV-04-Circulo D-ef - 1	6	<0.004		1916	878	0.58	1.3	10	0.11
2019-SV-04-Circulo D-ef - 3	20	<0.0047		2535	1158	0.8	1.7	13	0.17
2019-SV-06A-Circulo A-ef - 1	11	0.0025		1937	886	0.58	1.3	10	0.12
2019-SV-06A-Circulo A-ef - 2	5	<0.0034		1781	816	0.5	1.2	9	0.1
2019-SV-06A-Circulo A-ef - 3	9	<0.004		2193	993	0.6	1.4	11	0.13
UQAC-FeS-1 - 2	2.823544	6.134465		1767.8	818.2284	0.48972	1.111043	8.829434	0.111384
GSD-1G - 2	1.177898	1.041603		10458.99	4819.785	2.837595	6.335435	50.57801	0.568503
NIST610 - 2	9.879477	8.845456		4691.302	2154.309	1.380206	2.913063	23.37717	0.281871
2019-SV-06A-Circulo B-ef - 3	0.6	<0.004		1816	841	0.5	1.2	9	0.12
2019-SV-06A-Circulo B-ef - 4	3	<0.0037		1766	821	0.50	1	9	0.107
2019-SV-06A-Circulo C-ef - 1	2.3	<0.003		1786	835	0.56	1.2	9	0.11
2019-SV-06A-Circulo C-ef - 2	4.6	<0.0034		1852	862	0.55	1.2	10	0.1
2019-SV-06A-Circulo C-ef - 3	4	<0.0038		1800	843	0.5	1	9	0.11
2019-SV-06B-Circulo A-ef - 1	1.9	0.0023		1776	825	0.5	1.2	9	0.12
2019-SV-06B-Circulo A-ef - 2	7	<0.0037		1751	824	0.5	1.2	9	0.1
2019-SV-06B-Circulo A-ef - 3	20	<0.003		1780	831	0.5	1	10	0.1

Label	Pb208	Bi209	L.O.D. >	S33	S34	Cr53	Mn55	Fe57	Co59
2019-SV-06B-Circulo A-ef - 4	45	0.002		1775	827	0.55	1	10	0.1
2019-SV-06B-Circulo B-ef - 1	5.5	<0.0029		1709	796	0.5	1.1	9	0.11
2019-SV-06B-Circulo B-ef - 2	1	<0.0045		2484	1168	0.8	1.7	14	0.16
2019-SV-06B-Circulo B-ef - 3	11.0	0.0023		1834	863	0.56	1.2	10	0.1
2019-SV-06B-Circulo C-ef - 2	1.2	<0.003		1669	781	0.5	1.1	9	0.1
2019-SV-06B-Circulo C-ef - 3	5.7	<0.0038		1765	834	0.5	1.2	10	0.1
2019-SV-07-Circulo A-ef - 1	0.24	<0.0037		1783	841	0.56	1.2	9.9	0.12
2019-SV-07-Circulo A-ef - 2	0.47	<0.0037		1671	799	0.5	1	10	0.1
2019-SV-07-Circulo A-ef - 3	11	<0.0033		1764	835	0.55	1.2	10	0.12
2019-SV-07-Circulo A-ef - 4	1.4	<0.0033		1723	813	0.5	1.2	10	0.1
2019-SV-07-Circulo B-ef - 1	0.7	<0.0039		1765	841	0.55	1	10	0.12
2019-SV-07-Circulo B-ef - 2	5.7	0.0023		1688	802	0.5	1.2	10	0.12
2019-SV-07-Circulo B-ef - 3	45	0.0025		1614	779	0.50	1	10	0.1
2019-SV-07-Circulo B-ef - 4	25	0.0035		2505	1193	0.80	1.8	15	0.18
2019-SV-07-Circulo C-ef - 1	5	<0.003		1771	847	0.55	1.3	10	0.13
2019-SV-07-Circulo C-ef - 2	2	<0.0034		1920	918	0.58	1.4	11	0.14
2019-SV-07-Circulo C-ef - 3	2.2	<0.005		2011	968	0.7	1.4	12	0.1
UQAC-FeS-1 - 3	2.060843	3.830656		1804.555	873.088	0.54073	1.203997	10.25446	0.12434
GSD-1G - 3	0.797711	0.534566		4636.886	2219.041	1.321126	3.001939	25.06176	0.298188
NIST610 - 3	11.2558	9.625049		4820.39	2304.144	1.452527	3.202701	26.80611	0.340341
2019-SV-08A-Circulo A-ef - 2	3.5	<0.0033		1705	816	0.57	1.2	10	0.1
2019-SV-08A-Circulo A-ef - 3	11	0.0024		1708	811	0.5	1	10	0.13
2019-SV-08A-Circulo A-ef - 4	28	0.0027		1668	801	0.5	1.2	10	0.1
2019-SV-08A-Circulo C-ef - 1	8.8	0.0016		1633	777	0.5	1	10	0.1
2019-SV-08A-Circulo C-ef - 2	7.9	<0.0034		1544	730	0.48	1	9	0.11
2019-SV-08A-Circulo C-ef - 3	17	0.0019		1664	783	0.5	1.2	10	0.13
2019-SV-08A-Circulo D-ef - 1	2.7	<0.004		2100	992	0.69	1.5	13	0.17
2019-SV-08A-Circulo D-ef - 2	34	0.0027		1619	763	0.5	1.1	10	0.12
2019-SV-08A-Circulo D-ef - 3	16	0.0023		1652	774	0.5	1.2	10	0.12
2019-SV-08B-Circulo A-ef - 1	1.5	<0.0038		1750	825	0.58	1.2	11	0.12
2019-SV-08B-Circulo A-ef - 2	0.50	<0.0033		1631	775	0.56	1.2	10	0.1
2019-SV-08B-Circulo B-ef - 1	3.7	<0.003		1663	789	0.56	1.2	10	0.12

Label	Pb208	Bi209	L.O.D. >	S33	S34	Cr53	Mn55	Fe57	Co59
2019-SV-08B-Circulo B-ef - 3	18	0.0017		1613	761	0.55	1	10	0.1
2019-SV-08B-Circulo C-ef - 2	16	0.0028		1652	785	0.56	1.2	11	0.12
2019-SV-08B-Circulo C-ef - 3	2.3	<0.0034		1730	813	0.58	1	11	0.1
2019-SV-08B-Circulo D-ef - 1	5	0.0020		1659	773	0.56	1.2	11	0.12
2019-SV-08B-Circulo D-ef - 2	3.3	<0.003		1577	743	0.5	1.1	10	0.11
2019-SV-08B-Circulo D-ef - 3	2.6	<0.0034		1574	735	0.5	1.1	10	0.1
2019-SV-08B-Circulo D-ef - 4	4	<0.003		1733	811	0.59	1.2	11	0.13
2019-SV-08B-Circulo E-ef - 1	3.8	<0.0035		1795	840	0.6	1.3	12	0.1
2019-SV-08B-Circulo E-ef - 2	0.8	<0.003		1832	854	0.6	1.3	12	0.13
UQAC-FeS-1 - 4	2.37063	3.031411		1621.831	757.3147	0.506577	1.089002	9.852	0.121965
GSD-1G - 4	1.210641	0.809424		5368.278	2497.898	1.639949	3.49793	31.91697	0.389054
NIST610 - 4	12.39778	9.85728		4476.233	2097.683	1.45418	3.058365	27.92752	0.331806
2019-SV-08B-Circulo E-ef - 3	4.8	0.003		1874	876	0.58	1.3	12	0.14
2019-SV-08B-Circulo E-ef - 4	1.3	<0.0035		1689	790	0.5	1	11	0.1
2019-SV-09-Circulo A-ef - 1	1.5	<0.0034		1644	770	0.5	1.2	11	0.13
2019-SV-09-Circulo A-ef - 2	1.3	<0.0034		1666	768	0.55	1.2	11	0.13
2019-SV-09-Circulo A-ef - 3	0.7	<0.0033		1633	764	0.5	1.2	11	0.13
2019-SV-09-Circulo A-ef - 4	2.3	<0.0038		1774	824	0.55	1.3	11	0.13
2019-SV-09-Circulo B-ef - 1	2.0	<0.0038		1745	818	0.58	1.3	12	0.1
2019-SV-09-Circulo B-ef - 2	1.0	<0.003		1621	759	0.5	1	11	0.1
2019-SV-09-Circulo B-ef - 3	6	0.0016		1554	726	0.50	1	10	0.1
2019-SV-09-Circulo B-ef - 4	21	0.0026		1779	828	0.6	1.3	12	0.1
2019-SV-09-Circulo C-ef - 1	22	<0.005		2278	1072	0.8	1.7	15	0.19
2019-SV-09-Circulo C-ef - 3	4.9	<0.0035		1683	788	0.5	1.3	11	0.1
2019-SV-011A-Circulo B-ef - 1	11	0.0017		1562	731	0.50	1.2	11	0.13
2019-SV-011A-Circulo B-ef - 2	5.6	<0.0028		1529	715	0.5	1.2	10	0.14
2019-SV-011A-Circulo B-ef - 3	3	0.0019		1586	744	0.5	1.2	11	0.13
2019-SV-011A-Circulo B-ef - 4	1.8	<0.0036		1547	724	0.5	1	10	0.1
2019-SV-011A-Circulo C-ef - 1	4.5	<0.0034		1491	696	0.47	1.2	10	0.13
2019-SV-011A-Circulo C-ef - 2	1	<0.0035		1474	691	0.48	1.2	10	0.1
2019-SV-011A-Circulo C-ef - 3	1.8	0.0017		1478	692	0.49	1.2	10	0.14
2019-SV-011A-Circulo C-ef - 4	1.3	<0.0039		1537	710	0.49	1.2	11	0.1

Label	Pb208	Bi209	L.O.D. >	S33	S34	Cr53	Mn55	Fe57	Co59
2019-SV-011B-Circulo A-ef - 1	0.77	<0.0036		1503	704	0.5	1.2	10	0.1
2019-SV-011B-Circulo A-ef - 2	5.7	0.0025		1504	709	0.5	1.2	10	0.1
2019-SV-011B-Circulo A-ef - 3	2	<0.0028		1396	651	0.47	1.1	10	0.1
2019-SV-011B-Circulo A-ef - 4	3.7	<0.003		1487	697	0.50	1	10	0.14
2019-SV-011B-Circulo A-ef - 5	33	<0.0036		1403	660	0.44	1.1	10	0.13
UQAC-FeS-1 - 5	0.748244	3.390265		1097.43	517.4163	0.544653	1.317883	10.84287	0.134688
GSD-1G - 5	0.476951	1.796482		7079.116	3312.874	3.342211	8.106982	67.40475	0.854073
NIST610 - 5	5.025372	23.7684		5554.524	2609.923	2.648893	6.559074	53.94795	0.672363
2019-SV-011B-Circulo B-ef - 2	1.4	<0.006		2122	993	1	2.5	21	0.3
2019-SV-011B-Circulo C-ef - 1	0.7	<0.007		2117	986	1	2.4	21	0.3
2019-SV-011B-Circulo C-ef - 2	2	<0.007		2147	998	1	2.4	20	0.26
2019-SV-011B-Circulo C-ef - 3	1.8	<0.0067		2057	967	0.9	2.3	20	0.25
2019-SV-011B-Circulo D-ef - 1	0.77	<0.0056		2003	941	0.89	2	19	0.229
2019-SV-011B-Circulo D-ef - 2	0.79	<0.007		2005	933	0.90	2.1	18	0.229
2019-SV-011B-Circulo D-ef - 3	0.80	0.004		2048	946	0.9	2.2	19	0.243
2019-SV-011C-Circulo A-ef - 1	0.80	<0.006		1887	872	0.8	2.0	17	0.2
2019-SV-011C-Circulo B-ef - 2	2.3	0.0028		1948	895	0.8	1.9	17	0.2
2019-SV-011C-Circulo C-ef - 1	1.5	<0.0060		1943	901	0.8	1.9	17	0.20
2019-SV-011C-Circulo C-ef - 2	1.4	<0.0046		1798	828	0.77	1.7	15	0.19
2019-SV-012A-Circulo A-ef - 1	19	<0.006		2294	1058	1	2	19	0.243
2019-SV-012A-Circulo A-ef - 2	0.4	<0.0039		1814	840	0.8	1.7	15	0.187
2019-SV-012A-Circulo B-ef - 1	0.6	<0.0056		2078	950	0.8	1.9	16	0.2
2019-SV-012A-Circulo C-ef - 1	5	<0.005		1905	866	0.7	1.7	15	0.2
2019-SV-012A-Circulo C-ef - 2	4.6	<0.0044		1785	831	0.69	1.6	14	0.2
2019-SV-012A-Circulo D-ef - 1	26	0.0034		1742	799	0.67	2	14	0.2
2019-SV-012A-Circulo D-ef - 2	12	0.0024		1722	792	0.68	1	13	0.16
2019-SV-012B-Circulo A-ef - 1	2.9	0.0028		1793	823	0.67	1.5	14	0.2
2019-SV-012B-Circulo A-ef - 2	2.0	<0.0036		1820	845	0.68	1.5	14	0.2
2019-SV-012B-Circulo B-ef - 1	2.8	<0.0046		1825	831	0.7	1.5	13	0.2
2019-SV-012B-Circulo B-ef - 2	2.5	<0.003		1632	749	0.57	1	12	0.15
NIST610 - 6	10.57073	10.58531		4124.722	1898.392	1.492014	3.303912	29.6512	0.367279
GSD-1G - 6	1.548377	1.258073		6636.947	3035.893	2.429255	5.235577	46.82428	0.585678
UQAC-FeS-1 - 6	3.336015	6.915938		1576.085	720.8568	0.547238	1.228364	10.81829	0.133952

Label	Pb208	Bi209	L.O.D. >	S33	S34	Cr53	Mn55	Fe57	Co59
UQAC-FeS-1 - 1	2.253711	4.362918		1857.988	880.7727	0.57893	0.863228	9.383542	0.085957
GSD-1G - 1	1.191782	0.729756		7163.075	3367.306	2.258017	3.322016	35.00538	0.325282
NIST610 - 1	13.385	11.33121		5247.185	2491.405	1.65668	2.564555	27.13027	0.278933
2019-SV-013-Circulo A-ef - 1	7	<0.004		1798	840	0.5	0.9	10	0.09
2019-SV-013-Circulo A-ef - 2	18	<0.0039		1785	840	0.56	0.9	10	0.1
2019-SV-013-Circulo B-ef - 1	34	0.0028		1787	837	0.56	0.9	10	0.10
2019-SV-013-Circulo B-ef - 2	6	<0.0037		1824	849	0.56	1.0	10	0.099
2019-SV-013-Circulo C-ef - 1	25	0.0026		1814	844	0.5	1.0	10	0.1
2019-SV-013-Circulo C-ef - 2	69	0.0025		1967	914	0.6	1.1	11	0.11
2019-SV-014-Circulo A-ef - 1	39	0.0024		1820	844	0.56	1.0	10	0.1
2019-SV-014-Circulo A-ef - 2	13	<0.0038		1818	857	0.5	1.0	10	0.1
2019-SV-014-Circulo B-ef - 1	23	0.0029		2337	1090	0.68	1.3	13	0.13
2019-SV-014-Circulo B-ef - 2	28	0.002		1791	840	0.5	1.0	10	0.10
2019-SV-014-Circulo C-ef - 1	19	0.002		1830	845	0.5	1.0	10	0.10
2019-SV-014-Circulo C-ef - 2	31	0.0022		2046	943	0.59	1.1	11	0.12
2019-SV-015A-Circulo A-ef - 1	8.0	<0.0066		3509	1617	1	1.9	19	0.19
2019-SV-015A-Circulo A-ef - 2	9	<0.0039		1949	901	0.58	1.1	10	0.10
2019-SV-015A-Circulo B-ef - 1	185	<0.0060		2790	1288	0.8	1.6	15	0.16
2019-SV-015A-Circulo B-ef - 2	0.45	0.002		1933	890	0.57	1.1	10	0.10
2019-SV-015A-Circulo B-ef - 3	2.6	<0.004		2015	936	0.58	1.2	11	0.12
2019-SV-015A-Circulo C-ef - 1	28	<0.0049		2598	1203	0.8	1.5	14	0.14
2019-SV-015A-Circulo D-ef - 1	39	<0.006		3242	1495	0.9	1.9	17	0.18
2019-SV-015A-Circulo D-ef - 2	0.3	<0.0035		2042	936	0.56	1.2	11	0.10
2019-SV-015A-Circulo D-ef - 3	0.025	<0.004		2496	1135	0.7	1	13	0.14
2019-SV-015A-Circulo E-ef - 1	1.5	<0.0047		2359	1076	0.68	1.4	12	0.13
2019-SV-015A-Circulo E-ef - 2	1.8	<0.004		2082	953	0.57	1.2	11	0.12
2019-SV-015A-Circulo E-ef - 3	2	<0.003		2032	935	0.5	1.2	10	0.12
2019-SV-015B-Circulo A-ef - 1	0.4	<0.0034		2104	958	0.57	1.2	11	0.12
2019-SV-015B-Circulo A-ef - 2	0.011	<0.0044		2472	1124	0.6	1	13	0.14
UQAC-FeS-1 - 2	4.214435	5.058873		2389	1082	0.564023	1.292286	11.20848	0.125036
GSD-1G - 2	0.895815	0.638622		6075	2769	1.49536	3.232173	27.20984	0.307368
NIST610 - 2	12.01932	10.47414		6607	3030	1.574316	3.67499	31.26345	0.363534
2019-SV-015B-Circulo A-ef - 3	3.3	<0.0040		2150	975	0.5	1.2	10	0.11

Label	Pb208	Bi209	L.O.D. >	S33	S34	Cr53	Mn55	Fe57	Co59
2019-SV-015B-Circulo B-ef- 1	0.15	<0.0036		2349	1077	0.55	1.4	11	0.13
2019-SV-015B-Circulo B-ef - 2	0.11	<0.0046		2634	1205	0.7	1.5	13	0.15
2019-SV-015B-Circulo B-ef - 3	0.7	<0.0038		2322	1063	0.59	1.4	12	0.13
2019-SV-015B-Circulo B-ef - 4	0.35	<0.0035		2249	1034	0.5	1.3	11	0.12
2019-SV-015B-Circulo B-ef- 5	12	0.003		2469	1126	0.6	1.5	12	0.15
2019-SV-015B-Circulo B-ef-2 - 1	0.017	<0.003		2108	964	0.55	1.3	11	0.11
2019-SV-015B-Circulo C-ef - 1	0.023	<0.004		2899	1326	0.77	1.7	15	0.18
2019-SV-015B-Circulo C-ef - 2	6	0.0020		2203	1015	0.57	1.3	12	0.13
2019-SV-015B-Circulo C-ef - 3	0.55	<0.003		2114	968	0.56	1.3	11	0.12
2019-SV-016-Circulo A-ef - 1	7.7	<0.0033		1905	872	0.49	1.2	10	0.11
2019-SV-016-Circulo A-ef - 2	36	0.0033		2562	1165	0.64	1.6	14	0.1
2019-SV-016-Circulo B-ef - 1	19	0.0023		1890	869	0.47	1.2	10	0.1
2019-SV-016-Circulo D-ef - 1	35	0.002		1999	919	0.5	1.2	11	0.12
2019-SV-016-Circulo D-ef - 1	22	<0.0037		2797	1281	0.7	1.7	15	0.17
2019-SV-016-Circulo E-ef - 2	4	0.0019		1876	853	0.49	1.1	10	0.1
2019-SV-016-Circulo E-ef - 3	2.6	<0.0029		1824	821	0.47	1.1	10	0.12
2019-SH-31-Circulo A-ef - 1	1.3	<0.004		2728	1237	0.7	1.7	15	0.19
2019-SH-31-Circulo A-ef - 2	10	0.0019		2055	937	0.5	1.3	11	0.13
2019-SH-31-Circulo A-ef - 3	2.4	<0.0055		2998	1360	0.79	1.8	17	0.21
2019-SH-31-Circulo A-ef - 4	0.15	<0.003		1925	881	0.48	1.2	11	0.12
2019-SH-31-Circulo B-ef - 1	25	0.0023		1893	859	0.49	1	11	0.13
2019-SH-31-Circulo B-ef - 2	2.6	<0.003		1874	845	0.46	1.2	11	0.14
2019-SH-31-Circulo B-ef - 3	0.9	<0.0037		1853	846	0.50	1.1	11	0.14
2019-SH-31-Circulo C-ef - 1	4.0	0.0025		2092	952	0.55	1	12	0.14
UQAC-FeS-1 - 3	3.764307	4.623669		2629.771	1193.951	0.620479	1.451991	13.20084	0.163482
GSD-1G - 3	0.788544	0.55668		6302.619	2865.501	1.431206	3.394561	30.5405	0.400595
NIST610 - 3	9.951083	8.44255		5597.194	2568.952	1.407041	3.188489	28.73092	0.338974
2019-SH-31-Circulo C-ef - 2	1.2	<0.0037		1945	888	0.48	1.1	10	0.12
2019-SH-31-Circulo C-ef - 3	4	<0.0033		1962	891	0.5	1.2	11	0.14
2019-SH-31-Circulo C-ef - 4	0.18	<0.0035		1976	894	0.5	1.2	11	0.13
2019-SH-120-Circulo A-ef - 1	1.4	<0.0030		1956	880	0.5	1.1	11	0.1
2019-SH-120-Circulo A-ef - 2	21	<0.003		2023	927	0.5	1.2	11	0.13

Label	Pb208	Bi209	L.O.D. >	S33	S34	Cr53	Mn55	Fe57	Co59
2019-SH-120-Circulo A-ef - 3	0.8	<0.0029		1825	827	0.47	1.1	10	0.1
2019-SH-120-Circulo B-ef - 1	0.2	<0.0045		2420	1089	0.6	1.4	13	0.16
2019-SH-120-Circulo B-ef - 2	6	<0.003		1869	860	0.48	1.1	10	0.1
2019-SH-120-Circulo B-ef - 3	5.8	0.0023		1861	854	0.5	1.1	10	0.1
2019-SH-167-Circulo A-ef - 1	0.88	<0.0030		1904	862	0.49	1	11	0.13
2019-SH-167-Circulo A-ef - 2	0.08	<0.0029		1830	839	0.49	1.1	10	0.12
2019-SH-167-Circulo A-ef - 3	0.27	0.0019		2025	924	0.5	1.2	11	0.13
2019-SH-167-Circulo A-ef - 4	2.6	<0.0047		2346	1073	0.6	1.4	13	0.16
2019-SH-167-Circulo B-ef - 1	0.38	<0.0039		2336	1046	0.6	1.4	13	0.16
2019-SH-167-Circulo B-ef - 2	5	0.0025		1965	884	0.5	1.2	11	0.14
2019-SH-167-Circulo B-ef - 3	5	<0.0029		1768	804	0.45	1	10	0.12
2019-SH-167-Circulo B-ef - 4	0.48	<0.0050		2317	1050	0.6	1.4	13	0.15
2019-SH-167-Circulo C-ef - 1	5.8	<0.003		1787	815	0.44	1	10	0.12
2019-SH-167-Circulo C-ef - 2	0.26	<0.0035		1842	835	0.49	1.1	10	0.12
2019-SH-167-Circulo C-ef - 3	0.5	<0.0030		1885	857	0.5	1.1	11	0.13
2019-SH-167-Circulo C-ef - 4	0.19	<0.0029		1806	813	0.48	1	10	0.12
2019-SH-187-Circulo A-ef - 1	3.4	<0.0033		1860	834	0.48	1	11	0.13
2019-SH-187-Circulo A-ef - 2	4	<0.0029		1926	863	0.49	1	11	0.13
2019-SH-187-Circulo A-ef - 3	0.068	<0.004		1950	880	0.5	1	11	0.1
2019-SH-187-Circulo A-ef - 4	0.9	0.0018		1974	887	0.5	1.2	12	0.143
2019-SH-187-Circulo C-ef - 1	1.2	<0.0035		2026	911	0.5	1	12	0.15
2019-SH-187-Circulo C-ef - 2	0.39	<0.0036		1957	881	0.5	1.2	11	0.14
UQAC-FeS-1 - 4	1.924961	2.789583		2352.83	1073.546	0.57596	1.258522	12.09502	0.15714
GSD-1G - 4	1.296395	1.042294		9628.443	4436.577	2.312901	5.055305	48.89222	0.611918
NIST610 - 4	9.638697	8.300378		5380.643	2462.221	1.360278	2.945047	28.78259	0.32248
2019-SH-187-Circulo C-ef - 3	6	<0.004		2011	923	0.5	1.1	11	0.136
2019-SH-212-Circulo A-ef - 1	0.056	<0.0036		1995	910	0.5	1.1	11	0.14
2019-SH-212-Circulo A-ef - 2	0.25	<0.0035		1941	889	0.48	1.1	11	0.13
2019-SH-212-Circulo A-ef - 3	0.01	<0.0037		2088	943	0.55	1	12	0.15
2019-SH-212-Circulo A-ef - 4	0.24	<0.003		1889	868	0.5	1.1	11	0.14
2019-SH-212-Circulo B-ef - 1	0.9	<0.0036		1914	869	0.49	1	11	0.14
2019-SH-212-Circulo B-ef - 2	0.39	<0.0034		1915	871	0.49	1.1	11	0.14

Label	Pb208	Bi209	L.O.D. >	S33	S34	Cr53	Mn55	Fe57	Co59
2019-SH-212-Circulo B-ef - 3	0.13	<0.0035		1831	844	0.49	1.1	11	0.13
2019-SH-212-Circulo B-ef - 4	0.14	<0.005		2471	1136	0.69	1.5	15	0.19
SH-227-Circulo B-ef - 1	0.1	<0.0029		1832	830	0.5	1.1	11	0.14
SH-227-Circulo B-ef - 2	0.66	<0.004		1880	861	0.56	1.2	11	0.13
SH-227-Circulo B-ef - 3	4	<0.003		1758	806	0.49	1.1	11	0.14
SH-227-Circulo A-ef - 1	0.11	<0.0040		1996	913	0.59	1.2	12	0.16
SH-227-Circulo A-ef - 2	0.40	<0.0028		1826	830	0.5	1.1	11	0.14
SH-227-Circulo A-ef - 3	3.0	<0.004		1879	845	0.50	1.2	11	0.14
NIST610 - 5	9.268843	8.140289		5067.607	2288.718	1.494961	3.147573	30.30902	0.39025
GSD-1G - 5	0.741445	0.555325		4565.744	2090.054	1.365523	2.85247	27.33076	0.327435
UQAC-FeS-1 - 5	2.652359	2.675755		1934.448	884.4741	0.55187	1.208731	11.5952	0.145885

*Values in red color have been discarded in pl

Label	Ni62	Cu65	Zn66	Ga71	Ge74	As75	Se77	Mo95	Ag107
UQAC-FeS-1 - 1	1.479012	3.386043	7.670772	0.020001	0.125148	0.114612	0.800785	0.019909	0.080284
GSD-1G - 1	2.705518	7.610429	16.98357	0.045098	0.28137	0.275273	1.805928	0.044965	0.180613
NIST610 - 1	3.077925	8.418922	19.20758	0.051938	0.309022	0.300498	1.929367	0.053388	0.202887
2019-SV-02-Circulo A-ef - 1	1.2	3	7	0.021	0.1	0.11	0.8	0.021	0.08
2019-SV-02-Circulo A-ef - 2	1.7	4.0	9	0.026	0.15	0.13	0.9	0.024	0.096
2019-SV-02-Circulo A-ef - 3	1.7	4.7	10	0.03	0.2	0.16	1.1	0.028	0.12
2019-SV-02-Circulo B-ef - 1	1.9	4	10	0.027	0.16	0.2	1.1	0.03	0.1
2019-SV-02-Circulo B-ef - 2	1.4	3.4	8	0.021	0.1	0.12	0.8	0.016	0.087
2019-SV-02-Circulo B-ef - 3	2.00	4.9	11	0.03	0.19	0.2	1.2	0.035	0.1
2019-SV-02-Circulo C-ef - 1	1.4	3.4	8	0.021	0.13	0.1	0.8	0.02	0.084
2019-SV-04-Circulo A-ef - 1	1	3	7	0.02	0.1	0.11	0.80	0.02	0.08
2019-SV-04-Circulo A-ef - 2	1.1	3	7	0.021	0.12	0.12	0.8	0.015	0.080
2019-SV-04-Circulo B-ef - 1	1.2	3	8	0.021	0.12	0.12	0.78	0.022	0.085
2019-SV-04-Circulo B-ef - 2	1.5	3.4	8	0.025	0.13	0.13	0.79	0.019	0.09
2019-SV-04-Circulo B-ef - 3	1.5	3	7	0.018	0.11	0.11	0.67	0.019	0.08
2019-SV-04-Circulo C-ef - 2	1.2	3	8	0.020	0.12	0.12	0.7	0.02	0.09
2019-SV-04-Circulo C-ef - 3	1.7	3.8	9	0.024	0.15	0.15	0.85	0.024	0.097
2019-SV-04-Circulo D-ef - 1	1.4	3.4	8	0.024	0.1	0.1	0.77	0.022	0.092
2019-SV-04-Circulo D-ef - 3	2	4.6	11	0.032	0.2	0.17	1	0.034	0.12
2019-SV-06A-Circulo A-ef - 1	1.2	3.4	8	0.02	0.13	0.1	0.7	0.024	0.088
2019-SV-06A-Circulo A-ef - 2	1.2	3	7	0.020	0.1	0.1	0.65	0.02	0.083
2019-SV-06A-Circulo A-ef - 3	1.6	3.8	9	0.03	0.15	0.14	0.9	0.028	0.10
UQAC-FeS-1 - 2	1.267831	2.92441	7.012061	0.019694	0.111012	0.104319	0.645798	0.016038	0.080507
GSD-1G - 2	7.147591	16.87387	40.32807	0.114868	0.658436	0.628122	4.16326	0.128332	0.447266
NIST610 - 2	3.242353	7.688339	18.23544	0.054189	0.298379	0.282913	1.76741	0.054006	0.203093
2019-SV-06A-Circulo B-ef - 3	1.3	3	7	0.023	0.1	0.1	0.67	0.022	0.086
2019-SV-06A-Circulo B-ef - 4	1.1	3	7	0.021	0.1	0.11	0.67	0.023	0.082
2019-SV-06A-Circulo C-ef - 1	1	3	7	0.02	0.1	0.12	0.77	0.025	0.083
2019-SV-06A-Circulo C-ef - 2	1.2	3	8	0.022	0.1	0.12	0.71	0.014	0.088
2019-SV-06A-Circulo C-ef - 3	1.4	3.3	7	0.022	0.12	0.1	0.7	0.025	0.088
2019-SV-06B-Circulo A-ef - 1	1.3	3	7	0.019	0.12	0.1	0.8	0.022	0.087
2019-SV-06B-Circulo A-ef - 2	1.5	3	7	0.020	0.1	0.11	0.7	0.021	0.089
2019-SV-06B-Circulo A-ef - 3	1.2	3.2	8	0.021	0.1	0.11	0.8	0.02	0.092

Label	Ni62	Cu65	Zn66	Ga71	Ge74	As75	Se77	Mo95	Ag107
2019-SV-06B-Circulo A-ef - 4	1.3	3.3	8	0.021	0.12	0.1	0.7	0.027	0.090
2019-SV-06B-Circulo B-ef - 1	1.2	3	7	0.020	0.1	0.1	0.8	0.026	0.087
2019-SV-06B-Circulo B-ef - 2	2	4.7	11	0.032	0.17	0.16	1.1	0.030	0.13
2019-SV-06B-Circulo B-ef - 3	1.5	3.5	8	0.02	0.13	0.1	0.7	0.025	0.096
2019-SV-06B-Circulo C-ef - 2	1.3	3	7	0.018	0.12	0.11	0.7	0.026	0.091
2019-SV-06B-Circulo C-ef - 3	1.4	3.5	8	0.024	0.13	0.13	0.8	0.022	0.096
2019-SV-07-Circulo A-ef - 1	1.4	3.6	8	0.022	0.12	0.11	0.77	0.025	0.096
2019-SV-07-Circulo A-ef - 2	1.3	3.4	7	0.022	0.1	0.12	0.7	0.02	0.094
2019-SV-07-Circulo A-ef - 3	1.3	3.6	8	0.02	0.13	0.12	0.7	0.018	0.099
2019-SV-07-Circulo A-ef - 4	1.3	3.6	8	0.023	0.12	0.11	0.78	0.023	0.10
2019-SV-07-Circulo B-ef - 1	1.6	3.7	8	0.023	0.13	0.12	0.78	0.025	0.10
2019-SV-07-Circulo B-ef - 2	1.3	3.6	8	0.02	0.1	0.12	0.74	0.024	0.10
2019-SV-07-Circulo B-ef - 3	1.4	3.5	7	0.020	0.12	0.1	0.77	0.023	0.1
2019-SV-07-Circulo B-ef - 4	2.5	5	11	0.03	0.19	0.2	1	0.036	0.15
2019-SV-07-Circulo C-ef - 1	1.4	3.8	8	0.022	0.1	0.1	0.9	0.023	0.11
2019-SV-07-Circulo C-ef - 2	1.4	4	9	0.02	0.1	0.14	0.9	0.025	0.12
2019-SV-07-Circulo C-ef - 3	2.4	4.5	9	0.029	0.15	0.15	1.0	0.03	0.13
UQAC-FeS-1 - 3	1.460797	3.8572	7.523019	0.022526	0.127095	0.124095	0.741869	0.020032	0.106575
GSD-1G - 3	3.555156	9.485273	18.78277	0.057707	0.314801	0.289491	1.922259	0.065445	0.270688
NIST610 - 3	4.752317	10.2643	20.04913	0.061916	0.339511	0.326677	1.978093	0.064627	0.279691
2019-SV-08A-Circulo A-ef - 2	1.3	3.8	7	0.022	0.1	0.12	0.8	0.024	0.10
2019-SV-08A-Circulo A-ef - 3	1.2	3.7	7	0.022	0.13	0.12	0.8	0.030	0.10
2019-SV-08A-Circulo A-ef - 4	1.6	3.8	7	0.02	0.13	0.12	0.7	0.027	0.10
2019-SV-08A-Circulo C-ef - 1	1.4	3.7	7	0.023	0.12	0.11	0.78	0.025	0.099
2019-SV-08A-Circulo C-ef - 2	1.3	3.5	7	0.020	0.1	0.1	0.7	0.028	0.093
2019-SV-08A-Circulo C-ef - 3	1.5	3.8	7	0.03	0.1	0.1	0.78	0.027	0.10
2019-SV-08A-Circulo D-ef - 1	2.2	4.8	9	0.030	0.2	0.15	1	0.036	0.1
2019-SV-08A-Circulo D-ef - 2	1.3	3.7	7	0.023	0.13	0.11	0.8	0.023	0.1
2019-SV-08A-Circulo D-ef - 3	1.4	3.7	7	0.024	0.13	0.12	0.77	0.030	0.10
2019-SV-08B-Circulo A-ef - 1	1.4	3.9	8	0.024	0.14	0.12	0.78	0.023	0.11
2019-SV-08B-Circulo A-ef - 2	1.1	3.6	7	0.022	0.13	0.11	0.77	0.023	0.098
2019-SV-08B-Circulo B-ef - 1	1.4	3.7	7	0.022	0.1	0.12	0.8	0.025	0.098

Label	Ni62	Cu65	Zn66	Ga71	Ge74	As75	Se77	Mo95	Ag107
2019-SV-08B-Circulo B-ef - 3	1.3	3.6	7	0.02	0.12	0.1	0.69	0.027	0.096
2019-SV-08B-Circulo C-ef - 2	1.1	3.6	7	0.024	0.13	0.12	0.7	0.027	0.099
2019-SV-08B-Circulo C-ef - 3	1.4	3.9	8	0.02	0.14	0.1	0.8	0.030	0.11
2019-SV-08B-Circulo D-ef - 1	1.4	3.7	8	0.022	0.1	0.12	0.8	0.025	0.097
2019-SV-08B-Circulo D-ef - 2	1.1	3.5	7	0.026	0.13	0.1	0.67	0.021	0.099
2019-SV-08B-Circulo D-ef - 3	1.2	3.4	7	0.02	0.12	0.11	0.7	0.023	0.093
2019-SV-08B-Circulo D-ef - 4	1.7	3.9	8	0.03	0.14	0.13	0.8	0.019	0.10
2019-SV-08B-Circulo E-ef - 1	1.5	4.0	8	0.026	0.14	0.13	0.8	0.03	0.11
2019-SV-08B-Circulo E-ef - 2	1.5	4	8	0.03	0.15	0.13	0.80	0.03	0.1
UQAC-FeS-1 - 4	1.217595	3.319618	6.502437	0.022172	0.118357	0.103702	0.697468	0.019952	0.090593
GSD-1G - 4	4.546494	11.11166	21.2952	0.082786	0.381699	0.359234	2.4168	0.074607	0.286001
NIST610 - 4	3.053039	9.396697	18.25287	0.064371	0.334031	0.289407	1.92931	0.067344	0.254514
2019-SV-08B-Circulo E-ef - 3	1.5	4	8	0.029	0.15	0.14	0.8	0.028	0.1
2019-SV-08B-Circulo E-ef - 4	1.6	3.7	7	0.024	0.1	0.12	0.8	0.025	0.098
2019-SV-09-Circulo A-ef - 1	1.5	3.8	7	0.025	0.13	0.12	0.70	0.020	0.099
2019-SV-09-Circulo A-ef - 2	1.2	3.8	7	0.026	0.1	0.13	0.7	0.023	0.1
2019-SV-09-Circulo A-ef - 3	1.4	3.7	7	0.02	0.1	0.12	0.7	0.028	0.10
2019-SV-09-Circulo A-ef - 4	1.4	4	8	0.026	0.14	0.13	0.7	0.029	0.11
2019-SV-09-Circulo B-ef - 1	1.7	4	8	0.027	0.15	0.13	0.8	0.030	0.1
2019-SV-09-Circulo B-ef - 2	1.3	3.7	7	0.027	0.13	0.12	0.78	0.026	0.11
2019-SV-09-Circulo B-ef - 3	1.3	3.7	7	0.025	0.12	0.11	0.7	0.027	0.10
2019-SV-09-Circulo B-ef - 4	1.6	4	8	0.03	0.1	0.14	0.77	0.03	0.11
2019-SV-09-Circulo C-ef - 1	1.9	6	10	0.04	0.18	0.18	1	0.036	0.15
2019-SV-09-Circulo C-ef - 3	1.5	4	8	0.03	0.14	0.13	0.8	0.027	0.11
2019-SV-011A-Circulo B-ef - 1	1.2	3.9	7	0.024	0.13	0.1	0.7	0.026	0.11
2019-SV-011A-Circulo B-ef - 2	1.3	3.9	7	0.025	0.13	0.12	0.7	0.03	0.1
2019-SV-011A-Circulo B-ef - 3	1.3	4	7	0.02	0.1	0.13	0.70	0.02	0.11
2019-SV-011A-Circulo B-ef - 4	1.5	3.8	7	0.025	0.13	0.1	0.7	0.026	0.11
2019-SV-011A-Circulo C-ef - 1	1	3.9	7	0.025	0.123	0.11	0.69	0.026	0.11
2019-SV-011A-Circulo C-ef - 2	1.1	3.9	7	0.023	0.1	0.11	0.66	0.024	0.11
2019-SV-011A-Circulo C-ef - 3	1.3	3.9	7	0.024	0.12	0.1	0.72	0.021	0.11
2019-SV-011A-Circulo C-ef - 4	1.6	3.9	7	0.025	0.13	0.12	0.7	0.033	0.11

Label	Ni62	Cu65	Zn66	Ga71	Ge74	As75	Se77	Mo95	Ag107
2019-SV-011B-Circulo A-ef - 1	1.4	4.0	7	0.024	0.13	0.12	0.7	0.026	0.11
2019-SV-011B-Circulo A-ef - 2	1.3	3.9	7	0.025	0.13	0.11	0.67	0.03	0.1
2019-SV-011B-Circulo A-ef - 3	1.3	3.6	7	0.022	0.12	0.11	0.6	0.024	0.11
2019-SV-011B-Circulo A-ef - 4	1.4	3.9	7	0.022	0.13	0.11	0.64	0.022	0.12
2019-SV-011B-Circulo A-ef - 5	1.1	3.6	7	0.021	0.1	0.11	0.68	0.026	0.1
UQAC-FeS-1 - 5	1.349686	4.566754	3.343637	0.023192	0.094709	0.12224	0.812613	0.028934	0.128048
GSD-1G - 5	9.457221	27.05918	20.87475	0.161233	0.567251	0.843459	5.024319	0.178896	0.766591
NIST610 - 5	7.831247	21.46733	16.91574	0.137346	0.465107	0.620576	4.135664	0.13576	0.629477
2019-SV-011B-Circulo B-ef - 2	2.8	8	7	0.051	0.2	0.2	1.4	0.05	0.24
2019-SV-011B-Circulo C-ef - 1	3	8	7	0.044	0.2	0.23	1	0.05	0.23
2019-SV-011B-Circulo C-ef - 2	2.2	8	7	0.052	0.19	0.2	1.5	0.05	0.24
2019-SV-011B-Circulo C-ef - 3	2.5	7.9	7	0.049	0.2	0.2	1	0.06	0.22
2019-SV-011B-Circulo D-ef - 1	2	7	7	0.042	0.2	0.22	1	0.043	0.22
2019-SV-011B-Circulo D-ef - 2	2.2	7	7	0.042	0.18	0.2	1	0.057	0.20
2019-SV-011B-Circulo D-ef - 3	2.8	7	7	0.043	0.18	0.2	1.2	0.058	0.21
2019-SV-011C-Circulo A-ef - 1	2	6	7	0.041	0.2	0.2	1	0.039	0.19
2019-SV-011C-Circulo B-ef - 2	1.9	6	7	0.041	0.17	0.19	1	0.040	0.19
2019-SV-011C-Circulo C-ef - 1	1.9	6	7	0.035	0.2	0.19	1.00	0.035	0.18
2019-SV-011C-Circulo C-ef - 2	2	5	7	0.04	0.16	0.2	1.0	0.04	0.16
2019-SV-012A-Circulo A-ef - 1	2.4	6.9	9	0.04	0.2	0.2	1.3	0.04	0.21
2019-SV-012A-Circulo A-ef - 2	1.9	5.5	7	0.035	0.16	0.2	1.0	0.04	0.16
2019-SV-012A-Circulo B-ef - 1	2.2	5.9	8	0.04	0.2	0.2	0.97	0.040	0.17
2019-SV-012A-Circulo C-ef - 1	1.8	5	8	0.04	0.17	0.2	1.0	0.039	0.17
2019-SV-012A-Circulo C-ef - 2	1.44	5	7	0.03	0.15	0.17	0.88	0.034	0.15
2019-SV-012A-Circulo D-ef - 1	1.6	4.8	7	0.03	0.15	0.2	0.9	0.03	0.14
2019-SV-012A-Circulo D-ef - 2	1.9	4.6	7	0.033	0.14	0.1	0.7	0.035	0.14
2019-SV-012B-Circulo A-ef - 1	1.8	4.8	7	0.033	0.2	0.15	0.88	0.038	0.14
2019-SV-012B-Circulo A-ef - 2	1.6	4.9	8	0.035	0.2	0.2	0.8	0.021	0.1
2019-SV-012B-Circulo B-ef - 1	1.8	4.8	8	0.033	0.15	0.15	0.80	0.04	0.14
2019-SV-012B-Circulo B-ef - 2	1.6	4	7	0.027	0.14	0.1	0.68	0.03	0.12
NIST610 - 6	3.411418	10.585	18.38327	0.07045	0.354585	0.351478	1.664634	0.05531	0.303527
GSD-1G - 6	5.430816	16.00233	29.95773	0.112909	0.589522	0.583984	2.821296	0.112835	0.49454
UQAC-FeS-1 - 6	1.404576	3.81987	7.091053	0.025459	0.129687	0.124588	0.666161	0.030594	0.112015

Label	Ni62	Cu65	Zn66	Ga71	Ge74	As75	Se77	Mo95	Ag107
UQAC-FeS-1 - 1	1.212571	3.235126	6.513427	0.020371	0.11716	0.140463	0.862065	0.024802	0.072673
GSD-1G - 1	5.294883	11.53096	24.72969	0.075666	0.43141	0.540531	3.252452	0.072719	0.279547
NIST610 - 1	3.944791	8.999321	19.00563	0.053796	0.329467	0.38952	2.581695	0.05242	0.219946
2019-SV-013-Circulo A-ef - 1	1.2	3.3	7	0.02	0.1	0.14	0.8	0.020	0.082
2019-SV-013-Circulo A-ef - 2	1.2	3	7	0.022	0.1	0.1	0.9	0.015	0.08
2019-SV-013-Circulo B-ef - 1	1.4	3.5	7	0.022	0.12	0.14	0.9	0.020	0.09
2019-SV-013-Circulo B-ef - 2	1.3	3.4	7	0.022	0.12	0.14	0.90	0.021	0.089
2019-SV-013-Circulo C-ef - 1	1.3	3.4	7	0.022	0.1	0.14	0.78	0.02	0.090
2019-SV-013-Circulo C-ef - 2	1.6	3.8	7	0.03	0.13	0.16	0.88	0.03	0.10
2019-SV-014-Circulo A-ef - 1	1.5	3.5	7	0.02	0.12	0.1	0.9	0.021	0.09
2019-SV-014-Circulo A-ef - 2	1.1	3.4	7	0.020	0.12	0.15	0.8	0.019	0.090
2019-SV-014-Circulo B-ef - 1	1.7	4.4	9	0.03	0.15	0.18	1	0.021	0.12
2019-SV-014-Circulo B-ef - 2	1.5	3.4	7	0.02	0.11	0.14	0.79	0.020	0.09
2019-SV-014-Circulo C-ef - 1	1.2	3	7	0.021	0.1	0.14	0.8	0.024	0.090
2019-SV-014-Circulo C-ef - 2	1.6	3.8	8	0.024	0.13	0.16	0.8	0.025	0.1
2019-SV-015A-Circulo A-ef - 1	2.9	7	13	0.042	0.21	0.28	1.7	0.05	0.18
2019-SV-015A-Circulo A-ef - 2	1.5	4	7	0.02	0.1	0.15	0.9	0.018	0.094
2019-SV-015A-Circulo B-ef - 1	2.0	5	10	0.032	0.18	0.2	1.3	0.039	0.14
2019-SV-015A-Circulo B-ef - 2	1.5	3.5	7	0.022	0.12	0.15	0.9	0.022	0.0960
2019-SV-015A-Circulo B-ef - 3	1.5	4	7	0.0233	0.12	0.15	0.9	0.025	0.10
2019-SV-015A-Circulo C-ef - 1	1.7	5	9	0.03	0.16	0.20	1.2	0.036	0.13
2019-SV-015A-Circulo D-ef - 1	2.5	6	12	0.035	0.20	0.2	1.5	0.04	0.16
2019-SV-015A-Circulo D-ef - 2	1.2	3.8	7	0.0221	0.13	0.15	0.9	0.021	0.10
2019-SV-015A-Circulo D-ef - 3	1.6	5	9	0.0272	0.15	0.2	0.95	0.027	0.1
2019-SV-015A-Circulo E-ef - 1	1.6	4	8	0.0292	0.14	0.2	1.1	0.033	0.12
2019-SV-015A-Circulo E-ef - 2	1.4	4	7	0.02	0.12	0.2	0.9	0.022	0.11
2019-SV-015A-Circulo E-ef - 3	1.4	4	7	0.025	0.13	0.15	0.78	0.023	0.10
2019-SV-015B-Circulo A-ef - 1	1.4	4	7	0.027	0.12	0.16	0.8	0.025	0.11
2019-SV-015B-Circulo A-ef - 2	1.6	4	9	0.028	0.1	0.2	1	0.024	0.1
UQAC-FeS-1 - 2	1.556445	4.037067	7.40798	0.026505	0.12679	0.159133	0.934669	0.028123	0.11532
GSD-1G - 2	3.515632	9.805616	18.33717	0.063286	0.317512	0.397477	2.288161	0.054835	0.282921
NIST610 - 2	4.446019	11.13936	21.57354	0.074116	0.371812	0.451	2.404889	0.063814	0.316274
2019-SV-015B-Circulo A-ef - 3	1.5	4	7	0.025	0.13	0.2	0.9	0.024	0.11

Label	Ni62	Cu65	Zn66	Ga71	Ge74	As75	Se77	Mo95	Ag107
2019-SV-015B-Circulo B-ef- 1	1.5	4	8	0.026	0.14	0.17	0.90	0.03	0.1
2019-SV-015B-Circulo B-ef - 2	1.7	5	9	0.03	0.15	0.2	1.1	0.03	0.1
2019-SV-015B-Circulo B-ef - 3	1.4	4	8	0.028	0.133	0.17	1.0	0.023	0.1
2019-SV-015B-Circulo B-ef - 4	1.6	4	8	0.027	0.13	0.2	0.85	0.03	0.1
2019-SV-015B-Circulo B-ef- 5	1.4	5	9	0.0279	0.14	0.2	1.0	0.033	0.13
2019-SV-015B-Circulo B-ef-2 - 1	1.4	4	7	0.024	0.12	0.16	0.90	0.022	0.11
2019-SV-015B-Circulo C-ef - 1	2	5	10	0.03	0.2	0.22	1	0.036	0.15
2019-SV-015B-Circulo C-ef - 2	1.4	4	8	0.027	0.13	0.2	0.82	0.02	0.12
2019-SV-015B-Circulo C-ef - 3	1.5	4	8	0.025	0.13	0.2	0.9	0.024	0.11
2019-SV-016-Circulo A-ef - 1	1.1	3.6	7	0.023	0.12	0.15	0.7	0.024	0.11
2019-SV-016-Circulo A-ef - 2	2	4.8	9	0.030	0.2	0.19	1	0.031	0.1
2019-SV-016-Circulo B-ef - 1	1.3	3.7	7	0.024	0.1	0.1	0.8	0.019	0.1
2019-SV-016-Circulo D-ef - 1	1.4	3.9	7	0.024	0.12	0.15	0.8	0.02	0.1
2019-SV-016-Circulo D-ef - 1	2	5.5	11	0.036	0.18	0.22	1.1	0.04	0.16
2019-SV-016-Circulo E-ef - 2	1.2	3.7	7	0.023	0.12	0.1	0.70	0.020	0.11
2019-SV-016-Circulo E-ef - 3	1.4	3.6	7	0.022	0.11	0.1	0.7	0.02	0.10
2019-SH-31-Circulo A-ef - 1	2.0	6	10	0.034	0.17	0.21	1.1	0.038	0.16
2019-SH-31-Circulo A-ef - 2	1.7	4	8	0.026	0.13	0.15	0.8	0.025	0.1
2019-SH-31-Circulo A-ef - 3	2	6	12	0.04	0.19	0.2	1.2	0.046	0.18
2019-SH-31-Circulo A-ef - 4	1.4	4.0	8	0.024	0.1	0.14	0.77	0.027	0.12
2019-SH-31-Circulo B-ef - 1	1.5	4.0	8	0.025	0.12	0.14	0.79	0.02	0.1
2019-SH-31-Circulo B-ef - 2	1.3	4	7	0.023	0.12	0.14	0.8	0.027	0.11
2019-SH-31-Circulo B-ef - 3	1.2	3.9	7	0.025	0.12	0.14	0.8	0.025	0.11
2019-SH-31-Circulo C-ef - 1	1.4	5	8	0.028	0.13	0.15	0.8	0.024	0.13
UQAC-FeS-1 - 3	1.6978	4.957829	9.428319	0.028619	0.1505	0.174924	0.976294	0.030761	0.14418
GSD-1G - 3	4.358025	11.36192	21.5441	0.067577	0.357453	0.399047	2.157389	0.050783	0.325049
NIST610 - 3	2.342284	10.45687	20.20824	0.057499	0.334072	0.388969	2.254717	0.069232	0.310484
2019-SH-31-Circulo C-ef - 2	1.2	4	7	0.023	0.12	0.14	0.7	0.020	0.11
2019-SH-31-Circulo C-ef - 3	1.3	4	8	0.024	0.13	0.1	0.77	0.024	0.12
2019-SH-31-Circulo C-ef - 4	1.4	4	8	0.023	0.12	0.1	0.78	0.027	0.12
2019-SH-120-Circulo A-ef - 1	1.5	4.0	7	0.02	0.1	0.15	0.8	0.026	0.11
2019-SH-120-Circulo A-ef - 2	1.5	4	8	0.023	0.12	0.2	0.8	0.026	0.12

Label	Ni62	Cu65	Zn66	Ga71	Ge74	As75	Se77	Mo95	Ag107
2019-SH-120-Circulo A-ef - 3	1.5	3.7	7	0.023	0.11	0.14	0.71	0.023	0.11
2019-SH-120-Circulo B-ef - 1	1.7	4.8	9	0.030	0.1	0.19	0.9	0.037	0.1
2019-SH-120-Circulo B-ef - 2	1.1	3.9	7	0.022	0.12	0.14	0.77	0.026	0.11
2019-SH-120-Circulo B-ef - 3	1.4	3.8	7	0.020	0.11	0.15	0.68	0.025	0.1
2019-SH-167-Circulo A-ef - 1	1.4	3.9	7	0.023	0.12	0.14	0.7	0.024	0.11
2019-SH-167-Circulo A-ef - 2	1.3	3.7	7	0.023	0.11	0.14	0.7	0.020	0.11
2019-SH-167-Circulo A-ef - 3	1.6	4.2	8	0.026	0.1	0.16	0.8	0.022	0.12
2019-SH-167-Circulo A-ef - 4	1.4	5.0	9	0.030	0.15	0.2	0.88	0.034	0.14
2019-SH-167-Circulo B-ef - 1	1.8	5	9	0.03	0.15	0.19	0.90	0.037	0.14
2019-SH-167-Circulo B-ef - 2	1.4	4	8	0.02	0.12	0.16	0.7	0.026	0.12
2019-SH-167-Circulo B-ef - 3	1.4	3.7	7	0.022	0.11	0.15	0.65	0.023	0.11
2019-SH-167-Circulo B-ef - 4	1.7	4.8	9	0.031	0.15	0.19	0.89	0.029	0.14
2019-SH-167-Circulo C-ef - 1	1.3	4	7	0.023	0.1	0.14	0.7	0.027	0.11
2019-SH-167-Circulo C-ef - 2	1.3	3.9	7	0.024	0.12	0.16	0.7	0.029	0.11
2019-SH-167-Circulo C-ef - 3	1.3	4	7	0.02	0.12	0.2	0.69	0.027	0.12
2019-SH-167-Circulo C-ef - 4	1.3	4	7	0.021	0.1	0.14	0.70	0.027	0.11
2019-SH-187-Circulo A-ef - 1	1.2	4	7	0.024	0.12	0.2	0.7	0.029	0.12
2019-SH-187-Circulo A-ef - 2	1.2	4	8	0.03	0.12	0.16	0.7	0.023	0.12
2019-SH-187-Circulo A-ef - 3	1.4	4.3	8	0.026	0.13	0.2	0.68	0.021	0.12
2019-SH-187-Circulo A-ef - 4	1.6	4.5	8	0.03	0.1	0.16	0.8	0.023	0.13
2019-SH-187-Circulo C-ef - 1	1.6	4.7	8	0.030	0.13	0.2	0.79	0.026	0.1
2019-SH-187-Circulo C-ef - 2	1.8	4.5	8	0.028	0.13	0.2	0.7	0.028	0.12
UQAC-FeS-1 - 4	1.94145	4.70143	8.347304	0.027627	0.140771	0.172492	0.840303	0.021908	0.129777
GSD-1G - 4	6.636601	17.83713	34.14591	0.115602	0.531836	0.726557	3.744762	0.098824	0.536918
NIST610 - 4	3.129051	10.6584	19.32076	0.064849	0.326378	0.427135	1.952026	0.069231	0.305265
2019-SH-187-Circulo C-ef - 3	1.1	4	8	0.025	0.1	0.16	0.77	0.027	0.12
2019-SH-212-Circulo A-ef - 1	1.6	4	8	0.024	0.13	0.2	0.8	0.027	0.13
2019-SH-212-Circulo A-ef - 2	1.3	4	7	0.025	0.13	0.15	0.78	0.03	0.12
2019-SH-212-Circulo A-ef - 3	1.7	4.5	8	0.03	0.13	0.16	0.8	0.029	0.1
2019-SH-212-Circulo A-ef - 4	1.1	4	7	0.025	0.12	0.16	0.7	0.024	0.12
2019-SH-212-Circulo B-ef - 1	1.4	4.2	8	0.025	0.12	0.2	0.7	0.023	0.12
2019-SH-212-Circulo B-ef - 2	1.3	4	8	0.02	0.12	0.16	0.7	0.026	0.12

Label	Ni62	Cu65	Zn66	Ga71	Ge74	As75	Se77	Mo95	Ag107
2019-SH-212-Circulo B-ef - 3	1.1	4.1	7	0.025	0.12	0.16	0.66	0.023	0.12
2019-SH-212-Circulo B-ef - 4	1.8	5.3	10	0.03	0.17	0.22	1	0.04	0.2
SH-227-Circulo B-ef - 1	1.5	3.9	7	0.03	0.12	0.15	0.7	0.028	0.12
SH-227-Circulo B-ef - 2	1.4	4	7	0.028	0.13	0.2	0.7	0.03	0.1
SH-227-Circulo B-ef - 3	1.4	4	7	0.026	0.12	0.15	0.68	0.024	0.1
SH-227-Circulo A-ef - 1	1.7	4.4	8	0.032	0.136	0.2	0.80	0.03	0.14
SH-227-Circulo A-ef - 2	1.3	4.0	7	0.03	0.1	0.16	0.64	0.027	0.12
SH-227-Circulo A-ef - 3	1.05	4	8	0.028	0.13	0.17	0.7	0.026	0.1
NIST610 - 5	4.161901	10.5344	20.11108	0.069051	0.33971	0.4802	1.953939	0.074891	0.331339
GSD-1G - 5	3.061855	9.780775	17.73527	0.068136	0.325614	0.421759	1.778343	0.054828	0.296228
UQAC-FeS-1 - 5	1.572398	4.161597	7.672614	0.028719	0.130706	0.183672	0.756582	0.026879	0.127471

*Values in red color have been discarded in pl

Label	Cd111	In115	Sn118	Sb121	Au197	Hg202	Tl205	Pb208	Bi209
UQAC-FeS-1 - 1	0.367057	0.004391	0.046412	0.029723	0.009858	0.1005	0.006476	0.009389	0.004498
GSD-1G - 1	0.767103	0.010588	0.103249	0.063236	0.025417	0.226295	0.013822	0.01873	0.008786
NIST610 - 1	0.875421	0.009466	0.116241	0.078137	0.025855	0.242451	0.015518	0.022047	0.010882
2019-SV-02-Circulo A-ef - 1	0.33	0.0059	0.043	0.031	0.011	0.080	0.01	0.008	0.004497
2019-SV-02-Circulo A-ef - 2	0.40	0.0066	0.057	0.0	0.013	0.11	0.0076	0.0109	0.0053
2019-SV-02-Circulo A-ef - 3	0.53	0.0079	0.070	0.039	0.015	0.12	0.008	0.01	0.005
2019-SV-02-Circulo B-ef - 1	0.48	0.0076	0.06	0.037	0.014	0.12	0.0071	0.013	0.005
2019-SV-02-Circulo B-ef - 2	0.37	0.0051	0.047	0.03	0.009	0.095	0.006	0.0092	0.0036
2019-SV-02-Circulo B-ef - 3	0.56	0.0081	0.071	0.04	0.018	0.13	0.009	0.014	0.007
2019-SV-02-Circulo C-ef - 1	0.35	0.0054	0.047	0.030	0.010	0.088	0.0064	0.0092	0.0040
2019-SV-04-Circulo A-ef - 1	0.35	0.005	0.04	0.025	0.009	0.096	0.0049	0.0094	0.004
2019-SV-04-Circulo A-ef - 2	0.330	0.0052	0.043	0.03	0.010	0.094	0.006	0.0087	0.0038
2019-SV-04-Circulo B-ef - 1	0.35	0.0054	0.045	0.028	0.0099	0.092	0.005	0.0091	0.0037
2019-SV-04-Circulo B-ef - 2	0.37	0.006	0.044	0.028	0.0089	0.10	0.005	0.0096	0.004
2019-SV-04-Circulo B-ef - 3	0.34	0.005	0.040	0.028	0.01	0.090	0.005	0.0088	0.0038
2019-SV-04-Circulo C-ef - 2	0.34	0.0058	0.048	0.029	0.01	0.094	0.005	0.0088	0.0037
2019-SV-04-Circulo C-ef - 3	0.40	0.0061	0.055	0.03	0.01	0.11	0.0061	0.010	0.0047
2019-SV-04-Circulo D-ef - 1	0.39	0.006	0.045	0.03	0.01	0.10	0.005	0.01	0.004
2019-SV-04-Circulo D-ef - 3	0.52	0.0072	0.06	0.035	0.013	0.1	0.008	0.014	0.004704
2019-SV-06A-Circulo A-ef - 1	0.39	0.0049	0.04	0.024	0.01	0.10	0.0057	0.0093	0.003666
2019-SV-06A-Circulo A-ef - 2	0.36	0.005	0.05	0.026	0.0088	0.10	0.0056	0.009	0.0034
2019-SV-06A-Circulo A-ef - 3	0.43	0.0070	0.056	0.03	0.011	0.12	0.0061	0.01	0.004
UQAC-FeS-1 - 2	0.305306	0.004881	0.042571	0.023677	0.008306	0.083368	0.004362	0.00689	0.003757
GSD-1G - 2	1.741143	0.031416	0.250669	0.147588	0.052234	0.535295	0.023166	0.045713	0.021529
NIST610 - 2	0.844918	0.011565	0.106878	0.06386	0.02242	0.229948	0.01121	0.01628	0.008354
2019-SV-06A-Circulo B-ef - 3	0.36	0.005697	0.04	0.027	0.01	0.092	0.0046	0.008	0.004
2019-SV-06A-Circulo B-ef - 4	0.33	0.0059	0.040	0.024	0.009	0.089	0.0049	0.008	0.0037
2019-SV-06A-Circulo C-ef - 1	0.33	0.005	0.045	0.026	0.0088	0.092	0.006	0.0080	0.003
2019-SV-06A-Circulo C-ef - 2	0.35	0.0059	0.04	0.029	0.008	0.094	0.0053	0.0073	0.0034
2019-SV-06A-Circulo C-ef - 3	0.34	0.006	0.04	0.025	0.009	0.096	0.005	0.008	0.0038
2019-SV-06B-Circulo A-ef - 1	0.35	0.0058	0.04	0.025	0.0089	0.095	0.0043	0.0085	0.0029
2019-SV-06B-Circulo A-ef - 2	0.35	0.006	0.044	0.026	0.0089	0.099	0.0048	0.008	0.003702
2019-SV-06B-Circulo A-ef - 3	0.3	0.0059	0.046	0.027	0.010	0.097	0.0050	0.0075	0.003

Label	Cd111	In115	Sn118	Sb121	Au197	Hg202	Tl205	Pb208	Bi209
2019-SV-06B-Circulo A-ef - 4	0.33	0.005	0.04	0.028	0.0090	0.10	0.0046	0.007799	0.004
2019-SV-06B-Circulo B-ef - 1	0.34	0.005	0.04	0.029	0.010	0.093	0.005	0.0076	0.0029
2019-SV-06B-Circulo B-ef - 2	0.52	0.009	0.07	0.036	0.016	0.14	0.007	0.01	0.0045
2019-SV-06B-Circulo B-ef - 3	0.37	0.0056	0.05	0.028	0.01	0.10	0.0044	0.00955	0.003702
2019-SV-06B-Circulo C-ef - 2	0.33	0.0059	0.04	0.025	0.009	0.094	0.0042	0.007604	0.003
2019-SV-06B-Circulo C-ef - 3	0.36	0.0064	0.05	0.026	0.012	0.10	0.0051	0.0080	0.0038
2019-SV-07-Circulo A-ef - 1	0.37	0.006	0.049	0.029	0.01	0.099	0.0046	0.0090	0.0037
2019-SV-07-Circulo A-ef - 2	0.34	0.0063	0.046	0.023	0.0099	0.095	0.004	0.0086	0.0037
2019-SV-07-Circulo A-ef - 3	0.37	0.006	0.050	0.027	0.011	0.097	0.004	0.0087	0.0033
2019-SV-07-Circulo A-ef - 4	0.35	0.0066	0.049	0.026	0.01	0.099	0.005	0.0082	0.0033
2019-SV-07-Circulo B-ef - 1	0.34	0.006	0.048	0.026	0.012	0.098	0.0040	0.008	0.0039
2019-SV-07-Circulo B-ef - 2	0.35	0.0062	0.05	0.023	0.01	0.098	0.004	0.0087	0.0030
2019-SV-07-Circulo B-ef - 3	0.35	0.006303	0.04	0.025	0.01	0.098	0.0043	0.0086	0.0030
2019-SV-07-Circulo B-ef - 4	0.6	0.0094	0.075	0.038	0.0178	0.15	0.0070	0.012	0.0044
2019-SV-07-Circulo C-ef - 1	0.37	0.0059	0.048	0.030	0.011	0.1	0.005	0.01	0.003
2019-SV-07-Circulo C-ef - 2	0.44	0.0067	0.05	0.034	0.013	0.11	0.005	0.01	0.0034
2019-SV-07-Circulo C-ef - 3	0.45	0.0081	0.06	0.038	0.014	0.1	0.005	0.012	0.005
UQAC-FeS-1 - 3	0.346099	0.005321	0.046258	0.028728	0.011533	0.113543	0.004248	0.009453	0.003775
GSD-1G - 3	0.904707	0.014561	0.121705	0.0707	0.02531	0.283628	0.010296	0.020234	0.009807
NIST610 - 3	0.936521	0.018842	0.128553	0.076952	0.029268	0.280872	0.012741	0.024034	0.010391
2019-SV-08A-Circulo A-ef - 2	0.33	0.0056	0.050	0.029	0.01	0.09	0.0040	0.0095	0.0033
2019-SV-08A-Circulo A-ef - 3	0.34	0.006198	0.049	0.026	0.01	0.090	0.0045	0.0091	0.003797
2019-SV-08A-Circulo A-ef - 4	0.34	0.0059	0.044	0.027	0.01	0.092	0.0048	0.0086	0.0027
2019-SV-08A-Circulo C-ef - 1	0.34	0.006	0.04	0.024	0.0094	0.09	0.0036	0.0087	0.0028
2019-SV-08A-Circulo C-ef - 2	0.31	0.0063	0.04	0.027	0.01	0.08	0.004	0.0074	0.0034
2019-SV-08A-Circulo C-ef - 3	0.37	0.0057	0.047	0.02	0.01	0.089	0.0043	0.010	0.0032
2019-SV-08A-Circulo D-ef - 1	0.45	0.008	0.06	0.037	0.014	0.12	0.006	0.012	0.004
2019-SV-08A-Circulo D-ef - 2	0.34	0.0054	0.044	0.024	0.01	0.09	0.0045	0.0083	0.0035
2019-SV-08A-Circulo D-ef - 3	0.32	0.0057	0.05	0.024	0.01	0.09	0.0044	0.0095	0.0027
2019-SV-08B-Circulo A-ef - 1	0.37	0.0064	0.05	0.028	0.01	0.11	0.0045	0.011	0.0038
2019-SV-08B-Circulo A-ef - 2	0.31	0.0068	0.043	0.029	0.01	0.10	0.0039	0.0089	0.0033
2019-SV-08B-Circulo B-ef - 1	0.33	0.006	0.050	0.026	0.011	0.10	0.0050	0.0093	0.003

Label	Cd111	In115	Sn118	Sb121	Au197	Hg202	Tl205	Pb208	Bi209
2019-SV-08B-Circulo B-ef - 3	0.33	0.006	0.047	0.025	0.01	0.097	0.0040	0.008404	0.0029
2019-SV-08B-Circulo C-ef - 2	0.33	0.006	0.05	0.03	0.01	0.10	0.0047	0.0083	0.0031
2019-SV-08B-Circulo C-ef - 3	0.34	0.006	0.045	0.029	0.011	0.11	0.0051	0.010	0.0034
2019-SV-08B-Circulo D-ef - 1	0.34	0.0066	0.04	0.030	0.011	0.10	0.0042	0.008	0.0029
2019-SV-08B-Circulo D-ef - 2	0.32	0.0064	0.047	0.023	0.01	0.098	0.0041	0.0084	0.003
2019-SV-08B-Circulo D-ef - 3	0.312	0.0058	0.041	0.027	0.01	0.093	0.0040	0.0088	0.0034
2019-SV-08B-Circulo D-ef - 4	0.33	0.0066	0.052	0.026	0.01	0.10	0.0050	0.009	0.003
2019-SV-08B-Circulo E-ef - 1	0.35	0.0081	0.050	0.028	0.012	0.11	0.0047	0.010	0.0035
2019-SV-08B-Circulo E-ef - 2	0.37	0.007	0.05	0.035	0.01	0.11	0.0051	0.01	0.003
UQAC-FeS-1 - 4	0.281497	0.006218	0.041995	0.024964	0.009449	0.086788	0.003469	0.008452	0.002671
GSD-1G - 4	0.933539	0.019481	0.144599	0.073895	0.02886	0.3004	0.01413	0.025153	0.010258
NIST610 - 4	0.867843	0.016571	0.127043	0.069519	0.027208	0.256567	0.011708	0.021779	0.008434
2019-SV-08B-Circulo E-ef - 3	0.36	0.0069	0.05	0.03	0.012	0.11	0.005	0.0086	0.004
2019-SV-08B-Circulo E-ef - 4	0.30	0.008	0.043	0.029	0.01	0.10	0.0044	0.0089	0.0035
2019-SV-09-Circulo A-ef - 1	0.31	0.0060	0.045	0.029	0.011	0.096	0.0041	0.0083	0.0034
2019-SV-09-Circulo A-ef - 2	0.32	0.006	0.05	0.028	0.009	0.09	0.0037	0.0098	0.0034
2019-SV-09-Circulo A-ef - 3	0.31	0.006	0.048	0.026	0.009	0.097	0.0038	0.008	0.0033
2019-SV-09-Circulo A-ef - 4	0.34	0.0080	0.053	0.03	0.011	0.11	0.0046	0.0086	0.0038
2019-SV-09-Circulo B-ef - 1	0.35	0.0070	0.05	0.025	0.012	0.11	0.005	0.010	0.0038
2019-SV-09-Circulo B-ef - 2	0.33	0.006	0.045	0.027	0.01	0.098	0.0040	0.0091	0.003
2019-SV-09-Circulo B-ef - 3	0.30	0.0063	0.046	0.029	0.009	0.099	0.0041	0.008	0.0028
2019-SV-09-Circulo B-ef - 4	0.35	0.0072	0.05	0.028	0.012	0.1	0.0048	0.0091	0.0036
2019-SV-09-Circulo C-ef - 1	0.45	0.01	0.06	0.04	0.014	0.14	0.0065	0.013	0.005
2019-SV-09-Circulo C-ef - 3	0.34	0.006	0.052	0.029	0.0099	0.10	0.0038	0.0086	0.003497
2019-SV-011A-Circulo B-ef - 1	0.30	0.0070	0.05	0.025	0.01	0.1	0.004	0.0080	0.002701
2019-SV-011A-Circulo B-ef - 2	0.29	0.0069	0.04	0.028	0.009	0.095	0.0042	0.0086	0.0028
2019-SV-011A-Circulo B-ef - 3	0.30	0.0071	0.043	0.029	0.01	0.093	0.0042	0.009	0.002905
2019-SV-011A-Circulo B-ef - 4	0.30	0.008	0.04	0.025	0.01	0.094	0.003895	0.0079	0.0036
2019-SV-011A-Circulo C-ef - 1	0.28	0.0068	0.05	0.027	0.0099	0.091	0.0038	0.0085	0.0034
2019-SV-011A-Circulo C-ef - 2	0.28	0.0067	0.045	0.026	0.01	0.09	0.0042	0.007	0.0035
2019-SV-011A-Circulo C-ef - 3	0.28	0.006	0.043	0.024	0.011	0.090	0.004395	0.0075	0.002804
2019-SV-011A-Circulo C-ef - 4	0.30	0.007	0.044	0.026	0.009	0.092	0.004	0.0082	0.0039

Label	Cd111	In115	Sn118	Sb121	Au197	Hg202	Tl205	Pb208	Bi209
2019-SV-011B-Circulo A-ef - 1	0.29	0.0069	0.043	0.026	0.01	0.098	0.0042	0.0082	0.0036
2019-SV-011B-Circulo A-ef - 2	0.30	0.007	0.046	0.023	0.01	0.099	0.0035	0.0095	0.003232
2019-SV-011B-Circulo A-ef - 3	0.28	0.0057	0.048	0.025	0.0089	0.091	0.0038	0.008	0.0028
2019-SV-011B-Circulo A-ef - 4	0.28	0.008	0.05	0.027	0.009	0.095	0.0042	0.0085	0.003
2019-SV-011B-Circulo A-ef - 5	0.3	0.0064	0.044	0.026	0.009	0.088	0.0033	0.0086	0.0036
UQAC-FeS-1 - 5	0.107509	0.007793	0.051861	0.026383	0.009736	0.10696	0.004797	0.001827	0.003536
GSD-1G - 5	0.656709	0.042679	0.313325	0.17114	0.06718	0.668212	0.025578	0.010329	0.022031
NIST610 - 5	0.511781	0.038868	0.272705	0.133044	0.054643	0.53314	0.021916	0.008064	0.017769
2019-SV-011B-Circulo B-ef - 2	0.22	0.01	0.1	0.055	0.020	0.18	0.008	0.0033	0.006
2019-SV-011B-Circulo C-ef - 1	0.22	0.014	0.09	0.05	0.018	0.19	0.0086	0.003	0.007
2019-SV-011B-Circulo C-ef - 2	0.23	0.01	0.1	0.058	0.02	0.18	0.0066	0.004	0.007
2019-SV-011B-Circulo C-ef - 3	0.24	0.01	0.09	0.05	0.02	0.2	0.007	0.0036	0.0067
2019-SV-011B-Circulo D-ef - 1	0.24	0.013	0.10	0.05	0.019	0.17	0.0082	0.0042	0.0056
2019-SV-011B-Circulo D-ef - 2	0.26	0.012	0.09	0.05	0.017	0.16	0.0064	0.0039	0.007
2019-SV-011B-Circulo D-ef - 3	0.24	0.013	0.088	0.04	0.019	0.17	0.0072	0.0041	0.006
2019-SV-011C-Circulo A-ef - 1	0.22	0.012	0.08	0.045	0.015	0.15	0.0057	0.0035	0.006
2019-SV-011C-Circulo B-ef - 2	0.25	0.012	0.078	0.04	0.016	0.15	0.0067	0.0038	0.0046
2019-SV-011C-Circulo C-ef - 1	0.26	0.012	0.066	0.04	0.016	0.2	0.0073	0.0046	0.0060
2019-SV-011C-Circulo C-ef - 2	0.24	0.009	0.06	0.040	0.015	0.13	0.0059	0.0038	0.0046
2019-SV-012A-Circulo A-ef - 1	0.32	0.01	0.08	0.05	0.02	0.17	0.006	0.0060	0.006
2019-SV-012A-Circulo A-ef - 2	0.27	0.01	0.074	0.036	0.015	0.13	0.0055	0.005	0.0039
2019-SV-012A-Circulo B-ef - 1	0.3	0.010	0.08	0.04	0.016	0.15	0.006	0.006	0.0056
2019-SV-012A-Circulo C-ef - 1	0.27	0.011	0.058	0.036	0.016	0.14	0.005	0.005	0.005
2019-SV-012A-Circulo C-ef - 2	0.28	0.01	0.062	0.035	0.015	0.12	0.005	0.0049	0.0044
2019-SV-012A-Circulo D-ef - 1	0.27	0.008	0.06	0.03	0.011	0.12	0.0053	0.0053	0.004305
2019-SV-012A-Circulo D-ef - 2	0.27	0.010	0.05	0.03	0.014	0.12	0.005	0.005597	0.0035
2019-SV-012B-Circulo A-ef - 1	0.31	0.009	0.06	0.03	0.012	0.12	0.0048	0.0063	0.003696
2019-SV-012B-Circulo A-ef - 2	0.32	0.009	0.055	0.036	0.013	0.12	0.005	0.0058	0.0036
2019-SV-012B-Circulo B-ef - 1	0.29	0.009	0.059	0.035	0.014	0.12	0.0048	0.0062	0.0046
2019-SV-012B-Circulo B-ef - 2	0.29	0.007	0.05	0.03	0.011	0.1	0.0042	0.0064	0.003
NIST610 - 6	0.813359	0.020907	0.122854	0.075072	0.031572	0.28146	0.013419	0.018263	0.008511
GSD-1G - 6	1.183916	0.031941	0.220395	0.114739	0.046599	0.430914	0.021452	0.02805	0.015169
UQAC-FeS-1 - 6	0.304734	0.007022	0.051401	0.032256	0.011082	0.094177	0.004317	0.007133	0.003746

Label	Cd111	In115	Sn118	Sb121	Au197	Hg202	Tl205	Pb208	Bi209
UQAC-FeS-1 - 1	0.297063	0.004987	0.050488	0.029872	0.010336	0.104664	0.007108	0.007611	0.004679
GSD-1G - 1	1.073862	0.018192	0.195721	0.10594	0.03364	0.41272	0.022987	0.026412	0.016471
NIST610 - 1	0.877111	0.014707	0.157444	0.081993	0.028053	0.309014	0.017087	0.019163	0.011911
2019-SV-013-Circulo A-ef - 1	0.30	0.0044	0.052	0.029	0.009	0.094	0.006	0.008003	0.004
2019-SV-013-Circulo A-ef - 2	0.32	0.0052	0.05	0.026	0.01	0.095	0.0054	0.007702	0.0039
2019-SV-013-Circulo B-ef - 1	0.316	0.0056	0.06	0.027	0.009	0.099	0.0048	0.0075	0.003597
2019-SV-013-Circulo B-ef - 2	0.317	0.0055	0.05	0.029	0.009	0.10	0.005	0.007	0.003695
2019-SV-013-Circulo C-ef - 1	0.31	0.01	0.06	0.028	0.009	0.099	0.006	0.0079	0.0034
2019-SV-013-Circulo C-ef - 2	0.329	0.0059	0.06	0.027	0.01	0.11	0.005797	0.0086	0.0035
2019-SV-014-Circulo A-ef - 1	0.34	0.0052	0.05	0.027	0.009	0.11	0.006	0.0086	0.0034
2019-SV-014-Circulo A-ef - 2	0.30	0.005	0.058	0.027	0.009	0.11	0.005	0.0077	0.0038
2019-SV-014-Circulo B-ef - 1	0.42	0.007	0.07	0.035	0.012	0.14	0.007	0.0099	0.0047
2019-SV-014-Circulo B-ef - 2	0.31	0.005	0.05	0.029	0.009	0.11	0.0055	0.0078	0.003
2019-SV-014-Circulo C-ef - 1	0.310	0.0049	0.054	0.023	0.008	0.11	0.0048	0.0086	0.003
2019-SV-014-Circulo C-ef - 2	0.340	0.0067	0.06	0.030	0.009	0.11	0.0055	0.0095	0.0035
2019-SV-015A-Circulo A-ef - 1	0.605	0.01	0.1	0.05	0.017	0.22	0.010	0.018	0.006603
2019-SV-015A-Circulo A-ef - 2	0.347	0.005	0.055	0.027	0.010	0.12	0.005	0.009	0.0039
2019-SV-015A-Circulo B-ef - 1	0.505	0.01	0.088	0.04	0.014	0.17	0.007	0.0137	0.0060
2019-SV-015A-Circulo B-ef - 2	0.333	0.0051	0.06	0.027	0.009	0.12	0.0062	0.0089	0.003
2019-SV-015A-Circulo B-ef - 3	0.354	0.0057	0.06	0.026	0.009	0.12	0.005	0.0094	0.004
2019-SV-015A-Circulo C-ef - 1	0.458	0.008	0.07	0.040	0.012	0.15	0.0062	0.013	0.0049
2019-SV-015A-Circulo D-ef - 1	0.573	0.0087	0.09	0.048	0.014	0.19	0.0076	0.018	0.006
2019-SV-015A-Circulo D-ef - 2	0.354	0.0060	0.051	0.030	0.008	0.12	0.0056	0.01	0.0035
2019-SV-015A-Circulo D-ef - 3	0.41	0.0066	0.071	0.034	0.011	0.14	0.0051	0.011	0.004
2019-SV-015A-Circulo E-ef - 1	0.433	0.0062	0.065	0.03	0.011	0.13	0.0047	0.0099	0.0047
2019-SV-015A-Circulo E-ef - 2	0.36	0.006	0.05	0.027	0.009	0.1	0.0053	0.0090	0.004
2019-SV-015A-Circulo E-ef - 3	0.367	0.0060	0.06	0.026	0.007	0.11	0.005	0.008	0.003
2019-SV-015B-Circulo A-ef - 1	0.37	0.0065	0.06	0.024	0.008	0.13	0.0049	0.01	0.0034
2019-SV-015B-Circulo A-ef - 2	0.427	0.0072	0.07	0.029	0.011	0.15	0.005	0.011	0.0044
UQAC-FeS-1 - 2	0.364776	0.006973	0.063162	0.025717	0.008259	0.115991	0.004274	0.00827	0.003439
GSD-1G - 2	0.857824	0.013621	0.148936	0.07765	0.023543	0.301018	0.011802	0.018173	0.01015
NIST610 - 2	1.060591	0.015609	0.17809	0.085965	0.026117	0.352038	0.014259	0.025416	0.009983
2019-SV-015B-Circulo A-ef - 3	0.354	0.0064	0.05	0.03	0.0090	0.11	0.0045	0.0076	0.0040

Label	Cd111	In115	Sn118	Sb121	Au197	Hg202	Tl205	Pb208	Bi209
2019-SV-015B-Circulo B-ef- 1	0.387	0.0073	0.064	0.03	0.009	0.13	0.005	0.0095	0.0036
2019-SV-015B-Circulo B-ef - 2	0.44	0.008	0.069	0.036	0.01	0.15	0.005	0.011	0.0046
2019-SV-015B-Circulo B-ef - 3	0.40	0.0078	0.07	0.027	0.009	0.13	0.0052	0.008	0.0038
2019-SV-015B-Circulo B-ef - 4	0.39	0.007197	0.07	0.03	0.0077	0.13	0.0043	0.0088	0.0035
2019-SV-015B-Circulo B-ef- 5	0.426	0.0078	0.07	0.03	0.01	0.14	0.005	0.0095	0.004
2019-SV-015B-Circulo B-ef-2 - 1	0.38	0.0060	0.05	0.024	0.008002	0.12	0.004	0.0077	0.003
2019-SV-015B-Circulo C-ef - 1	0.544	0.0086	0.080	0.045	0.011	0.16	0.0056	0.012	0.004
2019-SV-015B-Circulo C-ef - 2	0.392	0.0067	0.059	0.03	0.01	0.12	0.005	0.008	0.0031
2019-SV-015B-Circulo C-ef - 3	0.394	0.007	0.07	0.027	0.009	0.12	0.0034	0.0079	0.003
2019-SV-016-Circulo A-ef - 1	0.34	0.0059	0.057	0.027	0.008	0.11	0.0044	0.0080	0.0033
2019-SV-016-Circulo A-ef - 2	0.46	0.0079	0.069	0.032	0.0088	0.15	0.0047	0.0096	0.0037
2019-SV-016-Circulo B-ef - 1	0.34	0.0057	0.054	0.028	0.007	0.10	0.004198	0.0080	0.0028
2019-SV-016-Circulo D-ef - 1	0.37	0.006	0.06	0.03	0.01	0.11	0.004	0.008299	0.003
2019-SV-016-Circulo D-ef - 1	0.50	0.008	0.082	0.033	0.010	0.15	0.0055	0.012	0.0037
2019-SV-016-Circulo E-ef - 2	0.34	0.007	0.053	0.024	0.008	0.11	0.0038	0.008	0.0026
2019-SV-016-Circulo E-ef - 3	0.3	0.0059	0.05	0.023	0.01	0.10	0.003	0.0071	0.0029
2019-SH-31-Circulo A-ef - 1	0.53	0.01	0.08	0.0355	0.011	0.17	0.0055	0.011	0.004
2019-SH-31-Circulo A-ef - 2	0.387	0.0068	0.06	0.0309	0.008	0.2	0.005	0.0081	0.0029
2019-SH-31-Circulo A-ef - 3	0.61	0.01	0.09	0.0492	0.01	0.2	0.0072	0.013	0.0055
2019-SH-31-Circulo A-ef - 4	0.39	0.006	0.05	0.028	0.006	0.12	0.004	0.0087	0.003
2019-SH-31-Circulo B-ef - 1	0.35	0.0069	0.056	0.03	0.0066	0.12	0.0038	0.0072	0.0031
2019-SH-31-Circulo B-ef - 2	0.36	0.0077	0.054	0.0263	0.006	0.11	0.0044	0.0077	0.003
2019-SH-31-Circulo B-ef - 3	0.36	0.006	0.06	0.0256	0.006	0.14	0.0041	0.006996	0.0037
2019-SH-31-Circulo C-ef - 1	0.43	0.0089	0.058	0.0280	0.007	0.14	0.004	0.0085	0.0033
UQAC-FeS-1 - 3	0.462481	0.009238	0.070946	0.032085	0.009513	0.144598	0.004628	0.009877	0.003296
GSD-1G - 3	1.091805	0.018488	0.157489	0.063872	0.020605	0.362574	0.01049	0.025959	0.009004
NIST610 - 3	1.010657	0.018536	0.154377	0.074888	0.019837	0.325795	0.009637	0.018728	0.008811
2019-SH-31-Circulo C-ef - 2	0.38	0.0068	0.051	0.0303	0.0060	0.10	0.004	0.0073	0.0037
2019-SH-31-Circulo C-ef - 3	0.362	0.0069	0.054	0.03	0.008	0.13	0.0038	0.008	0.003296
2019-SH-31-Circulo C-ef - 4	0.375	0.0068	0.05	0.03	0.008	0.14	0.003	0.0073	0.0035
2019-SH-120-Circulo A-ef - 1	0.39	0.006	0.057	0.030096	0.007	0.15	0.0036	0.0076	0.0030
2019-SH-120-Circulo A-ef - 2	0.40	0.007	0.062	0.031	0.0079	0.16	0.0038	0.0069	0.003

Label	Cd111	In115	Sn118	Sb121	Au197	Hg202	Tl205	Pb208	Bi209
2019-SH-120-Circulo A-ef - 3	0.37	0.0056	0.053	0.031199	0.0068	0.1	0.0039	0.006	0.0029
2019-SH-120-Circulo B-ef - 1	0.49	0.0077	0.068	0.039	0.009	0.19	0.005	0.009	0.0045
2019-SH-120-Circulo B-ef - 2	0.39	0.0067	0.056	0.0285	0.0069	0.16	0.0036	0.006	0.003
2019-SH-120-Circulo B-ef - 3	0.34	0.006	0.053	0.03	0.008	0.2	0.004	0.0059	0.0027
2019-SH-167-Circulo A-ef - 1	0.373	0.0060	0.051	0.03	0.0066	0.15	0.0037	0.0064	0.0030
2019-SH-167-Circulo A-ef - 2	0.363	0.007	0.053	0.028	0.007	0.13	0.0033	0.006	0.0029
2019-SH-167-Circulo A-ef - 3	0.403	0.0075	0.06	0.028	0.009	0.14	0.0037	0.007196	0.0029
2019-SH-167-Circulo A-ef - 4	0.489	0.0078	0.07	0.0322	0.01	0.16	0.0049	0.0077	0.0047
2019-SH-167-Circulo B-ef - 1	0.49	0.0093	0.064	0.03	0.0099	0.16	0.0047	0.0078	0.0039
2019-SH-167-Circulo B-ef - 2	0.397	0.007	0.062	0.026	0.008	0.14	0.0045	0.006	0.0031
2019-SH-167-Circulo B-ef - 3	0.360	0.006	0.048	0.0249	0.008	0.1	0.004	0.005	0.0029
2019-SH-167-Circulo B-ef - 4	0.467	0.008002	0.066	0.03	0.008	0.15	0.0042	0.0070	0.0050
2019-SH-167-Circulo C-ef - 1	0.388	0.0060	0.05	0.026	0.0078	0.12	0.0035	0.0044	0.003
2019-SH-167-Circulo C-ef - 2	0.384	0.0059	0.05	0.044	0.0078	0.14	0.0036	0.0056	0.0035
2019-SH-167-Circulo C-ef - 3	0.420	0.007	0.05	0.034	0.009	0.13	0.0039	0.006	0.0030
2019-SH-167-Circulo C-ef - 4	0.372	0.006	0.05	0.03	0.008	0.1	0.0037	0.0058	0.0029
2019-SH-187-Circulo A-ef - 1	0.43	0.0061	0.057	0.03	0.0090	0.13	0.0033	0.0060	0.0033
2019-SH-187-Circulo A-ef - 2	0.417	0.007	0.055	0.0286	0.009002	0.1	0.004	0.006	0.0029
2019-SH-187-Circulo A-ef - 3	0.448	0.0068	0.056	0.03	0.009	0.1	0.0043	0.0056	0.004
2019-SH-187-Circulo A-ef - 4	0.410	0.008004	0.05	0.031	0.01	0.14	0.004	0.006	0.003099
2019-SH-187-Circulo C-ef - 1	0.45	0.008395	0.06	0.03	0.01	0.1	0.0037	0.0061	0.0035
2019-SH-187-Circulo C-ef - 2	0.445	0.0080	0.05	0.029	0.01	0.14	0.0046	0.0060	0.0036
UQAC-FeS-1 - 4	0.471247	0.007641	0.060921	0.033744	0.011573	0.143546	0.004398	0.008387	0.004204
GSD-1G - 4	1.877341	0.034554	0.287783	0.12615	0.04612	0.604054	0.017964	0.031357	0.016753
NIST610 - 4	1.06399	0.018289	0.149587	0.077098	0.023988	0.332238	0.008885	0.015411	0.009322
2019-SH-187-Circulo C-ef - 3	0.42	0.0070	0.06	0.03	0.01	0.12	0.0044	0.008	0.004
2019-SH-212-Circulo A-ef - 1	0.41	0.0077	0.056	0.032	0.009	0.17	0.004	0.0078	0.0036
2019-SH-212-Circulo A-ef - 2	0.42	0.0079	0.057	0.028	0.009	0.1	0.0040	0.0070	0.0035
2019-SH-212-Circulo A-ef - 3	0.43	0.009	0.06	0.029	0.01	0.14	0.005	0.008	0.0037
2019-SH-212-Circulo A-ef - 4	0.41	0.008	0.055	0.03	0.009	0.13	0.0047	0.0071	0.003
2019-SH-212-Circulo B-ef - 1	0.409	0.0082	0.06	0.03	0.008	0.13	0.0034	0.007	0.003601
2019-SH-212-Circulo B-ef - 2	0.41	0.008	0.054	0.026	0.009	0.1	0.0043	0.0075	0.003397

Label	Cd111	In115	Sn118	Sb121	Au197	Hg202	Tl205	Pb208	Bi209
2019-SH-212-Circulo B-ef - 3	0.41	0.0067	0.053	0.02	0.01	0.12	0.0036	0.0063	0.0035
2019-SH-212-Circulo B-ef - 4	0.56	0.01	0.08	0.038	0.014	0.2	0.0056	0.0085	0.005
SH-227-Circulo B-ef - 1	0.40	0.0077	0.05	0.026	0.01	0.12	0.0032	0.007	0.0029
SH-227-Circulo B-ef - 2	0.391	0.0075	0.054	0.0276	0.01	0.13	0.004	0.0073	0.004
SH-227-Circulo B-ef - 3	0.383	0.007	0.05	0.031	0.008	0.1	0.0037	0.008	0.003
SH-227-Circulo A-ef - 1	0.430	0.009	0.06	0.030	0.011	0.16	0.0044	0.0080	0.0040
SH-227-Circulo A-ef - 2	0.400	0.006	0.054	0.03	0.009	0.1	0.0040	0.0082	0.0028
SH-227-Circulo A-ef - 3	0.40	0.008	0.051	0.03	0.0089	0.14	0.0039	0.0069	0.004001
NIST610 - 5	1.126219	0.020891	0.150906	0.084996	0.02245	0.398412	0.009755	0.019898	0.00906
GSD-1G - 5	0.936328	0.01624	0.148508	0.077537	0.023388	0.330728	0.011232	0.016927	0.00958
UQAC-FeS-1 - 5	0.404014	0.008451	0.051804	0.028544	0.008556	0.117429	0.004108	0.008208	0.00391

*Values in red color have been discarded in pl